

AJNR

AMERICAN JOURNAL OF NEURORADIOLOGY

FEBRUARY 2014
VOLUME 35
NUMBER 2
WWW.AJNR.ORG

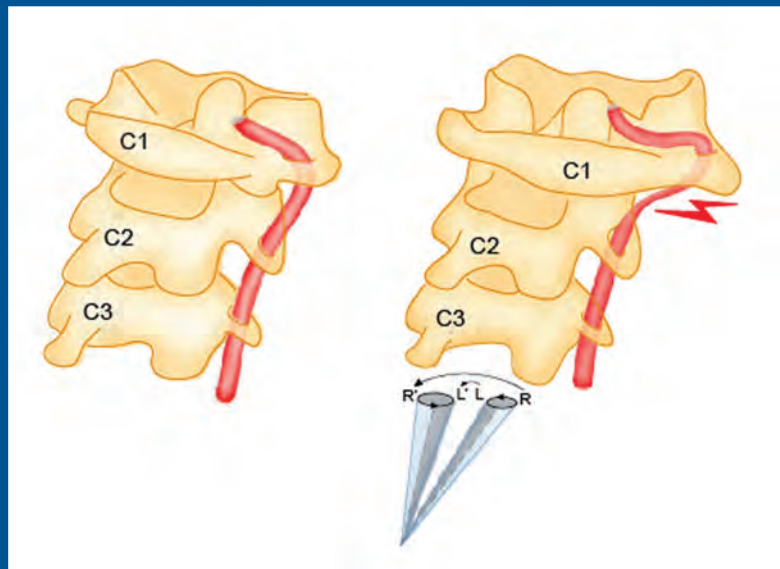
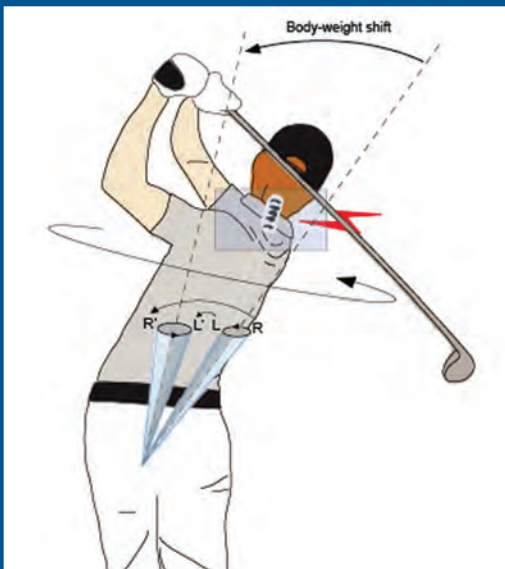
THE JOURNAL OF DIAGNOSTIC AND
INTERVENTIONAL NEURORADIOLOGY

White matter damage in boxers and
martial arts fighters

Perivascular spaces in the anterior
temporal lobes

Hyperattenuated lesions after mechanical
recanalization in acute stroke

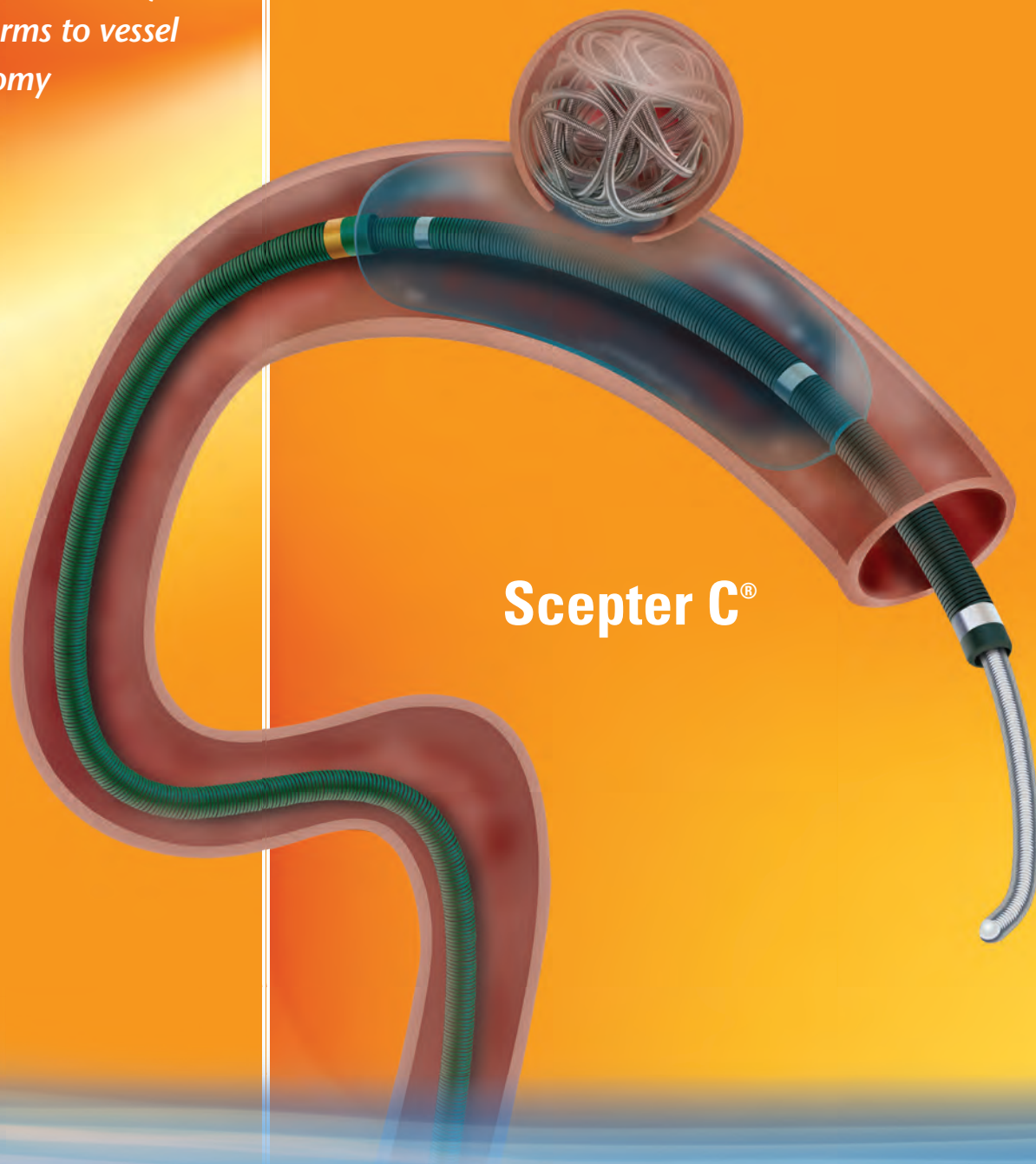
Official Journal ASNR • ASFNR • ASHNR • ASPNR • ASSR



Scepter C[®]
Occlusion Balloon
Catheter

The New Standard of Excellence, Redefining

*Compliant balloon
designed for reliable
vessel occlusion yet
conforms to vessel
anatomy*



Scepter C[®]

For more information or a product demonstration,
contact your local MicroVention representative:

MicroVention, Inc.
Worldwide Headquarters
1311 Valencia Avenue
Tustin, CA 92780 USA
MicroVention United Kingdom
MicroVention Europe, S.A.R.L.
MicroVention Deutschland GmbH
Web

PH +1.714.247.8000

PH +44 (0) 191 258 6777
PH +33 (1) 39 21 77 46
PH +49 211 210 798-0
microvention.com

Deliverability

Versatility

and

Control

Scepter XC[®]
Occlusion Balloon
Catheter

Occlusion Balloon with .014" Guidewire Compatibility

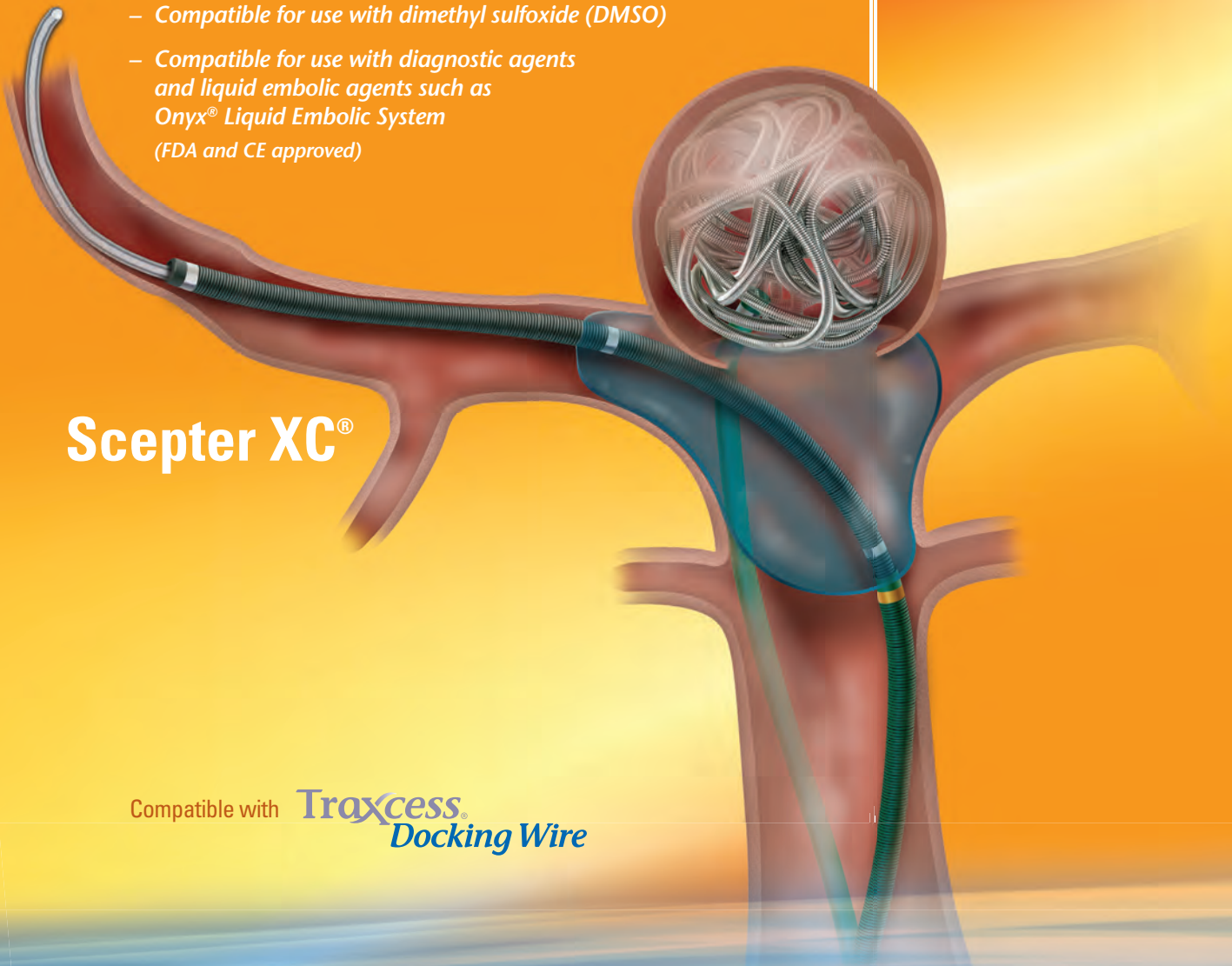
- Maximizing the utility of a unique coaxial shaft, Scepter Occlusion Balloon Catheter incorporates many new product features
- Balloon diameters range from 2mm to 6mm

Key Compatible Agents

- Compatible for use with dimethyl sulfoxide (DMSO)
- Compatible for use with diagnostic agents and liquid embolic agents such as Onyx[®] Liquid Embolic System (FDA and CE approved)

*Xtra Compliant
balloon conforms to
extremely complex
anatomies where
neck coverage is
more challenging*

Scepter XC[®]



Compatible with **Traxcess[®]**
Docking Wire

CE
0297

MICROVENTION, Scepter C, Scepter XC and Traxcess are registered trademarks of MicroVention, Inc. Onyx Liquid Embolic System is a registered trademark of Covidien. • Scientific and clinical data related to this document are on file at MicroVention, Inc. Refer to Instructions for Use for additional information. Federal (USA) law restricts this device for sale by or on the order of a physician. © 2013 MicroVention, Inc. 10/13

 **MicroVention[®]**
TERUMO



BARRICADE COIL SYSTEM™

COILING SIMPLIFIED, PERFORMANCE DELIVERED

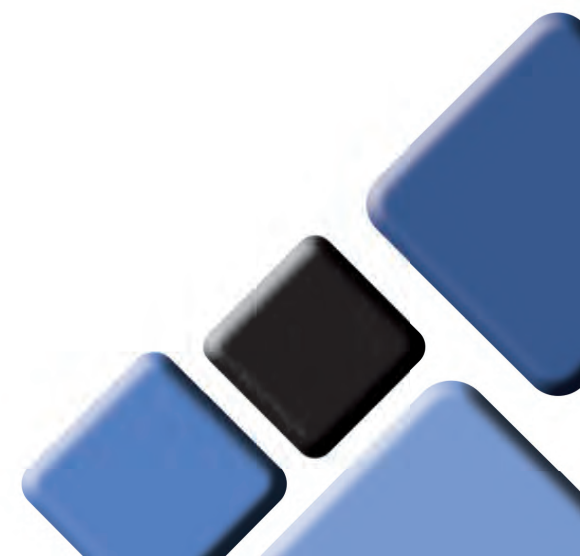


BLOCKADE
M E D I C A L

18 TECHNOLOGY DRIVE #169, IRVINE CA 92618 | P 949.788.1443
WWW.BLOCKADEMEDICAL.COM

 MADE IN AMERICA

CE
0297
MKTG-020 REV. A



AJNR

AMERICAN JOURNAL OF NEURORADIOLOGY

FEBRUARY 2014
VOLUME 35
NUMBER 2
WWW.AJNR.ORG

Publication Preview at www.ajnr.org features articles released in advance of print. Visit www.ajnrblog.org to comment on AJNR content and chat with colleagues and AJNR's News Digest at <http://ajnrndigest.org> to read the stories behind the latest research in neuroimaging.

EDITORIALS

PERSPECTIVES

- 211 **Trainees in Peer Review: Our Experience** *M. Castillo*

EDITORIALS

- 213 **Editorial Transition** *M. Castillo*
- 213 **Human Neuroimaging and the BRAIN Initiative: A Joint Statement from the ASNR and ASFNR, with the support of the RSNA, ACR, ARR, and ISMRM** *G. Sze, M. Wintermark, M. Law, P. Mukherjee, and C. Hess*

MEMORIAL

- 215 **Lucien Maurice Levy** *R.K. Tu, R. Bhojwani, R. Taheri, M. Monteferrante, and A. Ahmad*

REVIEW ARTICLES

- 216 **Imaging Features of Rhinoplasty** *C.J. Schatz and D.T. Ginat*
- 223 **Illustrated Review of the Embryology and Development of the Facial Region, Part 3: An Overview of the Molecular Interactions Responsible for Facial Development** *P.M. Som, A. Streit, and T.P. Naidich*

METHODOLOGIC PERSPECTIVES

- 230 **Toward an Endovascular Internal Carotid Artery Classification System** *M. Shapiro, T. Becske, H.A. Riina, E. Raz, D. Zumofen, J.J. Jafar, P.P. Huang, and P.K. Nelson*

PATIENT SAFETY

- 237 **Carotid CTA: Radiation Exposure and Image Quality with the Use of Attenuation-Based, Automated Kilovolt Selection** *A. Eller, W. Wuest, M. Kramer, M. May, A. Schmid, M. Uder, and M.M. Lell*

HEALTH CARE REFORM VIGNETTE

- 242 **The Medicare Conversion Factor** *D.J. Seidenwurm and J.H. Bursleson*

BRAIN

- 244 **Visual-Statistical Interpretation of ¹⁸F-FDG-PET Images for Characteristic Alzheimer Patterns in a Multicenter Study: Inter-Rater Concordance and Relationship to Automated Quantitative Evaluation** *T. Yamane, Y. Ikari, T. Nishio, K. Ishii, K. Ishii, T. Kato, K. Ito, D.H.S. Silverman, M. Senda, T. Asada, H. Arai, M. Sugishita, T. Iwatsubo, and the J-ADNI Study Group*
- 250 **Oxygen Extraction Fraction and Stroke Risk in Patients with Carotid Stenosis or Occlusion: A Systematic Review and Meta-Analysis** *A. Gupta, H. Baradaran, A.D. Schweitzer, H. Kamel, A. Pandya, D. Delgado, D. Wright, S. Hurtado-Rua, Y. Wang, and P.C. Sanelli*

 Indicates Editor's Choices selection

 Indicates Fellows' Journal Club selection

 Indicates open access to non-subscribers at www.ajnr.org

 Indicates article with supplemental on-line table

 Indicates article with supplemental on-line photo

 Indicates article with supplemental on-line video

 Indicates Evidence-Based Medicine Level 1

 Indicates Evidence-Based Medicine Level 2



Diagrams illustrate vulnerability of right vertebral artery during golf swing.

ASNR 52ND ANNUAL MEETING & THE FOUNDATION OF THE ASNR SYMPOSIUM 2014

MAY 17-22 | Montreal ■ Palais des congrés de Montreal

ASNR 2014 PROGRAM CHAIR/PRESIDENT-ELECT - Gordon K. Sze, MD, FACR

THE FOUNDATION OF THE ASNR



The Foundation of the ASNR Symposium 2014: Inflammatory and Infectious Diseases of the CNS

SYMPOSIUM 2014:

- The Role of Inflammation and Infections in Stroke, Seizures, White Matter Diseases, etc.
- Advanced Imaging Techniques in the Evaluation of Inflammatory CNS Diseases
- Infectious Agents for Human Good: Oncolytic Viruses, Viral Vector Gene Therapy and Advanced Imaging

ADDITIONAL NEW EDUCATIONAL COURSE PROGRAM IN 2014 (concurrent program with the Symposium 2014): Inflammatory and Infectious Diseases

EDUCATIONAL COURSE 2014: with world class speakers including

- Anne G. Osborn, MD, Thomas P. Naidich, MD, Donald Resnick, MD, James G. Smirniotopoulos, MD, Jeffrey S. Ross, MD, Kelly K. Koeller, MD, FACR, David M. Yousem, MD, MBA, Laurie A. Loevner, MD, Peter M. Som, MD, Patricia A. Hudgins, MD, Robert D. Zimmerman MD, FACR, Hugh D. Curtin, MD, M. Judith Donovan Post, MD, FACR, and More...

ANNUAL MEETING:

- One-day **MINI SYMPOSIUM on STROKE** - Organized by Pina C. Sanelli, MD, MPH and Max Wintermark, MD
- One-day **MINI SYMPOSIUM on TUMORS** - Organized by Girish M. Fatterpekar, MD, MBBS, DNB, Whitney B. Pope, MD, PhD and Gordon K. Sze, MD, FACR
- Nobel Prize Laureate, Stanley Prusiner, MD, Keynote Speaker, on Prions and Alzheimer's Disease, Parkinson's Disease, and Other Neurodegenerative Disorders
- More "Hands-On" Experience Applicable to Your Practices
- Young Professionals Programming
- Expanded Self-Assessment Module (SAM) Session Programming Throughout the Week

PROGRAMMING DEVELOPED IN COOPERATION WITH THE...

- American Society of Functional Neuroradiology (ASFNR) David J. Mikulis, MD
- American Society of Head and Neck Radiology (ASHNR) Yoshimi Anzai, MD, MPH
- American Society of Pediatric Neuroradiology (ASPNR) Richard L. Robertson, MD
- American Society of Spine Radiology (ASSR) Meng Law, MD, MBBS, FRACR
- Society of NeuroInterventional Surgery (SNIS) Peter A. Rasmussen, MD



ASFNR ASHNR ASPNR ASSR SNIS

TO REQUEST PROGRAMMING AND REGISTRATION MATERIALS FOR THE ASNR 52ND ANNUAL MEETING, CONTACT:

ASNR 52ND ANNUAL MEETING

c/o American Society of Neuroradiology
800 Enterprise Drive, Suite 205
Oak Brook, Illinois 60523-4216

Phone: 630-574-0220
Fax: 630-574-0661
Email: meetings@asnr.org
Website: www.asnr.org/2014



Scan Now
to visit our website

-    **256 Perfusion Measurement in Brain Gliomas with Intravoxel Incoherent Motion MRI** *C. Federau, R. Meuli, K. O'Brien, P. Maeder, and P. Hagmann*
-  **263 Assessment of Angiographic Vascularity of Meningiomas with Dynamic Susceptibility Contrast-Enhanced Perfusion-Weighted Imaging and Diffusion Tensor Imaging** *C.H. Toh, K.-C. Wei, C.N. Chang, Y.-W. Peng, S.-H. Ng, H.-F. Wong, and C.-P. Lin*
-  **270 Utility of Proton MR Spectroscopy for Differentiating Typical and Atypical Primary Central Nervous System Lymphomas from Tumefactive Demyelinating Lesions** *S.-S. Lu, S.J. Kim, H.S. Kim, C.G. Choi, Y.-M. Lim, E.J. Kim, D.Y. Kim, and S.H. Cho*
-    **278 ⁶²Cu-Diacetyl-Bis (N⁴-Methylthiosemicarbazone) PET in Human Gliomas: Comparative Study with [¹⁸F]Fluorodeoxyglucose and L-Methyl-[¹¹C]Methionine PET** *K. Tateishi, U. Tateishi, S. Nakanowatari, M. Ohtake, R. Minamimoto, J. Suenaga, H. Murata, K. Kubota, T. Inoue, and N. Kawahara*
-  **285 Diffusion Measures Indicate Fight Exposure-Related Damage to Cerebral White Matter in Boxers and Mixed Martial Arts Fighters** *W. Shin, S.Y. Mahmoud, K. Sakaie, S.J. Banks, M.J. Lowe, M. Phillips, M.T. Modic, and C. Bernick*
-    **291 Local and Global Fiber Tractography in Patients with Epilepsy** *C. Anastasopoulos, M. Reisert, V.G. Kiselev, T. Nguyen-Thanh, A. Schulze-Bonhage, J. Zentner, and I. Mader*
- 297 Tumor Consistency of Pituitary Macroadenomas: Predictive Analysis on the Basis of Imaging Features with Contrast-Enhanced 3D FIESTA at 3T** *J. Yamamoto, S. Kakeda, S. Shimajiri, M. Takahashi, K. Watanabe, Y. Kai, J. Moriya, Y. Korogi, and S. Nishizawa*
- 304 Frontotemporal Cortical Thinning in Amyotrophic Lateral Sclerosis** *A. d'Ambrosio, A. Gallo, F. Trojsi, D. Corbo, F. Esposito, M. Cirillo, M.R. Monsurrò, and G. Tedeschi*
-   **311 Use of FLAIR Imaging to Identify Onset Time of Cerebral Ischemia in a Canine Model** *X.-Q. Xu, Q.-Q. Zu, S.-S. Lu, Q.-G. Cheng, J. Yu, Y. Sheng, H.-B. Shi, and S. Liu*
-   **317 Subcortical Cystic Lesions within the Anterior Superior Temporal Gyrus: A Newly Recognized Characteristic Location for Dilated Perivascular Spaces** *S. Rawal, S.E. Croul, R.A. Willinsky, M. Tymianski, and T. Krings*
-   **323 Preferential Location for Arterial Dissection Presenting as Golf-Related Stroke** *M.H. Choi, J.M. Hong, J.S. Lee, D.H. Shin, H.A. Choi, and K. Lee*
- INTERVENTIONAL** *Published in collaboration with Interventional Neuroradiology*
-   **327 When Is Carotid Angioplasty and Stenting the Cost-Effective Alternative for Revascularization of Symptomatic Carotid Stenosis? A Canadian Health System Perspective** *M.A. Almekhlafi, M.D. Hill, S. Wiebe, M. Goyal, D. Yavin, J.H. Wong, and F.M. Clement*
-  **333 Quantifying the Large-Scale Hemodynamics of Intracranial Aneurysms** *G. Byrne, F. Mut, and J. Cebal*
- 339 Analysis of Complications and Recurrences of Aneurysm Coiling with Special Emphasis on the Stent-Assisted Technique** *H. Nishido, M. Piotin, B. Bartolini, S. Pistocchi, H. Redjem, and R. Blanc*
-  **345 Hyperattenuated Intracerebral Lesions after Mechanical Recanalization in Acute Stroke** *N. Lummel, G. Schulte-Altedorneburg, C. Bernau, T. Pfefferkorn, M. Patzig, H. Janssen, C. Opherk, H. Brückmann, and J. Linn*
- COMMENTARY**
- 352 Hyperattenuated Intracerebral Lesions after Mechanical Recanalization in Acute Stroke: Contrast and Compare** *T. Tomsick*

Letter from the President-Elect – Search for New *AJNR* Editor

In June, 2015, Mauricio Castillo, MD, FACR, will complete an eight-year term as the Editor-in-Chief of the *AJNR*. He follows a short list of illustrious neuroradiologists, from Dr. Juan Taveras to Dr. Michael Huckman to Dr. Robert Quencer to Dr. Robert Grossman.

One only has to pick up any random issue of the *AJNR* to realize what a tremendous mark Mauricio has made on the journal. His imprint starts on the first page of content with his column, Perspectives. Probing, erudite, at times very witty, and always brilliant, Mauricio turns out a monthly commentary on the state of neuroradiology, the state of our profession, and, at times, the state of the world. His references and quotations demonstrate a mind not only scientific and exacting but also knowledgeable in realms far beyond medicine.

Having worked with Mauricio very closely at the ASNR for the past two years, I can also attest to the fact that Mauricio is totally dedicated to the journal. At times, it seemed his reason for being. And the journal has benefitted immensely, in turn. From its look to its organization to the quality of the articles, Mauricio has brought the journal into the forefront of all radiology journals and it now ranks #2 in Impact Factor of all radiology journals. *AJNR* is the premier clinical neuroimaging journal with the highest circulation among all imaging-related subspecialty journals, publishing about 350 articles in 12 issues per year. It receives over 1400 original submissions annually and its Web site is accessed over 10 million times a year. In addition to the print version of the Journal, Mauricio also initiated its biannual Special Collections and monthly *AJNR* Digest. Other electronic activities which he began include its popular Case Collection (Case of the Week, Case of the Month, Classic Case, and Clinical Correlation), podcasts (editor's and fellows' journal club selections, traveling journal club, and Special Collections), and Fellows' Portal. With his international background, Mauricio has also been the ideal person to spread the word of the *AJNR* across the world. Finally, he has done all this and kept the journal in sound financial health through a period of difficult economic times.

Mauricio took over leadership of the journal at a time when the concept of the journal was beginning to enter a state of flux. One only has to look at your neighborhood newsstand to realize that this has been a time when many publications have been unable to adjust and have disappeared. In the past eight years, the demands on the journal have changed. Our current expectations are for instant gratification, not a lag time before publication. We require our information in more bite-size pieces, directed at us and easily accessible.

The new editor will face an even more rapidly evolving world. What is the future of radiology journals? We know that the *AJNR* will survive but in what form? What will be the best digital format? There will be an increased demand for electronic access and a further migration to tablets and smartphones. Preserving the brand of the *AJNR* will become more challenging. While in the past, publication was the end point, increasingly, publication today is the starting point, the beginning of an interactive discussion. How will this impact on the financial state of the journal, with decreasing print advertising? How will the *AJNR* respond to the demands of social media?

To assist the Executive Committee in the search for a new editor in these changing times, I will chair a search committee comprised, in part, of Tina Young-Poussaint, Chair of the Publications Committee, Laurie Lovner, Vice-President, Howard Rowley, Robert Quencer, Robert D. Zimmerman, James Barkovich, Tabbasum Kennedy, and some of the Senior Editors of the *AJNR*, Harry J. Cloft, Nancy Fischbein, Pamela W. Schaefer, Jody Tanabe, and Charles M. Strother, as well as James Gantenberg, Karen Halm, and Angelo Artemakis from the ASNR headquarters. The appointment of the new Editor-in-Chief will be announced in the spring of 2015.

All interested physicians are invited to send their curriculum vitae and an introductory letter of intent to Dr. Gordon Sze, American Society of Neuroradiology, 800 Enterprise Drive, Suite 205, Oak Brook, IL, 60523 and via email to gordon.sze@yale.edu and jgantenberg@asnr.org. In addition, we welcome nominations of candidates from the ASNR membership. The deadline for receipt of submissions is August 1, 2014 but earlier submissions are welcome. A position description for the *AJNR* Editor and basic qualifications are posted at: www.ajnr.org/site/misc/eic-search-2015.xhtml.

Gordon Sze, MD, FACR
Chair, Editor-in-Chief Search Committee
President-Elect
American Society of Neuroradiology

354 Angioarchitectural Characteristics Associated with Complications of Embolization in Supratentorial Brain Arteriovenous Malformation

J. Pan, H. He, L. Feng, F. Viñuela, Z. Wu, and R. Zhan

-  **360 Acute Bleeding in the Head and Neck: Angiographic Findings and Endovascular Management** *L.-B. Zhao, H.B. Shi, S. Park, D.g. Lee, J.H. Shim, D.H. Lee, and D.C. Suh*

-  **367 Recanalization of Symptomatic Vertebral Ostial Occlusion in Patients with Acute or Subacute Stroke** *S. Park, D.-G. Lee, J.H. Shim, D.H. Lee, and D.C. Suh*

HEAD & NECK

373 Imaging Findings of Head and Neck Dermatofibrosarcoma Protuberans

G.G. Millare, N. Guha-Thakurta, E.M. Sturgis, A.K. El-Naggar, and J.M. Debnam

379 Fractional Change in Apparent Diffusion Coefficient as an Imaging Biomarker for Predicting Treatment Response in Head and Neck Cancer Treated with Chemoradiotherapy

M. Matoba, H. Tuji, Y. Shimode, I. Toyoda, Y. Kuginuki, K. Miwa, and H. Tonami

386 Yield of Neck CT and Barium Esophagram in Patients with Globus Sensation

L. Alhilali, S.-h. Seo, B.F. Branstetter IV, and S. Fakhran

390 Actinomycosis in the Mandible: CT and MR Findings

Y. Sasaki, T. Kaneda, J.W. Uyeda, H. Okada, K. Sekiya, M. Suemitsu, and O. Sakai

PEDIATRICS

-   **395 Arterial Spin-Labeled Perfusion of Pediatric Brain Tumors** *K.W. Yeom, L.A. Mitchell, R.M. Lober, P.D. Barnes, H. Vogel, P.G. Fisher, and M.S. Edwards*

- 402 Bannayan-Riley-Ruvalcaba Syndrome: MRI Neuroimaging Features in a Series of 7 Patients** *R. Bhargava, K.J. Au Yong, and N. Leonard*

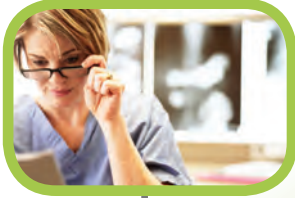
SPINE

407 Comparison of Dynamic Contrast-Enhanced 3T MR and 64-Row Multidetector CT Angiography for the Localization of Spinal Dural Arteriovenous Fistulas

S. Oda, D. Utsunomiya, T. Hirai, Y. Kai, Y. Ohmori, Y. Shigematsu, Y. Iryo, H. Uetani, M. Azuma, and Y. Yamashita

BOOK REVIEWS *R.M. Quencer, Section Editor*

Please visit www.ajnrblog.org to read and comment on Book Reviews.



Simplify the MOC Process



Manage your CME Credits Online

CMEgateway.org

Available to Members of Participating Societies

American Board of Radiology (ABR)
American College of Radiology (ACR)
American Roentgen Ray Society (ARRS)
American Society of Neuroradiology (ASNR)
Commission on Accreditation of Medical
Physics Educational Programs, Inc. (CAMPEP)
Radiological Society of North America (RSNA)
Society of Interventional Radiology (SIR)
SNM
The Society for Pediatric Radiology (SPR)

It's Easy and Free!

Log on to CME Gateway to:

- View or print reports of your CME credits from multiple societies from a single access point.
- Print an aggregated report or certificate from each participating organization.
- Link to SAMs and other tools to help with maintenance of certification.

American Board of Radiology (ABR) participation!

By activating ABR in your organizational profile, your MOC-fulfilling CME and SAM credits can be transferred to your own personalized database on the ABR Web site.

Sign Up Today!

go to CMEgateway.org

Official Journal:

American Society of Neuroradiology
American Society of Functional Neuroradiology
American Society of Head and Neck Radiology
American Society of Pediatric Neuroradiology
American Society of Spine Radiology

EDITOR-IN-CHIEF

Mauricio Castillo, MD

Professor of Radiology and Chief, Division of Neuroradiology, University of North Carolina, School of Medicine, Chapel Hill, North Carolina

SENIOR EDITORS

Harry J. Cloft, MD, PhD

Professor of Radiology and Neurosurgery, Department of Radiology, Mayo Clinic College of Medicine, Rochester, Minnesota

Nancy J. Fischbein, MD

Professor of Radiology, Otolaryngology-Head and Neck Surgery, Neurology, and Neurosurgery and Chief, Head and Neck Radiology, Department of Radiology, Stanford University Medical Center, Stanford, California

Jeffrey S. Ross, MD

Staff Neuroradiologist, Barrow Neurological Institute, St. Joseph's Hospital, Phoenix, Arizona

Pamela W. Schaefer, MD

Clinical Director of MRI and Associate Director of Neuroradiology, Massachusetts General Hospital, Boston, Massachusetts, and Associate Professor, Radiology, Harvard Medical School, Cambridge, Massachusetts

Charles M. Strother, MD

Professor of Radiology, Emeritus, University of Wisconsin, Madison, Wisconsin

Jody Tanabe, MD

Professor of Radiology and Psychiatry, Chief of Neuroradiology, University of Colorado, Denver, Colorado

EDITORIAL BOARD

Ashley H. Aiken, Atlanta, Georgia
A. James Barkovich, San Francisco, California
Walter S. Bartynski, Charleston, South Carolina
Barton F. Branstetter IV, Pittsburgh, Pennsylvania
Jonathan L. Brisman, Lake Success, New York
Julie Bykowski, San Diego, California
Donald W. Chakeres, Columbus, Ohio
Alessandro Cianfoni, Lugano, Switzerland
Colin Derdeyn, St. Louis, Missouri
Rahul S. Desikan, San Diego, California
Richard du Mesnil de Rochemont, Frankfurt, Germany
Clifford J. Eskey, Hanover, New Hampshire
Massimo Filippi, Milan, Italy
David Fiorella, Cleveland, Ohio
Allan J. Fox, Toronto, Ontario, Canada
Christine M. Glastonbury, San Francisco, California

John L. Go, Los Angeles, California
Wan-Yuo Guo, Taipei, Taiwan
Rakesh K. Gupta, Lucknow, India
Lotfi Hacein-Bey, Sacramento, California
David B. Hackney, Boston, Massachusetts
Christopher P. Hess, San Francisco, California
Andrei Holodny, New York, New York
Benjamin Huang, Chapel Hill, North Carolina
Thierry A.G.M. Huisman, Baltimore, Maryland
George J. Hunter, Boston, Massachusetts
Mahesh V. Jayaraman, Providence, Rhode Island
Valerie Jewells, Chapel Hill, North Carolina
Timothy J. Kaufmann, Rochester, Minnesota
Kenneth F. Layton, Dallas, Texas
Ting-Yim Lee, London, Ontario, Canada
Michael M. Lell, Erlangen, Germany
Michael Lev, Boston, Massachusetts
Karl-Olof Lovblad, Geneva, Switzerland
Lisa H. Lowe, Kansas City, Missouri
Franklin A. Marden, Chicago, Illinois
M. Gisele Matheus, Charleston, South Carolina
Joseph C. McGowan, Merion Station, Pennsylvania
Kevin R. Moore, Salt Lake City, Utah
Christopher J. Moran, St. Louis, Missouri
Takahisa Mori, Kamakura City, Japan

Suresh Mukherji, Ann Arbor, Michigan
Amanda Murphy, Toronto, Ontario, Canada
Alexander J. Nemeth, Chicago, Illinois
Laurent Pierot, Reims, France
Jay J. Pillai, Baltimore, Maryland
Whitney B. Pope, Los Angeles, California
M. Judith Donovan Post, Miami, Florida
Tina Young Poussaint, Boston, Massachusetts
Joana Ramalho, Lisbon, Portugal
Otto Rapalino, Boston, Massachusetts
Álex Rovira-Cañellas, Barcelona, Spain
Paul M. Ruggieri, Cleveland, Ohio
Zoran Rumboldt, Charleston, South Carolina
Amit M. Saindane, Atlanta, Georgia
Erin Simon Schwartz, Philadelphia, Pennsylvania
Aseem Sharma, St. Louis, Missouri
J. Keith Smith, Chapel Hill, North Carolina
Maria Vittoria Spampinato, Charleston, South Carolina
Gordon K. Sze, New Haven, Connecticut
Krishnamoorthy Thamburaj, Hershey, Pennsylvania
Kent R. Thielen, Rochester, Minnesota
Cheng Hong Toh, Taipei, Taiwan
Thomas A. Tomsick, Cincinnati, Ohio
Aquila S. Turk, Charleston, South Carolina
Willem Jan van Rooij, Tilburg, Netherlands
Arastoo Vossough, Philadelphia, Pennsylvania
Elysa Widjaja, Toronto, Ontario, Canada
Max Wintermark, Charlottesville, Virginia
Ronald L. Wolf, Philadelphia, Pennsylvania
Kei Yamada, Kyoto, Japan

EDITORIAL FELLOW

Falgun H. Chokshi, Atlanta, Georgia

YOUNG PROFESSIONALS ADVISORY COMMITTEE

Asim K. Bag, Birmingham, Alabama
Anna E. Nidecker, Sacramento, California
Peter Yi Shen, Sacramento, California

HEALTH CARE AND SOCIOECONOMICS EDITOR

Pina C. Sanelli, New York, New York

Founding Editor

Juan M. Taveras

Editors Emeriti

Robert I. Grossman, Michael S. Huckman,
Robert M. Quencer

Special Consultants to the Editor

Sandy Cheng-Yu Chen, Girish Fatterpekar,
Ryan Fitzgerald, Yvonne Lui,
Louise M. Henderson, Greg Zaharchuk

INR Liaisons

Timo Krings, Karel terBrugge

Managing Editor

Karen Halm

Electronic Publications Manager

Jason Gantenberg

Editorial Assistant

Mary Harder

Executive Director, ASNR

James B. Gantenberg

Director of Communications, ASNR

Angelo Artemakis

AJNR (Am J Neuroradiol ISSN 0195-6108) is a journal published monthly, owned and published by the American Society of Neuroradiology (ASNR), 800 Enterprise Drive, Suite 205, Oak Brook, IL 60523. Annual dues for the ASNR include \$170.00 for journal subscription. The journal is printed by Cadmus Journal Services, 5457 Twin Knolls Road, Suite 200, Columbia, MD 21045; Periodicals postage paid at Oak Brook, IL and additional mailing offices. Printed in the U.S.A. POSTMASTER: Please send address changes to American Journal of Neuroradiology, P.O. Box 3000, Denville, NJ 07834, U.S.A. Subscription rates: nonmember \$370 (\$440 foreign) print and online, \$300 online only; institutions \$430 (\$495 foreign) print and basic online, \$850 (\$915 foreign) print and extended online, \$355 online only (basic), extended online \$770; single copies are \$35 each (\$40 foreign). Indexed by PubMed/Medline, BIOSIS Previews, Current Contents (Clinical Medicine and Life Sciences), EMBASE, Google Scholar, HighWire Press, Q-Sensei, RefSeek, Science Citation Index, and SCI Expanded. Copyright © American Society of Neuroradiology.



Call for *AJNR* Editorial Fellowship Candidates

ASNR and *AJNR* are pleased once again in 2014 to join efforts with other imaging-related journals that have training programs on editorial aspects of publishing for trainees or junior staff (3–5 years after training) such as *Radiology* (Olmsted fellowship), *AJR* (Figley and Rogers fellowships [USA and international respectively]), and *Radiologia* (from Spain).

Goals:

1. Increase interest in “editorial” and publication-related activities in younger individuals.
2. Increase understanding and participation in the *AJNR* review process.
3. Incorporate into *AJNR*’s Editorial Board younger individuals who have previous experience in the review and publication process.
4. Fill a specific need in neuroradiology not offered by other similar fellowships.
5. Increase the relationship between “newer” generations of neuroradiologists and more established individuals.
6. Increase visibility of *AJNR* among younger neuroradiologists.

Activities of the Fellowship:

1. Serve as “Editorial Fellow” for one year. This individual will be listed on the masthead as such and will receive a certificate stating his/her activities at the end of the service period.
2. Review at least one manuscript per month for 12 months. Evaluate all review articles submitted to *AJNR*. Access to our electronic manuscript review system will be granted so that the candidate can learn how these systems work.
3. Be involved in the final decision of selected manuscripts together with the EIC.
4. Participate in all monthly telephone Senior Editor conference calls.
5. Participate in all meetings of the Editors and Publications Committee during the annual meetings of ASNR and RSNA as per candidate’s availability. *AJNR*/ASNR will not provide funding for this activity but may offer a discounted fee for its annual meeting.
6. Evaluate progress and adjust program to specific needs in biannual meeting or telephone conference with the EIC.
7. Write at least one editorial for *AJNR*.
8. Embark on an editorial scientific or bibliometric project that will lead to the submission of an article to *AJNR* or another appropriate journal as determined by *AJNR*’s EIC. This project can be done in conjunction with the EIC or one of the Senior Editors.
9. Serve as liaison between *AJNR* and ASNR’s Young Professionals Network and the 3 YPs appointed to *AJNR* as special consultants. Participate in meetings and telephone calls with this group. Design one electronic survey/year polling the group regarding readership attitudes and wishes.
10. Recruit trainees as reviewers as determined by the EIC.
11. Participate in Web improvement projects.
12. Potentially become a member of *AJNR*’s Editorial Board at the end of the fellowship.
13. Invite Guest Editors for *AJNR*’s News Digest to cover a variety of timely topics.

Qualifications:

1. Be a fellow in neuroradiology from North America, including Canada (this may be extended to include other countries).
2. Be a junior faculty neuroradiology member (<3 years) in either an academic and private environment.
3. Provide an “end” of fellowship report to *AJNR*’s EIC and ASNR’s Publications Committee.
4. Be an “in-training” or member of ASNR in any other category.

Application:

1. Include a short letter of intent with statement of goals and desired research project. CV must be included.
2. Include a letter of recommendation from the Division Chief or fellowship program director. A statement of protected time to perform the functions outlined is desirable.
3. Applications will be evaluated by *AJNR*’s Senior Editors and the Chair of the Publications Committee prior to the ASNR meeting. The name of the selected individual will be announced at the meeting.
4. Applications should be received by March 3, 2014 and sent to Ms. Karen Halm, *AJNR* Managing Editor, electronically at khalm@asnr.org.

Trainees in Peer Review: Our Experience

M. Castillo, *Editor-in-Chief*

The *American Journal of Neuroradiology (AJNR)* receives more than 1400 article submissions every year. When more than 2 years ago, we eliminated case reports, which accounted for between 25% and 35% of all submitted articles, we did not anticipate that this difference would be made up, almost instantly, by an increasing number of original, full-length investigations (we are very happy this happened). Today, nearly 1250 of the total submissions (89%) are full-length, original articles, and the rest are reviews, editorials, letters to the editor, and other types of articles. These have obviously resulted in increasing work for our Senior Editors and reviewers. Our reviewer data base contains the names of more than 2400 clinicians and scientists from all over the world, but in reality, only a relatively small number of them do most of our reviews. Why? Because they never say no, they are excellent reviewers, and neuroradiology has become so subspecialized that it is difficult to find reviewers for a growing number of sophisticated topics such as computer modeling of intra-aneurysm fluid-flow dynamics, kurtosis, and so forth. In this "Perspectives," my aim is to inform our readers about how we are trying to improve and expand our reviewer data base, especially as it pertains to using neuroradiology trainees in the peer-review process. This information was partially presented at the Radiology Editors Forum in 2012 (this group of editors from imaging-related journals meets once per year).

One can easily improve and increase the number of reviewers by recruiting fellows and residents, using the names of individuals found in the references of submitted articles, accepting personal references from other reviewers, asking the authors of previously submitted articles to contribute, and accepting those individuals who offer unsolicited help (*AJNR* uses all of these strategies). I have tried to recruit my own fellows who have left for private practice after their training but have found this disappointing because they soon become very busy and reviewing articles turns into a low priority. Once every 2 years, we look at Editorial Board performance in the reviewer data base and purge those individuals who have very low scores and often decline to review articles (you can ask for your scores, and we will be glad to send them). Using only our best reviewers is often problematic because it leads to fast burnout rates. Remember that each review generally takes anywhere from 3 to 8 hours to complete. Because our reviewers do not work exclusively for us, demanding more work from them only leads to their declining requests from other journals that may also need their expertise (there are currently 116 imaging-related journals).

The ever-increasing demands placed on these exceptional individuals requires constant positive feedback and encouragement from editors in the form of awards and "best of" lists published in

journals and on Web sites, reviewer scoring feedback, and personal encouragement in the form of praise and letters (we at *AJNR* do all of these). Unfortunately the intellectual rewards of reviewing may soon lose their initial importance, and we must try other forms of encouragement: payments, discounted subscriptions, discounted fees to annual meetings, discounted or free continuing medical education (CME) activities, and CME credit for reviewing (currently I am aware of 5 imaging journals that use this latter strategy; *AJNR* will start doing this sometime in the second semester of 2013).¹ Unfortunately, none of these strategies work well in the long run.

The reality is that all journals are facing a reviewer shortage. The total number of scientific articles submitted increases at a rate of 3.3% per year and doubles every 20 years.² More than 1.3 million articles undergo peer review every year. These may even be underestimated if one takes into account the growing number of "international" journals published in China, India, and Eastern Europe. Because less than 45% of all published articles will ever be cited, it seems that most of the reviewing and editing process is being spent on lesser quality science that will never be recognized as important. Reviewers not only contribute to journals but are asked to do similar jobs when they serve as experts on panels of foundations and government agencies. Junior and midlevel individuals end up with no time for activities needed for promotions, and peer review of articles is not one of these. We have found that as the number of review requests has increased, the percentage of individuals who do not respond or decline these requests has remained at about 50% for the past 3 years (Fig 1). Thus, although we have a larger number of reviewers, our success rate at getting them to accept review requests remains static.

Because of all of the aforementioned situations, it seems natural to tap into our trainees and younger members of our profession to review articles. In 2004, the United Nations Educational, Scientific and Cultural Organization created the International Forum of Young Scientists, and peer review has been addressed repeatedly there.³ The World Academy of Young Scientists agrees that junior members of different specialties should be involved in peer review of the scientific literature and considers it a critical activity in their education process, but medical schools and radiology departments do not give credit for it (at least in the United States).

At our annual meeting of the American Society of Neuroradiology (ASNR), during the luncheon for the Young Professionals Network, I usually ask these individuals for help with the peer-review process. These young volunteers are generally asked to serve as third (or fourth) reviewers; that is, they never review unless an article is being evaluated by 2 or 3 other senior reviewers. During 2010 and 2011, we were able to recruit 36 such collaborators (in 2012 their number was up to 41, but I will not include them here because we still do not have all of the information pertaining to their activities). All except 1 of these young reviewers lived in the United States. Each individual was assigned to 1 Editor, and I had 29 (83%) of them. Two Senior Editors who deal with brain and head and neck issues were responsible for the rest. No trainees volunteered to review articles related to neurointer-

<http://dx.doi.org/10.3174/ajnr.A3548>

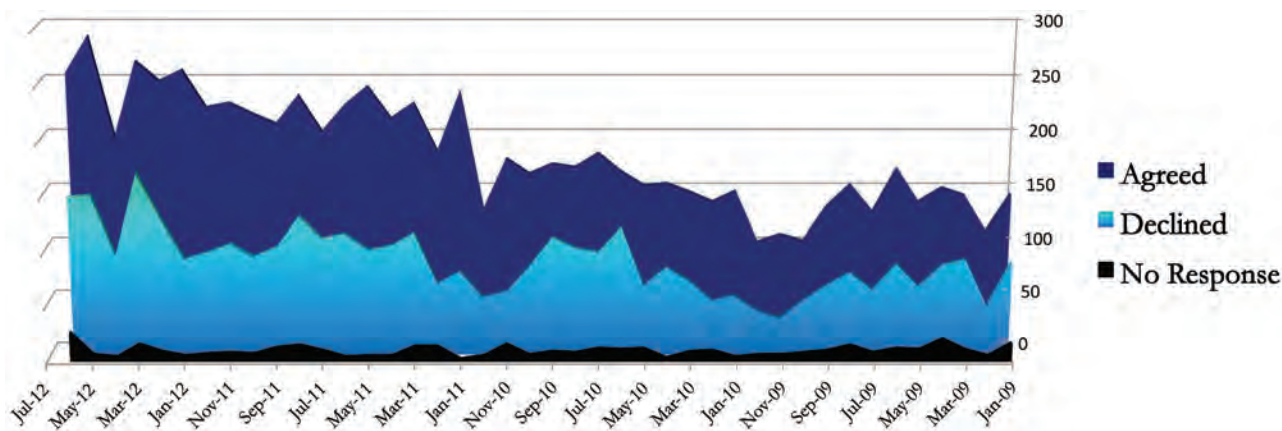


FIG 1. Response to request to review *AJNR* manuscripts, January 2009–June 2012.

ventional, spine, or advanced imaging techniques. Six of the 36 trainees declined all invitations to review articles. The remaining 30 did 261 total reviews (221 original research, 22 clinical reports, 14 case reports, 3 technical notes, and 1 review article), accounting for 9.3% of all submissions ($n = 2826$) during the same 2-year period. The time it took for these reviews to be completed was 5–17 days, below our allowed maximum of 21 days and perhaps less than it takes many of our more senior reviewers to complete their tasks. All reviews received by *AJNR* are scored by using a simple and subjective scale by the editor in charge of the article (1 = review was below average, 2 = review was sufficient, and 3 = review was highly relevant). The average score of reviews done by trainees was 2.3; but as is seen with those assigned to senior reviewers, scores varied significantly from individual to individual.

As with senior reviewers, we do not expect structured evaluations from trainees. It is the philosophy of the editors of *AJNR* that free-form review allows individuals to better express their opinions and thoughts. However, we do not deny that structured reviews may be useful to more neophyte reviewers. For guidance, we generally refer reviewers to the well-known articles on this topic by Proto⁴ and Provenzale and Stanley,⁵ which are posted on our peer-review Web site. We believe that adequate and continuous feedback leads to the development of well-defined and useful individual styles and results in reviews of high quality; however, this is controversial. In 1 study, neither reviewers with low nor high scores improved their evaluations when feedback was given to them, leading to the conclusion that feedback in this situation is ineffective.⁶

For purposes of assessing the quality of trainee reviewers with respect to more senior ones, it is helpful to compare their decisions. Trainee reviewers gave a “hard” rejection to 114 manuscripts, while senior reviewers gave these same articles the same “hard” rejection in 69 instances and a “reject/resubmit” disposition in 45 cases. Trainees gave 156 articles a decision of “revision needed” (either major or minor revision), and these matched the dispositions given by senior reviewers. One article was accepted without revision per both trainee and senior reviewers. Therefore, there were no significantly discordant decisions between the 2 groups of reviewers, and mild discordances in dispositions were seen in 17% of reviews. I was surprised by this because published

studies seem to indicate that there is no reproducibility of peer review in the neurosciences.⁷

After becoming reviewers, 25/36 trainees submitted articles to *AJNR* either as a principal or coauthor (82 total articles including 59 original research articles, 4 clinical reports, and 4 review articles). Of these, 39 were ultimately accepted, and 43, rejected (which is better than our usual 75% rejection rate). It is thus possible that reviewing made these young individuals better authors. One excellent trainee reviewer was asked to join our Editorial Board at the end of her fellowship. After 2 years, all of our trainee reviewers migrated to the pool of senior reviewers.

How can we improve trainee participation in our review process? Certainly, structured reports are a consideration. Structured review forms tell less-experienced reviewers not only what to look for but also (more important) what to ignore. Some journals that use this type of process have considered eliminating “false cues of quality” from their forms. “Significance tests” are one such cue because they are generally interpreted as reflecting “quality” in research when this is not always the case.⁸ Currently, the *American Journal of Roentgenology* and *Radiographics* are in the process of studying this issue and crafting structured guidelines for their reviewers. Greater communication with neuroradiology program directors could lead to further reviewer recruitment as well as granting young reviewers the time needed for the activity, credit for their work, and encouragement.

In addition, increasing the pool of international trainee reviewers would be desirable. From my experience, it seems that article reviewing is still an important and honorable activity in other countries, especially reviewing for an American journal. Asking members-in-training about their interest in reviewing articles at the time that they are filling out their society applications would simplify the process of identifying interested individuals (ASNR started doing this in 2012). One difficulty that we editors face when assigning articles to trainee reviewers is finding which ones are appropriate for them. In the past when we accepted case reports, these provided us with simple articles that served as a starting point for junior individuals. As the complexity of articles increases, assigning them is more difficult (but maybe I am underestimating the capacity of our trainee reviewers).

Special training programs for individuals may produce fewer, but highly qualified, reviewers and future editors. Currently, there

are 3 societies offering such programs. The oldest is the Figley Fellowship from the American Roentgen Ray Society, which is now geared to young individuals practicing in the United States; and the newer Rogers International Editorial Fellowship, which, as its name implies, is available to those residing outside the United States. Fifty-seven individuals (including myself) have participated in one of these fellowships, and 7 have become journal editors (S. Cappitelli, personal communication; December 2012). The Radiological Society of North America (RSNA) and *Radiology* have offered their Olmsted Fellowship to 7 individuals, but none serve on its Editorial Board (R. Arnold, personal communication; December 2012). The Eyer Fellowship from the RSNA is designed for midcareer individuals, and I have not included it in this discussion. In the Spanish-speaking world, the Spanish Society of Medical Radiology and its journal, *Radiologia*, are the only ones to offer an editorial fellowship. ASNR and *AJNR* have recently started a similar endeavor, and information about this can be found on our blog (www.ajnrblog.org) or Web site.

In conclusion, I think that we have had some degree of early, but encouraging, success by using trainees in the peer-review process of *AJNR*. Their participation has been limited, but the results of their timely reviews do not differ significantly from those of our more senior reviewers. We hope to start implementing new measures that will increase the number of trainee reviewers, standardize their contributions, and recognize their effort.

REFERENCES

1. Lee K, Bero L. **What authors, editors and reviewers should do to improve peer review.** *Nature* (2006), <http://www.nature.com/nature/peerreview/debate/nature05007.html>. Accessed May 13, 2013
2. Bauerlein M, Gad-el-Hak M, Grody H, et al. **We must stop the avalanche of low-quality research.** *The Chronicle of Higher Education*, June 13, 2010, <http://chronicle.com/article/We-Must-Stop-the-Avalanche-of/65890>. Accessed May 13, 2013
3. Mainguy G, Motamedi MR, Mietchen D. **Peer review: the newcomers' perspective.** *PLoS Biol* 2005;3:e326
4. Proto AV. **Radiology 2007: reviewing for Radiology.** *Radiology* 2007;244:7–11
5. Provenzale JM, Stanley RJ. **A systematic guide to reviewing a manuscript.** *J Nuclear Med Technol* 2006;34:92–99
6. Callahan ML, Knopp RK, Gallagher EJ. **Effect of written feedback by editors on quality of reviews: two randomized trials.** *JAMA* 2002;287:2781–83
7. Rothwell PM, Martyn CN. **Reproducibility of peer review in clinical neuroscience: is agreement between reviewers any greater than would be expected by chance alone?** *Brain* 2000;123 (pt 9):1964–69
8. Armstrong JS. **Peer review for journals: evidence on quality control, fairness, and innovation.** *Sci Eng Ethics* 1997;3:63–84

EDITORIAL

Editorial Transition

M. Castillo, *Editor-in-Chief*

As many of our readers may know by now, we are terribly saddened by the passing of our colleague and Senior Editor, Dr Lucien Levy. Lucien brought with him considerable enthusi-



asm and knowledge regarding advanced neuroimaging and was a true gentleman. An obituary with details about his life is also published in this issue of the *American Journal of Neuroradiology* (*AJNR*).

We welcome Dr Jody Tanabe as our new Senior Editor in charge of advanced imaging. She is currently Professor of Radiology, Psychiatry, and Neurology at the University of Colorado, where she is also Chief of Neuroradiology. She was a radiology resident at Cornell Medical School, a neuroradiology fellow at the University of California, San Francisco, and, before moving to Denver, a neuroradiologist at New York University. Dr Tanabe's main areas of interest are neuroimaging of psychiatric and personality disorders and drug addiction, for which she has been awarded 7 NIH and foundation grants as principal investigator. She is a regular member of an NIH study section. Please join us here at *AJNR* in welcoming her; we are indeed lucky to have such a respected researcher to help us make our journal even better.

EDITORIAL

Human Neuroimaging and the BRAIN Initiative: A Joint Statement from the ASNR and ASFNR, with the support of the RSNA, ACR, ARR, and ISMRM

G. Sze, M. Wintermark, M. Law, P. Mukherjee, and C. Hess

The BRAIN Initiative (Brain Research through Advancing Innovative Neurotechnologies), launched by President Obama on April 1, 2013, and developed by the National Institutes of Health, is the much publicized potentially multidecade Presidential focus, seeking to “revolutionize our understanding of the human brain.” Its official charge is “to accelerate the development and application of innovative new technologies to construct a dynamic picture of brain function that integrates neuronal and circuit activity over time and space. The goal is to build on the growing scientific foundation of neuroscience, genetics, physics,

engineering, informatics, nanoscience, chemistry, mathematics, and other advances of the past few decades, to catalyze an interdisciplinary effort of unprecedented scope.” This exciting multi-agency initiative will span the next decade and include funding commitments from the National Science Foundation (\$20 million per year) and the Defense Advanced Research Programs Agency (\$50 million per year). It is important that it demonstrates early successes to convince the public that the funds committed to this project are well-spent tax dollars. Also, and perhaps more important, it is crucial to demonstrate to the public that this initiative will truly impact patient care and ultimately improve the well-being of the American people.

The American Society of Neuroradiology (ASNR), representing more than 5000 neuroradiologists and brain imaging scientists, with the support of the Radiological Society of North America (RSNA), representing over 51,000 members; the American College of Radiology (ACR), representing more than 36,000 members; the International Society of Magnetic Resonance in Medicine (ISMRM), representing more than 8000 members; and the Academy of Radiology Research (ARR), which serves as the overall science policy and advocacy voice for the academic imaging research community, believes that to achieve these goals, a number of approaches need to be pursued concurrently. One approach needs to focus on cellular models and neural circuits to better understand the functioning of the brain from the bottom up. This approach will require molecular studies; large-scale recording technologies; the use of nonhuman models, such as the connectome of *Drosophila*; and viral tracer or microbial techniques to look at neurons in animal models.

A simultaneous, parallel approach is necessary to study the brain from the top down, including brain mapping and circuits. Human neuroimaging is well poised to tackle this task. We, as human brain imagers, have developed a wealth of information concerning systems integration that can be used to effectively probe the complexities of brain structure. Keep in mind that the human brain is a system that contains 100 billion neurons, each with an average of 7000 connections or synapses to other elements, regulated by more than 100 excitatory and inhibitory sets of modulators or neurotransmitters. The magnitude of this anatomic complexity is difficult to even contemplate and will surely defy attempts for accurate characterization unless the problem can be simplified by using evidence derived from functional and anatomic pathways that the brain imaging community has accumulated through decades of research.

Neuroimaging is essential for the treatment of most diseases of the brain, from acute traumatic brain injury to stroke to brain tumors to multiple sclerosis, epilepsy, and so forth. Indeed, the developers of CT and MR imaging have been awarded separate Nobel Prizes, and these tools have become indispensable for neurologic and neurosurgical care. Recently, new advances in microstructural, functional, and molecular human brain imaging have opened the way for a revolution in terms of diagnosis, outcome prediction, and treatment mon-

itoring in even more disorders. These disorders cause great morbidity and mortality, from neurodevelopmental conditions, such as autism, to the psychiatric diseases of schizophrenia, depression, substance abuse, and so forth, to the neurodegenerative diseases, such as Alzheimer disease and Parkinson disease. These new advances include imaging human brain structural and functional connectivity as well as the development of new methods of visualizing pathology at the molecular level, such as chemical exchange saturation transfer, hyperpolarized ^{13}C MR imaging, PET with novel amyloid and τ agents, and so forth.

Both the bottom up and top down approaches will converge in the sense that both involve big data and will require specific developments in terms of computing, which has been defined as the third axis of the Initiative.

The community of brain imagers, encompassing ASNR, RSNA, ACR, ISMRM, and ARR, would like to volunteer its help and support for the human brain imaging component of the Initiative. We have the advantage that as physicians taking care of patients, we can garner public support for this multidecade funding push by demonstrating the advantages to the public of short-term health benefits, while at the same time developing longer term research goals. We have the resources and the structures necessary to facilitate large-scale collaborative efforts in terms of human brain imaging.

Once our understanding of healthy brain organization and function has advanced through this process, we as imagers and “brain health care providers” can apply this knowledge to further generate major breakthroughs in the medical management of patients with a wide variety of disorders that can afflict the human brain. We are also fortunate to have principal investigators of the Human Connectome Project and the ENIGMA consortium, a worldwide network of more than 200 imaging and genetic scientists at 125 institutions, leading translation of brain imaging and genomics into the clinic. Finally, our participation may alleviate the concerns of groups who monitor animal experiments closely.

In conclusion, as physicians and scientists taking care of patients and experts in brain imaging, we would like to pledge our support to the BRAIN Initiative and hope that we will be able to contribute to new programs that will both revolutionize our understanding of the brain and fundamentally impact the care of patients with neurologic disease.

CONTRIBUTORS

Bibb Allen, Kimberly Applegate, Ronald Arenson, Daniel Barboriak, Michael Brant-Zawadzki, Kenneth Cammarata, Renee Cruea, Burton Drayer, Richard Ehman, Paul Ellenbogen, Scott Faro, Christopher Filippi, Gary Glover, Clifford Jack, Peter Jezard, Michael Kalutkiewicz, Lucien Levy, Jonathan Lewin, David Mikulis, Carolyn Meltzer, Jeff Neil, Harvey Neiman, Alex Norbash, Todd Parish, Vijay Rao, Bruce Rosen, Donald Rosen, Kamil Ugurbil, Mark Watson, Kirk Welker, Ona Wu.

Lucien Maurice Levy

Dr Lucien Levy passed away December 19, 2013, peacefully at his home in Columbia, Maryland. News spread within hours to the entire George Washington University family, and the abruptness and shock of it quickly moved from the nation's capital to the world of neuroradiology, which mourns the loss of an exceptional colleague and friend.

Lucien completed his undergraduate studies at McGill University in 1967, after earning his electrical engineering degree with honors and continued at the Massachusetts Institute of Technology, studying under Dr William Daggett in the cardiovascular unit and earning a doctorate in biomedical and electrical engineering in 1973. Lucien completed a Doctor of Medicine degree at Johns Hopkins University in 1981 and a neuroimaging fellowship under Dr Giovanni DiChiro at the National Institutes of Health and became an attending radiologist at Hopkins under Dr Nick Bryan. Lucien's academic career continued in Washington, DC, as an attending radiologist at Georgetown University for 5 years and thereafter as Professor of Radiology at The George Washington University since 1999. Lucien's final publications "MR Imaging of Papilledema and Visual Pathways: Effects of Increased Intracranial Pressure and Pathophysiologic Mechanisms" (2013;34:919–24) and "Pseudotumor Cerebri: Brief Review of Clinical Syndrome and Imaging Findings" (2013;34:919–24) appeared in the *American Journal of Neuroradiology (AJNR)*. He served as a Senior Editor of *AJNR* since 2007 and was an Associate Editor of *Radiology* since 2009. During his tenure with *AJNR*, he proved to be a conscientious, acute, and fair editor. He took pride in his work and always offered new ideas. His breadth of knowledge was spectacular, and as Editor Emeritus of *AJNR*, Dr Robert Quencer once said, "One could learn more from reading Lucien's evaluations than from the actual articles he was reviewing."

Lucien loved teaching, and this attracted neuroradiology fellows who sought his mentorship to The George Washington University from as far away as India, Iraq, and Israel. Lucien continued to teach residents, fellows, and students during his brave fight with colon cancer. Last year, the George Washington radiology residents honored him with the Golden Apple



Award for teaching excellence, an award that he treasured. A few days before his passing, he was happy to hear the good news that all of his senior residents had passed the recent American Board of Radiology resident examination. Lucien will be remembered for his wit and humor. He had the knack of engendering smiles from all of those whom he mentored, even on the most mundane of subjects. All of us who knew Lucien had a rare opportunity to work with such a special, unassuming, quiet, and private man. He will be missed immensely in the reading room and by his *AJNR* colleagues, his family, his trainees, and all those who encountered him.

R.K. Tu
R. Bhojwani
R. Taheri
M. Monteferrante
A. Ahmad

Neuroradiology Section
 The George Washington University
 Washington, DC

<http://dx.doi.org/10.3174/ajnr.A3881>

Imaging Features of Rhinoplasty

C.J. Schatz and D.T. Ginat



ABSTRACT

SUMMARY: Cosmetic rhinoplasty encompasses a diverse group of procedures, including alteration of the radix, nasal dorsum, nasal tip, and nasal base; premaxillary augmentation; septoplasty; and combinations thereof. Similarly, many different types of grafts and alloplastic materials can be used in cosmetic rhinoplasty, such as cartilage, bone, silicone, porous polyethylene, expanded polytetrafluoroethylene, and calcium hydroxylapatite. Complications of rhinoplasty that can be observed on imaging include retained metallic surgical instrument fragments, infection, implant extrusion, nerve impingement by implants, nasal valve collapse, and implant deformity. Knowledge of the basic surgical procedures and potential complications of cosmetic rhinoplasty is important for adequately interpreting postoperative radiologic imaging studies.

ABBREVIATION: K-wires = Kirschner wires

Cosmetic rhinoplasty consists of surgically modifying portions of the nose to ameliorate its appearance, while maintaining its function. The procedure is the second most commonly performed cosmetic surgery, with 243,772 cases recorded in 2011 in the United States.¹ Thus, it is not uncommon to encounter the sequelae of rhinoplasty on head and neck imaging. The imaging characteristics of the different types of rhinoplasty, augmentation materials, and associated complications are reviewed.

Types of Surgery

Rhinoplasty can be performed for cosmetic or functional purposes. The surgery can be classified as primary (performed for the first time) or secondary (revision), in which patients return for additional surgery to address over-resection, under-resection, delayed effects of shrink-wrapping, functional problems, and other complications.²⁻⁵ Furthermore, rhinoplasty can be performed via external (open) or endonasal (closed) approaches. Ultimately, rhinoplasty encompasses a diverse group of procedures, including the following types of techniques:

- Radix modification consists of reduction versus augmentation (Fig 1). The radix is typically altered in harmony with the nasal dorsum and tip. A rasp or osteotome can be used for reduction, while various implants and grafts can be used for augmentation.^{2,6}
- Nasal dorsum surgery consists of dorsal hump reduction versus augmentation. Reduction surgery consists of excising excess osteocartilaginous septum by using a rasp or chisel.^{2,7} The resected tissue can sometimes then be used as a columella strut, tip graft, or for radix augmentation.² On the other hand, augmentation can be performed with autografts or alloplastic implants (Fig 2).
- Tip modification procedures include elevation by using a columellar strut, shield or tip grafts, volume reduction via cartilage trimming, and altering the definition and projection (Fig 3).⁷
- Nasal base surgery includes narrowing the wide columella, wedge resection, nostril sill resection, rim excision, alar reshaping with a graft, and columella excision or grafting.² Augmentation of the columella is often performed in conjunction with nasal dorsum augmentation and can be accomplished by using L-strut implants (Fig. 4)
- Lateral osteotomy consists of creating fractures of the nasal processes of the maxillae and shifting the lateral nasal walls to narrow a wide nose, widen a narrow bony pyramid, straighten a deviated nose, and close an open roof deformity.⁸ The osteotomy sites are initially visible on CT as radiolucent defects and perhaps mild displacement of the nasal processes (Fig 5). Osteotomies are sometimes performed as a greenstick-type frac-

From the Department of Radiology (C.J.S.), Beverly Tower Wilshire Advanced Imaging, University of Southern California Keck School of Medicine, Los Angeles, California; and Department of Radiology (D.T.G.), Massachusetts General Hospital, Harvard Medical School, Boston, Massachusetts.

Please address correspondence to Daniel T. Ginat, MD, MS, Massachusetts General Hospital, 55 Fruit St, Boston, MA 02114; e-mail: ginatd01@gmail.com

Indicates open access to non-subscribers at www.ajnr.org

<http://dx.doi.org/10.3174/ajnr.A3443>

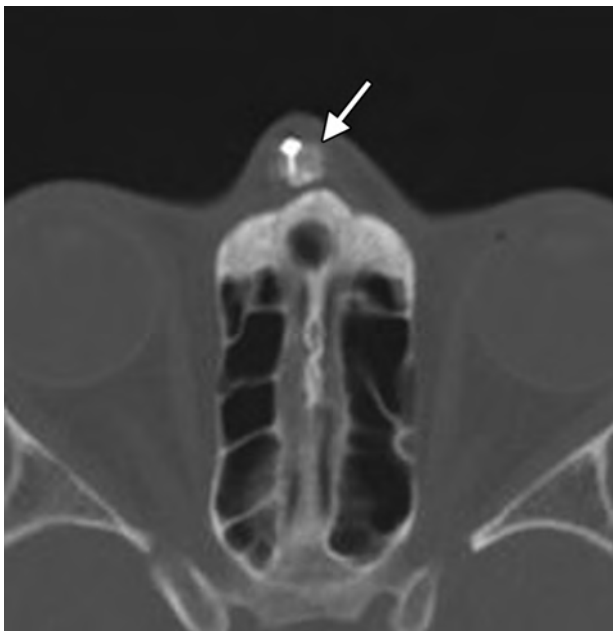


FIG 1. Radix implant. Axial CT image shows a bone graft positioned at the level of the nasal radix, secured by a metal plate and screws (arrow).



FIG 2. Dorsal nasal implant. Sagittal CT image shows a hyperattenuated expanded polytetrafluoroethylene nasal dorsum implant (arrow).

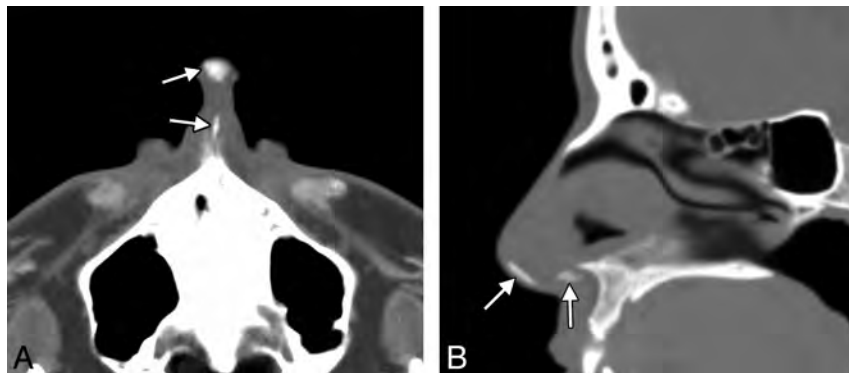


FIG 3. Tip augmentation with a columellar strut graft. Axial (A) and sagittal (B) CT images show hyperattenuated grafts within the infratip lobule and columella (arrows).

ture, resulting in stable bone stumps.⁹ The osteotomies generally heal by 6 months, and remodeling can be observed on CT.¹⁰

- Premaxillary augmentation can be performed as an adjunct to rhinoplasty to treat an excessively deep infranasal sulcus (premaxillary underprojection) and acute nasolabial angle. This can be accomplished by using autografts of implants positioned in the midline just inferior to the anterior nasal spine of the maxilla (Fig 6).^{11,12} The implants can have a linear or bat-wing configuration.¹²

Rhinoplasty can also be performed in conjunction with septoplasty for correcting concurrent nasal septal deviation (septorhinoplasty) and other cosmetic facial interventions to optimize esthetic balance.¹³ Septoplasty usually appears as a straight and thin septum without spurs on imaging (Fig 7).

Types of Graft and Implant Materials

A variety of materials are available for rhinoplasty, including autografts and alloplastic materials. Graft materials include bone and cartilage, which can be harvested from septal cartilage, auricular conchal cartilage, costal cartilage, calvarial bone, iliac crest bone, and costal bone and acellular dermal graft (AlloDerm; BioHorizons, Birmingham Alabama).¹⁴⁻¹⁷ “Turkish Delight” is a unique graft composed of diced cartilage mixed with a small amount of blood and wrapped in Surgicel (Ethicon, Raleigh North Carolina).¹⁸ Overgrafting is often intentionally performed with certain graft materials, especially AlloDerm, to compensate for eventual resorption and atrophy.¹⁴ However, cartilage transplanted with perichondrium has been shown to induce growth of new cartilage or bone.¹⁹ On CT, cartilage appears as soft-tissue attenuation, though calcification or ossification may form, rendering the graft hyperattenuated.²⁰ The cortex of bone grafts is hyperattenuated on CT, though the size and attenuation can diminish with time with resorption of the graft.²⁰ Bone grafts may contain marrow elements, which have soft-tissue attenuation on CT and can display fat signal characteristics on MR imaging.²⁰

Alloplastic implants used in facial cosmetic surgery include silicone (Silastic; Dow Corning, Auburn, Michigan), polyamide mesh (Supramid; S. Jackson, Alexandria, Virginia), polyethylene tetraphthalate mesh (Mersilene; Ethicon), expanded polytetrafluoroethylene (Gore-Tex; W.L. Gore & Associates, Newark, Delaware), and high-attenuation porous polyethylene (Med-

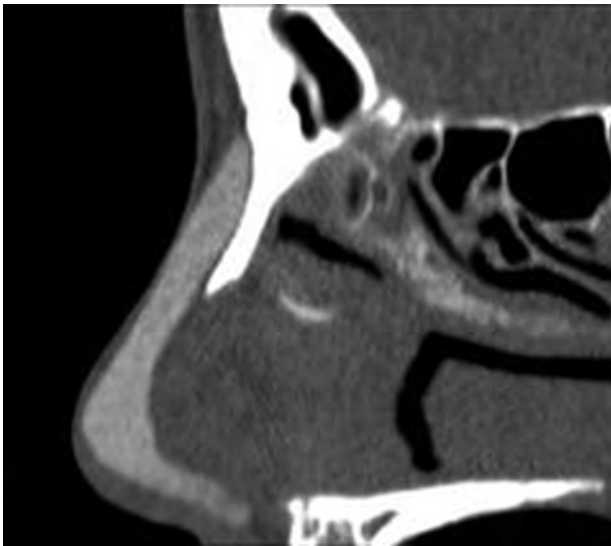


FIG 4. Silicone L-strut implant. Sagittal CT image shows the hyperattenuated L-shaped Silicone implant extending from the nasal dorsum to the columella.

por; Stryker, Mahwah, New Jersey).^{14,21-25} Silicone and expanded polytetrafluoroethylene are similarly hyperattenuating, intermediate in attenuation between soft tissue and bone.²⁰ On the other hand, high-attenuation porous polyethylene is hypoattenuating with attenuation intermediate between soft tissue and fat, and it has intermediate signal on T1 and T2 MR imaging sequences.²⁰ The material can appear to enhance due to fibrovascular in-growth.

Filler agents, such as calcium hydroxylapatite (Radiesse; Merz Aesthetics, San Mateo, California), can be used for minimally invasive cosmetic rhinoplasty or to modify prior rhinoplasty.^{26,27} The fillers can be injected by using a linear, threading, fanning, or cross-hatching technique.²⁷ Calcium hydroxylapatite displays high attenuation on CT (Fig 8).²⁸

Metallic Kirschner wires can be used for restoration of an im-

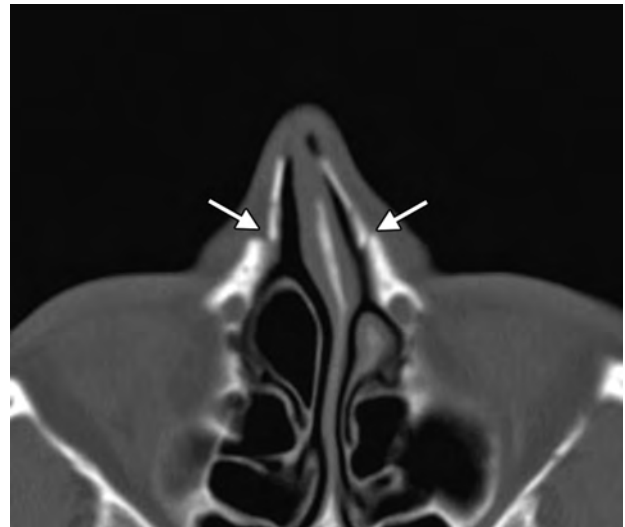


FIG 5. Lateral osteotomy. Axial CT image shows defects in the bilateral nasal processes of the maxillae (arrows). The lateral nasal walls are displaced medially (in-fractures).

packed nasal pyramid, fixation of intraoperative nasal septum fractures, and stabilization of costal cartilage grafts.²⁹⁻³¹ K-wires can be implanted in the nasal dorsum, columella, or both because in an L-strut configuration, a wire is positioned along the dorsum (Fig 9). The columellar K-wires are typically inserted into a maxillary drill hole in the area of the nasal spine, adjacent to the incisive canal.

Complications

Complications of rhinoplasty that can be found on imaging include retained metallic surgical instrument fragments, infection, implant extrusion, cranial nerve impingement by implants, nasal valve collapse, and implant deformity.²¹

Surgical paraphernalia used in rhinoplasty are rarely retained during surgery. This can occur, for instance, as a result of os-

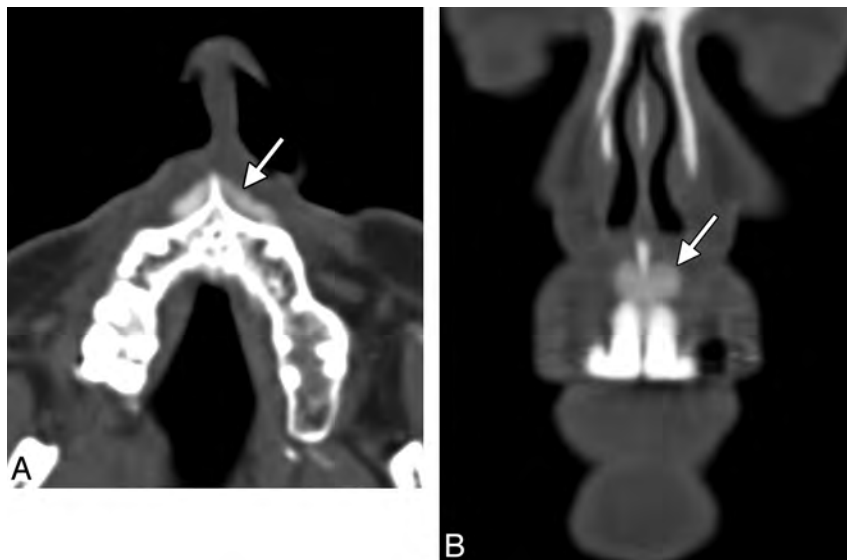


FIG 6. Premaxillary implant. Axial (A) and coronal (B) CT images show a hyperattenuated strip of silicone (arrows) positioned in the midline anterior to the nasal spine of the maxilla.



FIG 7. Septorhinoplasty. Axial CT image shows a very straight and thin nasal septum (*arrowheads*). A bone graft is present within the nasal dorsum (*arrow*).

teotome breakage during nasal osteotomy, leaving behind a fragment that can be difficult to find intraoperatively. However, ra-

diographs can readily confirm and localize retained metallic foreign bodies (Fig 10).

Infection is the most common objective complication of rhinoplasty and can occur early or late postoperatively.³² This complication is more common with alloplastic implants than autografts.¹⁴ The postoperative infections most often remain localized to the skin and subcutaneous tissues of the nose but occasionally extend intracranially or result in generalized septicemia.³² MR imaging or CT can be used to delineate the extent of infections, which can appear as fluid collections, sclerosis and enhancement of osseous structures, and soft-tissue inflammatory changes (Fig 11). Infection predisposes to skin ulceration and implant extrusion (Fig 12).^{33,34}

Lip dysesthesia can occur after certain types of rhinoplasty, but this is expected to resolve within 6 weeks without functional sequelae.³⁵ However, inadvertent drilling and insertion of columellar K-wires into the incisive canal can lead to dysesthesia in the distribution of the nasopalatine nerve. This complication can be observed on CT (Fig 13).

Various types of deformities have been described following cosmetic rhinoplasty, including nasal valve collapse, inverted-V deformity, saddle nose deformity, open roof, stairstep deformity,



FIG 8. Rhinoplasty with filler. Axial (A) and coronal (B) CT images show hyperattenuated hydroxylapatite filler (*arrows*) to the right of the Silastic nasal dorsum implant. Note the deviated nasal septum.

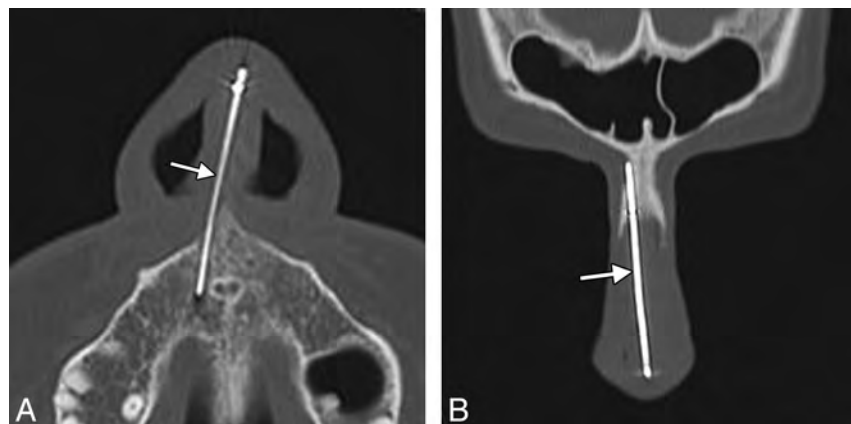


FIG 9. Kirschner wire strut. Axial (A) and coronal (B) CT images show a metallic wire (*arrow*) extending along the nasal dorsum and nasal base, where it inserts into the maxilla, lateral to the incisive canal.

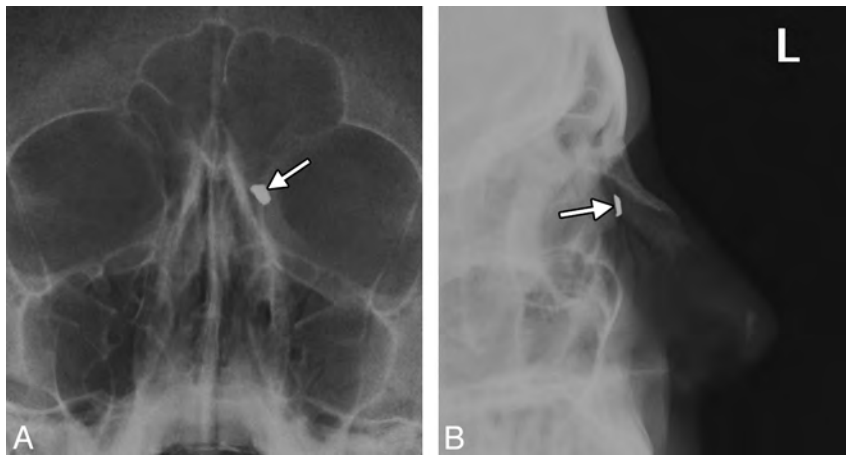


FIG 10. Retained osteotome fragment. Frontal (A) and lateral (B) radiographs show the retained metallic fragment (arrows) at the left lateral osteotomy site. Note the nasal-tip bone graft.

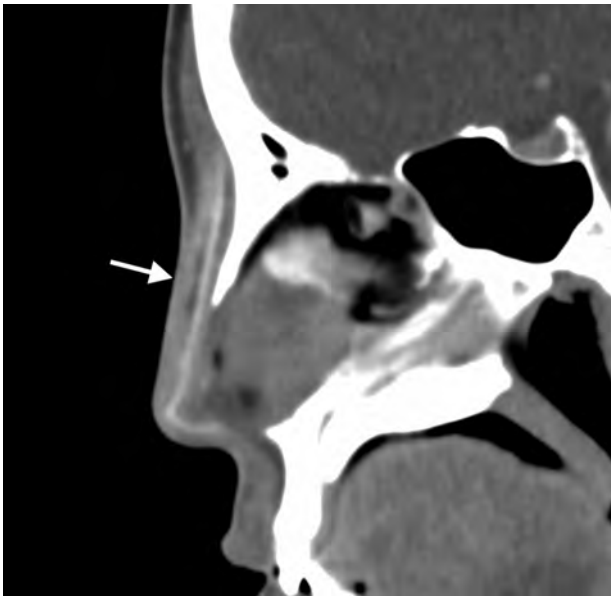


FIG 11. Implant infection. Sagittal postcontrast CT image shows a small fluid collection and associated inflammatory changes (arrow) in the nasal dorsum surrounding the implant.

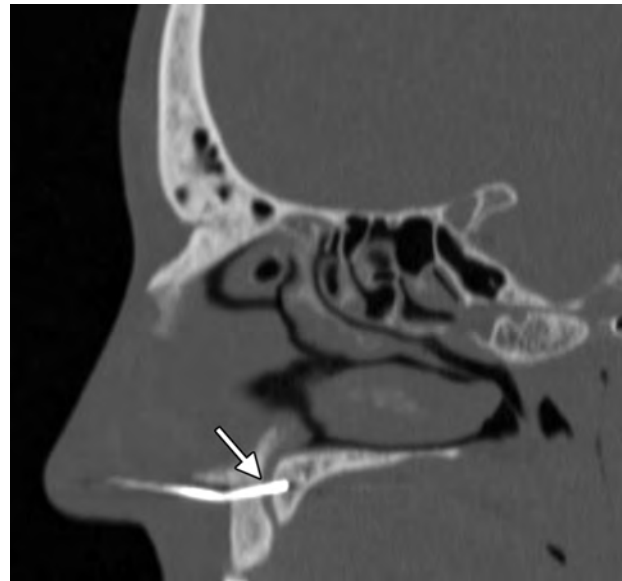


FIG 13. Nerve impingement. The patient presented with dysesthesias in the maxillary nerve distribution after rhinoplasty. Sagittal CT image shows that the K-wire traverses the incisive canal at the expected location of the nasopalatine nerve (arrow).



FIG 12. Implant extrusion. Sagittal CT image shows a porous polyethylene dorsal nasal implant (arrow) projecting through a cutaneous defect.



FIG 14. Deformed K-wire. The patient presented with trauma to the nose. Submentovertex radiograph shows a bend in the K-wire (arrow).

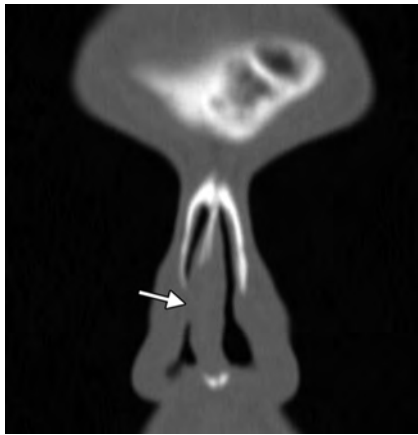


FIG 15. Nasal valve collapse. Coronal CT image shows stenosis of the right nasal valve (arrow). The left nasal valve remains patent.

hourglass deformity following dorsal hump surgery, and shrink-wrap effect of the soft tissues after nasal tip surgery.^{13,36-38} Postoperative deformity can also result from warping of grafts, particularly undiced cartilage grafts.³⁹ Furthermore, trauma can compromise the structural integrity and alignment of grafts and implants (Fig 14).

Postoperative nasal valve collapse can lead to dynamic or static obstruction and is evidenced by a decreased nasal valve angle, which is normally 10°-15°.^{36,38,40} The nasal valve angle can be more reliably determined on CT than via endoscopic methods (Fig 15).⁴¹ Furthermore, nasal-base-view reformatted CT images obtained in a plane perpendicular to the anterior aspect of the estimated acoustic axis are more accurate than traditional coronal CT images for measuring nasal valve angles.⁴⁰ Spreader grafts and suture techniques, splay grafts, alar batten grafts, lateral crural extension grafts, and lateral alar suspension can be used to correct this deformity.^{13,42}

CONCLUSIONS

A wide variety of techniques and augmentation materials are used for cosmetic rhinoplasty. Familiarity with the expected alterations, and complications from rhinoplasty is essential for satisfactory interpretation of postoperative imaging.

Disclosures: Charles Schatz—UNRELATED: Expert Testimony: various attorneys, Comments: 2-3 times per year, no conflict of interest, Stock/Stock Options: unrelated investments/retirement plan.

REFERENCES

- 2011 Cosmetic Plastic Surgery Statistics. American Society of Plastic Surgeons. <http://www.plasticsurgery.org/Documents/news-resources/statistics/2011-statistics/2011-cosmetic-procedures-trends-statistics.pdf>. Accessed September 1, 2012
- Bagheri SC. **Primary cosmetic rhinoplasty.** *Oral Maxillofac Surg Clin North Am* 2012;24:39-48
- Bagheri SC, Khan HA, Jahangirnia A, et al. **An analysis of 101 primary cosmetic rhinoplasties.** *J Oral Maxillofac Surg* 2012;70:902-09
- Cuzalina A, Qaqish C. **Revision rhinoplasty.** *Oral Maxillofac Surg Clin North Am* 2012;24:119-30
- Bracaglia R, Fortunato R, Gentileschi S. **Secondary rhinoplasty.** *Aesthetic Plast Surg* 2005;29:230-39
- Steiger JD, Baker SR. **Nuances of profile management: the radix.** *Facial Plast Surg Clin North Am* 2009;17:15-28, v
- Cervelli V, Bottini DJ, Gentile P. **Reconstruction of the nasal tip.** *J Craniofac Surg* 2007;18:1380-84
- Bohluli B, Moharamnejad N, Bayat M. **Dorsal hump surgery and lateral osteotomy.** *Oral Maxillofac Surg Clin North Am* 2012;24:75-86
- Giacomarra V, Russolo M, Arnez ZM, et al. **External osteotomy in rhinoplasty.** *Laryngoscope* 2001;111:433-38
- Daniel RK, Ethier R. **Rhinoplasty: a CT-scan analysis.** *Plast Reconstr Surg* 1987;80:175-84
- Kim WS, Kim CH, Yoon JH. **Premaxillary augmentation using autologous costal cartilage as an adjunct to rhinoplasty.** *J Plast Reconstr Aesthet Surg* 2010;63:e686-90
- Kim WS, Kim CH, Yoon JH. **Premaxillary augmentation using autologous costal cartilage as an adjunct to rhinoplasty.** *J Plast Reconstr Aesthet Surg* 2010;63:e686-90
- Waite PD. **Internal septorhinoplasty technique.** *Oral Maxillofac Surg Clin North Am* 2012;24:109-17
- Dresner HS, Hilger PA. **An overview of nasal dorsal augmentation.** *Semin Plast Surg* 2008;22:65-73
- Brenner MJ, Hilger PA. **Grafting in rhinoplasty.** *Facial Plast Surg Clin North Am* 2009;17:91-113, vii
- Gentile P, Cervelli V. **Nasal dorsum reconstruction with 11th rib cartilage and auricular cartilage grafts.** *Ann Plast Surg* 2009;62:63-66
- Bottini DJ, Gentile P, Donfrancesco A, et al. **Augmentation rhinoplasty with autologous grafts.** *Aesthetic Plast Surg* 2008;32:136-42
- Erol OO. **The Turkish delight: a pliable graft for rhinoplasty.** *Plast Reconstr Surg* 2000;105:2229-41, discussion 2242-43
- Breadon GE, Kern EB, Neel HB 3rd. **Autografts of uncrushed and crushed bone and cartilage: experimental observations and clinical implications.** *Arch Otolaryngol* 1979;105:75-80
- Schatz CJ, Ginat DT. **Imaging of cosmetic facial implants and grafts.** *AJNR Am J Neuroradiol* 2013;34:1674-81
- Conrad K, Torgerson CS, Gillman GS. **Applications of Gore-Tex implants in rhinoplasty reexamined after 17 years.** *Arch Facial Plast Surg* 2008;10:224-31
- Skouras A, Skouras G, Karypidis D, et al. **The use of Medpor alloplastic material in rhinoplasty: experience and outcomes.** *J Plast Reconstr Aesthet Surg* 2012;65:35-42
- Inanli S, Sari M, Baylancicek S. **The use of expanded polytetrafluoroethylene (Gore-Tex) in rhinoplasty.** *Aesthetic Plast Surg* 2007;31:345-48
- Erlich MA, Parhiscar A. **Nasal dorsal augmentation with silicone implants.** *Facial Plast Surg* 2003;19:325-30
- Berghaus A, Stelter K. **Alloplastic materials in rhinoplasty.** *Curr Opin Otolaryngol Head Neck Surg* 2006;14:270-77
- Humphrey CD, Arkins JP, Dayan SH. **Soft tissue fillers in the nose.** *Aesthet Surg J* 2009;29:477-84
- Siclovian HR, Jomah JA. **Injectable calcium hydroxylapatite for correction of nasal bridge deformities.** *Aesthetic Plast Surg* 2009;33:544-48
- Ginat DT, Schatz CJ. **Imaging features of midface injectable fillers and associated complications.** *AJNR Am J Neuroradiol* 2013;34:1488-95
- Murphy J, Marshall AH, Jones NS. **Restoration of the impacted nasal pyramid using a Kirschner wire.** *J Laryngol Otol* 2004;118:543-45
- Gunter JP, Cochran CS. **Management of intraoperative fractures of the nasal septal "L-strut": percutaneous Kirschner wire fixation.** *Plast Reconstr Surg* 2006;117:395-402
- Sarifakioglu N, Cigsar B, Aslan G. **K-wire: a simple and safe method for internal stabilization of costal cartilage in L-strut grafts.** *Ann Plast Surg* 2002;49:444
- Barat M, Shikowitz MJ. **Nasofrontal abscess following rhinoplasty.** *Laryngoscope* 1985;95:1523-25
- Graham BS, Thiringer JK, Barrett TL. **Nasal tip ulceration from infection and extrusion of a nasal alloplastic implant.** *J Am Acad Dermatol* 2001;44:362-64
- Herbst A. **Extrusion of an expanded polytetrafluoroethylene implant after rhinoplasty.** *Plast Reconstr Surg* 1999;104:295-96
- Bravo FG, Schwarze HP. **Closed-open rhinoplasty with extended lip**

- dissection: a new concept and classification of rhinoplasty.** *Plast Reconstr Surg* 2008;122:944–50
36. Sykes JM, Tapias V, Kim JE. **Management of the nasal dorsum.** *Facial Plast Surg* 2011;27:192–202
37. Lam SM, Williams EF 3rd. **Anatomic considerations in aesthetic rhinoplasty.** *Facial Plast Surg* 2002;18:209–14
38. Araco A, Gravante G, Gentile P, et al. **Iatrogenic collapse of the nasal valve after aesthetic rhinoplasty.** *Scand J Plast Reconstr Surg Hand Surg* 2007;41:293–96
39. Holt GR, Garner ET, McLarey D. **Postoperative sequelae and complications of rhinoplasty.** *Otolaryngol Clin North Am* 1987;20:853–76
40. Poetker DM, Rhee JS, Mocan BO, et al. **Computed tomography technique for evaluation of the nasal valve.** *Arch Facial Plast Surg* 2004;6:240–43
41. Suh MW, Jin HR, Kim JH. **Computed tomography versus nasal endoscopy for the measurement of the internal nasal valve angle in Asians.** *Acta Otolaryngol* 2008;128:675–79
42. Fischer H, Gubisch W. **Nasal valves—importance and surgical procedures.** *Facial Plast Surg* 2006;22:266–80

Illustrated Review of the Embryology and Development of the Facial Region, Part 3: An Overview of the Molecular Interactions Responsible for Facial Development

P.M. Som, A. Streit, and T.P. Naidich



ABSTRACT

SUMMARY: Parts 1 and 2 of this review discussed the complex morphogenesis of the face. However, the molecular processes that drive the morphology of the face were not addressed. Part 3 of this review will present an overview of the genes and their products that have been implicated in the developing face.

ABBREVIATIONS: *BMP* = bone morphogenic protein; *Fgf* = fibroblast growth factor; *PDGF* = platelet-derived growth factor; *Shh* = sonic hedgehog; *TGFβ* = transforming growth factor β

Parts 1 and 2 of this review discussed the complex morphogenesis of the face from the earliest closure of the anterior neuropore through the embryologic and fetal facial development to the changes that occur in the facial structure from the neonate to the adult. However, the topic of molecular processes that drive the morphology of the face is ever-emerging in complexity and is mostly foreign to our understanding. Yet, this molecular biology is the basis of vertebrate facial embryology. Part 3 of this review will present an overview of the genes and their products that have been implicated in the developing face. The major source of information regarding these genes comes from experiments that knockout or reduce or, in some cases, increase their presence in specific cell populations at differing times in early embryogenesis. The resulting morphologic changes are then observed. Although these genes can be implicated in facial development, their precise activation pathways and interactions remain mostly unclear. One of the most intriguing aspects of the present research in this field is that it is changing the traditional concepts of early craniofacial embryogenesis.

Complex Multistep Process

The dynamics of facial development is a multistep process that initiates with the creation of neural crest cells and prechordal mesenchyme, the migration of these cells, their epithelial-mesen-

chymal interactions that control growth, their patterning as they are allocated different cell fates while existing in a field of equivalent cells, the appearance of the facial primordia, and finally the subsequent development of the face. It is the presence of specific genes and the signaling of their gene products that coordinate this growth of the face.

The craniofacial development is unique from the rest of the body. First, the cranial neural crest cells give rise to skeletal structures unlike neural crest cells in the rest of the body. Second, with the exception of the tongue, which is formed from segmented somites as are the remaining muscles in the body, the craniofacial muscles are formed from prechordal mesenchyme and unsegmented paraxial mesoderm.^{1,2} The prechordal mesenchyme arises from the prechordal plate immediately anterior to the tip of the anterior notochord. Francis-West et al¹ in their detailed review of craniofacial development said, “The prechordal plate is the head organizer region. It lies directly under the developing forebrain and is essential for normal dorsal-ventral patterning of the brain and the subsequent appropriate development of the midline face” (Fig 1). Last, the craniofacial region has neurogenic placodes that are present only in the craniofacial region. These placodes give rise to the lens; inner ears; the olfactory epithelium; and neurons in the trigeminal, facial, glossopharyngeal, and vagal ganglia (epibranchial placodes).³

Early Development of the Craniofacial Region

In the early second embryonic week, the embryoblast begins to differentiate into 2 different cell layers. The epiblast layer develops first, and most of these cells will remain in this layer to become the embryo proper. In the late second to early third embryonic week, a new layer of cells begins to emerge underneath the epiblast (Fig 2), the hypoblast (or primitive endoderm). The hypoblast will

From the Department of Radiology (P.M.S., T.P.N.), Mount Sinai School of Medicine, New York University, New York, New York; and Department of Craniofacial Development and Stem Cell Biology (A.S.), King's College London, Guy's Campus, London, UK.

Please address correspondence to Peter M. Som, MD, Department of Radiology, The Mount Sinai Hospital, One Gustave Levy Place, New York, NY 10029; email: Peter.Som@MSSM.edu

Indicates open access to non-subscribers at www.ajnr.org

<http://dx.doi.org/10.3174/ajnr.A3453>

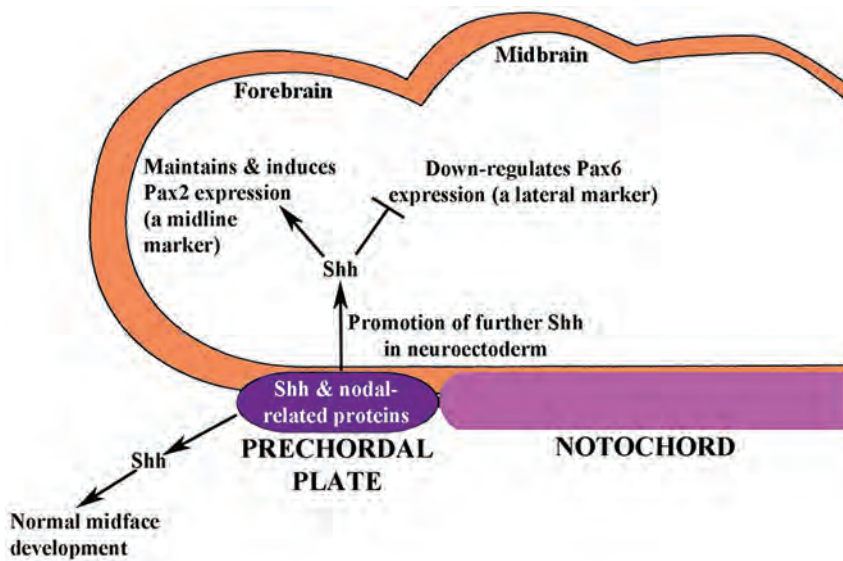


FIG 1. Sagittal diagram shows the craniofacial region and the relationship of the prechordal plate to the ventral notochord. Also shown is some of the signaling that originates in the prechordal plate to influence the optic field division and some of the signaling for normal midfacial development. (Modified from Fig 3, Francis-West PH, Robson L, Evans DJ. Craniofacial development: the tissue and molecular interactions that control development of the head. *Adv Anat Embryol Cell Biol* 2003;169:III-VI, 1–138. With permission from Springer Science+Business Media.)

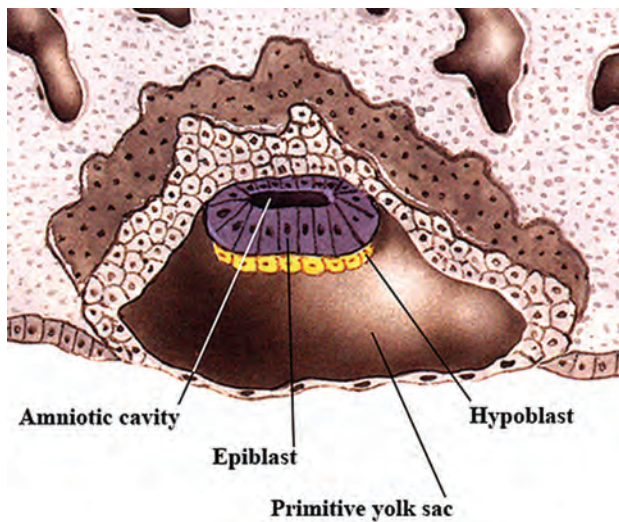


FIG 2. Sagittal drawing of a late 2-week-old embryo showing the embryonic disk with an epiblast layer and a the hypoblast below it. This is the bilaminar embryo just before gastrulation. (Modified with permission from Netter Illustration from www.netterimages.com. Elsevier Inc. © All rights reserved.^{16,17})

generate extraembryonic tissues, and one of its initial roles is to inhibit primitive streak formation. This early inhibition prevents future mesodermal cells (cells that can give rise to both endoderm and mesoderm) from premature ingress (migration) below the epiblast layer, while ensuring that future ectodermal cells remain in the epiblast and do not ingress at all. In addition, this early inhibition helps to separate mesodermal and neuroectodermal cells (cells that will eventually give rise to the central and peripheral nervous systems); the hypoblast also transiently induces expression of preneural markers in the epiblast. Next, in the

early third week, the hypoblast controls epiblast cell movement that leads to the formation of the primitive streak, the first obvious morphologic feature that develops in the embryonic disk.⁴ The presence of the primitive streak establishes bilateral symmetry in the embryo and marks the site of gastrulation, which is the process by which the hypoblast forms only extraembryonic tissues and the epiblast layer is converted into a trilaminar disk with all 3 germ layers. Shortly after the primitive streak is first visible, the primitive groove appears along its midline (Fig 3A).

Soon after primitive streak formation, the primitive node arises at its anterior end along with the primitive pit, a depression developing along the dorsal aspect of the node, which is continuous posteriorly with the primitive groove (Fig 3B). “Ingression” is the movement of cells through the primitive streak: Starting in the mid-third week, epiblast cells move into the streak and fan outward to become mesoderm or endoderm under the epiblast.

Cells ingressing at different positions along the anteroposterior length of the streak contribute to different mesodermal tissues. Those cells that migrate anteriorly via the primitive pit in the midline will form the axial mesoderm, the prechordal plate, and notochord (Fig 4). Precursors for both structures are initially intermixed but segregate eventually. Cells that ingress in the lateral node also participate in notochord formation and contribute to the medial portions of the somites (the paraxial mesoderm), while cells ingressing just posterior to the node form the lateral somites. Cells that move through the more posterior parts of the streak form the intermediate, lateral plate, and extraembryonic mesoderm, respectively. Thus, mesodermal cells with different ultimate fates are organized along the anteroposterior axis of the primitive streak: Axial precursors lie at its most rostral end, and lateral precursors, caudally. Once the primitive streak has reached its full length, it begins to regress posteriorly while ingression continues, and in its wake, it lays down the body axis. The primitive node is eventually absorbed into the tail bud.

As gastrulation occurs, the neural plate is induced by signals from the primitive node. Its appearance is the first morphologic manifestation of the forming central nervous system, and during neurulation, it will eventually form the neural tube and give rise to the brain and spinal cord.

In summary, during gastrulation, a trilaminar disk is formed with the epiblast cells that remain at the surface becoming the ectoderm, cells that ingress and replace the hypoblast becoming the endoderm, and the cells between these layers becoming the mesoderm. Table 1 gives an overview of events that lead to the formation of the trilaminar embryo. However, most of these processes are fluid and merge into each other, and some happen at the same time. After gastrulation, the remains of the hypoblast may protect some prospective forebrain cells from caudalizing signals,

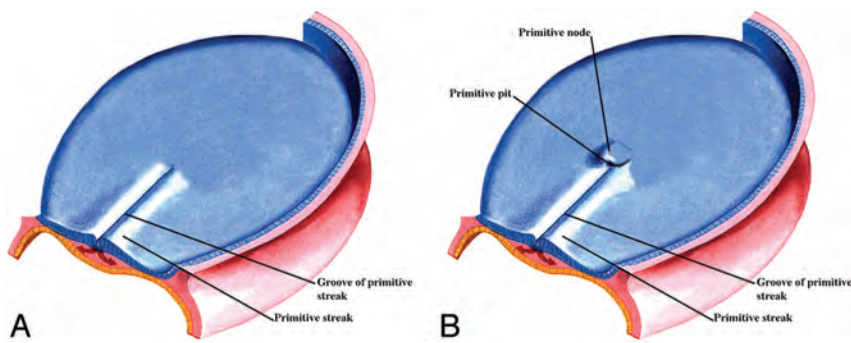


FIG 3. A, Oblique view from above of an early 3-week embryo shows the appearance of the primitive streak. Within the center of the primitive streak, a groove develops. Modified with permission from Cochard¹⁷ and Netter et al.¹⁸ B, Oblique view from above of an embryo a few days older than that in Fig 3A shows the development of the primitive node and the primitive pit at the ventral margin of the primitive streak. (Modified with permission from Netter Illustration from www.netterimages.com. Elsevier Inc. © All rights reserved.^{16,17})

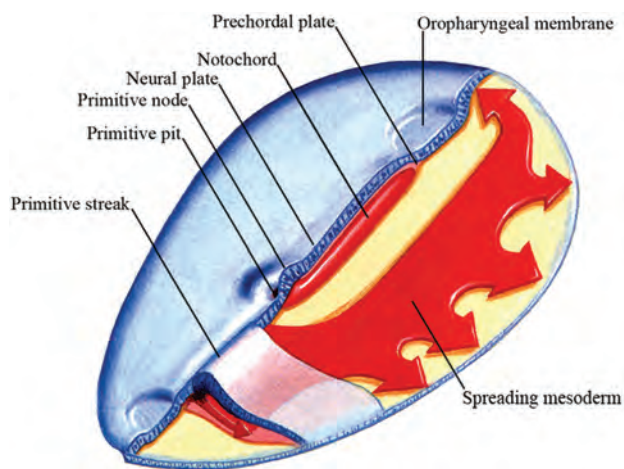


FIG 4. Oblique view from above of an embryo slightly older than that in Fig 3B showing the relative relationship of the neural plate, prechordal plate and notochord, primitive streak, and primitive node. Also shown is the mesoderm spreading out under the epiblast. (Modified with permission from Netter Illustration from www.netterimages.com. Elsevier Inc. © All rights reserved.^{16,17})

Table 1: Summary of the order of development of the trilaminar embryonic disk

Order
Epiblast
↓
Hyoblast (future extraembryonic tissue develops under epiblast)
↓
Primitive streak: marks beginning of gastrulation
↓
Primitive groove
↓
Primitive node with primitive pit
↓
Neural plate forms (induced by primitive node)
↓
Ingression of epiblast cells to form endoderm and mesoderm
↓
Trilaminar embryonic disk formed
↓
Primitive streak starts to regress
↓
Primitive node absorbed into tail bud

which would otherwise confer a posterior identity to neural tissue to generate mid-brain or hindbrain.

Formation of the Placodes

The placode precursors are induced at the edge of the anterior neural plate and then segregate into the cells with individual placode identities. By early gastrulation, this ectodermal border zone expresses both neural and non-neural markers. Within this zone, precursors for 4 cell populations—neural, neural crest, epidermal, and placode cells—are initially intermingled but segregate later through patterning events (Fig 5). With respect to placode formation, members of the *Six* and *Eya* families of nuclear

factors are key players and become expressed in this border zone, where the precursors for all placodes become concentrated. This region is now called the “preplacodal territory” or “zone.” Although the cells in the preplacodal zone are initially competent to form any placode, soon the placode precursors seem to acquire different regional characteristics as evidenced by differential gene expression. For example, *Pax6*, *Six3*, and *Otx2* are confined to anterior placode cells, while *Irx1/2/3* and *Gbx2* are found posteriorly. By the early somite stage, *Pax6* is concentrated in the cells that will give rise to the olfactory and lens placodes, while *Pax3* and *Pax2/8* are located in cells that will develop into the trigeminal, otic, and epibranchial placodes, respectively.⁵

In the early border zone, the decision of the multipotential cells to evolve into either neural crest cells or preplacodal cells is controlled by modulation of signals from the surrounding tissues. As discussed in the next paragraphs, signals from the head mesoderm provide antagonists to both *BMP* and *Wnt* that protect placode precursors from inhibitory influences, allowing them to develop. However, signals from the neural folds trigger neural crest development, and unlike the preplacodal zone, interaction between the neural plate and the ectoderm is sufficient to induce neural crest cells.⁶

During gastrulation, *BMPs* induce a set of factors that make the ectoderm competent to become placode precursors. In this context, competence means that a tissue can respond to an inducing signal from outside the cell, causing it to change its fate. These competence factors are important for the expression of *Six* and *Eya* genes as discussed above. Shortly thereafter *BMP* signaling must be completely blocked (during the late second and early third weeks) by antagonists to induce preplacodal rather than neural crest identity in cells bordering the neural plate.⁶ This blocking is important because the preplacodal zone is surrounded by inhibitory signals from the ectoderm laterally (*BMP*) and posteriorly (*Wnt*), from the neural folds medially (*Wnt* and *BMP*), and from the lateral and posterior mesoderm (*Wnt*). Both *Wnt* and *BMP* antagonists from the mesoderm underlying the preplacodal region protect the overlying ectoderm from these inhibitory signals, allowing the formation of the placodal precursors.⁵ Once placode precursors have formed, members of the *fibroblast growth factor* family of signaling molecules together with other signals play an important role, causing the emer-

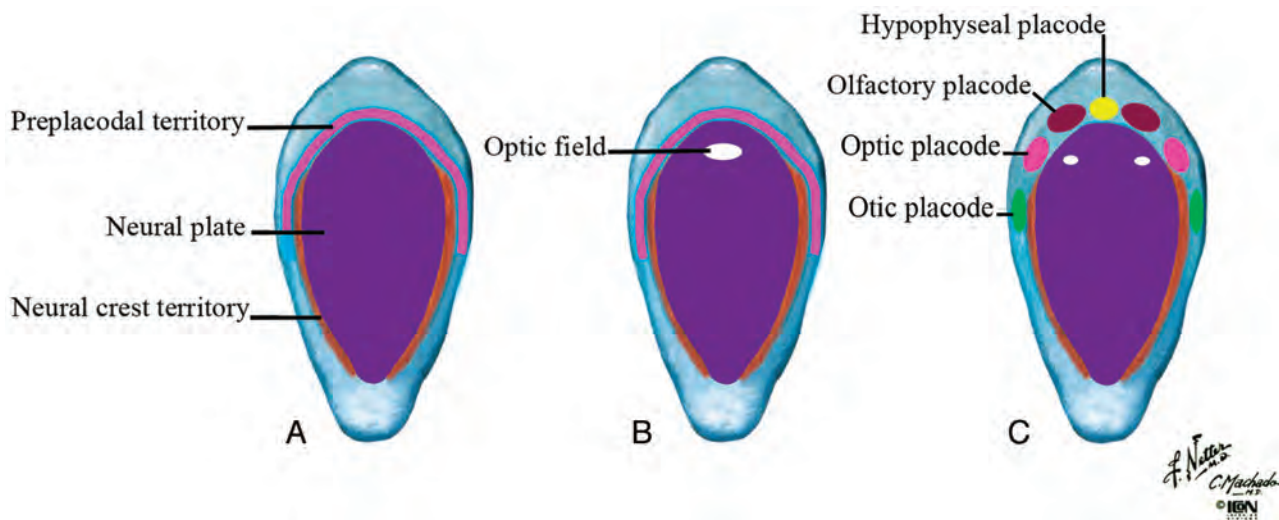


FIG 5. A, Location of the preplacodal territory and (B) the region around the anterior neural plate. The optic field develops to eventually be divided by signals from the prechordal plate. C, The placodes have separated from the preplacodal territory. (Modified with permission from Netter Illustration from www.netterimages.com. Elsevier Inc. © All rights reserved.^{16,17})

Table 2: Summary of the order of development of the placodes

Order
Early in gastrulation, ectodermal cells around the future neural plate express both neural and non-neural markers
↓
<i>Six</i> and <i>Eya</i> nuclear markers begin to be expressed after neural plate formation at its border; precursors for all placodes concentrate in the <i>Six</i> - and <i>Eya</i> -expressing territory
↓
<i>Pax6</i> , <i>Six3</i> , <i>Otx2</i> expression is concentrated anteriorly <i>Irx1/2/3</i> , <i>Gbx2</i> expression is concentrated posteriorly
↓
Signaling molecules (including <i>Fgfs</i>) from surrounding tissue induce the formation of the individual placodes

Table 3: Factor and receptor families known to play roles in placode induction

Placode	Inducer Families					
Adenohypophysis	<i>FGF</i>	<i>PDGF</i>	RA	<i>Shh</i>	<i>TGFβ</i> family	<i>Wnt</i> ^a
Lens	<i>FGFR</i>			<i>Shh</i>	Nodal, <i>BMP4</i>	
Olfactory	<i>FGF</i>				<i>BMP4</i> , <i>BMP7</i>	
Otic	<i>FGFR</i>					<i>Wnt</i>
	<i>FGF</i>					
Epibranchial (VII, IX, X)	<i>FGFR</i>					
Trigeminal	<i>FGF</i>	<i>PDGF</i>				<i>Wnt</i>
		<i>PDGFR</i>				

Note:—RA indicates retinoic acid; *PDGFR*, platelet-derived growth factor receptor; *FGFR*, fibroblast growth factor receptor; *PDGF*, platelet-derived growth factor.

^a Modified from Table 2 in McCabe KL, Bronner-Fraser M. Molecular and tissue interactions governing induction of cranial ectodermal placodes. *Dev Biol* 2009;332:189–95, Elsevier Inc. © All rights reserved.³

gence of the individual placodes. Different members of the family are responsible for inducing unique characteristics of each placode from the preplacodal territory.⁵ Table 2 summarizes the events that lead to the formation of the placodes, and Table 3 shows the current understanding of the factors and receptors that are implicated in induction of the placodes.

Craniofacial Development and Normal Neural Development

Current thinking is that initially there are common precursors for the central nervous system, neural crest, and the placodes. With

time, these precursors are exposed to different signals and they acquire distinct characteristics. Thus, the embryonic development of the craniofacial region is dependent on normal neural development. Thus, rostral-caudal patterning abnormalities of the neural crest will cause facial abnormalities because this neural crest gives rise to facial skeletal structures and the connective tissues of the face. Signaling from the prechordal plate mesoderm is required for normal development of the ventral diencephalon, which divides the eye (retinal) field into 2 components⁷—that is, prechordal plate signaling promotes *Pax2* and inhibits *Pax6* expression to promote division of the single optic field. One of the key signals mediating this process is *Shh*, which is expressed in the axial mesoderm and the prechordal plate. It promotes *Pax2* and inhibits *Pax6* expression (Fig 1).⁸ If prechordal signaling is interrupted, a single midline eye is formed and there is a resulting cyclops (Fig 5). The neural crest and its related gene products are also essential

for normal patterning of the craniofacial region.

Initially the developing face consists of the medial and lateral maxillary processes that together will form the upper jaw and the mandibular processes that will give rise to the lower jaw. The mesenchymal cells that form these processes are of neural crest origin. It is the coordinated outgrowth of these primordia and their ultimate fusion that is essential for the development of a normal face. In the beginning, these primordia consist of undifferentiated neural crest–derived mesenchyme covered by a layer of ectoderm. The control of these outgrowths is by epithelial-

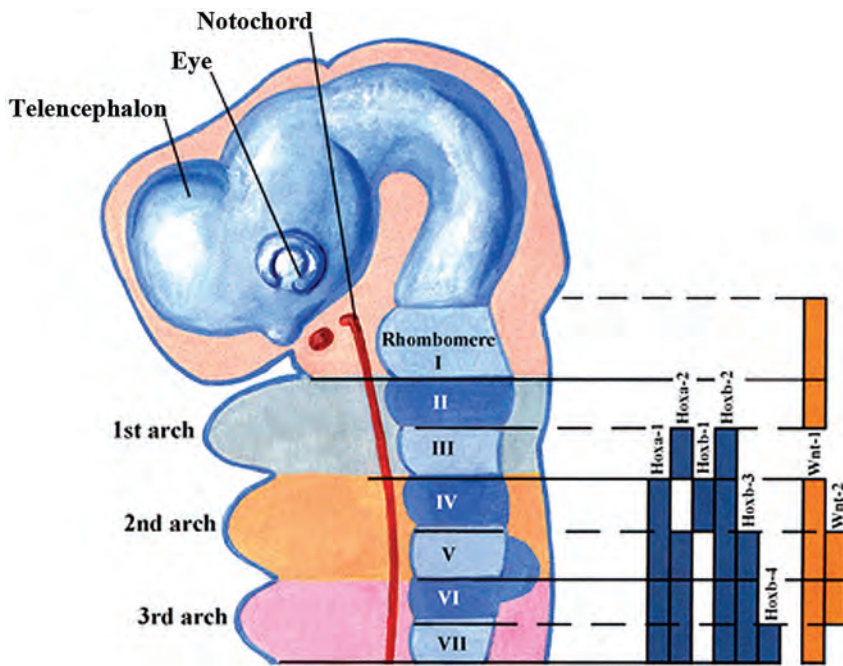


FIG 6. Sagittal drawing illustrating the *Hox* gene family signaling in the hindbrain and the pharyngeal arches. The solid bars represent the *Hox* gene expression in the neural crest cells and the neural tube. The downregulation of the *Hoxa-2* gene in the first arch of neural crest cells is necessary for normal first arch development. (Modified with permission from Netter Illustration from www.netterimages.com. Elsevier Inc. © All rights reserved.^{16,17})

Table 4: Summary of factors related to facial abnormalities discussed in the text

Factor	Some Observed Abnormalities
RA	Excess leads to fusion of 1st and 2nd branchial arches and acoustic-facial ganglia, small jaws, cleft palate, deformed pinna (Treacher-Collins syndrome); RA controls <i>Shh</i> and <i>Fgf8</i> levels
<i>Fgf</i>	Controls outgrowth of facial primordia and migration of neural (<i>Fgf</i>) crest cells to facial processes; a decrease in <i>FBGFR1</i> leads to midline clefting and Kallmann syndrome, small face and skull, achondroplasia, Crouzon syndrome, Apert syndrome
<i>TGF</i>	<i>TGFβ</i> required for fusion of lateral palatal processes; a decrease leads to defects in maxillary and mandibular development
<i>BMP</i>	A decrease leads to short frontal and nasal bones and small pterygoid processes, short stature, ear defects, odontogenic patterning defects, slower neural tube closure, small branchial arches, loss of incisor teeth
<i>Shh</i> protein	A decrease leads to holoprosencephaly, hypotelorism; an increase leads to a wide forehead, frontonasal dysplasia, Gorlin syndrome, Grieg cephalopolysyndactyly, Smith-Lemli-Opitz syndrome
<i>Wnts</i>	A decrease leads to loss of teeth, truncation of jaw, mesencephalic nucleus, and trigeminal nerve
<i>ET-1</i>	A decrease leads to aplasia of 1st and 2nd arches, defects in maxilla and cleft palate, malformations of middle and external ear; 22q11.2 deletion syndrome (CATCH22 syndrome)
<i>Jagged 1</i> and 2	A decrease leads to Alagille syndrome, failure of palatal shelves to elevate, and fusion of shelves with tongue
Platelet-derived growth factors	A decrease leads to loss of some facial bones
Homeobox-containing genes	A decrease leads to primitive facial morphology, cleft palate, short maxilla and mandible, loss of maxillary molar teeth, ankyloglossia

Note:—RA indicates retinoic acid; *FGFR*, fibroblast growth factor receptor; *PDGFR*, platelet-derived growth factor receptor.

mesenchymal interactions, and it is primarily the mesenchymal signaling that controls the outgrowth.⁹ In addition to retinoic acid, 5 key families of secreted growth factors have been

identified that control facial outgrowth via regulation of cell proliferation and survival. These factors include *fibroblast growth factors*, *transforming growth factor β* and *bone morphogenetic proteins*, *sonic hedgehog*, *Wnts*, and *endothelin-1* (*ET-1*). Last, there are the contributions of *jagged 1* and 2, *platelet-derived growth factors*, and *homeobox-containing genes* (Fig 6). Table 4 summarizes the effect of these factors on facial development. It may be that each region of the head can be viewed as a distinct module with its own unique set of signaling interactions.^{1,10}

Coordinated Growth-Factor Signaling

As can be surmised from the preceding paragraphs, these gene and gene products do not act alone. For normal facial growth and patterning, signaling of multiple growth factors must be highly coordinated. Thus as an example, expression of *ET-1* is dependent on *Fgf8* function in some regions of the facial primordium. On the other hand, antagonistic signaling interactions between *Fgf8* and *BMP4* outline the boundaries of gene expression for a number of *homeobox-containing genes*, and this can determine the position of the odontogenic field and odontogenic patterning.^{1,9} In addition, retinoic acid, *Fgf*, and *BMP* are responsible for controlling *Shh* and overall facial outgrowth.¹¹ In general, signaling is subject to precise spatial and temporal control: Too much or too little genetic input or input out of the regulated normal temporal sequence results in abnormalities.¹²

As an example of the multivariant signaling and its temporal organization needed for normal development, the following are some of the genetic factors required for correct palatal shelf formation and fusion. For initial budding of the palatal shelf, *Fgf-Shh* signaling needs to be coordinated. *Jagged-2*, the *paired box gene 9*, serotonin, and hyaluronan are required for palatal shelf formation and elevation. *Poliovirus receptor-related 1* and *TGFβ3* are expressed in the palatal shelf medial edge epithelium, while the homeobox proteins *Lhx-8* and *Msx-1* are expressed in the underlying mesenchyme. *TGFβ3*, *TGF-α*, and *epidermal growth factor* are required for the breakdown of the medial edge epithelium. In addition, derivatives of γ -aminobutyric acid signaling are critical to palatal formation, and loss of γ -aminobutyric

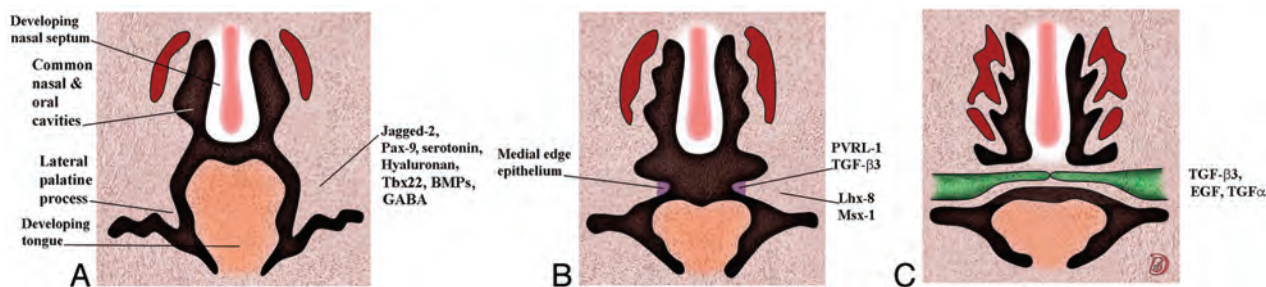


FIG 7. Serial coronal drawings showing the development of the palate and the genes associated with the stages of this development. A, The lateral palatal shelves emerge. B, The palatal shelves have elevated. C, The shelves have met in the midline, the medial edge epithelium dissolves, and the shelves eventually fuse.

Table 5: Gene mutations associated with cleft palate in humans^a

Genes	Associated Conditions
Collagen genes, <i>COL II</i> and <i>XI</i>	Otospondylomegapiphyseal dysplasia, achondrogenesis type II, Stickler syndrome types I-III, Diastrophic dysplasia
<i>Diastrophic dysplasia sulfate transporter</i>	
<i>FGFR2</i>	Apert syndrome
<i>Homeobox MSX1</i>	Cleft palate and hypodontia
<i>TGFβ R1</i> or <i>TGFβR2</i>	Aortic aneurysm, arterial tortuosity, hypertelorism, cleft palate, bifid uvula, craniosynostosis
<i>T-Box 1 (BX1)</i>	DiGeorge/Velo cardiofacial syndrome
<i>T-Box 22 (TBX22)</i>	X-linked cleft palate and ankyloglossia
<i>TCOF1</i>	Treacher Collins syndrome
<i>TWIST</i>	Saethre-Chatzen syndrome

Note:—*FGFR2* indicates fibroblast growth factor receptor 2.

^a Other genes and proteins associated with normal palatal formation include the following: *Fgf-Shh* signaling, *Tbx22*, *BMPs*, *Jagged-2*, *Pax-9*, serotonin, hyaluronan, *PVRL1*, *TGF-β3*, *TGF-α*, *EGF*, *Lhx-8*, *Msx-1*, and *GABA* (Fig 1). Table modified from Rice DP. Craniofacial anomalies: from development to molecular pathogenesis. *Curr Mol Med* 2005; 5:699–722, Table 2, © Bentham Science Publishers.¹⁶

Table 6: Gene mutations associated with cleft lip/cleft palate in humans^a

Gene	Condition
<i>DHCR7</i>	Smith-Lemli-Opitz syndrome
<i>EFNB1</i>	Craniofrontonasal syndrome
<i>FGFR1</i>	Kallmann syndrome
<i>IRF6</i>	van der Woude syndrome
<i>OFD1</i>	Oral-facial-digital syndrome type I
<i>MIDI1</i>	Opitz syndrome
<i>MSX1</i>	Cleft lip/palate with hypodontia
<i>PVRL1</i>	Margarita Island ectodermal dysplasia (part of cleft lip/palate-ectodermal dysplasia syndrome)
<i>TP73 L (p63)</i>	Ectrodactyly, ectodermal dysplasia, and cleft lip/palate, ankyloblepharon-ectodermal dysplasia-clefting syndrome
<i>SIX3</i>	HPE2
<i>TGIF</i>	HPE4
<i>PTCH1</i>	HPE7
<i>GLI2</i>	HPE-like features

Note:—HPE indicates holoprosencephaly.

^a Table modified from Rice DP. Craniofacial anomalies: from development to molecular pathogenesis. *Curr Mol Med* 2005;5:699–722, Table 1, © Bentham Science Publishers.¹⁶

acid signaling increases the risk of a cleft palate. Both excess and loss of retinoids also may result in a cleft palate. The formation of the palate is summarized in Fig 7. Tables 5 and 6 list some of the gene mutations associated with a cleft palate with and without a cleft lip in humans.^{1,9}

If any of the above normal signaling does not occur, a cleft

palate can occur either as an isolated entity or in combination with a cleft lip, and there are >300 syndromes in which such clefts are associated—that is, clefts occur when there are abnormalities in the normal process of development.

From the above discussion, it is clear that multiple genes and precise temporal occurrence are necessary for normal palatal development. Additional considerations are anteroposterior gradients and medial-lateral spacial gradients of gene products. This is especially evident along the fusion line of the lateral palatal shelves. Thus, *Osr1* and *Ors2* are expressed in a medial-lateral gradient in the palatal shelves, and loss of *Ors2* retards shelf elevation. Similarly, *fibroblast growth factor receptor 2* (*Fgfr2*) is concentrated in the medial aspect of the palatal shelf, suggesting that it plays a role in palatal elevation. Genetic heterogeneity is also noted along the anteroposterior axis with, as an example, *Fgf8* signaling selectively inducing expression of *Pax9* in the posterior palatal mesenchyme.

Ossification of the palate is also under genetic control. As an example, *Sox9* controls cartilage development and blocks the expression of *Runx2*, a transcription factor essential for normal osteoblast differentiation and bone formation. If *Sox9* is mutant, *Runx2* expression is not repressed and ossification of the palatal shelves occurs too early. Because they are prematurely ossified, they cannot grow together in the midline and a cleft palate results.

Similar rostral/caudal and medial/lateral segregation of genetic products occurs in almost all facial developmental regions. This is also especially noted in the development of the mandible primordia where *ET-1*, *BMP4*, *FGF-8*, and *Dix3* are rostral, while *Gsc*, *Msx1*, *Msx2*, *Barx1*, *Pax9*, and *Lhx6* are caudal.¹

How Does Signaling Affect the Cell?
The various signaling mentioned above needs a means of affecting specific cells to accomplish their programmed mission, and there is a variety of methods of cell communication that can occur. These proteins can be considered as external signals in the environment of the cells, and the signals may come from a number of sources, which include the following: a cell signaling to itself (autocrine), a nearby cell in the microenvironment (paracrine), from

a distant cell (hormones), or interactions of surface-specific signaling molecules. When one considers signaling molecules, there are 2 main types: those that diffuse into the cell and bind directly to internal receptors (steroids, retinoids [vitamin A]) and those signaling molecules that are called ligands and bind to the extracellular receptor component of a transmembrane protein. While the extracellular component of the transmembrane protein binds a specific signaling molecule, the intracellular portion in the cytosol of the cell activates proteins that eventually, via a variety of pathways, regulate gene transcription in the nucleus.^{13,14}

CONCLUSIONS

The purpose of this review was to give some insight into the complex world of molecular products and their interactions as they participate in the embryogenesis of the face. There is rarely only 1 gene that is responsible for a morphologic change. What is starting to be defined is a complex regulatory network that controls these events; and within this network, each step in the temporal hierarchy can be identified by a specific set of transcription factors that cross-regulate each other and that, in turn, are controlled by defined signaling inputs.¹⁵ Thus, facial patterning is controlled by complex and coordinated signaling between the mesenchyme and epithelium. However, the precise roles of these tissues remain incompletely understood. How neural crest cells influence gene expression in the epithelium once they have reached the facial primordia is just beginning to be understood. How patterning between different neural crest cell populations is coordinated and how patterning is related to cell differentiation are presently being intensely studied. Although many of the genes that control facial development are known, how these genes interact and how their malfunction influences cellular behavior are mostly unclear. Once these and other remaining questions are answered and there is a more complete understanding of the molecular changes involved in normal facial development, how and why facial malformations occur and how they may possibly be prevented will be better understood.^{1,9,10}

REFERENCES

1. Francis-West PH, Robson L, Evans DJ. **Craniofacial development: the tissue and molecular interactions that control development of the head.** *Adv Anat Embryol Cell Biol* 2003;169:III-VI, 1–138
2. Osumi-Yamashita N. **Retinoic acid and mammalian craniofacial morphogenesis.** *J Biosci* 1996;21:313–27
3. McCabe KL, Bronner-Fraser M. **Molecular and tissue interactions governing induction of cranial ectodermal placodes.** *Dev Biol* 2009;332:189–95
4. Stern CD, Downs KM. **The hypoblast (visceral endoderm): an evodevo perspective.** *Development* 2012;139:1059–69
5. Streit A. **The preplacodal region: an ectodermal domain with multipotential progenitors that contribute to sense organs and cranial sensory ganglia.** *Int J Dev Biol* 2007;51:447–61
6. Litsiou A, Hanson S, Streit A. **A balance of FGF, BMP and WNT signalling positions the future placode territory in the head.** *Development* 2005;132:4051–62
7. Li H, Tierney C, Wen L, et al. **A single morphogenetic field gives rise to two retina primordia under the influence of the prechordal plate.** *Development* 1997;124:603–15
8. Macdonald R, Barth KA, Xu Q, et al. **Midline signalling is required for Pax gene regulation and patterning of the eyes.** *Development* 1995;121:3267–78
9. Rice ME, Lee EJ, Choy Y. **High levels of ascorbic acid, not glutathione, in the CNS of anoxia-tolerant reptiles contrasted with levels in anoxia-intolerant species.** *J Neurochem* 1995;64:1790–99
10. Kim CH, Park HW, Kim K, et al. **Early development of the nose in human embryos: a stereomicroscopic and histologic analysis.** *Laryngoscope* 2004;114:1791–800
11. Liu B, Rooker SM, Helms JA. **Molecular control of facial morphology.** *Semin Cell Dev Biol* 2010;21:309–13
12. Yu W, Serrano M, Miguel SS, et al. **Cleft lip and palate genetics and application in early embryological development.** *Indian J Plast Surg* 2009;42(suppl):S35–50
13. Kimball JW. *Biology*. St. Louis: William C. Brown; 1994
14. Naidich TP, Blaser SI, Lien RJ, et al. **Embryology and congenital lesions of the midface.** In: Som PM, Curtin HD, eds. *Head and Neck Imaging*. Philadelphia: Elsevier; 2011:3–97
15. Grocott T, Tanbalo M, Streit A. **The peripheral sensory nervous system in the vertebrate head: a gene regulatory perspective.** *Dev Biol* 2012;370:3–23
16. Rice DP. **Craniofacial anomalies: from development to molecular pathogenesis.** *Curr Mol Med* 2005;5:699–722

Toward an Endovascular Internal Carotid Artery Classification System

M. Shapiro, T. Becske, H.A. Riina, E. Raz, D. Zumofen, J.J. Jafar, P.P. Huang, and P.K. Nelson

ABSTRACT

SUMMARY: Does the world need another ICA classification scheme? We believe so. The purpose of proposed angiography-driven classification is to optimize description of the carotid artery from the endovascular perspective. A review of existing, predominantly surgically-driven classifications is performed, and a new scheme, based on the study of NYU aneurysm angiographic and cross-sectional databases is proposed. Seven segments – cervical, petrous, cavernous, paraophthalmic, posterior communicating, choroidal, and terminus – are named. This nomenclature recognizes intrinsic uncertainty in precise angiographic and cross-sectional localization of aneurysms adjacent to the dural rings, regarding all lesions distal to the cavernous segment as potentially intradural. Rather than subdividing various transitional, ophthalmic, and hypophyseal aneurysm subtypes, as necessitated by their varied surgical approaches and risks, the proposed classification emphasizes their common endovascular treatment features, while recognizing that many complex, trans-segmental, and fusiform aneurysms not readily classifiable into presently available, saccular aneurysm-driven schemes, are being increasingly addressed by endovascular means. We believe this classification may find utility in standardizing nomenclature for outcome tracking, treatment trials and physician communication.

Until now, the ICA was subdivided into various segments, primarily on the basis of surgical considerations. Fischer's original classification (Fig 1),¹ with C1–C5 segments, in retrograde fashion, addressed the then-existing need for localization of regional pathology on the basis of mass effect on the ICA, as assessed by early angiographic imaging. It remained in widespread use until 1981, when Gibo et al,² in a report detailing superb dissections of the supraclinoid ICA designed to specifically address aneurysm considerations, introduced an antegrade alphanumeric system from C1–C4 (Fig 2). The extracranial ICA was recognized as the C1 segment, and extradural ICA was subdivided into petrous (C2) and cavernous (C3) segments, terminating at the distal dural ring. The entire intradural ICA was classified as supraclinoid (C4), with ophthalmic, communicating, and choroidal subsegments (Fig 2). Subsequently, a modified Fischer classification was proposed by Bouthillier et al³ in 1996, which became known

as the Bouthillier classification (Fig 3). Although substantially different from Fischer's, it also retained an antegrade alphanumeric designation of C1–C6 segments. Bouthillier introduced the new lacerum and, most importantly, clinoid segments, thereby formally recognizing a particularly complex region of carotid anatomy as it transitions from intracavernous to intradural spaces. Anatomic interest in this area was driven by refinement in microsurgical techniques, which allowed for the possibility of access to aneurysms of this paraophthalmic-paraclinoid region, albeit with mixed results. While Bouthillier's classification gained wide and enduring acceptance, new systems were proposed to address its perceived shortcomings. Ziyal et al⁴ advocated a classification (Fig 4) that dispensed with Bouthillier's lacerum segment, arguing on the basis of detailed microsurgical dissections that relationships between the carotid artery, foramen lacerum, petrolingual ligament, and proximal cavernous sinus left no room for a distinct lacerum segment.⁵ The ophthalmic segment was also discarded in favor of the cisternal segment because of variability in the index artery origin.⁴ Additional, surgically driven, subsegmental classifications, addressing primarily the paraclinoid and ophthalmic regions, were proposed, incorporating evolving surgical approaches in this challenging area.^{2,6-11}

A radically different approach was taken by Lasjaunias et al^{12,13} (Fig 5), emphasizing embryologic origins of various ICA segments. The system was part of an all-encompassing, conceptually brilliant embryologic framework, addressing all

Received February 28, 2013; accepted after revision May 11.

From the Department of Radiology (M.S., T.B., H.A.R., E.R., D.Z., P.K.N.), Bernard and Irene Schwartz Neurointerventional Radiology Section; and Departments of Neurology (M.S., T.B.), and Neurosurgery (H.A.R., D.Z., J.J., P.P.H., P.K.N.), NYU Langone Medical Center, New York, New York.

Please address correspondence to Maksim Shapiro, MD, Departments of Radiology and Neurology, Bernard and Irene Schwartz Neurointerventional Radiology Section, NYU Langone Medical Center, 660 First Ave, 7th Floor, New York, NY 10016; e-mail: shapim06@med.nyu.edu

<http://dx.doi.org/10.3174/ajnr.A3666>

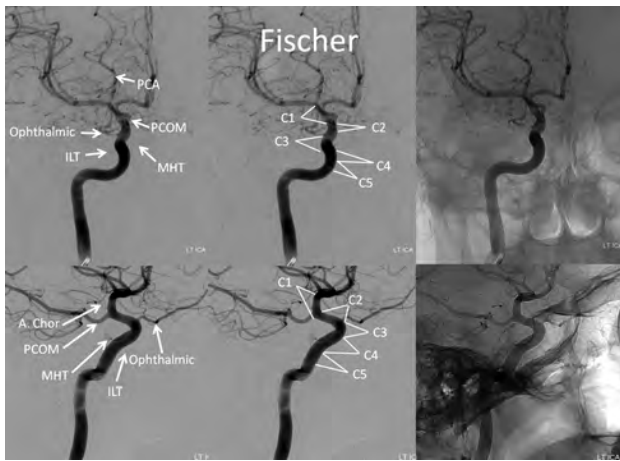


FIG 1. Frontal and lateral projection views of left ICA injection, depicting Fischer ICA nomenclature, including relevant osseous and branch relationships.

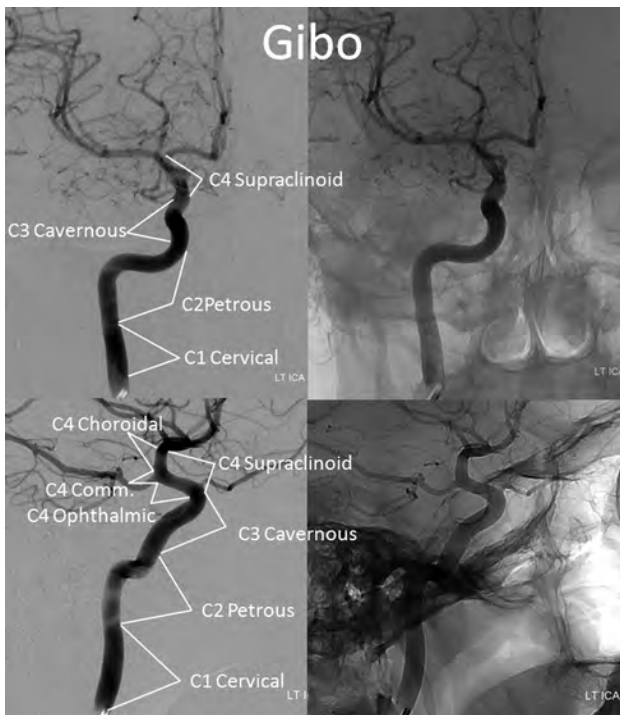


FIG 2. Gibo classification. The C4 supraclinoid segment is subdivided into ophthalmic, communicating, and choroidal subsegments.

manner of cerebrovascular development and variation, such as segmental ICA agenesis and reconstitution, the aberrant ICA, dorsal and ventral ophthalmic origin, and the primitive maxillary artery, to name a few. This unique view was derived from neither surgical nor endovascular experience and as such was not specifically designed for existing microsurgical or then-emerging endovascular considerations. Although the authors introduced a correlation between the embryologic segments and external anatomic landmarks, illustrated in Fig 5, the system did not achieve widespread use.

Our own view of the ICA, crystallized in the currently proposed scheme (Fig 6), emerged as a product of decades-long experience in angiographic and cross-sectional study of vari-

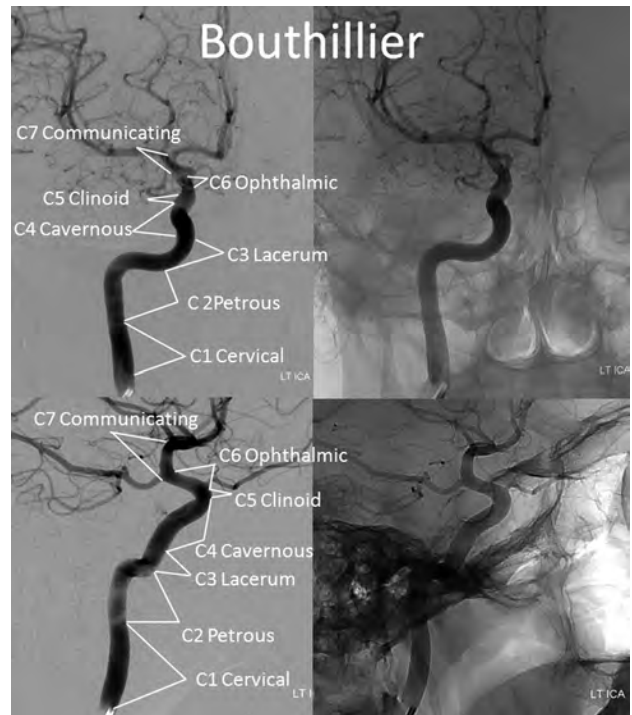


FIG 3. Bouthillier classification.

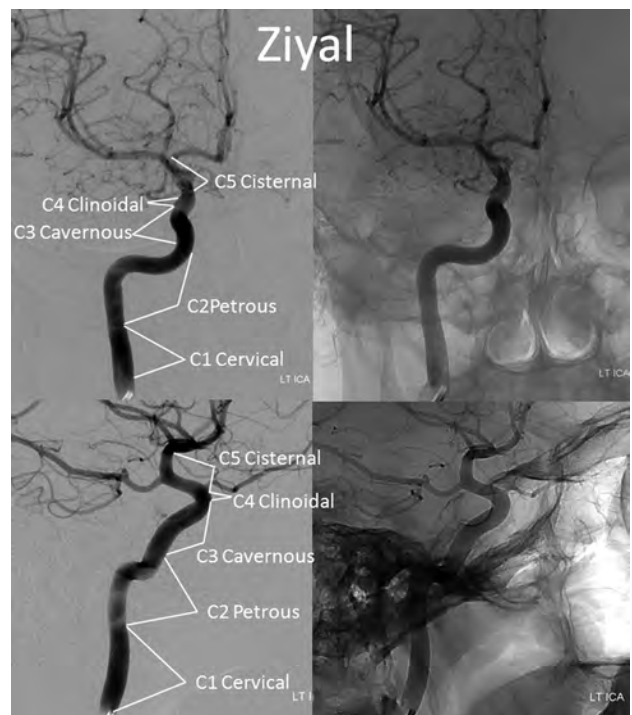


FIG 4. Ziyal classification.

ous ICA aneurysms and subsequent treatment-centered discussions. During this process, we have naturally gravitated toward certain descriptive terms, which seem to transmit most succinctly both anatomic information and subjective implications related to treatment considerations in a multidisciplinary forum, recognizing intrinsic uncertainties between angiographic and microsurgical landmarks. Concurrent refinement

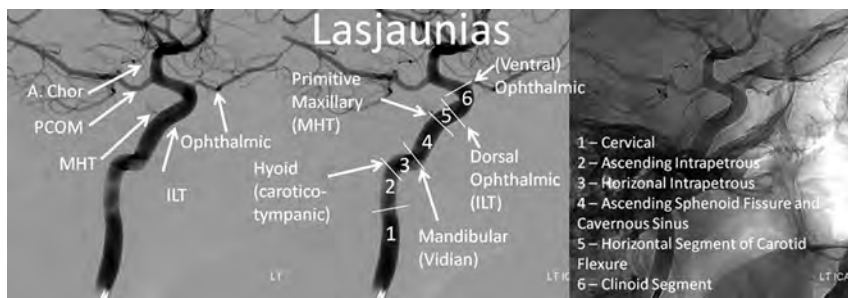


FIG 5. Lasjaunias and Santoyo-Vazquez, embryology-based classification.

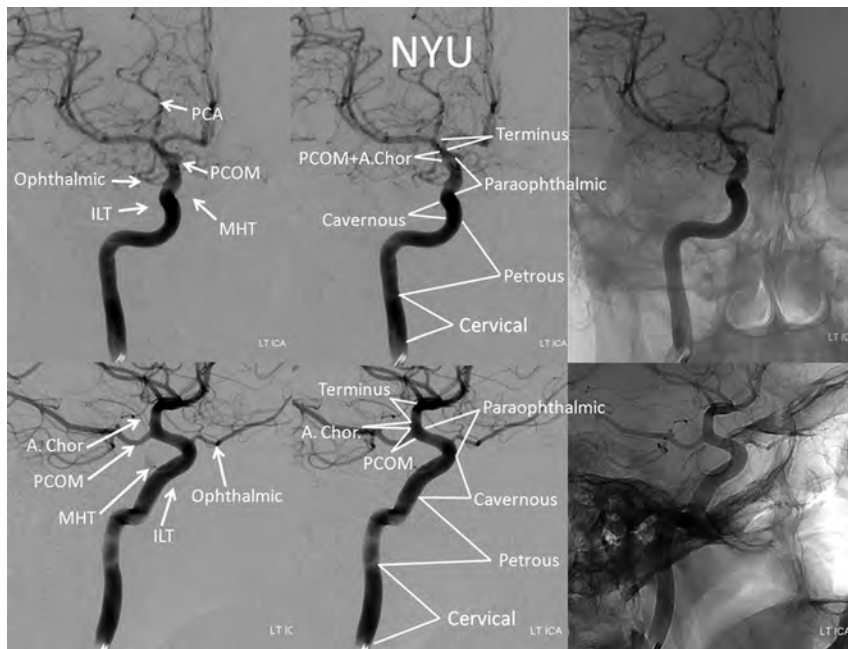


FIG 6. Proposed classification.

in endovascular techniques, most recently exemplified by development of endoluminal (flow diversion) methods, has meanwhile transformed cerebrovascular approaches to carotid siphon aneurysms, placing increasing emphasis on development of an ICA classification system particularly relevant to endovascular factors.¹⁴ The improved capability to definitively treat larger and increasingly complex ICA aneurysms and fusiform segments of the artery highlights the need for a conceptually flexible classification that suitably describes the transsegmental nature of many such formidable lesions, which frequently extend across various embryologically neutral, landmark-based segmental boundaries.

MATERIALS AND METHODS

A literature review of existing ICA classification systems and related works was conducted. Cerebral angiograms and cross-sectional studies performed at the New York University Langone Medical Center and Bellevue Health and Hospitals Center and outside studies forwarded for consultation were continuously reviewed and discussed at our multidisciplinary conference. Patterns of aneurysm formation and growth were

studied as a pathophysiologic guide to a clinically useful classification system.

RESULTS

The proposed system is presented in Fig 6. In this nomenclature, 7 segments are described—cervical, petrous, cavernous, paraophthalmic, posterior communicating, anterior choroïdal, and terminus—without alphanumeric correspondence.

The cervical segment is identical to that of Bouthillier and Ziyal, extending from cervical carotid bifurcation to the proximal margin of the carotid canal. Variations such as aberrant carotid artery (ie, ascending pharyngeal artery reconstitution of petrous carotid artery) can be described on their own terms.

The petrous segment is analogous to that of Ziyal, and, combining Bouthillier's petrous and lacerum segments, spans the ICA within the temporal bone and partially above the foramen lacerum, terminating at the petrolingual ligament. It contains the rarely visible (probably caused by temporal bone thickness rather than actual absence) carotico-tympanic branch and the more consistently demonstrated vidian branches. The precise location of the petrolingual ligament is not angiographically determinable, and the anterior aspect of the petrous ridge can be used as a landmark. We chose to dispense with a distinct lacerum segment,

in agreement with Ziyal, for 2 reasons. First, the preponderance of anatomic information argues against its unique character,^{5,15} whereas the petrolingual ligament best defines carotid transition into the cavernous segment. Second, from a pathophysiologic standpoint, among the nontraumatic temporal bone aneurysms evaluated by our group that involved the lacerum portion of the ICA, none were focal; all were fusiform lesions extending into the adjacent petrous or cavernous segments, rendering the distinction between Bouthillier's petrous and lacerum segments clinically neutral (Fig 7).

The cavernous segment extends from the estimated location of distal margin of the petrolingual ligament to the estimated location of the proximal dural ring. We recognize that neither proximal nor, more importantly, distal cavernous segment boundaries, can be reliably established on an angiographic or transaxial basis—a recurrent theme with regard to segmentation on the basis of external anatomic landmarks. Additionally, the morphology of both cavernous sinus and cavernous ICA are highly variable, with important endovascular implications. Broadly speaking, a proximal ascending segment, proximal (posterior) genu, horizontal segment, distal (anterior) genu, and distal ascending segment can

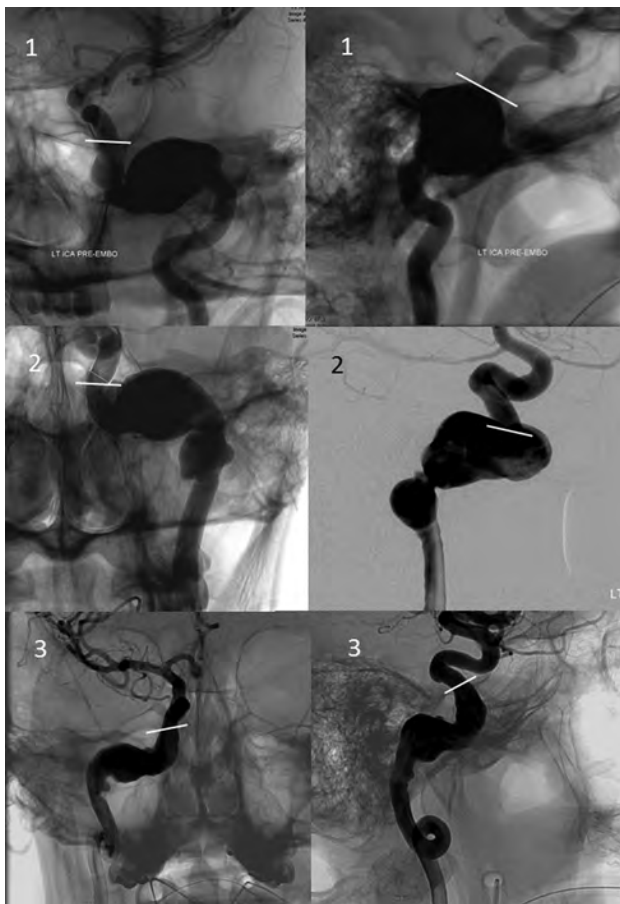


FIG 7. Frontal, transorbital (upper left image), and lateral views of 3 petrous segment aneurysms, demonstrating their extension into the vertical segment above the foramen lacerum, terminating adjacent to the superior margin of the petrous apex (white lines), corresponding to estimated location of the petrotingual ligament.

be described. The meningo-hypophyseal trunk or its component branches originate from the posterior genu, whereas the inferolateral trunk is most commonly found arising from the horizontal segment. It is interesting to note that aneurysms of the cavernous segment, regardless of size and morphology, appear to spare the proximal vertical portion, which extends from the petrotingual ligament to the proximal genu, even though this subsegment is anatomically located within the posterior compartment of the cavernous sinus (Fig 8). The reasons for this are unclear: an embryologic mechanism could be suggested from the Lasjaunias system, corresponding to segment 4 in Fig 5. The uncertainty in localizing the distal boundary of the cavernous segment is formally recognized in the next, encompassing paraophthalmic segment.

The paraophthalmic segment extends from the estimated distal border of the cavernous segment to the ostium of the posterior communicating artery, with all of its aneurysms regarded as clearly or potentially intradural. Our choice of this generalized term follows from 2 primary considerations. First, we formally accept the intrinsic uncertainty in angiographic or cross-sectional definition of traditional segmental boundaries (particularly relevant to delineation of the clinoid segment). Second, we propose that endovascular methods, in contrast to surgical ones, increas-

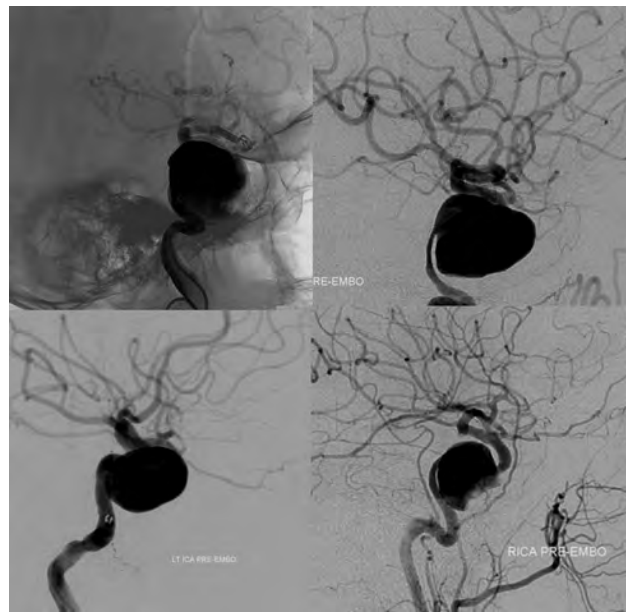


FIG 8. Four fusiform cavernous segment aneurysms, all sparing the proximal vertical subsegment of the cavernous ICA.

ingly tend to unite rather than divide treatment considerations of the various aneurysms arising from traditionally defined clinoid, ophthalmic, and superior hypophyseal segments.

Proximally, the paraophthalmic segment incorporates Bouthillier's clinoid segment, which can be microsurgically localized between the proximal and distal dural rings.^{3,16} This assimilation formally recognizes that neither location nor status of either ring is reliably demonstrable with presently available angiographic or transaxial imaging modalities. Attempts to define the position of a distal dural ring, by use of CT, MR imaging, or angiography,^{6,17-21} are limited by 2 key considerations. First, none of the clinically available imaging modalities can actually depict the distal dural ring itself; attempts to define its location instead rely on indirect morphometric and landmark relationships. As such, these methods become quite vulnerable to a high degree of local anatomic variation. No attempt has been made, so far as we know, to demonstrate the more nebulous and less clinically significant proximal ring. Second, and more importantly, regional anatomy is extensively modified by disease (aneurysm growth), which distorts landmarks by destroying or distorting adjacent tissues (dural ring dehiscence). For these reasons, short of surgical exposure, the exact state of affairs in this region cannot be determined by any currently available imaging technique. Finally, the subpopulation of larger and more complex aneurysms, which are increasingly addressed by endovascular methods, frequently transcend established segmental boundaries, leading to uncertainty as to whether a given lesion is partially or fully, primarily or secondarily, intradural (Fig 9). Our position is to consider all aneurysms distal to the anterior cavernous carotid artery genu as potentially intradural.

The endovascular considerations involved in treatment of proximal paraophthalmic segment aneurysms are separate and distinct from well-established microsurgical concerns of exposing the clinoid segment and cave aneurysms,^{7,16} which are different

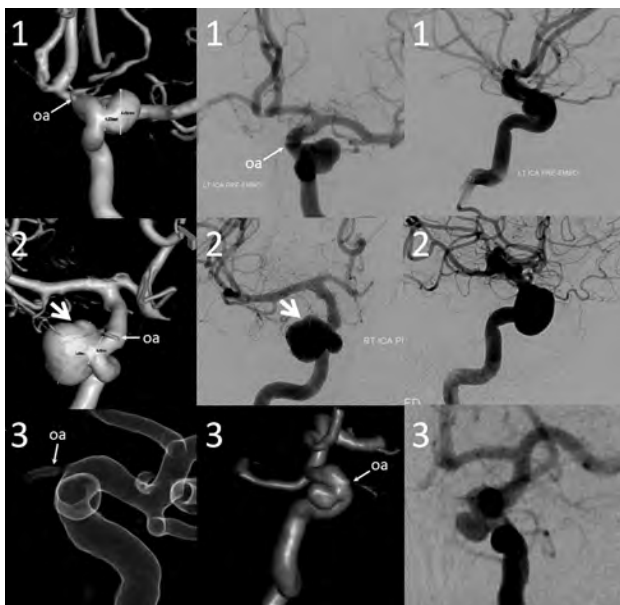


FIG 9. Three-dimensional DSA, frontal, and lateral projection views of 3 proximal paraophthalmic aneurysms, which would traditionally be considered in the clinoid (1, 2) and cave (3) families. An oblique indentation (*arrow*) of aneurysm 2 probably defines the dural ring, suggesting intradural extension.

from surgical approaches to various ophthalmic or superior hypophyseal region aneurysms. No such critical distinctions are relevant in the endovascular arena, in which the most important point is to decide whether a given aneurysm is extradural or intradural. In consequence, all intradural ICA subsegments proximal to the posterior communicating artery are consolidated into the paraophthalmic segment. This area is home to particularly varied and complex aneurysms, in which our experience suggests a lower baseline interobserver agreement as to their classification, becoming progressively more difficult with larger and frankly trans-segmental lesions (Fig 10). The proposed nomenclature also reflects the angiographic limitations of identifying the superior hypophyseal arteries, which serve to define their aneurysms in microsurgical dissections. These arteries are small and have a variable, typically medial origin along a comparatively long segment of the ICA. They tend to be superimposed on the parent ICA in lateral projections and therefore are rarely demonstrable on angiography. Furthermore, the amalgamation of all aneurysms proximal to the posterior communicating artery into the paraophthalmic segment encompasses infrequent but important aneurysms not necessarily associated with the superior hypophyseal arteries (such as treacherous ventral or dorsal blister lesions).

An awkward situation for use of the “paraophthalmic” term is created when the ophthalmic artery does not arise from its “classic” location in the very proximal intradural ICA. On the other hand, greater flexibility is now afforded for the location of ophthalmic artery ostium, with its intradural (traditional clinoid segment) variants remaining within the paraophthalmic segment. Our feeling is that other potential sites of orbital supply, which include the dorsal ophthalmic artery arising in the adult from the



FIG 10. Various 3D DSA examples of segmental ICA dysplasia. In traditional classifications, case 1 may be described as 3 separate aneurysms—distal cavernous (or transitional) and superior- and inferior-pointing superior hypophyseal aneurysms. We consider all of these as focal expressions of disease affecting the entire paraophthalmic segment. Case 2 may be considered as a discrete carotid-ophthalmic aneurysm; notice, however, the irregular, expanded morphology of the parent vessel below the “neck.” Case 3—apparently separate clinoid and ophthalmic aneurysms—can also be viewed as segmental dysplasia with a single aneurysm separated by the anterior clinoid process. Case 4 is a giant fusiform aneurysm spanning the entire carotid artery from cavernous to terminus segments.

inferolateral trunk, external carotid origin particularly from the middle meningeal artery (meningo-ophthalmic variant), and ventral ophthalmic variants arising from the anterior cerebral artery are sufficiently uncommon that descriptions of ICA pathology in this region may be customized accordingly, with minimal detriment to the system as a whole. The issue may be addressed by adoption of another term that makes no mention of the ophthalmic artery—as reflected in the Ziyal classification through the “cisternal” segment⁴; our preference is to emphasize the more common anatomic arrangement, made further flexible by extension of the paraophthalmic segment into the traditional clinoid region.

The posterior communicating segment extends from the proximal ostium of the posterior communicating artery to the anterior choroidal artery. A separate category for the posterior communicating segment recognizes the unique epidemiologic characteristics of its aneurysms.²² Furthermore, in contrast to preceding segments, the angiographic boundaries of this segment can be adequately defined under most circumstances. Continued vernacular description of aneurysms arising from the posterior communicating segment of the ICA as simply “posterior communicating” is fully acceptable because there is no uncertainty about what is meant by either name. Finally, both endosaccular and endoluminal treatment considerations—related to preservation, sacrifice, or jailing of the posterior communicating artery, as well

as issues of posttreatment recurrence and its management—are distinct from those of the subsequent choroidal segment.

The anterior choroidal segment consists of the ICA adjacent to the choroidal ostium and includes aneurysms recognized in the vernacular description as anterior choroidal. The distinct issues of maintaining anterior choroidal patency and risk stratification in cases of its compromise (intentional or not) are germane to both surgical and endovascular modalities.

The terminus segment extends from beyond the choroidal ostium to the carotid bifurcation and incorporates aneurysms arising from the carotid bifurcation. It contains a variable number of perforator vessels to the anterior perforated substance,²³ which, along with anterior choroidal branches, participate extensively in Moyamoya-type collateral reconstitution of the MCA and anterior cerebral artery. We believe that both clinical and management considerations of terminus aneurysms are sufficiently different from the choroidal type and thus merit placement in a separate category.

DISCUSSION

The proposed angiographic classification seeks to define each vascular segment in terms of its distinct angiographic and endovascular considerations. This leads to both amalgamation of commonly defined segments (clinoid, ophthalmic, and hypophyseal) and subdivision in the postcommunicating region. Cervical segment pathology is widely recognized as separate from cranial lesions. Petrous segment aneurysms, both traumatic and nontraumatic, likewise represent a unique set of pathology, as do various cavernous aneurysms. The full spectrum of paraophthalmic aneurysms, inclusive of the large and complex lesions that remained on the fringes of surgical classifications driven by more discrete saccular aneurysms, are thought to represent a sufficiently unified group from an endovascular perspective. The posterior communicating, anterior choroidal, and terminus segment aneurysms are all associated with their particular clinical and technical issues.

Our improving ability to definitively treat the increasingly complex and trans-segmental aneurysms requires adoption of a more flexible system, capable of comfortably accommodating these lesions within a descriptive framework. We hope that the proposed nomenclature will increase interobserver agreement in classification of ICA lesions, particularly desirable in epidemiologic and other research settings in addition to the clinical setting. Finally, we formally dispensed with numeric classification in favor of purely descriptive terms to minimize confusion with various already-existing schemes.

We remain acutely cognizant that despite our sincere effort, all landmark-based classification systems, including ours, remain intrinsically suboptimal when applied to description of increasingly complex, trans-segmental aneurysms. Therefore, in closing, we wish to re-emphasize that all classifications have a priori limitations and are most useful when they strike a balance between utility, accuracy, and flexibility—particularly stressing the latter quality—as demanded by the varied nature of the pathologies these systems are designed to address.

CONCLUSIONS

We propose a new, angiographically based classification system of the ICA, from cervical to intracranial bifurcations, to better serve the needs of present-day endovascular clinical and research efforts.

Disclosures: Tibor Becske—UNRELATED: Consultancy: Covidien, Comments: clinical proctorships related to Pipeline Embolization Device; Maksim Shapiro—UNRELATED: Consultancy: Covidien, Comments: clinical proctorships related to Pipeline Embolization Device; Howard Riina—UNRELATED: Board Membership: Reach Bionics; Grants/Grants Pending: Tomorrow Foundation*; Patents (planned, pending, or issued): None relevant to this area of work; Stock/Stock Options: Reach Bionics. Peter Nelson—UNRELATED: Consultancy: Covidien, Comments: Clinical proctorships related to Pipeline Embolization Device; Royalties: Stryker,* Comments: Royalties related to Neuroform and Wingspan Stents (*money paid to institution).

REFERENCES

1. Fischer E. Die Lageabweichungen der vorderen Hirnarterie im Gefäßbild. *Zentralbl Neurochir* 1938;3:300–13
2. Gibo H, Lenkey C, Rhoton AL. Microsurgical anatomy of the supraclinoid portion of the internal carotid artery. *J Neurosurg* 1981;55:560–74
3. Bouthillier A, van Loveren HR, Keller JT. Segments of the internal carotid artery: a new classification. *Neurosurgery* 1996;38:425–32
4. Ziyal IM, Ozgen T, Sekhar LN, et al. Proposed classification of segments of the internal carotid artery: anatomical study with angiographical interpretation. *Neurol Med Chir (Tokyo)* 2005;45:184–90
5. Ziyal IM, Salas E, Wright DC, et al. The petrolingual ligament: the anatomy and surgical exposure of the posterolateral landmark of the cavernous sinus. *Acta Neurochir (Wien)* 1998;140:201–04
6. Beretta F. The paraclinoid aneurysms and the distal dural ring: a new classification. *J Neurosurg Sci* 2004;48:161–75
7. Kobayashi S, Kyoshima K, Gibo H, et al. Carotid cave aneurysms of the internal carotid artery. *J Neurosurg* 1989;70:216–21
8. Kiris T, Sankhla S, Lawton M, et al. Microsurgical anatomy of the cavernous sinus. *Barrow Quarterly* 1996;12:1–7
9. Day AL. Aneurysms of the ophthalmic segment: a clinical and anatomical analysis. *J Neurosurg* 1990;72:677–91
10. Barami K, Hernandez VS, Diaz FG, et al. Paraclinoid carotid aneurysms: surgical management, complications, and outcome based on a new classification scheme. *Skull Base* 2003;13:31–41
11. De Jesús O, Sekhar LN, Riedel CJ. Clinoid and paraclinoid aneurysms: surgical anatomy, operative techniques, and outcome. *Surg Neurol* 1999;51:477–87
12. Lasjaunias PL, Berenstein A, Raybaud C. *Surgical Neuroangiography*. Berlin/New York: Springer-Verlag; 1987
13. Lasjaunias P, Santoyo-Vazquez A. Segmental agenesis of the internal carotid artery: angiographic aspects with embryological discussion. *Anat Clin* 1984;6:133–41
14. Fiorella D, Woo HH, Albuquerque FC, et al. Definitive reconstruction of circumferential, fusiform intracranial aneurysms with the Pipeline embolization device. *Neurosurgery* 2008;62:1115–20
15. Ferreira M, Feiz-Erfan I, Deshmukh P, et al. Microsurgical anatomy of the anterior cerebral circulation, part I: the infraclinoid internal carotid artery. *Barrow Quarterly*; 2002;18:1–7
16. Oikawa S, Kyoshima K, Kobayashi S. Surgical anatomy of the juxtadural ring area. *J Neurosurg* 1998;89:250–54
17. Thines L, Delmaire C, Le Gars D, et al. MRI localization of paraclinoid carotid aneurysms. *J Neuroradiol* 2006;33:115–20
18. Thines L, Gauthier JY, Leclerc X, et al. Usefulness of MR imaging for the assessment of nonophthalmic paraclinoid aneurysms. *AJNR Am J Neuroradiol* 2008;29:125–29
19. Thines L, Lee SK, Dehdashti AR, et al. Direct imaging of the distal dural ring and paraclinoid internal carotid artery aneurysms with

- high-resolution T2 turbo-spin echo technique at 3-T magnetic resonance imaging. *Neurosurgery* 2009;64:1059–64
20. Hirai T, Kai Y, Morioka M, et al. **Differentiation between paraclinoid and cavernous sinus aneurysms with contrast-enhanced 3D constructive interference in steady-state MR imaging.** *AJNR Am J Neuroradiol* 2008;29:130–33
21. Lee N, Jung JY, Huh SK, et al. **Distinction between intradural and extradural aneurysms involving the paraclinoid internal carotid artery with T2-weighted three-dimensional fast spin-echo magnetic resonance imaging.** *J Korean Neurosurg Soc* 2010;47:437–41
22. International Study of Unruptured Intracranial Aneurysms Investigators. **Unruptured intracranial aneurysms: risk of rupture and risks of surgical intervention.** *N Engl J Med* 1998;339:1725–33
23. Rhoton AL. **The supratentorial arteries.** *Neurosurgery* 2002;51:S53–120

Carotid CTA: Radiation Exposure and Image Quality with the Use of Attenuation-Based, Automated Kilovolt Selection

A. Eller, W. Wuest, M. Kramer, M. May, A. Schmid, M. Uder, and M.M. Lell



ABSTRACT

BACKGROUND AND PURPOSE: CTA is considered the imaging modality of choice in evaluating the supraaortic vessels in many institutions, but radiation exposure remains a matter of concern. The objective of the study was to evaluate a fully automated, attenuation-based kilovolt selection algorithm in carotid CTA in respect to radiation dose and image quality compared with a standard 120-kV protocol.

MATERIALS AND METHODS: Ninety-eight patients were included: 53 examinations (patient age, 66 ± 12 years) were performed by use of automated adaption of tube potential (80–140 kV) on the basis of the attenuation profile of the scout scan (study group), and 45 examinations (patient age, 67 ± 11 years) were performed by use of a standard 120-kV protocol (control group). CT dose index volume and dose-length product were recorded from the examination protocol. Image quality was assessed by ROI measurements and calculations of SNR and contrast-to-noise ratio. Subjective image quality was evaluated by 2 observers with the use of a 4-point scale (3, excellent; 0, not diagnostic).

RESULTS: Subjective image quality was rated as “excellent” or “good” in all examinations (study group, 2.8; control group, 2.8). The algorithm automatically selected 100 kV in 47% and 80 kV in 34%; 120 kV was retained in 19%. An elevation to 140 kV did not occur. Compared with the control group, overall CT dose index volume reduction was 33.7%; overall dose-length product reduction was 31.5%. In the low-kilovolt scans, image noise and mean attenuation of ROIs inside the carotid arteries were significantly higher than in 120-kV scans, resulting in a constant or increased (80-kV group) contrast-to-noise ratio.

CONCLUSIONS: The attenuation-based, kilovolt selection algorithm enables a dose reduction of >30% in carotid artery CTA while maintaining contrast-to-noise ratio and subjective image quality at adequate levels.

ABBREVIATIONS: CTDIvol = CT dose index volume; DLP = dose-length product; HU = Hounsfield unit; CNR = contrast-to-noise ratio; BMI = body mass index

CT angiography is recommended as a second-line imaging technique in patients with extracranial carotid artery disease after screening with Doppler sonography.¹ As the result of rapid technological evolution, the number of CT examinations is still rising,² even with the significant medical x-ray exposure^{2,3} and the increasing awareness of the potential risks of even relatively low radiation doses^{2,4}—especially in usage as a screening tool⁵ or in serial use.⁶ Biologic experiments have demonstrated that the

number of DNA double-strand breaks is closely related to the applied dose.^{3,7}

Several techniques for CT dose reduction, maintaining image quality on a diagnostic level, became a hot topic in clinical research.^{8–11} Automated attenuation-based tube current modulation or so-called automatic exposure control techniques are widely used.^{12,13} All major manufacturers provide iterative reconstruction algorithms, which are fast enough to be used in clinical practice and aim to compensate the increased image noise of low-dose CTA scans.^{14,15}

Besides minimizing tube current, the reduction of the tube voltage is a potent option to reduce radiation dose. Such low-kilovolt protocols are used in cerebral perfusion CT in the evaluation of patients with stroke¹⁶ and in pediatric CT.¹⁷ In phantom¹⁸ as well as in clinical studies, it has been demonstrated that this technique can also be used in chest and abdominal imaging in adults.^{19–24}

Lower tube voltage in CTA results in higher noise levels on one

Received February 18, 2013; accepted after revision April 30.

From the Department of Radiology, University Erlangen, Erlangen, Germany.

This paper was supported by the German Government, Bundesministerium für Bildung und Forschung, BMBF (01EX1012B, “Spitzencluster Medical Valley”).

Please address correspondence to Michael M. Lell, MD, Department of Radiology, University Erlangen, Maximiliansplatz 1, 91054 Erlangen, Germany; e-mail: michael.lell@uk-erlangen.de

Indicates open access to non-subscribers at www.ajnr.org

<http://dx.doi.org/10.3174/ajnr.A3659>

hand, but the attenuation of iodine is increased^{25,26} on the other hand. This relationship must be considered when trying to reduce radiation exposure by use of low-kilovolt scanning and to maintain image quality.^{24,27} The higher noise level in low-kilovolt scans will not be completely compensated by the higher iodine attenuation; therefore, additional adjustments of the tube current (milliamperage setting) are necessary. Optimal manual adjustment of these parameters is complex, which prevented low-kilovolt scanning from general use until now. New software solutions that automatically adjust the kilovolt and milliamperage setting to the individual patient anatomy by the attenuation profile of the scout scan may overcome this limitation.²⁰

In a previous study, significant dose reduction and higher attenuation profiles of the carotid arteries were reported but were limited in image quality at the level of the common carotid artery.²⁸

In the present study, we aimed to evaluate the effects on radiation exposure and image quality in CTA of the carotid arteries by use of a commercially available automated tube voltage and tube current adaption software tool.

MATERIALS AND METHODS

Ninety-eight patients were prospectively enrolled in this institutional review board–approved study and scheduled for CTA of the carotid arteries. All examinations were performed on a 128-section CT scanner (Somatom Definition AS+, Siemens, Erlangen, Germany) equipped with an automated attenuation-based kilovolt selection and milliamperage adaption algorithm (CAREkV, Siemens). Fifty-three examinations (mean patient age, 66 ± 12 years; range, 25–83 years; 36 male and 17 female patients) were performed by use of automated kilovolt and milliamperage adaption (study group); 45 examinations (mean patient age, 67 ± 11 ; range, 40–88 years; 30 male and 15 female patients) were performed by use of a standard 120-kV protocol (control group). Automated exposure control was used in both groups.

The scan range included the lateral ventricles to the aortic arch. Collimation was 128×0.6 mm and pitch, 0.6. The image quality level of the attenuation-based tube current modulation algorithm (CAREdose 4D) corresponded to 140 Ref. mA at 120 kV for all scans.

After the lateral scout scan, the individual kilovolt setting was calculated on the basis of the attenuation profile. Different settings of the algorithm can be selected; we chose a setting that aims to maintain the SNR constant and allows more aggressive dose reduction.

Circulation time was individually calculated by use of a test bolus injection with 10 mL of iodinated contrast medium (Imeron 350; Bracco, Milan, Italy) at a flow rate of 5 mL/s, chased by a 50-mL saline bolus at the same flow rate. The ROI to measure the TTP was placed in the aortic arch. The delay of the diagnostic scan was calculated by use of the formula $TTP + 2$ seconds. For the diagnostic scan, 50 mL of iodinated contrast medium and a 50-mL saline chaser were used at the same flow rate of 5 mL/s.

Radiation Dose

Values for milliamperes, the CT dose index volume (CTDIvol, milligray), and the dose-length product (DLP, milligray centime-

ters) were recorded from the patient protocol for the diagnostic scans, allowing a direct comparison of radiation dose exposure in the study group and the control group.

Image Quality

The objective assessment of the image quality was performed on a standard PACS workstation (Syngo Plaza, Siemens) in 3-mm images in the axial plane by use of a soft-tissue kernel. For each examination, 2 ROIs were bilaterally placed in the carotid arteries, in the musculature of the neck, and in the air right and left anterior to the neck. Calcifications of the carotid walls were carefully excluded in the ROI. ROIs were not placed in sections with severe artifacts (ie, caused by dental hardware or motion).

ROI size (cm^2), mean attenuation (Hounsfield Unit [HU]), and the standard deviation (HU) were obtained for each measurement. Standard deviation (HU) was considered as a measure of image noise. SNR (mean attenuation [HU] carotid artery/standard deviation [HU]) and contrast-to-noise ratio (CNR) (mean attenuation [HU] carotid artery–mean attenuation [HU] muscle)/standard deviation [HU]) for the carotid artery were calculated.

Subjective image quality assessment of all examinations was evaluated by means of a 4-grade scale (3, excellent; 2, good; 1, moderate; 0, not diagnostic). Artifacts (beam-hardening, windmill artifacts, etc) were grouped into 4 classes (3, no artifacts; 2, mild artifacts not affecting diagnostic value; 1, artifacts affecting diagnostic value; 0, strong artifacts, not diagnostic). Metal artifacts (caused by dental hardware) were not considered. The same evaluation system was used for the control group.

Image quality and the presence of artifacts were independently evaluated by 2 observers (both with more than 4 years of experience in CTA).

Statistical Analyses

Descriptive statistics were performed (SPSS 15.0, IBM, Armonk, New York). A Student *t* test was performed for dose assessment after testing for normal distribution of the data, and the Mann-Whitney *U* rank test was performed to evaluate the subjective image quality scores. A *P* value of $<.05$ was considered to be statistically significant.

Cohen κ was used to assess interobserver agreement in rating image quality and artifacts.

RESULTS

Automated kilovolt selection was successfully applied in all examinations without any user interaction or delay, thus not interfering with the clinical workflow. In the study group, in 10 (18.8%) patients, 120 kV was maintained; in 25 (47.2%) cases, 100 kV was used; and in 18 (34%) cases, 80 kV was used. No case was elevated to 140 kV.

Overall CTDI reduction was 33.7%: 55.8% in 80-kV and 31.6% in 100-kV examinations. In the 10 examinations of the study group scanned at 120 kV, the CTDI was 2.1% higher than in the control group.

Overall DLP reduction was 31.5%: 54% in the 80-kV group and 29.7% in the 100-kV group. In the 120-kV group, the DLP was 0.6% higher than in the control group.

Table 1: Dose parameters

Group	80 kV	100 kV	120 kV	Study Group	Control Group (120 kV)
<i>n</i>	18	25	10	53	45
kV	80	100	120	97 ± 14	120
Reference mAs	210	145	140	166 ± 32	140
Effective mAs	224 ± 14	165 ± 22	144 ± 11	181 ± 37	141 ± 9
CTDIvol, mGy ^b	4.2 ± 0.3 ^a	6.5 ± 0.9 ^a	9.7 ± 0.7	6.3 ± 2.1 ^a	9.5 ± 0.6
DLP, mGy cm ^b	134.5 ± 19.6 ^a	208.7 ± 40 ^a	299.5 ± 54.9	200.6 ± 69.4 ^a	292.8 ± 46.2

Note:—The Reference mAs are automatically adapted to match the image quality level of 140 mA at 120 kV.

^a *P* < .05.

^b CTDIvol and DLP referenced to 32-cm phantom.

Table 2: Results of ROI measurements

Group	80 kV	100 kV	120 kV	Study Group Complete	Control Group (120 kV)
<i>n</i>	18	24	10	53	45
ROI carotid	Mean 488.4 ± 93.3 ^a SD 12.7 ± 2.8 ^a SNR 40.1 ± 12.3 CNR 34.9 ± 11.5 ^a	Mean 340.9 ± 73.8 ^a SD 12.1 ± 2.7 ^a SNR 29.9 ± 9.4 CNR 24.4 ± 8.9	Mean 243 ± 83.2 ^a SD 7.9 ± 3.1 SNR 33.7 ± 13 CNR 25 ± 12.7	Mean 372.5 ± 122.1 ^a SD 11.5 ± 3.3 ^a SNR 34.1 ± 11.8 CNR 28.1 ± 11.5	Mean 293.9 ± 58 SD 8.8 ± 1.8 SNR 35.2 ± 11.7 CNR 28.3 ± 10.9
ROI muscle	Mean 61.4 ± 7.8 SD 9.7 ± 2.7 ^a	Mean 62.2 ± 11.2 SD 9.6 ± 2.8 ^a	Mean 61.4 ± 9.8 SD 6.5 ± 2.4	Mean 61.8 ± 9.7 SD 9.1 ± 2.9 ^a	Mean 58.9 ± 6.3 SD 6.7 ± 1.4
ROI air	Mean -1000.2 ± 1.8 ^a SD 6.2 ± 1.9 ^a	Mean -999.1 ± 2.2 SD 6.5 ± 2.2 ^a	Mean -999.2 ± 1.3 SD 4.1 ± 1.3	Mean -999.5 ± 2 SD 5.9 ± 2.1	Mean -998.7 ± 2.2 SD 4.6 ± 1

Note:—Values correspond to Hounsfield units.

^a *P* < .05.

Table 3: Results of the subjective image quality assessment

Group	80 kV	100 kV	120 kV	Study Group	Control Group (120 kV)
<i>n</i>	18	25	10	53	45
Grade 3, excellent	14/15	17/15	10/9	41/39	37/38
Grade 2, good	4/3	8/10	0/1	12/14	8/7
Grade 1, diagnostic	0	0	0	0	0
Grade 0, not diagnostic	0	0	0	0	0
Average	2.8	2.6 ^a	2.9	2.8	2.8

Note:—Counts are given for both observers (observer 1/observer 2).

^a *P* < .05.

Dose Evaluation

Dose evaluations specified for the different kilovolt groups are given in Table 1.

All CTA examinations were of high quality and fully diagnostic; no examination of the study group or control group was classified as “moderate” or “not diagnostic.” Mild beam-hardening artifacts, none of which affected diagnostic values, were found in all examinations in some sections (usually at the shoulder level) independent of the kilovolt setting, but all artifacts were classified as mild (grade 2) and were not exaggerated by use of the low-kilovolt technique.

CTA studies performed at 80 kV had quality scores similar to those in studies from the control group (120 kV). Interobserver agreement was substantial in the study group ($\kappa = 0.695$) and moderate in the control group ($\kappa = 0.6$).

The results for the objective image quality assessment by use of ROI measurements are given in Table 2; those for subjective image quality are given in Table 3.

In the study group, diagnostic findings included 24 with >70% stenosis or occlusion (22.6%; 13 right, 11 left) of the internal carotid arteries; 16 (15.1%; 9 right, 7 left) with stenosis between 50–70%; and in 66 (62.3%; 31 right, 35 left), stenosis <50% or no stenosis. Severe calcified plaques of the carotid bifurcation occurred in 52.8%.

In the control group, diagnostic findings included 37 with >70% stenosis or occlusion (41.1%; 19 right, 18 left) of the internal carotid arteries; 10 (11.1%; 3 right, 7 left) with stenosis between 50–70%; and in 43 cases (47.8%; 23 right, 20 left), <50% stenosis or no stenosis. Severe calcified plaques of the carotid bifurcation occurred in 53.3%.

Examples of the different kilovolt groups, comparing examinations by use of 80, 100, and 120 kV in the axial plane and sagittal maximum intensity projections are shown in Fig 1.

DISCUSSION

CTA is frequently used in the evaluation of carotid artery stenosis²⁹ and is meant to be the reference standard.³⁰ Anzidei et al³¹ reported that CTA was the most accurate technique for evaluating carotid stenosis in a large study group (*n* = 170 patients), with a slightly better performance

than MRA (97% versus 95% for steady-state MRA and 92% for first-pass MRA) and a greater accuracy than color Doppler ultrasonography (97% versus 76%). Although patients scheduled for carotid artery imaging are predominantly in the higher age group and radiation exposure is thought to be less critical, the ALARA (as low as reasonably achievable) concept should still be followed, and a variety of dose-reduction techniques in CT imaging have become available in recent years.^{32–35} There are abundant data that the low-kilovolt technique can significantly reduce radiation exposure and maintain image quality; however, until now, it is still not often used in clinical routine.

The main reason that most CT examinations including CTA are still performed with the 120-kV setting is that many users are not familiar with the required tube current adaption when scanning at low kilovolts. This adaption is important to keep the image noise level within an appropriate range. Elevating the tube current, on the other hand, limits or reverses the dose-reduction potential; therefore, scanning at 80 or 100 kV in every patient is not reasonable.

The software under evaluation is fully integrated in the scan protocols, tailoring the kilovolt and milliamperage settings to the respective examination situation and individual patient anatomy. No further user interaction is required. In most (81.2%), adaptations allowed overall dose reduction. The predefined image quality level (120 kV, 140 mA) was kept constant throughout the study and the control group. Objective image quality was comparably high, with no significant differences between the study group and the control group, though a significant reduction in dose (overall CTDIvol reduction in the study group, 33.7%) was achieved. CTDIvol reduction was 55.8% in the examinations at 80 kV and 31.6% at 100 kV.

The noise measurements revealed significantly increased image noise levels in the 80-kV and 100-kV examinations but also significantly higher iodine contrast. The CNR in the study group

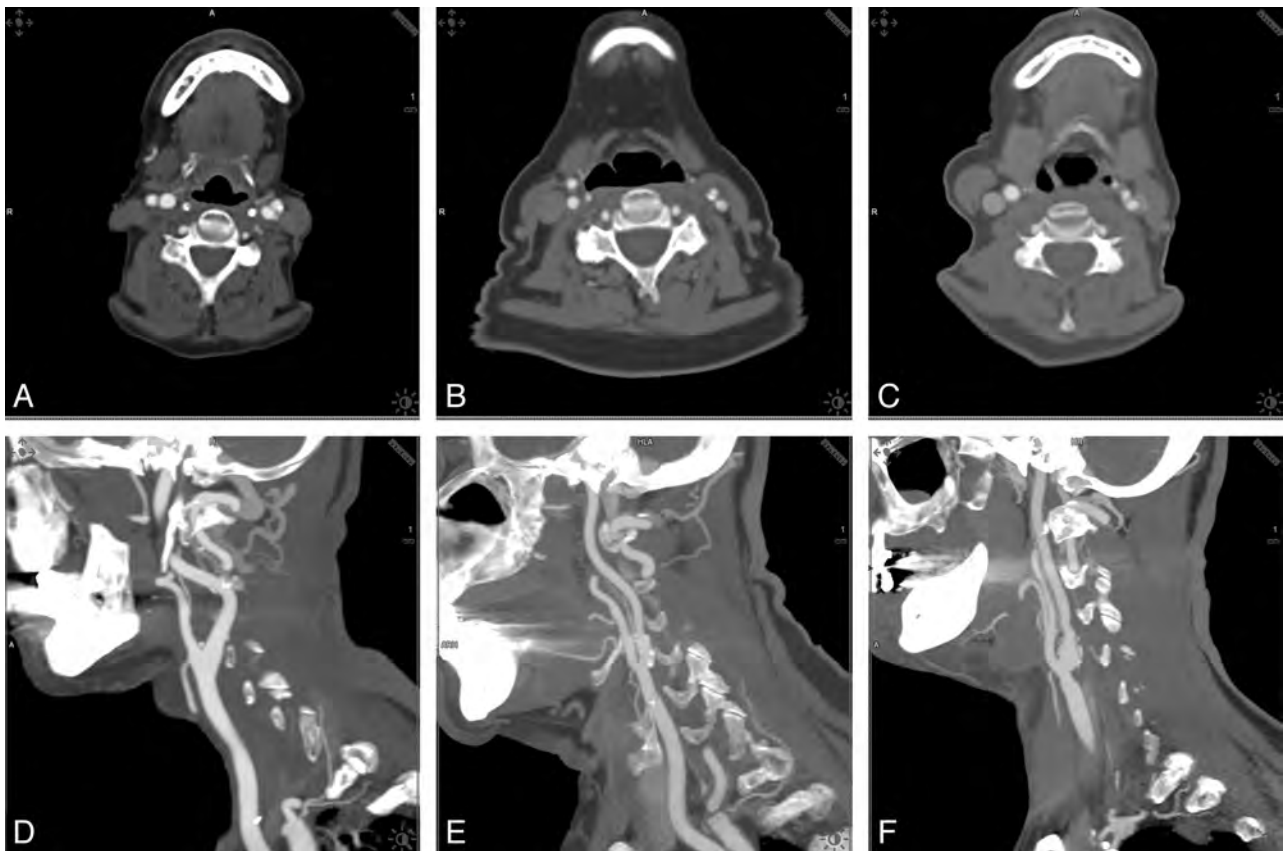


FIG 1. Examples of the different kilovolt groups. Comparison of examinations by use of 80, 100, and 120 kV in the axial plane and sagittal maximum intensity projections.

and the control group was comparable; in the 80-kV group, CNR increased. To compensate for the different image contrasts, the window-level setting also must be adapted. This is of special importance to differentiate calcified plaque from luminal contrast and to restore the familiar image aspect in low-kilovolt images, but this step can also be performed automatically by the software.

Subjective image quality was high in all CTA examinations, without any equivocal or nondiagnostic results. Image noise in the 100-kV group was similar to that at 80 kV on average, resulting in higher SNR and CNR and higher subjective scores for 80-kV examinations.

The fact that the HU values in the carotid arteries were significantly lower in the study group scanned at 120 kV as compared with the control group, in which all scans were performed at 120 kV, may be attributed to the small sample size ($n = 10$) and patient-specific factors.³⁶

The algorithm is designed to provide optimal parameter adjustment by the attenuation profile of the scout scan; thus, patient size is supposed to be one of the main influencing factors. In imaging the trunk, the body mass index (BMI) influences the kilovolt setting.²⁰ BMI does not play that role in carotid CTA or CT of the neck, because a short neck or elevated, muscular shoulders influence attenuation more profoundly and do not correlate well with the BMI. In our study cohort, patients up to a BMI of 42 (height, 185 cm; weight, 145 kg) were scanned successfully at 100 kV.

Low-kilovolt scanning is limited by tube output. If higher pitch values are applied, the high attenuation at the level of the

shoulders in larger persons may preclude the application of 80 kV. Iterative reconstruction has been demonstrated to compensate image noise in low-kilovolt scanning, maintaining high image quality.^{24,37} Adding iterative reconstruction techniques to 100-kV scanning may further improve dose reduction by compensation of the higher image noise. We did not investigate this option because we wanted to exclude all confounding effects from the different techniques. Another limitation may be that we used an aggressive setting of the algorithm, which balances image noise and vascular enhancement but leads to decreased CNR and SNR of tissue with less or no contrast material uptake. This makes the success of the approach also dependent on optimal contrast timing, which can be achieved with the use of either a test bolus or a bolus-tracking technique.

CONCLUSIONS

We demonstrated that an attenuation-based kilovolt selection with automated milliamperage adaption in CTA of the carotid arteries results in a significant dose reduction while preserving image quality. The significantly increased noise level of the images is compensated by increased iodine contrast, resulting in a comparably high or improved CNR. Further dose reduction might be achieved by combining the algorithm with other dose-saving techniques such as iterative reconstruction algorithms.

Disclosures: Michael Uder—UNRELATED: Payment for Lectures (including service on speakers bureaus): Bracco, Siemens, Bayer-Schering, Medtronic; Patents

REFERENCES

1. Brott TG, Halperin JL, Abbara S, et al. 2011 ASA/ACCF/AHA/AANN/AANS/ACR/ASNR/CNS/SAIP/SCAI/SIR/SNIS/SVM/SVS Guideline on the management of patients with extracranial carotid and vertebral artery disease: a report of the American College of Cardiology Foundation/American Heart Association Task Force on Practice Guidelines, and the American Stroke Association, American Association of Neuroscience Nurses, American Association of Neurological Surgeons, American College of Radiology, American Society of Neuroradiology, Congress of Neurological Surgeons, Society of Atherosclerosis Imaging and Prevention, Society for Cardiovascular Angiography and Interventions, Society of Interventional Radiology, Society of NeuroInterventional Surgery, Society for Vascular Medicine, and Society for Vascular Surgery, developed in collaboration with the American Academy of Neurology and Society of Cardiovascular Computed Tomography. *J Am Coll Cardiol* 2011;57:e16–94
2. Berrington de Gonzalez A, Mahesh M, Kim KP, et al. Projected cancer risks from computed tomographic scans performed in the United States in 2007. *Arch Intern Med* 2009;169:2071–77
3. Kuefner MA, Grudzinski S, Schwab SA, et al. DNA double-strand breaks and their repair in blood lymphocytes of patients undergoing angiographic procedures. *Invest Radiol* 2009;44:440–46
4. Brenner DJ, Hall EJ. Computed tomography: an increasing source of radiation exposure. *N Engl J Med* 2007;357:2277–84
5. Narvid J, Do HM, Blevins NH, et al. CT angiography as a screening tool for dural arteriovenous fistula in patients with pulsatile tinnitus: feasibility and test characteristics. *AJNR Am J Neuroradiol* 2011;32:446–53
6. van Gils MJ, Vukadinovic D, van Dijk AC, et al. Carotid atherosclerotic plaque progression and change in plaque composition over time: a 5-year follow-up study using serial CT angiography. *AJNR Am J Neuroradiol* 2012;33:1267–73
7. Lobrich M, Rief N, Kuhne M, et al. In vivo formation and repair of DNA double-strand breaks after computed tomography examinations. *Proc Natl Acad Sci U S A* 2005;102:8984–89
8. Coakley FV, Gould R, Yeh BM, et al. CT radiation dose: what can you do right now in your practice? *AJR Am J Roentgenol* 2011;196:619–25
9. Kalender WA, Buchenau S, Deak P, et al. Technical approaches to the optimisation of CT. *Phys Med* 2008;24:71–79
10. Kalra MK, Maher MM, Toth TL, et al. Strategies for CT radiation dose optimization. *Radiology* 2004;230:619–28
11. Manninen AL, Isokangas JM, Karttunen A, et al. A comparison of radiation exposure between diagnostic CTA and DSA examinations of cerebral and cervicocerebral vessels. *AJNR Am J Neuroradiol* 2012;33:2038–42
12. Soderberg M, Gunnarsson M. Automatic exposure control in computed tomography: an evaluation of systems from different manufacturers. *Acta Radiol* 2010;51:625–34
13. van Straten M, Deak P, Shrimpton PC, et al. The effect of angular and longitudinal tube current modulations on the estimation of organ and effective doses in x-ray computed tomography. *Med Phys* 2009;36:4881–89
14. Bittencourt MS, Schmidt B, Seltmann M, et al. Iterative Reconstruction in Image Space (IRIS) in cardiac computed tomography: initial experience. *Int J Cardiovasc Imaging* 2011;27:1081–87
15. Leipsic J, Heilbron BG, Hague C. Iterative reconstruction for coronary CT angiography: finding its way. *Int J Cardiovasc Imaging* 2012;28:613–20
16. Haberland U, Klotz E, Abolmaali N. Performance assessment of dynamic spiral scan modes with variable pitch for quantitative perfusion computed tomography. *Invest Radiol* 2010;45:378–86
17. Singh S, Kalra MK, Moore MA, et al. Dose reduction and compliance with pediatric CT protocols adapted to patient size, clinical indication, and number of prior studies. *Radiology* 2009;252:200–08
18. Kalender WA, Deak P, Kellermeier M, et al. Application- and patient size-dependent optimization of x-ray spectra for CT. *Med Phys* 2009;36:993–1007
19. Bjorkdahl P, Nyman U. Using 100- instead of 120-kVp computed tomography to diagnose pulmonary embolism almost halves the radiation dose with preserved diagnostic quality. *Acta Radiol* 2010;51:260–70
20. Eller A, May MS, Scharf M, et al. Attenuation-based automatic kilovolt selection in abdominal computed tomography: effects on radiation exposure and image quality. *Invest Radiol* 2012;47:559–65
21. Matsuoka S, Hunsaker AR, Gill RR, et al. Vascular enhancement and image quality of MDCT pulmonary angiography in 400 cases: comparison of standard and low kilovoltage settings. *AJR Am J Roentgenol* 2009;192:1651–56
22. Schindera ST, Graca P, Patak MA, et al. Thoracoabdominal-aortoiliac multidetector-row CT angiography at 80 and 100 kVp: assessment of image quality and radiation dose. *Invest Radiol* 2009;44:650–55
23. Wildberger JE, Mahnken AH, Schmitz-Rode T, et al. Individually adapted examination protocols for reduction of radiation exposure in chest CT. *Invest Radiol* 2001;36:604–11
24. Winklehner A, Goetti R, BaumueLLer S, et al. Automated attenuation-based tube potential selection for thoracoabdominal computed tomography angiography: improved dose effectiveness. *Invest Radiol* 2011;46:767–73
25. Ramgren B, Bjorkman-Burtscher IM, Holtas S, et al. CT angiography of intracranial arterial vessels: impact of tube voltage and contrast media concentration on image quality. *Acta Radiol* 2012;53:929–34
26. Marin D, Nelson RC, Samei E, et al. Hypervascular liver tumors: low tube voltage, high tube current multidetector CT during late hepatic arterial phase for detection: initial clinical experience. *Radiology* 2009;251:771–79
27. Ramgren B, Bjorkman-Burtscher IM, Holtas S, et al. CT angiography of intracranial arterial vessels: impact of tube voltage and contrast media concentration on image quality. *Acta Radiol* 2012;53:929–34
28. Beitzke D, Wolf F, Edelhauser G, et al. Computed tomography angiography of the carotid arteries at low kV settings: a prospective randomised trial assessing radiation dose and diagnostic confidence. *Eur Radiol* 2011;21:2434–44
29. Byrnes KR, Ross CB. The current role of carotid duplex ultrasonography in the management of carotid atherosclerosis: foundations and advances. *Int J Vasc Med* 2012 Mar 7 [Epub ahead of print]
30. Babiarz LS, Romero JM, Murphy EK, et al. Contrast-enhanced MR angiography is not more accurate than unenhanced 2D time-of-flight MR angiography for determining $\geq 70\%$ internal carotid artery stenosis. *AJNR Am J Neuroradiol* 2009;30:761–68
31. Anzidei M, Napoli A, Zaccagna F, et al. Diagnostic accuracy of colour Doppler ultrasonography, CT angiography and blood-pool-enhanced MR angiography in assessing carotid stenosis: a comparative study with DSA in 170 patients. *Radiol Med* 2012;117:54–71
32. Alkadhhi H, Leschka S. Radiation dose of cardiac computed tomography: what has been achieved and what needs to be done. *Eur Radiol* 2011;21:505–09
33. Kim JE, Newman B. Evaluation of a radiation dose reduction strategy for pediatric chest CT. *AJR Am J Roentgenol* 2010;194:1188–93
34. McCollough CH, Bruesewitz MR, Kofler JM Jr. CT dose reduction and dose management tools: overview of available options. *Radiographics* 2006;26:503–12
35. Silva AC, Lawder HJ, Hara A, et al. Innovations in CT dose reduction strategy: application of the adaptive statistical iterative reconstruction algorithm. *AJR Am J Roentgenol* 2010;194:191–99
36. Bae KT. Intravenous contrast medium administration and scan timing at CT: considerations and approaches. *Radiology* 2010;256:32–61
37. Hou Y, Xu S, Guo W, et al. The optimal dose reduction level using iterative reconstruction with prospective ECG-triggered coronary CTA using 256-slice MDCT. *Eur J Radiol* 2012;81:3905–11

The Medicare Conversion Factor

D.J. Seidenwurm and J.H. Burleson

ABBREVIATIONS: RVU = Relative Value Unit; CF = Conversion Factor; GPCI = Geographic Practice Cost Index; CMS = Centers for Medicare and Medicaid Services; MP = malpractice; RBRVS = Resource-Based Relative Value Scale; CPT = Current Procedural Terminology; SGR = Sustainable Growth Rate

To understand the Medicare compensation system for physician services, it is necessary to understand how the relative values of medical services are translated into fee schedule payment amounts. Basically, the relative value of a procedure multiplied by the number of dollars per Relative Value Unit (RVU) is the fee paid by Medicare for the procedure (RVU_W = physician work, RVU_{PE} = practice expense, RVU_{MP} = malpractice). The Conversion Factor (CF) is the number of dollars assigned to an RVU. It is calculated by use of a complex formula (Fig 1) that takes into account the overall state of the economy of the United States, the number of Medicare beneficiaries, the amount of money spent in prior years, and changes in the regulations governing covered services. Medicare fees are set according to a relative value scale rather than a free market, payments are made by third parties rather than consumers, and the labor market for physicians is illiquid, so the pricing mechanisms that regulate markets in other parts of the economy are not effective in rationalizing prices. The factors that influence the CF calculation are similar to those that are used in calculating global health care budgets; therefore the principles are durable, even if the precise formula might be altered in the future.

Annually, the CF is based on the previous year's CF and adjusted for the Medical Economic Index, the Update Adjustment Factor, Legislative Change, and Budget Neutrality. The Medical Economic Index is a calculation of the inflation rate for medical services, which is generally higher than inflation in consumer prices overall. The Update Adjustment Factor encompasses the Sustainable Growth Rate (SGR) that takes into account growth or decline in the Gross Domestic Product, changes in the number of beneficiaries, and certain regulatory adjustments that may affect

the demand for and costs of providing Medicare services. This is the mechanism through which the relative proportion of Part B Medicare spending is maintained at an acceptable level with respect to overall government spending and the size of the economy as a whole. The process of setting the CF each year balances increases in demand for medical services and the finite productive capacity of the economy. The calculation is then subject to Budget Neutrality, requiring any increase in the relative expenditures in one area of the Medicare program to be offset by cuts in other areas. The calculation must result in a budget for Medicare that is within \$20 million of the target.¹

What Is the CF?

The monetary CF is 1 of 3 key elements that determine physician payment under the Medicare Physician Fee Schedule, along with the Resource-Based Relative Value Scale and Geographic Practice Cost Indices (GPCIs) ($GPCI_W$ = physician work, $GPCI_{PE}$ = practice expense).

With the Resource-Based Relative Value Scale (RBRVS), an RVU is assigned for each Current Procedural Terminology (CPT) code on the basis of resource costs associated with 1) physician work, 2) practice expense, and 3) professional liability insurance. As determined by Congress at the inception of the RBRVS, all of the CPT codes on the Medicare Fee Schedule are subject to review on an annual basis.¹

Each Current Procedural Terminology code RVU is adjusted on the basis of the GPCI associated with each geographic area, adjusting for different medical costs and wage differentials. GPCIs are reviewed every 3 years.

The CF, a national dollar multiplier, is used to "convert" the geographically adjusted RVU to determine the Medicare-allowed payment amount for a particular physician service.

The CF is used separately to price facility and nonfacility payment amounts. Facility pricing typically covers services provided to inpatients or in a hospital outpatient clinic setting or other off-site hospital facilities. Nonfacility pricing covers services gen-

Received April 10, 2013; accepted after revision April 30.

From Radiological Associates of Sacramento, Auburn, California (D.S.); and Metrics Department, American College of Radiology, Reston, Virginia (J.B.).

Please address correspondence to Judy Burleson, MHSA, American College of Radiology, 1891 Preston White Dr, Reston, VA 20191; e-mail: jburleson@acr.org

<http://dx.doi.org/10.3174/ajnr.A3674>

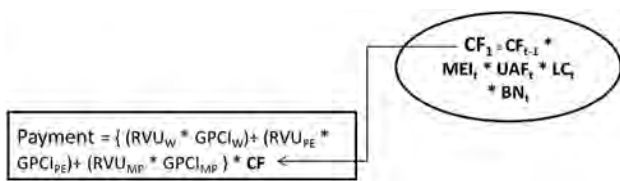


FIG 1. Role of the conversion factor in the Medicare fee schedule.

erally provided in a physician office or other freestanding setting such as an Independent Diagnostic Testing Facility.²

How Is the CF Calculated? Why Is the Calculation So Complex?

The CF is updated annually according to a complex formula set by statute. Every year, by use of the formula, the Centers for Medicare and Medicaid Services (CMS) must publish an estimated SGR and estimated CF applicable to Medicare payments for physician services for the following year, as well as the data underlying these estimates. CMS cannot change its overall budget by more than \$20 million. The use of this SGR target is intended to control growth of aggregate Medicare spending. The targets are not expenditure limits, but an update to the Physician Fee Schedule to reflect a comparison of actual to target expenditures. If RVU adjustment causes a differential greater than that \$20 million or exceeds the target, CMS uses the Budget Neutrality factor to bring overall payments down to an acceptable level.

Under statute, the update for each year is determined by comparing cumulative actual expenditures with cumulative target expenditures since April 1, 1996, through the end of the year before the year in question. As an example, the update for 2013 compares the cumulative actual with cumulative target expenditures from April 1, 1996, through December 31, 2012. The calculation is as follows for 2013:

2013 Non-Facility Pricing Amount = [(Work RVU * Work GPCI) + (Transitioned Non-Facility PE RVU * PE GPCI) + (malpractice expense [MP] RVU * MP GPCI)] * CF
 2013 Facility Pricing Amount = [(Work RVU * Work GPCI) + (Transitioned Facility PE RVU * PE GPCI) + (MP RVU * MP GPCI)] * CF.

The CF for calendar year 2013 is \$34.0230.

If the Formula Were Followed, What Would the CF Be for Next Year?

Under current law, the CF for 2014 would be similar to 2013, reduced by approximately 26.5% to \$25.0069 (compared with the current \$34.0230). This reduction would be effective January 1, 2014, unless Congress passes a legislative fix. The latest estimates of the cost of the so called “doc fix” are between \$150 and \$300 billion, depending on assumptions regarding economic performance, policy changes, and physician behavior.

What Happens Next?

Annually, the Sustainable Growth Rate–mandated cuts in the CF have been overridden by Congress, usually through last-minute negotiations that cover numerous contentious issues. Many interested in health policy recognize the need for a reform of this process to improve clarity and remove uncertainty from the annual determination of the CF. Because of the large and growing discrepancy between the statutory CF and the established CF, the budgetary need for a more permanent solution is also considered important, going forward. Recently, the magnitude of the adjustment required in the CF to maintain Budget Neutrality has been revised downward. It is likely that this is a temporary consequence of the disparate timing of effects on the various components of the Sustainable Growth Rate formula related to recent economic conditions. As the economy returns to more normal levels of growth, we can expect these short-term trends to revert to their prior patterns and continue to increase.

Some of the proposals on the table include cuts in the overall level of Medicare fees weighted heavily toward cuts in specialist services such as imaging and relatively sparing primary care. Others reduce costs by changing the calculation of Medicare premiums and/or means testing them. Another approach is to adjust the relationship between the CF and the rate of inflation and the rate of economic growth. Other proposals seek a more fundamental overhaul of the program, through premium support models similar to those already being used in Medicare Part D. Others seek to preserve the status quo. Regardless of the fate of the current CF formula and the precise relationships among the components, the ingredients of the CF are combined in recipes for global health care budgets under discussion in health care policy circles.³

Disclosures: David Seidenwurm—RELATED: Consulting Fee or Honorarium: CMI, ACR, Medical Legal, Medical Management, Comments: CMI is a consortium of radiology practices in California; meeting honoraria are paid to Dr Seidenwurm’s practice. Dr Seidenwurm performs medical legal consulting and medical management consulting. Dr Seidenwurm participates in the ACR MRI accreditation program; Support for Travel to Meetings for the Study or Other Purposes: NQF, ASNR, RAS, CMI, PCPI, ACR, Comments: Dr Seidenwurm receives travel reimbursement for participation in numerous activities related principally to performance measurement and quality improvement in medicine and radiology; Other: Hill Physicians Medical Group.* Comments: Utilization review for HMO, ACO and other activities; UNRELATED: Board Membership: CMI*; Consultancy: Medical Legal, Medical Management; Employment: RAS; Expert Testimony: Medical Legal; Payment for Development of Educational Presentations: Kluver, Comments: Textbook chapter; Stock/Stock Options: Aaken Labs.* Comments: Electrophysiology and imaging fusion. Judith H. Burleson—OTHER RELATIONSHIPS: Employed by the American College of Radiology.

REFERENCES

1. Woody I. The fundamentals of the US Medicare physician reimbursement process. *J Am Coll Radiol* 2005;2:139–50
2. American Medical Association. 2012 RBRVS: *The Physicians’ Guide*. Chicago: American Medical Association; 2012
3. Health policy brief: Medicare payments to physicians. *Health Affairs*. Updated February 13, 2013

Visual-Statistical Interpretation of ¹⁸F-FDG-PET Images for Characteristic Alzheimer Patterns in a Multicenter Study: Inter-Rater Concordance and Relationship to Automated Quantitative Evaluation

T. Yamane, Y. Ikari, T. Nishio, K. Ishii, K. Ishii, T. Kato, K. Ito, D.H.S. Silverman, M. Senda, T. Asada, H. Arai, M. Sugishita, T. Iwatsubo, and the J-ADNI Study Group



ABSTRACT

BACKGROUND AND PURPOSE: The role of ¹⁸F-FDG-PET in the diagnosis of Alzheimer disease is increasing and should be validated. The aim of this study was to assess the inter-rater variability in the interpretation of ¹⁸F-FDG-PET images obtained in the Japanese Alzheimer's Disease Neuroimaging Initiative, a multicenter clinical research project.

MATERIALS AND METHODS: This study analyzed 274 ¹⁸F-FDG-PET scans (67 mild Alzheimer disease, 100 mild cognitive impairment, and 107 normal cognitive) as baseline scans for the Japanese Alzheimer's Disease Neuroimaging Initiative, which were acquired with various types of PET or PET/CT scanners in 23 facilities. Three independent raters interpreted all PET images by using a combined visual-statistical method. The images were classified into 7 (FDG-7) patterns by the criteria of Silverman et al and further into 2 (FDG-2) patterns.

RESULTS: Agreement among the 7 visual-statistical categories by at least 2 of the 3 readers occurred in >94% of cases for all groups: Alzheimer disease, mild cognitive impairment, and normal cognitive. Perfect matches by all 3 raters were observed for 62% of the cases by FDG-7 and 76 by FDG-2. Inter-rater concordance was moderate by FDG-7 ($\kappa = 0.57$) and substantial in FDG-2 ($\kappa = 0.67$) on average. The FDG-PET score, an automated quantitative index developed by Herholz et al, increased as the number of raters who voted for the AD pattern increased ($\rho = 0.59, P < .0001$), and the FDG-PET score decreased as those for normal pattern increased ($\rho = -0.64, P < .0001$).

CONCLUSIONS: Inter-rater agreement was moderate to substantial for the combined visual-statistical interpretation of ¹⁸F-FDG-PET and was also significantly associated with automated quantitative assessment.

ABBREVIATIONS: AD = Alzheimer disease; J-ADNI = Japanese Alzheimer's Disease Neuroimaging Initiative; MCI = mild cognitive impairment; NC = cognitively normal subject

PET can visualize regional glucose metabolism by using ¹⁸F-FDG; and hypometabolism in the posterior cingulate/precuneus and temporoparietal cortices is regarded as a typical uptake

pattern of Alzheimer disease (AD).¹ These findings are considered useful for differentiating AD from other disorders presenting with dementia as well as for predicting conversion from mild cognitive impairment (MCI) to AD.^{2,3}

Three approaches for evaluating brain PET images are visual interpretation alone, visual interpretation with adjunctive statis-

Received February 21, 2013; accepted after revision May 2.

From the Division of Molecular Imaging (T.Y., Y.I., T.N., M. Senda), Institute of Biomedical Research and Innovation, Kobe, Japan; Department of Radiology (Kazunari Ishii), Kinki University Faculty of Medicine, Osakasayama, Japan; Positron Medical Center (Kenji Ishii), Tokyo Metropolitan Institute of Gerontology, Tokyo, Japan; Department of Brain Science and Molecular Imaging (T.K., K. Ito), National Center for Geriatrics and Gerontology, Obu, Japan; David Geffen School of Medicine (D.H.S.S.), University of California, Los Angeles, Los Angeles, California; Department of Psychiatry (T.A.), University of Tsukuba, Tsukuba, Japan; Department of Geriatrics and Gerontology (H.A.), Tohoku University, Sendai, Japan; Institute of Brain and Blood Vessels (M. Sugishita), Isezaki, Japan; Department of Neuropathology and Neuroscience (T.I.), University of Tokyo, Tokyo, Japan; Research Association for Biotechnology (Y.I., T.N.), Tokyo, Japan; and J-ADNI Core (T.Y., Y.I., T.N., Kazunari Ishii, Kenji Ishii, T.K., Kengo Ito, M.S., T.A., H.A., M.S., T.I.).

The Research Group of the Japanese Alzheimer's Disease Neuroimaging Initiative comprised investigators from 38 different facilities. The investigators contributed to the design and implementation of J-ADNI and/or provided data but did not participate in the analyses of this report.

T. Yamane contributed to concept and design, analyzed data, and wrote the manuscript. Y. Ikari and T. Nishio acquired and analyzed PET data. Kazunari Ishii, Kenji Ishii, T. Kato, and K. Ito acquired and interpreted PET data. D.H.S. Silverman critically revised the manuscript and enhanced its intellectual content. M. Senda critically revised the manuscript, enhanced its intellectual content, and approved

the final content of the manuscript. T. Asada, H. Arai, M. Sugishita, and T. Iwatsubo acquired clinical data and approved the final content of the manuscript.

This work is a part of the Translational Research Promotion Project/Research Project for the Development of a Systematic Method for the Assessment of Alzheimer's Disease, sponsored by the New Energy and Industrial Technology Development Organization of Japan. The Japanese Alzheimer's Disease Neuroimaging Initiative is also supported by a Grant-in-Aid for Comprehensive Research on Dementia from the Japanese Ministry of Health, Labour and Welfare, as well as by the grants from J-ADNI Pharmaceutical Industry Scientific Advisory Board companies.

Paper previously presented in part at: Annual Meeting of the Society of Nuclear Medicine, June 4–8, 2011; San Antonio, Texas.

Please address correspondence to Tomohiko Yamane, MD, PhD, Division of Molecular Imaging, Institute of Biomedical Research and Innovation, 2–2, Minatojima-minamimachi, Chuo-ku, Kobe, 650-0047, Japan; e-mail address: yamane@fbri.org

Indicates open access to non-subscribers at www.ajnr.org

Evidence-Based Medicine Level 2.

<http://dx.doi.org/10.3174/ajnr.A3665>

tical tools (visual-statistical), and automated quantitative analysis, but the relationship between the latter 2 of these approaches has been little explored, to our knowledge. Visual interpretation features comprehensive and flexible assessment of the qualitative radioactivity distribution by the reader, who may look into all features across the brain. This approach appears effective because patients with AD typically present with characteristic temporoparietal hypometabolism known as the “AD pattern.” However, inter-rater variability inevitably occurs because each rater has his or her own experience and criteria, especially for borderline cases, and this variability can potentially be increased or decreased when the reader also takes into account statistical information provided by various software display tools.

On the other hand, quantitative analysis traditionally extracts radioactivity uptake values of the region of interest, placement of which is a subjective matter requiring experience. Although a recently developed anatomic standardization technique can define ROIs automatically and further allows voxelwise statistical analysis to generate *Z*-maps, standardization may not always be accurate and may require adjustment by a human observer. Although these region-of-interest values can be processed into a numeric indicator such as an FDG-PET score^{4,5} and a cutoff level can be determined, a single indicator may not be as accurate as complex and comprehensive evaluation by expert readers. As a result, a “combined” approach of visual and quantitative evaluation is often used during image interpretation, in which the readers examine both the tomographic PET images and the result of region-of-interest analysis and/or a *Z*-map.

Inter-rater variability and comparison between visual reading and software-based evaluation have been studied by some investigators on brain ¹⁸F-FDG-PET. Ng et al⁶ studied the inter-rater variability of 15 patients with AD and 25 cognitively normal subjects (NCs) and reported that visual agreement between 2 readers was good ($\kappa = 0.56$). Tolboom et al⁷ studied the variability of 20 patients with AD and 20 NCs and reported that agreement between 2 readers was moderate ($\kappa = 0.56$). Rabinovici et al⁸ also reported the inter-rater agreement of ¹⁸F-FDG ($\kappa = 0.72$). However, the data of these preceding studies were acquired with a single scanner in a single site and were evaluated by the readers belonging to the institution who were used to the scanner and its image quality. In addition, the studied subjects did not include patients with MCI, in whom PET findings featuring AD, if any, are mild and may make the discrimination challenging. Furthermore, inter-rater variability for combined interpretation of visual and statistical analysis has never been reported, to our knowledge.

In the present study, we analyzed the baseline scans of ¹⁸F-FDG in a multicenter clinical project named Japanese Alzheimer’s Disease Neuroimaging Initiative (J-ADNI)⁹ and evaluated the inter-rater variability among 3 independent expert raters who were blinded to the clinical information and interpreted the PET images to evaluate the characteristic AD pattern in ¹⁸F-FDG-PET on the basis of a combined visual-statistical evaluation. The raters looked at the 3D stereotactic surface projection *Z*-map of ¹⁸F-FDG-PET visually as well as the ¹⁸F-FDG tomographic images because it is considered the standard means of human interpretation of ¹⁸F-FDG-PET images in Japan and therefore was adopted as the official interpretation method in J-ADNI. Images were also assessed by auto-

ated quantitative analysis by using an FDG-PET score, which was derived from ADtsum,^{4,5} and were compared with the visual-statistical rating by the 3 raters and with their consensus.

MATERIALS AND METHODS

Subjects

Data used in the present study were obtained from J-ADNI.⁹ This project was approved by the ethics committee of each site in which J-ADNI data were acquired, and written informed consent was obtained from each subject before participating in J-ADNI. All subjects were native Japanese speakers, 60–84 years of age, and were registered as 1 of 3 clinical groups (mild AD, MCI, or NC). Subjects of the mild AD group scored 20–26 in Mini-Mental State Examination-Japanese and 0.5–1.0 in the Clinical Dementia Rating-Japanese and were compatible with the probable AD criteria in the National Institute of Neurologic and Communicative Disorders and Stroke and the Alzheimer Disease and Related Disorders Association.¹⁰ Subjects of the MCI group scored 24–30 in the Mini-Mental State Examination-Japanese and 0.5 in the Clinical Dementia Rating-Japanese. Subjects of NC group scored 24–30 in the Mini-Mental State Examination-Japanese and 0 in the Clinical Dementia Rating-Japanese. The exclusion criteria were depression (Geriatric Depression Scale-Japan ≥ 6), cerebrovascular disorders (Hachinski Ischemic Score ≥ 5), and other neurologic or psychiatric disorders.

Enrollment in each clinical group for J-ADNI was primarily determined by the referring physician, and 303 consecutive subjects entered the study to undergo ¹⁸F-FDG-PET scanning. A thorough central review of the clinical and behavioral data by expert psychiatrists and psychologists excluded 29 cases that had erroneous assessment of the cognitive test results, depression or cerebrovascular disorders that had been overlooked, prohibited concomitant medications, or other deviations from the criteria. As a result, 274 baseline ¹⁸F-FDG-PET scans (67 mild AD, 100 MCI, and 107 NC) were analyzed in the present study.

PET Imaging

As a quality assurance measure necessary for the multicenter study, all PET sites in J-ADNI were qualified for the PET scanner and other devices, resting-state environment, quality of the on-site-produced PET drugs, and so forth before scanning of the first subject. Intersite differences were minimized by standardizing the imaging protocol, and interscanner differences were addressed with the Hoffmann 3D phantom data.¹¹ The data used for the analysis in the present study were acquired with 14 types of PET or PET/CT scanners in 23 PET centers.

In the ¹⁸F-FDG-PET scans, all subjects fasted for at least 4 hours and their preinjection blood glucose levels were confirmed to be <180 mg/dL. Intravenous administration of ¹⁸F-FDG (185 ± 37 MBq) was followed by a resting period of 30 minutes in a dimly lit and quiet room. Dynamic scans (300 seconds \times 6 frames) were obtained starting 30 minutes postinjection in the 3D mode. Attenuation was corrected for by a transmission scan with segmentation for dedicated PET and by a CT scan for PET/CT.

All the PET images acquired in each PET site went through the J-ADNI PET quality control process,¹¹ in which head motion between frames was corrected for and bad frames were removed to create sum frame images. Then the images were reoriented to the anterior/posterior commissure line with the same matrix size and

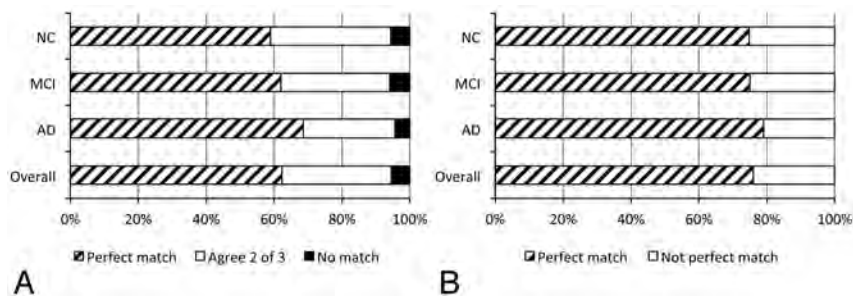


FIG 1. Breakdown of the ^{18}F -FDG-PET cases into degree of match by 3 raters in a combined visual-statistical human classification into 7 (FDG-7) (A) or 2 (FDG-2) (B) categories. A perfect match by the 3 raters is observed for 62% of the cases for FDG-7 and 76% for FDG-2 in total. The AD group shows the highest concordance followed by the MCI and NC groups, in this order, both for FDG-7 and FDG-2.

voxel size so that all camera models presented images of similar orientation and appearance to the viewer and were then passed on to image interpretation.

The ^{18}F -FDG-PET images that had passed through the quality control process above were also treated with a 3D stereotactic surface projection technique to generate z score maps (displayed with upper = 7 and lower = 0) by using iSSP software, Version 3.5 (Nihon Medi-physics, Tokyo, Japan). The normal data base used for generating the Z-maps was made by a method of leave-one-out cross-validation based on 25 healthy subjects of J-ADNI (11 men and 14 women; mean age, 66.0 ± 4.8 years) who were interpreted as having a normal pattern by one of the coauthors of the study. The Z-maps were used not for the automated quantification but for a part of the information for human raters in the visual-statistical interpretation.

Human Interpretation

Those ^{18}F -FDG images generated through the quality control process above were independently interpreted with the combined visual-statistical method by 3 expert raters blinded to the clinical group and other clinical and laboratory data. The raters were provided with the ^{18}F -FDG tomographic images on the viewer as well as the Z-map images in PDF format. Information about the age and sex was also provided to the raters. Moreover, T1-weighted MR images acquired in 3D mode by using MPRAGE or its equivalent and reformatted in axial sections were also provided together with axial T2WI and proton-attenuation images, in which the MR imaging sections did not correspond to the PET section positions. The experience of the 3 raters as physicians specializing in nuclear neuroimaging was 17, 19, and 19 years, respectively, when this project started.

After independent interpretation, consensus reads were performed by the 3 raters and 2 other discussants who are experienced nuclear medicine physicians specialized in neuroimaging. The experience of both discussants as physicians specializing in nuclear neuroimaging was 20 years. The same images and information as that in the independent interpretation were also provided for the discussants in the consensus reads. The 7 sessions of consensus reads lasted for 1.5 years in the order of subject enrollment in J-ADNI. In the consensus reads, the cases in which the evaluations by the 3 raters did not completely match were discussed, and the unified visual-statistical interpretation was determined as an official judgment by the J-ADNI PET Core.

For classification of ^{18}F -FDG-PET, the criteria of Silverman et al¹ were adopted for classifying the uptake pattern in J-ADNI. All 3 expert raters and the 2 discussants had attended a training course for the criteria organized by Silverman et al before starting the J-ADNI project. In the criteria of Silverman et al, ^{18}F -FDG uptake patterns were classified into 7 categories: progressive patterns: P1, P1+, P2, and P3, in which P1 represents the characteristic AD pattern and P1+ represents AD-variant pattern, including the characteristic Lewy body dementia pattern; and nonprogressive patterns: N1, N2 and N3, in which N1 represents the characteristic normal pattern. In addition to these original 7 categories (FDG-7), the present study defined a binary criteria (FDG-2) in which the 7 categories were dichotomized into posterior-predominant hypometabolism (AD and AD-variant) patterns (P1, P1+) and the other patterns (N1, N2, N3, P2, and P3).

patterns: N1, N2 and N3, in which N1 represents the characteristic normal pattern. In addition to these original 7 categories (FDG-7), the present study defined a binary criteria (FDG-2) in which the 7 categories were dichotomized into posterior-predominant hypometabolism (AD and AD-variant) patterns (P1, P1+) and the other patterns (N1, N2, N3, P2, and P3).

Automated Quantitative Evaluation

In the automated quantitative analysis, the FDG-PET score, as a measure of the AD pattern, was calculated from ADtsum⁴ by using the Alzheimer's Discrimination Tool in PMOD, Version 3.12 (PMOD Technologies, Zurich, Switzerland)^{4,5} by using the following equation: $\text{FDG-PET score} = \log_2 \{ (\text{ADtsum} / 11,089) + 1 \}$. The FDG-PET score was not calculated in 1 case because no significant clusters were determined for the image.⁴ This case was excluded from the quantitative analysis.

Statistical Analysis

Concordance among the 3 raters was evaluated by Cohen κ statistics. As comparisons between human and automated evaluation, the association between the FDG-PET score and the number of the raters who interpreted the case as P1 (AD pattern) in FDG-7 was evaluated by the Spearman rank correlation coefficient. Likewise, association between the FDG-PET score and the number of the raters who interpreted the case as N1 (normal pattern) was evaluated. The association was also examined between the FDG-PET score and the number of raters in FDG-2 classification (ie, how many raters judged the case as the AD and AD-variant patterns [P1, P1+] versus the other patterns [N1, N2, N3, P2, and P3]). A P value $< .05$ was considered significant. In addition, the FDG-PET score was compared with the final combined visual-statistical interpretation determined by the consensus read and with the clinical group. Receiver operating characteristic analysis was used to obtain the optimum cutoff level for the quantitative index for discrimination.

Neither iSSP nor the PMOD Alzheimer's Discrimination Tool was approved for clinical use by the US Food and Drug Administration.

RESULTS

Figure 1 summarizes concordance rates among the 3 raters. Agreement among the 7 visual-statistical categories by at least 2 of the 3 readers occurred in $>94\%$ of cases for all groups: NC, MCI,

and AD. The κ statistic \pm SE for each pair of the 3 raters was 0.59 ± 0.04 , 0.54 ± 0.04 , and 0.58 ± 0.04 in FDG-7 (average, 0.57), and 0.73 ± 0.04 , 0.65 ± 0.0 , and 0.64 ± 0.05 in FDG-2 (average, 0.67), respectively.

Figure 2 illustrates the relationship between the FDG-PET score and the number of raters who visually-statistically interpreted the ^{18}F -FDG-PET image as P1 (Fig 2A) and N1 (Fig 2B). A significant positive association was observed between the FDG-PET score and the number of P1 interpretations ($\rho = 0.59$, $P < .0001$). The mean FDG-PET score was 0.46 ± 0.37 ($n = 103$) for the scans no raters interpreted as P1, but it increased to 0.723 ± 0.39 ($n = 34$) for those that 1 rater interpreted as P1, to 0.99 ± 0.45 ($n = 31$) for 2 raters, and to 1.21 ± 0.73 ($n = 105$) for all 3 raters. Likewise, a significant negative association was observed between the FDG-PET score and the number of N1 interpretations ($\rho = -.64$, $P < .0001$). The FDG-PET score was 1.15 ± 0.69 ($n = 146$) for the scans no raters interpreted as N1, but it decreased to 0.80 ± 0.39 ($n = 28$) for those 1 rater interpreted as N1, 0.50 ± 0.25 ($n = 40$) for 2 raters, and 0.34 ± 0.22 ($n = 59$) for all 3 raters. A similar association was observed between the FDG-PET score and the number of raters who interpreted the case as AD and AD-variant patterns, including the Lewy body dementia pattern (P1, P1+) or the other patterns (N1, N2, N3, P2, and P3); and both showed significant positive and negative associations ($\rho = 0.60$, $P < .0001$; and $\rho = -0.60$, $P < .0001$).

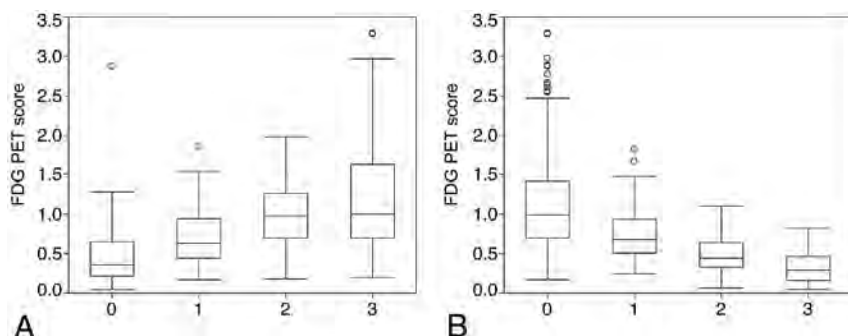


FIG 2. Boxplots of the FDG-PET score against the number of raters who interpreted the ^{18}F -FDG-PET images as P1 (A) and N1 (B) based on the FDG-7 criteria. The FDG-PET score gradually increases as the number of P1 (AD pattern) interpretations increases (Spearman rank correlation coefficient: $\rho = 0.59$, $P < .0001$). On the other hand, FDG-PET score gradually decreases as the number of N1 (normal pattern) interpretations increases ($\rho = -.64$, $P < .0001$).

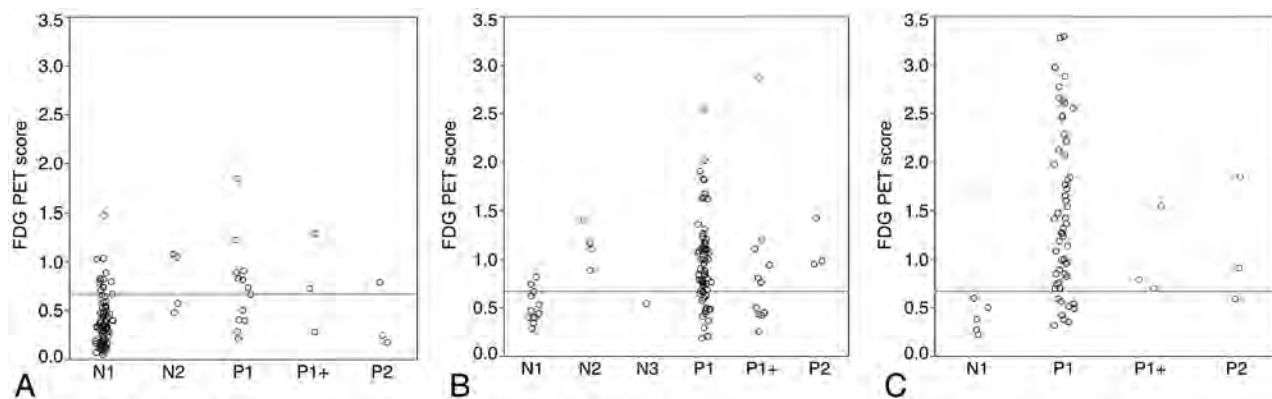


FIG 3. Scatterplot of the FDG-PET score as contrasted with the combined visual-statistical interpretation determined by the consensus read of ^{18}F -FDG-PET for each clinical group (A, NC; B, MCI; and C, AD). The horizontal line indicates the cutoff level of 0.67 derived by receiver operating characteristic analysis on P1 and N1 cases.

Figure 3 illustrates scatterplots of the FDG-PET scores as contrasted to the combined visual-statistical interpretation determined by the consensus read of ^{18}F -FDG-PET for each clinical group. For each group as well as for all subjects, cases with P1 interpretation showed higher FDG-PET scores than those with N1. Receiver operating characteristic analysis on P1 and N1 cases led to a cutoff FDG-PET score of 0.67 for discrimination between P1 and N1. As was expected, NC cases with P1 interpretation had lower FDG-PET scores than MCI and AD cases with P1 interpretation, and the ratio of the cases above-to-below the cutoff level was also lower. As for the cases with other patterns, a large fraction of the cases with N2 interpretation had FDG-PET scores above the cutoff level, though most were below 1.0. The FDG-PET scores of the cases with P1+ and P2 were variable.

DISCUSSION

Matches among 7 visual-statistical categories by at least 2 of 3 readers occurred in $>94\%$ of cases for each clinical group, and perfect matches among the 3 raters were observed for 62% of the cases for FDG-7 and 76% for FDG-2 categorization schemes in total. The mild AD group showed the highest concordance, followed by MCI and NC, in order, for both FDG-7 and FDG-2. The AD pattern in ^{18}F -FDG-PET is usually seen in the early stage of AD and is expected to predict the onset of AD.^{1,12} Because most of the subjects who are clinically diagnosed as having AD may have had an established AD pattern in ^{18}F -FDG-PET, it is reasonable for these results that AD showed the highest concordance.

Based on the classification of κ values described by Landis and Koch,¹³ agreements were considered to be moderate for FDG-7 and substantial for FDG-2. Inter-rater variability is one of the indices that are often used to evaluate the validity of methods of image interpretation, and it facilitates comparison with the other studies. The κ index of FDG-2 ($\kappa = 0.67$) of the present study showed values similar to those of the other studies ($\kappa = 0.56$ - 0.72) evaluated by the bi-

nary criteria.⁶⁻⁸ However, the values observed in the other studies are not the same as those in the present study because we analyzed the interpretation both visually and statistically. Recent studies have shown that the diagnostic capability of visual analysis of ¹⁸F-FDG-PET increases when the raters interpret the images in combination with 3D stereotactic surface projections.^{14,15} These kinds of visual-statistical methods seem to be a standard approach in clinical settings.

To increase the concordance rate and diagnostic capability, we need to overcome some problems. We had to degrade the image quality according to the PET with the lowest quality among the 23 facilities of J-ADNI.¹¹ Therefore, the quality of the images may be improved in the future. In addition to the image quality, development of new methods or new approaches to image interpretation may contribute to increasing the concordance.

This study showed a relationship between combined visual-statistical interpretation and automated quantitative assessment regarding the characteristic AD pattern in brain ¹⁸F-FDG-PET. Significant association was observed between the quantitative index (FDG-PET score) and the number of raters who interpreted the scans accordingly. This correlation may have been something expected from reports on similar/automated analysis.^{5,6} However, this association was observed in a large-scale multicenter study by using various camera models on a wide spectrum of subjects in the present study.

From the standpoint of detecting the AD pattern, cases evaluated as having positive AD findings by complete agreement of all 3 raters tended to show a higher quantitative index than the cases that fewer than 3 raters interpreted as having positive AD findings. From the standpoint of ruling out the AD pattern, cases evaluated as having negative AD findings by complete agreement of all 3 raters also tended to show a lower quantitative index than the cases that fewer than 3 raters interpreted as having negative AD findings. Therefore, the results suggest that interpretation by 3 raters may be better than that by 2 or fewer raters. The results also indicate that cases that only 1 rater interpreted as having positive (or negative) AD findings presented a different quantitative index from those that no raters interpreted as having positive (or negative) findings. This outcome suggests that there are cases in which the “minority opinion” may not be ignored.

Generally, the minority opinion is somewhat important when a subtle but definite finding is evaluated. However, most of the ¹⁸F-FDG-PET images for which the judgment did not agree among the raters showed ambiguous findings. Ng et al⁶ reported that experienced raters scored higher accuracy than nonexperienced raters in the interpretation of brain ¹⁸F-FDG-PET images for the diagnosis of AD.⁶ Such subtle findings in brain ¹⁸F-FDG-PET may be difficult to interpret. We need to analyze the difference in detail and develop new methods for interpretation or new diagnostic tools.

When the FDG-PET score of the cases judged as P1 in the consensus read were examined, NC subjects with P1 interpretation showed lower FDG-PET scores than MCI and AD subjects. This result is probably because many of the NC subjects with P1 interpretation presented with a very mild AD pattern that influenced the FDG-PET score to only a small extent. Those cases,

however, presented characteristic findings such as posterior cingulate hypometabolism, which led to the P1 interpretation.

The criterion standard used in this study was the clinical diagnosis at enrollment. Although dementia with Lewy body cases with the specific symptoms were excluded from enrollment in the J-ADNI beforehand, differentiating Lewy body dementia from AD is occasionally difficult in clinical settings.¹⁶ The typical Lewy body dementia pattern of ¹⁸F-FDG-PET, evaluated as occipital hypometabolism, is classified into P1+ by the criteria of Silverman et al.¹ Some cases classified into P1+, though limited in the present study, seem to have the possibility of Lewy body dementia. Moreover, the consensus read judged 16 of 107 cases of the NC group to be the AD pattern (P1 and P1+), and 8 of 67 cases in the AD group to be a non-AD pattern (N1 and P2). These disagreements might be either caused by inappropriate clinical diagnosis at enrollment or reflecting the limitation of FDG-PET as a diagnostic tool. While these diagnostic discrepancies are not critical in the present study, which analyzed inter-rater concordance, comparison with other criterion standards such as long-term follow-up or postmortem examination is important for this kind of multicenter study in the future.

The FDG-PET score of 1.0, by definition, is proposed as an optimum threshold for the differential diagnosis of AD from healthy subjects.⁵ Because the present study deals with comparison of combined visual-statistical human interpretation with automated quantitative analysis, we derived a cutoff level of 0.67 based on discrimination of the P1 from the N1 pattern. This discrepancy may be explained by the difference in the target of discrimination as well as in the profile of subjects, and the lower cutoff would be consistent with a higher sensitivity for visually detecting the AD pattern than for clinically identifying the diagnosis of AD, for which the 1.0 cutoff is designed. In addition, one of the essential factors for this discrepancy seems to be that decisions by visual-statistical interpretation are not completely consistent with the actual clinical diagnosis. Because the diagnostic capability of ¹⁸F-FDG-PET is not the subject of the present study, further studies are needed to elucidate the discrepancy.

CONCLUSIONS

Inter-rater agreement was moderate to substantial regarding the combined visual-statistical human interpretation of the characteristic AD pattern in ¹⁸F-FDG-PET. In addition, a significant relationship between human interpretation and automated quantitative assessment was found. The human rating as an AD or normal pattern was best predicted by the FDG-PET score when using a cutoff of 0.67.

ACKNOWLEDGMENTS

The authors thank the J-ADNI Imaging Pharmaceutical Industry Scientific Advisory Board and other organizations for their support of this work.

Disclosures: Tomohiko Yamane—RELATED: Grant: New Energy and Industrial Technology Development Organization of Japan,* Comments: This study is a part of the “Translational Research Promotion Project/Research Project for the Development of a Systematic Method for the Assessment of Alzheimer’s Disease,” sponsored by the New Energy and Industrial Technology Development Organization of Japan. The Japanese Alzheimer’s Disease Neuroimaging Initiative is also supported by a Grant-in-Aid for Comprehensive Research on Dementia from the Japanese Ministry of

Health, Labour and Welfare, as well as by grants from J-ADNI Pharmaceutical Industry Scientific Advisory Board companies. Yasuhiko Ikari—UNRELATED: Employment: Micron. Tomoyuki Nishio—UNRELATED: Employment: Micron. Takashi Kato—RELATED: Grant: government-based funding, Comments: Ministry of Health, Labour, and Welfare in Japan; Ministry of Education, Culture, Sports, Science & Technology in Japan. Kengo Ito—RELATED: Grant: “Translational Research Promotion Project/Research Project for the Development of a Systematic Method for the Assessment of Alzheimer’s Disease,” sponsored by the New Energy and Industrial Technology Development Organization of Japan, and a Grant-in-Aid for Comprehensive Research on Dementia from the Japanese Ministry of Health, and Labour and Welfare.* Michio Senda—RELATED: Grant: Research Association for Biotechnology.* UNRELATED: Grants/Grants Pending: GE Healthcare.* Eli Lilly.* Morihiro Sugishita—RELATED: Grant: New Energy and Industrial Technology Development Organization.* Support for Travel to Meetings for the Study or Other Purposes: New Energy and Industrial Technology Development Organization, UNRELATED: Consultancy: Eli Lilly Japan KK, Employment: Sugishita Co Ltd, Royalties: Nihon Bunka Kagakusha Co Ltd, Stock/Stock Options: Japan Air Line. *Money paid to the institution.

REFERENCES

- Silverman DH, Small GW, Chang CY, et al. **Positron emission tomography in evaluation of dementia: regional brain metabolism and long-term outcome.** *JAMA* 2001;286:2120–27
- Mosconi L, Perani D, Sorbi S, et al. **MCI conversion to dementia and the APOE genotype: a prediction study with FDG-PET.** *Neurology* 2004;63:2332–40
- Yuan Y, Gu ZX, Wei WS. **Fluorodeoxyglucose-positron-emission tomography, single-photon emission tomography, and structural MR imaging for prediction of rapid conversion to Alzheimer disease in patients with mild cognitive impairment: a meta-analysis.** *AJNR Am J Neuroradiol* 2009;30:404–10
- Herholz K, Salmon E, Perani D, et al. **Discrimination between Alzheimer dementia and controls by automated analysis of multi-center FDG-PET.** *Neuroimage* 2002;17:302–16
- Herholz K, Westwood S, Haense C, et al. **Evaluation of a calibrated ¹⁸F-FDG-PET score as a biomarker for progression in Alzheimer disease and mild cognitive impairment.** *J Nucl Med* 2011;52:1218–26
- Ng S, Villemagne VL, Berlangieri S, et al. **Visual assessment versus quantitative assessment of ¹¹C-PIB PET and ¹⁸F-FDG-PET for detection of Alzheimer’s disease.** *J Nucl Med* 2007;48:547–52
- Tolboom N, van der Flier WM, Boverhoff J, et al. **Molecular imaging in the diagnosis of Alzheimer’s disease: visual assessment of [¹¹C]PIB and [¹⁸F]FDDNP PET images.** *J Neurol Neurosurg Psychiatry* 2010;81:882–84
- Rabinovici G, Rosen H, Alkalay A, et al. **Amyloid vs FDG-PET in the differential diagnosis of AD and FTLD.** *Neurology* 2011;77:2034–42
- Iwatsubo T. **Japanese Alzheimer’s Disease Neuroimaging Initiative: present status and future.** *Alzheimers Dement* 2010;6:297–99
- McKhann G, Drachman D, Folstein M, et al. **Clinical diagnosis of Alzheimer’s disease: report of the NINCDS-ADRDA Work Group under the auspices of Department of Health and Human Services Task Force on Alzheimer’s Disease.** *Neurology* 1984;34:939–44
- Ikari Y, Nishio T, Makishi Y, et al. **Head motion evaluation and correction for PET scans with ¹⁸F-FDG in the Japanese Alzheimer’s Disease Neuroimaging Initiative (J-ADNI) multi-center study.** *Ann Nucl Med* 2012;26:535–44
- Silverman DH, Mosconi L, Ercoli L, et al. **Positron emission tomography scans obtained for the evaluation of cognitive dysfunction.** *Semin Nucl Med* 2008;38:251–61
- Landis JR, Koch GG. **The measurement of observer agreement for categorical data.** *Biometrics* 1977;33:159–74
- Lehman VT, Carter RE, Claassen DO, et al. **Visual assessment versus quantitative three-dimensional stereotactic surface projection fluorodeoxyglucose positron emission tomography for detection of mild cognitive impairment and Alzheimer disease.** *Clin Nucl Med* 2012;37:721–26
- Foster NL, Heidebrink JL, Clark CM, et al. **FDG-PET improves accuracy in distinguishing frontotemporal dementia and Alzheimer’s disease.** *Brain* 2007;130(pt 10):2616–35
- Ishii K, Soma T, Kono AK, et al. **Comparison of regional brain volume and glucose metabolism between patients with mild dementia with Lewy bodies and those with mild Alzheimer’s disease.** *J Nucl Med* 2007;48:704–11

Oxygen Extraction Fraction and Stroke Risk in Patients with Carotid Stenosis or Occlusion: A Systematic Review and Meta-Analysis

A. Gupta, H. Baradaran, A.D. Schweitzer, H. Kamel, A. Pandya, D. Delgado, D. Wright, S. Hurtado-Rua, Y. Wang, and P.C. Sanelli



ABSTRACT

BACKGROUND AND PURPOSE: Increased oxygen extraction fraction on PET has been considered a risk factor for stroke in patients with carotid stenosis or occlusion, though the strength of this association has recently been questioned. We performed a systematic review and meta-analysis to summarize the association between increased oxygen extraction fraction and ipsilateral stroke risk.

MATERIALS AND METHODS: A comprehensive literature search was performed. We included studies with baseline PET oxygen extraction fraction testing, ipsilateral stroke as the primary outcome, and at least 1 year of follow-up. A meta-analysis was performed by use of a random-effects model.

RESULTS: After screening 2158 studies, 7 studies with 430 total patients with mean 30-month follow-up met inclusion criteria. We found that 6 of 7 studies were amenable to meta-analysis. Although 4 of the 6 studies independently did not reach statistical significance, meta-analysis revealed a significant positive relationship between abnormal oxygen extraction fraction and future ipsilateral stroke, with a pooled OR of 6.04 (95% CI, 2.58–14.12). There was no statistically significant difference in OR in the subgroup analyses according to testing method or disease site.

CONCLUSIONS: Abnormal oxygen extraction fraction remains a powerful predictor of stroke in carotid stenosis or occlusion and is a valuable reference standard to compare and validate MR imaging–based measures of brain oxygen metabolism. However, there is a need for further evaluation of oxygen extraction fraction testing in patients with high-grade but asymptomatic carotid disease.

ABBREVIATIONS: CVR = cerebrovascular reserve; OEF = oxygen extraction fraction; COSS = Carotid Occlusion Surgery Study

Carotid atherosclerotic disease remains a significant cause of stroke, with extracranial carotid disease accounting for approximately 20% of all strokes.¹ The hemodynamic risk factors underlying stroke in patients with carotid disease^{2,3} include impairment in cerebrovascular reserve (CVR) and increase in oxy-

gen extraction fraction (OEF). Impairment in CVR, a measure of the vasodilatory capacity of vessels in the face of reduced cerebral perfusion pressure, may lead to a reduction in CBF, which can precede or occur alongside a compensatory increase in oxygen extraction state sometimes referred to as “misery perfusion.” Neuroimaging can measure both cerebrovascular and oxygen metabolic reserve, with the latter determined by OEF on PET.

Increased OEF on PET has long been considered a risk factor for the development of stroke in patients with symptomatic carotid occlusion.⁴ However, OEF-defined hemodynamic failure was a key inclusion criterion for patients enrolled in the Carotid Occlusion Surgery Study (COSS).⁵ This trial was recently terminated for futility, and concerns were raised regarding the specific OEF testing method that was used as a study inclusion criterion, thus sparking renewed debate in the literature^{6–9} regarding OEF testing methodology and its role in stroke risk assessment. The role of OEF in stroke risk prediction also deserves renewed attention, given its potential value as a reference standard for new MR imaging measures of brain oxygen metabolism.^{10–12} Some of the

Received March 21, 2013; accepted after revision April 29.

From the Departments of Radiology (A.G., H.B., A.D.S., Y.W., P.C.S.) and Neurology (H.K.), Weill Cornell Medical College, New York-Presbyterian Hospital, New York, New York; and Department of Public Health (A.P., S.H.-R., P.C.S.) and Samuel J. Wood Library and C.V. Starr Biomedical Information Center (D.D., D.W.), Weill Cornell Medical College, New York, New York.

Abstract previously presented at: Annual Meeting of the American Society of Neuroradiology, May 20–24, 2013; San Diego, California. The abstract for this paper won the Cornelius G. Dyke Memorial Award at the meeting.

This paper was supported in part by NIH grant R01EB013443.

Please address correspondence to Ajay Gupta, MD, 525 East 68th St, Starr 8A, Box 141, New York, NY 10065; e-mail: ajg9004@med.cornell.edu

Indicates open access to non-subscribers at www.ajnr.org

Indicates article with supplemental on-line tables

<http://dx.doi.org/10.3174/ajnr.A3668>

difficulties in drawing definite conclusions about the role of OEF in predicting stroke and its role in treating patients with carotid disease are based on small sample sizes in individual research studies on this topic and the heterogeneity of study designs implemented. For this reason, and in the light of several recently published studies^{5,9} following patients after OEF PET testing, a critical reappraisal of the OEF literature is warranted. We therefore performed a systematic review and meta-analysis to summarize the association between increased OEF and risk of future stroke (first-ever or recurrent) ipsilateral to a high-grade carotid artery stenosis or occlusion.

MATERIALS AND METHODS

We referred to the Preferred Reporting Items for Systematic Reviews and Meta-Analyses (PRISMA) statement¹³ as a guide for the methodologic approach in this study.

Study Eligibility Criteria

Studies with PET-based measurement of OEF and its association with stroke in patients with high-grade carotid stenosis ($\geq 70\%$) or occlusion were eligible. Specific inclusion criteria were 1) English-language published manuscripts; 2) original prospective or retrospective research studies; 3) subjects with high-grade carotid stenosis ($\geq 70\%$) or occlusion determined by any imaging technique; 4) measurement of OEF by means of ¹⁵O-PET scan; 4) mean follow-up of ≥ 1 year assessing development of ipsilateral stroke and/or TIA; and 5) nonsurgical treatment of patients. If surgical revascularization occurred during patient follow-up, we included the study only if the authors separately identified and analyzed these patients. In such a case, we included follow-up until the point of revascularization, at which time follow-up was censored. In cases in which outcome data or information about the OEF testing method could not be determined from the report, we attempted to contact the corresponding author for additional details. If 2 different testing methods were described in the original report, we applied the following rules: 1) the measure of OEF alone (eg, OEF alone instead of OEF plus additional hemodynamic parameters) was used in the overall analysis of pooled effect size; and 2) if 2 purely OEF-based testing methods were described in the same original report, the method that most accurately predicted stroke was used in the overall analysis of pooled effect size.

Information Sources and Search

A systematic search was performed to comprehensively identify studies predicting the risk of stroke or TIA on the basis of positive ¹⁵O-PET scans in patients with carotid stenosis or occlusion.

Potentially relevant articles were found by searching the biomedical electronic databases Ovid MEDLINE (1946 to October 2012), EMBASE (1974 to October 2012), and The Cochrane Library (updated October 2012). Relevant subject heading and free text terms were used. Published, unpublished, and ongoing trials were identified by search of ClinicalTrials.gov. Additional records were identified by use of the Related Citations feature in PubMed and the Cited Reference Search in Web of Science. To improve the retrieval of the relevant information and to ensure the methodologic quality of the literature search, there was an external peer

review of the primary MEDLINE search. The primary search was conducted in MEDLINE by use of the terms exp Positron-Emission Tomography/OR (positron adj2 emission adj2 tomograph\$.tw. OR (PET or PETCT\$one or PET CT\$1).tw. OR (Oxygen-15 or O-15).tw. AND (Oxygen adj3 (extract\$ or fraction\$ or ratio\$ or rate\$ or metaboli\$ or consumption)).tw. OR (OEF or OER or CMRO2).tw. OR (cerebr\$ adj3 (metaboli\$ or autoregulat\$ or reserve\$ or blood\$ or flow\$ or volume\$ or resistance\$ or pressure\$ or hemodynamic\$ or vasomotor\$ or impair\$)).tw. OR (CBF or rCBF or CVR or CPP).tw. AND exp Carotid Stenosis/ OR (carotid adj3 (stenos\$ or ulcer\$ or plaque\$ or narrow\$ or obstruct\$ or occlus\$ or constrict\$)).tw. OR (steno\$ occlus\$ or stenocclus\$).tw. OR exp Stroke/ OR Stroke\$.tw. OR cerebrovascular.tw. OR ((brain\$ or vascular\$ or lacunar\$ or venous\$ or cerebral\$ or ischemic\$) adj2 (accident\$ or infarct\$ or event\$ or attack\$)).tw. OR (cva\$ or cvas).tw.

Study Selection and Data Collection Process

All eligible reports were screened by a single reader on the basis of title and abstract for possible inclusion. These reports were reviewed in their entirety by 3 independent readers to determine final inclusion, with disagreements resolved by consensus. Qualitative and quantitative study data were extracted from selected studies by 2 independent readers by use of a predetermined data collection template. All disagreements were resolved by an independent third reader as a tie-breaker.

Assessment of Risk of Bias in Studies

On the basis of our literature search, no standardized tool exists to assess the risk of bias in observational time-to-event cohort studies. Therefore, we adapted bias assessment criteria used in a previously published meta-analysis¹⁴ of stroke risk on the basis of imaging findings. The following criteria were applied: 1) reference standard bias was assessed by noting whether observers were blinded to OEF results when stroke outcomes were determined; 2) confounding bias was assessed by noting whether potentially confounding co-existent vascular risk was collected and described; 3) completeness of follow-up data was determined by recording the number of subjects either censored or lost to follow-up for other reasons.

Statistical Analyses

A fixed-effects model was used if studies were found statistically homogeneous; otherwise, a random-effects model was chosen. The upper 95% confidence limit of the heterogeneity index ($I^2 > 30\%$) was used as a cutoff for accepting studies that were relatively homogeneous. Heterogeneity across studies was also examined by means of the Breslow-Day method, with $P < .05$ as the threshold for statistically significant heterogeneity. Continuity correction was used for sparse tables before pooling the OR. Publication bias was examined with the use of Begg-Mazumdar tests. We performed subgroup analyses stratified by 1) disease site, 2) symptomatic disease versus never-symptomatic disease, and 3) absolute measures of OEF versus hemispheric ratio-based measures of OEF. All analyses were conducted by a biostatistician with the use of R: A Language and Environment for Statistical Computing, version 2.15.2 (<http://www.r-project.org/>).

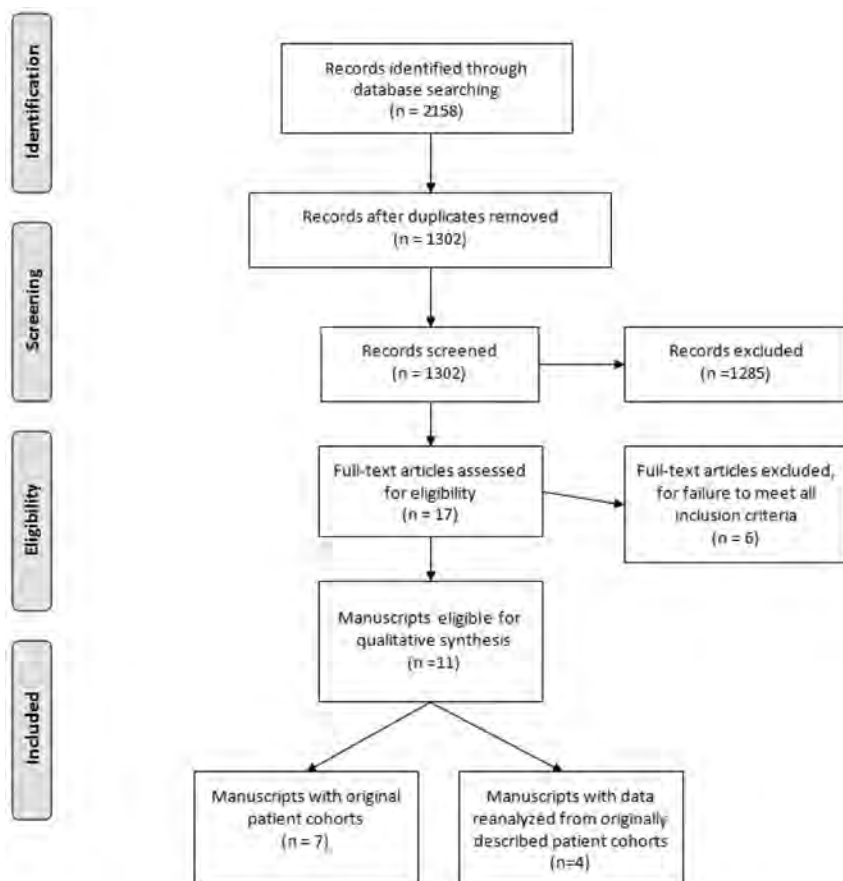


FIG 1. Study selection flow diagram. Figure adapted from the Preferred Reporting Items for Systematic Reviews and Meta-Analyses (PRISMA) group statement.

RESULTS

Study Selection

A total of 2158 reports were initially screened, of which 17 potentially eligible reports were selected for further review (Fig 1). Of these 17 reports, 6 did not meet inclusion criteria when read in their entirety because they did not include patient cohorts followed for development of stroke after baseline OEF testing. Of the remaining 11 reports, 7 reports^{4,5,9,15-18} were included in the final systematic review. The remaining 4 of 11 reports^{3,8,19,20} reanalyzed data originally presented in an original patient cohort.⁴ Two^{9,16} of 7 of these original cohort studies described more than 1 OEF testing method for the cohort, whereas the other 5 described only 1 method of OEF testing. Of the 7 original cohort studies for systematic review, 6 of 7 studies reported ipsilateral stroke incidence in a fashion amenable to meta-analysis. One study (the Carotid Occlusion Surgery Study⁵) reported stroke outcomes only in patients with abnormal OEF, which prevented calculation of an OR for inclusion in the meta-analysis. The stroke outcomes data for patients with normal OEF who were excluded from the randomized trial could not be obtained after contacting the study authors.

Qualitative Assessment and Study Characteristics

Of the 7 original cohort reports meeting eligibility for qualitative review, 6 were nonrandomized, observational, time-to-event studies, and 1 was observational data extracted from a randomized, controlled trial.⁵ Four studies were conducted in the United

States^{4,5,15,17} and the remaining 3 studies in Japan.^{9,16,18} A total of 430 unique patients were included, with a mean follow-up of 30 months. All studies had similar mean subject ages (range, 58–66 years) and a similar increased preponderance of male subjects (range, 62–77%). Most patients enrolled in these studies had occlusive ICA disease, with 3 studies exclusively studying this population.^{4,7,17} The remaining 4 studies^{9,15,16,18} had mixed disease sites and severity, including high-grade stenosis and/or occlusion of the middle cerebral and carotid arteries. In studies with mixed vessel site and severity, most patients had occlusive as opposed to stenotic vascular disease (comprising 83.3%,¹⁵ 80%,¹⁶ 75%,¹⁸ and 67.3%⁹ of each of the cohorts); however, stroke outcomes were not consistently reported in all of these studies by vessel disease site or severity. All but 1 study¹⁷ evaluated patients with symptomatic disease, which was defined by the presence of prior TIA or stroke with variable days since last symptoms. On-line Table 1 provides an overview of the patient characteristics in each study.

Variable cutoff values for abnormal OEF were used, with major testing categories including 1) quantitative, arterial catheterization–dependent versus non–arterial-dependent count–based OEF techniques and 2) absolute versus hemispheric ratio OEF techniques (On-line Table 2).

All studies presented outcomes in terms of ipsilateral stroke. Original cohort data from Grubb et al⁴ were reanalyzed 6 times in 4 subsequent reports^{3,7,19} (On-line Tables 3–5). In 2 reports by Yamauchi et al,^{9,16} more than 1 OEF testing method was presented.

Assessment of Study Methods

In only 2 observational cohort studies^{4,17} were researchers explicitly blinded to OEF results when assessing for ipsilateral stroke. In 4^{9,15,16,18} of the remaining 5 studies, outcomes were not assessed while blinded to OEF results, and in the Carotid Occlusion Surgery Study participants were selected on the basis of known pre-existing OEF elevation. All 7 studies measured and described potentially confounding pre-existing vascular factors. Finally, in the assessment of the completeness of follow-up, the COSS trial⁵ lost 1 patient to follow-up at 21 months. In the other 6 studies, no explicit loss to follow-up was described.

Meta-Analysis Results

After pooling the 6 studies amenable for meta-analysis, the I^2 statistic and Breslow-Day statistic showed low heterogeneity ($I^2 = 0$; CI = 0–38.3% and Breslow-Day = 2.39, $df = 5$, $P = .66$). The Begg-Mazumdar test did not reveal significant publication bias

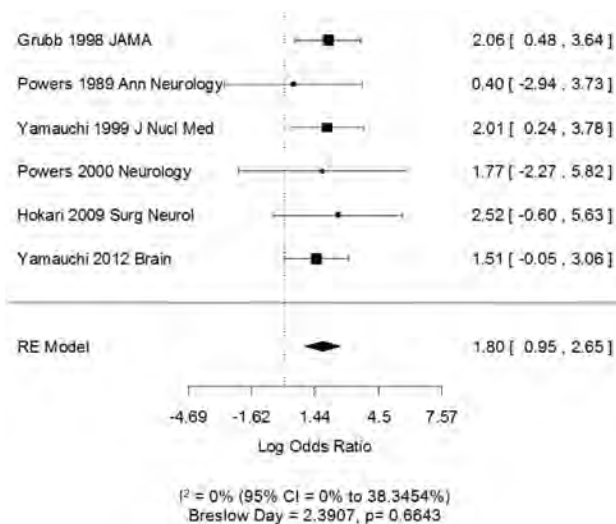


FIG 2. Forest plot of the association between increased OEF and ipsilateral first-ever or recurrent stroke determined by a random effects (RE) model. Squares represent point estimates for effect size expressed as log of the OR, with the size proportional to the inverse variance of the estimate (note, $OR = \exp[\log OR]$). Diamonds represent pooled estimate. Lines represent 95% CIs. Vertical line indicates null effect ($OR = 1$ or log odds = 0). I^2 and Breslow-Day statistic for heterogeneity is listed below the forest plot.

(Kendall $\tau = .067$, $P = 1.00$). The pooled random effects odds ratio of 6.04 (CI, 2.58–14.12) indicates a significant positive relationship between increased OEF and future ipsilateral stroke (Fig 2). Each study had a positive association between OEF increase and stroke, though importantly, 75% of the studies (4/6), when viewed independently, did not have a statistically significant OR.

Subset Analysis

Additional subset analyses with measures of heterogeneity were performed. The OR remained statistically significant in all of the subset analyses: 1) symptomatic patients only (Fig 3A) (only 1 study, Powers et al¹⁷ from 2000 studied asymptomatic patients and was not alone statistically significant), 2) disease site involving only the carotid artery (Fig 3B) versus patients with carotid and MCA disease (Fig 3C), and 3) testing by use of absolute OEF measures (Fig 4A) versus testing by use of OEF hemispheric ratio-based measures (Fig 4B).

DISCUSSION

In patients with carotid artery stenosis or occlusion, accurate measures of stroke risk are important for guiding management and treatment decisions. Though structural neuroimaging can play a role in measuring the degree of vessel narrowing, imaging of downstream hemodynamic factors can provide additional insight into stroke risk, including impairments in CVR.¹⁴ Often considered to be the end-stage of hemodynamic failure, increases in OEF as measured on PET were recently used to select patients for the COSS trial, randomly assigning subjects to surgical vascular bypass or medical therapy. With the recent early termination of this trial, there has been renewed interest in the predictive value of OEF increase because some authors⁶ have attributed the trial's futility to methodologic failure of the OEF PET selection criteria. In addition, with multiple MR imaging–based surrogate mea-

asures of OEF being developed with techniques such as susceptibility-weighted MR imaging,¹⁰ functional MR imaging,¹¹ and MR spectroscopy,¹² it is important to summarize the value of OEF as a reference standard to predict stroke by which future technologies can be assessed. If shown to be accurate markers of cerebral oxygen metabolism compared with PET-derived OEF, these potentially more widely available MR imaging techniques can then be tested as potential stroke risk prediction tools.

In our systematic review and meta-analysis of 430 patients with a mean follow-up of 30 months, increased OEF was strongly associated with the risk of ipsilateral stroke, though when viewed independently, only 2 of the 6 studies included in the meta-analysis reached statistical significance. The pooled OR suggests that despite variability in results of individual studies in the literature, patients with increased OEF are approximately 6 times more likely to have ipsilateral stroke than those without increased OEF. Most patients in this study had symptomatic occlusive arterial disease; only 1 study¹⁷ contained a cohort of never-symptomatic patients. This study did not find a significant association between increased OEF and stroke but was limited by its small sample size. The need for stroke prediction in patients with carotid occlusion, the disease state in which most OEF investigation has been done, appears questionable, given the results of COSS. However, the strong performance of OEF in predicting stroke in this population suggests that it may also be useful in patients with high-grade but asymptomatic carotid stenosis, for whom accurate stroke prediction is likely to prove important in deciding between intervention and medical therapy.²¹ Our study emphasizes the need for prospective investigation evaluating the role of OEF testing in predicting stroke risk in asymptomatic carotid stenosis, especially in light of data that impairment of CVR has been associated with stroke in such patients.¹⁴

We also found no significant difference in broad categories of OEF testing method and stroke risk prediction. Specifically, we did not find a significant difference in OR when absolute values of OEF were calculated versus hemispheric-ratio–based techniques (On-line Table 2). This is of note because Carlson et al⁶ recently commented that semiquantitative hemispheric OEF ratios for patient selection in COSS probably contributed to trial failure, which suggests that this method is inferior to quantitative, absolute measures of OEF. Although our study was not designed specifically to analyze this issue, we found insufficient evidence to claim superiority of one of these methods over the other. Even in a study by Yamauchi et al,¹⁶ in which absolute OEF testing performed better than ratio-based techniques in predicting stroke in the same patients, this difference was not statistically significant. As far as optimizing thresholds for classification of abnormal OEF test results, it is interesting to note that studies that had repeated analyses of patient data suggest that adding measures of cerebral blood volume and CBF to OEF may help to further define higher hemodynamic risk categories.^{3,9}

Our study has some limitations. Although the outcome measure (ipsilateral stroke) was the same across studies, the exact definition of stroke was not uniform, given the variable criteria for each study, and in only 2 of the 6 included studies were adjudication of stroke outcomes made blinded to OEF data. Similarly, stroke outcomes were not consistently reported broken down by

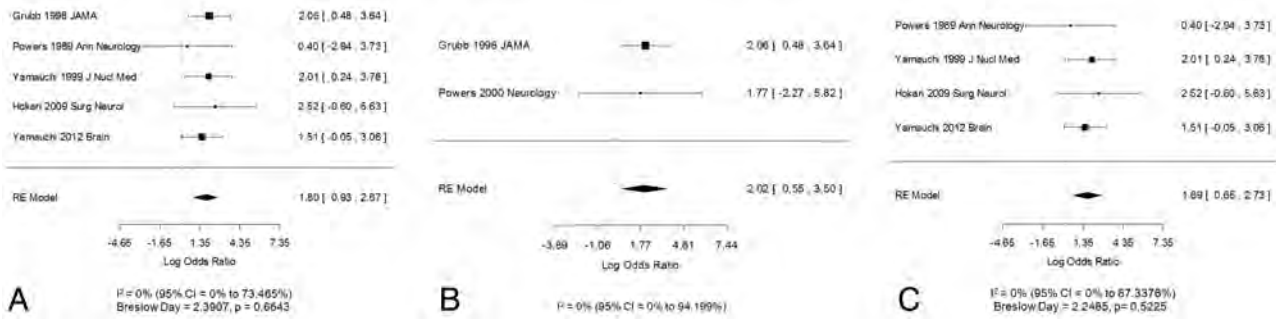


FIG 3. A, Symptomatic patients only, with the OR representing the strength of association between increased OEF and risk of either recurrent stroke or stroke preceded by prior TIA in the symptomatic territory. B, Carotid artery disease only. C, Carotid and MCA disease. Log OR and 95% CI for studies divided by the presence of disease in symptomatic patients only (A), in the carotid artery only (B), or in the carotid artery and MCA (C). Note that a Breslow-Day statistic could not be calculated for the forest plot in B, given the small outcome events. Squares represent point estimates for effect size expressed as log of the OR, with the size proportional to the inverse variance of the estimate (note, $OR = \exp[\log OR]$). Diamonds represent pooled estimate. Lines represent 95% CIs. Vertical line indicates null effect ($OR = 1$ or log odds = 0). I^2 and Breslow-Day statistic for heterogeneity is listed below the forest plot.

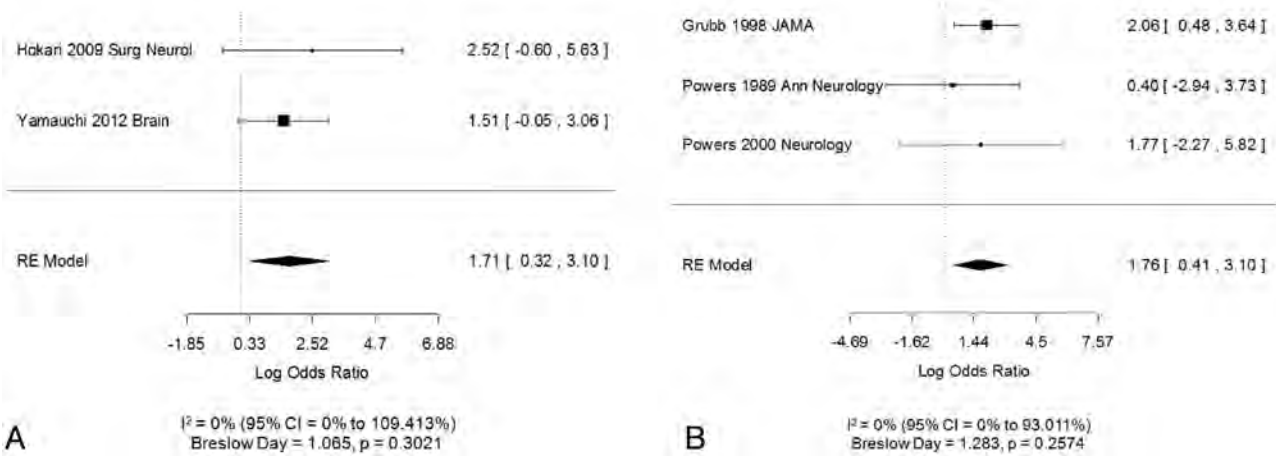


FIG 4. A, Testing by use of absolute OEF measures. B, Testing by use of hemispheric ratio-based measures. Log OR and 95% CI for studies divided by the OEF testing by use of absolute measures of OEF (A) or hemispheric ratio-based measure of OEF (B). Squares represent point estimates for effect size expressed as log of the OR, with the size proportional to the inverse variance of the estimate (note, $OR = \exp[\log OR]$). Diamonds represent pooled estimate. Lines represent 95% CIs. Vertical line indicates null effect ($OR = 1$ or log odds = 0). I^2 and Breslow-Day statistic for heterogeneity is listed below the forest plot.

vessel disease site or severity in those studies with mixed patient characteristics thereby preventing more detailed subset analyses in these studies. In addition, though most studies focused on occlusive disease, in those cohorts in which stenosis was present, individual patient-level results are confounded, in part, by the fact that groups with and without OEF elevation did not have exact matching degrees of arterial stenosis. In addition, as the within-cohort subset analyses demonstrate, definitions of abnormal OEF can vary and significantly affect the resulting OR. Unfortunately, the data were not amenable to comparisons of receiver operating-characteristic curves, a potentially more useful measure of diagnostic test performance. Beyond this, comparing imaging test data across different PET scanners and techniques prevents deriving specific cutoffs for defining abnormal OEF that could be broadly applied to various institutions. Finally, these studies all analyzed a hemodynamic risk factor underlying stroke and did not differentiate strokes that may have arisen from embolic phenomena, potentially overstating the strength of the association between OEF elevation and stroke.

Despite these limitations, our study suggests that increased

OEF remains a robust predictor of ipsilateral stroke in patients with symptomatic carotid disease across multiple disease sites and across broad categories of testing methodology. Furthermore, our study has shown that oxygen metabolism and stroke risk in asymptomatic carotid stenosis requires further study, given the paucity of OEF literature in this patient population in which the identifying high-risk subgroups could be of significant value. Despite the challenges of routinely implementing ^{15}O -PET scanning, our study supports the use of testing as a marker of stroke risk and emphasizes the need for continued investigation of newer techniques to measure cerebral oxygen metabolism.

ACKNOWLEDGMENT

The Association of University Radiologists General Electric Radiology Research Academic Fellowship (GERRAF) is acknowledged for supporting a portion of Dr Gupta's efforts.

Disclosures: Ajay Gupta—RELATED: Grant: AUR-GE Radiology Research Academic Fellowship.* Comments: Part of Dr Gupta's effort for this study was supported by a AUR-GERRAF award from 2012–2014. Yi Wang—RELATED: Grant: NIH R01EB013443*;

UNRELATED: Patents (planned, pending or issued): One of the inventors on QSM patent application.* Pina Sanelli—RELATED: Grant: NIH NINDS* (*money paid to institution).

REFERENCES

1. Petty GW, Brown RD Jr, Whisnant JP, et al. **Ischemic stroke subtypes: a population-based study of incidence and risk factors.** *Stroke* 1999;30:2513–16
2. Silvestrini M, Vernieri F, Pasqualetti P, et al. **Impaired cerebral vasoreactivity and risk of stroke in patients with asymptomatic carotid artery stenosis.** *JAMA* 2000;283:2122–27
3. Derdeyn CP, Videen TO, Yundt KD, et al. **Variability of cerebral blood volume and oxygen extraction: stages of cerebral haemodynamic impairment revisited.** *Brain* 2002;125:595–607
4. Grubb RL Jr, Derdeyn CP, Fritsch SM, et al. **Importance of hemodynamic factors in the prognosis of symptomatic carotid occlusion.** *JAMA* 1998;280:1055–60
5. Powers WJ, Clarke WR, Grubb RL Jr, et al. **Extracranial-intracranial bypass surgery for stroke prevention in hemodynamic cerebral ischemia: the Carotid Occlusion Surgery Study randomized trial.** *JAMA* 2011;306:1983–92
6. Carlson AP, Yonas H, Chang YF, et al. **Failure of cerebral hemodynamic selection in general or of specific positron emission tomography methodology? Carotid Occlusion Surgery Study (COSS).** *Stroke* 2011;42:3637–39
7. Powers WJ, Clarke WR, Adams HP Jr, et al. **Commentary: extracranial-intracranial bypass for stroke in 2012: response to the critique of the carotid occlusion surgery study “it was deja vu all over again.”** *Neurosurgery* 2012;71:E772–76
8. Powers WJ. **Letter by Powers regarding article, “Failure of cerebral hemodynamic selection in general or of specific positron emission tomography methodology? Carotid Occlusion Surgery Study (COSS).”** *Stroke* 2012;43:e43
9. Yamauchi H, Higashi T, Kagawa S, et al. **Is misery perfusion still a predictor of stroke in symptomatic major cerebral artery disease?** *Brain* 2012;135:2515–26
10. Zaitsev Y, Kudo K, Terae S, et al. **Mapping of cerebral oxygen extraction fraction changes with susceptibility-weighted phase imaging.** *Radiology* 2011;261:930–36
11. Gauthier CJ, Desjardins-Crepeau L, Madjar C, et al. **Absolute quantification of resting oxygen metabolism and metabolic reactivity during functional activation using QUO2 MRI.** *Neuroimage* 2012;63:1353–63
12. Zhu XH, Chen JM, Tu TW, et al. **Simultaneous and noninvasive imaging of cerebral oxygen metabolic rate, blood flow and oxygen extraction fraction in stroke mice.** *Neuroimage* 2013;64:437–47
13. Liberati A, Altman DG, Tetzlaff J, et al. **The PRISMA statement for reporting systematic reviews and meta-analyses of studies that evaluate health care interventions: explanation and elaboration.** *Ann Intern Med* 2009;151:W65–94
14. Gupta A, Chazen JL, Hartman M, et al. **Cerebrovascular reserve and stroke risk in patients with carotid stenosis or occlusion: a systematic review and meta-analysis.** *Stroke* 2012;43:2884–91
15. Powers WJ, Tempel LW, Grubb RL Jr. **Influence of cerebral hemodynamics on stroke risk: one-year follow-up of 30 medically treated patients.** *Ann Neurol* 1989;25:325–30
16. Yamauchi H, Fukuyama H, Nagahama Y, et al. **Significance of increased oxygen extraction fraction in five-year prognosis of major cerebral arterial occlusive diseases.** *J Nucl Med* 1999;40:1992–98
17. Powers WJ, Derdeyn CP, Fritsch SM, et al. **Benign prognosis of never-symptomatic carotid occlusion.** *Neurology* 2000;54:878–82
18. Hokari M, Kuroda S, Shiga T, et al. **Impact of oxygen extraction fraction on long-term prognosis in patients with reduced blood flow and vasoreactivity because of occlusive carotid artery disease.** *Surg Neurol* 2009;71:532–8
19. Derdeyn CP, Videen TO, Simmons NR, et al. **Count-based PET method for predicting ischemic stroke in patients with symptomatic carotid arterial occlusion.** *Radiology* 1999;212:499–506
20. Derdeyn CP, Videen TO, Grubb RL Jr, et al. **Comparison of PET oxygen extraction fraction methods for the prediction of stroke risk.** *J Nucl Med* 2001;42:1195–97
21. Abbott AL. **Medical (nonsurgical) intervention alone is now best for prevention of stroke associated with asymptomatic severe carotid stenosis: results of a systematic review and analysis.** *Stroke* 2009;40:e573–83

Perfusion Measurement in Brain Gliomas with Intravoxel Incoherent Motion MRI

C. Federau, R. Meuli, K. O'Brien, P. Maeder, and P. Hagmann



ABSTRACT

BACKGROUND AND PURPOSE: Intravoxel incoherent motion MRI has been proposed as an alternative method to measure brain perfusion. Our aim was to evaluate the utility of intravoxel incoherent motion perfusion parameters (the perfusion fraction, the pseudodiffusion coefficient, and the flow-related parameter) to differentiate high- and low-grade brain gliomas.

MATERIALS AND METHODS: The intravoxel incoherent motion perfusion parameters were assessed in 21 brain gliomas (16 high-grade, 5 low-grade). Images were acquired by using a Stejskal-Tanner diffusion pulse sequence, with 16 values of b ($0-900 \text{ s/mm}^2$) in 3 orthogonal directions on 3T systems equipped with 32 multichannel receiver head coils. The intravoxel incoherent motion perfusion parameters were derived by fitting the intravoxel incoherent motion biexponential model. Regions of interest were drawn in regions of maximum intravoxel incoherent motion perfusion fraction and contralateral control regions. Statistical significance was assessed by using the Student t test. In addition, regions of interest were drawn around all whole tumors and were evaluated with the help of histograms.

RESULTS: In the regions of maximum perfusion fraction, perfusion fraction was significantly higher in the high-grade group (0.127 ± 0.031) than in the low-grade group (0.084 ± 0.016 , $P < .001$) and in the contralateral control region (0.061 ± 0.011 , $P < .001$). No statistically significant difference was observed for the pseudodiffusion coefficient. The perfusion fraction correlated moderately with dynamic susceptibility contrast relative CBV ($r = 0.59$). The histograms of the perfusion fraction showed a "heavy-tailed" distribution for high-grade but not low-grade gliomas.

CONCLUSIONS: The intravoxel incoherent motion perfusion fraction is helpful for differentiating high- from low-grade brain gliomas.

ABBREVIATIONS: D = diffusion coefficient; D^* = pseudodiffusion coefficient; f = perfusion fraction; fD^* = flow-related parameter; IVIM = intravoxel incoherent motion

An estimated 69,720 new cases of primary central nervous system tumors are expected to be diagnosed in the United States in 2013, of which an estimated 24,620 new cases will be malignant

(13,630 in males and 10,990 in females).¹ The 5-year relative survival rate following diagnosis of primary malignant CNS tumors, mostly gliomas, is poor, with an average of 33.8%, but it is age-dependent, decreasing monotonically from 73% for 0–19 years of age to 10% for 65–74 years of age (data from 1995–2009).²

The assessment of perfusion characteristics of those lesions by using dynamic susceptibility MR imaging has become an important part of the initial evaluation and follow-up because cerebral blood volume has been shown to correlate with the degree of neovascularization³ and increased local perfusion has been shown to correlate with tumor grading⁴ and prognosis.⁵ Histologically, the assessment of microvascularity is important for the grading of a primary brain tumor⁶ because high-grade neoplasms produce a pathologic microvascular network through neoangiogenesis to satisfy a growing need for nutrients and oxygen.

Le Bihan et al⁷ have proposed measuring microvascular perfusion with an MR imaging–based method called intravoxel incoherent motion (IVIM) imaging. The incoherent motion of spins, which can be understood as the spatial “mixing” of spins

Received March 30, 2013; accepted after revision June 2.

From the Department of Diagnostic and Interventional Radiology (C.F., R.M., P.M., P.H.), Centre Hospitalier Universitaire Vaudois and University of Lausanne, Lausanne, Switzerland; and Center for Biomedical Imaging (K.O.), University of Geneva, Geneva, Switzerland.

P. Maeder and P. Hagmann contributed equally to this work.

This work was supported by the Centre d'Imagerie BioMédicale of the University of Lausanne, University of Geneva, Hôpitaux Universitaires de Genève, Centre Hospitalier Universitaire Vaudois, École polytechnique fédérale de Lausanne and the Leenaards and Jeantet Foundations. C. Federau was supported by the Faculté de biologie et de médecine of the University of Lausanne. P. Hagmann was supported by a grant from Leenaards Foundation.

Please address correspondence to Christian Federau, MD, Department of Diagnostic and Interventional Radiology, Centre Hospitalier Universitaire Vaudois, Rue du Bugnon 46, 1011 Lausanne, Switzerland; e-mail: christian.federau@chuv.ch

Indicates open access to non-subscribers at www.ajnr.org

Indicates article with supplemental on-line appendix.

Indicates article with supplemental on-line figure.

<http://dx.doi.org/10.3174/ajnr.A3686>

Table 1: Patient demographics, tumor localization, and histologic diagnosis

Grade	Age (yr)	Sex	Localization	Sample Obtained	Pathologic Diagnosis	WHO Grade
High						
1	77	Male	Left parietal lobe	Surgical resection	Glioblastoma multiforme	IV
2	67	Male	Right parietal lobe	Surgical resection	Glioblastoma multiforme	IV
3	84	Female	Left parietal lobe	Stereotaxic biopsy	Glioblastoma multiforme	IV
4	61	Female	Right frontal lobe	Surgical resection	Glioblastoma multiforme	IV
5	60	Male	Right frontal lobe	Surgical resection	Glioblastoma multiforme	IV
6	68	Male	Right insula	Surgical resection	Glioblastoma multiforme	IV
7	73	Male	Right frontotemporal lobes	Surgical resection	Anaplastic oligoastrocytoma	III
8	36	Male	Left insula	Stereotaxic biopsy	Diffuse glioma	III
9	50	Male	Left temporal lobe	Stereotaxic biopsy	Glioblastoma multiforme	IV
10	43	Male	Left temporal lobe	Surgical resection	Glioblastoma multiforme	IV
11	73	Male	Left temporal lobe	Surgical resection	Glioblastoma multiforme	IV
12	53	Male	Left parietal lobe	Surgical resection	Glioblastoma multiforme	IV
13	60	Female	Left operculum	Stereotaxic biopsy	Glioblastoma multiforme	IV
14	24	Male	Left cingulum	Stereotaxic biopsy	Anaplastic oligoastrocytoma	III
15	61	Male	Left temporal lobe	Surgical resection	Glioblastoma multiforme	IV
16	63	Female	Right frontal lobe	Surgical resection	Glioblastoma multiforme	IV
Low						
1	38	Male	Right frontal lobe	Surgical resection	Oligoastrocytoma	II
2	58	Male	Right frontal lobe	Surgical resection	Neuroglial tumor	II
3	54	Male	Left temporo-occipital lobes	Stereotaxic biopsy	Diffuse astrocytoma	II
4	38	Male	Left frontal lobe	Stereotaxic biopsy	Oligodendroglioma	II
5	2	Male	Centered on 3rd ventricle	Stereotaxic biopsy	Pilomyxoid astrocytoma	II

Note:—WHO indicates World Health Organization.

during the time of measurement, reduces exponentially the signal amplitude obtained from a diffusion-weighted sequence such as the Stejskal-Tanner sequence.⁸ This incoherent motion arises inevitably from the thermal diffusion characterized by diffusion coefficient (D) and, in biologic perfused tissue, from movements of blood in the microvasculature, called by analogy pseudodiffusion and characterized by pseudodiffusion coefficient (D^*).

Therefore, an IVIM biexponential signal equation⁷ has been proposed to model incoherent motion in biologic tissue, with the perfusion fraction (f) describing the fraction of incoherent signal arising from the vascular compartment in each voxel over the total incoherent signal. Furthermore, under the assumption of an isotropic, randomly laid microvascular network, a linear relationship were derived⁹ between D^* and fD^* (the scalar multiplication of f and D^* , referred to as the flow-related parameter) and CBV, MTT^{-1} , and CBF, respectively.

Recently, IVIM showed promising results in helping discriminate high- and low-grade tumors, for example in the salivary gland, among Warthin tumors, pleomorphic adenomas, and malignant tumors¹⁰; in the pancreas between healthy pancreas and pancreatic cancer¹¹; or between renal¹² and breast tumor subtypes.¹³ In the brain, where initial reports were made,^{7,14-19} IVIM perfusion parameters showed recently a gradual increase in response to gradual increase of hypercapnia.²⁰

The purpose of this study was to evaluate the utility of IVIM perfusion parameters (f , D^* , and fD^*) to differentiate high- and low-grade brain gliomas.

MATERIALS AND METHODS

Patient Demographics

The present study was approved by the local ethics committee at University of Lausanne. Patient consents were waived. From May 2011 to December 2012, our clinical glioma protocol included an IVIM sequence, which replaced the standard diffusion-weighted

sequence. This provided apparent diffusion maps, which are part of the standard glioma evaluation, as well as perfusion-weighted maps, which allowed our exploratory work. Our clinical glioma protocol also included T1-weighted, T2-weighted, DSC perfusion, and T1-weighted postgadolinium sequences. Twenty-one consecutive patients (17 males, 4 females; mean age, 52.3 ± 21.3 years; age range, 2–84 years; Table 1) who had preoperative MR imaging examination, had no relevant treatment history at the time of imaging (such as radio-, chemo-, or antiangiogenic therapy), and had consecutive histopathologic diagnoses were included in the study. The tumor grading was based on World Health Organization criteria and yielded 16 high-grade and 5 low-grade gliomas. Because of the low number of low-grade gliomas found, a complementary study was performed and included 6 further low-grade gliomas diagnosed on radiologic criteria only (On-line Appendix).

Conventional MR Imaging

Conventional MR imaging, DSC, and IVIM were performed during the same procedure to allow direct comparison. The imaging was performed on 3T MR imaging scanners (Trio, Verio, or Skyra; Siemens, Erlangen, Germany) equipped with 32 multi-channel receiver head coils. Before the examination, an 18- to 20-ga needle was inserted in either the right or the left antecubital vein. Afterward, T1-weighted sagittal and T2-weighted axial images were acquired.

IVIM MR Imaging

A Stejskal-Tanner diffusion-weighted spin-echo EPI pulse sequence¹⁵ was used, with multiple b-values (0, 10, 20, 40, 80, 110, 140, 170, 200, 300, 400, 500, 600, 700, 800, 900 s/mm^2) in 3 orthogonal directions, and the corresponding trace was calculated. A single acquisition was obtained (no average). The images were orientated axially with a section thickness of 4 mm, an FOV of $297 \times 297 mm^2$, and a matrix size of 256×256 ,

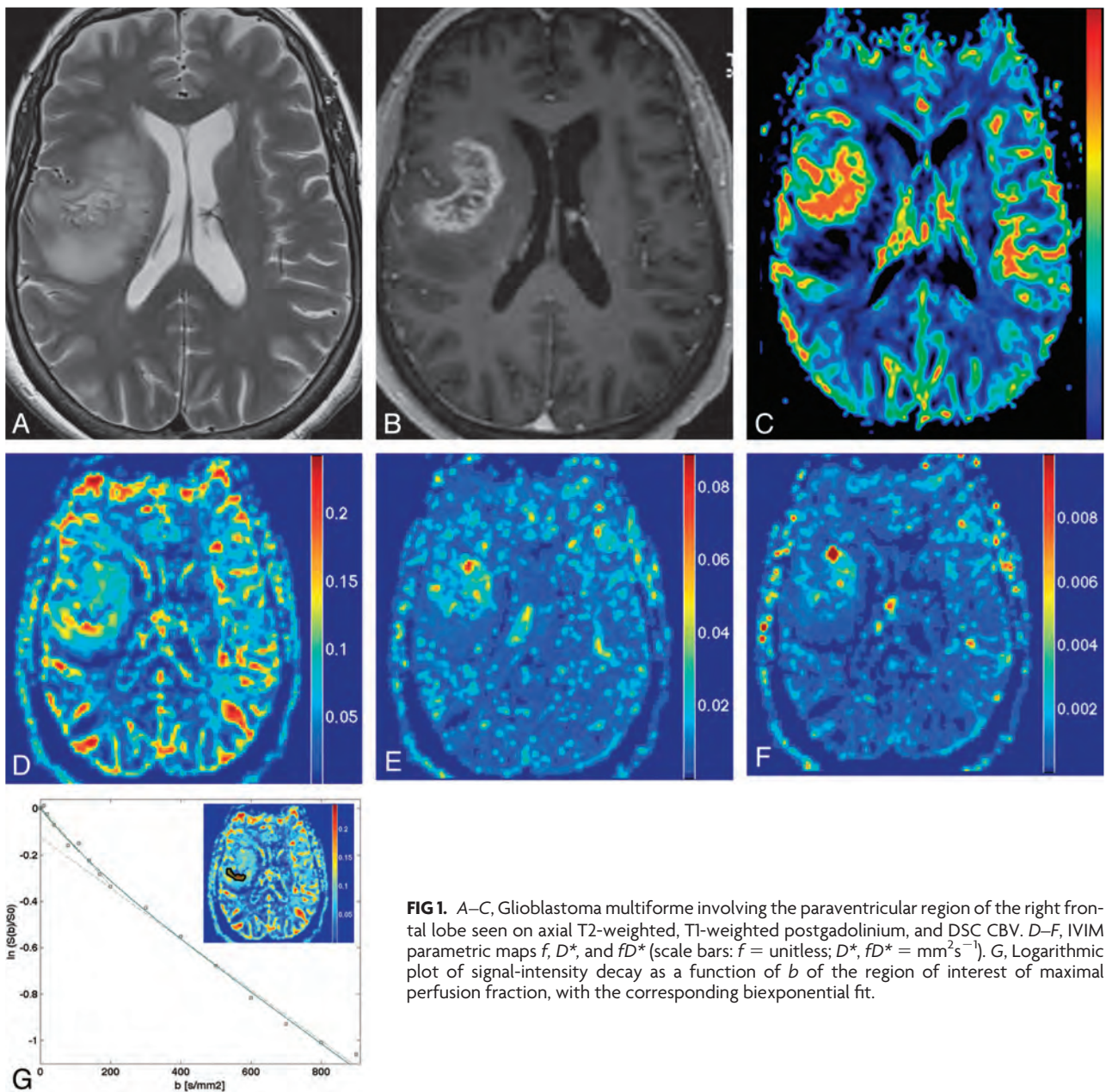


FIG 1. A–C, Glioblastoma multiforme involving the paraventricular region of the right frontal lobe seen on axial T2-weighted, T1-weighted postgadolinium, and DSC CBV. D–F, IVIM parametric maps f , D^* , and fD^* (scale bars: f = unitless; D^* , fD^* = mm^2s^{-1}). G, Logarithmic plot of signal-intensity decay as a function of b of the region of interest of maximal perfusion fraction, with the corresponding biexponential fit.

yielding an in-plane resolution of $1.2 \times 1.2 \text{ mm}^2$. Parallel imaging, with an acceleration factor of 2 and a 75% partial Fourier encoding allowed $\text{TR/TE} = 4000/99 \text{ ms}$. The receiver bandwidth was 1086 Hz/pixel, and fat was suppressed with a spectrally selective saturation routine. Total acquisition time was 3 minutes 7 seconds.

DSC MR Imaging

A gadolinium-based agent (gadoterate meglumine, Dotarem; Guerbet, Paris, France) was intravenously injected at a dose of 0.2 mL per kilogram of body weight and at a rate of 3 mL/s, followed by a 20-mL saline flush. Standard echo-planar images were consecutively acquired ($\text{TR} = 1950 \text{ ms}$, $\text{TE} = 43 \text{ ms}$, section thickness = 6 mm, $\text{FOV} = 230 \times 230$, acquisition matrix = 128×128). No leakage correction was performed. CBV, MTT, and CBF maps were computed from the DSC MR imaging data by using the commercially available software,

syngoMR (Siemens). On the section of interest, a region of interest was placed on an identified artery. We selected ≥ 4 voxels containing the best arterial input function curves, from which the average was built. We then set the time ranges defining baseline, gadolinium entry, and recovery, before the DSC perfusion maps were automatically calculated on the basis of a γ variate fitting of the time-concentration curve.

Regions of Interest

Brain gliomas have very heterogeneous structures and, accordingly, only the region with the highest malignancy defines the pathologic grade of the lesion. Therefore, a region of interest was manually placed on each tumor area in consensus by 2 experienced neuroradiologists (P.M. and P.H.) who were blinded to the histopathology, in the region of the tumor with maximal IVIM

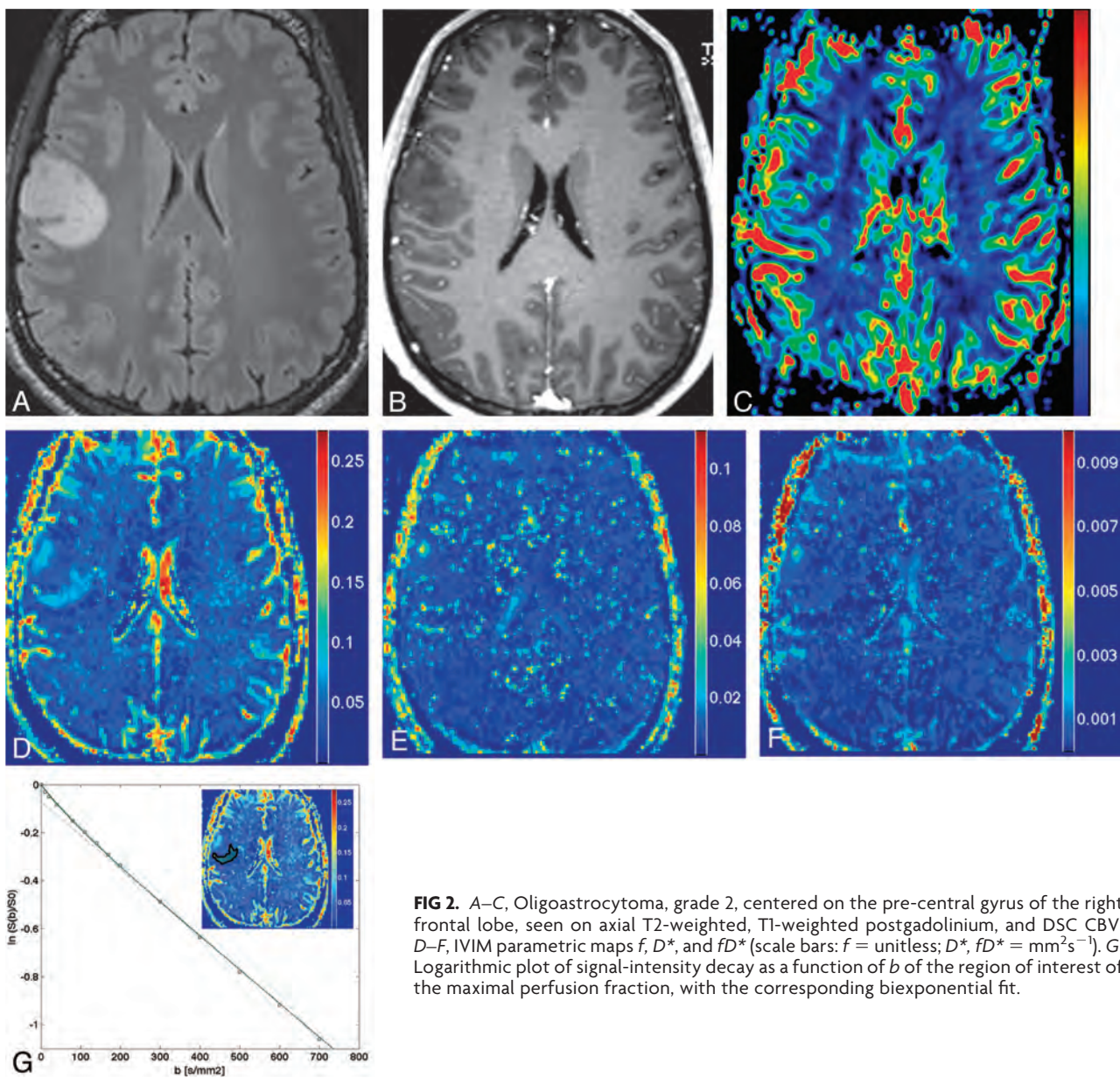


FIG 2. A–C, Oligoastrocytoma, grade 2, centered on the pre-central gyrus of the right frontal lobe, seen on axial T2-weighted, T1-weighted postgadolinium, and DSC CBV. D–F, IVIM parametric maps f , D^* , and fD^* (scale bars: f = unitless; D^* , fD^* = mm^2s^{-1}). G, Logarithmic plot of signal-intensity decay as a function of b of the region of interest of the maximal perfusion fraction, with the corresponding biexponential fit.

perfusion fraction and in the contralateral white matter, both on a single axial section. Cystic, hemorrhagic, or necrotic areas were avoided by using conventional pre- and postcontrast MR images. If a tumor was centered on the midline, a region of interest was chosen in the white matter of one of both hemispheres. Mean IVIM region-of-interest size was $322 \pm 187 \text{ mm}^2$. The corresponding ROIs were then drawn on the DSC images, manually matching the images by using anatomic landmarks. The relative CBV was calculated by dividing the value of the region of interest in the tumor by the value of the contralateral normal-appearing white matter. The mean DSC region-of-interest size was $342 \pm 151 \text{ mm}^2$.

We also produced histograms by placing a region of interest on all whole tumors on the IVIM b_0 images, including all sections where the tumor was visible, and encompassing as much of the tumor area as possible but excluding cystic or necrotic areas, with the help of conventional pre- and postcontrast MR images. For

the control histogram, a region of interest was placed in all patients to comprise the full white matter of an axial section of the contralateral hemisphere to the tumor.

All ROIs were placed so that they included as little CSF or as few large vessels as possible.

IVIM Image Processing

The standard IVIM 2-compartment diffusion model was assumed,⁷ with a “microvascular” and a “nonvascular” compartment, having, respectively, a pseudodiffusion coefficient and an apparent diffusion coefficient. The percentage of incoherent signal arising from the microvascular compartment f is called the perfusion fraction. To obtain the IVIM parameters, the IVIM signal equation

$$\frac{S(b)}{S_0} = f \times e^{-bD^*} + (1 - f) \times e^{-bD}$$

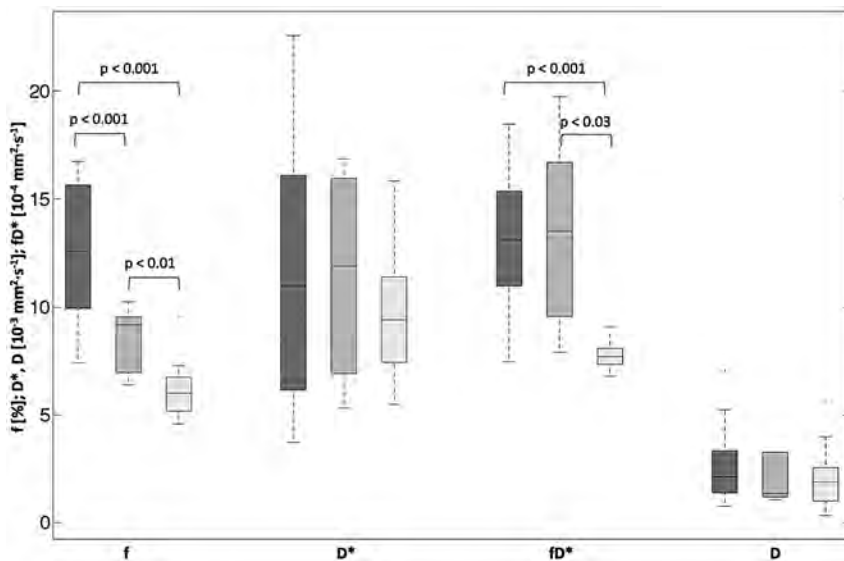


FIG 3. Box-and-whisker plot (median, 25th and 75th percentiles, minimum, maximum, and outliers) of f , D^* , fD^* , and D , as measured in ROIs of the maximum perfusion fraction. Dark gray indicates high-grade tumors; medium gray, low-grade tumors; light gray, contralateral control region of both high- and low-grade. P values are indicated when $<.05$.

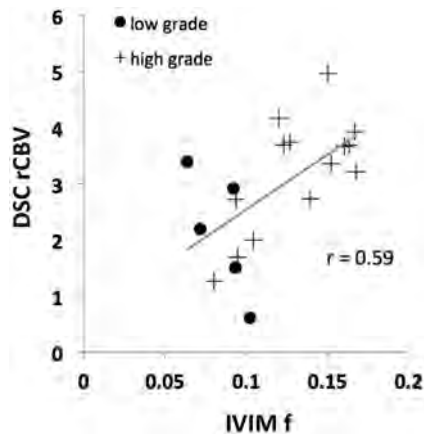


FIG 4. Scatterplots comparing relative DSC CBV (y-axis) with absolute IVIM f (x-axis). Pearson r correlation coefficient is given.

was fitted in 2 steps, as previously described,²⁰ first for $b > 200$ s/mm² for the single parameter D , then for all b and all parameters, while keeping D constant. This fit was done on a voxel-by-voxel basis, by using the Levenberg-Marquardt algorithm²¹ implemented within Matlab (MathWorks, Natick, Massachusetts). This 2-step method increases robustness under biologic conditions and assumes that D^* is significantly greater than D so that the influence of pseudodiffusion on signal decay can be neglected for b -values > 200 s/mm². Values under 0 for f , D , and D^* , and values with $f > 0.3$ and $D^* > 0.05$ mm²/s were considered not physiologic and were set to 0.²³ This step excluded poorly fitted voxels ($< 1\%$ of the voxels) and was necessary to ensure that a single artifactually very high value in a single voxel could not be responsible for the measured effect, while also increasing the contrast of the IVIM maps.

Statistical Analysis

Statistical analysis was performed with Excel (Microsoft, Redmond, Washington). A normal distribution of the data was

assumed. Single-tailed, pair-wise Student t tests were calculated when data were compared with the contralateral region. Single-tailed, 2-sample, unequal-variance Student t tests were calculated between high- and low-grade tumor groups. Statistical significance was defined at $P < .05$. The Pearson r correlation coefficient between IVIM perfusion fraction f and DSC CBV was calculated.

RESULTS

High-resolution IVIM perfusion maps were produced, and in tumorous regions, increased perfusion similar to DSC CBV could be observed (Figs 1 and 2).

In the region of interest of the maximum IVIM perfusion fraction, f was significantly higher in high-grade (0.127 ± 0.031) compared with low-grade gliomas (0.084 ± 0.016 , $P = .0006$), as well as in both glioma groups compared with the contralateral region (0.061 ± 0.011 , $P < .0001$) (Fig 3). Those results could be confirmed in the complementary study including the cohort of low-grade gliomas diagnosed on radiologic criteria only (On-line Fig 1).

f correlated moderately with DSC relative CBV ($r = 0.59$, Fig 4). The normalized histogram analysis of f over all whole tumor volumes showed an obvious “heavy-tailed” distribution for the high-grade gliomas in comparison with the low-grade and the reference contralateral white matter of an axial section (Fig 5).

No statistically significant difference was observed for D^* (0.0117 ± 0.0058 mm²s⁻¹ versus 0.0114 ± 0.0050 mm²s⁻¹ versus 0.0098 ± 0.0029 mm²s⁻¹, for high-, low-grade, and contralateral brain, respectively; Fig 3). The flow-related parameter fD^* was not statistically significantly different between high- and low-grade tumors (0.00132 ± 0.00032 mm²s⁻¹ versus 0.00133 ± 0.00046 mm²s⁻¹, respectively; $P = .46$), but it was significantly different between both glioma groups and the contralateral brain region (0.00077 ± 0.00007 mm²s⁻¹, $P < .001$).

DISCUSSION

This report demonstrates that the IVIM perfusion fraction can help differentiate high- and low-grade gliomas. Of interest is the fact that this was obtained with a direct measurement in the tumor, without normalization with a measure in the contralateral white matter, as is currently done with DSC. While more data will be required for a detailed analysis, the following can be deduced from this small cohort: No low-grade tumor showed a value of f above 0.103, suggesting a probable high-grade histology when above this value, with a sensitivity of 75%. No control region showed an f value above 0.096, suggesting tumor when above this value, with a sensitivity of 69%.

Further, f correlated moderately with DSC CBV, confirming earlier results.²³ In the histogram analysis of all whole tumors, the heavy-tailed distribution for the high-grade in comparison with the low-grade gliomas and the reference white matter demon-

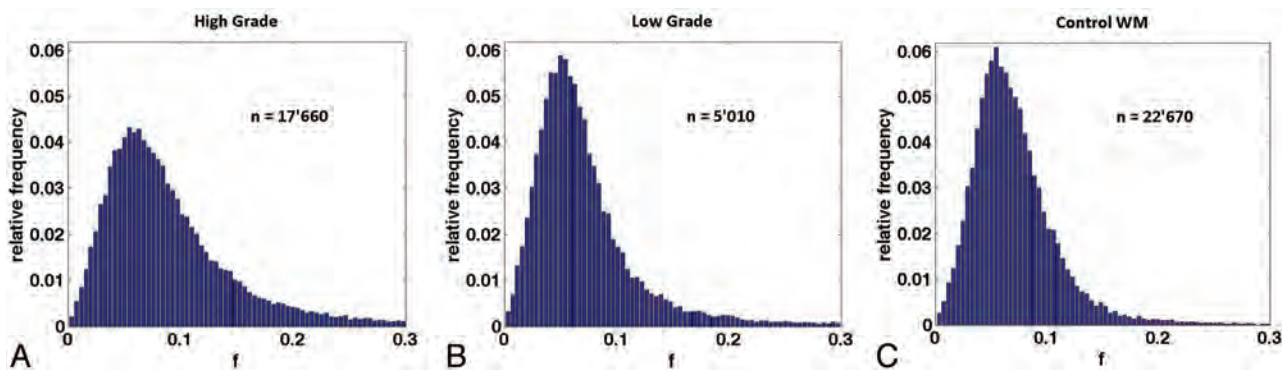


FIG 5. Normalized histograms of the perfusion fraction comprising the voxels of all whole tumor volumes for the high-grade (A) and low-grade (B) groups and for the control group (C). The total number of voxels included is indicated by n . An increase in the normalized number of highly perfused voxels can be observed in the high-grade tumor group in comparison with the low-grade and control groups.

stated that the presented effect can be measured independent of region-of-interest placement.

Single whole-tumor statistical analysis might be of interest but should be explored with care because tumor heterogeneity is a known property of gliomas and the region of highest malignancy defines the tumor grade.

There was no statistically significant difference between D^* in the different groups in this small cohort, which might be due to low signal-to-noise ratio. D^* has been shown to be less reproducible than f in the liver.²⁴ Nevertheless, in selected cases with high image quality (which was not an inclusion criterion for this study), we were able to produce D^* maps that were consistent with the known histologic diagnosis.²⁵ Furthermore, in a larger study with healthy volunteers over large regions of interest, a strong dependence of D^* (and no statistically significant dependence of f) on the cardiac cycle could be shown.²⁶ Together, these findings indicate that there is still hope that D^* could provide clinically relevant information when image quality is high enough.

There was also no statistically significant difference in D among the different groups. While regions with minimum apparent diffusion coefficient are thought to reflect the sites of highest cellularity within heterogeneous tumors and hence correlate with glioma grade,^{27–29} those regions do not have to correspond necessarily to the regions of highest vascularity, which were studied here.

The known linear relationship⁹ between the standard perfusion parameters and the IVIM perfusion parameters is dependent on the structure of the microvascular network, for example, on the mean vascular segment length or on the number and orientation of bifurcations. Neovascular vessels in tumors are known to have a fundamentally different network structure than normal vessels.^{30,31} This might, therefore, introduce a bias in the comparison with standard perfusion parameters, and further studies evaluating the exact relationship between IVIM and standard perfusion parameters in pathologic conditions should be pursued. The IVIM perfusion parameters should be considered as a new set of microperfusion parameters that, though related to the standard perfusion parameters, might differ in given cases, depending on the local microvascular network structure.

IVIM perfusion measurement in the brain remains technically challenging. It is obviously highly dependent on the immobility of the patient during the entire acquisition. Susceptibility inhomogeneities, such as around the petrous apex or the paranasal sinuses or due to the presence of metal or blood, for example, postoper-

atively, can harm the IVIM signal but are also problematic when performing DSC.

On the other hand, the IVIM method has many theoretic advantages over currently used DSC. It is intrinsically quantitative, and, because of the intravoxel excitation and readout, it does not require a precise knowledge of the arterial input function, which is challenging to measure.^{32–34} It does not require contrast media and enables the acquisition of perfusion and diffusion information in a single sequence.

This study has several limitations. The cohort studied is relatively small, especially the low-grade tumors, because those tumors are usually followed without biopsy or operation at our institution. The results of a complementary study, including low-grade tumors as diagnosed on radiologic criteria only, can be found in the On-line Appendix and showed results similar to the ones presented. The placement of the ROIs was subjective in nature but reflected the usual clinical practice. Furthermore, the comparison between IVIM f and DSC CBV is limited by the fact that the DSC sections were positioned in the anterior/posterior commissure plane, while the IVIM sections were placed strictly transverse, but the regions of interest were sufficiently large to be identified reliably by using anatomic landmarks. In the future, the orientation and FOV of the different sequences could be aligned to ease comparison; however, this could be at the cost of optimal parameter settings, which are often sequence-specific. Coregistration and interpolation could improve the accuracy of the correspondence of the regions.

CONCLUSIONS

This report demonstrates that the IVIM perfusion fraction might be of value to differentiate high- and low-grade gliomas.

Disclosures: Christian Federau—UNRELATED: Patents (planned, pending or issued): patent pending on IVIM.* Philippe Maeder—UNRELATED: Patents (planned, pending or issued): patent pending on IVIM.* Patric Hagmann—UNRELATED: patents (planned, pending or issued): patent pending on IVIM.* *Money paid to the institution.

REFERENCES

1. The Central Brain Tumor Registry of the United States. <http://www.cbtrus.org>. Accessed November 11, 2012
2. Surveillance, Epidemiology, and End Results (SEER) Program. National Cancer Institute. www.seer.cancer.gov. Accessed November 11, 2012

3. Aronen HJ, Gazit IE, Louis DN, et al. **Cerebral blood volume maps of gliomas: comparison with tumor grade and histologic findings.** *Radiology* 1994;191:41–51
4. Law M, Yang S, Wang H, et al. **Glioma grading: sensitivity, specificity, and predictive values of perfusion MR imaging and proton MR spectroscopic imaging compared with conventional MR imaging.** *AJNR Am J Neuroradiol* 2003;24:1989–98
5. Law M, Young RJ, Babb JS, et al. **Gliomas: predicting time to progression or survival with cerebral blood volume measurements at dynamic susceptibility-weighted contrast-enhanced perfusion MR imaging.** *Radiology* 2008;247:490–98
6. Kumar V, Abbas AK, Aster JC, et al. *Robbins & Cotran Pathologic Basis of Disease*. 7th ed. Paris, France: Elsevier Saunders; 2005
7. Le Bihan D, Breton E, Lallemand D, et al. **Separation of diffusion and perfusion in intravoxel incoherent motion MR imaging.** *Radiology* 1988;168:497–505
8. Stejskal EO, Tanner JE. **Spin diffusion measurements: spin echoes in the presence of a time-dependent field gradient.** *J Chem Phys* 1965;42:288–92
9. Le Bihan D, Turner R. **The capillary network: a link between IVIM and classical perfusion.** *Magn Reson Med* 1992;27:171–78
10. Sumi M, Van Cauteren M, Sumi T, et al. **Salivary gland tumors: use of intravoxel incoherent motion MR imaging for assessment of diffusion and perfusion for the differentiation of benign from malignant tumors.** *Radiology* 2012;263:770–77
11. Lemke A, Laun FB, Klauss M, et al. **Differentiation of pancreas carcinoma from healthy pancreatic tissue using multiple b-values: comparison of apparent diffusion coefficient and intravoxel incoherent motion derived parameters.** *Invest Radiol* 2009;44:769–75
12. Chandarana H, Kang SK, Wong S, et al. **Diffusion-weighted intravoxel incoherent motion imaging of renal tumors with histopathologic correlation.** *Invest Radiol* 2012;47:688–96
13. Sigmund EE, Cho GY, Kim S, et al. **Intravoxel incoherent motion imaging of tumor microenvironment in locally advanced breast cancer.** *Magn Reson Med* 2011;65:1437–47
14. Henkelman RM, Neil JJ, Xiang QS. **A quantitative interpretation of IVIM measurements of vascular perfusion in the rat brain.** *Magn Reson Med* 1994;32:464–69
15. Turner R, Le Bihan D, Maier J, et al. **Echo-planar imaging of intravoxel incoherent motion.** *Radiology* 1990;177:407–14
16. Neil JJ, Bosch CS, Ackerman JJ. **An evaluation of the sensitivity of the intravoxel incoherent motion (IVIM) method of blood flow measurement to changes in cerebral blood flow.** *Magn Reson Med* 1994;32:60–65
17. Chenevert TL, Pipe JG, Williams DM, et al. **Quantitative measurement of tissue perfusion and diffusion in vivo.** *Magn Reson Med* 1991;17:197–212
18. Le Bihan D, Moonen CT, van Zijl PC, et al. **Measuring random microscopic motion of water in tissues with MR imaging: a cat brain study.** *J Comput Assist Tomogr* 1991;15:19–25
19. Wirestam R, Brockstedt S, Lindgren A, et al. **The perfusion fraction in volunteers and in patients with ischaemic stroke.** *Acta Radiol* 1997;38:961–64
20. Federau C, Maeder P, O'Brien K, et al. **Quantitative measurement of brain perfusion with intravoxel incoherent motion MR imaging.** *Radiology* 2012;265:874–81
21. Seber GA, Wild CJ. *Nonlinear Regression*. Hoboken, New Jersey: Wiley-Interscience; 2003
22. Le Bihan D, Turner R, MacFall JR. **Effects of intravoxel incoherent motions (IVIM) in steady-state free precession (SSFP) imaging: applications to molecular diffusion imaging.** *Magn Reson Med* 1989;10:324–37
23. Wirestam R, Borg M, Brockstedt S, et al. **Perfusion-related parameters in intravoxel incoherent motion MR imaging compared with CBV and CBF measured by dynamic susceptibility-contrast MR technique.** *Acta Radiol* 2001;42:123–28
24. Andreou A, Koh DM, Collins DJ, et al. **Measurement reproducibility of perfusion fraction and pseudodiffusion coefficient derived by intravoxel incoherent motion diffusion-weighted MR imaging in normal liver and metastases.** *Eur Radiol* 2013;23:428–34
25. Federau C, O'Brien K, Meuli R, et al. **Measuring brain perfusion with intravoxel incoherent motion (IVIM): initial clinical experience.** *J Magn Reson Imaging* 2013. In press
26. Federau C, O'Brien K, Müller M, et al. **Pulsatile microvascular perfusion demonstrated in the human brain with intravoxel incoherent motion (IVIM) MRI.** In: *Proceedings of the 21st Annual Meeting of the International Society for Magnetic Resonance in Medicine*, Salt Lake City, Utah. April 20–26, 2013
27. Sugahara T, Korogi Y, Kochi M, et al. **Usefulness of diffusion-weighted MRI with echo-planar technique in the evaluation of cellularity in gliomas.** *J Magn Reson Imaging* 1999;9:53–60
28. Higano S, Yun X, Kumabe T, et al. **Malignant astrocytic tumors: clinical importance of apparent diffusion coefficient in prediction of grade and prognosis.** *Radiology* 2006;241:839–46
29. Murakami R, Sugahara T, Nakamura H, et al. **Malignant supratentorial astrocytoma treated with postoperative radiation therapy: prognostic value of pretreatment quantitative diffusion-weighted MR imaging.** *Radiology* 2007;243:493–99
30. Scatliff JH, Radcliffe WB, Pittman HH, et al. **Vascular structure of glioblastomas.** *Am J Roentgenol Radium Ther Nuclear Med* 1969;105:795–805
31. Jain RK, di Tomaso E, Duda DG, et al. **Angiogenesis in brain tumours.** *Nat Rev Neurosci* 2007;8:610–22
32. Calamante F, Gadian DG, Connelly A. **Quantification of perfusion using bolus tracking magnetic resonance imaging in stroke: assumptions, limitations, and potential implications for clinical use.** *Stroke* 2002;33:1146–51
33. Knutsson L, Stahlberg F, Wirestam R. **Absolute quantification of perfusion using dynamic susceptibility contrast MRI: pitfalls and possibilities.** *MAGMA* 2010;23:1–21
34. Petersen ET, Zimine I, Ho YC, et al. **Non-invasive measurement of perfusion: a critical review of arterial spin labelling techniques.** *Br J Radiol* 2006;79:688–701

Assessment of Angiographic Vascularity of Meningiomas with Dynamic Susceptibility Contrast-Enhanced Perfusion-Weighted Imaging and Diffusion Tensor Imaging

C.H. Toh, K.-C. Wei, C.N. Chang, Y.-W. Peng, S.-H. Ng, H.-F. Wong, and C.-P. Lin



ABSTRACT

BACKGROUND AND PURPOSE: The roles of DTI and dynamic susceptibility contrast-enhanced-PWI in predicting the angiographic vascularity of meningiomas have not been studied. We aimed to investigate if these 2 techniques could reflect the angiographic vascularity of meningiomas.

MATERIALS AND METHODS: Thirty-two consecutive patients with meningiomas who had preoperative dynamic susceptibility contrast-enhanced-PWI, DTI, and conventional angiography were retrospectively included. The correlations between angiographic vascularity of meningiomas, classified with a 4-point grading scale, and the clinical or imaging variables—age and sex of patient, as well as size, CBV, fractional anisotropy, and ADC of meningiomas—were analyzed. The meningiomas were dichotomized into high-vascularity and low-vascularity groups. The differences in clinical and imaging variables between the 2 groups were compared. Receiver operating characteristic curve analysis was used to determine the diagnostic performance of these variables.

RESULTS: In meningiomas, angiographic vascularity correlated positively with CBV but negatively with fractional anisotropy. High-vascularity meningiomas demonstrated significantly higher CBV but lower fractional anisotropy as compared with low-vascularity meningiomas. In differentiating between the 2 groups, the area under the curve values were 0.991 for CBV and 0.934 for fractional anisotropy on receiver operating characteristic curve analysis.

CONCLUSIONS: CBV and fractional anisotropy correlate well with angiographic vascularity of meningiomas. They may differentiate between low-vascularity and high-vascularity meningiomas.

ABBREVIATIONS: AUC = area under the curve; FA = fractional anisotropy; ROC = receiver operating characteristic

Meningiomas account for approximately one-third of primary brain tumors.¹ Preoperative evaluation of meningioma with conventional angiography, the reference standard for tumor vasculature assessment, may help in surgical planning by providing important information such as tumor vascularity, vascular anatomy of feeding arteries, and draining veins. However,

cerebral conventional angiography is invasive and not without risk. A previous study reported that there were 1.3% neurologic complications, among which 0.5% were permanent.²

Several MR imaging techniques have been shown to be able to provide some of the vascular information of meningiomas that could only be obtained with conventional angiography in the past. Arterial spin-labeling and regional perfusion imaging techniques could determine if the vascular supply of a meningioma was from the external carotid artery, the ICA, or both.³ MRA, on the other hand, helped to identify the arterial branches primarily supplying the meningiomas.⁴ To our knowledge, there is no report on the use of quantitative MR techniques to predict the degree of angiographic vascularity of meningiomas.

In contrast to conventional MR imaging, which provides only structural information, advanced MR techniques such as dynamic susceptibility contrast-enhanced PWI and DTI may provide physiologic information that helps in lesion characterization. The attenuation of T2-weighted signal measured with DTI after 2 extra gradient pulses can be linked to water diffusivity. Fractional

Received March 15, 2013; accepted after revision April 27.

From the Departments of Medical Imaging and Intervention (C.H.T., Y.-W.P., S.-H.N., H.-F.W.) and Neurosurgery (K.-C.W., C.N.C.), Chang Gung Memorial Hospital, Linkou and Chang Gung University College of Medicine, Tao-Yuan, Taiwan; and Department of Biomedical Imaging and Radiological Sciences (C.H.T., C.-P.L.) and Brain Connectivity Laboratory (C.H.T., C.-P.L.), Institute of Neuroscience, National Yang-Ming University, Taipei, Taiwan.

This work was partly supported by grants from the National Science Council Taiwan (NSC-102-2314-B-182-055 to C.H.T.).

Please address correspondence to Cheng Hong Toh, MD, Department of Medical Imaging and Intervention, Chang Gung Memorial Hospital, Linkou and Chang Gung University College of Medicine, No. 5, Fuxing St, Guishan Township, Taoyuan County 333, Taiwan; e-mail: eldomtoh@hotmail.com

Indicates open access to non-subscribers at www.ajnr.org

<http://dx.doi.org/10.3174/ajnr.A3651>

anisotropy (FA) and ADC are quantitative metrics derived from DTI for water diffusivity measurement.⁵ DSC-PWI, on the other hand, measures T2*-weighted signal intensity loss that occurs dynamically over bolus injection of contrast medium, from which relative CBV, a quantitative marker of tumor angiogenesis, can be computed.⁶

Both DTI^{7,8} and DSC-PWI⁹⁻¹¹ had been reported to be useful in subtyping meningiomas. The microvessel area of meningiomas determined by histopathology was found to correlate with relative CBV derived from DSC-PWI.¹¹ In the present study, we aimed to investigate if DTI and DSC-PWI could reflect the angiographic vascularity of meningiomas. To our knowledge, the roles of DTI and DSC-PWI in assessing the angiographic vascularity of meningiomas have never been studied.

MATERIALS AND METHODS

Patients

Between 2009–2012, a total of 46 patients underwent surgery for intracranial meningiomas in our institution. A routine MR protocol including conventional MR imaging, DSC-PWI, and DTI has been used to assess all patients with intracranial mass lesions since 2009. In our institution, conventional angiography has been a routine preoperative study in patients with meningioma who do not have iodinated contrast medium allergy or renal insufficiency. Nine patients whose MR studies were performed at outside hospitals were excluded. Thirty-seven patients whose preoperative MR imaging and conventional angiography were performed in our institution were retrospectively included. Signed informed consent was obtained from all patients for imaging and surgical procedures performed. Approval for reviewing the patient clinical data, findings of preoperative MR imaging studies, and catheter cerebral angiography was obtained from the institutional review board. Images with motion artifacts from 2 patients were excluded. Three patients with purely calcified tumors as seen on SWI or noncontrast CT images were excluded. Therefore, a total of 32 patients (17 men, 15 women; mean age, 54.5 years; age range, 24–80 years) with meningioma (mean size, 5.3 ± 1.5 cm; range, 2–8 cm) were analyzed. Histologic diagnosis was obtained in all patients by surgical resection. The histologic subtypes included 11 meningothelial, 8 transitional, 4 fibroblastic, 2 psammomatous, 3 microcystic, 2 atypical, and 2 anaplastic meningiomas. None of the patients had begun corticosteroid treatment, radiation therapy, or chemotherapy or had any previous brain biopsy at the time of MR imaging. Patients with estimated glomerular filtration rate <60 mg/min per 1.72 m^2 were excluded before enrollment.

MR Imaging

All MR studies were performed by use of a 3T unit (Magnetom Tim Trio; Siemens, Erlangen, Germany) with a 12-channel phased-array head coil. The conventional MR pulse sequences included transverse T1WI, transverse T2WI, and transverse FLAIR. DTI was performed in the axial plane by use of single-shot EPI with the following parameters: TR ms/TE ms, 5800/83; diffusion gradient encoding in 20 directions; $b = 0$, 1000 seconds/ mm^2 ; FOV, 256×256 mm; matrix size, 128×128 ; section thickness, 2 mm; and number of signals acquired, 4. A total of 50–60

sections without intersection gap were used to cover the cerebral hemispheres, upper brain stem, and cerebellum. Generalized autocalibrating partially parallel acquisitions (reduction factor = 2) were used during DTI acquisitions.

The DSC-PWI was obtained with a T2*-weighted gradient-echo EPI sequence during the bolus injection of a standard dose (0.1 mmol/kg) of intravenous gadopentetate dimeglumine (Magnevist; Schering, Berlin, Germany). The injection rate was 4 mL/s for all patients and was immediately followed by a bolus injection of saline (total of 20 mL at the same rate). DSC-PWI sequence parameters included the following: TR/TE, 1640/40 ms; flip angle, 90°; FOV, 230×230 mm; section thickness, 4 mm; 20 sections; and acquisition time of 1 minute, 28 seconds. Fifty measurements were acquired, allowing acquisition of at least 5 measurements before bolus arrival. No contrast agent was administered before DSC-PWI. Postcontrast magnetization-prepared rapid acquisition gradient echo (TR/TE, 2000/2.63 ms; section thickness, 1 mm; TI, 900 ms; acquisition matrix, 224×256 ; and FOV, 224×256 mm) sequences were acquired after completion of the PWI sequence.

Conventional angiography was performed by interventional neuroradiologists through the femoral approach. Biplanar intra-arterial DSA was performed by selective catheterization of bilateral internal and external carotid arteries as well as bilateral vertebral arteries. Images were obtained with a 1024×1024 matrix and a 17-cm FOV. The temporal resolution of the images was 3 frames per second. A bolus of 5–9 mL of undiluted iodinated contrast material was injected for each projection by use of a power injector.

Image Postprocessing

The perfusion and diffusion-tensor data were transferred to an independent workstation and processed by use of the software nordicICE (Version 2, NordicNeuroLab, Bergen, Norway). The diffusion-weighted images were co-registered to the non-diffusion-weighted ($b = 0$) images to minimize the artifacts induced by eddy-current and subject motion. FA and ADC were calculated from diffusion-tensor data by use of standard algorithms described previously.^{5,12,13}

The CBV for each voxel was estimated by integrating the relaxation-time curve converted from the dynamic signal intensity curve. Contrast leakage correction was performed by use of a technique outlined by Boxerman et al.^{14,15}

Image Analysis

Two independent interventional neuroradiologists blinded to the DTI and DSC-PWI findings assessed the tumor vascularity by evaluating the entire series of angiographic images. On the basis of the attenuation of tumor stain, the degree of angiographic vascularity of meningioma is graded as the following: 0 indicated none; 1, minimal; 2, moderate; and 3, marked (Fig 1). For meningiomas with grade 0 or 1 vascularity, preoperative embolization or even diagnostic conventional angiography is considered not to be necessary. Meningiomas with grade 2 or 3 vascularity were candidates for embolization, provided that their feeders derived from the external carotid artery or dural branches that were safe to be embolized. Interobserver differences were resolved by consensus.

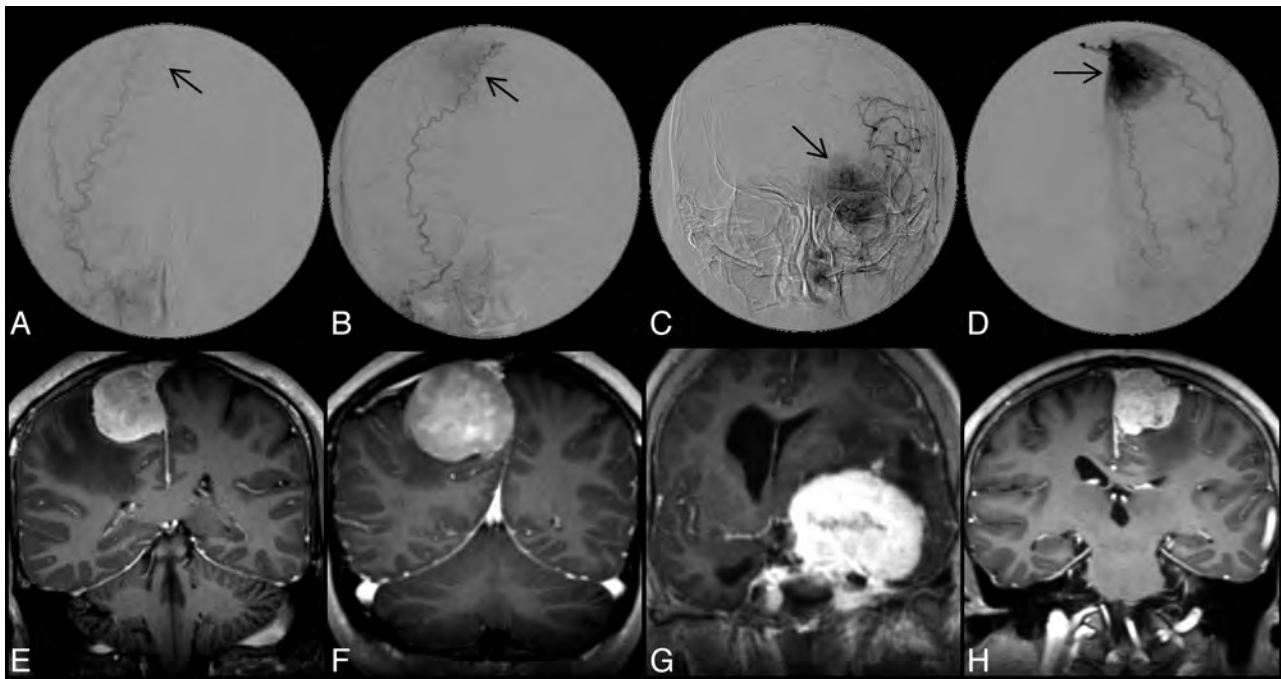


FIG 1. Upper panel shows DSA images of 4 different meningiomas, demonstrating grade 0 (A), 1 (B), 2 (C), and 3 (D) angiographic vascularity, respectively. Arrows indicate locations of meningiomas; lower panel shows the corresponding postcontrast MPRAGE images in coronal view.

A diagnostic neuroradiologist blinded to the angiographic results measured the size, ADC, FA, and CBV of the meningiomas. For tumor size, the largest diameter of the contrast-enhancing lesion on axial postcontrast MPRAGE was measured. Before all quantitative measurements, the ADC, FA, and CBV maps were coregistered to postcontrast MPRAGE on the basis of 3D nonrigid transformation and mutual information with the use of Statistical Parametric Mapping 2 (SPM2; Wellcome Department of Imaging Neuroscience, London, United Kingdom).

On the basis of postcontrast MPRAGE, a polygonal ROI was first drawn to include the entire enhancing lesion on every section. A threshold pixel value was then manually chosen to create a volumetric ROI to segment the entire enhancing tumor. The mean ADC, FA, and CBV of the whole tumor were subsequently measured with the tumor ROI. All ROIs did not include areas of necrosis or nontumor macrovessels evident on postcontrast MPRAGE. Examples of 2 meningiomas with grade 1 and grade 3 vascularity, respectively, are shown in Fig 2.

The ADC, FA, and CBV were normalized and expressed as ratios to contralateral normal-appearing white matter before all quantitative comparisons. The ratios were calculated by dividing the mean values of whole tumor by the values obtained from a region of interest (size range, 30–50 mm²) placed in the contralateral normal-appearing white matter.

Statistical Analysis

The level of interobserver agreement for angiographic vascularity was determined by calculating the κ coefficient. The correlations between angiographic vascularity of meningiomas on the basis of consensus readings and the clinical or imaging variables—age and sex of patient, as well as size, CBV, FA, and ADC of meningiomas—were analyzed with the Spearman rank correlation coefficient.

The degree of angiographic tumor vascularity was further dichotomized into low-vascularity (grade 0 and 1) and high-vascularity (grade 2 and 3) groups. Between the 2 groups, the size, ADC, FA, and CBV of meningiomas, as well as the patient age, were compared by means of a 2-sample *t* test. The difference in sex was analyzed with χ^2 analysis. The diagnostic performance of clinical and imaging variables with statistical significance was further determined by receiver operating characteristic (ROC) curve analysis. A commercially available statistical software package (SPSS 16; IBM, Armonk, New York) was used for analysis, and *P* values <.05 were considered to indicate a statistically significant difference.

RESULTS

Interobserver agreement was excellent ($\kappa = 0.824$; $P < .001$) for degree of angiographic vascularity. The angiographic vascularity on consensus readings was grade 0 in 4, grade 1 in 6, grade 2 in 8, and grade 3 in 14 meningiomas. Angiographic vascularity correlated positively with CBV (Spearman $\rho = 0.891$; $P < .001$; Fig 3A) but negatively with FA (Spearman $\rho = -0.861$; $P < .001$; Fig 3B). There was no correlation between angiographic vascularity and the patient sex (Spearman $\rho = 0.151$; $P = .410$), tumor size (Spearman $\rho = -0.186$; $P = .307$), or ADC (Spearman $\rho = 0.287$; $P = .111$; Fig 3C).

The clinical and imaging data of the meningiomas are summarized in Table 1. There were 10 patients with low-vascularity meningiomas (grade 0 and 1) and 22 with high vascularity (grades 2 and 3). There were no significant differences in the sex, age, and tumor size between the 2 groups. The high-vascularity meningiomas demonstrated significantly higher CBV (Fig 4A) but lower FA (Fig 4B) as compared with low-vascularity meningiomas. The 2 groups showed no difference in their ADC values (Fig 4C). In differentiating between low- and high-vascularity meningiomas, the sensitivity and specificity were 90.9% and 100%, respectively,

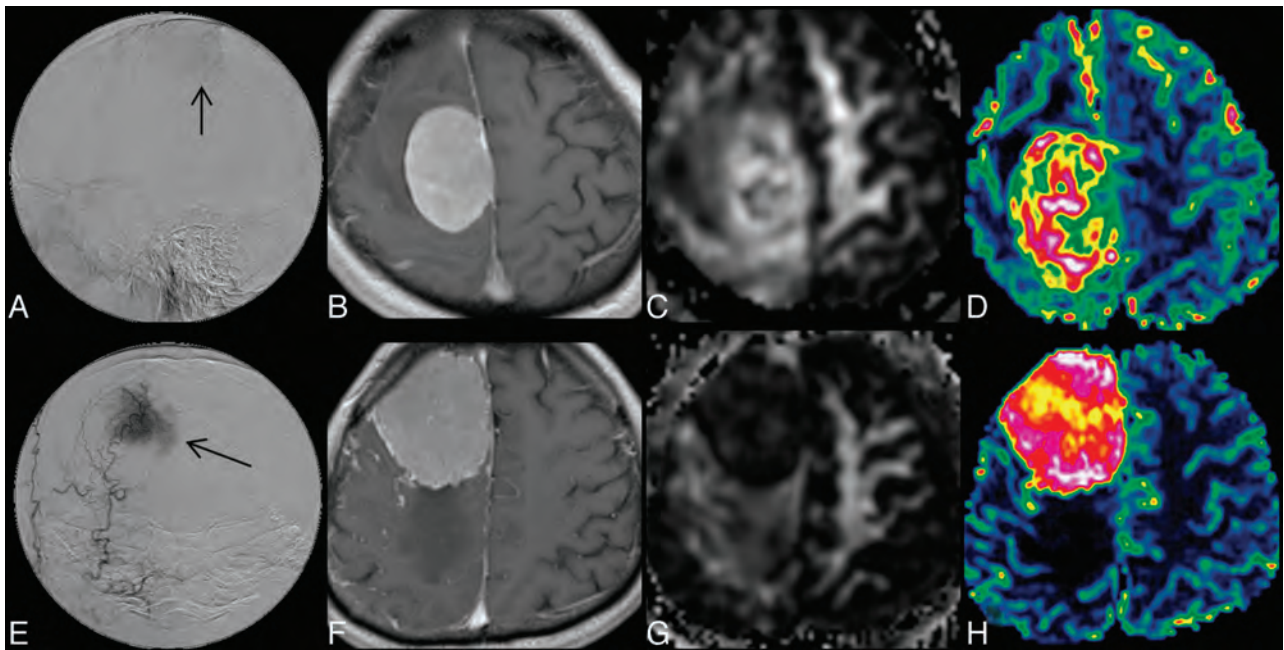


FIG 2. Upper panel shows DSA (A), contrast-enhanced MPRAGE (B), FA (C), and CBV (D) images of a meningioma with grade 1 angiographic vascularity; lower panel (E–H) shows the corresponding images from a meningioma with grade 3 angiographic vascularity.

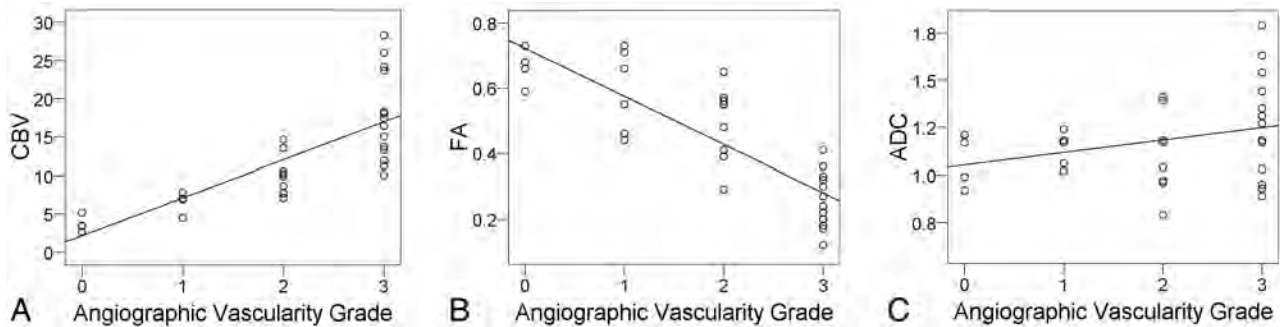


FIG 3. Scatterplots with regression lines show a correlation (Spearman $\rho = 0.891$) between CBV and angiographic vascularity (A) and an inverse correlation (Spearman $\rho = -0.861$) between FA and angiographic vascularity (B). There is no correlation between ADC and angiographic vascularity.

Table 1: Comparison of clinical and imaging data between low-vascularity and high-vascularity meningiomas

Group	Low-Vascularity Meningioma	High-Vascularity Meningioma	P Value	95% CI
Sex	6 women, 4 men	9 women, 13 men	.450	NA
Age, y	49.7 ± 16.7	56.7 ± 14.5	.237	−18.91 to 4.86
Size, cm	5.45 ± 1.69	5.27 ± 1.57	.781	−1.08 to 1.42
CBV	5.06 ± 2.05	13.97 ± 5.67	<.001	−12.71 to −5.10
ADC	1.114 ± 0.107	1.213 ± 0.258	.253	−0.27 to 0.07
FA	0.621 ± 0.106	0.339 ± 0.147	<.001	0.17 to 0.38

Note:—Data are mean ± standard deviation. Units are $\times 10^{-3}$ mm²/s for ADC values.

for CBV and were 100% and 77%, respectively, for FA. When combining CBV and FA, the sensitivity and specificity were 95.2% and 100%, respectively. The results of ROC analysis are summarized in Table 2 and illustrated in Fig 5.

DISCUSSION

Our study showed that angiographic vascularity of meningiomas correlated with tumoral CBV and FA. Low-vascularity meningiomas demonstrated significantly lower CBV but higher FA when

compared with high-vascularity meningiomas. Our results suggest that CBV and FA of meningiomas could reflect angiographic vascularity of the tumors.

Preoperative angiography evaluation and embolization of meningiomas is currently performed in some institutions, even though its value has not been established by randomized trials.^{16–18} Two very recent studies reported that patients may benefit from preoperative meningioma embolization. Shah et al¹⁷ reviewed 36 studies comprising 459 patients published between 1990–2011; they concluded that embolization may reduce rates of surgical morbidity and mortality in the management of meningiomas. In another study, Borg et al¹⁸ reported that complete devascularization resulted in lower blood transfusion requirements in their 107 patients with meningioma operated on between 2001–2010.¹⁸ We found that DSC-PWI and DTI could provide quantitative information about angiographic vascularity in a noninvasive way. Angiographic vascularity, which visualized as tumor stain, aids tumor localization during angiographic procedures and frequently serves as a reference of the degree of devascular-

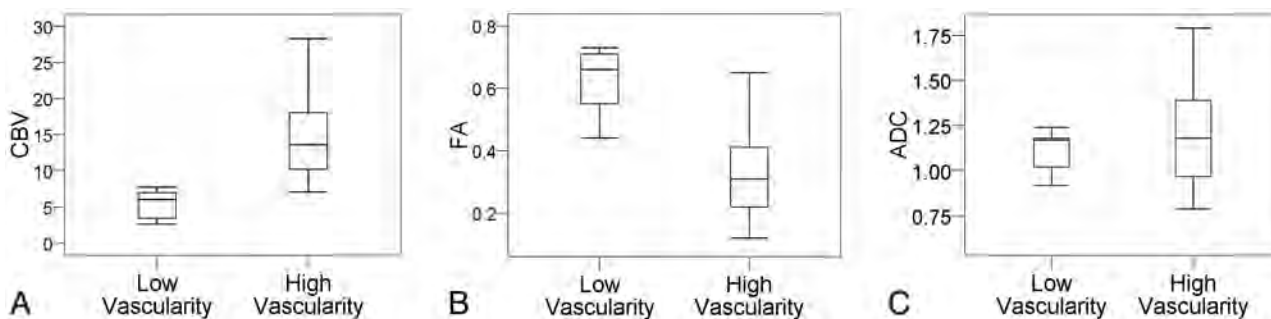


FIG 4. Boxplots of CBV (A), FA (B), and ADC (C) according to angiographic vascularity.

Table 2: ROC analysis of CBV and FA in differentiating meningiomas with high vascularity from those with low vascularity

Parameter	AUC	95% CI	P Value	CV	SEN	SPE
CBV	0.991	0.967–1.015	<.001	8.21	90.9	100
FA	0.934	0.852–1.016	<.001	0.425	100	77

Note:—CV indicates cutoff value; SEN, sensitivity; SPE, specificity. Data of sensitivity, specificity, and accuracy are in percentages.

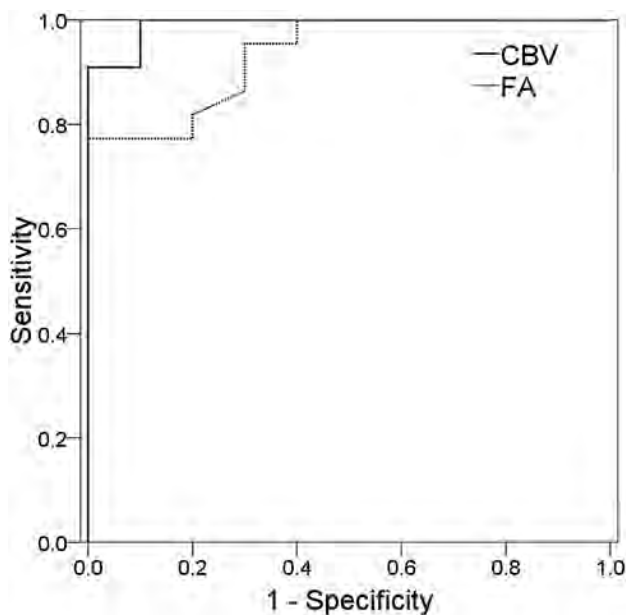


FIG 5. ROC curve analysis of the diagnostic performance of CBV and FA in differentiating between low-vascularity and high-vascularity meningiomas.

ization. Therefore, findings in our study may be helpful to institutions in which preoperative conventional angiography evaluation and embolization of meningiomas is practiced.

In the present study, all meningiomas demonstrated increased CBV, a finding similar to what has been reported in the literature.¹⁰ However, not all meningiomas with increased CBV demonstrated tumor stain visible on conventional angiography. Rather, angiographic vascularity was absent in (grade 0) 12.5% of meningiomas and only slightly increased (grade 1) in 18.8% of cases. If a meningioma is identified to be low or absent of angiographic vascularity by DSC-PWI or DTI, embolization or even conventional angiography may not be needed because tumor feeders are frequently absent or difficult to identify. In contrast, if a meningioma is found to have high angiographic vascularity by

DSC-PWI or DTI, tumor embolization may be planned, and its associated risk and benefit can be discussed in advance with the patient.

CBV has been shown to be a surrogate marker of angiogenesis in gliomas. It has been found to correlate with microvascular proliferation^{19–22} and vascular endothelial growth factor expression, a major regulator of tumor angiogenesis.²³ In meningiomas, both angiographic vascularity²⁴ and CBV²⁵ correlated with vascular endothelial growth factor expression. Therefore, it is not surprising when there is a positive correlation between CBV and angiographic vascularity in meningiomas, as demonstrated in the present study. To our knowledge, such correlation has not been reported in meningiomas, though it was observed in gliomas.²⁶

The inverse correlation between FA and angiographic vascularity, as demonstrated in the present study, had allowed the use of FA to differentiate meningiomas of different angiographic vascularity, with diagnostic performance close to that of DSC-PWI. Therefore, DTI may serve as an alternative to DSC-PWI when administration of gadolinium-based contrast medium is a contraindication in patients who are subject to development of nephrogenic systemic fibrosis caused by low glomerular filtration rate. Previous studies investigated the roles of ADC and FA in subtyping meningiomas, but the results were controversial.^{7,8,27} In the present study, we found that angiographic vascularity of meningiomas correlated with FA but not with ADC. Whereas ADC measures the average changes of water diffusivity, FA quantifies the diffusion anisotropy. High FA indicates coherent diffusion, whereas low FA suggests disorganized or incoherent diffusion. The inverse correlation between FA and angiographic vascularity suggested that water diffusion in meningiomas became more disorganized as the angiographic vascularity increased.

It has been proposed that both pure diffusion of water molecules and microcirculation of the blood in the capillary network (perfusion-related diffusion) contribute to the signal decay observed on the source image of DTI.²⁸ The perfusion-related diffusion can be considered as an incoherent motion caused by random capillary organization, and its contribution to the ADC measurement can be assessed by use of an intravoxel incoherent motion model.^{29,30} However, to our knowledge, there is no well-established model to evaluate the effect of perfusion on diffusion anisotropy. We speculate that higher perfusion resulted in greater incoherent motion and subsequently lower FA in meningiomas with high angiographic vascularity. On the other hand, the contribution of perfusion to the ADC measurement was limited at b values >100 seconds/mm².²⁹ This, perhaps, may explain the ab-

sence of correlation between angiographic vascularity and ADC obtained with a b value of 1000 seconds/mm² in the present study.

The purpose of preoperative evaluation with conventional angiography is to obtain information such as the degree of angiographic vascularity and the origin of arterial feeders of meningiomas. It has been reported that the information about vascular supply of meningiomas could be obtained with arterial spin-labeling, regional perfusion imaging, and MRA.^{3,4} Our results show that CBV and FA may complement arterial spin-labeling, regional perfusion imaging, and MRA by providing information about the degree of angiographic vascularity and may enhance the role of MR imaging in the preoperative assessment of meningiomas. Although the presence intratumoral vessels seen as flow voids on T2WI or enhancing vascular structures on postcontrast T1WI as well as the intensity of contrast enhancement may help to assess the vascularity of meningiomas, these imaging features cannot predict the angiographic vascularity of the tumor in a quantitative manner. In contrast, we have successfully demonstrated that CBV and FA could serve as quantitative markers to assess angiographic vascularity of meningiomas.

There are some limitations in the present study. First, there is no objective measurement of the degree of angiographic vascularity. Although the 4-point grading scale used in this study may be inherently subjective, it appears to be an optimal method, on the basis of its high interobserver agreement. Second, we did not have histologic findings to support the correlations between angiographic vascularity and FA or CBV. However, it is not a caveat to our study because we aimed to investigate the relationship between findings from different imaging modalities, for example, conventional angiography and MR imaging, and not between imaging findings and the pathologic changes. Although CBV and FA can predict angiographic vascularity of meningiomas, they cannot identify meningiomas with high angiographic vascularity but without accessible feeding arteries or meningiomas with a large arterial supply but with low angiographic vascularity. However, this limitation may be overcome in future studies if arterial spin-labeling, regional perfusion imaging and MRA are included in the MR protocol.

CONCLUSIONS

CBV and FA correlate well with angiographic vascularity of meningiomas. They may serve as noninvasive, quantitative tools to assess angiographic vascularity of meningiomas.

ACKNOWLEDGMENTS

The authors acknowledge support from Molecular Imaging Center, Chang Gung Memorial Hospital, Linkou, Taiwan.

Disclosures: Cheng Hong Toh—RELATED: Grant: National Science Council, Taiwan* (*money paid to institution).

REFERENCES

1. Wiemels J, Wrensch M, Claus EB. **Epidemiology and etiology of meningioma.** *J Neurooncol* 2010;99:307–14
2. Willinsky RA, Taylor SM, TerBrugge K, et al. **Neurologic complications of cerebral angiography: prospective analysis of 2,899 procedures and review of the literature.** *Radiology* 2003;227:522–28
3. Sasao A, Hirai T, Nishimura S, et al. **Assessment of vascular supply of hypervascular extra-axial brain tumors with 3T MR regional perfusion imaging.** *AJNR Am J Neuroradiol* 2010;31:554–58
4. Uetani H, Akter M, Hirai T, et al. **Can 3T MR angiography replace DSA for the identification of arteries feeding intracranial meningiomas?** *AJNR Am J Neuroradiol* 2013;34:765–72
5. Mukherjee P, Berman JI, Chung SW, et al. **Diffusion tensor MR imaging and fiber tractography: theoretic underpinnings.** *AJNR Am J Neuroradiol* 2008;29:632–41
6. Zaharchuk G. **Theoretical basis of hemodynamic MR imaging techniques to measure cerebral blood volume, cerebral blood flow, and permeability.** *AJNR Am J Neuroradiol* 2007;28:1850–58
7. Toh CH, Castillo M, Wong AM, et al. **Differentiation between classic and atypical meningiomas with use of diffusion tensor imaging.** *AJNR Am J Neuroradiol* 2008;29:1630–35
8. Wang S, Kim S, Zhang Y, et al. **Determination of grade and subtype of meningiomas by using histogram analysis of diffusion-tensor imaging metrics.** *Radiology* 2012;262:584–92
9. Zhang H, Rodiger LA, Shen T, et al. **Preoperative subtyping of meningiomas by perfusion MR imaging.** *Neuroradiology* 2008; 50:835–40
10. Zhang H, Rodiger LA, Shen T, et al. **Perfusion MR imaging for differentiation of benign and malignant meningiomas.** *Neuroradiology* 2008;50:525–30
11. Kimura H, Takeuchi H, Koshimoto Y, et al. **Perfusion imaging of meningioma by using continuous arterial spin-labeling: comparison with dynamic susceptibility-weighted contrast-enhanced MR images and histopathologic features.** *AJNR Am J Neuroradiol* 2006;27:85–93
12. Toh CH, Wei KC, Ng SH, et al. **Differentiation of brain abscesses from necrotic glioblastomas and cystic metastatic brain tumors with diffusion tensor imaging.** *AJNR Am J Neuroradiol* 2011;32:1646–51
13. Toh CH, Wei KC, Ng SH, et al. **Differentiation of tumefactive demyelinating lesions from high-grade gliomas with the use of diffusion tensor imaging.** *AJNR Am J Neuroradiol* 2012;33:846–51
14. Boxerman JL, Schmainda KM, Weisskoff RM. **Relative cerebral blood volume maps corrected for contrast agent extravasation significantly correlate with glioma tumor grade, whereas uncorrected maps do not.** *AJNR Am J Neuroradiol* 2006;27:859–67
15. Toh CH, Wei KC, Chang CN, et al. **Differentiation of primary central nervous system lymphomas and glioblastomas: comparisons of diagnostic performance of dynamic susceptibility contrast-enhanced perfusion MR imaging without and with contrast-leakage correction.** *AJNR Am J Neuroradiol* 2013;34:1145–49
16. Sluzewski M, van Rooij WJ, Lohle PN, et al. **Embolization of meningiomas: comparison of safety between calibrated microspheres and polyvinyl-alcohol particles as embolic agents.** *AJNR Am J Neuroradiol* 2013;34:727–29
17. Shah AH, Patel N, Raper DM, et al. **The role of preoperative embolization for intracranial meningiomas.** *J Neurosurg* 2013;119:364–72
18. Borg A, Ekanayake J, Mair R, et al. **Preoperative particle and glue embolization of meningiomas: indications, results and lessons learned from 117 consecutive patients.** *Neurosurgery* 2013 Feb 25 [Epub ahead of print]
19. Hu LS, Eschbacher JM, Dueck AC, et al. **Correlations between perfusion MR imaging cerebral blood volume, microvessel quantification, and clinical outcome using stereotactic analysis in recurrent high-grade glioma.** *AJNR Am J Neuroradiol* 2012;33:69–76
20. Liao W, Liu Y, Wang X, et al. **Differentiation of primary central nervous system lymphoma and high-grade glioma with dynamic susceptibility contrast-enhanced perfusion magnetic resonance imaging.** *Acta Radiol* 2009;50:217–25
21. Sadeghi N, D'Haene N, Decaestecker C, et al. **Apparent diffusion coefficient and cerebral blood volume in brain gliomas: relation to tumor cell density and tumor microvessel density based on stereotactic biopsies.** *AJNR Am J Neuroradiol* 2008;29:476–82

22. Barajas RF Jr, Phillips JJ, Parvataneni R, et al. **Regional variation in histopathologic features of tumor specimens from treatment-naïve glioblastoma correlates with anatomic and physiologic MR imaging.** *Neuro Oncol* 2012;14:942–54
23. Maia AC Jr, Malheiros SM, da Rocha AJ, et al. **MR cerebral blood volume maps correlated with vascular endothelial growth factor expression and tumor grade in nonenhancing gliomas.** *AJNR Am J Neuroradiol* 2005;26:777–83
24. Bitzer M, Opitz H, Popp J, et al. **Angiogenesis and brain oedema in intracranial meningiomas: influence of vascular endothelial growth factor.** *Acta Neurochir (Wien)* 1998;140:333–40
25. Ginat DT, Mangla R, Yeane G, et al. **Correlation between dynamic contrast-enhanced perfusion MRI relative cerebral blood volume and vascular endothelial growth factor expression in meningiomas.** *Acad Radiol* 2012;19:986–90
26. Sugahara T, Korogi Y, Kochi M, et al. **Correlation of MR imaging-determined cerebral blood volume maps with histologic and angiographic determination of vascularity of gliomas.** *AJR Am J Roentgenol* 1998;171:1479–86
27. Tropine A, Dellani PD, Glaser M, et al. **Differentiation of fibroblastic meningiomas from other benign subtypes using diffusion tensor imaging.** *J Magn Reson Imaging* 2007;25:703–08
28. Le Bihan D, Breton E, Lallemand D, et al. **MR imaging of intravoxel incoherent motions: application to diffusion and perfusion in neurologic disorders.** *Radiology* 1986;161:401–07
29. Koh DM, Collins DJ, Orton MR. **Intravoxel incoherent motion in body diffusion-weighted MRI: reality and challenges.** *AJR Am J Roentgenol* 2011;196:1351–61
30. Chavarria L, Alonso J, Garcia-Martinez R, et al. **Biexponential analysis of diffusion-tensor imaging of the brain in patients with cirrhosis before and after liver transplantation.** *AJNR Am J Neuroradiol* 2011;32:1510–17

Utility of Proton MR Spectroscopy for Differentiating Typical and Atypical Primary Central Nervous System Lymphomas from Tumefactive Demyelinating Lesions

S.-S. Lu, S.J. Kim, H.S. Kim, C.G. Choi, Y.-M. Lim, E.J. Kim, D.Y. Kim, and S.H. Cho



ABSTRACT

BACKGROUND AND PURPOSE: It may be challenging to differentiate primary CNS lymphomas, especially primary CNS lymphomas with atypical MR features, from tumefactive demyelinating lesions by the use of conventional MR. This study aimed to investigate the usefulness of ¹H-MR spectroscopy for making this discrimination.

MATERIALS AND METHODS: Forty-four patients with primary CNS lymphomas and 21 with tumefactive demyelinating lesions were enrolled. Single-voxel (TE = 144 ms) ¹H-MR spectroscopy scans with the use of the point-resolved spectroscopy sequence were retrospectively analyzed. The Cho/Cr and Cho/NAA area ratios were calculated. The lipid and/or lactate peak was visually categorized into 5 grades on the basis of comparison with the height of the Cr peak. The ¹H-MR spectroscopy findings were compared in all of the primary CNS lymphomas and the tumefactive demyelinating lesions and in the subgroup of atypical primary CNS lymphomas and tumefactive demyelinating lesions. The thresholds and added value of ¹H-MR spectroscopy to conventional MR were calculated by use of receiver operating characteristic curves.

RESULTS: Discrepancies between all of the primary CNS lymphomas and tumefactive demyelinating lesions were found in the Cho/Cr ratio ($P = .000$), Cho/NAA ratio ($P = .000$), and the lipid and/or lactate peak grade ($P = .000$). Lymphoma rather than tumefactive demyelinating lesions was suggested when the Cho/Cr ratio was >2.58 , the Cho/NAA ratio was >1.73 , and a high lipid and/or lactate peak grade (grade >3) was seen. Higher Cho/Cr ratios, Cho/NAA ratios, and lipid and/or lactate peak grades were found in atypical primary CNS lymphomas when compared with those of tumefactive demyelinating lesions. The area under the receiver operating characteristic curve of conventional MR was improved from 0.827 to 0.870 when Cho/NAA ratio was added in the uncertain cases.

CONCLUSIONS: ¹H-MR spectroscopy may be useful for differentiating primary CNS lymphomas from tumefactive demyelinating lesions. Cho/NAA ratio could provide added value to conventional MR imaging.

ABBREVIATIONS: PCNSL = primary central nervous system lymphoma; TDL = tumefactive demyelinating lesion; lip-lac = lipid and/or lactate peak; ROC = receiver operating characteristic; AUC = area under the receiver operating characteristic curve

Primary central nervous system lymphomas (PCNSLs) are aggressive tumors that represent approximately 1–6% of primary intracranial neoplasms.¹ Their incidence has been increasing during the past 2 decades not only in immunocompromised patients but also in immunocompetent patients.^{2,3} Typical MR

imaging features of PCNSLs are characterized by their periventricular locations, well-defined margin, moderate or marked edema, and intense and homogeneous nodular enhancement and are usually easy to correctly diagnose.^{4–6} However, some patients present with atypical MR imaging features, commonly those of heterogeneous enhancement, such as patchy enhancement, streaky enhancement without mass formation, or even no enhancement.^{6–9}

Demyelinating diseases of the CNS are pathologic entities that are frequently encountered in clinical practice. When such lesions appear as solitary masses >2 cm in the longest diameter, they are defined as tumefactive demyelinating lesions (TDLs), and they can cause symptoms mimicking brain neoplasms and can be associated with variable enhancement on MR imaging.¹⁰ Differentiation between PCNSLs and TDLs by use of conventional MR can sometimes be challenging, especially when there are atypical MR

Received February 7, 2013; accepted after revision April 29.

From the Department of Radiology and Research Institute of Radiology (S.-S.L., S.J.K., H.S.K., C.G.C., D.Y.K., S.H.C.), and Department of Neurology (Y.-M.L.), University of Ulsan College of Medicine, Asan Medical Center, Seoul, Korea; Department of Radiology (S.-S.L.), The First Affiliated Hospital of Nanjing Medical University, Nanjing, Jiangsu Province, China; and Philips Healthcare (E.J.K.), Seoul, Korea.

Please address correspondence to Sang Joon Kim, MD, PhD, Department of Radiology and Research Institute of Radiology, University of Ulsan College of Medicine, Asan Medical Center, 88 Olympic-ro 43-gil, Songpa-Gu, Seoul 138-736, Korea; e-mail: sjkimjb@amc.seoul.kr

<http://dx.doi.org/10.3174/ajnr.A3677>

imaging features in PCNSLs. Considering the rapid progress of PCNSLs, early differentiation is important because both the treatment effectiveness and the patient survival rate will substantially decrease if there is delayed radiation therapy and/or chemotherapy.⁷ Accurate differentiation is also important to avoid unnecessary biopsies of TDLs.

¹H-MR spectroscopy can provide noninvasive biochemical information regarding *in vivo* tissue. Some authors have suggested that ¹H-MR spectroscopy is helpful for discriminating tumors and pseudotumors,^{11,12} whereas others argue that it may not be so, because there is some overlap of the metabolites.^{13,14} There are many published ¹H-MR spectroscopy studies of PCNSLs as well as TDLs^{3,10,15,16}; however, to our knowledge, there is still no ¹H-MR spectroscopy study that distinguishes PCNSLs from TDLs. Our current study attempts to investigate the potential clinical utility of ¹H-MR spectroscopy for differentiating PCNSLs from TDLs and further focuses on evaluating whether ¹H-MR spectroscopy is also helpful for discriminating PCNSLs with atypical MR imaging features from TDLs.

MATERIALS AND METHODS

This retrospective study was approved by our institutional review board, and the requirement for informed consent was waived.

Study Subjects

Sixty-nine patients with PCNSL and 35 patients with TDL, all of whom had undergone conventional MR imaging and ¹H-MR spectroscopy between June 2006 and May 2012, were selected from our institution data base. The inclusion criteria were as follows: 1) histologically proven PCNSLs by stereotactic biopsy or surgical resection; 2) histologically proven or clinically diagnosed TDLs; with 3) ¹H-MR spectroscopy on intermediate TE (144 ms) and conventional MR including T1WI, T2WI, FLAIR, and contrast-enhanced T1WI. The clinical diagnosis of TDL was based on the following criteria: 1) acute or subacute onset of neurologic symptoms and signs; 2) at least 1 brain lesion with the longest diameter ≥ 2 cm seen on MR; 3) no evidence of systemic illness, vasculitis, toxic or metabolic disease, or CNS infection seen on extensive laboratory testing. The final diagnosis of TDL was made on the basis of histopathologic findings or a strong clinical suspicion supported by the patient's clinical course and the follow-up MR findings.

For a subgroup comparison of PCNSLs with TDLs, patients with PCNSL were further divided into 2 subgroups on the basis of enhancement patterns seen on conventional MR: 1) typical PCNSLs had nodular and homogeneous enhancement; and 2) atypical PCNSLs with various types of heterogeneous enhancement, including patchy infiltrative, streaky infiltrative, ring enhancement, or lack of enhancement.

Fourteen patients with PCNSL and 6 patients with TDL with unsatisfactory ¹H-MR spectroscopy, including noisy baseline, motion artifact, and inappropriate ROI that contained too much normal tissue, were excluded. Eight patients with PCNSL and 3 patients with TDL with only multivoxel ¹H-MR spectroscopy were excluded. Three patients with PCNSLs without pathologic confirmation and 5 patients with TDL who neither met all the

clinical diagnostic criteria nor had pathologic confirmation were also excluded.

A total of 44 patients with PCNSL (31 men, 13 women; 13–76 years of age) and 21 patients with TDL (10 women, 11 men; 22–66 years of age) were finally identified according to all of the criteria we used. Among the patients with PCNSLs, there were 24 patients with typical PCNSLs (16 men, 8 women; 13–76 years of age) and 20 patients with atypical PCNSLs (15 men, 5 women; 26–68 years of age). Forty-two patients (95.5%) with PCNSLs were confirmed as having diffuse large B-cell lymphoma, whereas the other 2 patients were confirmed as having malignant lymphoma with atypical large cells and histiocytic sarcoma. TDLs were diagnosed by brain biopsy in 6 patients (28.6%) and by clinical follow-up and repeat MR imaging in 15 patients (71.4%).

Acquisition and Analysis of Conventional MR Imaging

Conventional MR imaging was performed in all of the study patients with the use of a 3T MR system (Achieva; Philips Healthcare, Best, the Netherlands), including fast spin-echo T1WI (TR, 500 ms; TE, 10 ms; section thickness, 5 mm; FOV, 230 mm; matrix, 512 \times 512), T2WI (TR, 3000 ms; TE, 80 ms; section thickness, 5 mm; FOV, 230 mm; matrix, 512 \times 512), FLAIR (TR, 10,000 ms; TE, 125 ms; section thickness, 5 mm; inversion time, 2200 ms; FOV, 230 mm; matrix, 512 \times 512), and contrast-enhanced T1WI after intravenous injection of 0.1 mmol/kg gadoterate meglumine (Dotarem; Guerbet, Paris, France).

Two readers (D.Y.K., S.H.C.) with 9 and 5 years of experience in radiology, respectively, and blinded to the diagnosis, evaluated the conventional MR images by use of a 5-point confidence scale on the basis of lesion number, location, signal intensity, and mass effect on T1WI, T2WI, and FLAIR, as well as enhancement pattern on contrast-enhanced T1WI: grade 1: quite certainly TDL; grade 2: probably TDL; grade 3: equivocal; grade 4: probably PCNSL; grade 5: quite certainly PCNSL. Final decisions were made by consensus of the 2 readers and used for analysis.

Acquisition and Analysis of Proton MR Spectroscopy

Single-voxel ¹H-MR spectroscopy with the use of the point-resolved spectroscopy sequence was performed (TR, 2000 ms; TE, 144 ms; average 128). A volume of interest was placed on the basis of the abnormal signal intensity lesions seen on T2WI, FLAIR, and the enhancing portion of lesions seen on contrast-enhanced T1WI. The voxel size ranged from 3–8 mL. Spectrum analysis was performed with baseline correction, phase correction, and noise filtering to improve the quality of ¹H-MR spectroscopy in SpectroView software (Philips Healthcare).

The metabolites assessed were Cho at 3.22 ppm, Cr at 3.02 ppm, NAA at 2.02 ppm, lipid at 0.8 to 1.3 ppm, and lactate at 1.33 ppm. Lactate peak is identified as an inverted doublet peak at TE = 144 ms. However, the anomalous J modulation can cause signal loss for lactate, which leads to complicated assessment of the presence or absence of lactate in the voxel, particularly complicated by the presence of lipid resonances. This problem has been identified previously.^{16–18} Therefore, they were not separated in this study and were recorded as the lipid and/or lactate (lip-lac) peak.

For the analysis of ¹H-MR spectroscopy, Cho/Cr and Cho/

NAA peak area ratios were calculated. For the analysis of the lip-lac peak, the height of the lip-lac peaks was used instead of the peak area because it was not possible to accurately measure the areas. Lip-lac peaks were visually categorized into 5 grades on the basis of comparison with the height of the Cr peak by 2 readers (D.Y.K., S.H.C.): grade 1, no definite lip-lac peak; grade 2, any single peak (upward or downward) smaller than the Cr peak; grade 3, both peaks smaller than the Cr peak; grade 4, any single peak 1 to 3 times higher than the Cr peak; and grade 5, any single peak >3 times higher than the Cr peak. Final decisions were made by consensus of the 2 readers and used for analysis.

Statistical Analysis

Inter-rater agreement was measured by use of weighted κ statistics. Conventional MR imaging features and grades of PCNSLs and TDLs were compared by means of Pearson χ^2 test when appropriate or Fisher exact test. The Cho/Cr and Cho/NAA ratios were compared by use of the Student *t* test in all the PCNSLs and the TDLs. The Mann-Whitney *U* test was used to evaluate the difference of lip-lac grades between the 2 groups. Receiver operating characteristic curve (ROC) analyses were used to determine the optimum thresholds of the ratios and to evaluate their diagnostic performance for differentiating the 2 entities. The area under the receiver operating characteristic curve (AUC), sensitivity, and specificity were then calculated. The same statistical analysis was repeated in the atypical PCNSLs and TDLs groups.

The receiver operating characteristic curve was also constructed to assess the added value of ¹H-MR spectroscopy to conventional MR imaging in the differential diagnosis between PCNSLs and TDLs. The diagnostic performance of conventional MR alone was evaluated first. Afterward, we tested whether combined ¹H-MR spectroscopy and conventional MR could improve the diagnosis when the conventional imaging results were uncertain (grades 2–4).

All the statistical analyses were performed with the use of commercially available software (SPSS, version 13.0, IBM, Armonk, New York, and MedCalc, version 12.3.0, Mariakerke, Belgium). A difference of *P* < .05 was considered statistically significant.

RESULTS

Conventional MR Imaging Manifestations and Grades

On conventional MR images, a single lesion was observed in 24 PCNSLs and in 8 TDLs, whereas multiple or diffuse lesions were found in 14 and 6 patients with PCNSL and in 9 and 4 patients with TDL, respectively. No statistical difference was found between PCNSLs and TDLs (*P* = .463).

Variable enhancement patterns were observed in both PCNSLs and TDLs, including homogeneous enhancement, opening or ring enhancement, patchy infiltrative enhancement, streaky infiltrative enhancement, and no contrast enhancement. Twenty-four PCNSLs were considered as typical PCNSLs (grade 5) that were homogeneously enhanced and certainly diagnosed on the basis of conventional MR imaging, whereas the remaining 20 PCNSLs were uncertain cases. Five TDLs were evaluated as grade 1, and 16 TDLs were considered as grade 2–5. The weighted

Table 1: Conventional MR imaging features and grades of PCNSLs and TDLs

	PCNSLs (n = 44)	TDLs (n = 21)
No. of lesions	^a <i>P</i> = .463	
Single lesion	24 (54.5%)	8 (38.1%)
Multiple focal lesions	14 (31.8%)	9 (42.9%)
Diffuse lesions	6 (13.6%)	4 (19.0%)
Enhancing pattern	^a <i>P</i> = .000	
Homogeneous	24 (54.5%)	2 (9.5%)
Ring	4 (9.1%)	1 (4.8%)
Open ring	0 (0.0%)	5 (23.8%)
Patchy infiltrative	11 (25.0%)	4 (19.0%)
Streaky infiltrative	3 (6.8%)	0 (0.0%)
No enhancement	2 (4.5%)	9 (42.9%)
Conventional MR grades	^a <i>P</i> = .000	
Grade 1	0 (0.0%)	5 (23.8%)
Grade 2	5 (11.4%)	5 (23.8%)
Grade 3	7 (15.9%)	6 (28.6%)
Grade 4	8 (18.2%)	4 (19.0%)
Grade 5	24 (54.5%)	1 (4.8%)

Note:—Grade 1: quite certainly TDL; grade 2: probably TDL; grade 3: equivocal; grade 4: probably PCNSL; grade 5: quite certainly PCNSL.

^a *P* values represent the comparison results of PCNSLs and TDLs by use of Pearson χ^2 test or Fisher exact test.

κ value for inter-rater agreement was 0.602. Both enhancing patterns and conventional MR grades between PCNSLs and TDLs were significantly different (*P* = .000 and *P* = .000, respectively).

The conventional MR imaging features and grades of the PCNSLs and TDLs are summarized in Table 1.

Quantitative Analysis of ¹H-MR Spectroscopy

The diagnostic performance of the Cho/Cr ratio, Cho/NAA ratio, and lip-lac grade are summarized in Table 2.

The Cho/Cr ratio and Cho/NAA ratio were significantly different between PCNSLs and TDLs (*P* = .000 and *P* = .000, respectively). PCNSLs demonstrated higher Cho/Cr and Cho/NAA ratio than TDLs (Figs 1 and 2). The AUC of the Cho/Cr ratio and the Cho/NAA ratio was 0.849 and 0.885, respectively. The optimal cutoff values for differentiating PCNSLs from TDLs were 2.58 for the Cho/Cr ratio and 1.73 for the Cho/NAA ratio.

Higher Cho/Cr and Cho/NAA ratios were consistently found in the atypical PCNSLs compared with those of the TDLs (*P* = .003 and *P* = .001, respectively, Fig 3). The AUC of the Cho/Cr ratio and the Cho/NAA ratio was 0.785 and 0.883, respectively. The optimum threshold value was 2.39 for the Cho/Cr ratio and 1.73 for the Cho/NAA ratio. In 2 nonenhancing PCNSLs, the Cho/Cr ratios or Cho/NAA ratios were not higher than the threshold values for PCNSLs. Differences of the Cho/Cr ratio and Cho/NAA ratio among all of the PCNSLs, atypical PCNSLs, and TDLs are displayed in Fig 4.

The weighted κ value for inter-rater agreement of lip-lac grade was 0.739. Lip-lac peaks were noted in 40 of the 44 (90.9%) patients with PCNSL and in 12 of the 21 (57.1%) patients with TDL. A substantial difference in lip-lac grades was found when all of the patients were analyzed (*P* = .000). High lip-lac peaks (> grade 3) were mostly observed in PCNSLs (*n* = 21), especially in nodular enhancing PCNSLs (*n* = 14) (Fig 1), whereas only one high lip-lac peak (grade 4) was found in a TDL, which had central necrosis. Very high lip-lac peaks (grade 5) were only observed in 10 of 44

Table 2: Diagnostic performance of the Cho/Cr ratio, Cho/NAA ratio, and lip-lac grade

	P Value ^a	AUC	Cutoff Value	Sensitivity (%)	Specificity (%)
Comparison of all PCNSLs and TDLs					
Cho/Cr ratio	.000	0.849 (0.739, 0.926)	2.58	75.0 (59.7, 86.8)	81.0 (58.1, 94.4)
Cho/NAA ratio	.000	0.885 (0.782, 0.951)	1.73	88.6 (75.4, 96.2)	76.2 (52.8, 91.7)
Lip-lac grade	.000	0.801 (0.684, 0.890)	3	47.7 (32.5, 63.3)	95.2 (76.2, 99.9)
Comparison of atypical PCNSLs and TDLs					
Cho/Cr ratio	.003	0.785 (0.628, 0.897)	2.39	70.0 (45.7, 88.0)	71.4 (47.8, 88.6)
Cho/NAA ratio	.001	0.883 (0.744, 0.962)	1.73	90.0 (68.3, 98.5)	76.2 (52.8, 91.7)
Lip-lac grade	.005	0.745 (0.585, 0.868)	3	35.0 (15.4, 59.2)	95.2 (76.2, 99.9)

Note:—Numbers in parentheses are the 95% confidence intervals.

^a P values represent comparison results of PCNSLs and TDLs by use of the Student t test for the Cho/Cr ratio, the Cho/NAA ratio, and the Mann-Whitney U test for the lip-lac grade.

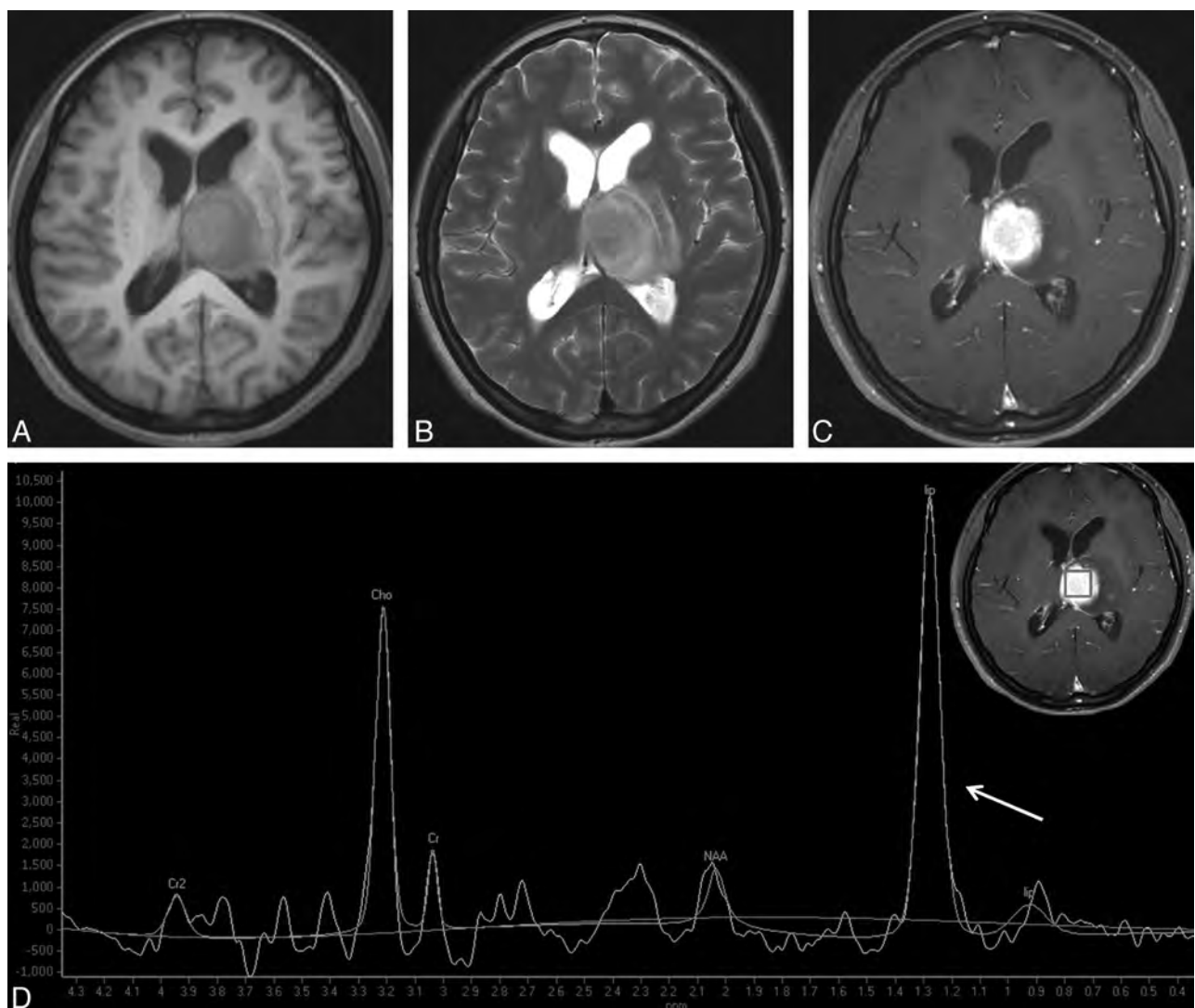


FIG 1. Typical PCNSL in a 47-year-old woman. A round mass is located in the left thalamus and with hypointensity on T1WI (A) and hyperintensity on T2WI (B). Homogeneous enhancement is observed on contrast-enhanced T1WI (C). D, ¹H-MR spectroscopy demonstrates the remarkably increased Cho peak and the decreased NAA peak, both of which give rise to a high Cho/Cr ratio (6.47) and a high Cho/NAA ratio (3.57). A very high lip-lac peak (grade 5) is shown (arrow).

(22.7%) PCNSLs, including 8 typical PCNSLs and 2 atypical PCNSLs. The lip-lac grades of atypical PCNSLs were also higher than those of TDLs ($P = .005$).

In addition, the Cho/Cr ratio of typical PCNSLs were found to be higher than those of atypical PCNSLs ($P = .018$), whereas no differences of the Cho/NAA ratio and lip-lac grade were found between the typical and atypical PCNSLs ($P = .152$ and $P = .058$, respectively).

Assessment of the Added Value of ¹H-MR Spectroscopy

The AUC for conventional MR imaging alone to differentiate PCNSLs from TDLs was 0.827 (95% CI, 0.713, 0.910).

Thirty-five cases were classified as grade 2–4 according to the conventional MR imaging, including 20 PCNSLs and 15 TDLs. When Cho/NAA ratio was added to conventional MR imaging in those cases, the diagnosis could be improved in 29 of 35 cases

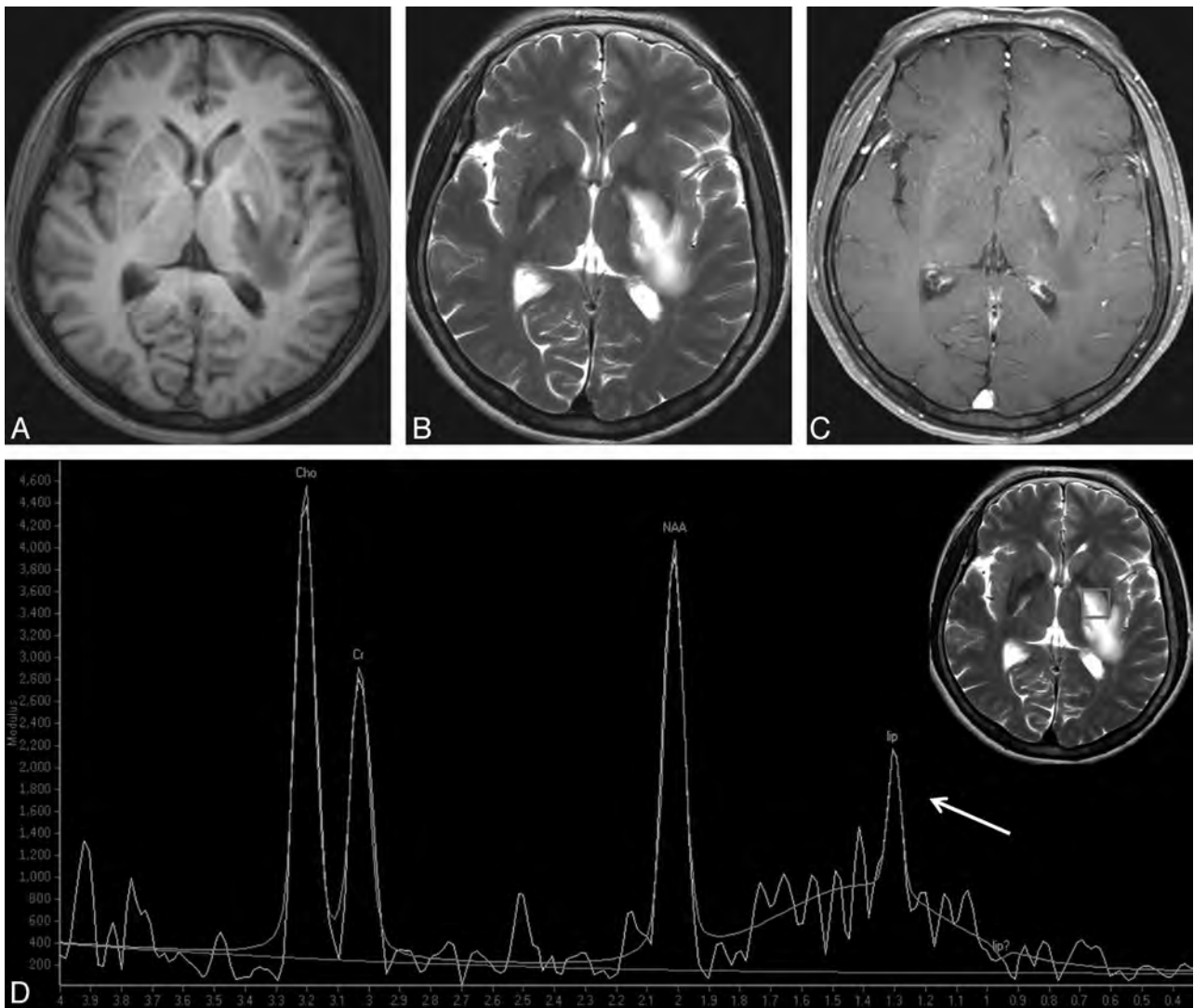


FIG 2. TDL in a 35-year-old woman. A well-defined lesion is shown in the left basal ganglia, and with predominant hypointensity on TIWI (A), hyperintensity on T2WI (B), and focal peripheral enhancement on contrast-enhanced TIWI (C). Spectrum (D) demonstrates an elevated Cho resonance. The Cho/Cr ratio is not as high as that of PCNSL (1.62). The low Cho/NAA ratio (1.09) strongly supports the diagnosis of TDL. A grade 2 lip-lac peak, caused by the necrosis component, is observed (arrow).

(82.9%), and the AUC was improved to 0.870 (95% CI, 0.713, 0.959). However, the Cho/Cr ratio and lip-lac grade did not improve the diagnostic accuracy of conventional MR imaging.

DISCUSSION

We intended to investigate whether ^1H -MR spectroscopy was useful for discriminating PCNSLs and TDLs and was also useful for discriminating PCNSLs with atypical MR features and TDLs. Our results suggest that the Cho/Cr ratio, the Cho/NAA ratio, and the lip-lac grade were significantly different between PCNSLs and TDLs. PCNSL rather than TDL was suggested when the Cho/Cr ratio was >2.58 , the Cho/NAA ratio was >1.73 , and when there was a high lip-lac grade (grade >3) seen on MR spectroscopy. ^1H -MR spectroscopy was also useful in discriminating atypical PCNSLs and TDLs. Cho/NAA ratio could provide added value to conventional MR imaging.

Discrimination between PCNSLs and TDLs has important diagnostic and therapeutic implications, and conventional MR imaging is a successful technique for evaluating both. However, dif-

ferentiation can be complicated by atypical or ambiguous MR imaging features. Many advanced imaging techniques are now used clinically in the attempt to distinguish the 2 entities. DWI has been used with success. PCNSLs tend to have a low ADC value because of high cellularity, whereas TDLs are usually associated with elevated ADC values.^{10,19} However, at times, an acute demyelinating lesion may also have areas of low ADC values, which makes it difficult to differentiate from tumors.²⁰ Cha et al^{21,22} summarized the perfusion MR imaging features of brain tumors. The typical PWI feature of PCNSL is low relative CBV compared with that of high-grade gliomas and metastasis. However, TDLs are also reported to have low relative CBV. Although in the Cha et al²³ report, PCNSLs tended to have higher relative CBV than TDLs, the difference was less pronounced.

^1H -MR spectroscopy provides noninvasive assessment of lesion metabolism, which makes it a potentially useful adjunct tool. In our study, elevated Cho and decreased NAA peak were observed in both PCNSLs and TDLs and are consistent with the

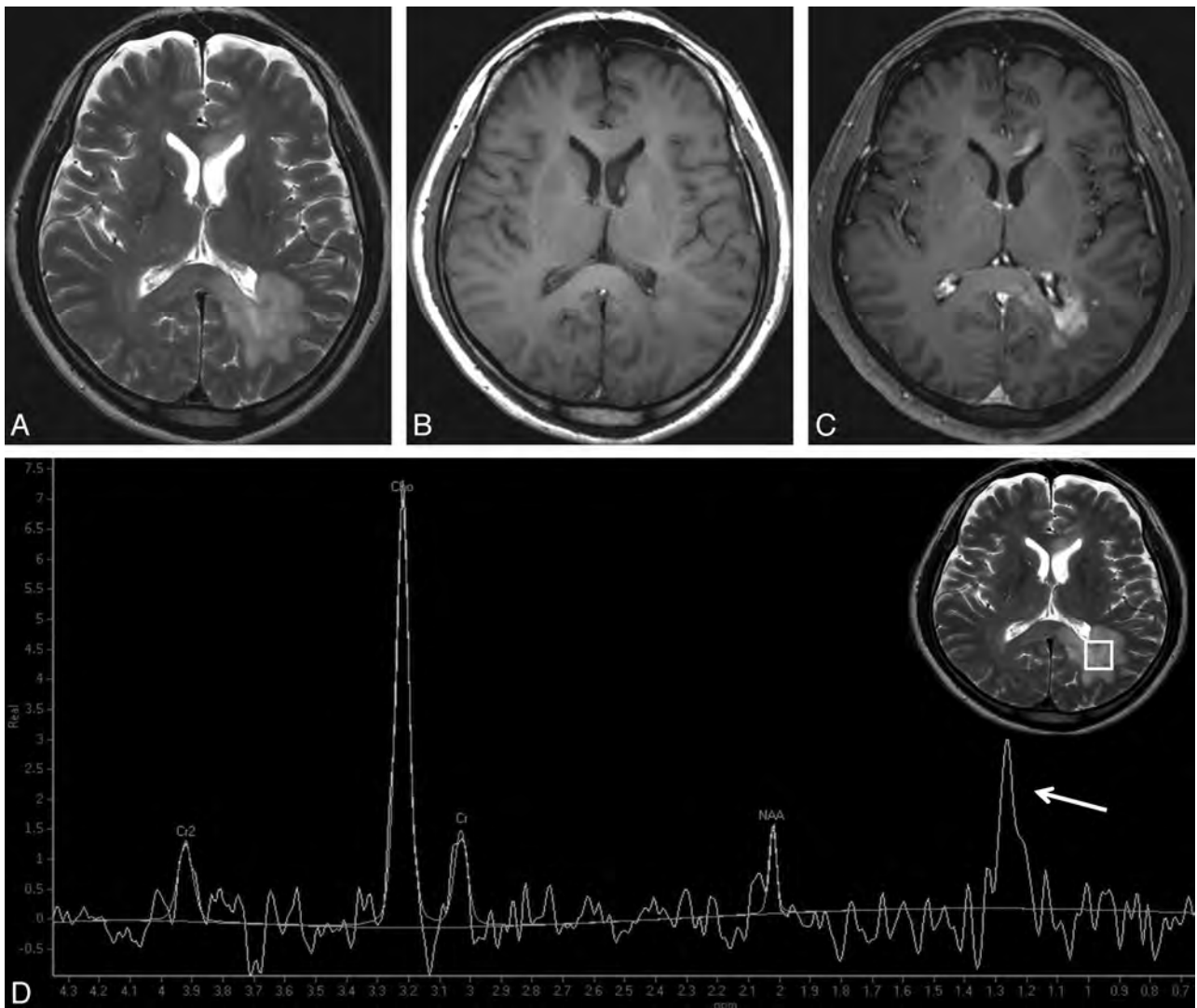


FIG 3. Atypical PCNSL in a 59-year-old man. Multiple lesions are observed in left parieto-occipital periventricular white matter, genu, and splenium of the corpus callosum, with hyperintensity on T2WI (A), isointensity on TIWI (B), and patchy infiltrative enhancement on contrast-enhanced TIWI (C). D, The Cho/Cr ratio and the Cho/NAA ratio are 4.55 and 8.46, respectively. Both obvious elevation of the Cho peak and reduction of the NAA peak strongly suggest tumor rather than TDL. A high lip-lac peak (grade 4) is observed in this case (arrow).

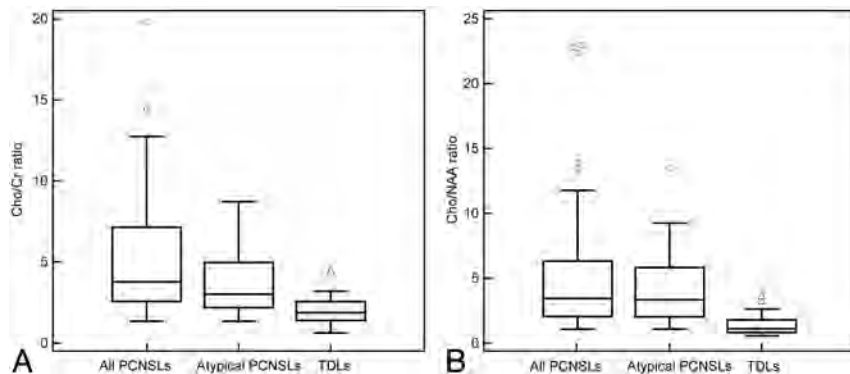


FIG 4. Box lots of the Cho/Cr ratio and the Cho/NAA ratio of all the PCNSLs, atypical PCNSLs, and TDLs. All of the PCNSLs as well as atypical PCNSLs reveal a higher Cho/Cr ratio (A) and higher Cho/NAA ratio (B) than TDLs. Some very high Cho/Cr and Cho/NAA ratios are observed exclusively in PCNSLs (circles).

findings of previous reports.^{10,15,16} The increase in Cho is thought to result from rapid membrane turnover, high mitotic activity, and dense cellularity in PCNSL and from inflammatory cellular

infiltration, reactive astrogliosis, and demyelination in TDL.^{13,16,24} The decreased NAA reflects the neuronal destruction, axonal damage, early axonal degeneration, and decreased axonal density.^{13,24} Our results suggest that an increase of Cho and a decrease of NAA in PCNSLs were more obvious than those seen in TDLs. This is probably because PCNSLs have a more increased phosphocholine turnover as the result of the membrane biosynthesis caused by proliferating cells, dense cellularity, and larger loss, dysfunction, or displacement of normal neuronal tissue, compared with TDLs.

A high lipid peak in PCNSLs and a variable lip-lac peak in patients with TDL have been previously noted by many other researchers.^{1,3,10,15,16} In our study, we classified the lip-lac grade

by visual judgment, which could easily be applied in daily clinical practice. We found that a high-grade lip-lac (grade >3) was mostly shown in PCNSLs regardless of whether there was necrosis. In a previous report, Raizer et al¹⁶ stated that a markedly elevated lipid in lymphoma might be helpful in differentiating it from glioma, and our observation was similar to theirs. A high lip-lac peak was suggestive of PCNSL rather than of TDL.

Although the origin of the lipid is still unclear, it is thought to be associated with necrosis and membrane breakdown.^{25,26} However, a very high lipid peak in PCNSL may result from an increased turnover of the membrane components in transformed lymphoid cells rather than from necrosis, which has been reported in many homogeneously enhancing PCNSLs.¹⁶ In our study, 8 nodular enhancing PCNSLs showed a very high lip-lac peak (grade 5), which was consistent with that seen in previous reports. It is also possible that PCNSL is composed of numerous macrophages that also contribute to the lipid signal.²⁷ The increase of lactate results from anaerobic metabolism, which is thought to be related to several mechanisms such as necrosis, demyelination, the inflammatory process, or mitochondrial dysfunction.^{14,25,28} In our study, the only patient with TDL with a high lactate peak had necrosis.

We also observed that the Cho/Cr ratio of typical, nodular PCNSLs was higher than that of atypical PCNSLs. This may be because homogeneously enhancing PCNSLs had more densely packed lymphoma cells than heterogeneously enhancing PCNSLs,²⁹ such that they had more active cell division, rapid cell turnover with synthesis of membrane phospholipids, and higher Cho/Cr ratios. The lower Cho/Cr ratios of atypical PCNSLs may result in the decreased diagnostic performance of the Cho/Cr ratio for discriminating between atypical PCNSLs and TDLs.

In our 2 nonenhancing PCNSLs, ¹H-MR spectroscopy was not helpful in differentiating them from TDLs. Nonenhancing PCNSLs were considered to be low-grade PCNSLs, less aggressive than typical PCNSLs in some previous studies.^{8,30} An autopsy report of a patient with PCNSL suggested that only scattered infiltration of malignant lymphomatous cells was observed in the nonenhancing tumor portion.²⁹ Therefore, we speculate that the low cellularity and low invasiveness contributed to the nonspecific MR spectrum in those cases.

There are a number of limitations to our study. First, all the spectra in our study were based on intermediate TE ¹H-MR spectroscopy. It has been reported that metabolites on short TE ¹H-MR spectroscopy, such as the glutamate/glutamine peak, can help to differentiate TDL from neoplasm.¹³ Further study with the combination of long and short TE ¹H-MR spectroscopy will be helpful for better discrimination of the 2 conditions. Second, pathology confirmation was lacking in 15 patients with TDL. However, supportive clinical and laboratory information as well as follow-up imaging helped us to make the final diagnosis. Third, our analysis of the lip-lac peak was not based on quantitative evaluation but was based on visual assessment. Because in many of our patients, accurate quantification was not possible, we considered it practical to use visual assessment. Difficulty in the assessment of the lipid or lactate in ¹H-MR spectroscopy is well known, especially in a single TE study. Multiple TE studies (TE = 20, 144, and 288 ms) are desirable to accurately separate the lipid

and lactate peak. Finally, the retrospective nature of our study should also be considered as a limitation.

CONCLUSIONS

In our study, PCNSLs showed differences from TDLs on ¹H-MR spectroscopy. A higher Cho/Cr ratio (>2.58), higher Cho/NAA ratio (>1.73), and high lip-lac grade (grade >3) therefore suggest PCNSL rather than TDL. The ¹H-MR spectroscopy findings are also helpful for discriminating PCNSLs with atypical MR features from TDLs. When conventional MR imaging features do not differentiate between PCNSLs and TDLs with certainty, the Cho/NAA ratio can provide added value. ¹H-MR spectroscopy may be a useful tool for differentiating PCNSLs from TDLs.

REFERENCES

1. Kuker W, Nagele T, Korfel A, et al. **Primary central nervous system lymphomas (PCNSL): MRI features at presentation in 100 patients.** *J Neurooncol* 2005;72:169–77
2. Kawai N, Okubo S, Miyake K, et al. **Use of PET in the diagnosis of primary CNS lymphoma in patients with atypical MR findings.** *Ann Nucl Med* 2010;24:335–43
3. Zacharia TT, Law M, Naidich TP, et al. **Central nervous system lymphoma characterization by diffusion-weighted imaging and MR spectroscopy.** *J Neuroimaging* 2008;18:411–17
4. Buhning U, Herrlinger U, Krings T, et al. **MRI features of primary central nervous system lymphomas at presentation.** *Neurology* 2001;57:393–96
5. Haldorsen IS, Espeland A, Larsson EM. **Central nervous system lymphoma: characteristic findings on traditional and advanced imaging.** *AJNR Am J Neuroradiol* 2011;32:984–92
6. Haldorsen IS, Krakenes J, Krossnes BK, et al. **CT and MR imaging features of primary central nervous system lymphoma in Norway, 1989–2003.** *AJNR Am J Neuroradiol* 2009;30:744–51
7. Erdag N, Bhorade RM, Alberico RA, et al. **Primary lymphoma of the central nervous system: typical and atypical CT and MR imaging appearances.** *AJR Am J Roentgenol* 2001;176:1319–26
8. Lachenmayer ML, Blasius E, Niehusmann P, et al. **Non-enhancing primary CNS lymphoma.** *J Neurooncol* 2011;101:343–44
9. Trendelenburg G, Zimmer C, Forschler A, et al. **Atypical appearance of a primary central nervous system lymphoma.** *Arch Neurol* 2006;63:908–09
10. Given CA 2nd, Stevens BS, Lee C. **The MRI appearance of tumefactive demyelinating lesions.** *AJR Am J Roentgenol* 2004;182:195–99
11. Butzen J, Prost R, Chetty V, et al. **Discrimination between neoplastic and nonneoplastic brain lesions by use of proton MR spectroscopy: the limits of accuracy with a logistic regression model.** *AJNR Am J Neuroradiol* 2000;21:1213–19
12. Majos C, Aguilera C, Alonso J, et al. **Proton MR spectroscopy improves discrimination between tumor and pseudotumoral lesion in solid brain masses.** *AJNR Am J Neuroradiol* 2009;30:544–51
13. Cianfoni A, Niku S, Imbesi SG. **Metabolite findings in tumefactive demyelinating lesions utilizing short echo time proton magnetic resonance spectroscopy.** *AJNR Am J Neuroradiol* 2007;28:272–77
14. Law M, Meltzer DE, Cha S. **Spectroscopic magnetic resonance imaging of a tumefactive demyelinating lesion.** *Neuroradiology* 2002;44:986–89
15. Malhotra HS, Jain KK, Agarwal A, et al. **Characterization of tumefactive demyelinating lesions using MR imaging and in-vivo proton MR spectroscopy.** *Mult Scler* 2009;15:193–203
16. Raizer JJ, Koutcher JA, Abrey LE, et al. **Proton magnetic resonance spectroscopy in immunocompetent patients with primary central nervous system lymphoma.** *J Neurooncol* 2005;71:173–80
17. Lange T, Dydak U, Roberts TP, et al. **Pitfalls in lactate measurements at 3T.** *AJNR Am J Neuroradiol* 2006;27:895–901
18. Yablonskiy DA, Neil JJ, Raichle ME, et al. **Homocoupling**

- effects in volume localized NMR spectroscopy: pitfalls and solutions. *Magn Reson Med* 1998;39:169–78
19. Calli C, Kitis O, Yuntun N, et al. **Perfusion and diffusion MR imaging in enhancing malignant cerebral tumors.** *Eur J Radiol* 2006;58:394–403
 20. Balashov KE, Lindzen E. **Acute demyelinating lesions with restricted diffusion in multiple sclerosis.** *Mult Scler* 2012;18:1745–53
 21. Cha S. **Perfusion MR imaging of brain tumors.** *Top Magn Reson Imaging* 2004;15:279–89
 22. Cha S, Knopp EA, Johnson G, et al. **Intracranial mass lesions: dynamic contrast-enhanced susceptibility-weighted echo-planar perfusion MR imaging.** *Radiology* 2002;223:11–29
 23. Cha S, Pierce S, Knopp EA, et al. **Dynamic contrast-enhanced T2*-weighted MR imaging of tumefactive demyelinating lesions.** *AJNR Am J Neuroradiol* 2001;22:1109–16
 24. Bitsch A, Bruhn H, Vougioukas V, et al. **Inflammatory CNS demyelination: histopathologic correlation with in vivo quantitative proton MR spectroscopy.** *AJNR Am J Neuroradiol* 1999;20:1619–27
 25. Horska A, Barker PB. **Imaging of brain tumors: MR spectroscopy and metabolic imaging.** *Neuroimaging Clin North Am* 2010;20:293–310
 26. Howe FA, Barton SJ, Cudlip SA, et al. **Metabolic profiles of human brain tumors using quantitative in vivo 1H magnetic resonance spectroscopy.** *Magn Reson Med* 2003;49:223–32
 27. Tang YZ, Booth TC, Bhogal P, et al. **Imaging of primary central nervous system lymphoma.** *Clin Radiol* 2011;66:768–77
 28. Soares DP, Law M. **Magnetic resonance spectroscopy of the brain: review of metabolites and clinical applications.** *Clin Radiol* 2009;64:12–21
 29. Sugie M, Ishihara K, Kato H, et al. **Primary central nervous system lymphoma initially mimicking lymphomatosis cerebri: an autopsy case report.** *Neuropathology* 2009;29:704–07
 30. Jahnke K, Schilling A, Heidenreich J, et al. **Radiologic morphology of low-grade primary central nervous system lymphoma in immunocompetent patients.** *AJNR Am J Neuroradiol* 2005;26:2446–54

^{62}Cu -Diacetyl-Bis (N^4 -Methylthiosemicarbazone) PET in Human Gliomas: Comparative Study with ^{18}F Fluorodeoxyglucose and L-Methyl- ^{11}C Methionine PET

K. Tateishi, U. Tateishi, S. Nakanowatari, M. Ohtake, R. Minamimoto, J. Suenaga, H. Murata, K. Kubota, T. Inoue, and N. Kawahara



ABSTRACT

BACKGROUND AND PURPOSE: ^{62}Cu -diacetyl-bis(N^4 -methylthiosemicarbazone) was developed as a hypoxic radiotracer in PET. We compared imaging features among MR imaging and ^{62}Cu -diacetyl-bis(N^4 -methylthiosemicarbazone)-PET, FDG-PET, and L-methyl- ^{11}C methionine-PET in gliomas.

MATERIALS AND METHODS: We enrolled 23 patients who underwent ^{62}Cu -diacetyl-bis(N^4 -methylthiosemicarbazone)-PET and FDG-PET and 19 (82.6%) who underwent L-methyl- ^{11}C methionine-PET, with all 23 patients undergoing surgery and their diagnosis being then confirmed by histologic examination as a glioma. Semiquantitative and volumetric analysis were used for the comparison.

RESULTS: There were 10 newly diagnosed glioblastoma multiforme and 13 nonglioblastoma multiforme (grades II and III), including 4 recurrences without any adjuvant treatment. The maximum standardized uptake value and tumor/background ratios of ^{62}Cu -diacetyl-bis(N^4 -methylthiosemicarbazone), as well as L-methyl- ^{11}C methionine, were significantly higher in glioblastoma multiforme than in nonglioblastoma multiforme ($P = .03$ and $P = .03$, respectively); no significant differences were observed on FDG. At a tumor/background ratio cutoff threshold of 1.9, ^{62}Cu -diacetyl-bis(N^4 -methylthiosemicarbazone) was most predictive of glioblastoma multiforme, with 90.0% sensitivity and 76.9% specificity. The positive and negative predictive values, respectively, for glioblastoma multiforme were 75.0% and 85.7% on ^{62}Cu -diacetyl-bis(N^4 -methylthiosemicarbazone), 83.3% and 60.0% on L-methyl- ^{11}C methionine, and 72.7% and 75.0% on MR imaging. In glioblastoma multiforme, volumetric analysis demonstrated that ^{62}Cu -diacetyl-bis(N^4 -methylthiosemicarbazone) uptake had significant correlations with FDG ($r = 0.68$, $P = .03$) and L-methyl- ^{11}C methionine ($r = 0.87$, $P = .03$). However, the ^{62}Cu -diacetyl-bis(N^4 -methylthiosemicarbazone)-active region was heterogeneously distributed in 50.0% (5/10) of FDG-active and 0% (0/6) of L-methyl- ^{11}C methionine-active regions.

CONCLUSIONS: ^{62}Cu -diacetyl-bis(N^4 -methylthiosemicarbazone) may be a practical radiotracer in the prediction of glioblastoma multiforme. In addition to FDG-PET, L-methyl- ^{11}C methionine-PET, and MR imaging, ^{62}Cu -diacetyl-bis(N^4 -methylthiosemicarbazone)-PET may provide intratumoral hypoxic information useful in establishing targeted therapeutic strategies for patients with glioblastoma multiforme.

ABBREVIATIONS: ^{62}Cu -ATSM = ^{62}Cu -diacetyl-bis(N^4 -methylthiosemicarbazone); GBM = glioblastoma multiforme; MET = L-methyl- ^{11}C methionine; non-GBM gliomas = World Health Organization grade II and III gliomas; SUV_{max} = maximum standardized uptake value; T/B ratio = tumor/background ratio

Gliomas have heterogeneously infiltrative and proliferative features, among which glioblastoma multiforme (GBM) is the most common and has the worst prognosis in adults.¹ From a histopathologic standpoint, microvascular proliferation and/or

necrosis is essential for the diagnosis of GBM.¹ However, random tissue sampling may not always lead to an accurate diagnosis because of tissue heterogeneity. Therefore, other diagnostic modalities to predict highly malignant regions, such as PET imaging, can provide complementary diagnostic and therapeutic information and guide selective target tissue sampling or resection.

Malignant tumor cells display an increased flux of glucose metabolism by increased expression of glucose transporters and hexokinase, as well as an increased rate of amino acid uptake and metabolism.² This increased transport and high metabolism oc-

Received April 3, 2013; accepted after revision June 2.

From the Departments of Neurosurgery (K.T., S.N., M.O., J.S., H.M., N.K.) and Radiology (U.T., T.I.), Graduate School of Medicine, Yokohama City University, Yokohama, Japan; and Division of Nuclear Medicine (R.M., K.K.), Department of Radiology, National Center for Global Health and Medicine, Tokyo, Japan.

This work was supported by Japan Advanced Molecular Imaging Program (J-AMP) of the Ministry of Education, Culture, Sports, Science and Technology (MEXT), Japan, and was partly funded by a Grant-in-Aid for Scientific Research from the Japan Society for the Promotion of Sciences (No. 24791515).

Please send correspondence to Nobutaka Kawahara, MD, PhD, Department of Neurosurgery, Graduate School of Medicine, Yokohama City University, 3-9 Fukuura, Kanazawa-ku, Yokohama, Kanagawa 236-0004, Japan; e-mail: nkawa@yokohama-cu.ac.jp

Indicates open access to non-subscribers at www.ajnr.org

Indicates article with supplemental on-line tables.

Indicates article with supplemental on-line figure.

<http://dx.doi.org/10.3174/ajnr.A3679>

cur commonly in GBM and can be detected by widely used techniques, such as FDG-PET and L-methyl-[¹¹C]methionine (MET)-PET.³⁻⁹ However, the predictive value of these PET imaging techniques has not been adequate for a diagnosis of GBM because uptake of these tracers is not specific in GBM.^{3,4} On the other hand, tissue hypoxia and necrosis are cardinal features of GBM that are often associated with resistance to radiation therapy and chemotherapy.¹⁰ Thus, intratumoral hypoxic information may be useful for an accurate diagnosis and establishment of effective therapeutic strategies for gliomas.

Some clinical investigations by use of [¹⁸F]fluoromisonidazole-PET have been recently undertaken to detect tissue hypoxia noninvasively in gliomas.¹¹⁻¹³ On the other hand, we previously reported the clinical usefulness of ⁶²Cu-diacetyl-bis(N⁴-methylthiosemicarbazone) (⁶²Cu-ATSM)-PET imaging for gliomas.¹⁴ Our preliminary study revealed a relationship between ⁶²Cu-ATSM uptake values and hypoxia-inducible factor-1 α expression, which is increased under hypoxia,¹⁴ suggesting that ⁶²Cu-ATSM-PET is a practical hypoxic imaging technique in gliomas. However, whether ⁶²Cu-ATSM uptake is specific in GBM was not determined, and the correlation of ⁶²Cu-ATSM findings with FDG and MET remained unclear in GBM. In addition, to assess whether ⁶²Cu-ATSM uptake is dependent on BBB breakdown and to evaluate an additional value over MR imaging findings, we volumetrically and qualitatively compared ⁶²Cu-ATSM-PET imaging with T1-weighted MR imaging with Gd-DTPA.

MATERIALS AND METHODS

Patients

This study was approved by the local ethics committee (Institutional Review Board no. B1001111026) after written informed consent was obtained from all patients. Between December 2010 and December 2012, we prospectively performed ⁶²Cu-ATSM-PET in 68 patients with malignant brain tumors. Among them, 23 consecutive patients with pathologically confirmed gliomas (10 men and 13 women; age range, 19–81 years; mean age, 54.2 \pm 17.5 years) who received FDG-PET and/or MET-PET with ⁶²Cu-ATSM-PET were retrospectively analyzed. FDG-PET and MET-PET imaging were performed in 23 patients (100%) and 19 patients (82.6%), respectively. Of the 23 patients, 19 (82.6%) were newly diagnosed, and the remaining 4 patients (17.4%), who previously underwent biopsy but had not received any radiation therapy or chemotherapy, were diagnosed as having tumor recurrence. Histologic diagnosis and tumor grade were classified according to the following 2007 World Health Organization criteria: 8 (34.8%) grade II (3 diffuse astrocytomas, 3 oligoastrocytomas, and 2 oligodendrogliomas); 5 (21.7%) grade III (1 anaplastic oligoastrocytoma and 4 anaplastic oligodendrogliomas); and 10 (43.5%) grade IV (GBM). All 10 patients with GBM were newly diagnosed. Thirteen grade II and III gliomas (56.5%) were classified as non-GBM gliomas. The oligodendroglial component was found in 10 (76.9%) of 13 non-GBM gliomas.

Intervals from the MR imaging investigation to ⁶²Cu-ATSM-PET, FDG-PET, and MET-PET were 5.4 \pm 4.1, 4.3 \pm 3.2, and 5.4 \pm 3.4 days, respectively (mean \pm SD). All patients underwent surgery the day after a repeated MR imaging study for neuronavi-

gation, and their diagnosis was confirmed on histologic examination. On-Line Table 1 summarizes the patient characteristics.

PET and MR Image Acquisition

Preparation of ⁶²Cu-ATSM, FDG, and MET has been described in previous reports.^{15,16} To acquire ⁶²Cu-ATSM-PET and FDG-PET/CT images, a whole-body PET/CT scanner (Aquiduo PCA-7000B; Toshiba, Tokyo, Japan) with a 16-row detector in the CT component was used at the Yokohama City University Hospital (Yokohama, Japan). MET-PET imaging was performed with PET/CT scans (Biograph 16; Siemens, Erlangen, Germany) at the National Center for Global Health and Medicine (Tokyo, Japan). An image quality phantom (NU 2–2001; National Electrical Manufacturers Association) was used for cross-calibration because such phantoms are widely used and allow estimation of optimal acquisition times.

For ⁶²Cu-ATSM-PET/CT and FDG-PET/CT, the following conditions were used for acquisition of low-dose CT data: 120 kVp, an auto-exposure control system, a beam pitch of 0.875 or 1, and a 1.5- or 2-mm \times 16-row mode. No iodinated contrast material was administered. After intravenous injection of 740 MBq of ⁶²Cu-ATSM, the patients were placed in a supine “arm-up” position. Dynamic data acquisition was carried out for 30–40 minutes, and PET/CT images were reconstructed from the data. For studies of FDG, the patients received an intravenous injection of 370 MBq of FDG after at least 6 hours of fasting, followed by an uptake phase of approximately 60 minutes. For MET-PET/CT, the following conditions were used for acquisition of low-dose CT data: 120 kVp, an auto-exposure control system, a beam pitch of 0.875, and a 3-mm \times 16-row mode. After 6 hours of fasting, 370 MBq of MET was intravenously injected, followed by data acquisition at 20 minutes after the injection. The following acquisition settings were used for ⁶²Cu-ATSM-PET/CT and FDG-PET/CT: 3D data acquisition mode; 180 seconds/bed; field of view, 500 mm; 4 iterations; 14 subsets; matrix size, 128 \times 128; 8-mm Gaussian filter, full width at half maximum; and reconstruction, ordered subset expectation maximization. For MET-PET/CT, the following acquisition settings were used: 3D data acquisition mode; 180 seconds/bed; field of view, 300 mm; 4 iterations; 14 subsets; matrix size, 256 \times 256; 4-mm Gaussian filter, full width at half maximum; and reconstruction, ordered subset expectation maximization. The estimated internal absorbed doses of ⁶²Cu-ATSM, FDG, and MET were approximately 10, 2.5, and 1.9 mSv, respectively.

MR imaging was performed on a 1.5T system (Magnetom Symphony; Siemens). 3D T1-weighted MR imaging with a MPRAGE sequence was used with the following parameters to acquire axial T1-weighted images after administration of 0.2 mL/kg of Gd-DTPA: field of view, 250 \times 250 mm²; matrix size, 512 \times 512; TR, 1960 ms; TE, 3.9 ms; TI, 1100 ms; and flip angle, 15°. In total, 120 contiguous 2-mm images were obtained from each patient.

Image Interpretation

Four board-certified nuclear medicine specialists who were unaware of the clinical information assessed the PET images semiquantitatively and volumetrically in consensus (⁶²Cu-ATSM and

FDG, U.T. and T.I.; MET, R.M. and T.I.). MR imaging findings were also assessed by board-certified radiologists (U.T. and T.I.), who interpreted the tumors as either GBM or non-GBM gliomas. A volume of interest was outlined within areas of increased tracer uptake and was measured on each section. In extensively heterogeneous lesions, regions of interest covered all components. For semiquantitative interpretations, the standardized uptake value was determined by a standard formula. The tumor/background ratio (T/B ratio) of ^{62}Cu -ATSM and MET was calculated relative to the uptake in the contralateral frontal cortex. The FDG T/B ratio was calculated relative to the uptake in the contralateral white matter. The uptake values of the ^{62}Cu -ATSM, FDG, and MET tracers were determined by assessment of the maximum standardized uptake value (SUV_{max}) values and T/B ratios.

Dr. View version R 2.5 for LINUX (Infocom, Tokyo, Japan) software was used to merge the PET images with the MR images,^{4,13,14} and each PET and MR image was volumetrically compared. To evaluate volumetric analysis, we extracted the uptake regions of the ^{62}Cu -ATSM images on the basis of the optimal T/B ratio thresholds of ≥ 1.8 , a cutoff value for predicting hypoxia-inducible factor-1 α expression in our previous study.¹⁴ The uptake regions of the FDG and MET images were extracted on the basis of the T/B ratio thresholds of ≥ 1.5 and ≥ 1.3 , respectively, in accordance with previous reports.^{5,9} These uptake regions were rated as metabolically active volumes. For GBM, we extracted the tumor volume by measuring a completely covered contrast-enhanced region with necrotic and cystic components on MR imaging. The contrast-enhanced volume was also separately extracted by measuring a contrast-enhanced region without any necrotic and cystic components. Metabolically active regions shown by each PET tracer were overlaid on the MR images for qualitatively comparing metabolically active regions among the 3 tracers. Tumors with ^{62}Cu -ATSM-active regions that demonstrated $\leq 50\%$ volumetric overlap with the active regions of FDG and MET were rated as heterogeneous with respect to intratumoral oxygenation. Correlations among ^{62}Cu -ATSM, FDG, and MET were also volumetrically analyzed. On the basis of the optimal cutoff value for prediction of GBM (T/B ratio, 1.9), which was defined by receiver operating characteristic analysis, tumors having ^{62}Cu -ATSM T/B ratios ≥ 1.9 were rated as GBM. The optimal cutoff threshold of the MET T/B ratio was set by receiver operating characteristic analysis, and tumors having MET T/B ratios ≥ 3.0 were rated as GBM. To assess the clinical value of ^{62}Cu -ATSM-PET findings relative to those of MET-PET and MR imaging findings for prediction of GBMs, we evaluated the positive and negative predictive values independently.

Statistical Analysis

All parameters were expressed as means \pm SDs. Two-way repeated measures ANOVA was used to compare the mean uptake values of each tracer. To determine the optimal radio-tracer for prediction of GBM by semiquantitative analysis, we performed receiver operating characteristic analysis. To evaluate volumetric correlations of ^{62}Cu -ATSM with FDG and MET, we used linear regression analysis. The Wilcoxon signed rank test was used to compare the mean tumor volume, con-

trast-enhanced volume, and metabolically active volumes determined by the 3 PET tracers. The Fisher exact probability test was used to compare the ^{62}Cu -ATSM-PET with contrast-enhanced MR imaging and MET-PET imaging features. The level of statistical significance was set at $P < .05$. JMP 10 statistical software (SAS Institute, Cary, North Carolina) was used for statistical analyses.

RESULTS

Semiquantitative Analysis of PET Studies According to Tumor Classification

A summary of the uptake values for each PET tracer is presented in On-Line Table 2. Representative images are shown in Fig 1 and in the On-Line Figure. The average ^{62}Cu -ATSM SUV_{max} values in GBM and non-GBM gliomas were 1.68 ± 0.94 and 0.98 ± 0.52 , respectively. The ^{62}Cu -ATSM SUV_{max} was significantly higher for GBM than for non-GBM gliomas ($P = .03$; Fig 2A). A significant difference in SUV_{max} was also detected between GBM and non-GBM gliomas for MET (5.23 ± 1.11 and 3.25 ± 1.66 , respectively; $P = .02$; Fig 2A) but not for FDG (7.31 ± 3.22 and 5.72 ± 2.25 , respectively; $P = .18$; Fig 2A).

The mean ^{62}Cu -ATSM T/B ratios in GBM and non-GBM gliomas were 3.10 ± 2.37 and 1.47 ± 0.57 , respectively, which were also significantly different ($P = .03$; Fig 2B). Receiver operating characteristic analysis indicated that a ^{62}Cu -ATSM T/B ratio cutoff threshold of 1.9 was most predictive of GBM, with 90.0% sensitivity and 76.9% specificity (area under the curve, 0.88). Similar to the SUV_{max} results, there was a significant difference in the T/B ratio between GBM and non-GBM gliomas for MET (3.53 ± 0.70 and 2.27 ± 0.97 , respectively; $P = .01$; Fig 2B) but not for FDG (2.71 ± 1.56 and 2.44 ± 1.28 , respectively; $P = .65$; Fig 2B). Receiver operating characteristic analysis showed an optimal T/B ratio of 3.0 for MET (sensitivity, 83.3%; specificity, 76.9%; area under the curve, 0.83, respectively), which was slightly less than that for ^{62}Cu -ATSM.

Volumetric and Qualitative Comparison among 3 Tracers in GBM

A summary of tumor volume and contrast-enhanced volume on MR imaging and the active volume for each PET tracer is presented in On-Line Table 3. Table 1 shows the relationships of the metabolically active volumes in GBM: for ^{62}Cu -ATSM (T/B ratio ≥ 1.8), FDG (T/B ratio ≥ 1.5), and MET (T/B ratio ≥ 1.3); the volumes were 8.2 ± 14.0 , 11.0 ± 12.0 , and $38.0 \pm 19.0 \text{ cm}^3$, respectively. The mean active volume of ^{62}Cu -ATSM in GBM was not significantly different from that of FDG ($P = .63$) but was significantly less than that of MET ($P = .03$). In addition, the active volume of ^{62}Cu -ATSM in GBM correlated significantly with that of FDG ($r = 0.68$, $P = .03$) and MET ($r = 0.87$, $P = .03$). However, compared with the active regions of FDG and MET, those of ^{62}Cu -ATSM were heterogeneously distributed ($\leq 50\%$ volumetric overlap with the active regions of FDG and MET) in 50% (5/10) and 0% (0/6) of the tumors with metabolically active regions, respectively. The ^{62}Cu -ATSM-active regions were fully covered within the MET-active regions in all cases.

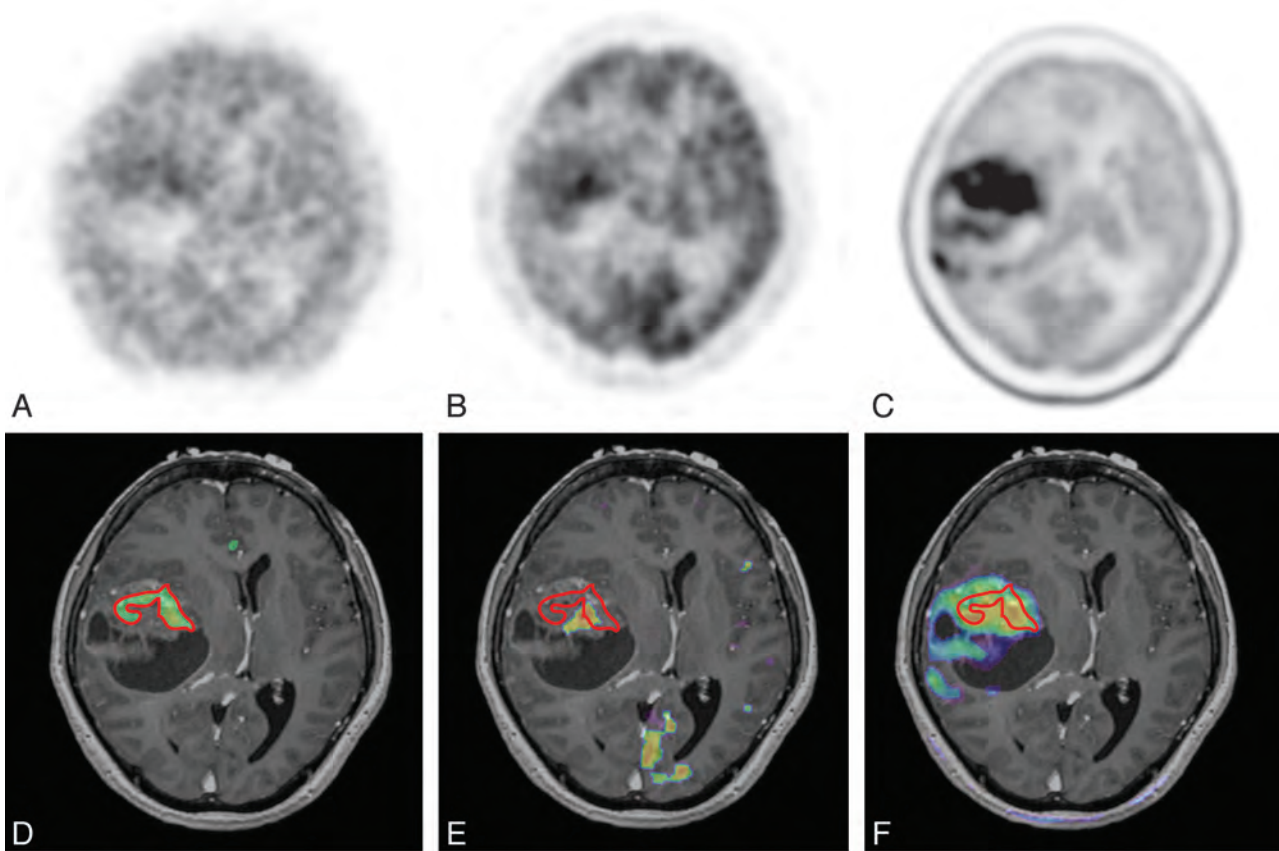


FIG 1. Case 21. A 59-year-old woman with GBM in the right temporal lobe (tumor volume, 79.6 cm³). PET images of ⁶²Cu-ATSM (A), FDG (B), and MET (C) are shown; the ⁶²Cu-ATSM-active regions are outlined by red lines (D–F, respectively). ⁶²Cu-ATSM-PET/MR imaging fusion image (D) showing the intratumoral hypoxic region (11.8 cm³), which is less than that of the contrast-enhanced volume (30.9 cm³), FDG-PET/MR imaging fusion image (E) also indicating the intratumoral active region (4.6 cm³), which is heterogeneously distributed compared with the ⁶²Cu-ATSM-active region. MET-PET/MR imaging fusion image (F) showing the more extensive active region (73.1 cm³), which completely covered the ⁶²Cu-ATSM-active regions.

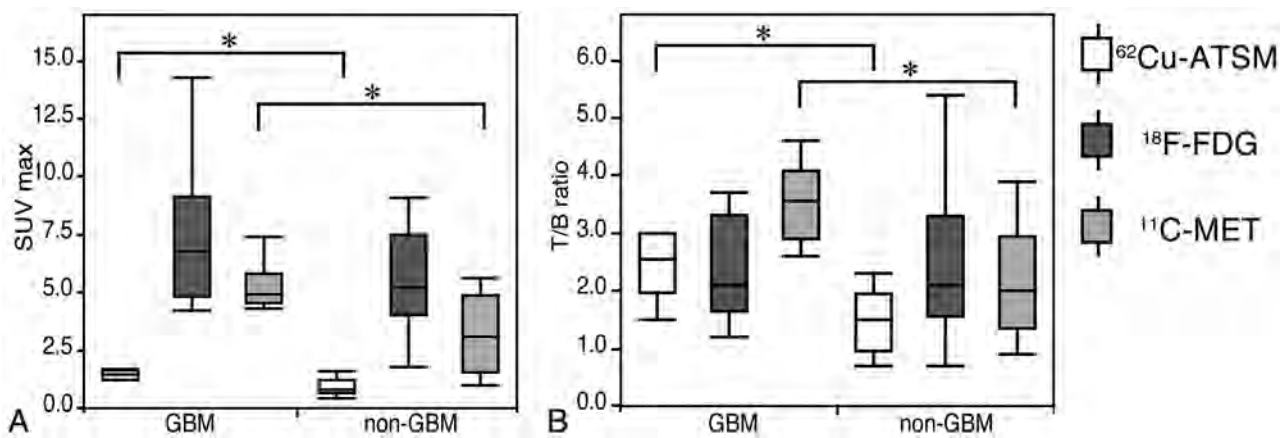


FIG 2. Boxplots comparing uptake values between GBM and non-GBM gliomas. The ⁶²Cu-ATSM and MET SUV_{max} values show significant differences ($P = .03$ and $P = .02$); however, FDG SUV_{max} values are not significantly different ($P = .18$; A). The ⁶²Cu-ATSM and MET T/B ratios also show significant differences ($P = .03$ and $P = .01$), but no significant difference is observed in the FDG T/B ratio ($P = .65$; B). * $P < .05$.

Volumetric Comparison with MR Imaging

The mean tumor volume and contrast-enhanced volume in GBMs were 45.4 ± 26.5 and 21.6 ± 14.3 cm³, respectively (Table 2), which were significantly greater than those of the metabolically active volumes for ⁶²Cu-ATSM ($P = .002$ and $P = .002$, respectively) and FDG ($P = .002$ and $P = .006$, respectively). The mean active volume of MET was not significantly different from

the mean tumor volume ($P = .56$) and contrast-enhanced volume ($P = .06$).

Predictive Values of ⁶²Cu-ATSM-PET, MET-PET, and MR Imaging for Distinguishing GBM

In 19 newly diagnosed gliomas, tumors having ⁶²Cu-ATSM-active regions and strongly contrast-enhanced regions on MR imaging

Table 1: Volumetric correlation of ⁶²Cu-ATSM with FDG and MET in GBM

GBM (n=10)	Volume (cm ³)	r	P Value	Heterogeneous Metabolism (%) ^a
⁶² Cu-ATSM	8.2 ± 14.0	—	—	—
FDG	11.0 ± 12.0	0.68	.03	5/10 (50%)
MET	38.0 ± 19.0	0.87	.03	0/6 (0%)

Note:—r indicates correlation coefficient when compared with ⁶²Cu-ATSM.

^aHeterogeneous metabolism indicates an overlap of ≤50% of the active volume of ⁶²Cu-ATSM with those of FDG and MET.

Table 2: Volumetric comparison of radiotracers in MRI for GBM

GBM (n=10)	TV (45.4 ± 26.5 cm ³) ^a	CEV (21.6 ± 14.3 cm ³) ^b
⁶² Cu-ATSM (8.2 ± 14.0 cm ³)	P = .002	P = .002
FDG (11.0 ± 12.0 cm ³)	P = .002	P = .006
MET (38.0 ± 19.0 cm ³)	P = .56	P = .06

Note:—The mean tumor volume (TV) and contrast-enhanced volume (CEV) were compared with the active volume of ⁶²Cu-ATSM (T/B cutoff threshold ≥1.8), FDG (T/B cutoff threshold of ≥1.5), and MET (T/B cutoff threshold of ≥1.3). P values < .05 were considered to indicate statistical significance.

^aTV was measured as a completely covered contrast-enhanced region with necrotic and cystic components.

^bCEV was measured as a contrast-enhanced region without necrotic and cystic components on T1-weighted MRI with Gd-DTPA.

were detected in 63.2% (12/19) and 57.9% (11/19), respectively. No statistical correlation was observed between the 2 modalities ($P = .07$). The positive predictive values of ⁶²Cu-ATSM and MR imaging for distinguishing GBM were 75.0% and 72.7%, respectively. In contrast, the negative predictive values of ⁶²Cu-ATSM and MR imaging were 85.7% and 75.0%, respectively. On the other hand, when tested by the optimal cutoff threshold on MET (T/B ratio, 3.0), the positive and negative predictive values for a diagnosis of GBM were 83.3% and 60.0%, respectively. We found no significant correlation between ⁶²Cu-ATSM and MET ($P = .59$).

DISCUSSION

Our present PET study demonstrated that ⁶²Cu-ATSM is a predictive radiotracer for GBM. Many clinical PET studies with FDG and MET have been conducted to discriminate among World Health Organization grades of gliomas.^{4,5,7,8} Several imaging studies have demonstrated the usefulness of FDG-PET in the differentiation between low-grade and high-grade gliomas and even between grade III and grade IV gliomas.^{5,7,8} Because of the associated increased glucose uptake and high rates of glycolysis, FDG-PET shows high FDG uptake in GBM.⁸ However, FDG-PET has a low signal-to-noise ratio in brain tumors, which is a result of the high glucose metabolism in normal brain tissue.⁴ Moreover, because FDG uptake reflects an increased glycolytic rate in rapidly growing brain tumor cells even in grade II and III gliomas,^{7,12} it may not be a suitable radiotracer to predict GBM. On the other hand, malignant gliomas demonstrate increased rates of amino acid uptake and metabolism. MET readily crosses the intact BBB through a neutral amino acid transporter and is incorporated into active tumor areas, which allows tumor visualization even in low-grade gliomas.⁹

In our current study, MET-PET revealed a significant difference between GBM and non-GBM despite the high frequency of oligodendroglial tumors. However, these oligodendroglial tumors are reported to show relatively high uptake of MET irrespec-

tive of their grade with MET-PET,^{3,4} which is not yet established as a standard imaging technique for a diagnosis of GBM. Recently, another technique, hypoxic imaging, has been used clinically and may be another diagnostic tool to discriminate GBM from non-GBM gliomas because poor microcirculation with respect to metabolic demand induces relative tissue hypoxia and necrosis, a cardinal feature of GBM.¹⁰

Hypoxic PET studies with [¹⁸F]fluoromisonidazole and ⁶²Cu-ATSM have demonstrated their usefulness separately in hypoxic imaging. Under hypoxic conditions, ⁶²Cu-ATSM retention is induced by microsomal cytochrome reductase enzymes, which is different from [¹⁸F]fluoromisonidazole retention by mitochondrial nitroreductase enzymes.¹⁷ Cu-ATSM was developed as a radiotracer to detect regional hypoxia in the ischemic myocardium and hypoxic tissues in tumors,^{18,19} and its image contrast may be greater than that of [¹⁸F]fluoromisonidazole, because Cu-ATSM has rapid blood clearance and is retained in hypoxic tissues with a high hypoxic/normoxic tissue-to-activity ratio.²⁰ On the other hand, [¹⁸F]fluoromisonidazole can detect a wider range of partial oxygen tension values than ⁶¹Cu-ATSM.¹⁷ Experimental investigations with glioma models have demonstrated that ^{61,64,67}Cu-ATSM uptake correlates with tissue hypoxia.¹⁹ Our preliminary clinical study also showed that ⁶²Cu-ATSM uptake values correlated highly with hypoxia-inducible factor-1 α expression, which is a biomarker of tissue hypoxia,¹⁴ and the optimal cutoff threshold to predict hypoxia-inducible factor-1 α expression (T/B ratio, 1.8) was similar to that of our present study in the prediction of GBM (T/B ratio, 1.9). It has been well established that overexpression of hypoxia-inducible factor-1 α , a transcription factor that is part of the stress response mechanism, is initiated in the presence of low oxygen tensions and induces hypoxia-regulated molecules, such as vascular endothelial growth factor, glucose transporters, and carbonic anhydrase IX,²¹ which correlate with treatment resistance and are highly expressed in GBM.¹⁰ Therefore, ⁶²Cu-ATSM-PET may be a radiotracer useful in the identification of treatment-resistant hypoxic regions in patients with glioma. Our present study also demonstrated that hypoxic imaging by use of ⁶²Cu-ATSM for discrimination of GBM from non-GBM gliomas may be as effective as [¹⁸F]fluoromisonidazole,¹² indicating that hypoxic imaging, including ⁶²Cu-ATSM, would be a better choice than FDG in the prediction of GBM.

However, to our knowledge, correlations between hypoxic regions depicted by PET studies and high-uptake regions in FDG or MET have not been precisely studied in GBM. In our present study, we showed that ⁶²Cu-ATSM uptake in GBM correlates significantly with FDG by volumetric assessments, but half of the uptake regions were distributed heterogeneously. Under hypoxia, glycolysis is increased by hypoxia-inducible factor-1 α activation,²¹ whereas in malignant tumor cells, aerobic glycolysis is driven even under nonhypoxic conditions.² Therefore, FDG uptake might indirectly and partially reflect hypoxic regions as well as nonhypoxic regions.²²

In line with these observations, several clinical studies on lung and cervical cancers have directly compared ⁶²Cu-ATSM-PET with FDG-PET and suggested that intratumoral distribution and uptake values may be different, depending on the histopathologic type of the tumor.^{15,23} In addition, a previous study using a lung

cancer model demonstrated that ^{64}Cu -ATSM was predominantly accumulated in hypoxic and quiescent tumor cells, a finding that differs from the FDG distribution with features of high proliferation.²⁴ In accordance with these findings, a hypoxic imaging study by use of [^{18}F]fluoromisonidazole revealed a positive relationship but not a precisely matched uptake to that of FDG in gliomas,¹¹ which seems to be similar to the results of our present study. These findings imply that the positive relationship between FDG-PET and hypoxic-PET may indicate increased glycolysis, glucose uptake, and hypoxia in GBM. In contrast, the parts of hypoxic regions not shown on FDG-PET might indicate severe ischemia and hypoxia where glucose delivery is also severely disturbed, an idea that should be explored in future investigations.

In contrast, no PET study has compared ^{62}Cu -ATSM and MET. Our present study showed that MET had larger active volumes than did ^{62}Cu -ATSM in GBM, which was fully covered within MET-active regions. There was also a significant volumetric correlation between ^{62}Cu -ATSM and MET. A volumetric correlation of MET-PET–delineated regions with hypoxic PET by [^{18}F]fluoromisonidazole has also been documented,¹³ which corroborates our results. However, it is not clear why hypoxic regions delineated by ^{62}Cu -ATSM not depicted by FDG-PET still show high MET uptake. If disturbance of substrate delivery such as that of glucose is the mechanism leading to FDG-PET–negative hypoxic regions, MET delivery should also be disturbed. Multifactorial effects of tracer kinetics, such as a switch from a metabolic to a catabolic state in hypoxic tumor cells,²⁵ as well as a threshold setting, would cause this discrepancy in complex and heterogeneous GBMs.

From a clinical point of view, MET-PET enables more accurate delineation of glioma extension than MR imaging,^{6,9} suggesting that MET is a practical radiotracer for the detection of infiltrative regions around contrast-enhanced regions on MR imaging, which can provide important clinical information for treatment. By combining ^{62}Cu -ATSM- and MET-PET imaging, delineation of hypoxic regions within MET-PET–active regions would provide additional value to delineate therapeutic targets as treatment-resistant hypoxic regions for more intensive therapy (ie, intensity-modulated radiation therapy and chemotherapy by use of convection-enhanced delivery as well as biopsy targets in GBM). However, the hypoxic mechanism is not fixed in time, and variability in spatial uptake can occur among repeated PET scans.²⁶ Therefore, it is crucial for PET imaging to elucidate the mechanism of changes in intratumoral radiotracer distribution as a clinical application. In addition, to confirm the differences among ^{62}Cu -ATSM, FDG, and MET in GBM, further precise metabolic evaluation within GBM is required.

Among these available imaging modalities, it is not clear which is best for distinguishing GBM from non-GBM. Contrast enhancement on MR imaging might provide a simple index; however, it is sometimes ambiguous.²⁷ To compare diagnostic reliability, we compared positive and negative predictive values for MR imaging, MET-PET, and ^{62}Cu -ATSM-PET and showed that for the prediction of GBM, both were higher in ^{62}Cu -ATSM than in MR imaging, indicating that ^{62}Cu -ATSM-PET is a better imaging technique for the prediction of GBM than is MR imaging. In addition, the negative predictive value was also higher for ^{62}Cu -

ATSM-PET (85.7%) vs MET-PET (60.0%), though the positive values were lower. This finding would suggest that combined assessment by use of ^{62}Cu -ATSM and MET may provide a more accurate diagnosis. However, because of the small number of patients in our present study, further clinical evaluation in a larger group of patients is required to confirm these hypotheses.

Study Limitations

One of the limitations of our study was that it is unknown how BBB disruption affects ^{62}Cu -ATSM kinetics. To gain some insight, we demonstrated that the ^{62}Cu -ATSM–active volumes in GBM were significantly less than those of the contrast-enhanced volumes on MR imaging, which are dependent on BBB breakdown accompanying neovascularization in gliomas.⁶ Thus, it is suggested that ^{62}Cu -ATSM uptake would be determined by other factors in addition to BBB breakdown. Indeed, it has been shown that the oxygen pressure in GBM is relatively lower than the pressure in the surrounding cortex.²⁸ Thus, ^{62}Cu -ATSM is likely to be a tracer that reflects part of the hypoxic region. Further clinical validation of the relationship between ^{62}Cu -ATSM uptake and tissue oxygen tension is required to determine the precision of hypoxic imaging.

In addition, our present study may have been affected by several biases, including threshold settings and MET-PET not being performed in all cases. Moreover, no published studies have compared ^{62}Cu -ATSM and [^{18}F]fluoromisonidazole for clinical use. Finally, ^{62}Cu -ATSM is rarely applicable for every institution because of limited radionuclide production. Nonetheless, multiple PET imaging by use of ^{62}Cu -ATSM, FDG, and MET may provide complementary valuable intratumoral metabolic information, all of which is important in the establishment of targeted therapeutic strategies for patients with GBM.

CONCLUSIONS

The results of our study suggest that ^{62}Cu -ATSM-PET is predictive of GBM. In addition to the information obtained by FDG-PET, MET-PET, and MR imaging, ^{62}Cu -ATSM-PET may provide intratumoral hypoxic information useful in establishing targeted therapeutic strategies for patients harboring GBM.

ACKNOWLEDGMENTS

We thank Tsuneo Saga, Masayuki Inubishi, Toshimitsu Fukumura, and Yasuhisa Fujibayashi of the Diagnostic Imaging and Molecular Probe Groups, Molecular Imaging Center, National Institute of Radiologic Sciences, Chiba, Japan; Hidehiko Okazawa of the Department of Radiology, Biomedical Imaging Research Center, Faculty of Medical Sciences, University of Fukui, Fukui, Japan; and Hirofumi Fujii, Functional Imaging Division, Research Center for Innovative Oncology, National Cancer Center Hospital East, Chiba, Japan, for their assistance.

Disclosures: Satoshi Nakanowatari—RELATED: Grant: Grant-in-Aid for Scientific Research from the Japan Society for the Promotion of Sciences (No. 24791515).* Nobutaka Kawahara—RELATED: Grant: Ministry Education, Culture, Sports, Science and Technology.* Comments: This grant is a public research grant offered from the Government. *Money paid to institution.

REFERENCES

1. Louis DN, Ohgaki H, Wiestler OD, et al. **The 2007 WHO classification of tumours of the central nervous system.** *Acta Neuropathol* 2007;114:97–109
2. Plathow C, Weber WA. **Tumor cell metabolism imaging.** *J Nucl Med* 2008;49 Suppl 2:43S–63S
3. Nariai T, Tanaka Y, Wakimoto H, et al. **Usefulness of L-[methyl-11C] methionine-positron emission tomography as a biological monitoring tool in the treatment of glioma.** *J Neurosurg* 2005;103:498–507
4. Kato T, Shinoda J, Nakayama N, et al. **Metabolic assessment of gliomas using 11C-methionine, [18F] fluorodeoxyglucose, and 11C-choline positron-emission tomography.** *AJNR Am J Neuroradiol* 2008;29:1176–82
5. Delbeke D, Meyerowitz C, Lapidus RL, et al. **Optimal cutoff levels of F-18 fluorodeoxyglucose uptake in the differentiation of low-grade from high-grade brain tumors with PET.** *Radiology* 1995;195:47–52
6. Miwa K, Shinoda J, Yano H, et al. **Discrepancy between lesion distributions on methionine PET and MR images in patients with glioblastoma multiforme: insight from a PET and MR fusion image study.** *J Neurol Neurosurg Psychiatry* 2004;75:1457–62
7. Padma MV, Said S, Jacobs M, et al. **Prediction of pathology and survival by FDG PET in gliomas.** *J Neurooncol* 2003;64:227–37
8. Singhal T, Narayanan TK, Jacobs MP, et al. **11C-methionine PET for grading and prognostication in gliomas: a comparison study with 18F-FDG PET and contrast enhancement on MRI.** *J Nucl Med* 2012;53:1709–15
9. Kracht LW, Miletic H, Busch S, et al. **Delineation of brain tumor extent with [11C]L-methionine positron emission tomography: local comparison with stereotactic histopathology.** *Clin Cancer Res* 2004;10:7163–70
10. Jensen RL. **Brain tumor hypoxia: tumorigenesis, angiogenesis, imaging, pseudoprogression, and as a therapeutic target.** *J Neurooncol* 2009;92:317–35
11. Cher LM, Murone C, Lawrentschuk N, et al. **Correlation of hypoxic cell fraction and angiogenesis with glucose metabolic rate in gliomas using 18F-fluoromisonidazole, 18F-FDG PET, and immunohistochemical studies.** *J Nucl Med* 2006;47:410–18
12. Hirata K, Terasaka S, Shiga T, et al. **(18)F-Fluoromisonidazole positron emission tomography may differentiate glioblastoma multiforme from less malignant gliomas.** *Eur J Nucl Med Mol Imaging* 2012;39:760–70
13. Kawai N, Maeda Y, Kudomi N, et al. **Correlation of biological aggressiveness assessed by 11C-methionine PET and hypoxic burden assessed by 18F-fluoromisonidazole PET in newly diagnosed glioblastoma.** *Eur J Nucl Med Mol Imaging* 2011;38:441–50
14. Tateishi K, Tateishi U, Sato M, et al. **Application of ⁶²Cu-diacetyl-bis (N4-methylthiosemicarbazone) PET imaging to predict highly malignant tumor grades and hypoxia-inducible factor-1 α expression in patients with glioma.** *AJNR Am J Neuroradiol* 2013;34:92–99
15. Minagawa Y, Shizukuishi K, Koike I, et al. **Assessment of tumor hypoxia by ⁶²Cu-ATSM PET/CT as a predictor of response in head and neck cancer: a pilot study.** *Ann Nucl Med* 2011;25:339–45
16. Morooka M, Kubota K, Kadowaki H, et al. **11C-methionine PET of acute myocardial infarction.** *J Nucl Med* 2009;50:1283–87
17. Bowen SR, van der Kogel AJ, Nordmark M, et al. **Characterization of positron emission tomography hypoxia tracer uptake and tissue oxygenation via electrochemical modeling.** *Nucl Med Biol* 2011;38:771–80
18. Fujibayashi Y, Taniuchi H, Yonekura Y, et al. **Copper-62-ATSM: a new hypoxia imaging agent with high membrane permeability and low redox potential.** *J Nucl Med* 1997;38:1155–60
19. Lewis JS, Sharp TL, Laforest R, et al. **Tumor uptake of copper-diacetyl-bis(N(4)-methylthiosemicarbazone): effect of changes in tissue oxygenation.** *J Nucl Med* 2001;42:655–61
20. Lewis JS, McCarthy DW, McCarthy TJ, et al. **Evaluation of ⁶⁴Cu-ATSM in vitro and in vivo in a hypoxic tumor model.** *J Nucl Med* 1999;40:177–83
21. Ke Q, Costa M. **Hypoxia-inducible factor-1 (HIF-1).** *Mol Pharmacol* 2006;70:1469–80
22. Christian N, Deheneffe S, Bol A, et al. **Is (18)F-FDG a surrogate tracer to measure tumor hypoxia? Comparison with the hypoxic tracer (14)C-EF3 in animal tumor models.** *Radiother Oncol* 2010;97:183–88
23. Lohith TG, Kudo T, Demura Y, et al. **Pathophysiologic correlation between ⁶²Cu-ATSM and 18F-FDG in lung cancer.** *J Nucl Med* 2009;50:1948–53
24. Oh M, Tanaka T, Kobayashi M, et al. **Radio-copper-labeled Cu-ATSM: an indicator of quiescent but clonogenic cells under mild hypoxia in a Lewis lung carcinoma model.** *Nucl Med Biol* 2009;36:419–26
25. Frezza C, Zheng L, Tennant DA, et al. **Metabolic profiling of hypoxic cells revealed a catabolic signature required for cell survival.** *PLoS One* 2011;6:e24411
26. Nehmeh SA, Lee NY, Schroder H, et al. **Reproducibility of intratumor distribution of (18)F-fluoromisonidazole in head and neck cancer.** *Int J Radiat Oncol Biol Phys* 2008;70:235–42
27. Behin A, Hoang-Xuan K, Carpentier AF, et al. **Primary brain tumours in adults.** *Lancet* 2003;361:323–31
28. Kayama T, Yoshimoto T, Fujimoto S, et al. **Intratumoral oxygen pressure in malignant brain tumor.** *J Neurosurg* 1991;74:55–59

Diffusion Measures Indicate Fight Exposure–Related Damage to Cerebral White Matter in Boxers and Mixed Martial Arts Fighters

W. Shin, S.Y. Mahmoud, K. Sakaie, S.J. Banks, M.J. Lowe, M. Phillips, M.T. Modic, and C. Bernick



ABSTRACT

BACKGROUND AND PURPOSE: Traumatic brain injury is common in fighting athletes such as boxers, given the frequency of blows to the head. Because DTI is sensitive to microstructural changes in white matter, this technique is often used to investigate white matter integrity in patients with traumatic brain injury. We hypothesized that previous fight exposure would predict DTI abnormalities in fighting athletes after controlling for individual variation.

MATERIALS AND METHODS: A total of 74 boxers and 81 mixed martial arts fighters were included in the analysis and scanned by use of DTI. Individual information and data on fight exposures, including number of fights and knockouts, were collected. A multiple hierarchical linear regression model was used in region-of-interest analysis to test the hypothesis that fight-related exposure could predict DTI values separately in boxers and mixed martial arts fighters. Age, weight, and years of education were controlled to ensure that these factors would not account for the hypothesized effects.

RESULTS: We found that the number of knockouts among boxers predicted increased longitudinal diffusivity and transversal diffusivity in white matter and subcortical gray matter regions, including corpus callosum, isthmus cingulate, pericalcarine, precuneus, and amygdala, leading to increased mean diffusivity and decreased fractional anisotropy in the corresponding regions. The mixed martial arts fighters had increased transversal diffusivity in the posterior cingulate. The number of fights did not predict any DTI measures in either group.

CONCLUSIONS: These findings suggest that the history of fight exposure in a fighter population can be used to predict microstructural brain damage.

ABBREVIATIONS: TBI = traumatic brain injury; FA = fractional anisotropy; LD = longitudinal diffusivity; TD = transversal diffusivity; MD = mean diffusivity

Traumatic brain injury (TBI) has been reported in athletes involved in combat sports who are frequently exposed to repetitive blows to the head, such as boxers.^{1–8} This cumulative head trauma is thought to cause chronic traumatic encephalopathy as a result of chronic axonal injury.⁹ The clinical syndrome related to chronic traumatic encephalopathy in boxing is characterized by impulsive behavior, cognitive dysfunction, and in some cases, violence or suicide.¹⁰

Conventional MR imaging, such as T1-weighted and T2-weighted anatomic scans, cannot assess mild white matter disruption. Because DTI is sensitive to microstructural changes in white matter, this technique is often used to investigate white matter

integrity in patients with TBI.^{11–17} Previous studies have found that fractional anisotropy (FA) values in the corpus callosum,^{14,16,17} internal capsule,^{11,14,16,17} cingulum,¹⁴ and centrum semiovale^{11,14,16,17} are decreased in patients with TBI versus healthy control subjects. A longitudinal TBI study found that FA was decreased in the white matter of study participants because of decreased longitudinal diffusivity (LD) and increased transversal diffusivity (TD).¹³ Another study demonstrated that the peaks of whole-brain ADC histograms were significantly correlated with scores on the Glasgow Coma Scale in patients with TBI, indicating that a change in DTI values can predict functional deficit.¹⁸

A limited number of studies have investigated diffusion changes in the white matter of fighting athletes.^{7,8,19} These studies found that among fighting athletes, whole-brain diffusion is increased,⁸ FA is reduced in the genu and splenium of the corpus callosum and the posterior internal capsule,⁷ and FA is reduced and ADC increased in the lower brain, the splenium of the corpus callosum, and the lateral and dorsolateral cortical regions.¹⁹ Although these studies used age- and sex-matched control groups,

Received December 21, 2012; accepted after revision May 10, 2013.

From the Imaging Institute (W.S., S.Y.M., K.S., M.J.L., M.P.) and Neurological Institute (C.B.), Cleveland Clinic, Cleveland, Ohio; and Lou Ruvo Center for Brain Health (S.J.B., M.T.M.), Cleveland Clinic, Las Vegas, Nevada.

Please address correspondence to Wanyong Shin, PhD, Imaging Institute, 9500 Euclid Ave, Mail Code U-15, Cleveland, OH 44195; e-mail: wanyong.shin@gmail.com

<http://dx.doi.org/10.3174/ajnr.A3676>

Table 1: Pearson correlation between predictors

	Age	Years of Education	Weight	Number of Knockouts	Number of Fights	Years of Fighting
Age		0.288 ^b	0.268 ^a	0.321 ^b	0.092	0.511 ^b
Years of education			0.283 ^b	-0.009	0.013	0.055
Weight				0.061	0.025	0.010
Number of knockouts					0.057	0.250 ^a
Number of fights						0.520 ^b
Years of fighting						

^a Correlation is significant at the .01 level (2-tailed).

^b Correlation is significant at the .001 level (2-tailed).

variations among fighters in number of fights and number of knockouts have not been fully investigated. Zhang et al⁸ found that the number of hospitalizations for boxing injuries was positively correlated with the peak of the Gaussian-fitted brain tissue compartment in a whole-brain diffusion histogram in 24 professional boxers. However, this finding did not offer information regarding which regions were affected in hospitalized boxers.

In the present study, we sought to assess previous fight history and regional MR diffusion parameters to evaluate the relationship between microstructural brain damage and fight-related exposure. We hypothesized that previous fight exposure would predict DTI changes suggestive of microstructural damage in fighter populations.

MATERIALS AND METHODS

Fighter Population

The Professional Fighters' Brain Health Study was approved by the local institutional review board, and all participants provided informed consent. Participants in the Professional Fighters' Brain Health Study are athletes ages 18 and older who have achieved at least a fourth-grade reading level and are licensed in Nevada to fight professionally in one of the combat sports (boxing, mixed martial arts). In the Professional Fighters' Brain Health Study protocol, participants are scanned for a baseline evaluation and then annually over 4 years. Eligible participants in the current study had no MR-visible central nervous system disease or neurologic disorder.

Data from the first 199 professional fighters who visited for the baseline evaluation were used for this study. Information on sex, age, weight, years of education, type of fighting (boxing or mixed martial arts), years of fighting, number of fights, and number of knockouts was collected for each participant. Fifteen female fighters were excluded from the study to eliminate sex effects, and a 71-year-old male fighter was also excluded because his age made him an outlier. Missing data of individual information were deleted list-wise from 183 fighters in the analysis. A total of 155 male fighters (74 boxers and 81 mixed martial arts fighters) were included in the final analysis (Table 1).

MR Protocols

MR images were performed on a 3T Verio scanner with a 32-channel head coil (Siemens, Erlangen, Germany). 3D T1-weighted scans (voxel size = 1 × 1 × 1.2 mm³; TR/TE/TI = 2300/2.98/900 ms; flip angle = 9°; scan time = 9:14), T2-weighted scans (voxel size = 0.8 × 0.8 × 4 mm³; TR/TE = 5000/84 ms; 38 sections; scan time = 0:57), and FLAIR scans (voxel size = 0.8 × 0.8 × 4 mm³; TR/TE/TI = 7000/81/2220 ms; 38 sections; scan time = 2:36) were performed. A single-shot EPI scan was used to

acquire diffusion tensor mapping (TR/TE = 7000/91 ms; FOV = 240 × 240 mm²; voxel size = 2.5 × 2.5 × 2.5 mm³; 49 axial sections with no gap between sections; partial Fourier factor = 5/8; NEX = 1; 71 nonlinear diffusion-weighting gradients with b-value = 1000 seconds/mm² and eight b = 0 volumes for averaging; scan time = 8:24).

DTI Postprocessing

Field map-based distortion correction²⁰ was applied in the time-series diffusion images to unwarp EPI geometric distortion, and an iterative motion and eddy current artifact correction method was used²¹ before DTI parameter calculation. Subsequently, the diffusion tensor was calculated at each voxel with log-linear ordinary least squares.²² The tensors were diagonalized, yielding eigenvalues from which LD, TD, mean diffusivity (MD), and FA were calculated with the use of in-house software.²³ The detailed definition of DTI parameters is described with 3 eigenvectors ($\lambda_{1,2,3}$, and $\lambda_1 \geq \lambda_2 \geq \lambda_3$); LD = λ_1 , TD = $(\lambda_2 + \lambda_3)/2$, MD = $(\lambda_1 + \lambda_2 + \lambda_3)/3$, and FA = $\{[(\lambda_1 - \lambda_2)^2 + (\lambda_2 - \lambda_3)^2 + (\lambda_3 - \lambda_1)^2]/(\lambda_1^2 + \lambda_2^2 + \lambda_3^2)/2\}^{1/2}$.

ROI Analysis

Seventy-three ROIs in white matter (3 corpus callosum areas and 35 white matter regions in each hemisphere) and 7 subcortical gray matter regions in each hemisphere were defined in T1-weighted image space with the use of the FreeSurfer software package (<http://surfer.nmr.mgh.harvard.edu/>). The defined ROIs were aligned in DTI space by use of the Linear Image Registration Tool FLIRT (<http://www.fmrib.ox.ac.uk/>).²⁴ Average DTI values were calculated in each ROI. After a visual check, the caudal middle frontal, lateral orbitofrontal, medial orbitofrontal, parsorbitalis, rostral middle frontal, superior frontal, and frontal pole regions were excluded because of imperfect coregistration between the anatomic image and the unwrapped EPI image, caused by EPI geometric distortion in the frontal lobe area.

Statistical Analysis

Pearson correlation was calculated for fighter information (age, years of education, weight, number of knockouts, number of fights, and years of fighting). Years of fighting was highly correlated with age (correlation = 0.511; $P < .001$) and with number of fights (correlation = 0.520; $P < .001$); therefore, number of knockouts and number of fights were selected as fight-related predictors. Age, weight, years of education, number of knockouts, and number of fights were chosen as predictors to represent variance in independent measures (Table 1).

Multiple hierarchical linear regression analyses were performed to test the hypothesis that fight-related exposure (number

of knockouts and number of fights) could predict average DTI values in different regions. Age, weight, and years of education were controlled to ensure that they would not account for the hypothesized effects. Therefore, model 1 used age, weight, and years of education as predictors for DTI value ($DTI = \text{constant} + a_1 \times \text{age} + a_2 \times \text{weight} + a_3 \times \text{years of education}$). Model 2A used age, weight, years of education, and number of knockouts as predictors ($DTI = \text{constant} + b_1 \times \text{age} + b_2 \times \text{weight} + b_3 \times \text{years of education} + b_4 \times \text{number of knockouts}$), and model 2B

used age, weight, years of education, and number of fights as predictors ($DTI = \text{constant} + c_1 \times \text{age} + c_2 \times \text{weight} + c_3 \times \text{years of education} + c_4 \times \text{number of fights}$). Regions were defined as activated (ie, a fight-related exposure predicted DTI values) when the following criteria were met: 1) the significance change from model 1 to model 2A or 2B was significant, and 2) the linear regression result of model 2A or 2B was significant.

RESULTS

We found no significant ($P > .05$) differences between boxers and mixed martial arts fighters in age, weight, number of fights, or number of knockouts, but there was a significant difference between the groups in years of education ($P = .0045$; Table 2).

The number of knockouts among boxers predicted increased LD in the inferior parietal, isthmus cingulate, pericalcarine, precuneus, and amygdala areas and increased TD in the middle and posterior corpus callosum, isthmus cingulate, pericalcarine, precuneus, and amygdala regions after we

controlled for individual variations in age, weight, and years of education (Table 3). There was increased MD and decreased FA in the corresponding areas. Interestingly, in mixed martial arts fighters, the number of knockouts predicted only decreased FA in the posterior corpus callosum and increased TD in the posterior cingulate. In the posterior corpus callosum of both boxers and mixed martial arts fighters, the number of knockouts predicted decreasing FA, but the decreasing tendency or the magnitude of coefficient of the number of knockouts over FA was larger in boxers than in mixed martial arts fighters ($-18.90 \times 10^{-6} \text{ mm}^2/\text{s}$ versus $-7.27 \times 10^{-6} \text{ mm}^2/\text{s}$; Table 4).

The number of knockouts predicted decreased LD in the pars triangularis, decreased LD and TD in the pallidum, and increased FA in the caudate and putamen regions. The number of fights did not predict DTI values in boxers or mixed martial arts fighters. The average DTI values for the regions in which the number of knockouts predicted DTI values are presented in Table 5.

DISCUSSION

We found that the number of knockouts in fighting athletes, most prominently in the boxing group, predicted DTI changes after we controlled for age, weight, and education effects. This finding suggests that the number of knockouts experienced by boxers can predict microstructural damage in the brain, as represented by increased LD and TD. In contrast, the number of fights did not account for microstructural injury.

Table 2: Demographic data

	Boxers	Mixed Marital Arts Fighters
Age, y	28.0 ± 6.3	28.2 ± 4.8
Years of education ^a	12.7 ± 3.0	14.0 ± 2.4
Weight, kg	74.5 ± 15.8	78.7 ± 10.9
Number of fights	13.2 ± 15.7	12.1 ± 14.1
Number of knockouts	1.1 ± 2.0	1.0 ± 2.1

^aSignificantly different between groups ($P < .01$).

Table 3: Areas in which number of knockouts predicted DTI values after controlling for individual variation

ROI	Boxers				Mixed Martial Arts Fighters	
	LD	TD	MD	FA	TD	FA
Corpus callosum posterior		a		b		a
Corpus callosum central		a	a			
Cuneus				L ^a		
Inferior parietal	L ^a					
Isthmus cingulate	L ^c , R ^b	L ^c , R ^c	L ^c , R ^c			
Pars triangularis	L ^a					
Pericalcarine	L ^b , R ^a	L ^c , R ^b	L ^c , R ^b			
Posterior cingulate					R ^a	
Precuneus	R ^a	R ^a	L ^a , R ^a			
Caudate				L ^a		
Putamen				L ^a , R ^a		
Pallidum	L ^a , R ^b	L ^a , R ^a	L ^a , R ^b			
Amygdala	L ^a , R ^c	R ^b	L ^a , R ^c			

Note:—L and R represent the left and right hemispheres, respectively.

^a $P < .05$.

^b $P < .01$.

^c $P < .001$.

Table 4: Coefficients for number of knockouts for the areas in which number of knockouts predicted DTI values after controlling for individual variation

ROI	Boxers				Mixed Martial Arts Fighters	
	LD	TD	MD	FA	TD	FA
Corpus callosum posterior		26.48		-18.9		-7.27
Corpus callosum central		20.28	18.19			
Cuneus				(L) -4.60		
Inferior parietal	(L) 6.56					
Isthmus cingulate	(L) 24.24 (R) 16.73	(L) 19.25 (R) 22.61	(L) 20.91 (R) 20.65			
Pars triangularis	(L) -7.61					
Pericalcarine	(L) 15.80 (R) 10.05	(L) 24.26 (R) 15.92	(L) 21.44 (R) 13.96			
Posterior cingulate					(R) 5.49	
Precuneus	(R) 8.34	(R) 9.90	(L) 6.63 (R) 9.38			
Caudate				(L) 5.72		
Putamen				(L) 3.30 (R) 4.74		
Pallidum	(L) -14.60 (R) -19.30	(L) -10.10 (R) -18.20	(L) -11.60 (R) -18.60			
Amygdala	(L) 12.38 (R) 29.06	(R) 12.80	(L) 10.12 (R) 18.22			

Note:—L and R represent the left and right hemispheres, respectively.

A coefficient unit is $10^{-6} \text{ mm}^2/\text{s}$ for LD, TD, and MD, and 10^{-3} for FA.

Table 5: Average DTI values for the areas in which number of knockouts predicted DTI values

ROI	Boxers				Mixed Martial Arts Fighters	
	LD	TD	MD	FA	TD	FA
Corpus callosum posterior	1.617	0.689	0.998	0.525	0.656	0.546
Corpus callosum central	1.533	0.679	0.964	0.506	0.653	0.512
Cuneus	0.966	0.727	0.807	0.189	0.712	0.194
Inferior parietal	1.007	0.657	0.774	0.280	0.648	0.284
Isthmus cingulate	1.292	0.569	0.810	0.481	0.540	0.498
Pars triangularis	0.956	0.650	0.752	0.266	0.635	0.270
Pericalcarine	1.128	0.787	0.901	0.238	0.769	0.250
Posterior cingulate	1.209	0.570	0.783	0.448	0.543	0.463
Precuneus	1.086	0.647	0.793	0.326	0.631	0.337
Caudate	1.235	0.966	1.056	0.170	0.949	0.168
Putamen	0.879	0.610	0.700	0.240	0.602	0.246
Pallidum	0.808	0.515	0.613	0.323	0.518	0.315
Amygdala	1.125	0.864	0.951	0.181	0.854	0.184

Note:—A coefficient unit is $10^{-3} \text{ mm}^2/\text{s}$ for LD, TD, and MD and 0–1 for FA.

We found that increased TD resulted in increased MD and decreased FA in the corpus callosum among boxers. The corpus callosum is an area known to be involved in TBI.^{7,16,17,25–30} Several studies have demonstrated increased MD and/or decreased FA in various white matter regions among patients with mild TBI versus matched control subjects.^{7,17,31} Inglese et al¹⁷ found a significant reduction in FA in the corpus callosum, internal capsule, and centrum semiovale and a significant increase in MD in the corpus callosum and internal capsule in 46 patients with mild TBI. In a study of 49 professional boxers who had been exposed to repeated blows to the head, Zhang et al⁷ observed a significant decrease in FA in the anterior and posterior corpus callosum, as well as a significant decrease in FA and an increase in MD in the internal capsule. In a study of 24 boxers, Zhang et al⁸ also found that the mean diffusion constant of the brain tissue was significantly correlated with the times of hospitalization for boxing injuries ($P < .05$) but not with age when boxing was started, total rounds, years of fighting, or number of wins and losses. Cubon et al³¹ reported that college athletes with mild TBI (5 men and 5 women) who had concussion showed significantly increased MD in the left hemisphere, spanning the sagittal striatum, retrolenticular section of the internal capsule, and the posterior thalamic radiation (by use of tract-based spatial statistics), but there was no significant change in FA. In a recent study, Zhang et al³² found no significant differences in fMRI and DTI results among patients with mild TBI versus control subjects; the authors suggested that these regional variations in FA and MD changes in patients with mild TBI might be the result of differing timeframes, technological issues involved in DTI, and different methodologic approaches.

Besides the corpus callosum, the areas in which increased LD was predicted by the number of knockouts among boxers were identical to the regions in which increased TD was predicted by the number of knockouts with the exception of the inferior parietal region. Our results of increased LD and TD among boxers suggests that knockouts could induce irreversible myelin damage, as has been discussed previously.³⁰ Kraus et al³⁰ found that patients with mild to severe TBI showed increased TD and LD in all white matter regions; patients with mild TBI also showed increased LD in the sagittal striatum and superior longitudinal fasciculus but not TD in any regions versus control subjects. This

study also found that moderate to severe TBI groups showed severe impairment of neuropsychological assessment, compared with mild TBI and control groups. We have performed cognitive testing for the participants in our study, and further analyses will be conducted to assess whether our DTI findings are correlated with individual cognitive assessments.

In our study, decreased LD and/or TD in the pars triangularis and pallidum were predicted by the number of knockouts. In a previous study, Bazarian et al³³ found decreased median MD and increased median FA in the posterior corpus callosum in 6 patients with mild TBI when scans were performed within 4 hours after the injury; MD was also decreased in the left anterior internal capsule in ROI analysis. Wilde et al³⁴ found increased FA in adolescents with mild TBI who were scanned within an average of 2.7 days (1–6 days) after the injury. McAllister et al³⁵ showed that strain rate positively predicted FA changes before and 10 days after head injury in the corpus callosum in 10 athletes. Mayer et al³⁶ also found increased FA in patients with mild TBI during the semi-acute injury period (average of 12 days after injury) and confirmed this finding in a replicate experiment (average of 15.6 days after injury).³⁷ This increased FA in semi-acute mild TBI may be induced by inflammation and/or cytotoxic edema and could be transient. A recent study by Wilde et al³⁸ assessed FA values in patients with mild TBI over time during the semi-acute period (from day 1 to days 7–8 after injury). Our study did not consider time after the onset of head injury (eg, the latest knockout). However, boxers who are exposed to repeated blows to the head, should be considered separately from patients with mild TBI, who generally have a single incidence of head injury. The decreased LD and TD among boxers in our study might be related to this repeated pattern of brain tissue injury and recovery. Further studies are needed to assess this possibility.

Although boxers in our study had increased LD and TD in various white matter regions predicted by number of knockouts, mixed martial arts fighters had decreased FA in the posterior corpus callosum and increased TD in the posterior cingulate region only predicted by the number of knockouts. Furthermore, when considering the posterior corpus callosum where the number of knockouts predicted FA in both boxers and the mixed martial arts fighters, the higher magnitude of coefficient for the number of knockouts over FA in boxers versus mixed martial arts fighters was

observed ($-18.90 \times 10^{-6} \text{ mm}^2/\text{s}$ versus $-7.27 \times 10^{-6} \text{ mm}^2/\text{s}$). This may reflect the different natures of boxing and mixed martial arts. Boxers mainly target the head of their opponent, which exposes the boxers to a higher risk of repetitive head injuries; mixed martial arts fighters use striking and grappling techniques.

DTI is known to be affected by a patient sex,³⁹ age,³⁹⁻⁴² intelligence level,^{43,44} and body weight.⁴⁵ We therefore included only male fighters in our study and used multiple hierarchical linear regression analyses to control for age, years of education, and weight. Although we assumed that body weight was an individual factor for the purpose of this analysis, it is possible that weight plays a role in the severity of brain injury, as a blow from a heavy-weight fighter would be expected to cause more damage than a blow from a light-weight fighter. In future research, weight class should be considered as an individual factor. We also plan to recruit an age- and education-matched control group for future studies of longitudinal MR changes, but we believe that our findings in the current study are not limited by the absence of a control group.

A previous study suggested that sports-related concussions are often unreported by athletes.⁴⁶ For this study, we used the number of knockouts in both the amateur and professional career periods, and the number of knockouts includes not only the loss of consciousness, leading to down more than 10 counts, but also the technical knockout including referee stop, corner stop, and multiple knockdowns caused by lack of the self-defense ability. The information of the number of knockouts from professional fights was collected and verified from the fighters' official log, whereas the information from amateur fights was collected through a self-reporting questionnaire. Inaccuracy in self-reporting may therefore be a confounding variable. Additionally, there probably are differences in the threshold of trauma required to cause a knockout in individuals, a factor we plan to address in future research.

This study involved data from one time point, but we intend to follow these fighters for at least 4 years. Although we do not know which, if any, of these fighters will have development of chronic traumatic encephalopathy, the results of the current study suggest that measurable microstructural changes or diffusion metrics can be predicted by history of repeated head injuries or severity in fighters' careers after controlling for individual variations.

ACKNOWLEDGMENTS

This work was supported by the Imaging Institute, Cleveland Clinic. The authors gratefully acknowledge Megan Griffiths for editing the manuscript and Dr HangJoon Jo for the helpful discussion of the data analysis. The authors also thank MR imaging technologist Trish Lake for technical support and research assistants Triny Cooper and Isaac Santa Ana for their work.

Disclosures: Wanyong Shin—RELATED: Grant: Lincy Foundation.* Ken Sakaie—UNRELATED: Grants/Grants Pending: NIH, NMSS, DOD. Mark Lowe—RELATED: Grant: Lincy Foundation.* Michael Phillips—RELATED: Grant: Lincy Foundation.* Charles Bernick—RELATED: Grant: Lincy Foundation*; UNRELATED: Consultancy: Bayer; Payment for Lectures (including service on speakers bureaus): Novartis, UCB, Teva (*money paid to institution).

REFERENCES

- Bledsoe GH, Li G, Levy F. Injury risk in professional boxing. *South Med J* 2005;98:994–98
- Blonstein JL. Letter: Traumatic encephalopathy in a young boxer. *Lancet* 1974;2:1213
- Guterman A, Smith RW. Neurological sequelae of boxing. *Sports Med* 1987;4:194–210
- Handratta V, Hsu E, Vento J, et al. Neuroimaging findings and brain-behavioral correlates in a former boxer with chronic traumatic brain injury. *Neurocase* 2010;16:125–34
- Harvey PK, Davis JN. Traumatic encephalopathy in a young boxer. *Lancet* 1974;2:928–29
- Saing T, Dick MC, Nelson PT, et al. Frontal cortex neuropathology in dementia pugilistica. *J Neurotrauma* 2012;29:1054–70
- Zhang L, Heier LA, Zimmerman RD, et al. Diffusion anisotropy changes in the brains of professional boxers. *AJNR Am J Neuroradiol* 2006;27:2000–04
- Zhang L, Ravdin LD, Relkin N, et al. Increased diffusion in the brain of professional boxers: a preclinical sign of traumatic brain injury? *AJNR Am J Neuroradiol* 2003;24:52–57
- McKee AC, Cantu RC, Nowinski CJ, et al. Chronic traumatic encephalopathy in athletes: progressive tauopathy after repetitive head injury. *J Neuropathol Exp Neurol* 2009;68:709–35
- Mendez MF. The neuropsychiatric aspects of boxing. *Int J Psychiatr Med* 1995;25:249–62
- Yuan W, Holland SK, Schmithorst VJ, et al. Diffusion tensor MR imaging reveals persistent white matter alteration after traumatic brain injury experienced during early childhood. *AJNR Am J Neuroradiol* 2007;28:1919–25
- Wu TC, Wilde EA, Bigler ED, et al. Longitudinal changes in the corpus callosum following pediatric traumatic brain injury. *Dev Neurosci* 2010;32:361–73
- Sidaros A, Engberg AW, Sidaros K, et al. Diffusion tensor imaging during recovery from severe traumatic brain injury and relation to clinical outcome: a longitudinal study. *Brain* 2008;131:559–72
- Rutgers DR, Toulgoat F, Cazejust J, et al. White matter abnormalities in mild traumatic brain injury: a diffusion tensor imaging study. *AJNR Am J Neuroradiol* 2008;29:514–19
- Matthews PM. Brain imaging of multiple sclerosis: the next 10 years. *Neuroimaging Clin North Am* 2009;19:101–12
- Xu J, Rasmussen IA, Lagopoulos J, et al. Diffuse axonal injury in severe traumatic brain injury visualized using high-resolution diffusion tensor imaging. *J Neurotrauma* 2007;24:753–65
- Inglese M, Makani S, Johnson G, et al. Diffuse axonal injury in mild traumatic brain injury: a diffusion tensor imaging study. *J Neurosurg* 2005;103:298–303
- Shanmuganathan K, Gullapalli RP, Mirvis SE, et al. Whole-brain apparent diffusion coefficient in traumatic brain injury: correlation with Glasgow Coma Scale score. *AJNR Am J Neuroradiol* 2004;25:539–44
- Chappell MH, Ulug AM, Zhang L, et al. Distribution of microstructural damage in the brains of professional boxers: a diffusion MRI study. *J Magn Reson Imaging* 2006;24:537–42
- Jezzard P, Balaban RS. Correction for geometric distortion in echo planar images from B0 field variations. *Magn Reson Med* 1995;34:65–73
- Sakaie KE, Shin W, Curtin KR, et al. Method for improving the accuracy of quantitative cerebral perfusion imaging. *J Magn Reson Imaging* 2005;21:512–19
- Basser PJ, Mattiello J, LeBihan D. MR diffusion tensor spectroscopy and imaging. *Biophys J* 1994;66:259–67
- Basser PJ, Pierpaoli C. Microstructural and physiological features of tissues elucidated by quantitative-diffusion-tensor MRI. *J Magn Reson* 1996;111:209–19
- Jenkinson M, Smith S. A global optimisation method for robust affine registration of brain images. *Med Image Analysis* 2001;5:143–56
- Rutgers DR, Fillard P, Paradot G, et al. Diffusion tensor imaging characteristics of the corpus callosum in mild, moderate, and severe traumatic brain injury. *AJNR Am J Neuroradiol* 2008;29:1730–35

26. Schaefer PW, Huisman TA, Sorensen AG, et al. **Diffusion-weighted MR imaging in closed head injury: high correlation with initial Glasgow Coma Scale score and score on modified Rankin Scale at discharge.** *Radiology* 2004;233:58–66
27. Wilde EA, Chu Z, Bigler ED, et al. **Diffusion tensor imaging in the corpus callosum in children after moderate to severe traumatic brain injury.** *J Neurotrauma* 2006;23:1412–26
28. Farbota KD, Bendlin BB, Alexander AL, et al. **Longitudinal diffusion tensor imaging and neuropsychological correlates in traumatic brain injury patients.** *Front Hum Neurosci* 2012;6:160
29. Wang JY, Bakhadirov K, Abdi H, et al. **Longitudinal changes of structural connectivity in traumatic axonal injury.** *Neurology* 2011;77:818–26
30. Kraus MF, Susmaras T, Caughlin BP, et al. **White matter integrity and cognition in chronic traumatic brain injury: a diffusion tensor imaging study.** *Brain* 2007;130:2508–19
31. Cubon VA, Putukian M, Boyer C, et al. **A diffusion tensor imaging study on the white matter skeleton in individuals with sports-related concussion.** *J Neurotrauma* 2011;28:189–201
32. Zhang K, Johnson B, Pennell D, et al. **Are functional deficits in concussed individuals consistent with white matter structural alterations: combined FMRI & DTI study.** *Exp Brain Res Experimentelle Hirnforschung* 2010;204:57–70
33. Bazarian JJ, Zhong J, Blyth B, et al. **Diffusion tensor imaging detects clinically important axonal damage after mild traumatic brain injury: a pilot study.** *J Neurotrauma* 2007;24:1447–59
34. Wilde EA, McCauley SR, Hunter JV, et al. **Diffusion tensor imaging of acute mild traumatic brain injury in adolescents.** *Neurology* 2008;70:948–55
35. McAllister TW, Ford JC, Ji S, et al. **Maximum principal strain and strain rate associated with concussion diagnosis correlates with changes in corpus callosum white matter indices.** *Ann Biomed Eng* 2012;40:127–40
36. Mayer AR, Ling J, Mannell MV, et al. **A prospective diffusion tensor imaging study in mild traumatic brain injury.** *Neurology* 2010;74:643–50
37. Ling JM, Pena A, Yeo RA, et al. **Biomarkers of increased diffusion anisotropy in semi-acute mild traumatic brain injury: a longitudinal perspective.** *Brain* 2012;135:1281–92
38. Wilde EA, McCauley SR, Barnes A, et al. **Serial measurement of memory and diffusion tensor imaging changes within the first week following uncomplicated mild traumatic brain injury.** *Brain Imaging Behav* 2012;6:319–28
39. Chepuri NB, Yen YF, Burdette JH, et al. **Diffusion anisotropy in the corpus callosum.** *AJNR Am J Neuroradiol* 2002;23:803–08
40. Pfefferbaum A, Sullivan EV. **Increased brain white matter diffusivity in normal adult aging: relationship to anisotropy and partial voluming.** *Magn Reson Med* 2003;49:953–61
41. Ardekani S, Kumar A, Bartzokis G, et al. **Exploratory voxel-based analysis of diffusion indices and hemispheric asymmetry in normal aging.** *Magn Reson Imaging* 2007;25:154–67
42. Giorgio A, Santelli L, Tomassini V, et al. **Age-related changes in grey and white matter structure throughout adulthood.** *NeuroImage* 2010;51:943–51
43. Mabbott DJ, Noseworthy MD, Bouffet E, et al. **Diffusion tensor imaging of white matter after cranial radiation in children for medulloblastoma: correlation with IQ.** *Neuro-Oncology* 2006;8:244–52
44. Yu C, Li J, Liu Y, et al. **White matter tract integrity and intelligence in patients with mental retardation and healthy adults.** *NeuroImage* 2008;40:1533–41
45. Xu J, Li Y, Lin H, et al. **Body mass index correlates negatively with white matter integrity in the fornix and corpus callosum: a diffusion tensor imaging study.** *Hum Brain Mapp* 2013;34:1044–52
46. McCrea M, Hammeke T, Olsen G, et al. **Unreported concussion in high school football players: implications for prevention.** *Clin J Sport Med* 2004;14:13–17

Local and Global Fiber Tractography in Patients with Epilepsy

C. Anastasopoulos, M. Reisert, V.G. Kiselev, T. Nguyen-Thanh, A. Schulze-Bonhage, J. Zentner, and I. Mader



ABSTRACT

BACKGROUND AND PURPOSE: Fiber tractography is increasingly used in the preoperative evaluation of endangered fiber bundles. From a clinical point of view, an accurate and methodologically transparent procedure is desired. Our aim was to evaluate the recently described global tracking algorithm compared with other established methods, such as deterministic and probabilistic tractography.

MATERIALS AND METHODS: Twenty patients, candidates for excision of epileptogenic lesions, were subjected to higher-angular resolution diffusion imaging–based fiber tractography. Seed points were created without manual bias, predominantly by FreeSurfer and voxel-based atlases. We focused on 2 important fiber bundles, namely the descending motor pathways and the optic radiation. Postoperatively, the accuracy of the predicted fiber route was controlled by structural MR imaging and by inflicted functional deficits.

RESULTS: Among the 3 evaluated methods, global tracking was the only method capable of reconstructing the full extent of the descending motor pathways, including corticobulbar fibers from the area of face representation. Still, probabilistic tractography depicted the optic radiation better, especially the Meyer loop. The deterministic algorithm performed less adequately.

CONCLUSIONS: The probabilistic method seems to be the best balance between computational time and effectiveness and seems to be the best choice in most cases, particularly for the optic radiation. If, however, a detailed depiction of the fiber anatomy is intended and tract crossings are implicated, then the computationally time-consuming global tracking should be preferred.

ABBREVIATIONS: DMP = descending motor pathways; FA = fractional anisotropy; FACT = Fiber Assignment by Continuous Tractography; OR = optic radiation; SLF = superior longitudinal fascicle

Before neurosurgical operations, especially those demanding resection of lesions adjacent to functionally critical areas, the structural and functional anatomy of the region must be evalu-

ated. In epilepsy neurosurgery, where protection of “eloquent” brain areas is essential, knowledge of the fiber course in altered anatomic conditions is beneficial. Therefore, diffusion tractography has been increasingly used for neurosurgical planning.¹

Tractography algorithms use the information that is obtained by multiple-gradient DWI on the basis of the anisotropic character of motion of free water molecules along myelinated fibers.² Various tractography algorithms are available, with 2 main categories being local (further subdivided into deterministic and probabilistic) and global methods (On-Line Fig 1). The deterministic fiber assignment by continuous tractography (FACT) algorithm is increasingly used for preoperative and intraoperative tractography.^{3,4} Most deterministic algorithms follow the principal orientation of diffusion. This approach leads to erroneous results, if there are fibers within a voxel running in different directions.⁵ In addition, fibers with a strong curvature may be difficult to reconstruct. For example, the extent of the optic radiation (OR) of the Meyer loop is frequently underestimated.⁶ Probabilistic tractography assesses the probability that a voxel is connected to a given start point, by means of iterative random walks.⁷ This method exploits the statistical nature of the information ob-

Received February 21, 2013; accepted after revision April 24.

From the Clinic of Neuropediatrics and Neuromuscular Diseases (C.A.), Medical Physics, Department of Radiology (M.R., V.G.K.), Epilepsy Center (A.S.-B.), and Departments of Neurosurgery (J.Z.), and Neuroradiology (I.M.), University Medical Center Freiburg, Freiburg, Germany; and Department of Radiology (T.N.-T.), Hue University College of Medicine and Pharmacy, Hué, Vietnam.

T.N.T. and I.M. were supported by the Comprehensive Cancer Center Freiburg, Freiburg, Germany (Seeding Grant 1027013110). V.G.K. and I.M. were supported by the German Research Council (DFG: KI 1089/3-1, MA 2343/4-1).

Paper previously presented in part at: 8th Annual World Congress of IBMISPS on Brain, Spinal Cord Mapping and Image Guided Therapy, June 8–10, 2011; San Francisco, California.

Please address correspondence to Constantin Anastasopoulos, Clinic of Neuropediatrics and Neuromuscular Diseases, Pediatric Hospital, University Medical Center Freiburg, Mathildenstr. 1, 79106 Freiburg, Germany; e-mail: constantin.anastasopoulos@uniklinik-freiburg.de

 Indicates open access to non-subscribers at www.ajnr.org

 Indicates article with supplemental on-line table.

 Indicates article with supplemental on-line figures.

<http://dx.doi.org/10.3174/ajnr.A3752>

tained by DWI and determines the most probable mathematic pathway.⁸ In contrast, global methods process the entire diffusion information simultaneously and generate a whole-brain reconstruction. Global tracking simulates an annealing procedure where—during a “decrease of temperature”—line elements of subvoxel size, representing the diffusion anisotropy, bind together. Finally, only aligned elements remain bound to each other according to the diffusion information of the brain.⁹ It has been suggested that global tractography overcomes the common issue of fiber crossings.¹⁰ The superiority of this algorithm has been proven in a study comparing 10 different algorithms on a phantom that mimics fiber crossing and bending.¹¹ The main disadvantage of global methods is the long calculation time, whereas the disadvantage of local methods, particularly the FACT algorithm, is the accumulation of errors during the algorithm propagation.⁵

Newer tractography algorithms outrank certain features of older algorithms. For example, probabilistic tractography is more robust than deterministic tractography in areas of high uncertainty (ie, areas of high signal noise or fiber crossings).¹² To date, it is not clear which particular tractographic approach has the appropriate features for certain anatomic or clinical questions. Therefore, it is essential to perform comparisons, not only by means of phantoms,¹¹ but also in an appropriate clinical setting. This study aimed at evaluating the clinical usefulness of global tractography as a preoperative tool and compared its performance with the widely used FACT and a probabilistic algorithm. The focus was on the depiction of the major fiber structures’ descending motor pathways (DMP) or OR.

MATERIALS AND METHODS

Patients

A total of 20 prospectively recruited consecutive patients (mean age, 27 years; age range, 3–66 years; 11 women) with drug-resistant epilepsy due to various supratentorial lesions were investigated. The inclusion criteria were 1) the presence of a benign-appearing lesion, adjacent to either the corticospinal tract or the OR; and 2) intended total lesion resection or minor loss of function postoperatively. The exclusion criterion was a malignant appearance (eg, major space-occupying lesion) with perifocal edema. Seven patients presented with focal cortical dysplasia, 5 with cavernoma, 3 with intra-axial low-grade tumors, 2 with hippocampal sclerosis, 1 with perinatal ischemic stroke, 1 with schizencephaly, and 1 with an arteriovenous malformation (On-line Table). The treatment procedure in each patient was individually determined in consensus decision-making sessions among neurologists, neuroradiologists, and neurosurgeons in the Neurocenter of the University Medical Center (Freiburg, Germany). All available information, including tractography results, was taken into account. The interval between preoperative evaluation and operation ranged from 3–19 days. The rationale behind tractography in the preoperative planning was the concern about the extent of the intended resection and subsequent functional outcome. The tractography analysis was performed by 2 neuroradiologists in training (C.A. and T.N.T.) under supervision of a senior neuroradiologist (I.M.). Preoperative and postoperative visual fields were assessed by Goldmann perimetry. The postop-

erative seizure outcome was assessed from 6–17 months after surgery (mean, 10 months) and was categorized according to the Engel and the International League Against Epilepsy classifications.^{13,14} The procedures were approved by the local ethics committee.

Image Acquisition

All measurements were performed by means of a 3T scanner (Magnetom Trio; Siemens, Erlangen, Germany). For DWI, a single-shot spin-echo-planar imaging sequence by use of a 12-channel head coil was applied (TR, 10.5 s; TE, 96 ms; resolution, 2³ mm³; 61 diffusion-encoding directions; effective b-value, 1000 s/mm²). The orientation distribution function in each voxel was extracted from higher-angular resolution diffusion imaging.¹⁵ In all patients, a T1WI magnetization prepared rapid acquisition of gradient-echo sequence with a 1-mm³ resolution was obtained (TR, 2.2 s; TE, 2.15 ms; TI, 1.1 ms) preoperatively and postoperatively. Preoperative structural images were coregistered with the DWI and were subsequently segmented into white matter, gray matter, and CSF by use of Statistical Parametric Mapping 8 (Wellcome Department of Imaging Neuroscience, London, UK), running under Matlab2009b (MathWorks, Natick, Massachusetts). A brain mask was created, restricting the algorithms’ calculations to the white matter and the adjacent 2 voxels of gray matter volume.

Seed Point Selection

A 2-seed point procedure was used for fiber tractography. For each of the 2 fiber structures, 2 ROIs served as end points: 1 cortical and 1 either in the ipsilateral brain stem for the DMP or the thalamus for the OR. In patients with obvious anatomic deviations (patients 3 and 9), motor cortex seed points were derived from fMRI. For fMRI, contiguous multisection echo-planar imaging was used (TR, 2.61 s; TE, 30 ms, 3³ mm³, active fist-clenching and tongue movement vs rest, respectively, 1 Hz, 9 measurements). After preprocessing, the peak maxima of the t-values of the statistical maps ($P_{\text{corr(FWE)}} < .05$) were enlarged by 3 mm in every direction to extend into white matter and were taken as seed points for the primary motor area.

In all other patients, cortical seed points were obtained by a standard automated parcellation with the FreeSurfer (<http://surfer.nmr.mgh.harvard.edu/>) algorithm.¹⁶ Brain stem/thalamic seed points were derived from a voxel-based atlas.¹⁷ The ROIs were registered to the individual coordinate system of the patients’ T1WI and DWI datasets. The precentral gyrus served as the cortical origin and the ipsilateral cerebral crus ROI as the second end point of the DMP in patients #1–10; the pericalcarine cortex served as the cortical end point for the OR and the lateral geniculate nucleus as the second end point for the OR in patients #11–20. Although the ROIs were atlas derived, some minor corrections were made: 1) the size of the brain stem ROI was halved to the ipsilateral cerebral peduncle; and 2) the lateral geniculate nucleus ROI was enlarged in every direction up to 4 mm, correcting its relatively small atlas size to match neuroanatomic studies.¹⁸

Fiber Tractography

We made no manual interference when we applied the tractography methods. All 3 tractography methods were successively used

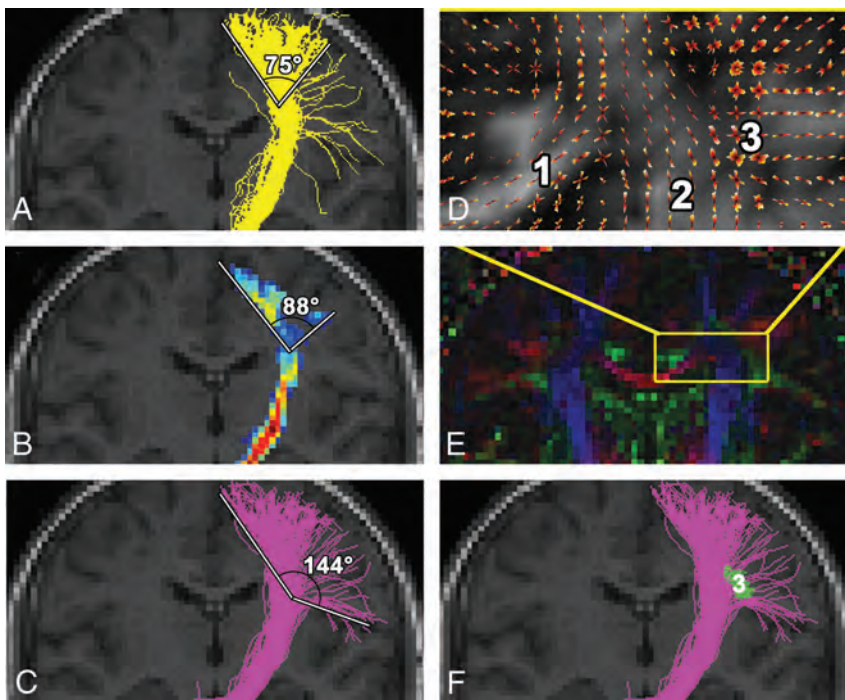


FIG 1. Depiction of the left descending motor pathways on the healthy side in patient 3 and the fan angle measurement performed. FACT (A), probabilistic (B), and global (C and F) tractography show approximately the same route and extent along the internal capsule. Note differences in the reconstruction of fibers arising from the lateral area of face cortical representation. These corticobulbar fibers are best depicted by global tracking, as this method is least susceptible to fiber crossings in the semiovale center (D) (orientation distribution function of the diffusion signal) and (E) (principal direction of the diffusion tensor shown as color-coded map) between the corpus callosum (1), corona radiata (2), and SLF (3). FACT and probabilistic tractography cannot overcome the crossing with the SLF (3, green in F, oriented perpendicular to the plane of the figure), with the results shown in On-Line Fig 2 in mind.

under the same conditions: 1) all algorithms were applied on the same diffusion data; and 2) the brain mask and 3) the pair of ROIs used were the same. The computation time span on a standard 64-bit platform was 30 minutes for FACT, 3 hours for probabilistic maps of connectivity, and 20 hours for global tracking. The results of tractography in the preoperative planning were analyzed by the same in-house visualization tool (http://www.uniklinik-freiburg.de/mr/live/arbeitsgruppen/diffusion/fibertools_en.html) and were superimposed on preoperative and, in a second step, postoperative structural imaging. For comparison of the tractography results for the DMP, the fan angle from the fibers arising in the foot area to the fibers from the face area was measured (Fig 1). The results of the different tractography methods for the OR were compared based on the presence of the Meyer loop and its distance to the tip of the temporal pole.

For FACT, particular stopping criteria were fractional anisotropy (FA) < 0.1 and a curvature between 2 consecutive steps $\geq 90^\circ$. The liberal curvature was chosen to allow the detection of strong fiber bending.

In our current study, an extension to the probabilistic index of connectivity method⁷ was adopted, which calculates the probability that a voxel is connected to the selected ROI by performing random walk iterations and counting the visits. At the same time, the directional information of the curves passing through the voxel is preserved. The probability information of voxels receiving visits from opposing directions creates probabilistic maps of

connectivity.⁸ It allows the depiction of the mathematically most probable pathway between 2 ROIs (On-Line Fig 1). Parameters were 10^5 random walk iterations from every seed region voxel and applying an exponent of 4 to the eigenvalues, whereas the stopping criterion was FA < 0.1.

Global fiber tractography methods reconstruct all brain fibers simultaneously by finding a configuration that best describes the diffusion data.^{9,10,19} In global tracking, the reconstructed fibers are built by small line segments (initially hundreds in each voxel) that represent the diffusion anisotropy (On-Line Fig 1E–G). During optimization, an iterative process is repeated with an order of 10^8 iterations, and the elements bind together in an annealing simulation. This behavior is governed by an interaction between the line elements and the measured data. A detailed description of global tracking is given by Reisert et al.¹⁰

RESULTS

Fiber Tractography in Presurgical Planning

In patients 1–10, preoperative reconstruction of the DMP by FACT and probabilistic algorithm, in both healthy and pathologic hemispheres, involved fibers arising from the precentral gyrus. Pre-

dominantly fibers from the arm and foot cortical representation, through the internal capsule and to the cerebral peduncle, were reconstructed. The mean fan angle for FACT was 92° (range, 66 – 114°) and for the probabilistic algorithm, 97° (range, 50 – 122° ; Fig 1). In contrast, the extent of the DMP pathways achieved by global tracking was broader in all patients, with multiple fibers starting from the foot, trunk, arm, and face areas of the precentral gyrus, achieving a mean fan angle of 138° (range, 118 – 156° ; Fig 1). This algorithm was thus capable of depicting corticospinal, as well as corticobulbar, pathways.

In patients 11–20, the FACT algorithm depicted the stem of the OR running from the lateral geniculate nucleus caudally toward the ipsilateral pericalcarine cortex. The Meyer loop could be partially depicted in 3 of 10 patients (mean distance to the tip of the temporal pole, 41 mm; range, 39–43 mm). The probabilistic maps of connectivity depicted the OR in all 10 patients, including the Meyer loop in 9 of 10 patients (mean distance to the tip of the temporal pole, 34 mm; range, 23–40 mm). Global tracking reconstructed only the main part of the OR and failed to reconstruct the Meyer loop in all 10 patients. In patient #13, reconstruction of the Meyer loop was missing in all methods because of impaired image quality caused by motion artifacts.

Postoperative Evaluation

In 7 of 10 patients with tractography of the DMP and in 8 of 10 patients with tractography of the OR, an excision of the alleged or

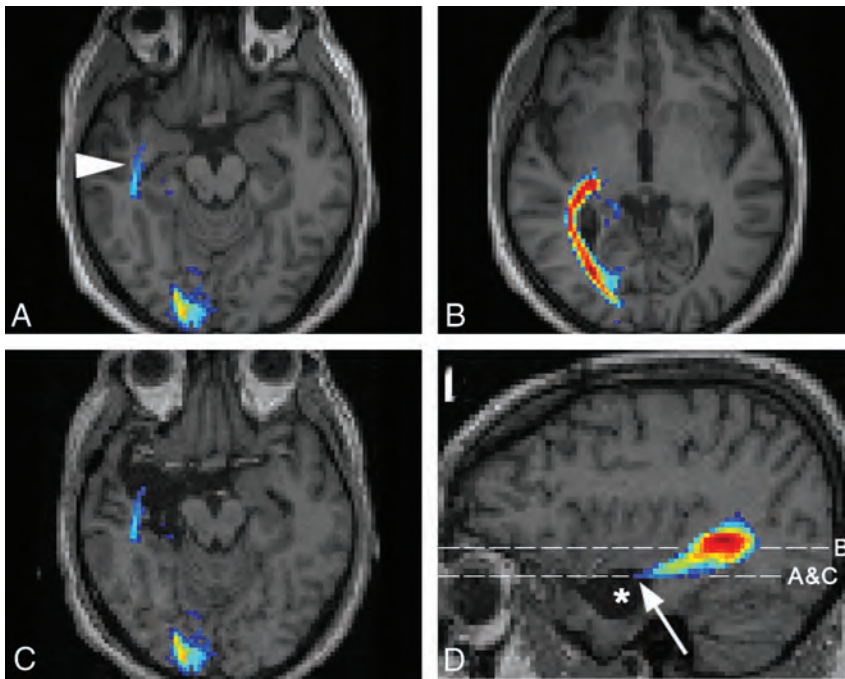


FIG 2. Assessment of the OR in patient 14 with a right hippocampal sclerosis. Results of probabilistic tractography (A) for the right Meyer loop (arrowhead) and (B) for the main part of the OR are shown. The preoperative OR reconstruction by the probabilistic algorithm is superimposed onto postoperative images (C and D, asterisk = resection area, arrow = anterior extent of Meyer loop). Postoperatively, the patient presented with a partial visual field defect in the left upper quadrant.

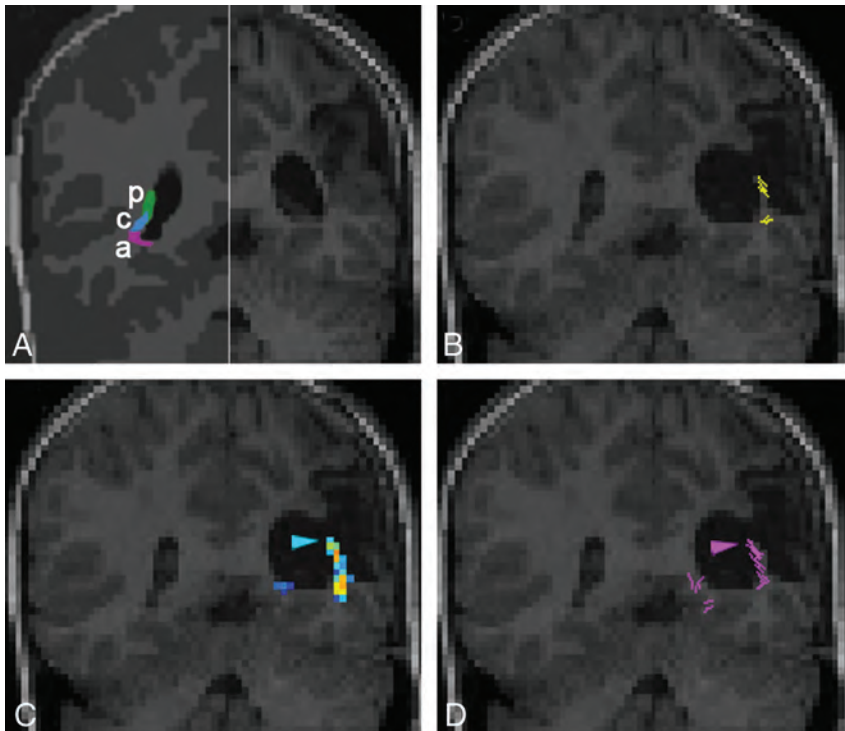


FIG 3. Coronal sections through the OR at the level of the trigone of the lateral ventricle in patient 15 with a perinatal stroke. Scheme drawing (A) of the functional organization of the OR on the healthy side (redrawn²⁶), indicating the course of the posterior (p), anterior (a), and central (c) bundles, carrying fibers of the lower quadrant, upper quadrant, and center of the contralateral visual field, respectively. Preoperative T1WI of the pathologic side (right half, A). Postoperatively, the patient had a lower right quadrant anopia. Preoperative tractography superimposed on the postoperative coronal T1 (B–D). The arrowhead indicates that the posterior bundle of the OR was within the resection area. It is missed by FACT (B) but is depicted by probabilistic (C) and global (D) tractography.

suspected epileptogenic focus was performed. During postoperative follow-up, 9 patients remained seizure-free; 5 patients had less frequent seizures than before surgery; and, in 1 patient, the seizure type and frequency remained unchanged. Surgical treatment was thought to be inappropriate in 5 patients (3 with tractography of the DMP and 2 of the OR), as a functional impairment may have ensued, because of the vicinity to the main part of the fiber pathways or to the respective cortex.

To re-evaluate our findings, we superimposed preoperative tractographic results on the postoperative imaging in patients having received surgery. In 2 patients, the detected fibers were presumably damaged during the operation. In patient 14, a right selective amygdalohippocampectomy was performed. Preoperatively, only the probabilistic algorithm successfully depicted the OR, including the Meyer loop (Fig 2). Postoperatively, the patient had a small left upper visual field defect. The preoperative probabilistic OR reconstruction was superimposed on the T1WI acquired 3 months postoperatively. The anterior extent of the reconstructed Meyer loop was now situated in the area that had been excised. In patient 15, a left-sided extended perisylvian lesionectomy of perinatal infarcted tissue was performed (Fig 3). Preoperatively, reconstruction of the OR was intended by the 3 algorithms. Probabilistic and global reconstruction was more detailed and included the posterior bundle of the OR. Postoperatively, the patient had a lower quadrant anopia. At 3 months after the operation, T1WI revealed that a small part of the sagittal stratum had been removed. The area corresponding to the posterior bundle of the OR, responsible for the contralateral lower quadrant field, coincided with the part of the surgically excised area.

DISCUSSION

The reliability of tractography algorithms as a tool for patient assessment is dependent on factors such as anatomic deviation and compression, intracellular and extracellular edema, tissue infiltration by tumors, fiber degeneration, and inflammation.²⁰ Our motivation to include patients with drug-resistant structural epi-

lepsy being planned for lesion resection includes 2 important points. First, epileptogenic lesions are often circumscribed and are the result of either benign pathologic conditions or low-grade tumors without gross mass effect and changes of the microstructure. Thus, the influence of pathologic microstructure on the performance of the fiber tractography algorithms is thought to be negligible. Second, the postoperative resection area represents an accurately defined lesion in the vicinity of the depicted fiber bundle. Therefore, a verification of the fiber course can be derived in conjunction with the postoperative functional outcome. In 2 patients (patients 14 and 15), this approach could be successfully applied. Some patients were not operated on, because the depicted anatomic course of the fiber tracts was adjacent to the pathologic condition.

The global tracking algorithm successfully reconstructed the DMP arising from the entire convexity of the precentral gyrus. A wider fan angle for the DMP indicates that the crossing with the superior longitudinal fascicle (SLF) and the callosal fiber has been resolved. In particular, the reconstruction of the corticobulbar fibers was established exclusively by this method. They originate in the lateral precentral gyrus, cross the SLF, and terminate in the nuclear areas of the dorsal pons. The large crossing area with the SLF is crucial for tractography algorithms. As expected from the phantom studies, the global tracking efficiently overcame this crossing area.¹¹ The success of global tracking lies in its design. Hundreds of segments per voxel represent even those fiber orientations with smaller diffusion weight. The individual line elements are longer than the voxel size, and most importantly, a global model has to be fulfilled in which the reconstructed fibers are hindered to end in the white matter. Thus, the entire fiber system is forced into a configuration where crossings are needed to explain the whole diffusion anisotropy. The reconstruction of the corticobulbar fibers by the other 2 algorithms was inadequate (Fig 1 and On-Line Fig 2). It has been established already that the deterministic FACT cannot solve the problem of fiber crossings with the result of stop of propagation.⁵ Probabilistic algorithms can only partially solve this problem such that the true course of the investigated pathway remains uncertain (supplementary material in¹¹ and²¹). Postoperatively, no functional deficits were present and no further conclusions could be drawn for the DMP.

For reconstruction of the OR, the probabilistic algorithm performed best. Until now, probabilistic approaches were able to reconstruct its full extent only with an additional manual placement of an ROI anterolateral to the lateral geniculate nucleus.²² The probabilistic maps of connectivity used in this study reconstructed the entire extent of the Meyer loop in 9 of 10 patients solely by using the parcellation/atlas-derived ROIs. The distance between the temporal pole tip and the anterior limit of the Meyer loop was in accordance with previous findings²³ and was an indicator for the detection of the Meyer loop. It has been commonly accepted that the FACT algorithm generally underestimates the Meyer loop.⁶ To exclude effects of the FA threshold of 0.1, the FACT algorithm was also assessed without it, and this trend did not result in a more reliable detection of the Meyer loop. Global tracking also failed to reconstruct the Meyer loop. This finding is

attributed to the rigid alignment of the line elements hindering reconstruction of a sharp bending. A correlation between postoperative visual field defects and the extent of Meyer loop excision has been described before.²² In 68%–100% of patients with amygdalohippocampectomy, visual field defects were observed.²³ One patient subjected to selective amygdalohippocampectomy (patient 14) showed a small upper visual field defect because the Meyer loop was partially damaged. A postoperative lesion was manifest where, in probabilistic maps of connectivity, the most anterior extent of the Meyer loop had been seen correctly. FACT and global tracking showed false-negative results.

In 8 of 10 patients, the estimation of the Meyer loop was not the main aim of tractography because the pathologic condition was located in the occipital lobe or the occipital-temporal region. From this group of patients, 6 were operated on, and a lower quadrant anopia developed in one of these patients (patient 15) postoperatively. In this patient, with a perinatal infarction, the comparison of the postoperative resection area and the preoperatively depicted fibers provided information about the true course of the posterior bundle of the OR. Probabilistic maps of connectivity and global tracking depicted correctly this part of the OR, whereas FACT showed false-negative results for the posterior bundle (Fig 3). Without the FA threshold, the results of FACT were also disappointing. It can be argued that FACT is susceptible to changes of axial and radial diffusivity, which has been recently shown in patients presenting with glioma.²¹ In patient 15, the course of the OR wound through a postischemic gliotic area visible on T2- and FLAIR-weighted sequences in the sagittal stratum along the ventricle. This finding comprised the whole OR but was most prominent in the posterior bundle.

Our study had several limitations. From a theoretic point of view, it may not have been advisable to compare the simplistic FACT algorithm with the 2 more sophisticated methods.¹¹ However, the approach to this study was practical, as it used in vivo data where additional effects of the tissue environment such as anatomic field inhomogeneities may overlay more subtle effects. It was difficult to define similar limiting conditions for all 3 methods. In global tracking, an internal factor, which reflects the brain-averaged anisotropic signal component, serves as an FA threshold. It was chosen such that spurious fibers appear only within areas of $FA < 0.1$. For comparability, an FA threshold of 0.1 was applied to the other 2 methods. Another clear limitation of this study was the relatively low number of patients because patients with high-grade tumors were not included in the study. Mass effect and low perifocal FA in high-grade tumors⁴ and changes of diffusion metrics in anaplastic gliomas²¹ have been described as confounding factors for fiber tractography. Therefore, the focus of our study was on well-circumscribed pathologic conditions in patients without mass effect and without gross changes of the microstructure. The validation of tractography approaches still remains a critical issue to be solved. Transcranial magnetic stimulation was contraindicated because of the epilepsy. Intraoperative subcortical mapping is predominantly used in sleep-awake patients²⁴ and has not been applied in our institution. Therefore, the course of major fiber bundles could be validated only by postoperative functional deficits. Despite the above-mentioned limitations, the comparison of these methods in a clinical setting is

new, especially because it considers a global method, which has not been clinically proven so far.

CONCLUSIONS

The choice of a suitable tractographic algorithm should be a trade-off between the fiber tract of interest and the available computational time. FACT might be sufficient if a fast tractography is required. However, for the Meyer loop of the OR and fiber bundles with strong bending characteristics, probabilistic tractography should be the method of choice. The probabilistic method seems to be the best balance between computational time and effectiveness, and it might be the best choice in most clinical cases. Where a detailed fiber depiction and a resolution of fiber crossings are intended, global tracking should be applied even if it comes along with a prolonged computation time.

Disclosures: Valerij Kiselev—RELATED: Grant: German Research Council.* Comments: Research Grant KI1089/3—one for development of fiber tracking. Irina Mader—RELATED: Grant: German Research Council.* Comments: German Research Council, MA 2343/4-1; Comprehensive Cancer Centre Freiburg, Germany, Seeding Grant 1027013110. *Money paid to institution.

ACKNOWLEDGMENTS

The authors are grateful to Mr. Hans-Joerg Mast for the MR imaging acquisitions and to Ms. Sophie Aslan for valuable philological suggestions.

REFERENCES

1. Yogarajah M, Duncan JS. Diffusion-based magnetic resonance imaging and tractography in epilepsy. *Epilepsia* 2008;49:189–200
2. Basser PJ. Inferring microstructural features and the physiological state of tissues from diffusion-weighted images. *NMR Biomed* 1995;8:333–44
3. Mori S, Crain BJ, Chacko VP, et al. Three-dimensional tracking of axonal projections in the brain by magnetic resonance imaging. *Ann Neurol* 1999;45:265–69
4. Nimsky C, Ganslandt O, Hastreiter P, et al. Preoperative and intraoperative diffusion tensor imaging-based fiber tracking in glioma surgery. *Neurosurgery* 2005;56:130–37; discussion 138
5. Anderson AW. Theoretical analysis of the effects of noise on diffusion tensor imaging. *Magn Reson Med* 2001;46:1174–88
6. Yamamoto T, Yamada K, Nishimura T, et al. Tractography to depict three layers of visual field trajectories to the calcarine gyri. *Am J Ophthalmol* 2005;140:781–85
7. Parker GJ, Haroon HA, Wheeler-Kingshott CA. A framework for a streamline-based probabilistic index of connectivity (PICO) using a structural interpretation of MRI diffusion measurements. *J Magn Reson Imaging* 2003;18:242–54
8. Kreher BW, Schnell S, Mader I, et al. Connecting and merging fibres: pathway extraction by combining probability maps. *Neuroimage* 2008;43:81–89
9. Kreher BW, Mader I, Kiselev VG. Gibbs tracking: a novel approach for the reconstruction of neuronal pathways. *Magn Reson Med* 2008;60:953–63
10. Reisert M, Mader I, Anastasopoulos C, et al. Global fiber reconstruction becomes practical. *Neuroimage* 2011;54:955–62
11. Fillard P, Descoteaux M, Goh A, et al. Quantitative evaluation of 10 tractography algorithms on a realistic diffusion MR phantom. *Neuroimage* 2011;56:220–34
12. Behrens TE, Woolrich MW, Jenkinson M, et al. Characterization and propagation of uncertainty in diffusion-weighted MR imaging. *Magn Reson Med* 2003;50:1077–88
13. Engel J, Van Ness PC, Rasmussen TB, et al. *Outcome With Respect to Epileptic Seizures*. New York: Raven Press;1993:609–21
14. Wieser HG, Blume WT, Fish D, et al. ILAE Commission Report. Proposal for a new classification of outcome with respect to epileptic seizures following epilepsy surgery. *Epilepsia* 2001;42:282–86
15. Aganj I, Lenglet C, Sapiro G, et al. Reconstruction of the orientation distribution function in single- and multiple-shell Q-ball imaging within constant solid angle. *Magn Reson Med* 2010;64:554–66
16. Destrieux C, Fischl B, Dale A, et al. Automatic parcellation of human cortical gyri and sulci using standard anatomical nomenclature. *Neuroimage* 2010;53:1–15
17. Maldjian JA, Laurienti PJ, Kraft RA, et al. An automated method for neuroanatomic and cytoarchitectonic atlas-based interrogation of fMRI data sets. *Neuroimage* 2003;19:1233–39
18. Andrews TJ, Halpern SD, Purves D. Correlated size variations in human visual cortex, lateral geniculate nucleus, and optic tract. *J Neurosci* 1997;17:2859–68
19. Fillard P, Poupon C, Mangin JF. A novel global tractography algorithm based on an adaptive spin glass model. *Med Image Comput Comput Assist Interv* 2009;12:927–34
20. Alexander AL, Lee JE, Lazar M, et al. Diffusion tensor imaging of the brain. *Neurotherapeutics* 2007;4:316–29
21. Nguyen-Thanh T, Reisert M, Anastasopoulos C, et al. Global tracking in human gliomas: a comparison with established tracking methods. *Clin Neuroradiol* 2013;23:263–75
22. Yogarajah M, Focke NK, Bonelli S, et al. Defining Meyer's loop—temporal lobe resections, visual field deficits and diffusion tensor tractography. *Brain* 2009;132:1656–68
23. Mandelstam SA. Challenges of the anatomy and diffusion tensor tractography of the Meyer loop. *AJNR Am J Neuroradiol* 2012;33:1204–10
24. Bello L, Gambini A, Castellano A, et al. Motor and language DTI fiber tracking combined with intraoperative subcortical mapping for surgical removal of gliomas. *Neuroimage* 2008;39:369–82
25. Palmieri A, Najm I, Avanzini G, et al. Terminology and classification of the cortical dysplasias. *Neurology* 2004;62:S2–8
26. Ebeling U, Reulen HJ. Neurosurgical topography of the optic radiation in the temporal lobe. *Acta Neurochir (Wien)* 1988;92:29–36

Tumor Consistency of Pituitary Macroadenomas: Predictive Analysis on the Basis of Imaging Features with Contrast-Enhanced 3D FIESTA at 3T

J. Yamamoto, S. Kakeda, S. Shimajiri, M. Takahashi, K. Watanabe, Y. Kai, J. Moriya, Y. Korogi, and S. Nishizawa

ABSTRACT

BACKGROUND AND PURPOSE: Preoperative evaluation of pituitary macroadenoma tumor consistency is important for neurosurgery. Thus, we aimed to retrospectively assess the role of contrast-enhanced FIESTA in predicting the tumor consistency of pituitary macroadenomas.

MATERIALS AND METHODS: Twenty-nine patients with pituitary macroadenomas underwent conventional MR imaging sequences and contrast-enhanced FIESTA before surgery. Two neuroradiologists assessed the contrast-enhanced FIESTA, contrast-enhanced T1WI, and T2WI. On the basis of surgical findings, the macroadenomas were classified by the neurosurgeons as either soft or hard. Finally, Fisher exact probability tests and unpaired *t* tests were used to compare predictions on the basis of the MR imaging findings with the tumor consistency, collagen content, and postoperative tumor size.

RESULTS: The 29 pituitary macroadenomas were classified as either solid or mosaic types. Solid type was characterized by a homogeneous pattern of tumor signal intensity without intratumoral hyperintense dots, whereas the mosaic type was characterized by many intratumoral hyperintense dots on each MR image. Statistical analyses revealed a significant correlation between tumor consistency and contrast-enhanced FIESTA findings. Sensitivity and specificity were higher for contrast-enhanced FIESTA (1.00 and 0.88–0.92, respectively) than for contrast-enhanced T1WI (0.80 and 0.25–0.33, respectively) and T2WI (0.60 and 0.38–0.54, respectively). Compared with mosaic-type adenomas, solid-type adenomas tended to have a hard tumor consistency as well as a significantly higher collagen content and lower postoperative tumor size.

CONCLUSIONS: Contrast-enhanced FIESTA may provide preoperative information regarding the consistency of macroadenomas that appears to be related to the tumor collagen content.

ABBREVIATIONS: CE = contrast-enhanced; PCC = percentage of collagen content; SI = signal intensity

The transsphenoidal approach of removing pituitary adenomas has been widely adopted as a safe and effective method.^{1,2} Recently, the endoscopic transsphenoidal technique has been applied as a minimally invasive surgery to remove pituitary adenomas.³ Most pituitary adenomas are soft and thus can be adequately removed by aspiration and curettage via the transsphenoidal route. However, 5–15% of pituitary adenomas are firm and fibrous. This can occur quite often, and, unfortunately, there are no preoperative predictors of its occurrence.⁴ Thus, pre-

operative evaluation of tumor consistency is essential for neurosurgeons.

Previous studies have attempted to predict pituitary macroadenoma tumor consistency by use of conventional MR imaging techniques.^{5–7} However, the ability of MR images to predict pituitary macroadenoma consistency is controversial.⁸ FIESTA can provide strong T2 contrast, emphasizing the water content signal, including CSF. This sequence also has a high signal intensity-to-noise ratio, inherent flow compensation, and is suitable for direct 3D imaging.^{9,10} Although FIESTA is predominantly used for T2WI, it also enables T1 contrast and portrays contrast enhancement with increased concentration of gadolinium-based contrast reagents.¹¹ Therefore, previous studies have reported that contrast-enhanced (CE) FIESTA can enable visualization of the boundary between brain tumors and surrounding structures, and CE-FIESTA is effective for preoperative evaluation of skull base tumors.^{12,13}

Received March 19, 2013; accepted after revision May 14.

From the Departments of Neurosurgery (J.Y., M.T., K.W., S.N.), Radiology (S.K., Y.Kai, J.M., Y.Korogi), and Surgical Pathology (S.S.), University of Occupational and Environmental Health, Kitakyushu, Japan.

Please address correspondence to Junkoh Yamamoto, MD, PhD, Department of Neurosurgery, University of Occupational and Environmental Health, 1-1 Iseigaoka, Yahatanishi-ku, Kitakyushu, Fukuoka 807-8555, Japan; e-mail: yama9218@mub.biglobe.ne.jp

<http://dx.doi.org/10.3174/ajnr.A3667>

In the clinic, we have previously noticed that pituitary macroadenomas have various CE-FIESTA signal intensities. Therefore, we hypothesized that CE-FIESTA might allow identification of the water content or vascularity within tumors to give an indication of tumor consistency. The purpose of this retrospective study was to assess the ability of CE-FIESTA to predict pituitary macroadenoma tumor consistency.

MATERIALS AND METHODS

Patients and Clinical Data

This study was approved by our institutional review board. We retrospectively evaluated 32 consecutive patients with pituitary macroadenomas who underwent surgery between September 2006 and May 2011. All patients underwent brain MR imaging, including CE-FIESTA, before surgery. Pituitary macroadenomas were defined as adenomas that exceeded 10 mm in diameter, on the basis of preoperative MR imaging. Subjects who had received previous surgery or any other therapy (chemotherapy or radiation therapy) for the pituitary macroadenoma were excluded from this study because the tumors might have induced fibrous changes.

Imaging Data Acquisition

MRI was performed by use of a 3T unit (Signa Excite; GE Healthcare, Milwaukee, Wisconsin) with a dedicated 8-channel phased-array coil (USA Instruments, Aurora, Ohio) after intravenous administration of 0.1 mmol/kg body weight gadodiamide hydrate (Omniscan; Daiichi Pharmaceutical, Tokyo, Japan) or gadopentetate dimeglumine (Magnevist; Bayer Schering-Pharma, Berlin, Germany). The FIESTA sequence was performed by use of the following parameters: repetition time, 5.4 ms; echo time, 2.4 ms (5.4/2.4); acquisitions, 2; flip angle, 50°; bandwidth, 662.5 kHz; matrix, 224 × 224; 100% image; section thickness, 0.8 mm; field of view, 14 × 14 cm; resolution, 0.6 × 0.6 × 0.8 mm; and imaging time, 5 minutes, 6 seconds. CE-FIESTA of all patients was acquired in the coronal plane. In addition, all patients underwent our standard brain MR imaging protocol for suprasellar tumors, including coronal T2WI with 3.0-mm-thick sections, coronal T1WI, and CE-T1WI (coronal CE spin-echo or axial CE-3D fast spoiled gradient-echo imaging). The CE-3D fast spoiled gradient-echo imaging data were reconstructed in the sagittal and coronal planes. The following imaging parameters were used for coronal T2WI: 4000/85 msec; flip angle, 90°; bandwidth, 62.5 kHz; section thickness, 3.0 mm; matrix, 512 × 224; field of view, 18 × 18 cm; and imaging time, 2 minutes, 16 seconds. The following imaging parameters were used for CE spin-echo imaging: 400/4 msec; flip angle, 100°; bandwidth, 62.5 kHz; section thickness, 3.0 mm; matrix, 224 × 224; field of view, 18 × 18 cm; and imaging time, 2 minutes, 40 seconds. The following parameters were used for CE spoiled gradient-echo imaging: 10/4 msec; flip angle, 10°; bandwidth, 42 kHz; section thickness, 1.2 mm; matrix, 256 × 256; field of view, 24 × 24 cm; and imaging time, 3 minutes, 56 seconds. Parallel imaging techniques (a reduction factor of 2) were used only for T2WI and CE spoiled gradient-echo images.

Image Analyses

First, we hypothesized that CE-FIESTA of pituitary macroadenomas would correlate with tumor consistency, in particular with the degree of hardness. Therefore, an experienced neuroradiolo-

gist (S.K., with 16 years of experience in neuroradiology) was blinded to the clinical information (ie, tumor consistency at surgery). The soft-tissue compartments of the pituitary macroadenomas were subjectively classified on the basis of CE-FIESTA, CE-T1WI, and T2WI data into 2 types, solid and mosaic, by the neuroradiologist. “Solid” was defined as a relatively homogeneous lesion (Fig 1–1) and “mosaic” was defined as a lesion containing small multiple hyperintense dots (ranging in size from 0.5 mm to <2 mm) that were uniformly distributed throughout the soft-tissue compartment of the adenoma (Fig 1–2). Subsequently, 2 other neuroradiologists (Y. Kai and J.M., with 17 and 10 years of experience in neuroradiology, respectively) independently reviewed the CE-FIESTA, CE-T1WI, and T2WI data. These reviewers were also blinded to the clinical data. Two training cases (1 adenoma with a solid pattern and 1 with a mosaic pattern) were presented before the tests, and reviewers underwent sufficient training on CE-FIESTA, CE-T1WI, and T2WI to be familiar with the 2 patterns. The reviewers then independently classified each adenoma on the basis of the findings from these images. For both sequences, each image was analyzed separately, and only 1 sequence was shown at a time. Data from the first read were used to calculate the sensitivity, specificity, positive predictive value, and negative predictive value for the MR imaging prediction of hard adenomas.

In accordance with previous research, ROIs for signal intensity (SI) analyses were drawn directly on the images obtained from the T2WI and CE-FIESTA sequences.⁷ All ROIs were an arbitrarily chosen (by the first neuroradiologist S.K.) uniform shape and size (elliptical, 50 mm²). ROIs were anatomically identified in the central and solid-appearing portions of the macroadenomas. ROIs were also placed in the normal white matter of the temporal lobe on the same section. To avoid scaling problems on each MR image, we calculated SI ratios for all images by use of the following formula: SI ratio = SI of tumor/SI of normal white matter. After the surgery, the maximum craniocaudal size of the pituitary macroadenomas was measured on the sagittal midline CE-T1WI before and after transsphenoidal surgery. To determine whether preoperative CE-FIESTA findings could affect surgical outcome, we calculated the percentage of relative postoperative tumor size by use of the following formula: (size after surgery/size before surgery) × 100.

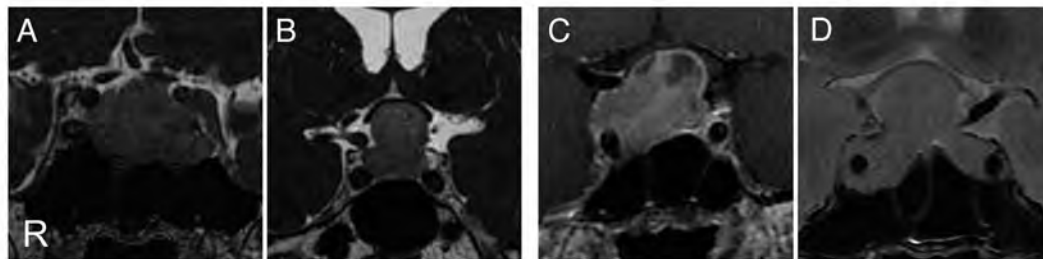
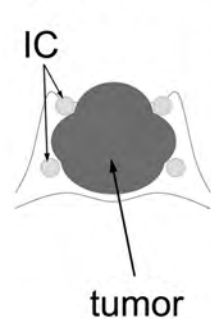
Surgery

A skilled neurosurgeon (S.N., with 35 years of experience in brain surgery) performed direct transsphenoidal surgery. Immediately after surgical treatment, this neurosurgeon (S.N.) and another experienced neurosurgeon (J.Y., with 16 years of experience in brain surgery and who also assisted during surgery) together assessed tumor consistency by use of surgical notes and the DVD recordings from the operation. Tumors were classified into 2 groups: tumors with soft consistency (easily removable through aspiration or curettage) and tumors with hard consistency (not removable through aspiration and/or curettage and requiring piecemeal resection by use of a microdissector or tumor forceps).

Histologic Study

A pathologist (S.S., with 18 years of experience) performed the subsequent histologic studies. Routine specimen processing

1) solid



2) mosaic

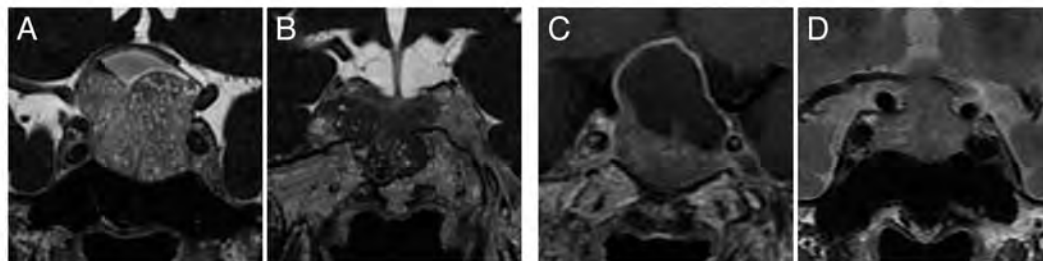
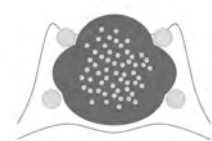


FIG 1. Classification of pituitary macroadenomas by use of CE-FIESTA, CE-T1WI, and T2WI. 1, Solid type. Schematic drawing and coronal images of CE-FIESTA (A and B), CE-T1WI (C), and T2WI (D) show homogeneous patterns of SI without intratumoral hyperintense dots. 2, Mosaic type. Schematic drawing and coronal images of CE-FIESTA (A and B), CE-T1WI (C), and T2WI (D) show intratumoral hyperintense dots within the tumor.

Table 1: Clinical and operative features of pituitary macroadenomas

	Hard (5 Cases)	Soft (24 Cases)	P Value
Age ^a	46.4 ± 20.8 (5)	56.0 ± 16.7 (24)	.2687
Sex			
Male (18)	4	14	.6221
Female (11)	1	10	
Preoperative clinical symptoms			
Visual disturbance (16)	3	13	>.9999
Others (13)	2	11	
Headache (6)			
Hormone abnormality (4)			
Incidental (3)			
Clinical endocrine classification			
Functioning (11)	2	9	>.9999
Nonfunctioning (18)	3	15	
Maximum tumor size, mm ^a	27.8 ± 6.4 (5)	29.1 ± 8.9 (24)	.7679
Relative postoperative tumor size, % ^a	72.0 ± 24.4 (4)	28.2 ± 12.1 (23)	<.0001

Note:—Numbers in parentheses indicate number of cases in each category.

^a Data are mean ± SD.

involved staining the slides with hematoxylin and eosin, followed by immunohistochemical analyses by use of antibodies for pituitary hormones. Tumor specimens were also histochemically examined for collagen content by use of Masson trichrome staining. To perform quantitative analyses of collagen content, photomicrographs were captured in 5 random regions of each specimen by use of a digital virtual microscope system (NanoZoomer Digital Pathology; Hamamatsu Photonics K.K., Hamamatsu, Japan). The area of collagen stained blue was measured by use of an image processing software program (Image J; National Institute of Mental Health, Bethesda, Maryland). The percentage of collagen content (PCC) was calculated by use of the following formula: PCC =

(collagen area/total tumor area) × 100. PCC was calculated in 5 random regions in each specimen, and the mean value was defined as a representative value for each specimen.

Statistical Analyses

Statistical analyses were performed by use of a statistical software package (StatView 5.0; SAS Institute, Cary, North Carolina). For pituitary macroadenoma demographics, correlations between tumor consistency, age, maximum tumor size, and relative postoperative tumor size were tested by use of Fisher exact probability tests. Correlations between tumor consistency, sex, preoperative clinical symptoms, and

clinical endocrine classification were tested by use of unpaired *t* tests. Correlations between MR findings (solid and mosaic types) and tumor consistency on surgery were tested by use of Fisher exact probability tests. Correlations between MR findings and relative postoperative tumor size were tested by use of unpaired *t* tests. Correlations between tumor consistency, PCC, and the SI ratio were also tested by use of unpaired *t* tests. A *P* value of <.05 was considered statistically significant. Diagnostic values for predicting hard adenomas were calculated according to the MR imaging findings, and the accuracies were compared by use of Fisher exact tests. Kendall *W* tests were used to assess interobserver agreement between radiologists. Interobserver agreement was

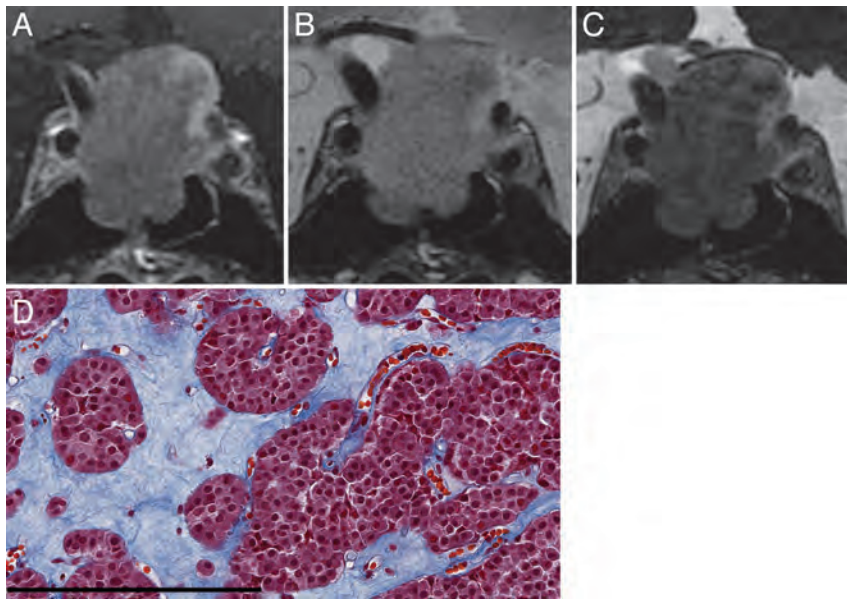


FIG 2. Macroadenoma with hard consistency in a 77-year-old male patient (case 13). *A*, Coronal CE-T1WI shows a large heterogeneous enhanced pituitary mass. *B*, Coronal T2WI shows an isointense mass with respect to normal white matter. *C*, Coronal CE-FIESTA shows a homogeneous tumor SI pattern without intratumoral hyperintense dots. *D*, Histologic examination of the resected tumor indicates small size and the formation of multiple nests surrounded by attenuated collagen tissue (Masson trichrome stain; scale bar, 200 μ m).

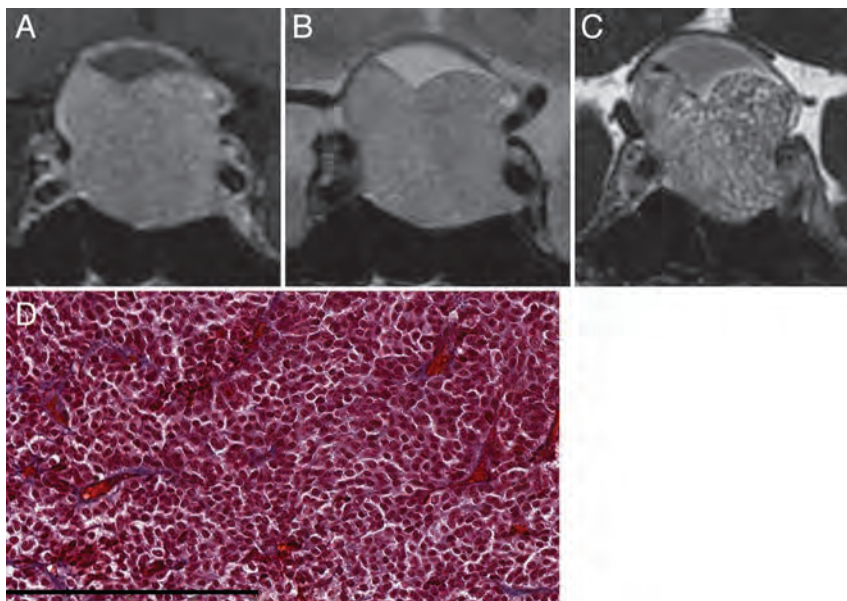


FIG 3. Macroadenoma with soft consistency in a 51-year-old female patient (case 28). *A*, Coronal CE-T1WI shows a large, homogeneous, enhanced pituitary mass. *B*, Coronal T2WI shows a relatively hyperintense mass with respect to normal white matter. *C*, Coronal CE-FIESTA shows numerous hyperintense dots within the tumor. *D*, Histologic examination of the resected tumor indicates small cells with scant collagen in a small, restricted perivascular area (Masson trichrome stain; scale bar, 200 μ m).

classified as follows: Kendall W values <0.20 indicated poor agreement, values of $0.21-0.40$ indicated fair agreement, values of $0.41-0.60$ indicated moderate agreement, values of $0.61-0.80$ indicated good agreement, and values of $0.80-1.00$ indicated excellent agreement. For the Kendall W coefficients by the 2 radiologists, CE-FIESTA was compared with the CE-T1WI and T2WI by means of χ^2 tests.

RESULTS

Of the 32 patients, 3 did not meet the inclusion criteria and were excluded from the study. Therefore, 29 patients with pituitary macroadenomas (18 men, 11 women; mean age, 54.4 ± 17.5 years) were included in this study. The demographic characteristics of the patients are summarized in Table 1. Of the 29 patients, tumor consistency at the time of surgery was classified as hard macroadenoma in 5 patients (17%) and soft macroadenoma in 24 patients (83%) (Table 1). Surgery preserved preoperative anterior and posterior pituitary functions. There were no surgical complications in any of the cases. Two patients did not undergo postoperative MR imaging; thus, the relative postoperative tumor sizes of these patients were not available. Regarding the clinical and operative features of pituitary macroadenomas, there was a significant difference in only relative postoperative tumors between hard and soft adenomas ($P < .01$) (Table 1). However, there were no significant differences in age, sex, preoperative clinical symptoms, clinical endocrine classification, and maximum tumor size.

MR Imaging Findings

All acquired images provided acceptable diagnostic image quality. CE-FIESTA, CE-T1WI, and T2WI showed isointense to hyperintense pituitary macroadenomas with or without hyperintense dots (Figs 2 and 3).

For evaluation of the CE-FIESTA and T2WI data, the interobserver agreements between reviewers were acceptable, with Kendall W values of 0.73 and 0.613, respectively. In contrast, for the CE-T1WI, the interobserver agreement between the reviewers was fair, with Kendall W values of 0.32. The 5 cases of hard macroadenomas were classified as solid types by use of CE-FIESTA images, whereas 21 (for radiologist 1) or 22 (for radiologist 2) of the 24 soft macroadenomas were deemed mosaic types (Table 2). There was a significant correlation between tumor consistency at the time of surgery and the CE-FIESTA findings by each reviewer ($P < .01$) but not between tumor consistency and the CE-T1WI and T2WI findings. Moreover, regarding the CE-FIESTA data, the percentage of relative postoperative tumor size in the solid group was significantly higher than that of the mosaic group ($P < .01$). In

Table 2: Effectiveness of CE-FIESTA and CE-T1WI findings for surgery of pituitary macroadenomas

MR Sequences	MR Findings	Radiologist 1			Radiologist 2			
		Tumor Consistency at Surgery			Tumor Consistency at Surgery			
		Hard (n = 5)	Soft (n = 24)	P Value	Hard (n = 5)	Soft (n = 24)	P Value	
CE-FIESTA	Solid	5	3	.0005	Solid	5	2	.0002
	Mosaic	0	21		Mosaic	0	22	
CE-T1WI	Solid	4	18	>.9999	Solid	4	16	>.9999
	Mosaic	1	6		Mosaic	1	8	
T2WI	Solid	3	15	>.9999	Solid	3	11	.6513
	Mosaic	2	9		Mosaic	2	13	

MR Sequences	MR Findings	Relative Postoperative Tumor Size, %		P Value	Relative Postoperative Tumor Size, %		P Value	
		Hard (n = 5)	Soft (n = 24)		Hard (n = 5)	Soft (n = 24)		
CE-FIESTA	Solid (7)	53.4 ± 29.5		.0040	Solid (6)	58.2 ± 28.8		.0008
	Mosaic (20)	28.2 ± 12.6			Mosaic (21)	28.0 ± 12.5		
CE-T1WI	Solid (22)	36.6 ± 22.7		.3458	Solid (22)	36.9 ± 21.2		.4533
	Mosaic (5)	26.5 ± 8.3			Mosaic (5)	30.3 ± 21.4		
T2WI	Solid (18)	38.4 ± 24.7		.2021	Solid (14)	36.0 ± 27.1		.7565
	Mosaic (9)	27.3 ± 7.0			Mosaic (13)	33.4 ± 12.7		

Note:—Numbers in parentheses indicate number of cases in each category. Data are mean ± SD.

Table 3: Diagnostic accuracy in prediction of tumor consistency

	Radiologist 1	Radiologist 2
CE-FIESTA		
Sensitivity	1.00 (0.83–1.00)	1.00 (0.83–1.00)
Specificity	0.88 (0.84–0.88)	0.92 (0.88–0.92)
Accuracy	0.90 (0.87–0.90)	0.93 (0.9–0.93)
Positive predictive value	0.63 (0.56–0.67)	0.71 (0.63–0.75)
Negative predictive value	1.00 (0.95–1.00)	1.00 (0.96–1.00)
CE-T1WI		
Sensitivity	0.80 (0.67–0.83)	0.80 (0.67–0.83)
Specificity	0.25 (0.24–0.28)	0.33 (0.32–0.36)
Accuracy	0.34 (0.33–0.37)	0.41 (0.40–0.43)
Positive predictive value	0.18 (0.17–0.28)	0.20 (0.19–0.31)
Negative predictive value	0.86 (0.75–0.88)	0.89 (0.80–0.90)
T2WI		
Sensitivity	0.60 (0.38–0.66)	0.60 (0.38–0.66)
Specificity	0.38 (0.36–0.40)	0.54 (0.48–0.56)
Accuracy	0.41 (0.4–0.43)	0.55 (0.47–0.57)
Positive predictive value	0.17 (0.16–0.21)	0.21 (0.20–0.27)
Negative predictive value	0.82 (0.75–0.83)	0.87 (0.81–0.88)

Note:—Numbers in parentheses indicate number of cases in each category.

contrast, analyses of the reviewers revealed no correlation between CE-T1WI and T2WI findings and the percentage of relative postoperative tumor size.

The diagnostic accuracy of analyses for the reviewers is outlined in Table 3. Regarding the prediction of hard adenomas, the mean sensitivity, specificity, and accuracy of CE-FIESTA were 1.00, 0.90, and 0.92, respectively. Accuracy by use of CE-FIESTA data was significantly higher than the accuracy value by use of CE-T1WI and T2WI ($P < .01$). Only 1 patient with a soft macroadenoma underwent both unenhanced and CE-FIESTA imaging (Fig 4). This patient had intratumoral hyperintense dots that were only apparent with CE-FIESTA; unenhanced-3D FIESTA displayed no intratumoral hyperintense dots.

Findings of CE-FIESTA, Surgery, and Histologic Analyses

On histologic examination, tumors displayed trabecular, papillary, or sheetlike patterns, with some variance of perivascular fibrosis. Masson trichrome staining revealed significant fibrosis in the perivascular tissue consisting of collagen (Figs 2D, 3D, and 4C). Macroadenomas in the hard tumor consistency group exhibited low cel-

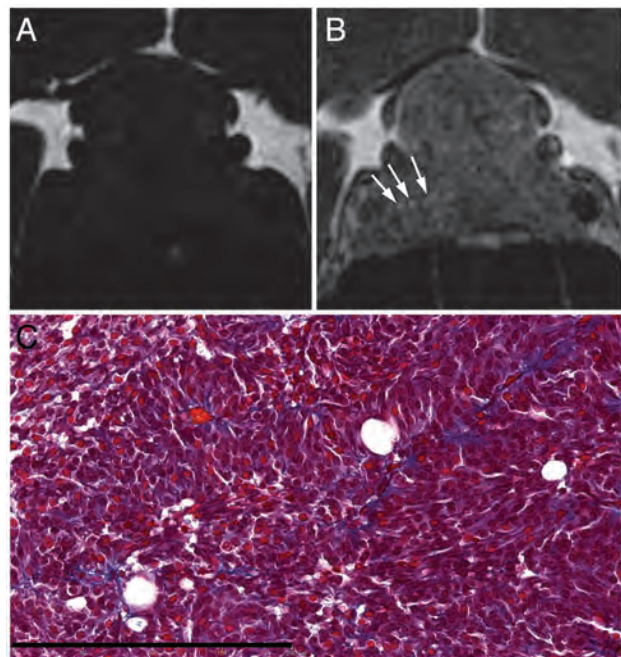


FIG 4. Macroadenoma with soft consistency in a 44-year-old female patient (case 29). A, Unenhanced coronal FIESTA image, and B, corresponding coronal CE-FIESTA image. Intratumoral hyperintense dots are shown on CE-FIESTA (arrows in B) but not on unenhanced FIESTA. C, Histologic examination of the resected tumor shows scant collagenous tissues in a perivascular area (Masson trichrome stain; scale bar, 200 μ m).

lularity and abundant collagenous stroma (Fig 2D). In contrast, macroadenomas in the soft tumor consistency group exhibited high cellularity and scant collagenous stroma (Figs 3D and 4C). The collagen content of hard macroadenomas was significantly higher than that of soft macroadenomas ($P = .0002$) (Table 4). The SI ratio on CE-FIESTA showed significant differences between hard and soft macroadenomas ($P = .0106$). However, no significant differences in the SI ratio on T2WI were found between the groups ($P = .3271$) (Table 4).

With regard to the tumor classifications on the basis of CE-AJNR Am J Neuroradiol 35:297–303 Feb 2014 www.ajnr.org 301

Table 4: Tumor consistency, SI ratio, and CE-FIESTA findings compared with collagen contents

		Tumor Consistency at Surgery			
		Hard (n = 5)		Soft (n = 24)	P Value
Collagen contents, %		46.6 ± 20.2		14.4 ± 14.5	.0002
T2WI SI ratio ^a		1.20 ± 0.16		1.29 ± 0.19	.3271
CE-FIESTA SI ratio ^a		1.32 ± 0.35		1.85 ± 0.17	.0106

MR Sequences	MR Findings	Radiologist 1		Radiologist 2		
		Collagen Contents, %	P Value	MR Findings	Collagen Contents, %	P Value
CE-FIESTA	Solid (8)	40.9 ± 26.3	<.0001	Solid (7)	35.7 ± 25.2	.012
	Mosaic (21)	12.0 ± 7.5		Mosaic (22)	14.9 ± 15.0	
CE-T1WI	Solid (22)	21.1 ± 21.2	.5733	Solid (20)	22.2 ± 20.4	.3642
	Mosaic (7)	16.2 ± 14.5		Mosaic (9)	14.9 ± 18.0	
T2WI	Solid (18)	20.8 ± 23.5	.7632	Solid (14)	20.6 ± 21.7	.8734
	Mosaic (11)	18.5 ± 11.7		Mosaic (15)	19.4 ± 18.2	

Note:—Numbers in parentheses indicate number of cases in each category.

Data are mean ± SD.

^aSI on T2WI and CE-FIESTA of tumor to SI on each of white matter, respectively.

FIESTA findings, the percentage of collagen content in the solid and mosaic types were 40.9 ± 26.3% (mean ± SD; n = 8) and 12.0 ± 7.5% (n = 21) for radiologist 1, respectively, and 35.7 ± 25.2% (n = 7) and 14.9 ± 15.0% (n = 22) for radiologist 2, respectively (Table 4). There were significant differences between both types (P < .01). In contrast, analyses from both radiologists revealed no correlation between CE-T1WI and T2WI findings and the percentage of collagen content (Table 4).

DISCUSSION

In the present study, we evaluated whether CE-FIESTA could predict tumor consistency in pituitary macroadenomas. Our results suggest that CE-FIESTA is a useful imaging sequence for this estimation. To the best of our knowledge, this is the first study to assess pituitary macroadenoma tumor consistency on the basis of CE-FIESTA findings.

Previous studies have histologically evaluated tumor consistency by assessing the amount of collagen or reticulin within macroadenomas.^{5,6,14} In the present study, we also performed histologic examinations by use of Masson trichrome staining. Our results indicate that the collagen content in hard macroadenomas is higher than that in soft adenomas, which is consistent with previous reports.^{5,14} On the basis of Azan, van Gieson, and Sirius red staining methods, previous studies have reported mean percentages of collagen contents of 7.23–26.1% for hard adenomas and 0.22–6.5% for soft adenomas.^{5,14} Our results found that the mean percentages of collagen content for both hard and soft adenomas were higher than those seen in previous studies. However, these discrepancies might be caused by differences in staining techniques. Moreover, we found that the collagen content correlated with tumor consistency, as evaluated by the subjective judgment of neurosurgeons with substantial experience with pituitary macroadenomas.

Our results suggest that tumor classification by use of CE-FIESTA more accurately predicts the consistency of pituitary macroadenomas than do conventional MR imaging methods, such as CE-T1WI and T2WI. Moreover, the percentages of relative postoperative tumor size in the solid group on the basis of CE-FIESTA data were significantly higher than in the mosaic group. The SI ratio on CE-FIESTA for soft tumors was higher

than that for hard tumors, though there was no correlation between the SI ratio on T2WI and tumor consistency. However, it is important to note that qualitative assessments of hyperintense dots on CE-FIESTA were able to discriminate between soft tumors and hard tumors with high accuracy. Quantitative assessment of the SI ratio typically varies with the individual. These results suggest that it is possible to diagnose tumor consistency on an individual basis from MR images without quantitative SI assessment.

The ability of DWI to predict tumor consistency in pituitary macroadenomas has been controversial. Only 3 studies by use of DWI to evaluate tumor consistency in pituitary macroadenomas have been reported.^{6,7,15} Two of 3 studies suggested a significant correlation between tumor consistency and ADC values in pituitary macroadenomas,^{6,7} whereas the third study indicated no relationship between tumor consistency and ADC values.¹⁵ DWI has lower spatial resolution compared with other conventional MR images. Moreover, for evaluation of the pituitary gland, artifacts that relate to bone structure or sinus aeration can degrade the image quality of DWI. Thus, placement of the ROI to measure the ADC value in pituitary macroadenomas may strongly affect the results in the previous studies. In contrast, FIESTA sequences, with high spatial resolution and reduced susceptibility artifacts, may be appropriate for assessing pituitary macroadenomas.

Although only 1 patient with soft macroadenomas underwent both unenhanced and CE-FIESTA, we found that hyperintense dots were identified by use of CE-FIESTA but not unenhanced FIESTA (Fig 4). This suggests that hyperintense dots may reflect water content but also might be the result of enhancement caused by contrast reagents. Histologically, the pituitary gland exhibits a distinct acinar architecture composed of rigid reticulin walls. Generally, pituitary adenomas proliferate and destroy these walls and present a variety of growth patterns.¹⁶ In the present study, in contrast to hard macroadenomas (Fig 2D), soft macroadenoma pathologic specimens showed typical destruction and thinning of the rigid reticulin walls and the presence of low collagen content (Figs 3D and 4C). Although the mechanism involved in CE-FIESTA is controversial, we speculate that the hyperintense dots apparent on CE-FIESTA may reflect enhancement of macroadenoma parenchyma as well as leakage and retention of contrast reagents into loose connective tissue and extra-

cellular space that no longer have rigid reticulin walls. In addition, the hyperintense dots were more frequently observed on CE-FIESTA compared with CE-T1WI, which may be explained by differences in the effect of contrast material between both sequences. Moreover, the high spatial resolution of CE-FIESTA, including thinner sections and reduction of the partial volume effects, may allow increased detection of hyperintense dots.

Our study has several limitations. First, histopathological confirmation of the entire tumor architecture was not obtained. Therefore, it was not possible to correlate the pathologic and radiologic findings. Moreover, it is unknown how specific pathologic changes in the macroadenoma are related to the hyperintense dots observed on CE-FIESTA. In addition, it was difficult to preserve intact tissue architecture because very little tissue is typically obtained from transphenoidal surgery. Second, this study was a retrospective analysis with a relatively small sample size. In particular, the incidence of hard adenomas was very low. Thus, future studies should consider the use of a larger sample size. Third, the FIESTA sequence was developed by only 1 vendor. However, previous studies have reported that other balanced steady-state free precession techniques, such as constructive interference in steady state by Siemens Medical Solutions and balanced fast field-echo by Philips Medical Systems, also provide strong T1 and T2 contrast^{9,17,18} and show contrast enhancement with gadolinium-based contrast reagents.¹¹ This suggests that results similar to those of our study may be reproducible with the use of these sequences developed from different vendors. Fourth, CE-FIESTA was performed after CE-T1WI in all cases. Although the observation of hyperintense dots occurred more frequently on CE-FIESTA compared with CE-T1WI, our results may have been affected by differences in so-called delayed enhancement effects² caused by the time lag after gadoteridol administration. Therefore, future studies of CE-FIESTA should consider the use of time-intensity curve analysis.

CONCLUSIONS

Our study reveals a distinct relationship between CE-FIESTA and intraoperative findings. We propose that CE-FIESTA findings are able to predict tumor consistency in pituitary macroadenomas. Furthermore, we deduced that macroadenomas with many hyperintense dots were indicative of a soft tumor consistency because they contained lower amounts of collagen. Thus, this study indicates that CE-FIESTA is a beneficial and practical MR imaging technique for preoperative evaluation of pituitary macroadenomas.

REFERENCES

1. Chacko G, Chacko AG, Lombardero M, et al. **Clinicopathologic correlates of giant pituitary adenomas.** *J Clin Neurosci* 2009;16:660–65
2. Schorner W, Laniado M, Niendorf HP, et al. **Time-dependent changes in image contrast in brain tumors after gadolinium-DTPA.** *AJNR Am J Neuroradiol* 1986;7:1013–20
3. D'Haens J, Van Rompaey K, Stadnik T, et al. **Fully endoscopic transphenoidal surgery for functioning pituitary adenomas: a retrospective comparison with traditional transphenoidal microsurgery in the same institution.** *Surg Neurol* 2009;72:336–40
4. Youssef AS, Agazzi S, van Loveren HR. **Transcranial surgery for pituitary adenomas.** *Neurosurgery* 2005;57(1 Suppl):168–75
5. Iuchi T, Saeki N, Tanaka M, et al. **MRI prediction of fibrous pituitary adenomas.** *Acta Neurochir (Wien)* 1998;140:779–86
6. Boxerman JL, Rogg JM, Donahue JE, et al. **Preoperative MRI evaluation of pituitary macroadenoma: imaging features predictive of successful transphenoidal surgery.** *AJR Am J Roentgenol* 2010;195:720–28
7. Pierallini A, Caramia F, Falcone C, et al. **Pituitary macroadenomas: preoperative evaluation of consistency with diffusion-weighted MR imaging: initial experience.** *Radiology* 2006;239:223–31
8. Bahuleyan B, Raghuram L, Rajshekhkar V, et al. **To assess the ability of MRI to predict consistency of pituitary macroadenomas.** *Br J Neurosurg* 2006;20:324–26
9. Haacke EM, Wielopolski PA, Tkach JA, et al. **Steady-state free precession imaging in the presence of motion: application for improved visualization of the cerebrospinal fluid.** *Radiology* 1990;175:545–52
10. Jayakumar PN, Kovoor JM, Srikanth SG, et al. **3D steady-state MR cisternography in CSF rhinorrhoea.** *Acta Radiol* 2001;42:582–84
11. Shigematsu Y, Korogi Y, Hirai T, et al. **Contrast-enhanced CISS MRI of vestibular schwannomas: phantom and clinical studies.** *J Comput Assist Tomogr* 1999;23:224–31
12. Yamamoto J, Kakeda S, Takahashi M, et al. **Dural attachment of intracranial meningiomas: evaluation with contrast-enhanced three-dimensional fast imaging with steady-state acquisition (FIESTA) at 3 T.** *Neuroradiology* 2011;53:413–23
13. Watanabe K, Kakeda S, Yamamoto J, et al. **Delineation of optic nerves and chiasm in close proximity to large suprasellar tumors with contrast-enhanced FIESTA MR imaging.** *Radiology* 2012;264:852–58
14. Naganuma H, Satoh E, Nukui H. **Technical considerations of transphenoidal removal of fibrous pituitary adenomas and evaluation of collagen content and subtype in the adenomas.** *Neurol Med Chir (Tokyo)* 2002;42:202–12
15. Suzuki C, Maeda M, Hori K, et al. **Apparent diffusion coefficient of pituitary macroadenoma evaluated with line-scan diffusion-weighted imaging.** *J Neuroradiol* 2007;34:228–35
16. Beatriz LW, McCarthy BJ. **Messenger RNA complexity in *Drosophila melanogaster*.** *Biochemistry* 1975;14:2440–46
17. Chung HW, Chen CY, Zimmerman RA, et al. **T2-weighted fast MR imaging with true FISP versus HASTE: comparative efficacy in the evaluation of normal fetal brain maturation.** *AJR Am J Roentgenol* 2000;175:1375–80
18. Tsuchiya K, Aoki C, Hachiya J. **Evaluation of MR cisternography of the cerebellopontine angle using a balanced fast-field-echo sequence: preliminary findings.** *Eur Radiol* 2004;14:239–42

Frontotemporal Cortical Thinning in Amyotrophic Lateral Sclerosis

A. d'Ambrosio, A. Gallo, F. Trojsi, D. Corbo, F. Esposito, M. Cirillo, M.R. Monsurrò, and G. Tedeschi

ABSTRACT

BACKGROUND AND PURPOSE: The extensive application of advanced MR imaging techniques has undoubtedly improved our knowledge of the pathophysiology of amyotrophic lateral sclerosis. Nevertheless, the precise extent of neurodegeneration throughout the central nervous system is not fully understood. In the present study, we assessed the spatial distribution of cortical damage in amyotrophic lateral sclerosis by using a cortical thickness measurement approach.

MATERIALS AND METHODS: Surface-based morphometry was performed on 20 patients with amyotrophic lateral sclerosis and 18 age- and sex-matched healthy control participants. Clinical scores of disability and disease progression were correlated with measures of cortical thickness.

RESULTS: The patients with amyotrophic lateral sclerosis showed a significant cortical thinning in multiple motor and extramotor cortical areas when compared with healthy control participants. Gray matter loss was significantly related to disease disability in the left lateral orbitofrontal cortex ($P = .04$), to disease duration in the right premotor cortex ($P = .007$), and to disease progression rate in the left parahippocampal cortex ($P = .03$).

CONCLUSIONS: Cortical thinning of the motor cortex might reflect upper motor neuron impairment, whereas the extramotor involvement seems to be related to disease disability, progression, and duration. The cortical pattern of neurodegeneration depicted resembles what has already been described in frontotemporal dementia, thereby providing further structural evidence of a continuum between amyotrophic lateral sclerosis and frontotemporal dementia.

ABBREVIATIONS: ALS = amyotrophic lateral sclerosis; ALSFRS-R = ALS Functional Rating Scale-Revised; CTh = cortical thickness; FrSBe = Frontal Systems Behavior Scale; FTD = frontotemporal dementia; HCs = healthy control participants; PMC = primary motor cortex; SBM = surface-based morphometry; TDP-43 = transactivating responsive sequence DNA-binding protein 43-kDa; UMN = upper motor neuron; VBM = voxel-based morphometry

Despite the common view of amyotrophic lateral sclerosis (ALS) as a neurodegenerative disease that exclusively affects motor functions, convincing evidence supports the notion that ALS is a multisystem disease also affecting behavior, language,

and cognition.¹⁻⁶ Indeed, among patients with ALS, as many as 15% meet criteria for frontotemporal dementia (FTD), whereas up to 35% show a mild to moderate cognitive impairment.^{5,7} From the histochemical and genetic points of view, recent findings suggest that ALS may belong to a broader clinicopathologic spectrum, known as transactivating responsive sequence DNA-binding protein 43-kDa (TDP-43) proteinopathy, which also includes FTD.⁸⁻¹⁰

Structural and functional MR imaging studies have corroborated the theory of a relevant frontotemporal impairment in ALS with approximately half of the patients displaying at least mild abnormalities.¹¹⁻²⁰

The development of advanced automated imaging analysis techniques, on the basis of construction of statistical parametric maps, has allowed detailed anatomic studies of brain morphometry. Voxel-based morphometry (VBM) allows a fully automated whole-brain measurement of regional brain atrophy by voxelwise

Received March 28, 2013; accepted after revision May 29.

From the Department of Medical, Surgical, Neurological, Metabolic and Aging Sciences (A.d'A., A.G., F.T., M.R.M., M.C., G.T.), Second University of Naples, Naples, Italy; MRI Research Center SUN-FISM—Neurological Institute for Diagnosis and Care "Hermitage Capodimonte," (A.d'A., A.G., F.T., D.C., F.E., M.C., M.R.M., G.T.), Naples, Italy; Department of Medicine and Surgery (F.E.), University of Salerno, Salerno, Italy; and Department of Cognitive Neuroscience (F.E.), Maastricht University, Maastricht, The Netherlands.

A.d'A. and A.G. contributed equally to this study.

Please address correspondence to Prof. Gioacchino Tedeschi, MD, Department of Medical, Surgical, Neurological, Metabolic and Aging Sciences, Second University of Naples, Piazza Miraglia 2, 80138 Naples, Italy; e-mail: gioacchino.tedeschi@unina2.it

<http://dx.doi.org/10.3174/ajnr.A3753>

Table 1: Demographics and clinical features

	Group	
	HC	ALS
<i>n</i>	18	20
M/F	10/8	10/10
Mean age, y (SD)	60 (10.5)	61.5 (9.1)
Disease duration, mean y (SD)	n/a	2.6 (2.7)
Upper limbs onset	n/a	10
Lower limbs onset	n/a	10
ALSFRS-R, mean (SD)	n/a	36.2 (8.7)
48-ALSFRS-R/months of disease duration, mean (SD)	n/a	0.64 (0.7)
UMN score, mean (SD)	n/a	7.1 (3.9)
FrSBe, mean (SD)	n/a	102.3 (18.5)

Note:—n/a indicates not applicable; SD, standard deviation.

comparison of GM and WM volumes between groups of participants.²¹ The most consistent finding of VBM studies in ALS involves GM atrophy in several regions of the frontal (ie, anterior cingulate, middle and inferior frontal gyrus) and temporal lobes (ie, temporal poles, superior temporal gyrus, temporal isthmus, hippocampus),^{11-13,16,17,19} reporting significant correlations between GM atrophy and cognitive dysfunction mainly in patients with an ALS-plus syndrome (ie, ALS with cognitive and behavioral symptoms).²⁰ However, the lack of agreement on cortical atrophy distribution²² has prompted the application of other advanced MR imaging approaches. Surface-based morphometry (SBM), allowing cortical thickness (CTh) measurements,²³ has shown several advantages compared with VBM in reconstructing the cortical surface. This technique, indeed, allows decomposition of cortical volume into both thickness and surface area, respecting the cortical topology and enhancing reliability and sensitivity.²⁴ Therefore, mainly to identify a more sensitive marker of upper motor neuron (UMN) degeneration, CTh analysis has been applied to the study of ALS, revealing cortical thinning not only in the precentral gyrus,^{18,25-27} but also within the numerous fronto-temporal, parietal, and occipital areas.²⁶⁻²⁸ It is noteworthy that, so far, the correlation between regional cortical thinning and clinical features has not been fully assessed. On this background, we aimed to further investigate—without any a priori hypothesis—the pattern of both motor and extramotor cortical involvement in patients with sporadic ALS and to explore the relationship between MR imaging data and clinical and neuropsychological features.

MATERIALS AND METHODS

Study Population

We investigated 20 patients with ALS (10 women and 10 men), who fulfilled the diagnostic criteria for probable or definite ALS, according to the revised El Escorial Criteria of the World Federation of Neurology. (See Table 1 for clinical and demographic data.)²⁹

The site of disease onset was the upper limbs in 10 patients and lower limbs in the remaining patients. All had a “classic” phenotype including bulbar signs in 9 patients. We excluded from the analysis patients with dominant lower motor neuron impairment (ie, progressive muscular atrophy, flail leg syndrome, pseudopolyneuritic form), progressive bulbar palsy, primary lateral sclerosis, postpoliomyelitis ALS, and motor neuron disease with multi-

system involvement (ie, ALS dementia). The mean disease duration between the first symptom and study visit was 2.6 years. However, we included 5 patients with a survival time of longer than 4 years, 2 of whom were receiving artificial respiratory support (mean duration of noninvasive ventilation, 68 months). None of the patients needed percutaneous endoscopic gastrostomy, and none had other neurologic diseases. All patients were receiving treatment with riluzole (50 mg twice daily).

The average functional status, as measured by the ALS Functional Rating Scale-Revised (ALSFRS-R),³⁰ ranged from 18–47. The disease progression rate, as measured by the ratio 48–ALSFRS-R/months of disease duration,³¹ ranged from 0.03–2.5. The quantitative assessment of clinical UMN involvement was based on a scale used in previous ALS neuroimaging studies,^{17,32} which evaluates the number of pathologic reflexes, elicited from 15 body sites: glabellum, orbicularis oris, masseter (jaw jerk), biceps, triceps and finger jerks bilaterally, and knee, ankle, and Babinski responses bilaterally. In our population this score ranged from 1–14.

No subjects had familial ALS or tested positive for the most common mutations related to ALS (ie, superoxide dismutase 1 or *SOD1*, transactive response DNA-binding protein or *TARDBP*, fused in sarcoma/translocated in liposarcoma or *FUS/TLS* and *C9ORF72*).

All patients with ALS underwent a brief neuropsychological assessment, including the Mini-Mental State Examination³³ and phonemic and semantic fluency tasks,^{33,34} which showed normal cognitive performances (cutoff values were 24, 17.35, and 7.25, and mean values were 28.5 ± 1.7 , 26.8 ± 9 , and 15 ± 4.3 , respectively, for the Mini-Mental State Examination and phonemic and semantic fluency tasks). The Frontal Systems Behavior (FrSBe) scale evaluation,³⁵ a questionnaire that measures apathy, disinhibition, and executive dysfunction and quantifies changes with time by comparing baseline (retrospective) and current assessments of behavior in a standardized T score ($T > 65$ is defined as impaired behavior and executive functions), was also administered to our patients and their caregivers. In our population, the mean total T score was 110.8 ± 21.7 , derived from the caregiver and referring to the present time; the T score was > 65 in 19 of 20 patients.

Eighteen age- and sex-matched healthy control participants (HCs) with no history of neurologic or psychiatric diseases and with a normal neuropsychological evaluation were enrolled in the study.

Informed consent was obtained from all participants before study entry, according to the Declaration of Helsinki. The study was approved by the ethical committee of the Second University of Naples.

3T MR Imaging

Images were obtained on a 3T HDx scanner (GE Healthcare, Milwaukee, Wisconsin) equipped with an 8 channel-coil. The following sequences were acquired: 2D axial FSE double-echo proton density/T2; 2D axial T2-FLAIR; 3D T1-weighted sagittal images (GE sequence IR-FSPGR: TR, 6.988 ms; TI, 650 ms; TE, 3.9 ms; flip angle, 10°; voxel size, $1 \times 1 \times 1.2$ mm³).

Measurements of Brain Cortical Thickness

FreeSurfer software version 4.5 (<http://surfer.nmr.mgh.harvard.edu>) running on a 64-bit Linux CentOS-4 (<http://www.centos.org>) was used to process anatomic 3D-T1 sagittal images and to measure whole-brain CTh.

In brief, after registration to the Talairach space and intensity normalization, the process involves automatic skull stripping by use of a hybrid method combining watershed algorithms and deformable surface models. Then, the WM/GM boundary was tessellated, and the surface was deformed following GM/CSF intensity gradients to optimally place WM/GM and GM/CSF borders. The results of these segmentations were inspected visually and, if needed, edited manually by adding control points. An automatic reconstruction of the cortex was produced and CTh estimated by computing the average shortest distance between the WM boundary and the GM/CSF surface. Surface maps were generated following registration of all participants' cortical reconstructions to a common average surface. Finally, surface maps were smoothed by use of default kernel of 10 mm.

The statistical parametric analysis was performed by the built-in Qdec module implemented in FreeSurfer, by use of a general linear model. Age and sex were used as covariates. Maps showing significant group differences between patients with ALS and HCs were generated by thresholding the images of *t* statistics at a .05 significance level, corrected for a false discovery rate.

A region-of-interest approach, by use of areas where significant CTh differences emerged from the between-group analysis, was used for the correlation analysis.

Each specific area (coming from the between-group analysis) was then labeled and projected into the original space of each participant, to measure the average CTh (for each area, in each participant). These measures were then transposed in a spreadsheet to run the correlation analysis.

Regional CTh data were corrected for total brain volume without finding any significant difference. A 2-tail analysis was used. Pearson correlation coefficients were calculated to evaluate the relationship between the clinical variables (UMN score, ALSFRS-R, FrSBe scale, disease duration, and disease progression rate) and the average CTh values within the motor and extramotor areas found to be thinner in patients compared with HCs. *P* values < .05 were considered statistically significant after correction for multiple comparisons with the Bonferroni method.

RESULTS

We found multiple brain areas of significant cortical thinning in patients with ALS when compared with HCs (Fig 1–4 and, for details, Table 2). These cortical regions localized in the bilateral frontal and prefrontal cortex (Fig 1, areas 1–4; Fig 2, areas 1–11; Fig 3, areas 1–4; Fig 4, areas 1–4), including the primary motor cortex (PMC); the bilateral temporal cortex (Fig 1, area 5; Fig 3, areas 5, 8; Fig 4, area 8); and the bilateral parieto-occipital cortex (Fig 3, areas 6, 7; Fig 4, areas 5–7). Conversely, CTh was found to be increased in patients with ALS compared with HCs in few and scattered cortical areas localized in the right hemisphere (lateral and medial surface, Figs 1 and 3).

Regarding correlations between CTh measurements and clinical characteristics of patients, we found that CTh of the left fron-

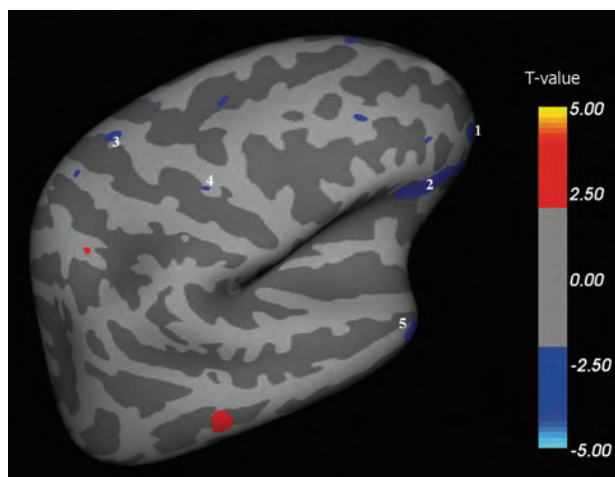


FIG 1. Right hemisphere, lateral surface. Areas showing a significant cortical thinning in patients with ALS ($P < .05$) are colored in blue. Areas 1–4 are localized in the frontal region. Area 5 is localized in the temporal region.

tal lateral cortex (Fig 2, area 1, orbitofrontal lateral cortex) correlated with disease disability ($P = .04$) (ALSFRS-R); CTh of the right medial frontal cortex (Fig 3, area 4, premotor cortex) correlated with disease duration ($P = .007$); and CTh of the left medial temporal cortex (Fig 4, area 8, inferior temporal and parahippocampal cortex) correlated with the disease progression rate ($P = .03$) ($48 - \text{ALSFRS-R}/\text{months of disease duration}$). No other correlations were found between CTh and other clinical and neuropsychological parameters (ie, UMN scores, FrSBe T-scores and subscores for apathy, disinhibition, and executive dysfunction).

DISCUSSION

Cortical damage in ALS has been shown not to be limited to motor areas alone but to involve extramotor areas as well.^{6–10} In vivo, independent of the structural neuroimaging approach used (VBM or SBM), the most commonly affected extramotor cortical areas were identified in the frontal and temporal lobes.^{11–20,26–28} However, significant correlations between cortical involvement and disease progression^{18,26,27} or cognitive impairment^{2,14,15,20,28} were reported only in a few studies.

Our findings resemble previous CTh results showing a significant PMC thinning in patients with ALS when compared with HCs.^{18,25–27} The cortical thinning of this region appears to be a radiologic correlate of Betz cells shrinkage and loss with reactive gliosis reported by neuropathologic studies.^{36–38}

Regarding morphometric results of the extent of cortical impairment in patients with ALS, VBM studies showed GM changes in several regions of the frontal and temporal lobes,^{11,13–16,19,20} whereas SBM studies indicated a more consistent involvement of the PMC.^{18,25–27} In this respect, the mildly divergent results obtained by VBM and SBM in analyzing the topography of GM atrophy in ALS could be the result of methodologic differences between the 2 techniques, intrinsic complexity of the pathologic process,³⁷ and clinical heterogeneity of the studied populations. It is important to note that VBM explores the between-group differences in regional GM concentration, which can depend on both CTh and amounts of cortical folding.²¹ Conversely, SBM

Table 2: Spatial coordinates, extent, and average CTh of areas showing significant cortical thinning between patients with ALS and HCs

Area	Talairach Coordinates (x, y, z)	Surface Extension (mm ²)	ALS Mean CTh (mm)	HC Mean CTh (mm)
Right hemisphere, lateral surface (see Fig 1 for reference)				
1	0, 97, -35	178	2.778	2.891
2	13, 74, -33	713	2.482	2.687
3	-12, -2, 69	39	2.462	2.793
4	22, 13, 39	15	2.662	2.952
5	23, 27, -69	269	3.152	3.387
Left hemisphere, lateral surface (see Fig 2 for reference)				
1	5, 85, -45	501	2.398	2.651
2	-13, 78, -32	37	3.050	3.134
3	-14, 88, -17	65	2.039	2.323
4	-20, 73, -3	206	1.860	2.116
5	-12, 76, 13	69	2.527	2.796
6	-12, 38, -42	175	3.350	3.652
7	-14, 37, -16	154	2.271	2.434
8	-22, 3, 43	22	1.389	1.557
9	11, 28, 61	57	2.164	2.522
10	-40, -4, 15	232	2.569	2.817
11	-33, -21, 31	152	2.293	2.507
Right hemisphere, medial surface (see Fig 3 for reference)				
1	-32, 82, 0	116	2.250	2.516
2	-31, 62, 26	131	2.347	2.510
3	-31, 40, 40	139	2.336	2.664
4	-31, 15, 38	67	2.187	2.450
5	2, 11, -64	159	3.342	3.970
6	-29, -57, 18	72	2.536	2.724
7	-25, -93, -19	204	1.571	1.797
8	17, -44, -52	65	2.697	2.928
Left hemisphere, medial surface (see Fig 4 for reference)				
1	28, 93, -39	179	2.288	2.668
2	33, 51, 24	55	2.063	2.509
3	30, 41, 49	40	2.769	2.929
4	28, 13, 66	44	2.407	2.747
5	28, -68, 25	67	2.411	2.614
6	28, -63, 17	43	2.634	2.769
7	20, -102, -28	155	1.685	1.826
8	-4, -3, -64	558	3.012	3.470

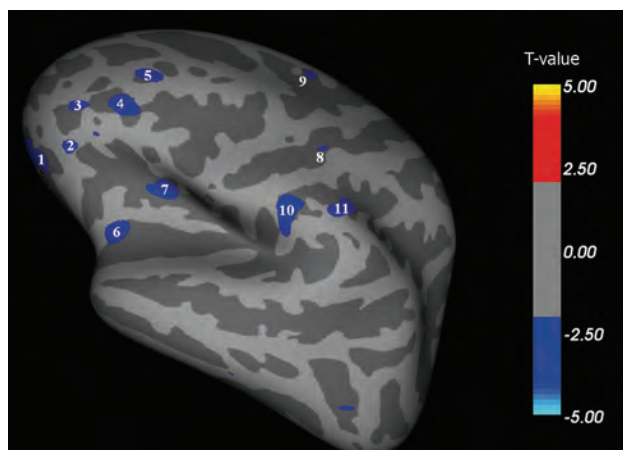


FIG 2. Left hemisphere, lateral surface. Areas showing a significant cortical thinning in patients with ALS ($P < .05$) are colored in blue. Areas 1–11 are localized in the frontal region. CTh in area 1 (orbitofrontal lateral cortex) correlated with disease disability ($P = .04$).

explores the actual cortical thinning, avoiding errors attributable to the complex brain cortical folding.²³ Therefore, compared with SBM, VBM measures have been found to have a lower signal-to-

noise ratio with a lower sensitivity to cortical atrophy localized in brain sulci.³⁹ Against this background, we designed our study, believing that SBM could be a valuable tool for investigating in vivo the cortical damage in ALS. However, although our present study does not aim to compare SBM and VBM methods when applied to ALS, we have run a VBM analysis with the SPM8 software package (Wellcome Department of Imaging Neuroscience, London, UK) of the same group of participants analyzed by SBM. In this analysis, we have observed that the main difference between the 2 approaches was in the extent of frontal, temporal, and parietal damage, more widely depicted by CTh measurements (data not shown).

In our present study, PMC thinning did not show any significant correlation with clinical scores of UMN impairment, disability, and disease progression. This finding is in agreement with that of Roccatagliata et al,²⁵ who reported a similar lack of correlations. This negative result might reflect the small number of studied patients on one hand but, on the other, the effect of a likely “ceiling phenomenon” that hinders the chance to explore a correlation with clinical scores and to assess a progressive cortical thinning of primary motor areas in longitudinal measures.²⁶ It is probable that reactive gliosis in the deep layers of the motor cortex, described in most neuropathologic studies,

^{37,38,40} may occur to a degree enough to “mask” tissue loss especially in the later stages of disease, as observed in our population. Finally, it should also be considered that PMC degeneration seems to affect or reduce CTh even before the onset of clinical symptoms, supporting the hypothesis that ALS might start in the cerebral cortex.⁴⁰ In fact, the previously reported observation that cortical hyperexcitability precedes the development of clinical symptoms in presymptomatic carriers of a *SOD1* mutation⁴¹ allows us to hypothesize that early ALS abnormalities occur within the PMC, with a subsequent anterograde excitotoxicity (often referred to as “dying forward” degeneration). For the above-mentioned reason, PMC thinning might have the potential to be a marker for UMN involvement in the diagnostic phase and possibly in the preclinical phase, but it could have limited value in the later stages of ALS, when a significant neurodegenerative threshold has already been reached, as likely occurred in our population.

Another relevant limitation of the correlation analysis between CTh measures and UMN signs was the lack of clinical scores highly specific for the detection of corticomotor neuron degeneration in ALS. Indeed, it has been shown that prominent clinical disability may occur even in the absence of impairment of the pyramidal pathway, and vice versa.^{37,41}

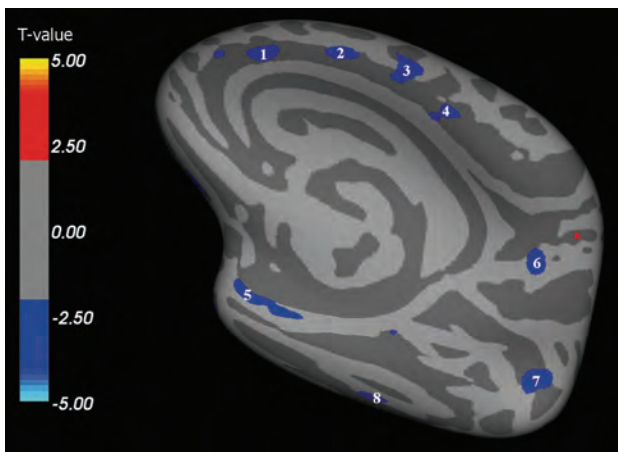


FIG 3. Right hemisphere, medial surface. Areas showing a significant cortical thinning in patients with ALS ($P < .05$) are colored in blue. Areas 1–4 are localized in the frontal region. Areas 5 and 8 are localized in the temporal region. Areas 6 and 7 are localized in the parietooccipital region. CTh in area 4 (premotor cortex) correlated with disease duration ($P = .007$).

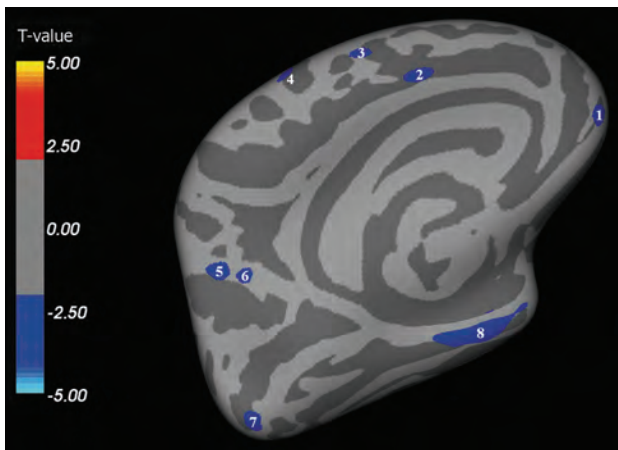


FIG 4. Left hemisphere, medial surface. Areas showing a significant cortical thinning in patients with ALS ($P < .05$) are colored in blue. Areas 1–4 are localized in the frontal region. Areas 7 and 8 are localized in the temporal region. Areas 5 and 6 are localized in the parietooccipital region. CTh in area 8 (inferior temporal and parahippocampal cortex) correlated with the rate of disease progression ($P = .0265$).

In addition to PMC, we detected a significant cortical thinning in multiple extramotor areas, particularly in the frontotemporal regions. These findings confirm previous neuroimaging studies in ALS,^{6,11,13-15,19,20} where the spatial distribution of neurodegeneration closely resembled patterns identified in FTD variants.⁴² Furthermore, the widespread cortical damage found in our ALS population overlaps *ex vivo* findings related to the expression of a TDP-43 pathologic feature. However, although our finding of a distributed involvement of the frontal, temporal, parietal, and occipital lobes is in keeping with the known spectrum of cognitive^{3,5} and pathologic¹⁰ overlap between ALS and FTD, none of our participants had overt dementia. Here we should acknowledge a limit of our present study, in which extensive neuropsychological testing (ie, including assessment of executive functioning, language, and memory) was not acquired given that

ALS-related physical symptoms could have affected the evaluation.

Our correlation analysis, in agreement with some previous results,^{26,27} showed that cortical thinning in temporal regions (inferior temporal and parahippocampal cortices) was significantly related to a faster disease course. Moreover, we described for the first time significant correlations between cortical thinning in the right medial frontal area (premotor cortex) and disease duration, and in the left lateral frontal area (orbitofrontal lateral cortex) and disability (ALSFRS-R).

If we take these results together, our data could suggest an increased vulnerability to neurodegeneration of both the frontal and temporal extramotor areas, depicting a pattern of cortical thinning similar to what was observed in the behavioral variant of frontotemporal dementia⁴² or in ALS-FTD⁴³ and confirming that frontotemporal involvement is a consistent feature of ALS. Specifically, the above-mentioned correlation between inferior temporal and parahippocampal thinning and disease progression rate may recall the recent finding of a widespread atrophy of the same temporal areas in patients with the behavioral variant of FTD.⁴⁴ Moreover, the significant thinning of the orbitofrontal and premotor areas, which we found to correlate with ALSFRS-R and disease duration, may reflect a similar cortical degeneration pattern reported in both the behavioral variant of FTD and primary-progressive aphasia, in which atrophy of the orbitofrontal and premotor areas was found to correlate with the occurrence of severely disabling behavioral changes (ie, aberrant eating and motor behaviors).⁴⁵⁻⁴⁷

It is remarkable that no correlations were found between cortical thinning of the frontotemporal areas and frontal impairment (evaluated by T-score and subscores of FrSBe scale). By contrast, previous studies have reported an association between regional volume loss in several frontotemporal areas and cognitive and behavioral symptoms in both ALS^{2,14,15,20} and the behavioral variant of FTD.^{45,48,49} However, we are only in apparent disagreement with previous VBM studies conducted in patients with ALS.^{2,14,15,20} In fact, the different methodologic approaches used, the heterogeneity of the populations studied, and the intrinsic limitation of the FrSBe scale (because it contains questions that may be influenced by disease-related somatic symptoms⁵⁰) could explain such discordance. Moreover, the idea of specific structural changes in the individual frontotemporal areas underlying behavioral impairment in ALS is only partially accepted. Instead, it should be considered that although apathy is considered the most prominent behavioral feature in patients with ALS,^{2-4,51} consistent neuroanatomic correlates are lacking.^{50,52,53}

Finally, our results also showed areas of CTh in patients with ALS when compared with HCs. Such areas, albeit few and scattered, might speculatively suggest that compensatory mechanisms (associated with structural remodeling) might take place in the ALS cortex, as already observed in other neurologic and psychiatric diseases such as stroke,⁵⁴ traumatic brain injury,⁵⁵ and obsessive-compulsive disorder.⁵⁶

CONCLUSIONS

Our present study supports the hypothesis that clinical disability in ALS is linked with both motor and extramotor cortical degen-

eration. Our data further support the potential role of extramotor frontal and temporal areas in influencing outcomes of ALS, suggesting that the more widespread the cortical damage, the more aggressive the disease. The pattern of cortical neurodegeneration described in our sample of patients with ALS, which covers many disease features especially in the advanced stages, provides further structural evidence of a continuum between ALS and FTD. However, the limited number of patients studied and the lack of a complete neuropsychological assessment might have partially hindered such an effort.

Longitudinal studies on groups of several ALS subtypes or phenotypes in the early stages of the disease are warranted to further characterize the spatial and temporal evolution of cortical damage, the correlations of MR imaging data with clinical and neuropsychological features, and the reliability of CTh as a biomarker of disease progression.

Disclosures: Mario Cirillo—UNRELATED: Payment for Lectures (including service on speaker bureaus): Bayer Schering Pharma,* Comments: €1600. Gioacchino Tedeschi—UNRELATED: Grants/Grants Pending: Novartis,* Comments: Research fellowships (pending, €145,000). Payment for Lectures (including service on speaker bureaus): Novartis,* Merck Serono,* Biogen Idec*; Comments: €20,000; Travel/Accommodations/Meeting Expenses Unrelated to Activities Listed: Novartis,* Merck Serono,* Biogen Idec.* *Money paid to institution.

REFERENCES

- Kiernan MC, Vucic S, Cheah BC, et al. **Amyotrophic lateral sclerosis.** *Lancet* 2011;377:942–55
- Grossman M, Anderson C, Khan A, et al. **Impaired action knowledge in amyotrophic lateral sclerosis.** *Neurology* 2008;71:1396–401
- Phukan J, Pender NP, Hardiman O. **Cognitive impairment in amyotrophic lateral sclerosis.** *Lancet Neurol* 2007;6:994–1003
- Gibbons ZC, Richardson A, Neary D, et al. **Behaviour in amyotrophic lateral sclerosis.** *Amyotroph Lateral Scler* 2008;9:67–74
- Ringholz GM, Appel SH, Bradshaw M, et al. **Prevalence and patterns of cognitive impairment in sporadic ALS.** *Neurology* 2005;65:586–90
- Tsermentseli S, Leigh PN, Goldstein LH. **The anatomy of cognitive impairment in amyotrophic lateral sclerosis: more than frontal lobe dysfunction.** *Cortex* 2012;48:166–82
- Murphy JM, Henry RG, Langmore S, et al. **Continuum of frontal lobe impairment in amyotrophic lateral sclerosis.** *Arch Neurol* 2007;64:530–34
- Geser F, Martinez-Lage M, Robinson J, et al. **Clinical and pathological continuum of multisystem TDP-43 proteinopathies.** *Arch Neurol* 2009;66:180–89
- Geser F, Brandmeir NJ, Kwong LK, et al. **Evidence of multisystem disorder in whole-brain map of pathological TDP-43 in amyotrophic lateral sclerosis.** *Arch Neurol* 2008;65:636–41
- Ludolph AC, Brettschneider J, Weishaupt JH. **Amyotrophic lateral sclerosis.** *Curr Opin Neurol* 2012;25:530–35
- Agosta F, Pagani E, Rocca MA, et al. **Voxel-based morphometry study of brain volumetry and diffusivity in amyotrophic lateral sclerosis patients with mild disability.** *Hum Brain Mapp* 2007;28:1430–38
- Kassubek J, Unrath A, Huppertz HJ, et al. **Global brain atrophy and corticospinal tract alterations in ALS, as investigated by voxel-based morphometry of 3-D MRI.** *Amyotroph Lateral Scler Other Motor Neuron Disord* 2005;6:213–20
- Ellis CM, Suckling J, Amaro E Jr, et al. **Volumetric analysis reveals corticospinal tract degeneration and extramotor involvement in ALS.** *Neurology* 2001;57:1571–78
- Mezzapesa DM, Ceccarelli A, Dicuonzo F, et al. **Whole-brain and regional brain atrophy in amyotrophic lateral sclerosis.** *AJNR Am J Neuroradiol* 2007;28:255–59
- Tsujimoto M, Senda J, Ishihara T, et al. **Behavioral changes in early ALS correlate with voxel-based morphometry and diffusion tensor imaging.** *J Neurol Sci* 2011;307:34–40
- Thivard L, Pradat P-F, Lehericy S, et al. **Diffusion tensor imaging and voxel based morphometry study in amyotrophic lateral sclerosis: relationships with motor disability.** *J Neurol Neurosurg Psychiatry* 2007;78:889–92
- Filippini N, Douaud G, Mackay CE, et al. **Corpus callosum involvement is a consistent feature of amyotrophic lateral sclerosis.** *Neurology* 2010;75:1645–52
- Verstraete E, van den Heuvel MP, Veldink JH, et al. **Motor network degeneration in amyotrophic lateral sclerosis: a structural and functional connectivity study.** *PLoS One* 2010;5:e13664
- Tedeschi G, Trojsi F, Tessitore A, et al. **Interaction between aging and neurodegeneration in amyotrophic lateral sclerosis.** *Neurobiol Aging* 2012;33:886–98
- Mioshi E, Lillo P, Yew B, et al. **Cortical atrophy in ALS is critically associated with neuropsychiatric and cognitive changes.** *Neurology* 2013;80:1117–23
- Ashburner J, Friston KJ. **Voxel-based morphometry—the methods.** *NeuroImage* 2000;11:805–21
- Turner MR, Grosskreutz J, Kassubek J, et al. **Towards a neuroimaging biomarker for amyotrophic lateral sclerosis.** *Lancet Neurol* 2011;10:400–03
- Fischl B, Dale AM. **Measuring the thickness of the human cerebral cortex from magnetic resonance images.** *Proc Natl Acad Sci U S A* 2000;97:11050–55
- Pereira JB, Ibarretxe-Bilbao N, Marti MJ, et al. **Assessment of cortical degeneration in patients with Parkinson's disease by voxel-based morphometry, cortical folding, and cortical thickness.** *Hum Brain Mapp* 2012;33:2521–34
- Roccatagliata L, Bonzano L, Mancardi G, et al. **Detection of motor cortex thinning and corticospinal tract involvement by quantitative MRI in amyotrophic lateral sclerosis.** *Amyotroph Lateral Scler* 2009;10:47–52
- Verstraete E, Veldink JH, Hendrikse J, et al. **Structural MRI reveals cortical thinning in amyotrophic lateral sclerosis.** *J Neurol Neurosurg Psychiatry* 2012;83:383–88
- Agosta F, Valsasina P, Riva N, et al. **The cortical signature of amyotrophic lateral sclerosis.** *PLoS One* 2012;7:e42816
- Libon DJ, McMillan C, Avants B, et al. **Deficits in concept formation in amyotrophic lateral sclerosis.** *Neuropsychology* 2012;26:422–29
- Brooks BR, Miller RG, Swash M, et al. **El Escorial revisited: revised criteria for the diagnosis of amyotrophic lateral sclerosis.** *Amyotroph Lateral Scler Other Motor Neuron Disord* 2000;1:293–99
- Cedarbaum JM, Stambler N, Malta E, et al. **The ALSFRS-R: a revised ALS functional rating scale that incorporates assessments of respiratory function. BDNF ALS Study Group (Phase III).** *J Neurol Sci* 1999;169:13–21
- Ellis CM, Simmons A, Jones DK, et al. **Diffusion tensor MRI assesses corticospinal tract damage in ALS.** *Neurology* 1999;53:1051–58
- Turner MR, Cagnin A, Turkheimer FE, et al. **Evidence of widespread cerebral microglial activation in amyotrophic lateral sclerosis: an [(11)C](R)-PK11195 positron emission tomography study.** *Neurobiol Dis* 2004;15:601–09
- Pasqualetti P, Moffa F, Chioyenda P, et al. **Mini-mental state examination and mental deterioration battery: analysis of the relationship and clinical implications.** *J Am Geriatr Soc* 2002;50:1577–81
- Borkowski JG, Benton AL, Spreen O. **Word fluency and brain damage.** *Neuropsychologia* 1967;5:135–40
- Grace J, Stout JC, Malloy PF. **Assessing frontal lobe behavioral syndromes with the frontal lobe personality scale.** *Assessment* 1999;6:269–84
- Kiernan JA, Hudson AJ. **Changes in sizes of cortical and lower motor neurons in amyotrophic lateral sclerosis.** *Brain* 1991;114:843–53
- Ince PG, Wharton SB. **Cytopathology of the motor neuron.** In: Eisen AA, Shaw PJ, eds. *Motor Neuron Disorders and Related Diseases: Hand-*

book of Clinical Neurology, 3rd ed. Amsterdam, the Netherlands: Elsevier;2007:89–119

38. Ince PG, Highley JR, Kirby J, et al. **Molecular pathology and genetic advances in amyotrophic lateral sclerosis: an emerging molecular pathway and the significance of glial pathology.** *Acta Neuropathol* 2011;122:657–71
39. Hutton C, Draganski B, Ashburner J, et al. **A comparison between voxel-based cortical thickness and voxel-based morphometry in normal aging.** *Neuroimage* 2009;48:371–80
40. Eisen A, Weber M. **The motor cortex and amyotrophic lateral sclerosis.** *Muscle Nerve* 2001;24:564–73
41. Vucic S, Nicholson GA, Kiernan MC. **Cortical hyperexcitability may precede the onset of familial amyotrophic lateral sclerosis.** *Brain* 2008;131:1540–50
42. Agosta F, Canu E, Sarro L, et al. **Neuroimaging findings in frontotemporal lobar degeneration spectrum of disorders.** *Cortex* 2012;48:389–413
43. Mahoney CJ, Beck J, Rohrer JD, et al. **Frontotemporal dementia with the C9ORF72 hexanucleotide repeat expansion: clinical, neuroanatomical and neuropathological features.** *Brain* 2012;135:736–50
44. Seeley WW, Crawford R, Rascofsky K, et al. **Frontal paralimbic network atrophy in very mild behavioral variant frontotemporal dementia.** *Arch Neurol* 2008;65:249–55
45. Rosen HJ, Allison SC, Schauer GF, et al. **Neuroanatomical correlates of behavioural disorders in dementia.** *Brain* 2005;128:2612–25
46. Whitwell JL, Sampson EL, Loy CT, et al. **VBM signatures of abnormal eating behaviours in frontotemporal lobar degeneration.** *Neuroimage* 2007;35:207–13
47. Rohrer JD, Warren JD. **Phenomenology and anatomy of abnormal behaviours in primary progressive aphasia.** *J Neurol Sci* 2010;293:35–38
48. Williams GB, Nestor PJ, Hodges JR. **Neural correlates of semantic and behavioural deficits in frontotemporal dementia.** *NeuroImage* 2005;24:1042–51
49. Zamboni G, Huey ED, Krueger F, et al. **Apathy and disinhibition in frontotemporal dementia: insights into their neural correlates.** *Neurology* 2008;71:736–42
50. Woolley SC, Zhang Y, Schuff N, et al. **Neuroanatomical correlates of apathy in ALS using 4 Tesla diffusion tensor MRI.** *Amyotroph Lateral Scler* 2011;12:52–58
51. Lillo P, Mioshi E, Zoing MC, et al. **How common are behavioural changes in amyotrophic lateral sclerosis?** *Amyotroph Lateral Scler* 2011;12:45–51
52. Meier SL, Charleston AJ, Tippett LJ. **Cognitive and behavioural deficits associated with the orbitomedial prefrontal cortex in amyotrophic lateral sclerosis.** *Brain* 2010;133:3444–57
53. Levy R, Dubois B. **Apathy and the functional anatomy of the prefrontal cortex–basal ganglia circuits.** *Cereb Cortex* 2006;16:916–28
54. Brodtmann A, Pardoe H, Li Q, et al. **Changes in regional brain volume three months after stroke.** *J Neurol Sci* 2012;322:122–28
55. Wilde EA, Merkley TL, Bigler ED, et al. **Longitudinal changes in cortical thickness in children after traumatic brain injury and their relation to behavioral regulation and emotional control.** *Int J Dev Neurosci* 2012;30:267–76
56. Fan Q, Palaniyappan L, Tan L, et al. **Surface anatomical profile of the cerebral cortex in obsessive-compulsive disorder: a study of cortical thickness, folding and surface area.** *Psychol Med* 2013;43:1081–91

Use of FLAIR Imaging to Identify Onset Time of Cerebral Ischemia in a Canine Model

X.-Q. Xu, Q.-Q. Zu, S.-S. Lu, Q.-G. Cheng, J. Yu, Y. Sheng, H.-B. Shi, and S. Liu



ABSTRACT

BACKGROUND AND PURPOSE: Stroke is a leading cause of death and disability, and many studies have focused on the evolution of FLAIR imaging in the acute and chronic time window. The purpose of this study was to evaluate the potential efficacy of FLAIR-related techniques in identifying the onset time of cerebral ischemia in a canine embolic stroke model.

MATERIALS AND METHODS: An embolic ischemic model was generated through the use of an autologous clot in 20 beagle dogs. Both FLAIR and DWI were performed at 3 hours, 4 hours, 5 hours, 6 hours, and 24 hours after embolization, respectively. Visual “DWI-FLAIR mismatch” was defined as hyperintense signal detected on DWI but not on FLAIR. The relative signal intensity of FLAIR-positive lesions and the degree of DWI-FLAIR mismatch was calculated as relative FLAIR = relative signal intensity of FLAIR positive lesions, mismatch degree = $(100 - V_{\text{FLAIR}}/V_{\text{DWI}}) \times 100\%$.

RESULTS: The ischemic model was successfully established in all animals. FLAIR-positive lesions were seen in 3, 11, 16, 19, and 20 beagle dogs at 5 time points after embolization, respectively. There was significant correlation between the relative FLAIR, degree of DWI-FLAIR mismatch, and the onset time (relative FLAIR: $r = +0.42$; 95% CI, 0.20–0.60; mismatch degree: $r = -0.85$; 95% CI, 0.89–0.78). Receiver operating characteristic curves showed that the degree of DWI-FLAIR mismatch could identify the hyperacute ischemic lesions with a sensitivity range from 1.00–0.76; visual DWI-FLAIR mismatch sensitivity ranged from 0.85–0.39, whereas specificity was 0.83–0.95 versus 0.85–1.00.

CONCLUSIONS: The relative FLAIR and DWI-FLAIR mismatch values were useful in predicting the onset time in our canine embolic stroke model. The degree of DWI-FLAIR mismatch proposed in our study could be a good indicator with high sensitivity for identifying the hyperacute ischemic stroke.

ABBREVIATIONS: rSI = relative signal intensity; DWI-FLAIR mismatch = DWI positive and FLAIR negative; ROC = receiver operating characteristic; rFLAIR = relative signal intensity of FLAIR positive lesions; SI = signal intensity; rADC = relative ADC

Intravenous administration of tPA is the only proven, effective treatment for acute ischemic stroke within the first 4.5 hours after onset of symptoms.^{1,2} However, an estimated 25% of ischemic strokes occur during sleep, and the exact time of the onset of symptoms is unclear, which means that a large group of patients is precluded from the time-based thrombolytic therapy, especially

in developing countries.³ Therefore, a new diagnostic method that can identify the onset time of stroke is urgently required.

Recently, FLAIR sequences of MR imaging in acute stroke have attracted more attention as a potential surrogate marker for time since stroke onset.⁴⁻⁵ Specifically, a visual mismatch between DWI and FLAIR images has been shown to identify patients likely to be within a time window of 4.5 hours.⁶⁻⁸ Although these findings showed the high specificity of a “DWI-FLAIR mismatch” as a “tissue clock” to identify patients potentially eligible for thrombolytic therapy, some limitations of the method remained, such as different interobserver agreement rate, patient selection bias, and especially the relatively low sensitivity.

To overcome these limitations, we performed several quantitative measurements with the use of FLAIR images, including relative signal intensity (rSI) of FLAIR lesions, degree of DWI-FLAIR mismatch, and also visual DWI-FLAIR mismatch, to evaluate the potential efficacy of FLAIR-related techniques and to identify the onset time of acute cerebral ischemia in a beagle dog model.^{9,10}

Received April 20, 2013; accepted after revision May 23.

From the Department of Radiology, First Affiliated Hospital of Nanjing Medical University, Nanjing, China.

This research was supported by National Natural Science Foundation of China (81000653 to S. Liu; 30870710 to H.B. Shi).

Xiao-quan Xu and Qing-quan Zu contributed equally to this work.

Please address correspondence to Sheng Liu, MD, PhD, Department of Radiology, First Affiliated Hospital of Nanjing Medical University, 300 Guangzhou Rd, Nanjing 210029, China; e-mail: liusheng@njmu.edu.cn

Indicates open access to non-subscribers at www.ajnr.org

<http://dx.doi.org/10.3174/ajnr.A3689>

MATERIAL AND METHODS

Animal Preparation and Model Establishment

The surgical procedures and experimental protocol were approved by the Institutional Animal Care and Use Committee of Nanjing Medical University (Nanjing, China). Effective actions were taken for reducing pain or discomfort during the experiments.

A total of 20 adult healthy beagle dogs of either sex, weighing 12–15 kg, were anesthetized with intravenous injection of 3 mg/kg of pentobarbital (Pentobarbital Sodium Salt, Chemical Reagent Company, Shanghai, China). The airways were secured by means of oral endotracheal tubes with spontaneous respiration. Bilateral femoral arterial and left femoral venous accesses were obtained by use of 5F sheaths for catheterization, physiologic monitoring, and drug administration. Body temperature was maintained at 37–39°C during the interventional procedures and the duration of recovery after procedures by use of heating blankets. Sterile procedures were strictly used in all cases.

The beagle dog's cerebral ischemic models were established through the use of a method similar to the one used in our previous reports.^{9,10} Briefly, a prepared autologous clot (approximately 1.7 mm in diameter and 5 mm in length) was injected into the left proximal MCA under live fluoroscopy, and embolization was confirmed by angiography. After that, a 5F catheter was guided to 2 cm distal to the orifice of the ipsilateral ICA to block the blood flow for 2 hours. The animals were then transported to the MR imaging suite for imaging studies.

MR Imaging

Imaging was performed with a 3T MR system (Magnetom Trio; Siemens, Erlangen, Germany), with the use of a transmit-receive extremity coil with a diameter of 15 cm. Imaging acquisitions were performed serially at 3 hours, 4 hours, 5 hours, 6 hours, and 24 hours after the left MCA embolization, respectively. The same medications and doses were used to maintain immobility and sleep during the MR imaging scan. We checked T2-weighted images (acquisition matrix = 320 × 320, TR = 5000 ms, TE = 76 ms), FLAIR (acquisition matrix = 320 × 320, TR = 8000 ms, TE = 97 ms), and DWI (acquisition matrix = 320 × 320, TR = 5500 ms, TE = 97.3 ms). After MR examination, all animals recovered and were kept in the animal facility for other studies.

Imaging Assessment

FLAIR-positive (FLAIR+) or DWI-positive (DWI+) was defined as new hyperintense signals detected on FLAIR or DWI. For signal intensity (SI) changes of ischemic lesions on FLAIR, an ROI was defined on 1–3 sections showing the most obvious lesion completely covering the ischemic area. Control SI values were obtained from an ROI drawn contralaterally. Two independent raters (Y. Sheng, Q.G. Cheng) judged FLAIR+ according to acute lesions on DWI. Relative SI was obtained from FLAIR images according to the following formula: $rSI = \text{lesion SI}/\text{contralateral SI}$.

For ADC changes of ischemic lesion on DWI, an ROI was also defined on the sections showing the most obvious lesion. Control ADC values were obtained from an ROI drawn contralaterally. The relative ADC (rADC) value was obtained according to the following formula: $rADC = \text{lesion ADC}/\text{contralateral ADC}$.

“DWI-FLAIR mismatch” was defined as new hyperintense signal detected on DWI but not on FLAIR. The sensitivity and specificity values were calculated for the allocation of dogs to time interval from symptom onset to MR imaging scan within 3 hours, 4 hours, 5 hours, and 6 hours by DWI-FLAIR mismatch.

The volume of DWI+ and FLAIR+ lesions at each time point were also calculated. For the quantification of lesion size on DWI and FLAIR, the lesions in the same section were delineated by 3 authors (X.-Q. Xu, S.-S. Lu, Q.-Q. Zu), with consensus by use of an operator-defined ROI on each of the lesion-containing sections. The lesion volumes were obtained by multiplying the lesion areas by the section and gap thickness. Through the use of the volume of DWI+ and FLAIR+ lesions, the degree of DWI-FLAIR mismatch was calculated according to the following formula: Degree = $(100 - V_{\text{FLAIR}}/V_{\text{DWI}}) \times 100\%$. During the whole imaging assessment process, if any discrepant results occurred between 2 evaluators, the third and senior evaluator (S. Liu) would make the final decision.

Statistical Analysis

Interobserver and intraobserver agreement for the rating of FLAIR, DWI, and ADC images was assessed by means of Pearson correlation coefficient. The correlation between rFLAIR and onset time of stroke, and the correlation between the degree of DWI-FLAIR mismatch and the onset time were assessed by Spearman ρ analysis. The linear regression curve was plotted by use of GraphPad Prism statistical analysis software (GraphPad Software, San Diego, California). An optimal cutoff value was determined from the receiver operating characteristic (ROC) curve to analyze if there were critical ADC values that were sensitive or specific for FLAIR positivity. An ROC curve was used to identify the optimal cutoff value to allocate the ischemic lesions within 3 hours, 4 hours, 5 hours, and 6 hours with degree of DWI-FLAIR mismatch. The numeric data were averaged over all animals and reported as mean \pm standard deviation. A significant difference was considered if the *P* value was $<.05$. Statistical analysis was carried out with SPSS 17.0 (IBM, Armonk, New York).

RESULTS

Ischemic Model

All 20 cerebral ischemic models were established successfully without any procedure-related complications or casualties (Fig 1). DWI+ lesions were seen in all 20 beagle dogs starting from 3 hours after embolization. The DWI indicated that the cerebral ischemic lesions were located on the ipsilateral caudate nucleus and the cortical area of the temporal lobe. Generally, the ischemic lesions were first found at the caudate nucleus, followed by the lesions located in the cortical area of the temporal lobe (Fig 2).

Correlations Between rFLAIR with Time after the Model Was Established

Intraobserver agreement for qualitative judgment of FLAIR lesion visibility of observer 1 and observer 2 was 87% ($k = 0.78$; 95% CI, 0.77–0.98) and 85% ($k = 0.77$; 95% CI, 0.75–0.96), respectively. Intraobserver agreement for quantitative judgment of FLAIR+ lesions of observer 1 and observer 2 was 89% ($k = 0.81$; 95% CI, 0.80–0.99) and 91% ($k = 0.84$; 95% CI, 0.82–0.98), respectively.

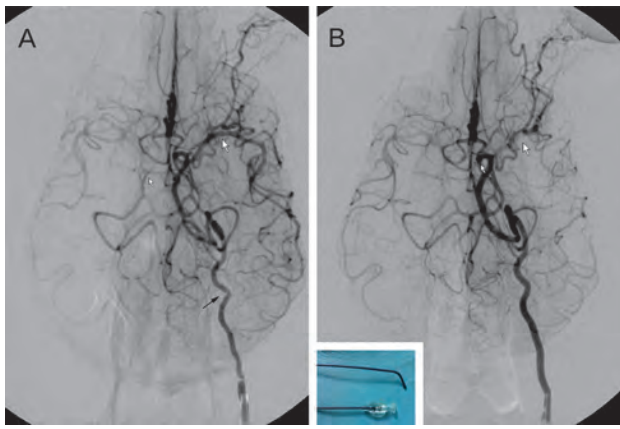


FIG 1. Representative real-time DSA images before and after MCA embolization in beagle dogs. *A*, Angiography clearly demonstrated the anatomy of intracranial arteries, including the left MCA trunk (*large arrowhead*), tortuous ICA (*black arrowhead*), and cerebral circulation (*small arrowhead*) through the left ICA injection before embolization. *B*, At the arterial phase, angiography immediately after thrombus injection through the catheter, the main trunk of MCA was completely occluded (*small and large arrowheads*). After that, a 5F catheter was guided to 2 cm distal to the orifice of ipsilateral ICA to block the blood flow for 2 hours. The catheter used in our study is displayed in left-bottom inset.

Interobserver agreement for qualitative judgment of FLAIR lesion visibility was 80.1% ($k = 0.52$; 95% CI, 0.56–0.91). Interobserver agreement for quantitative judgment of rFLAIR lesion was 86% ($k = 0.77$; 95% CI, 0.76–0.98).

FLAIR+ lesions were seen in 3 of the 20 (15%) beagles at 3 hours after embolization, 11 of the 20 (55%) beagles at 4 hours after embolization, 16 of the 20 (80%) beagles at 5 hours after embolization, 19 of the 20 (95%) beagles at 6 hours after embolization, and all 20 (100%) beagles at 24 hours after embolization, respectively (Fig 3).

All 69 FLAIR+ lesions had a mean rSI of 1.40 ± 0.27 . The rFLAIR values were 1.40 ± 0.04 , 1.23 ± 0.13 , 1.27 ± 0.03 , 1.59 ± 0.09 , and 1.43 ± 0.07 at 3 hours, 4 hours, 5 hours, 6 hours, and 24 hours after embolization, respectively. In a linear regression model, there were significant correlations between rFLAIR lesions and onset time ($P < .05$). The Spearman correlation coefficient for rFLAIR and onset time was $+0.42$ (95% CI, 0.20–0.60) (Fig 4).

Correlation Between FLAIR+ Images and the rADC Threshold Value

The ROC curve analysis results indicated that the rADC value of 0.54 might be the critical threshold value. With the rADC value of 0.54 set as the diagnostic threshold value, the best sensitivity and specificity for judging FLAIR positivity were 0.52 and 0.68, respectively (Fig 5).

Application of DWI-FLAIR Mismatch in the Ischemic Model

According to the pattern of DWI-FLAIR mismatch, the interval time between onset and image acquisition was presumed to be within 3 hours, sensitivity of 0.85 and specificity of 0.85; within 4 hours, sensitivity of 0.65 and specificity of 0.92; within 5 hours, sensitivity of 0.50 and specificity of 0.97; and within 6 hours, sensitivity of 0.39 and specificity of 1.00.

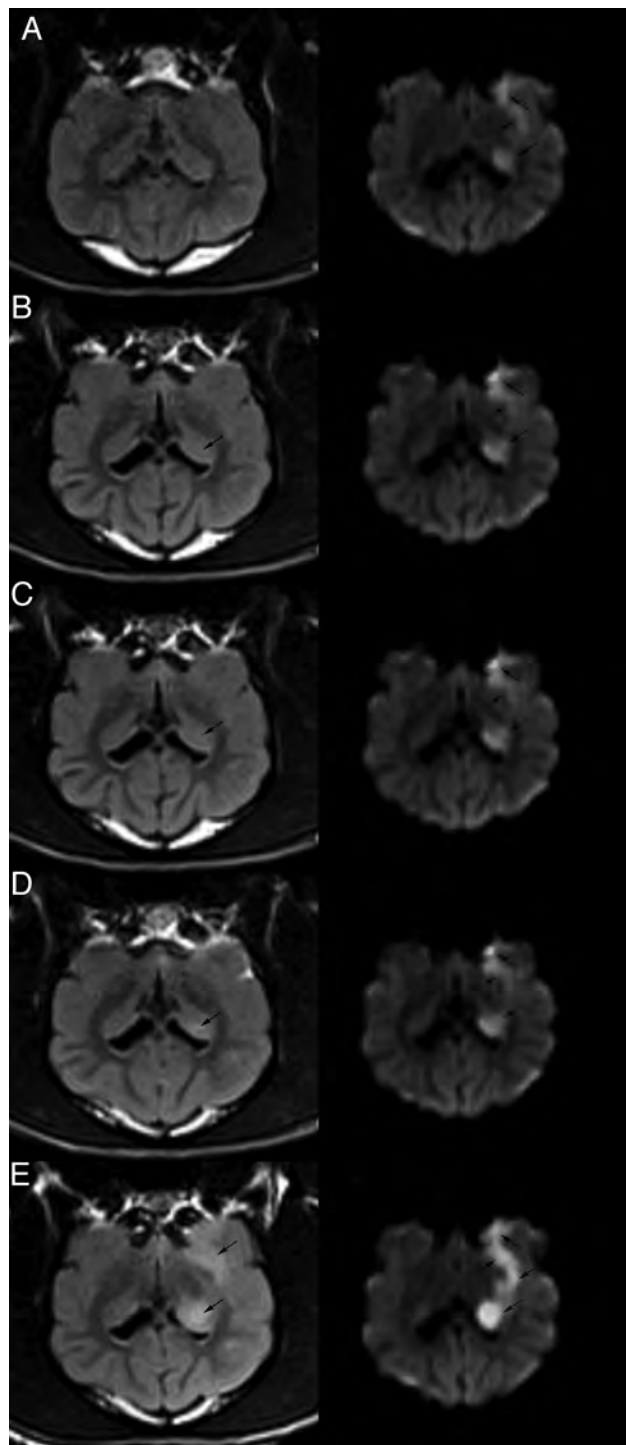


FIG 2. Sequential DWI and FLAIR images of coronal sections. The DWI and FLAIR were performed at 3 hours (*A*), 4 hours (*B*), 5 hours (*C*), 6 hours (*D*), and 24 hours (*E*) after embolization, respectively. There was no signal abnormality at 3 hours on the FLAIR image (*A*, left). Relative slightly high signal intensity area (*arrow*) with ovoid shape was observed in the left caudate nucleus on 4-hour FLAIR image (*B*, left). Increased high signal intensity was seen at 5 hours, 6 hours, and 24 hours on the FLAIR image (*C–E*, left), and lesions in the cortical area were seen on the 24-hour FLAIR image (*E*, left). Sequential DWI of coronal sections was all positive from 3 hours to 24 hours after model establishment (*A–E*, right).

Meanwhile, the degree of DWI-FLAIR mismatch was also calculated by means of the formula: $\text{degree} = (100 - V_{\text{FLAIR}} / V_{\text{DWI}}) \times 100\%$. Interobserver agreement for quantitative judgment

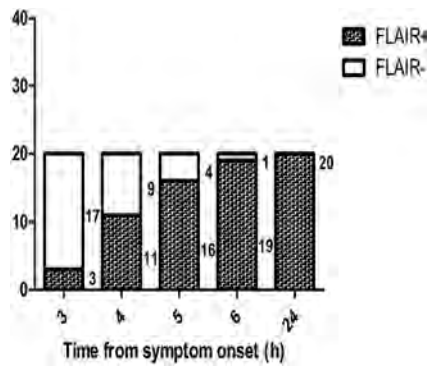


FIG 3. Proportion of FLAIR-negative and FLAIR-positive results on the basis of the 5 onset time points in the 20 beagle dogs. Number of FLAIR-negative and FLAIR-positive dogs are presented in bars.

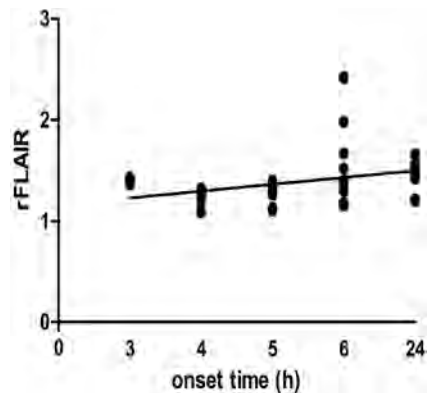


FIG 4. Relative SI on FLAIR images and time interval from onset to MR imaging scanning. Significant correlation between the rFLAIR and the onset time was found ($r = +0.42$; 95% CI, 0.20–0.90).

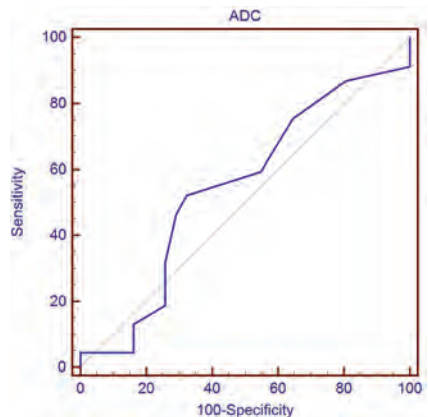


FIG 5. ROC of the rADC value in identifying the FLAIR+ lesions. ROC curve showed that the rADC value of 0.54 might be the critical threshold value that could quantify FLAIR+ lesions with the optimal sensitivity and specificity (0.52 and 0.68, respectively).

ment of “degree of mismatch” was 79% ($k = 0.77$; 95% CI, 0.72–0.84). The degree of DWI-FLAIR mismatch was 0.99 ± 0.00 , 0.93 ± 0.01 , 0.81 ± 0.11 , 0.67 ± 0.06 , and 0.42 ± 0.10 at 3 hours, 4 hours, 5 hours, 6 hours, and 24 hours after embolization, respectively. In a linear regression model, there is a significant correlation between degree of DWI-FLAIR mismatch and onset time ($P < .05$). The Spearman correlation coefficient for degree of

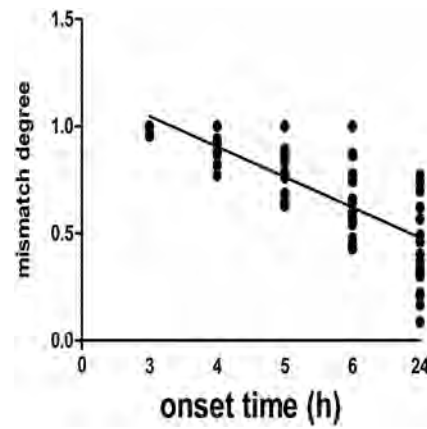


FIG 6. Degree of DWI-FLAIR mismatch and time interval from onset to MR imaging scanning. Significant correlation between the degree of DWI-FLAIR mismatch and the onset time was found ($r = -0.85$; 95% CI, 0.89–0.78).

DWI-FLAIR mismatch and onset time was -0.85 (95% CI, 0.89–0.78) (Fig 6).

The ROC analysis results indicated that the mismatch degree value of 0.95 might be the critical threshold value to identify the ischemic lesion within 3 hours, with a sensitivity and specificity of 100% and 82.5%, respectively. The mismatch degree value of 0.90 might be the critical threshold value to identify the ischemic lesion within 4 hours, with a sensitivity and specificity of 85% and 91.7%, respectively. The mismatch degree value of 0.79 might be the critical threshold value to identify the ischemic lesion within 5 hours, with a sensitivity and specificity of 83.3% and 90%, respectively. The mismatch degree value of 0.75 might be the critical threshold value to identify the ischemic lesion within 6 hours, with a sensitivity and specificity of 76.2% and 95%, respectively (Fig 7).

DISCUSSION

Our study demonstrates several major findings. First, the sensitivity of FLAIR for detecting hyperacute ischemic lesions clearly increases over time after embolization. Second, there is a significant correlation between the rFLAIR and the interval time from ischemic onset to MR imaging scanning. Thus, the rSI may be useful to predict the onset time of ischemic stroke. Third, also the most important, the new parameter, the degree of DWI-FLAIR mismatch proposed in our study, could be a better indicator for identifying the hyperacute ischemic stroke than visual DWI-FLAIR mismatch. To our knowledge, this is the first study to test the potential efficacy of a FLAIR-related technique, especially DWI-FLAIR mismatch and degree of DWI-FLAIR mismatch in identifying the onset time of cerebral ischemia on the basis of an ischemic stroke animal model with known onset time. Our study design can effectively avoid the selection bias as reported by previous retrospective clinical studies.

Whether rFLAIR can serve as an indicator to predict the onset time of cerebral ischemia is still debated. Ebinger et al¹¹ insisted that there was no significant correlation between rFLAIR and the onset interval time ($r = -0.15$, $P = .128$), after analyzing 102 FLAIR+ and 203 DWI+ lesions of 94 consecutive patients. However, Cheng et al¹² declared that there was a moderately significant correlation between

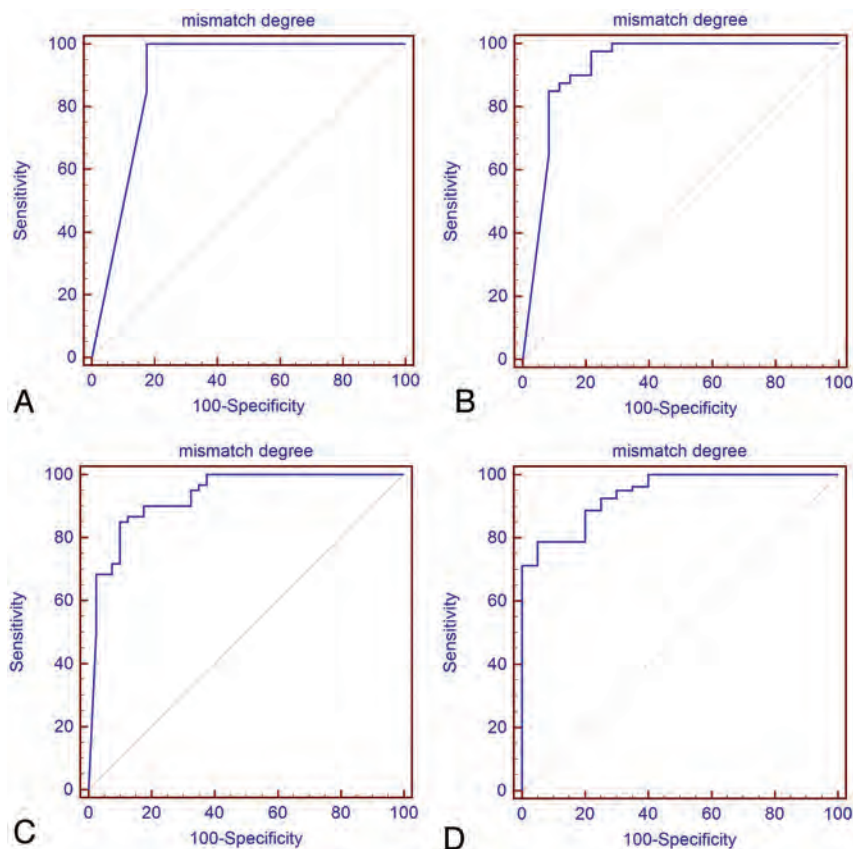


FIG 7. ROC of the DWI-FLAIR mismatch in identifying the hyperacute ischemic lesions within different onset time points. ROC showed that the cutoff values of DWI-FLAIR mismatch degree were 0.95, 0.90, 0.79, and 0.75, respectively, giving sensitivity of 1.00, 0.85, 0.83, and 0.76 for identifying the hyperacute ischemic lesion at 3 hours, 4 hours, 5 hours, and 6 hours after embolization, respectively.

the rFLAIR and onset interval time ($r = 0.38$, $P < .001$), which is similar to opinions of Petkova et al¹³ ($r = 0.63$, $P < .001$). Interestingly, the correlation ratio in our study was located between that of the latter 2 studies. Discrepancies in the results of correlations may partly be explained by patient characteristics. The median volume of FLAIR+ lesions in the Cheng et al study was larger than that of the Ebinger et al study (4.5–10.5 mL versus 0.86–1.65 mL). As a matter of course, the NIHSS score in the Cheng et al study was higher than that of the Ebinger et al study (7.3–8.8 versus 3–4). The larger ischemic volume and higher NIHSS score sometimes mean longer intervals in time from onset to MR imaging; therefore, more patients would be in the later time interval. Furthermore the statistical results would be different consequentially. However, in the Cheng et al study, data analysis was performed on images from multiple centers. This condition might lead to a heterogeneous set of FLAIR sequence parameters, which might contribute to a decreased homogeneity of rFLAIR, thus explaining a lesser correlation than that reported by Petkova et al¹³ and our study. Altogether, we think that a perspective, multiple center study with the uniform sequence parameters was needed to verify whether rSI of the FLAIR+ lesions can serve as an alternative indicator to predict the onset time of cerebral ischemia.

Recently, a visual mismatch between DWI and FLAIR in acute stroke has attracted increased attention. Previous studies indicated that DWI-FLAIR mismatch could serve as a surrogate marker of lesion age.^{6–8} In our study, by use of this mismatch

pattern to identify the hyperacute lesions within 3 hours, 4 hours, 5 hours, and 6 hours, we recorded specificities of 0.85, 0.92, 0.97, and 1.00, respectively, which were similar to those in previous studies. As we know, onset time of acute ischemic stroke is critical for guidance of thrombolysis therapy.^{1,14,15} Earlier management sometimes means better prognosis and fewer complications.¹⁶ However, if patients whose onset time is beyond the time window receive thrombolytic therapy, the risk of intracranial hemorrhage would increase and the thrombolysis therapy would be harmful or even lethal. Because of this, high specificity of the pattern of DWI-FLAIR mismatch appears to be crucial in improving the safety of the thrombolytic therapy, especially for patients with unknown symptom onset. However, also similar to the previous study, the sensitivity of the use of DWI-FLAIR mismatch to identify the hyperacute lesions is relatively low (0.39–0.85). So, if we choose the visual DWI-FLAIR mismatch as the criteria for identifying the acute stroke patients, only 39% of the patients (within 6 hours) would meet the criteria. As a result, more than half (61%) of the patients would lose the chance of thrombolytic therapy.

Considering that visual DWI and FLAIR mismatch is a binary concept—and the varied interobserver agreement rate among previous studies—our study proposes the utility of a new quantitative parameter, degree of DWI-FLAIR mismatch, for determining the onset time of stroke. With the use of the new index, we found that there were significant correlations between degree of DWI-FLAIR mismatch and onset time ($r = -0.85$; 95% CI, 0.78–0.89). Meanwhile, by use of the optimal mismatch degree threshold identified by ROC analysis to identify the hyperacute ischemic lesions, we acquired markedly enhanced sensitivity compared with the initial visual mismatch analysis. At the same time, an increase of sensitivity did not result in an obvious decrease in specificity. Why the new mismatch index could effectively enhance the sensitivity is, we think, because the visual DWI-FLAIR mismatch represents the concept of “all or nothing.” According to the criteria of visual DWI-FLAIR mismatch, there are just 2 results (“mismatch” or “no mismatch”), regardless of the ischemic lesions volume. Therefore, in our study, we transformed the binary DWI-FLAIR concept to a quantitative mismatch degree. The new mismatch degree index could effectively narrow the differences between each individual and each time point, rectify the influence of the lesion volume, and thus capture the difference that was omitted by the simple “yes or no” concept.

DWI and FLAIR techniques are more effective in identifying hyperacute strokes. First, we spent only approximately 45

seconds and 3 minutes, 8 seconds, on DWI and FLAIR techniques, respectively. In general, approximately 4 minutes was needed to get the DWI and FLAIR image information. Considering the time spent on image processing and analysis, this could save more time in identifying patients with hyperacute stroke than some other functional MR modalities. Second, both DWI and FLAIR techniques are contrast-free image modalities, which make them safer and with fewer contrast-related complications in an emergency.

There are still several limitations in our study that should be discussed. First, the ischemic model established in our study resembles the situation of a tandem occlusion in humans that will seriously impair collateral flow and cause more severe perfusion impairment. This mechanism may be only suitable for part of the stroke event. Second, we acquired the images at the interval of 1 hour, and the magic threshold of 4.5 hours for clinical thrombolysis was excluded from acquisition. Some other MR imaging sequences such as PWI, TOF, and SWI were also acquired in 1 session (the acquisition time was nearly 35 minutes in 1 instance), and we were concerned about the quality of the DWI and FLAIR images influenced by the contrast; therefore, we believe that the time point of 4.5 hours should be included in future studies. More animal studies are needed to confirm the reproducibility of our study.

CONCLUSIONS

From our study, we found that there was significant correlation between the rFLAIR and the onset time of acute stroke. The rFLAIR might be helpful to predict the onset time of ischemic events. Meanwhile, a new parameter, the degree of DWI-FLAIR mismatch proposed in our study, could be a better indicator for identifying hyperacute ischemic stroke than was the previous visual DWI-FLAIR mismatch.

ACKNOWLEDGMENTS

We thank Zhan Zhang and Jun-cheng Dai (Nanjing Medical University, Nanjing, China) for their help in statistics and Zhan-long Ma (Nanjing Medical University, Nanjing, China) for discussion.

REFERENCES

1. National Institute of Neurological Disorders and Stroke rt-PA Stroke Study Group. **Tissue plasminogen activator for acute ischemic stroke.** *N Engl J Med* 1995;24:1581–87
2. Wahlgren N, Ahmed N, Davalos A, et al. **Thrombolysis with alte-**

- plase 3–4.5 h after acute ischemic stroke (SITS-ISTR): an observational study.** *Lancet* 2008;372:1303–09
3. Barreto AD, Martin-Schild S, Hallevi H, et al. **Thrombolytic therapy for patients who wake-up with stroke.** *Stroke* 2009;3:827–32
4. Lee KY, Latour LL, Luby M, et al. **Distal hyperintense vessels on FLAIR: an MRI marker for collateral circulation in acute stroke?** *Neurology* 2009;72:1134–39
5. Gauvrit JY, Leclerc X, Girot M, et al. **Fluid-attenuated inversion recovery (FLAIR) sequences for the assessment of acute stroke: inter observer and inter technique reproducibility.** *J Neurol* 2006;253: 631–35
6. Aoki J, Kimura K, Iguchi Y, et al. **FLAIR can estimate the onset time in acute ischemic stroke patients.** *J Neurol Sci* 2010;293:39–44
7. Thomalla G, Rossbach P, Rosenkranz M, et al. **Negative fluid-attenuated inversion recovery imaging identifies acute ischemic stroke at 3 hours or less.** *Ann Neurol* 2009;65:724–32
8. Thomalla G, Cheng B, Ebinger M, et al. **DWI-FLAIR mismatch for the identification of patients with acute ischemic stroke within 4.5 h of symptom onset (PRE-FLAIR): a multicenter observational study.** *Lancet Neurol* 2011;10:978–86
9. Lu SS, Liu S, Zu QQ, et al. **In vivo MR imaging of intraarterially delivered magnetically labeled mesenchymal stem cells in a canine stroke model.** *PLoS ONE* 2013;8:e54963
10. Liu S, Hu WX, Zu QQ, et al. **A novel embolic stroke model resembling lacunar infarction following proximal middle cerebral artery occlusion in beagle dogs.** *J Neurosci Methods* 2012;209:90–96
11. Ebinger M, Galinovic I, Rozanski M, et al. **Fluid-attenuated inversion recovery evolution within 12 hours from stroke onset: a reliable tissue clock?** *Stroke* 2010;41:250–55
12. Cheng B, Brinkmann M, Forkert ND, et al. **Quantitative measurements of relative fluid-attenuated inversion recovery (FLAIR) signal intensities in acute stroke for the prediction of time from symptom onset.** *J Cereb Blood Flow Metab* 2013;33:76–84
13. Petkova M, Rodrigo S, Lamy C, et al. **MR imaging helps predict time from symptom onset in patients with acute stroke: implications for patients with unknown onset time.** *Radiology* 2010;257:782–92
14. Moonis M. **Intraarterial thrombolysis within the first three hours after acute ischemic stroke in selected patients.** *Stroke* 2009;40: 2611–12
15. Meyers PM, Schumacher HC, Higashida RT, et al. **Indications for the performance of intracranial endovascular neurointerventional procedures: a scientific statement from the American Heart Association Council on Cardiovascular Radiology and Intervention, Stroke Council, Council on Cardiovascular Surgery and Anesthesia, Interdisciplinary Council on Peripheral Vascular Disease, and Interdisciplinary Council on Quality of Care and Outcomes Research.** *Circulation* 2009;119:2235–49
16. Hacke W, Kaste M, Bluhmki E, et al. **Thrombolysis with alteplase 3 to 4.5 hours after acute ischemic stroke.** *N Engl J Med* 2008;13: 1317–29

Subcortical Cystic Lesions within the Anterior Superior Temporal Gyrus: A Newly Recognized Characteristic Location for Dilated Perivascular Spaces

S. Rawal, S.E. Croul, R.A. Willinsky, M. Tymianski, and T. Krings



ABSTRACT

SUMMARY: Cystic parenchymal lesions may pose an important diagnostic challenge, particularly when encountered in unexpected locations. Dilated perivascular spaces, which may mimic cystic neoplasms, are known to occur in the inferior basal ganglia and mesencephalothalamic regions; a focal preference within the subcortical white matter has not been reported. This series describes 15 cases of patients with cystic lesions within the subcortical white matter of the anterior superior temporal lobe, which followed a CSF signal; were located adjacent to a subarachnoid space; demonstrated variable surrounding signal change; and, in those that were followed up, showed stability. Pathology study results obtained in 1 patient demonstrated chronic gliosis surrounding innumerable dilated perivascular spaces. These findings suggest that dilated perivascular spaces may exhibit a regional preference for the subcortical white matter of the anterior superior temporal lobe. Other features—lack of clinical symptoms, proximity to the subarachnoid space, identification of an adjacent vessel, and stability with time—may help in confidently making the prospective diagnosis of a dilated perivascular space, thereby preventing unnecessary invasive management.

ABBREVIATION: SAS = subarachnoid space

Cystic lesions of the brain parenchyma pose an important diagnostic challenge, because the differentiation between benign and malignant lesions is often difficult on neuroimaging alone. In the classic sense, the differential diagnosis includes benign acquired lesions (enlarged perivascular spaces or Virchow-Robin spaces, porencephalic cysts or cystic encephalomalacia, chronic lacunar infarctions, or parasitic cysts), benign congenital lesions (neuroglial cysts or ependymal cysts), and cystic neoplasms.

Dilated Virchow-Robin spaces are expansions of the normal perivascular space that may mimic a cystic neoplasm. Previous literature has demonstrated a predilection for involvement of the mesencephalothalamic region,¹ and although these structures may involve the subcortical white matter of the cerebral hemispheres, this location is less common. A focal preference within the subcortical white matter has not been reported previously.

At our institution, we identified 15 sequential cases of cystic lesions within the subcortical white matter of the anterior superior

temporal lobes, all demonstrating nearly identical location and morphologic and imaging features. Here, we discuss their imaging characteristics and differential diagnosis, and propose that these lesions may be representative of a newly identified preferential location for a dilated perivascular space.

CASE SERIES

Case Selection

We obtained institutional research ethics board approval for this study. A total of 15 consecutive cases were identified at our institution with the presence of a subcortical cystic lesion within the anterior superior temporal gyrus, with imaging performed between November 2011 and January 2013. The corresponding patient records for each case were retrospectively reviewed for prior imaging studies indicating imaging follow-up. Information on demographic features, clinical symptoms prompting initial imaging, and any subsequent development of neurologic symptoms was also noted.

Imaging Acquisition

All imaging studies were performed on either a 1.5T Signa Excite HD (GE Healthcare, Milwaukee, Wisconsin) or a 1.5T Magnetom Avanto or 3T Magnetom Verio (Siemens, Erlangen, Germany) MR imaging scanner. Sequences performed in all MR imaging acquisitions included sagittal T1, axial FLAIR, and DWI sequences. Depending on the scanner used, either a gradient-echo

Received April 2, 2013; accepted after revision May 9.

From the Division of Neuroradiology (S.R., R.A.W., T.K.); and Department of Neuropathology (S.E.C.), University Health Network; and Division of Neurosurgery (M.T.), Toronto Western Hospital, University of Toronto, Toronto, Canada.

Please send correspondence to Sapna Rawal, Department of Medical Imaging, University of Toronto, 263 McCaul St, 4th Floor, Toronto, Ontario M5T 1W7, Canada; e-mail: sapna.rawal@hotmail.com

 Indicates article with supplemental on-line table

<http://dx.doi.org/10.3174/ajnr.A3669>

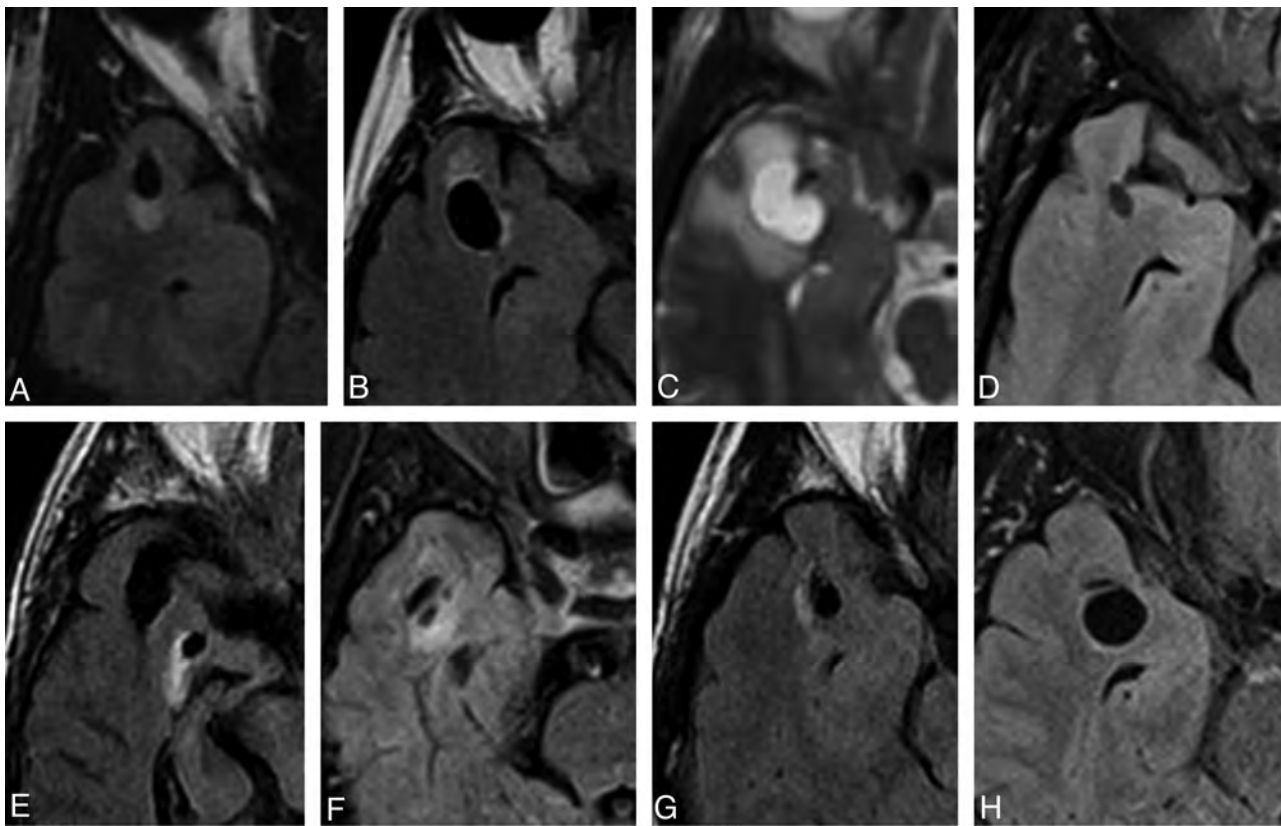


FIG 1. Selected axial FLAIR/T2 images of right-sided lesions within the anterior superior temporal gyrus as identified in case 1 (A), 2 (B), 7 (C), 8 (D), 9 (E), 10 (F), 12 (G), and 14 (H). All lesions were located adjacent to the SAS. The images illustrate the variability in the degree of surrounding signal change. Note the proximity to the adjacent middle cerebral artery and more prominent surrounding signal hyperintensity seen in case 7 (C).

sequence or a susceptibility-weighted sequence was obtained. T2 sequences were occasionally performed (these are not routinely performed at our institution in follow-up examinations of previously recognized lesions). Gadolinium-enhanced imaging was obtained in all patients within the period of follow-up.

RESULTS

In all 15 cases, the lesions demonstrated signal characteristics following that of CSF on all sequences (Figs 1 and 2; Table 1). All lesions were noted to closely appose the adjacent subarachnoid space (SAS). Most lesions (13/15) were elongated morphologically. None of the lesions showed associated enhancement, restricted diffusion, or susceptibility artifacts throughout the follow-up period. In those with imaging follow-up, no change in size was noted in any patient throughout the follow-up period (range, 6–112 months), either involving the lesion itself, or the degree of surrounding signal change. Finally, all lesions except for 1 lesion (identified in case 7) demonstrated either no perilesional FLAIR/T2 signal change, or mild perilesional signal change. On the basis of these findings, the diagnosis of a dilated perivascular space was suggested in each case, with a limited differential diagnosis provided. Of note, 2 patients (cases 6 and 11) had multiple adjacent, smaller, linearly-oriented lesions that followed a CSF signal on all sequences—these were thought to represent smaller prominent Virchow-Robin spaces (Fig 3). In case 7, there was extensive surrounding perilesional signal change, thought to represent perilesional

edema; this patient ultimately underwent surgical resection because of suspicion of a low-grade neoplasm (Fig 1C).

Corresponding clinical findings for each patient were also obtained (On-line Table). In most cases, on the basis of neurologic or neurosurgical evaluation, the lesions were felt to be incidental or were not felt to account for the patients' presenting symptoms (headache, etc). However, in 2 patients (cases 2 and 7) the presenting clinical symptoms could potentially have been attributed to the identified lesion. In case 2, the patient presented with seizures typical of temporal lobe epilepsy localized to the right temporal region, coinciding with the location of the cystic subcortical lesion. On the basis of the clinical work-up, it was thought plausible that these seizures might be arising from the lesion with potential associated cortical irritation; however, the patient remained seizure-free while receiving medication, and given the stability of the imaging findings and clinical course, surgical management was not indicated. For the patient in case 7, the combination of the clinical presentation suggesting possible temporal lobe seizures and the atypical imaging feature of extensive perilesional signal change prompted surgical management, following which the patient's symptoms completely resolved.

As a result, pathology study was obtained in only 1 patient (case 7). Results demonstrated a region of chronic demyelination and gliosis surrounding innumerable dilated perivascular spaces, which, aside from the dominant large perivascular space, were presumably below the resolution of MR imaging (Fig 4).

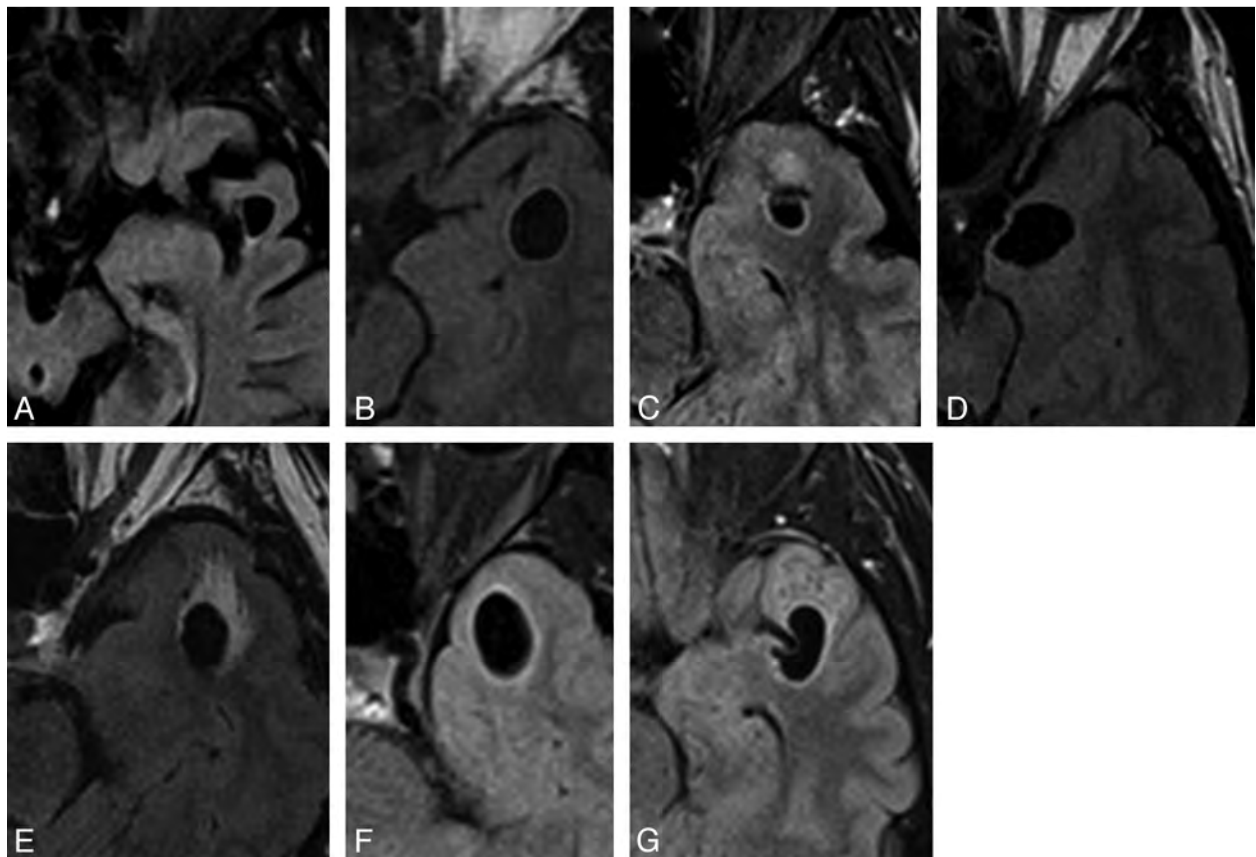


FIG 2. Selected axial FLAIR images of left-sided lesions within the anterior superior temporal gyrus as identified in case 3 (A), 4 (B), 5 (C), 6 (D), 11 (E), 13 (F), and 15 (G). All lesions were located adjacent to the SAS. Again, the images illustrate the variability in the degree of surrounding signal change.

Table 1: MR imaging characteristics of lesions identified within the anterior superior temporal subcortical white matter

Case	Location (R/L)	Maximal Dimension (cm)	Morphologic Feature	Adjacent to SAS (Y/N)	FLAIR Suppression (Y/N)	DWI Restriction (Y/N)	SWI/GRE Blooming (Y/N)	Gadolinium Enhancement (Y/N)	Perilesional FLAIR Signal Change	Imaging Follow-Up (mo)	Change over Follow-Up Period
1	R	1.0	Elongated	Y	Y	N	N	N	Mild	14	N
2	R	1.5	Elongated	Y	Y	N	N	N	Mild	38	N
3	L	0.9	Elongated	Y	Y	N	N	N	Mild	35	N
4	L	1.5	Elongated	Y	Y	N	N	N	Mild	22	N
5	L	0.9	Round	Y	Y	N	N	N	Mild	0	N/A
6	L	1.7	Elongated	Y	Y	N	N	N	None	11	N
7	R	1.8	Elongated	Y	Y	N	N	N	Extensive	0	N/A
8	R	0.7	Elongated	Y	Y	N	N	N	None	6	N
9	R	0.6	Elongated	Y	Y	N	N	N	Mild	99	N
10	R	0.5	Elongated	Y	Y	N	N	N	Mild	0	N/A
11	L	1.7	Elongated	Y	Y	N	N	N	Mild	7	N
12	R	1.1	Elongated	Y	Y	N	N	N	Mild	0	N/A
13	L	1.9	Elongated	Y	Y	N	N	N	None	0	N/A
14	R	1.3	Round	Y	Y	N	N	N	None	0	N/A
15	L	1.6	Elongated	Y	Y	N	N	N	Mild	112	N

Note:—GRE indicates gradient-recalled echo; L, left; N, no; N/A, not applicable; R, right; Y, yes.

DISCUSSION

Perivascular spaces are leptomeningeal-lined spaces that surround penetrating arteries as they course within the brain parenchyma. The leptomeningeal layers that line these spaces create a small, fluid-filled space around the arterial wall that is distinct from the subpial and SAS, allowing for a slightly different fluid composition than that present in CSF. These structures are usually identified in normal, healthy patients on high-resolution MR

imaging and often demonstrate a curvilinear morphologic pattern along the trajectory of penetrating vessels.²

Dilated perivascular spaces are benign expansions of these normal structures, typically located at the inferior basal ganglia along the anterior commissure.³ Giant perivascular spaces, measuring 1.5 cm, most commonly occur within the mesencephalothalamic region, where they may manifest with obstructive hydrocephalus.¹ Although less common, these lesions have been reported to exist focally else-

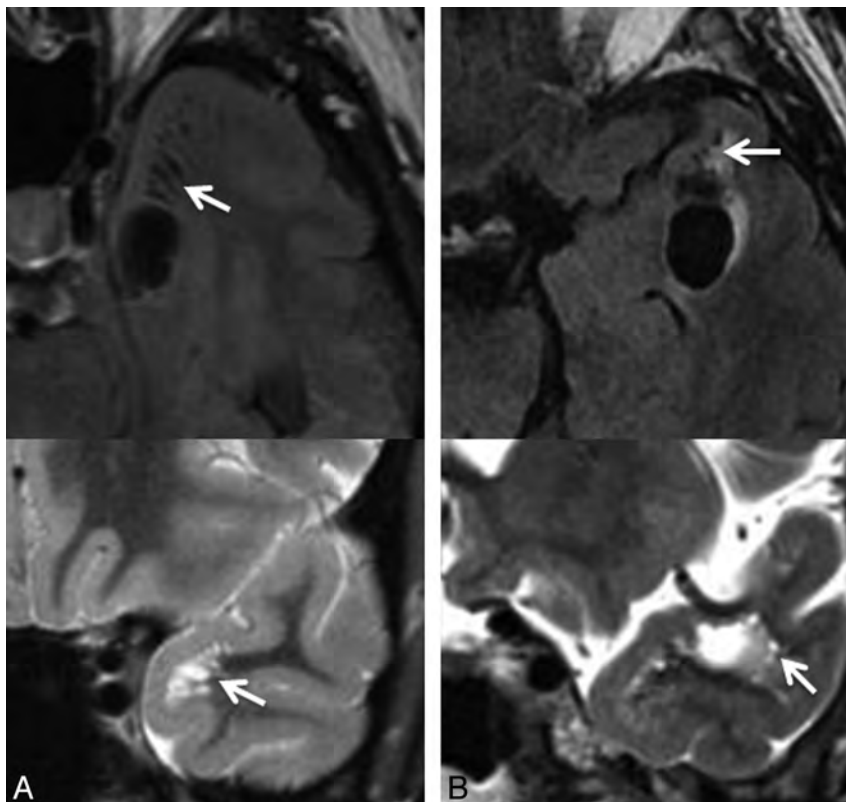


FIG 3. Selected axial FLAIR images demonstrating the presence of a cystic lesion within the anterior temporal gyrus as identified in case 6 (A) and case 11 (B), with adjacent smaller cystic lesions, suggestive of a dominant enlarged perivascular space with adjacent smaller prominent perivascular spaces (arrows). Corresponding coronal T2 images (below) through the region of interest confirm these findings (arrows). In case 11 (B), the proximity to the adjacent middle cerebral artery is identified on the coronal T2 image.

where in the brain parenchyma, including the subcortical white matter.¹ Regardless of specific location, enlarged perivascular spaces have been noted to abut either the ventricular margin or the SAS, as seen in the cases of all of our patients.¹ Diffusely enlarged perivascular spaces have also been reported, which have been hypothesized to occur in the context of certain pathologic conditions, including chronic microvascular ischemia, Alzheimer dementia, cerebral amyloid angiopathy, CADASIL (cerebral autosomal dominant arteriopathy with subcortical infarcts and leukoencephalopathy), and mucopolysaccharidoses.⁴⁻⁸

Regarding the function of perivascular spaces, several theories have been proposed. They are thought to play a role in immunologic processes in the brain, to provide a drainage route for interstitial fluid, and to provide a mechanism for equalization of intracranial pressure.⁹ However, the cause of their enlargement, and the reason for regional predilection to dilation, is poorly understood. Proposed mechanisms of enlargement include those related to the associated vessels, namely arterial elongation or increased vascular permeability; those related to the surrounding brain parenchyma, such as volume loss with ex vacuo enlargement; or those related to CSF or interstitial fluid dynamics, including altered or increased CSF pulsations with increased pressure within the perivascular space, or obstruction to flow of interstitial fluid on the basis of amyloid deposition.¹ However, the mechanisms by which these processes may occur focally in some cases, and diffusely in others, remain unexplained.

Previous literature on dilated perivascular spaces has demonstrated the tendency of these lesions to exhibit a regional preference. The largest series of dilated perivascular spaces, reported by Salzman et al,¹ described 37 cases, of which 21 (57%) were located in the mesencephalothalamic region, whereas only 8 (22%) were within the subcortical white matter. It is interesting to note that of all lesions located within the white matter, 50% exhibited surrounding perilesional signal change on FLAIR/T2 sequences, but none of the mesencephalothalamic lesions demonstrated this associated finding. This supports our findings because most of our cases demonstrated perilesional signal alteration. However, Salzman et al¹ did not describe a temporal predominance of the subcortical lesions because only 2 of the white matter lesions were identified within the temporal lobe. A smaller series reported by Cerase et al¹⁰ described 3 cases of dilated perivascular spaces where the lesions regressed with time: All were located in the anterior superior temporal lobe, corresponding exactly to the location we describe in our series, and one of the lesions exhibited perilesional signal

change on FLAIR sequence.

The cause of perilesional signal change has also been discussed previously, with a proposed theory being that of accelerated white matter ischemic change resulting from compression of the adjacent parenchymal vessels by the enlarged perivascular space.¹¹ A more interesting theory, however, and one that is reflected in our MR imaging and pathologic findings, is that the high signal may be the result of gliosis in addition to multiple prominent perivascular spaces that are below the resolution of MR imaging.^{1,12} Although we were able to prospectively identify prominent perivascular spaces surrounding the dominant lesion in 2 patients only (cases 6 and 11), our pathologic specimen was far more revealing. It is interesting to note that our patient (case 7) underwent surgical excision partially on the basis of MR imaging findings that suggested perilesional vasogenic edema, which was demonstrated on pathologic findings to be nothing more than the presence of multiple prominent perivascular spaces amid diffuse gliosis.

The ultimate objective of studying perivascular spaces is to elucidate imaging features that may help distinguish these benign lesions from more ominous pathologic conditions in a prospective manner. The predilection for certain locations is an important distinguishing feature of dilated perivascular spaces. Although previously only reported to favor the mesencephalothalamic region, our findings, in conjunction with several other reported cases, propose that the anterior superior temporal subcortical white matter is an additional pref-

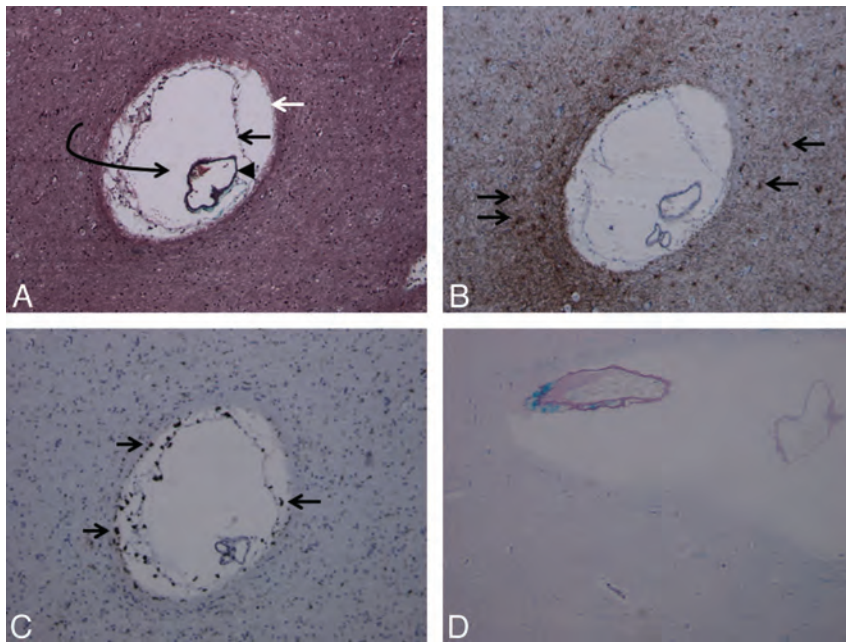


FIG 4. Trichrome stain (A) demonstrates the presence of an enlarged perivascular space (white arrow, glia limitans; black arrow, inner pial membrane; black arrowhead, vessel lined by outer pial membrane; curved arrow, perivascular space). Multiple such lesions were seen in the surgical specimen. Glial fibrillary acidic protein stain (B) and CD68 stain (C) demonstrate reactive astrocytes (arrows in B) and perivascular microglia (arrows in C) as multiple brown-staining dots, confirming chronicity of the pathophysiologic process. Luxol fast blue stain (D) demonstrates diffuse absence of blue staining (myelin staining), indicating demyelination and gliosis in the brain parenchyma surrounding the dilated perivascular space (magnification of all slides, 20 \times).

erential site for dilated perivascular spaces. Other features may also be helpful in identification of these structures, including their orientation and shape, which may often be elongated or fusiform in morphologic appearance, suggesting their association with a penetrating vessel.¹³ In our cases, the proximity to the SAS with the identification of the adjacent middle cerebral artery is an additional attribute that helps to distinguish these lesions, such that they may be associated with the course of a perforating vessel. Finally, the lack of associated enhancement or restricted diffusion, as well as the stability of these lesions with time, also act as key indicators of the underlying pathologic condition. Our cases, as well as those reported in the literature, demonstrate that perilesional FLAIR/T2 signal change may be identified in the context of dilated perivascular spaces and should not, in itself, prompt alternative diagnoses to be entertained.

It is important to note that only 5 of our patients had adequate imaging follow-up (range, 22–112 months) to indicate stability with time. Four patients had follow-up ranging from 6–14 months, and 5 patients did not undergo imaging follow-up at our institution (1 patient [case 7] without follow-up underwent surgery). For the cases that did not undergo imaging follow-up, one cannot rely on imaging stability to aid in diagnosis; however, given that these patients were asymptomatic regarding the lesion, and all other suggestive imaging features were present, including location within the anterior superior temporal lobe, the diagnosis of dilated perivascular spaces can be strongly suspected. In these situations in which the diagnosis of dilated perivascular spaces is highly favored but not proven, surgical management may still be avoided in favor of a more conservative approach.

Other benign lesions in the differential diagnosis that may have a similar imaging appearance include neuroglial or gliependymal cysts, which include the subtype of ependymal cysts. These rare lesions are thought to develop from sequestered embryologic remnants of neuroectoderm or neural tube elements.¹⁴ Although they demonstrate regional preferences—ependymal cysts are commonly identified in a juxtaventricular location, whereas other neuroglial cysts demonstrate frontal lobe predominance—these locations do not coincide with that of dilated perivascular spaces, thereby providing another basis on which to distinguish these pathologic conditions.^{14,15} Acquired lesions, on the other hand, including porencephalic cysts, cystic encephalomalacia, or sequelae of lacunar infarctions, would not be expected to demonstrate a regional preference, given that they are the result of prior insults to the brain that would not necessarily occur in a specific location. Finally, infectious cysts and cystic neoplasms would not necessarily follow a CSF signal on all sequences, could

demonstrate associated enhancement, and would be expected to enlarge or change with time.

CONCLUSIONS

This series of cases suggests that dilated perivascular spaces may exhibit a regional preference for the subcortical white matter of the anterior superior temporal lobe. In addition to location, other imaging features—including proximity to the SAS, identification of an adjacent vessel, absence of enhancement or restricted diffusion, and stability with time—may help in confidently making the diagnosis of a dilated perivascular space, thereby preventing unnecessary invasive management. The presence of a perilesional FLAIR/T2 signal change should not exclude this diagnosis, because this feature may be present in the context of a dilated perivascular space and does not necessarily suggest a more worrisome pathologic condition.

REFERENCES

1. Salzman KL, Osborn AG, House P, et al. **Giant tumefactive perivascular spaces.** *AJNR Am J Neuroradiol* 2005;26:298–305
2. Groeschel S, Chong WK, Surtees R, et al. **Virchow-Robin spaces on magnetic resonance images: normative data, their dilatation, and a review of the literature.** *Neuroradiology* 2006;48:745–54
3. Adachi M, Hosoya T, Haku T, et al. **Dilated Virchow-Robin spaces: MRI pathological study.** *Neuroradiology* 1998;40:27–31
4. Cumurciuc R, Guichard JP, Reizine D, et al. **Dilation of Virchow-Robin spaces in CADASIL.** *Eur J Neurol* 2006;13:187–90
5. Patankar TF, Mitra D, Varma A, et al. **Dilatation of the Virchow-Robin space is a sensitive indicator of cerebral microvascular disease: study in elderly patients with dementia.** *AJNR Am J Neuroradiol* 2005;26:1512–20

6. Rouhl RP, van Oostenbrugge RJ, Knottnerus IL, et al. **Virchow-Robin spaces relate to cerebral small vessel disease severity.** *J Neurol* 2008;255:692–96
7. Zhu YC, Dufouil C, Soumaré A, et al. **High degree of dilated Virchow-Robin spaces on MRI is associated with increased risk of dementia.** *J Alzheimers Dis* 2010;22:663–72
8. Calleja Gero ML, González Gutiérrez-Solana L, López Marín L, et al. **Neuroimaging findings in patient series with mucopolysaccharidosis** [in English, Spanish]. *Neurologia* 2012;27:407–13
9. Abbott NJ. **Evidence for bulk flow of brain interstitial fluid: significance for physiology and pathology.** *Neurochem Int* 2004;45:545–52
10. Cerase A, Vallone IM, Muccio CF, et al. **Regression of dilated perivascular spaces of the brain.** *Surg Radiol Anat* 2010;32:555–61
11. Shiratori K, Mrowka M, Toussaint A, et al. **Extreme, unilateral widening of Virchow-Robin spaces: case report.** *Neuroradiology* 2002;44:990–92
12. Elster AD, Richardson DN. **Focal high signal on MR scans of the midbrain caused by enlarged perivascular spaces: MR-pathologic correlation.** *AJR Am J Roentgenol* 1991;156:157–60
13. Tsutsumi S, Ito M, Yasumoto Y, et al. **The Virchow-Robin spaces: delineation by magnetic resonance imaging with considerations on anatomofunctional implications.** *Childs Nerv Sys* 2011;27:2057–66
14. Osborn AG, Preece MT. **Intracranial cysts: radiologic-pathologic correlation and imaging approach.** *Radiology* 2006;239:650–64
15. Boockvar JA, Shafa R, Forman MS, et al. **Symptomatic lateral ventricular ependymal cysts: criteria for distinguishing these rare cysts from other symptomatic cysts of the ventricles: case report.** *Neurosurgery* 2000;46:1229–32; discussion 1232–33

Preferential Location for Arterial Dissection Presenting as Golf-Related Stroke

M.H. Choi, J.M. Hong, J.S. Lee, D.H. Shin, H.A. Choi, and K. Lee



ABSTRACT

SUMMARY: Golf-related stroke has not been systematically reviewed. The purpose of our study was to describe in detail this particular stroke syndrome. Seven patients were analyzed at a university hospital and 7 patients were reviewed from MEDLINE literature. General demographics, symptom onset, neurologic signs, radiologic findings, and outcome were investigated. A total of 14 patients including 7 patients from the MEDLINE search were analyzed; all were men, with a mean age of 46.9 ± 12.8 years. Symptom onset was classified as during the golf swing ($n = 9$), unknown ($n = 3$), and after playing golf ($n = 2$). Most patients ($n = 12$) showed involvement of the vertebral artery and 2 patients showed involvement of the internal carotid artery ($P = .008$). Nine dissections were found on the right side, 3 on the left side, and 2 were bilateral ($P = .046$). Twelve patients had extracranial involvement and 2 patients had intracranial involvement ($P = .008$). Seven patients returned to normal, 5 returned to independence, 1 had unknown status, and 1 died. The anatomic preference of golf-related craniocervical arterial dissection is associated with the extracranial and vertebrobasilar system with a right-sided tendency as the result of stereotypical rotational movement during a golf swing.

ABBREVIATION: VA = vertebral artery

As more people golf, golf-related injuries have become more prevalent, even in amateur golfers.¹⁻³ Golf-related injuries are caused by either overuse or mechanical trauma, with most neurologic injuries being confined to the vertebral column.³ Several case series of cervicocranial artery dissection associated with golf playing have been reported recently and referred to as “golfer’s stroke.”³⁻⁶ Previous case studies have reported cervical artery dissection associated with sudden hyperextension or rotation of the neck, including painting a ceiling, coughing, vomiting, sneezing, receiving anesthesia, and during cardiopulmonary resuscitation.⁷⁻⁹ Cervical artery dissection caused by physical activity represents a coincidental environmental trigger, and certain risk factors such as connective tissue disorders or hyperhomocysteinemia are associated with this type of injury.¹⁰ Because the golf swing is a habitual body motion that includes rapid head and body rotation, it may lead to repetitive mechanical com-

pression of the extracranial cervical arteries during each swing.² We investigated the clinical characteristics and radiologic findings in patients with golf-related stroke from cervicocranial arterial dissection.

MATERIALS AND METHODS

We retrospectively analyzed computerized data of a prospective registry that included 5469 patients with ischemic stroke from March 2001 to June 2011. Seven patients had a history of acute ischemic stroke caused by cervicocranial arterial dissection associated with golfing. Acute ischemic stroke was confirmed by diffusion-weighted MR imaging of the brain. All patients underwent a battery of diagnostic studies, including intracerebral and extracerebral vessel studies, routine blood tests, and a cardiologic work-up (electrocardiogram, transthoracic echocardiography, 24-hour Holter monitoring). Comorbidities and autoimmune markers were investigated to exclude underlying vasculopathy. Various auto-antibody screening tests such as rheumatoid factor and antinuclear, antiphospholipid, and antineutrophil cytoplasmic antibodies were analyzed. In addition, a MEDLINE search was performed from 1990 to December 2010 by use of the search terms “golfer’s stroke,” “golf-induced stroke,” and “golf-induced dissection.” This study was approved by the local institutional review board of the hospital.

We investigated general demographics, personal history of golf playing, handedness, situations at symptom onset, neuro-

Received April 16, 2013; accepted after revision June 3.

From the Department of Neurology, Ajou University School of Medicine, Suwon, South Korea (M.H.C., J.M.H., J.S.L.); Department of Neurology, Gachon Gill Medical Center, Gachon University School of Medicine, Incheon, South Korea (D.H.S.); and Department of Neurosurgery, The University of Texas Health Science Center, Houston, Texas (H.A.C., K.L.).

Please address correspondence to Ji Man Hong, MD, PhD, Department of Neurology, School of Medicine, Ajou University, 5 San, Woncheon-dong, Yongtong-gu, Suwon-si, Kyunggi-do, 442-749, South Korea; e-mail: dacda@hanmail.net

Indicates article with supplemental on-line table.

<http://dx.doi.org/10.3174/ajnr.A3768>

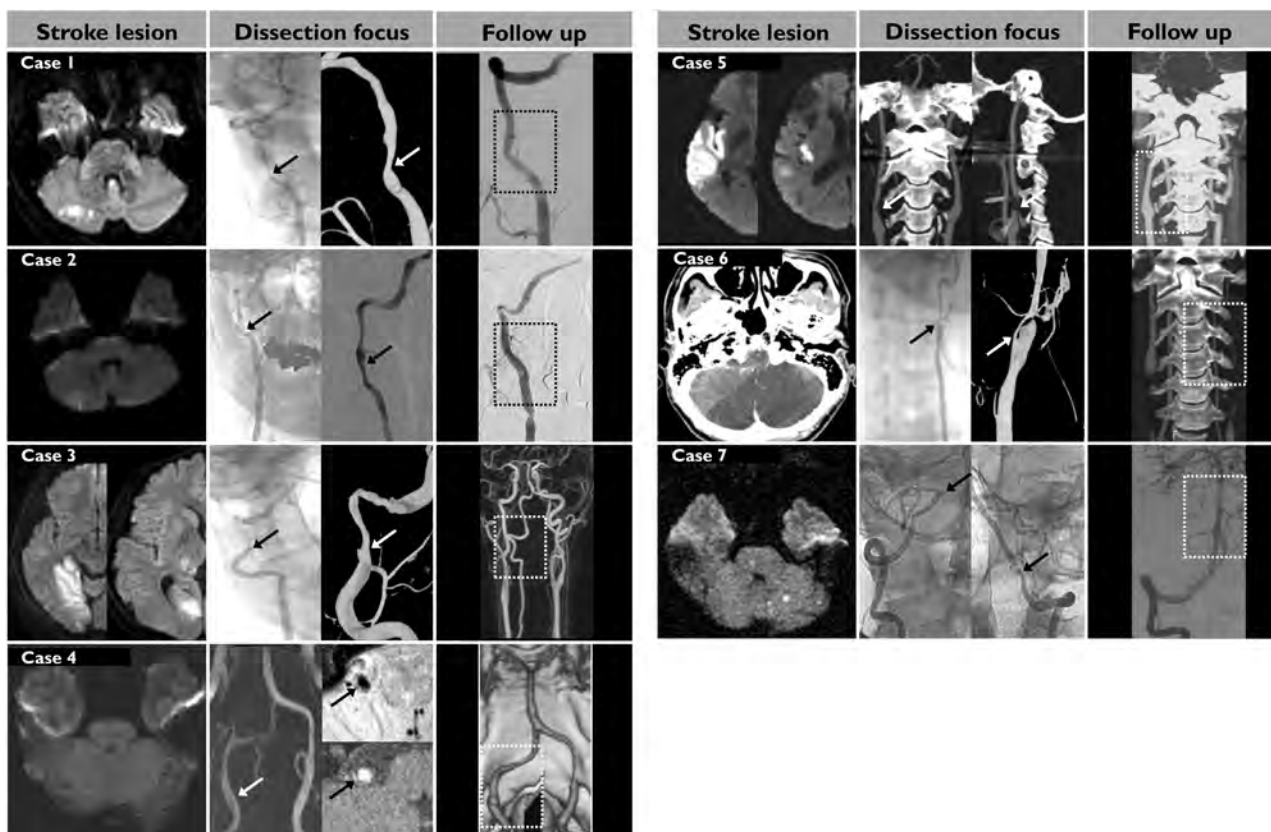


FIG 1. Radiologic findings (stroke location, dissection focus, and follow-up) of our 7 cases. Five cases had right-sided involvement: 3 patients (cases 1–3) with extracranial vertebral artery, 1 with intracranial VA (case 4), and 1 with extracranial carotid artery (case 5). One patient (case 6) had a left extracranial VA and 1 patient (case 7) had bilateral intracranial VA involvement. Black arrows indicate the dissection focus or foci. Dotted rectangles indicate follow-up images of dissection focus or foci.

logic signs and symptoms, treatment, and clinical outcomes. We also analyzed radiologic findings such as stroke location (anterior or posterior circulation), side of arterial dissection (right, left, or both), and anatomic location of the dissection (extracranial or intracranial). Status at symptom onset was classified as during swing, after golf exercise, and unknown. Clinical outcome was categorized as returned to normal (mRS = 0–1), independent (mRS = 2–3), dependent (mRS = 4–5), and death (mRS = 6) at discharge.¹¹ Differences between the stroke location, side of dissection, and anatomic location of the dissection were analyzed by use of the χ^2 test. Statistical significance was considered at $P < .05$.

RESULTS

Fourteen male patients were examined. The demographic and clinical-radiologic findings are provided in the On-line Table. The mean age of the patients was 46.9 ± 12.8 years, which was younger than that of the general stroke population. Seven patients were right-handed. Of the 7 patients, 2 were professional golfers with 15–17 years of experience, and the remaining patients were amateur players with playing experience for approximately 7 years (range, 0.1–30 years). None of the patients had a history of hypertension, diabetes, or autoimmune disorder. Symptom onset occurred during the golf swing ($n = 9$), at an unknown time ($n = 3$), or after golf playing ($n = 2$). Twelve patients had posterior circulation symptoms such as vertigo, nystagmus, and body tilt-

ing. Eight patients had localized pain at symptom onset. A potential source for vasculopathies and cardioembolic stroke was excluded from laboratory and cardiologic studies.

The location of arterial dissection was confirmed by cerebral angiography ($n = 11$), MR angiography ($n = 2$), and Doppler ultrasound ($n = 1$). The imaging studies revealed that 12 patients had involvement of the vertebral artery (VA) and 2 patients had ICA involvement ($P = .008$). Nine patients had arterial dissections on the right side, of which 2 had ICA involvement; 3 had left side involvement; and 2 had bilateral lesions ($P = .046$). There were 12 extracranial and 2 intracranial cases ($P = .008$). Normal activity was possible in 7 patients, but the other cases revealed 5 independent patients and 1 death (On-line Table). Radiologic findings (stroke location and dissection focus) of our 7 cases are shown in Fig 1.

DISCUSSION

Our study illustrates that arterial dissection from golf-related stroke was more likely to be on the right side and predominantly in the extracranial vertebrobasilar system. This preference may be explained by the anatomic vulnerability of the vertebrobasilar system and the biomechanics of the golf swing.

Recent studies on ethnic differences in spontaneous vertebral artery dissection have shown that intracranial dissection is more common than extracranial dissection in East Asian populations.⁷ Our study of golf-related vertebral artery dissection shows that

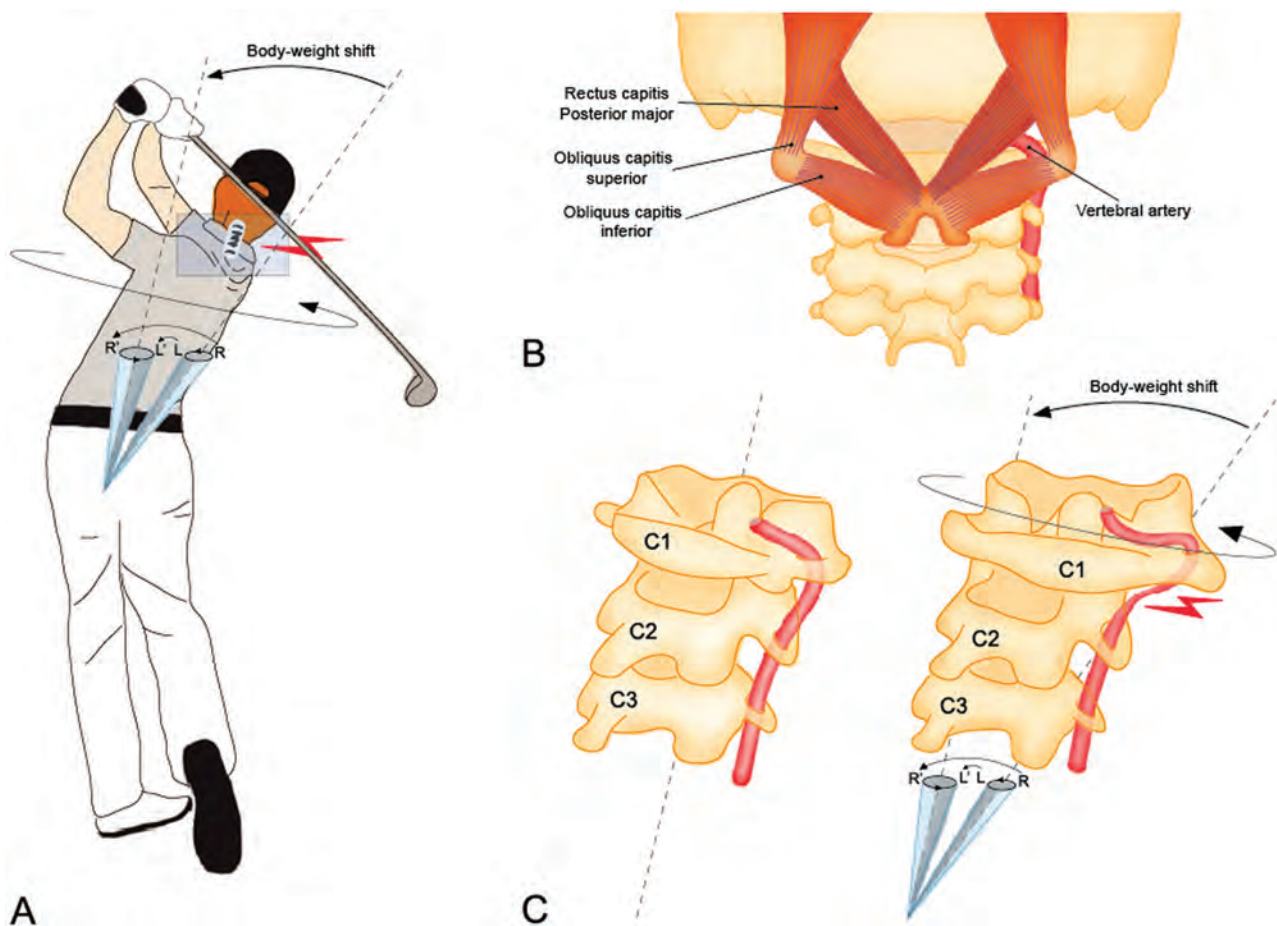


FIG 2. Mechanical explanation for the predominance of the right vertebral artery (VA) dissection during a golf swing. *A*, Late follow-through phase. *B*, Anatomy of neck muscles adjacent to the hypermobile segment (V3) of the VA. *C*, Vulnerability of the right VA during the golf swing. In a right-handed swing, there is a combination of right-to-left body-weight shift and counter-clockwise body rotation. This gives the right shoulder (R to R') a longer arch compared with the left shoulder (L to L'). In the same setting of force (F), the right VA receives a greater torque (τ) than does the left VA because it has a longer distance (r) from the central axis (dotted line). The anatomic preference for this specific stroke syndrome can be explained by a momentary high torque ($\tau = r \times F$) during body-weight shift and forceful rotation of the body and neck.

extracranial involvement is more frequent than intracranial involvement. As compared with either their intracranial segments or extracranial arteries of similar caliber, greater mobility of the extracranial segments of the carotid and vertebral arteries leads to increased susceptibility for injury by surrounding hard structures including bones, ligaments, and contracted muscles.^{6,8} Even with an external elastic lamina and a thickened media in the extracranial arteries, various studies have found that the atlantic (V3) portion of the vertebral artery is susceptible to VA dissection during trauma.⁸ This V3 portion is exposed without the support of bony structures and rotates freely during inadvertent head movement. Extracranial vertebral artery dissection has also been reported in patients who have undergone chiropractic manipulation, fixed neck posture caused by long-lasting surgery, or chest compressions during cardiopulmonary resuscitation.^{9,10} In addition, dynamic imaging studies show that the VA is compressed and even occluded at the extracranial portion during contralateral head rotation.^{12,13} These reasons support direct mechanical injury of the extracranial vessels as the etiology for golf-related stroke.

VA injuries during sports activities with repetitive neck movement have been reported in yoga, tennis, volleyball, judo, bowl-

ing, and wrestling.^{3,14,15} Most sports-related vessel damage is caused by dissection or thromboembolism.³ A similar case of right VA dissection associated with unidirectional stereotypical movement was reported in a right-handed archer and is known as "bow hunter's stroke."¹⁵ As compared with other sports, the golf swing is a high-speed, unidirectional, stereotypical rotational movement. Force is proportional to mass and acceleration of an object, as stated by Newton's second law. Torque (τ : torque) is a moment of force in rotating movement, and its magnitude depends on the length of the lever arm (r : length) and the force (F : force). Therefore, the driving torque of the golf swing is calculated as the cross-product of the distance and force, which tends to generate rotation, as expressed in the following equation: $\tau = r \times F$.¹⁶ Our patients were all right-handed. In a right-handed swing, the central axis (hub) of the right leg during the back swing is changed to the left leg because of the body-weight shift from right to left to obtain forceful impact of the ball. As compared with the left VA, the right VA is distant from the central axis during the body-weight shift and receives a greater torque during the golf swing. This swing trajectory also causes repetitive mechanical stress to the adjacent tissues including muscles, ligaments, and

vessels.⁶ The increased stress of neck muscles adjacent to the right VA can lead to vessel injury by acting as a hammer when a golfer has greater torso-pelvic separation, misses the shot, or has insufficient warm-up.¹⁷ In the present study, symptoms occurred during the golf swing in many of the cases (On-line Table).¹⁸ Our 2 professionals and 1 player with low handicap self-reported attempts to maximize torso-pelvic separation to get more distance. From this perspective, a right-sided preference for this specific type of stroke can be explained by a momentary high torque status in relation to the forceful hitting phases (downswing, impact, and follow-through) and an anatomic vulnerability at the hypermobile portion of the right VA (Fig 2).

Our study has several limitations. Given the small number of patients with golf-related stroke in this study, investigations with more cases are needed for a balanced interpretation. Moreover, the handedness of half of the patients was unknown despite the significant association with the laterality of the golfer's stroke. Finally, video analyses of swing phases were not investigated in a biomechanical laboratory. Five cases (36%) had no relationship with the direct golf swing even though the mechanical injury was suspicious for the development of arterial dissection during the swing.

CONCLUSIONS

Golf-related craniocervical arterial dissection occurs most often in the right extracranial vertebrobasilar system. Possible mechanisms are high mobility of the extracranial portion of the VA against a head rotation and mechanical injury to the respective vessels associated with high-speed, unidirectional, and stereotypical body rotation. Future studies are required not only to investigate detailed observations of the swing phase but to focus on other nonmechanical factors such as insufficient warm-up and incorrect posture.

REFERENCES

1. McCarroll JR. **The frequency of golf injuries.** *Clin Sports Med* 1996;15:1-7
2. Theriault G, Lachance P. **Golf injuries: an overview.** *Sports Med* 1998;26:43-57
3. Maroon JC, Gardner P, Abla AA, et al. **"Golfer's stroke": golf-induced stroke from vertebral artery dissection.** *Surg Neurol* 2007;67:163-68
4. Choi KD, Oh SJ, Yang TI, et al. **Golfer's stroke from internal carotid artery dissection.** *Arch Neurol* 2008;65:1122-23
5. Guptha SH, Promnitz AD, Warner A, et al. **A 'collapsing' golfer.** *Cerebrovasc Dis* 2005;19:281-82
6. Hong JM, Kim TJ, Lee JS. **Neurological picture: repetitive internal carotid artery compression of the hyoid: a new mechanism of golfer's stroke?** *J Neurol Neurosurg Psychiatry* 2011;82:233-34
7. Kim BM, Kim SH, Kim DI, et al. **Outcomes and prognostic factors of intracranial unruptured vertebrobasilar artery dissection.** *Neurology* 2011;76:1735-41
8. Schievink WI. **Spontaneous dissection of the carotid and vertebral arteries.** *N Engl J Med* 2001;344:898-906
9. Sherman DG, Hart RG, Easton JD. **Abrupt change in head position and cerebral infarction.** *Stroke* 1981;12:2-6
10. Tettenborn B, Caplan LR, Sloan MA, et al. **Postoperative brainstem and cerebellar infarcts.** *Neurology* 1993;43:471-77
11. Wilson JT, Hareendran A, Grant M, et al. **Improving the assessment of outcomes in stroke: use of a structured interview to assign grades on the modified Rankin Scale.** *Stroke* 2002;33:2243-46
12. Choi KD, Shin HY, Kim JS, et al. **Rotational vertebral artery syndrome: oculo-graphic analysis of nystagmus.** *Neurology* 2005; 65:1287-90
13. Sakaguchi M, Kitagawa K, Hougaku H, et al. **Mechanical compression of the extracranial vertebral artery during neck rotation.** *Neurology* 2003;61:845-47
14. DeBehnke DJ, Brady W. **Vertebral artery dissection due to minor neck trauma.** *J Emerg Med* 1994;12:27-31
15. Sorensen BF. **Bow hunter's stroke.** *Neurosurgery* 1978;2:259-61
16. Sharp RS. **On the mechanics of the golf swing.** *Proc R Soc A* 2009;465:551-70
17. Myers J, Lephart S, Tsai YS, et al. **The role of upper torso and pelvis rotation in driving performance during the golf swing.** *J Sports Sci* 2008;26:181-88
18. Ono Y, Arai K, Nishino A, et al. **Bilateral dissections of the vertebral arteries followed by MRI.** *Prog Comput Imaging* 2000;22: 199-204

When Is Carotid Angioplasty and Stenting the Cost-Effective Alternative for Revascularization of Symptomatic Carotid Stenosis? A Canadian Health System Perspective

M.A. Almekhlafi, M.D. Hill, S. Wiebe, M. Goyal, D. Yavin, J.H. Wong, and F.M. Clement



ABSTRACT

BACKGROUND AND PURPOSE: Carotid revascularization procedures can be complicated by stroke. Additional disability adds to the already high costs of the procedure. To weigh the cost and benefit, we estimated the cost-utility of carotid angioplasty and stenting compared with carotid endarterectomy among patients with symptomatic carotid stenosis, with special emphasis on scenario analyses that would yield carotid angioplasty and stenting as the cost-effective alternative relative to carotid endarterectomy.

MATERIALS AND METHODS: A cost-utility analysis from the perspective of the health system payer was performed by using a Markov analytic model. Clinical estimates were based on a meta-analysis. The procedural costs were derived from a microcosting data base. The costs for hospitalization and rehabilitation of patients with stroke were based on a Canadian multicenter study. Utilities were based on a randomized controlled trial.

RESULTS: In the base case analysis, carotid angioplasty and stenting were more expensive (incremental cost of \$6107) and had a lower utility (−0.12 quality-adjusted life years) than carotid endarterectomy. The results are sensitive to changes in the risk of clinical events and the relative risk of death and stroke. Carotid angioplasty and stenting were more economically attractive among high-risk surgical patients. For carotid angioplasty and stenting to become the preferred option, their costs would need to fall from more than \$7300 to \$4350 or less and the risks of the periprocedural and annual minor strokes would have to be equivalent to that of carotid endarterectomy.

CONCLUSIONS: In the base case analysis, carotid angioplasty and stenting were associated with higher costs and lower utility compared with carotid endarterectomy for patients with symptomatic carotid stenosis. Carotid angioplasty and stenting were cost-effective for patients with high surgical risk.

ABBREVIATIONS: BURST = Burden of Ischemic Stroke; CAS = carotid angioplasty and stenting; CEA = carotid endarterectomy; CREST = Carotid Revascularization Endarterectomy versus Stenting Trial; EVA-3S = Endarterectomy versus Angioplasty in Patients with Symptomatic Severe Carotid Stenosis; MI = myocardial infarction; QALY = quality-adjusted life years; SAPPHERE = Stenting and Angioplasty with Protection in Patients at High Risk for Endarterectomy

Stroke is a costly illness. Stroke prevention among patients with symptomatic carotid stenosis requires carotid revascularization. This can be done surgically as carotid endarterectomy (CEA)¹ or less invasively through carotid angioplasty and stent placement (CAS).² Both are used in combination with optimal medical therapy. Approximately 5000 CEA procedures were per-

formed in Canada in 2005.³ Stroke is an uncommon but feared complication of carotid revascularization.⁴ Stroke is more common after CAS, and though most of these periprocedural strokes are clinically minor, they contribute to the cumulative disability associated with the procedure.⁵ The largest randomized trial comparing CAS versus CEA (the Carotid Revascularization Endarterectomy versus Stenting Trial [CREST]) concluded that the outcomes after CEA versus CAS were similar because a higher risk of myocardial infarction (MI) after CEA was balanced by a higher risk of stroke after CAS.²

Increased costs of CAS due to the costs of devices and the higher costs of stroke as a complication may be balanced by a slightly longer length of stay after CEA.^{6–9} These outcomes have different impacts on the patient's quality of life.^{10,11} We sought to determine the cost-utility of CAS compared with CEA in symptomatic patients and to understand what circumstances make CAS a cost-effective procedure.

Received April 19, 2013; accepted after revision May 29.

From the Departments of Clinical Neurosciences (M.A.A., M.D.H., S.W., M.G., D.Y., J.H.W.), Medicine (M.D.H.), Community Health Sciences (M.D.H., S.W., F.M.C.), and Radiology (M.G., M.D.H.), Hotchkiss Brain Institute, University of Calgary, Calgary, Alberta, Canada; and Department of Internal Medicine (M.A.A.), King Abdulaziz University, Jeddah, Saudi Arabia.

Please address correspondence to Mohammed A. Almekhlafi, MD, MSc, FRCP(C), Foothills Medical Center, 1403 29th St NW, Calgary, Alberta, Canada T2N 2T9; e-mail: malmekhlafi@kau.edu.sa



Indicates article with supplemental on-line tables.



Evidence-Based Medicine Level 1.

<http://dx.doi.org/10.3174/ajnr.A3682>

MATERIALS AND METHODS

The cost per quality-adjusted life years (QALY) gained with CAS compared with CEA in the treatment of patients with symptomatic carotid stenosis was assessed. The perspective of the Canadian health care system payer was adopted. The costs and clinical outcomes were modeled by using a Markov process. A lifetime time horizon was used¹² to capture all relevant costs and benefits.

Model

Figure 1 presents the model structure. Given the higher risk of adverse outcomes in the initial 30 days after CAS or CEA, the first 30-day outcomes were modeled separately from long-term outcomes. Patients who survive the initial period will be in 1 of 4 health states: healthy, major stroke, minor stroke, or MI. The costs and clinical outcomes were assessed at 1-year intervals.

All clinical outcomes were taken from published randomized trials comparing CEA and CAS. Major stroke was defined as stroke that results in disability interfering with independent living. Minor stroke was defined as stroke that causes no disability or causes a disability that does not interfere with independent living.¹³ Myocardial infarction was defined as chest pain associated with electrocardiographic changes or elevated cardiac enzymes. The healthy state described individuals who did not have stroke or MI or die following the carotid revascularization procedure. The healthy state included patients who might have had known transient complications not typically affecting a durable quality of life, such as cranial nerve palsy following CEA or groin hematoma following CAS.

The base case analysis simulated a cohort of patients at an average age of 65 years with symptomatic carotid stenosis eligible for revascularization with either CAS or CEA. All costs and utili-

ties were discounted at 5% annually. Costs were inflated to 2012 costs by using the Canadian Consumer Price Index for health and personal care.¹⁴ Decision analysis software (TreeAge Software, Williamstown, Massachusetts) was used to construct a Markov model. The study was approved by the Conjoint Health Research Ethics Board at the University of Calgary.

Clinical Data

The estimates of the clinical outcomes in the periprocedural (30-day) period were pooled from the results of a recent meta-analysis,⁴ which included 12 major carotid revascularization trials enrolling 6973 patients (Table 1). This meta-analysis did not separately report the rates of periprocedural major and minor strokes. Data from this recent meta-analysis were reanalyzed to provide estimates of periprocedural major and minor strokes.⁴ The long-term clinical outcomes in those who survived the periprocedural period reported in included studies by Yavin et al⁴ were pooled to estimate the annual incidence of major stroke, minor stroke, and death, excluding the first 30 days. The annual risk of each outcome was calculated by dividing the total number of patients with the outcome by the number of follow-up years (excluding outcomes occurring in the first 30 days).

The risk of MI beyond the first 30 days was not reported in major randomized trials of CAS versus CEA and therefore was assumed similar among patients undergoing either procedure. Survival data beyond the follow-up of the clinical trials (≤ 4 years of follow-up) were based on the study by Caro et al.¹⁵

Cost Data

Procedural Costs. Using microcosting data from the Calgary Health Zone, we selected a cohort of consecutive patients with carotid stenosis who underwent carotid revascularization (2005–2007). Costs estimates reflected the direct costs incurred by the health system. Inpatient costing data include those for investigations and treatments. Investigation costs included laboratory, imaging, and cardiac investigations. Treatment costs included the operating room and angiography suite costs; nursing care; and medications, devices, and materials used. Human resources costs (including nurses, therapists, and social workers) were also captured. Physician claims for endarterectomy, stent placement, and anesthesia were obtained from the Alberta Ministry of Health schedule of medical benefits. Hospitalization costs were cal-

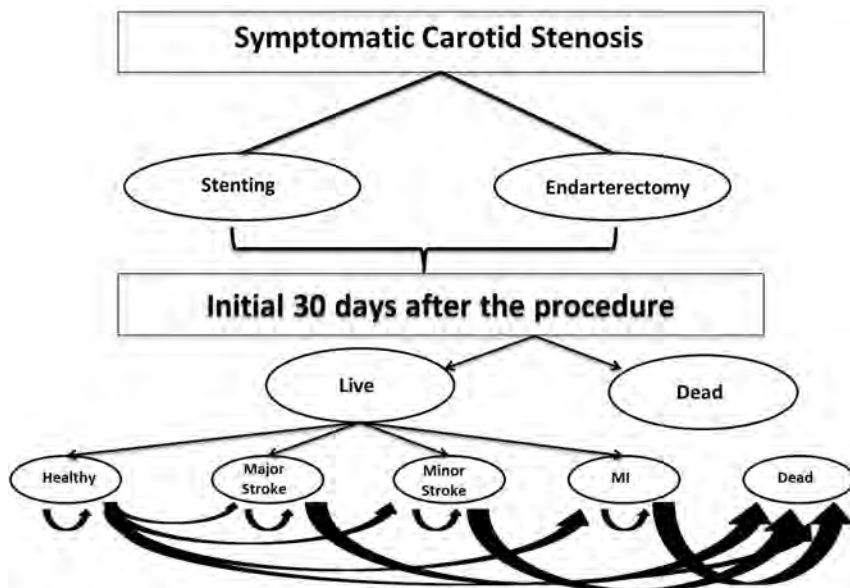


FIG 1. The Markov model structure.

Table 1: Clinical estimates for the periprocedural and annual outcomes

Outcome	Periprocedural Risk (CI ₉₅) after CEA	Annual Risk (CI ₉₅) after CEA	Periprocedural OR (CI ₉₅) of CAS vs CEA	Annual OR (CI ₉₅) of CAS vs CEA	References
Death	0.009 (0.008–0.01)	0.018 (0.016–0.02)	1.11 (0.82–1.40)	1.02 (0.94–1.10)	2,4,21,22,27,28
Major stroke	0.006 (0.005–0.008)	0.013 (0.012–0.015)	1.645 (0.89–2.1)	1.1 (0.58–2.10)	
Minor stroke	0.022 (0.019–0.025)	0.0515 (0.05–0.052)	1.91 (1.17–3.11)	1.3 (0.75–2.08)	
MI	0.018 (0.015–0.02)	N/A	0.47 (0.38–0.56)	N/A	

Note:—CI₉₅ indicates 95% confidence interval; N/A, not available.

Table 2: Cost estimates (2012)

	Base Case Cost Estimates (CDN\$)	Reference
CAS procedure	7303	Calgary cohort
CAS hospitalization	2243	
CEA procedure	4483	
CEA hospitalization	3703	
Major stroke		
1st year	83164	BURST study ^{16,29}
Annually after 1st year	31267	
Minor stroke		
1st year	31136	BURST study ^{16,29}
Annually after 1st year	13488	
MI		
1st year	4937	Conly et al ¹⁸
Annually after 1st year	1455	
Doppler US	237	Government of Alberta
Clopidogrel (daily)	1.18	Government of Alberta

Note.—CDN\$ indicates cost estimates; US, ultrasound.

Table 3: Utility estimates

	Base Case Utility Estimate	Reference
Baseline	0.86	Beaver Dam study ¹⁹
Healthy	0.86	
MI	0.74	SAPPHIRE ¹¹
Major stroke	0.28	Tengs and Linn meta-analysis ²⁰
Minor stroke	0.64	
Death	0	

culated from the asymptomatic patients and those presenting with TIAs. This calculation was performed to avoid double-counting the rehabilitation costs associated with patients presenting with minor or major strokes. Outpatient follow-up costs were assumed similar among patients with uncomplicated carotid revascularization.

Ongoing Costs of Care. The direct costs for hospitalization and readmissions for patients having minor and major strokes were based on the findings of the multicenter Canadian Burden of Ischemic Stroke (BURST) study.¹⁶ For the base case analysis, only direct costs for patients with major and minor strokes were used (Table 2). These included costs for hospitalizations, rehabilitation, diagnostic imaging, medications, physician services, home care, changes of residence, and paid caregivers. The costs for hospitalization of patients who had MI were based on the Alberta Provincial Project for Outcome Assessment in Coronary Heart Disease data base.^{17,18}

Utilities

Utility scores were quoted from the published literature (Table 3). The Stenting and Angioplasty with Protection in Patients at High Risk for Endarterectomy (SAPPHIRE) trial used the baseline utility reported by the Beaver Dam Health Outcomes Study utility score for “healthy” patients with hypertension. For the baseline utility, we used an average utility score (0.86) of those reported by the Beaver Dam Health Outcomes Study for subjects with-versus-without hypertension in the age group corresponding to the base case analysis.¹⁹ The utility scores of major and minor strokes were based on the results of a meta-analysis.²⁰ The utility score for MI was derived from the SAPPHIRE trial.

Table 4: Clinical characteristics of the local treatment cohorts

	Carotid Stenting (n = 134)	Carotid Endarterectomy (n = 66)
Mean age (yr) (SD)	72.2 (8.5)	69 (8.8)
Women	28.4 (38/134)	22.7 (15/66)
Risk factors		
Coronary artery disease	45.5 (61/134)	18.2 (12/66)
Diabetes	30.6 (40/134)	43.9 (29/66)
Hypertension	88.1 (118/134)	68.2 (45/66)
Current smoking	32.1 (43/134)	31.8 (21/66)
Qualifying event		
Retinal events	18.7 (25/134)	16.7 (11/66)
TIA	32.7 (44/134)	39.4 (26/66)
Stroke	29.9 (40/134)	25.7 (17/66)
Asymptomatic	18.7 (25/134)	18.2 (12/66)

Sensitivity Analyses

To address the model assumptions and uncertainties, we performed multiple 1-way sensitivity and scenario analyses over plausible ranges based on the confidence intervals of clinical outcome measures, costs, utility scores, and discount rates.

Given that cost-utility estimates may vary by health care setting, we explored the impact of high surgical risk and high procedural risk outcomes by using risk estimates from major carotid revascularization trials (CREST,² Endarterectomy versus Angioplasty in Patients with Symptomatic Severe Carotid Stenosis [EVA-3S],²¹ and SAPPHIRE²²) obtained in different populations.

Monte Carlo Simulation

A Monte Carlo simulation by using a hypothetical cohort of 10,000 patients was performed to investigate the overall uncertainty in the model. Normal distributions were used for the risks, costs, and utility estimates.

RESULTS

Model Validation

The baseline characteristics of the costing cohorts for CAS and CEA are summarized in Table 4. The cost of a CAS procedure was estimated at \$7303, while the hospitalization cost was \$2240. Compared with CAS, the cost of a CEA procedure was lower at \$4483 but had a higher hospitalization cost of \$3703. The decision model structure, estimates, and assumptions were reviewed by experts in the field of cerebrovascular diseases (M.D.H., J.H.W.) and health economics (F.M.C.). The internal validity of the model was verified by comparison of predicted outcomes and input clinical risks. External validity was evaluated by comparing the predicted clinical outcomes with observed clinical outcomes at 4 years from the major clinical trials (On-line Table 1). Our predicted probabilities matched the observed probabilities within 20%.

Base Case Cost-Utility Analysis

In the base case analysis, CAS was more expensive than CEA (incremental cost of \$6107) and had a lower effectiveness (−0.12 QALYs); CAS was dominated by CEA. (Table 5).

One-Way Sensitivity Analyses

The model results were not affected by varying the discount rate or periprocedural or annual risk of major or minor stroke

Table 5: Base case and scenario analyses

Strategy	Cost	Incremental Cost (\$)	Effectiveness (QALYs)	Incremental Effectiveness	Incremental Cost-Effectiveness	ICER
Base case						
CEA	\$24,624		6.83		3605	
CAS	\$30,731	\$ 6107.00	6.71	-0.12	4580	Dominated ^a
SAPPHIRE						
CEA	\$77,377	\$14,801.48	5.14	-1.96	15049	Dominated ^a
CAS	\$62,576		7.1		8814	
EVA-3S						
CEA	\$22585		6.82		\$3312	
CAS	\$30,832	\$ 8246.38	6.67	-0.15	\$4695	Dominated ^a
CREST						
CEA	\$22,259		6.89		\$3227	
CAS	\$25,846	\$ 3587.00	6.63	-0.27	\$3900	Dominated ^a

Note:—ICER indicates incremental cost-effectiveness ratio.

^a “Dominated” means that the treatment modality was associated with more cost and less effectiveness.

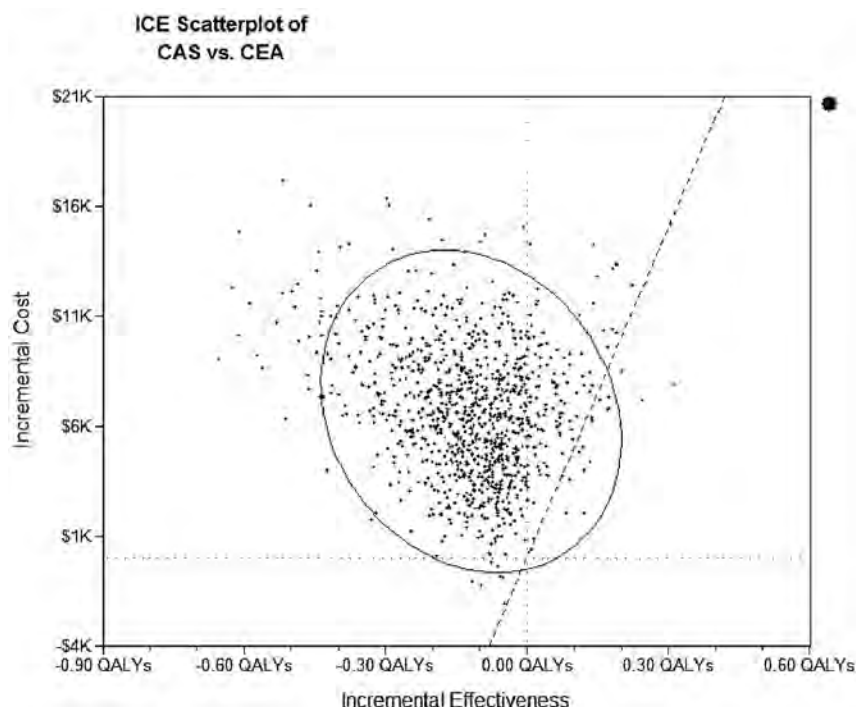


FIG 2. Scatterplot of the cost-effectiveness plane.

(On-line Table 2). The cost of MI did not impact the results. The procedural cost of CAS did not influence these results even when costs as low as \$1000 per procedure were used.

The model results were sensitive to variation in the annual mortality risk. When CAS was associated with a lower risk of death compared with CEA, at a threshold relative risk of 0.85, CAS was associated with an incremental cost-effectiveness ratio of \$32,839 per QALY gained compared with CEA.

Scenario Analyses Based on Major Trials

When estimates from trials of high-procedure-risk populations (EVA-3S) or of patients treated with the North American standards (CREST trial) were used (On-line Table 3), the results were unchanged. With estimates from the high surgical risk population (SAPPHIRE trial), CAS was cost-effective relative to CEA (Table 5). The higher risk of death and major strokes associated with CEA described in that trial led to higher costs and reduced QALYs.

Threshold Analyses

Only after simultaneously reducing CAS procedural costs from \$7300 to \$4350, the relative risks of minor periprocedural strokes (relative risk = 1.0), and the annual relative risk of stroke (relative risk = 1.15) does CAS become the preferred option.

In the Monte Carlo simulation, the estimated net costs in the simulated cohort were \$28,615 (95% CI, \$28,556–\$28,674) for CAS and \$22,948 (95% CI, \$22,919–\$22,976) for CEA. Almost all simulations fell in the upper quadrants, indicating the presence of incremental costs associated with CAS in most simulations (Fig 2). However, the scatter across the horizontal plane indicates uncertainty in the effectiveness of CAS versus CEA.

DISCUSSION

Overall, CAS was associated with higher costs and lower effectiveness compared with CEA among patients with symptomatic carotid stenosis. These results were driven by the costs of both the procedure and the associated periprocedural adverse outcomes (primarily major and minor stroke). The costs associated with MI did not impact the results. These results were sensitive to annual survival following the procedure. Longer survival is associated with greater cost-effectiveness for CAS.²³

CAS was cost-effective under certain circumstances. Among patients with high-surgical-risk features, CAS was associated with both lower costs and higher QALY gains. This was largely influenced by the lower risk of major and minor periprocedural stroke associated with CAS.

While careful patient selection is an important factor in reducing procedural complications, the risk of periprocedural stroke remains higher with CAS across many major trials. If and when the safety of CAS is improved through the development of the technology and procedural innovation, CAS may become cost-effective relative to CEA.

Monte Carlo simulated cohort analysis showed some uncertainty around the effectiveness of CAS compared with CEA, but costs were always higher with CAS. Distal protection devices, balloons, stents, and guiding catheters used for CAS are expensive, collectively approaching \$4500. These costs outweigh any savings associated with shorter hospitalization after CAS. Therefore, improving CAS safety is an alternative approach to improving its cost-effectiveness.

There are multiple steps involved in performing CAS; some of these are the subject of ongoing debate because of safety concerns. For example, the use of distal protection devices and poststent

balloon angioplasty are 2 procedural steps that are not universally performed. While angioplasty balloons cost approximately \$300 per device, the cost of the distal protection device is \$1900.²⁴ Identifying the safety of these instruments is important to enable the assessment of the potential clinical and economic impact of eliminating such steps that might be hazardous.

These results are concordant with reports from other jurisdictions.^{10,11,25,26} The higher procedural cost associated with CAS was unanimously reported by these studies, and the cost of stroke care was a major driver of the cost-utility analyses. The cost estimates used in this analysis for patients with major and minor stroke were significantly higher compared with other reports. The BURST trial estimates included costs for postdischarge care, which were not reported in many other trials and provide a novel Canadian context.

This study has limitations. The analysis was based on clinical estimates from a meta-analysis that combined patients with variable clinical characteristics treated via different protocols. While the effects of this variability were examined by performing multiple sensitivity and scenario analyses, the base case results should be interpreted bearing in mind the limitations of available evidence. Moreover, the model provides outcomes and costing data beyond what is known from these trials. The analysis adopts a public health system perspective, and indirect costs were not included in this analysis. Therefore, the reported costs represent an underestimate of the actual total costs associated with both procedures. Some adverse outcomes occasionally seen with CEA, such as cranial nerve injuries, which are rarely disabling, were not considered in this analysis. Despite these limitations, this analysis not only provides an assessment of the cost-utility of CAS in the Canadian health system but it also explored factors influencing these costs and suggests potential saving strategies.

CONCLUSIONS

Overall, CEA was the cost-effective procedure relative to CAS for patients with symptomatic carotid stenosis. CAS provides an attractive incremental cost-effectiveness ratio in the high-surgical-risk population. Effort should be focused on reducing the periprocedural stroke risk and procedural costs to improve CAS cost-effectiveness.

Disclosures: Michael D. Hill—*RELATED: Other*: site for the Carotid Revascularization Endarterectomy vs. Stenting Trial (CREST) study (local site principal investigator). **Comments*: money from National Institutes of Health grant to pay for per-patient costs for the CREST study, *UNRELATED: Board Membership*: Heart and Stroke Foundation Alberta, Northwest Territories, Nunavut, *Comments*: provincial advisory board, no remuneration, volunteer work, *Payment for Lectures (including service on Speakers Bureaus)*: Sanofi Canada, Bristol-Meyers Squibb Canada, *Comments*: honoraria for lecturing at continuing medical education events, *Stock/Stock Options*: Calgary Scientific Inc, *Comments*: stockholder in this company (an image-processing company), Samuel Wiebe—*UNRELATED: Travel/Accommodations/Meeting Expenses Unrelated to Activities Listed*: International League against Epilepsy, *Comments*: executive board member. Mayank Goyal—*UNRELATED: Consultancy*: Covidien/ev3, *Comments*: for speaking engagement, trial design, and so forth, *Grants/Grants Pending*: Covidien/ev3, **Comments*: partial funding of the ESCAPE (Endovascular treatment for Small Core and Anterior circulation Proximal occlusion with mphasis on minimizing CT to recanalization times) trial, *Payment for Lectures (including service on Speakers Bureaus)*: Covidien/ev3, *Comments*: for lectures related to acute stroke treatment, *Stock/Stock Options*: NoNo Inc, Calgary Scientific Inc. *Money paid to the institution.

REFERENCES

- Rothwell PM, Eliasziw M, Gutnikov SA, et al. Analysis of pooled data from the randomised controlled trials of endarterectomy for symptomatic carotid stenosis. *Lancet* 2003;361:107–16
- Brott TG, Hobson RW 2nd, Howard G, et al. Stenting versus endarterectomy for treatment of carotid-artery stenosis. *N Engl J Med* 2010;363:11–23
- Dai S, Bancej C, Bienek A, et al. Tracking heart disease and stroke in Canada 2009. *Chronic Diseases in Canada* Ottawa, Ontario: Public Health Agency of Canada 2009;29:192–93
- Yavin D, Roberts DJ, Tso M, et al. Carotid endarterectomy versus stenting: a meta-analysis of randomized trials. *Can J Neurol Sci* 2011;38:230–35
- Blackshear JL, Cutlip DE, Roubin GS, et al. Myocardial infarction after carotid stenting and endarterectomy: results from the carotid revascularization endarterectomy versus stenting trial. *Circulation* 2011;123:2571–78
- Jordan WD Jr, Roye GD, Fisher WS 3rd, et al. A cost comparison of balloon angioplasty and stenting versus endarterectomy for the treatment of carotid artery stenosis. *J Vasc Surg* 1998;27:16–22, discussion 22–14
- Kilaru S, Korn P, Kasirajan K, et al. Is carotid angioplasty and stenting more cost effective than carotid endarterectomy? *J Vasc Surg* 2003;37:331–39
- Ecker RD, Brown R Jr, Nichols DA, et al. Cost of treating high-risk symptomatic carotid artery stenosis: stent insertion and angioplasty compared with endarterectomy. *J Neurosurg* 2004;101:904–07
- Park B, Mavanur A, Dahn M, et al. Clinical outcomes and cost comparison of carotid artery angioplasty with stenting versus carotid endarterectomy. *J Vasc Surg* 2006;44:270–76
- Vilain KR, Magnuson EA, Li H, et al. Costs and cost-effectiveness of carotid stenting versus endarterectomy for patients at standard surgical risk: results from the Carotid Revascularization Endarterectomy Versus Stenting Trial (CREST). *Stroke* 2012; 43:2408–16
- Mahoney EM, Greenberg D, Lavelle TA, et al. Costs and cost-effectiveness of carotid stenting versus endarterectomy for patients at increased surgical risk: results from the SAPPPIRE trial. *Catheter Cardiovasc Interv* 2011;77:463–72
- Guidelines for the Economic Evaluation of Health Technologies. 3rd ed. Ottawa, Ontario, Canada: Canadian Agency for Drugs and Technologies in Health; 2006
- Kwon S, Hartzema AG, Duncan PW, et al. Disability measures in stroke: relationship among the Barthel Index, the Functional Independence Measure, and the Modified Rankin Scale. *Stroke* 2004;35:918–23
- Consumer Price Index, health and personal care, by province (monthly). Statistics Canada. <http://www.statcan.gc.ca/tables-tableaux/sum-som/l01/cst01/cpis13a-eng.htm>. Accessed January 2012
- Caro JJ, Ishak KJ, Migliaccio-Walle K. Estimating survival for cost-effectiveness analyses: a case study in atherothrombosis. *Value Health* 2004;7:627–35
- Mittmann N, Seung SJ, Hill MD, et al. Impact of disability status on ischemic stroke costs in Canada in the first year. *Can J Neurol Sci* 2012;39:793–800
- Ghali WA, Knudtson ML. Overview of the Alberta Provincial Project for Outcome Assessment in Coronary Heart Disease: on behalf of the APPROACH investigators. *Can J Cardiol* 2000;16:1225–30
- Conly J, Clement F, Tonelli M, et al. Cost-effectiveness of the use of low- and high-potency statins in people at low cardiovascular risk. *CMAJ* 2011;183:E1180–88
- Fryback DG, Dasbach EJ, Klein R, et al. The Beaver Dam Health Outcomes Study: initial catalog of health-state quality factors. *Med Decis Making* 1993;13:89–102
- Tengs TO, Lin TH. A meta-analysis of quality-of-life estimates for stroke. *Pharmacoeconomics* 2003;21:191–200
- Mas JL, Trinquart L, Leys D, et al. Endarterectomy Versus Angioplasty in Patients with Symptomatic Severe Carotid Stenosis (EVA-

- 3S) trial: results up to 4 years from a randomised, multicentre trial.** *Lancet Neurol* 2008;7:885–92
22. Gurm HS, Yadav JS, Fayad P, et al. **Long-term results of carotid stenting versus endarterectomy in high-risk patients.** *N Engl J Med* 2008;358:1572–79
23. Hobson RW 2nd, Howard VJ, Roubin GS, et al. **Carotid artery stenting is associated with increased complications in octogenarians: 30-day stroke and death rates in the CREST lead-in phase.** *J Vasc Surg* 2004;40:1106–11
24. Jacobs P, Fassbender K. **The measurement of indirect costs in the health economics evaluation literature: a review.** *Int J Technol Assess Health Care* 1998;14:799–808
25. Janssen MP, de Borst GJ, Mali WP, et al. **Carotid stenting versus carotid endarterectomy: evidence basis and cost implications.** *Eur J Vasc Endovasc Surg* 2008;36:258–64, discussion 265–66
26. Maud A, Vazquez G, Nyman JA, et al. **Cost-effectiveness analysis of protected carotid artery stent placement versus endarterectomy in high-risk patients.** *J Endovasc Ther* 2010;17:224–29
27. Brooks WH, McClure RR, Jones MR, et al. **Carotid angioplasty and stenting versus carotid endarterectomy: randomized trial in a community hospital.** *J Am Coll Cardiol* 2001;38:1589–95
28. Steinbauer MG, Pfister K, Greindl M, et al. **Alert for increased long-term follow-up after carotid artery stenting: results of a prospective, randomized, single-center trial of carotid artery stenting vs carotid endarterectomy.** *J Vasc Surg* 2008;48:93–98
29. Seung S, Mittmann N, Sharma M, et al. **The methodology behind a prospective, observational study of the economic burden of ischemic stroke.** *Value Health* 2005;8:A153

Quantifying the Large-Scale Hemodynamics of Intracranial Aneurysms

G. Byrne, F. Mut, and J. Cebal



ABSTRACT

BACKGROUND AND PURPOSE: Hemodynamics play an important role in the mechanisms that govern the initiation, growth, and possible rupture of intracranial aneurysms. The purpose of this study was to objectively characterize these dynamics, classify them, and connect them to aneurysm rupture.

MATERIALS AND METHODS: Image-based computational fluid dynamic simulations were used to re-create the hemodynamics of 210 patient-specific intracranial aneurysm geometries. The hemodynamics were then classified according to their spatial complexity and temporal stability by using quantities derived from vortex core lines and proper orthogonal decomposition.

RESULTS: The quantitative classification was compared with a previous qualitative classification performed by visual inspection. Receiver operating characteristic curves provided area-under-the-curve estimates for spatial complexity (0.905) and temporal stability (0.85) to show that the 2 classifications were in agreement. Statistically significant differences were observed in the quantities describing the hemodynamics of ruptured and unruptured intracranial aneurysms. Specifically, ruptured aneurysms had more complex and more unstable flow patterns than unruptured aneurysms. Spatial complexity was more strongly associated with rupture than temporal stability.

CONCLUSIONS: Complex-unstable blood flow dynamics characterized by longer core line length and higher entropy could induce biologic processes that predispose an aneurysm for rupture.

ABBREVIATIONS: IA = intracranial aneurysm; POD = proper orthogonal decomposition; CFD = computational fluid dynamic; ROC = receiver operating characteristic; AUC = area under the curve

Endothelial cells in blood vessel walls continuously sense and respond to hemodynamic wall shear stresses. Responses to normal wall shear stresses typically involve short-term vessel adaptation through vasodilation, or long-term, nonpathologic tissue remodeling. Under abnormal wall shear stresses, degenerative processes can take place in the vessel wall and lead to the pathologic formation, growth, and rupture of an intracranial aneurysm (IA).¹⁻⁶ The coupling between the local (near wall) and global (far from wall) hemodynamics makes it possible to identify large-scale spatiotemporal blood flow patterns that result in dangerous wall shear stress conditions.

The connection between large-scale hemodynamics and aneurysm rupture was previously studied.^{7,8} Qualitative descriptions of spatial flow complexity and temporal flow stability were outlined and used to visually assess the hemodynamics of patient-specific IA geometries. The clinical history of each patient was used to correlate rupture events with spatially complex and temporally unstable flow patterns.

In this study, we use vortex core lines and proper orthogonal decomposition (POD) to quantify the large-scale hemodynamics of IAs. These methods are commonly used to visualize spatially complex fluid flows^{9,10} and create low-dimensional models of turbulence.^{11,12} However, their use in analyzing biofluids is novel. Quantitative representations of spatial flow complexity and temporal flow stability are outlined and used to provide a more objective hemodynamic classification. This quantitative approach also allows us to connect specific large-scale dynamical quantities to rupture.

MATERIALS AND METHODS

Hemodynamic Modeling

Patient-specific geometries of cerebral aneurysms were reconstructed from 3D rotational angiography images.¹³ Digital sub-

Received February 19, 2013; accepted after revision May 20.

From the Center for Computational Fluid Dynamics, College of Science, George Mason University, Fairfax, Virginia.

This work was supported by the National Institutes of Health, grant No. R01NS059063.

Please address correspondence to Greg Byrne, PhD, Center for Computational Fluid Dynamics, George Mason University, 4400 University Dr, MSN 6A2, Fairfax, VA 22030; e-mail: gr3g.byrne@gmail.com

Indicates open access to non-subscribers at www.ajnr.org

<http://dx.doi.org/10.3174/ajnr.A3678>

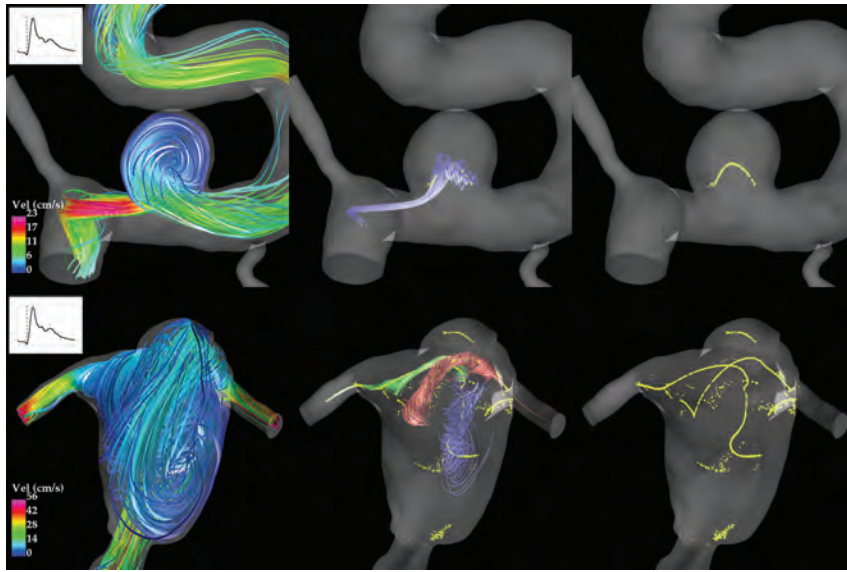


FIG 1. Qualitative assessments of spatial flow complexity were made by visually inspecting streamline plots. Top left: This flow formed a single vortex and was classified as simple. Bottom left: This flow formed multiple vortices and was classified as complex. Center column: Streamline trajectories around the vortex core lines help to distinguish the individual vortices. Right column: Core lines are also known as vortex skeletons because they provide simplified representations of the large-scale flow structure.

traction imaging was performed by use of a constant injection of contrast agent at 24 mL/s for a 180° rotation in 8 seconds. Imaging was performed at 15 frames per second. Data from these images was transferred to a workstation (Phillips Healthcare, Best, The Netherlands) and reconstructed into 3D voxel data with the use of the standard proprietary software. 3D reconstructions were compared with views from the conventional angiogram to assess the completeness of the rendering. Cases with incomplete rendering or inadequate filling of the parent artery or the aneurysm were discarded.

Unstructured grids composed of tetrahedral elements were generated with a resolution of approximately 0.1 mm, resulting in grids of roughly 2–5 million elements. Vessel walls were assumed rigid, and blood flow was considered incompressible and Newtonian. Numeric solutions of the unsteady 3D Navier-Stokes equations were obtained under “typical” pulsatile flow conditions.¹⁴ The inlet boundaries of all models were located in the internal carotid artery, the vertebral artery, or the basilar artery.

Two cardiac cycles were simulated with a time-step size of 0.01 second for a heart rate of 60 bpm. The analysis in this work was based on 100 snapshots of the velocity vector field generated during the second cycle. IA necks were identified on the reconstructed vascular models and used to label the aneurysm and the parent artery.¹⁵ Subsequent flow characterizations were restricted to the aneurysm.

Qualitative Assessments of Spatial Complexity and Temporal Stability

The hemodynamics of 210 IA geometries (83 ruptured) were classified according to Cebal et al.^{7,16} Flows were classified according to visual assessments of spatial complexity and temporal stability, on the basis of the following qualitative criteria.

Flow Complexity. “Simple” refers to flow patterns that consist of a single recirculation zone or vortex structure within the IA. “Com-

plex” refers to flow patterns that exhibit flow divisions or separations within the aneurysm sac and contain more than one recirculation zone or vortex structure.

Flow Stability. “Stable” refers to flow patterns that persist (do not move or change) during the cardiac cycle. “Unstable” refers to flow patterns in which the flow divisions and/or vortex structures move or are created or destroyed during the cardiac cycle.

Streamline plots were used to assess spatial flow complexity. Two examples are shown in Fig 1. Temporal flow stability was assessed by animating the streamline plots over the cardiac cycle.

Quantifying Spatial Flow Complexity

Many algorithms have been proposed to visualize vortices in datasets generated by computational fluid dynamic (CFD) simulations.¹⁰ Vortices were identified in this study by constructing vortex core

lines: 1D sets that pass through centers of swirling flow. Vortex core lines provide a simple but accurate way of representing the spatial structures that underpin blood flow patterns in an aneurysm.

Vortex core lines were identified by use of a co-linearity condition between the instantaneous vorticity $\vec{\omega}$ and velocity \vec{v} vectors. Mathematically, this condition can be expressed as

$$1) \quad \vec{\omega} \times \vec{v} = 0$$

where $\vec{\omega} = \nabla \times \vec{v}$.

Our numeric algorithm consisted of a parallel search across multiple processors for tetrahedral mesh elements that satisfied Equation 1. Each processor formed and diagonalized the velocity gradient tensor in an element. If a pair of complex conjugate eigenvalues was found, the vorticity vector $\vec{\omega}$ was formed to test whether Equation 1 was satisfied in the element. Reduced velocities¹⁷ were formed at the element nodes by subtracting the velocity component in the direction of the vorticity vector. Element faces that contained a point where the reduced velocity was zero were marked. If 2 or more faces of an element were found to contain a zero, a vortex core line passes through the element. A segment approximating this core line was constructed by connecting the points along the faces containing the zeros of the reduced velocity.

The vortex core line segments in each mesh element at the i^{th} snapshot were summed up to produce a total length L_i . Spatial complexity was quantified taking the average vortex core line length over the N snapshots

$$2) \quad \langle L \rangle = \frac{1}{N} \sum_{i=1}^N L_i$$

Complex flows (with multiple vortices) are expected to have longer average vortex core lines than simple flows (with a single vor-

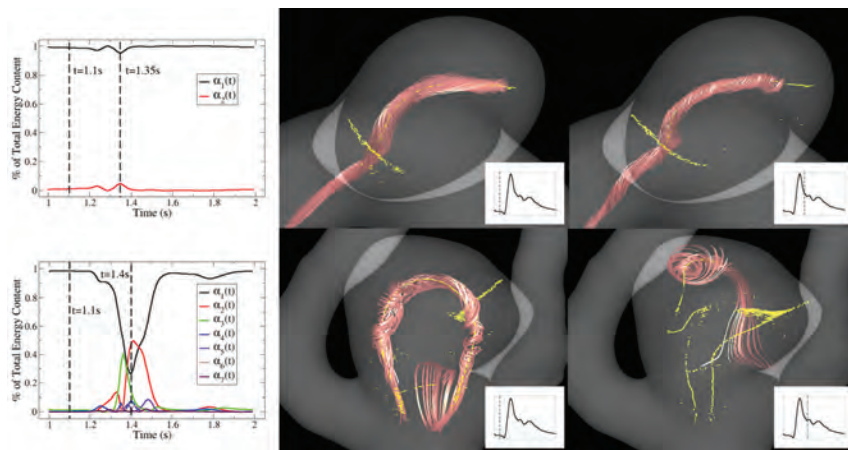


FIG 2. The temporal coefficients accounting for 99% of the total energy are plotted for stable (top) and unstable (bottom) flows. Vortex core lines (yellow) and neighboring streamline trajectories (red) are used to visualize the spatial structure of the flow at 2 instants during the cardiac cycle. The stable flow retains its spatial structure during the cardiac cycle. Very little energy is transferred between the temporal coefficients resulting in an entropy of $S = 0.0713$. The unstable flow undergoes large fluctuations and changes its spatial structure. Large amounts of energy are transferred between the temporal coefficients resulting in an entropy of $S = 0.674$.

text). Fig 1 shows the vortex core lines for a simple and a complex flow. The simple flow (top) contains a single core line with an average length $\langle L \rangle = 0.93$, whereas the complex flow (bottom) contains multiple core lines with an average length $\langle L \rangle = 17.5$.

Quantifying Temporal Flow Stability

Temporal flow stability is characterized by the creation, destruction, or motion of spatial flow patterns during the cardiac cycle. These patterns are defined by both vortex structures and flow divisions created by inflow jets. Temporal tracking of the vortex core lines was not used to quantify flow stability because of an alternate method that captures both flow divisions and recirculation zones.

The first step in quantifying the temporal flow stability was to separate the temporal dynamics from the spatial dynamics. This was achieved by expressing the velocity vector field ensemble as a linear combination of orthogonal, vector-based modes $\varphi(x)$ and scalar coefficients $\alpha_i(t_j)$ that govern their temporal evolution

$$3) \quad u(x, t_j) = \sum_{i=1}^N \alpha_i(t_j) \varphi_i(x), \quad j = 1, \dots, N$$

where N is the number of snapshots in the ensemble. POD was used to generate the orthogonal set of basis modes $\varphi_i(x)$.¹¹ Although this decomposition may not be unique, we chose the POD procedure to form the basis set because it identifies fundamental spatial flow patterns that, on average, capture more of the fluid kinetic energy per mode than any other basis set.

The POD basis was computed by use of a snapshot method that builds an $N \times N$ 2-point velocity correlation tensor.¹⁸ When diagonalized, the correlation tensor forms an energy matrix η with energy eigenvalues λ_i running along the diagonal in decreasing order. Each mode $\varphi_i(x)$ is associated with energy eigenvalue λ_i that can be recovered from the mean squared value of the corresponding temporal coefficients $\lambda_i = (\alpha_i(t_j), \alpha_i(t_j))/N$, where (\cdot, \cdot)

is the Euclidean inner product. The trace of the energy matrix $Tr(\eta) = \sum_{i=1}^N \lambda_i$ is a measure of the total fluid kinetic energy in the aneurysm.

The relative energy $P_i = \lambda_i / \sum_{j=1}^N \lambda_j$ quantifies the energy content of the i th mode, whereas the entropy

$$4) \quad S = - \sum_{i=1}^N P_i \ln(P_i)$$

quantifies the average energy distributed across the N modes. It is used here to measure the temporal stability of hemodynamic flows. Entropy is maximized when the energy is evenly spread over the modes and minimized when it is concentrated in a single mode.

An example is provided in Fig 2. The first column contains plots of the temporal coefficients $\alpha_i(t_j)$ for a stable (top) and unstable (bottom) flow. The tempo-

ral coefficients were scaled to plot the fractional energy content contained in each corresponding basis mode. For visualization purposes, only the temporal coefficients accounting for 99% of the total energy are plotted. The vortex core lines and a few neighboring streamlines are shown in the center and right hand columns at 2 different points in the cardiac cycle. Two coefficients are required to meet the 99% energy threshold for the stable flow while 7 coefficients are required for the unstable flow.

The value of the entropy for the stable flow is $S = 0.0713$. Most of the energy during the cardiac cycle is concentrated in the first spatial mode $\varphi_1(x)$. No flow structures are created, destroyed, or undergo significant motion. The value of the entropy for the unstable flow is $S = 0.674$, approximately 9.5 times greater than the stable flow. Large amounts of energy are transferred from $\alpha_1(t)$ to the remaining 6 coefficients. Significant changes are also observed to occur in the spatial organization of the flow during the cardiac cycle.

RESULTS

The spatial flow complexity and temporal flow stability in all 210 IA geometries were quantified by use of the average core line length $\langle L \rangle$ and entropy S . Flow classification was based on discrimination thresholds for each of the 2 variables. True- and false-positive rates were computed by sweeping over the discrimination thresholds and comparing the quantitative classifications to the qualitative classifications. The results are summarized by the 2 receiver operating characteristic (ROC) curves in Fig 3. The accuracy of the qualitative classification was measured by integrating the ROC curves. The resulting areas under the curve (AUCs) are presented in Table 1. An AUC of 1 indicates exact agreement for all cases. The AUC is 0.905 for spatial complexity and 0.86 for temporal stability. These results are considered "excellent" and "very good."¹⁹

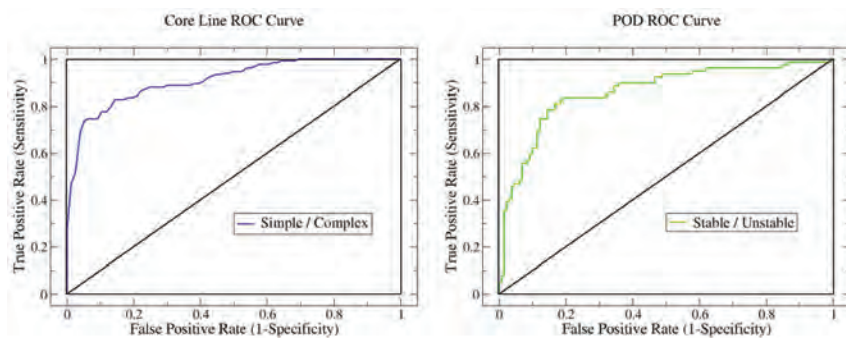


FIG 3. ROC curves summarizing the ability of our flow variables to correctly identify spatially simple (left) and temporally stable (right) hemodynamic flows in our aneurysm data base. The ROC curves were generated by comparing the quantitative classification against qualitative classification.

Table 1: Summary and performance statistics of the variables used to quantify spatial flow complexity and temporal flow stability

Category	Mean Core Line Length	Category	Mean Entropy
Simple	0.4564	Stable	0.1224
Complex	3.2094	Unstable	0.2458
<i>P</i> value	$<2.12 \times 10^{-22}$	<i>P</i> value	$<8.4 \times 10^{-19}$
AUC	0.905	AUC	0.86

Table 2: Summary and performance statistics of the variables used to quantify spatial flow complexity and temporal flow stability in ruptured and unruptured aneurysms

Category	Mean Core Line Length	Mean Entropy	Combined
Unruptured	1.4551	0.181	–
Ruptured	3.407	0.2275	–
<i>P</i> value	$<7.6 \times 10^{-8}$	<0.0002	–
AUC	0.72	0.648	0.716

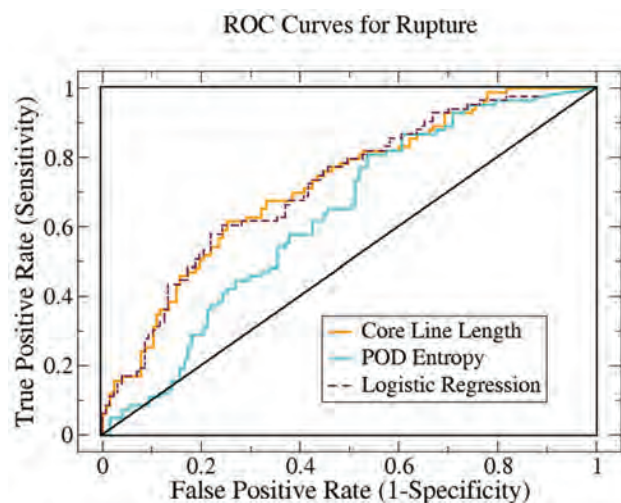


FIG 4. ROC curves summarizing the ability of our flow variables to discriminate between ruptured and unruptured aneurysms. The average core line length (L) measured the flow complexity and the entropy S measured flow stability. A logistic regression was used to combine these 2 variables into a third variable that was tested for enhanced predictive power.

Table 1 also compares the variable means for each flow group as established by the qualitative classification. The *P* values were generated by use of the Wilcoxon rank sum test. The mean core line length is higher in the complex flow group than in the

simple flow group. Likewise, the mean entropy is higher in the unstable flow group than in the stable flow group. The differences between the means are statistically significant ($P < .05$).

The same statistical comparison was applied to the group means of the ruptured and unruptured IAs. These results, presented in Table 2, indicate that ruptured IAs tend to have larger core line lengths (ie, more complex spatial flow patterns) and larger entropies (ie, more temporally unstable flow patterns) than unruptured IAs. Again, the differences between the means are statistically significant.

Rupture prediction was based on the ability to quantitatively discriminate between ruptured and unruptured aneurysms. The true- and false-positive rates were established by comparing the predicted state of rupture to the clinical records. A third variable, based on a logistic regression of spatial complexity and temporal stability, was also developed and tested for enhanced predictive power. The 3 ROC curves for rupture are shown in Fig 4. The corresponding AUCs are reported in Table 2. The average vortex core line length had the highest AUC, suggesting that spatial complexity may play a more important role than temporal stability in the rupture of IAs.

DISCUSSION

The results presented in this report confirm and extend previous results that compared qualitative flow characteristics in ruptured and unruptured IAs. Important spatiotemporal flow features (ie, flow complexity and flow stability) previously identified by visual inspection were successfully extracted from the velocity vector fields by using objective quantitative methods based on vortex core lines and POD. Quantitative results confirmed previous observations that ruptured aneurysms tend to have complex-unstable flows and that unruptured aneurysms tend to have simple-stable flows. The results also indicated that flow complexity is a better discriminant of rupture state than flow stability.

The effect of rupture on IA geometries was previously studied.²⁰ The results indicated small changes in 20% of the IAs and no changes in 80% of the IAs between the pre-ruptured and post-ruptured state. The small changes found in 20% of the ruptured IAs' geometry were assumed to have a negligible impact on the large-scale hemodynamic properties.

Isosurface methods have been used to visualize vortices in aortic aneurysms.^{21,22} However, the frequent need for a user supplied threshold to construct these surfaces led us to use line-type methods for visualizing and analyzing the spatial structure of hemodynamic flows.²³⁻²⁶ Irregular aneurysm geometries make the task of identifying a "characteristic length" difficult and subjective. As a result, we used the unnormalized length.

Our metric for spatial complexity is limited in the sense that it does not measure the number of discrete vortices formed within the aneurysm or account for their topologic structure. Other measures of spatial complexity on the basis of a more detailed analysis

of the core line structure (geometry, connectivity, or topology) are also possible and may provide a more accurate representation of the original qualitative criteria.

Discontinuities between neighboring core line segments were observed because the velocity gradient is piecewise linear over the computational domain. Segments oriented end-to-end created well-defined vortex core lines. Segments that were not oriented end-to-end often formed 2D structures that resembled vortex sheets. Vortices smaller than the mesh elements are unable to be resolved and were ignored in our study. Isolated segments in the domain that were not part of any visible fluid structure could be the result of noise produced by the computation of numeric derivatives.

Mesh sensitivity studies were not performed. The core lines extracted and analyzed in this work were consistent with the degree of approximation of the CFD simulations. Mesh refinement should capture smaller vortices and improve the linear approximation used for the vortex core segments. It should also reduce the gaps in vortex segments between neighboring elements.

The AUC values in Table 2 represent the probability that a ruptured aneurysm randomly selected from the data base will be ranked as “higher risk” than a randomly selected unruptured aneurysm. They indicate that the logistic regression variable performed about the same as the spatial complexity variable. This is an interesting result that further highlights the fact that most spatially complex flows are unstable and that most simple flows are stable. We attribute the lack of improvement in the AUC of the logistic variable to this correlation. One of the limitations of the rupture prediction study was the lack of long-term clinical data. As a result, we would like to point out that caution must be used when interpreting the low values of the AUCs found in Table 2. Artificially high false-positive rates can be generated by IAs that were quantitatively classified as “high risk,” but that have not yet undergone a rupture. A study with an extended clinical history would be required to make a more accurate assessment of rupture prediction on the basis of these variables.

CFD calculations were carried out under pulsatile flow condition at 2 heart rates (60 bpm and 100 bpm). For each heart rate, the corresponding flow waveforms were prescribed from measurements in the cerebral arteries reported in the literature.²⁷ Under these different flow conditions, the vortex core line lengths were not significantly different, and the statistical results were largely unaffected (within a 1% difference). This suggests that the large-scale hemodynamics are independent of relatively small variations in the physiologic conditions.

CONCLUSIONS

The observations and methods described in this study can better help us to understand the underlying mechanisms that govern IA initiation, evolution, and rupture. Our quantitative approach for assessing spatial flow complexity and temporal flow stability was consistent with the assessments made using well-defined qualitative approach. Statistically significant differences were found in the variables quantifying the hemodynamics of ruptured and unruptured aneurysms. Complex-unstable flow dynamics were more commonly observed in ruptured aneurysms, whereas sim-

ple-stable flow dynamics were more commonly observed in unruptured aneurysms. Spatial complexity was found to be more strongly associated with rupture than temporal stability. This result indicates that complex flows producing high spatial gradients of the wall shear stress vector may play a more fundamental role in predisposing the aneurysm wall for rupture than unstable flows producing temporal oscillations of the wall shear stress vector.

Disclosures: Greg Byrne—RELATED: Grant: NIH.* Comments: Research grant; Support for Travel to Meetings for the Study or Other Purposes: George Mason University. Comments: GMU student travel fund for the March APS conference 2012. Fernando Mut—RELATED: Grant: NIH.* Juan Cebal—RELATED: Grant: NIH.* Comments: Research grant; UNRELATED: Consultancy: Cardiatis; Grants/Grants Pending: NIH.* Philips* (*money paid to institution).

REFERENCES

1. Sforza D, Putman CM, Cebal JR. **Hemodynamics of cerebral aneurysms.** *Annu Rev Fluid Mech* 2009;41:91–107
2. Chalouhi N, Ali MS, Jabbour PM, et al. **Biology of intracranial aneurysms: role of inflammation.** *J Cereb Blood Flow Metab* 2012;32:1659–76
3. Penn DL, Komotar RJ, Connolly ES. **Hemodynamic mechanisms underlying cerebral aneurysm pathogenesis.** *J Clin Neurosci* 2011;18:1435–38
4. Kadirvel R, Ding YH, Dai D, et al. **The influence of hemodynamic forces on biomarkers in the walls of elastase-induced aneurysms in rabbits.** *Neuroradiology* 2007;49:1041–53
5. Hashimoto T, Meng H, Young WL. **Intracranial aneurysms: links among inflammation, hemodynamics and vascular remodeling.** *Neurol Res* 2006;28:372–80
6. Frosen J, Tulamo R, Paetau A, et al. **Saccular intracranial aneurysm: pathology and mechanisms.** *Acta Neuropathol* 2012;123:773–86
7. Cebal JR, Mut F, Weir J, et al. **Association of hemodynamic characteristics and cerebral aneurysm rupture.** *AJNR Am J Neuroradiol* 2011;32:264–70
8. Cebal JR, Castro MA, Burgess JE, et al. **Characterization of cerebral aneurysm for assessing risk of rupture using patient-specific computational hemodynamics models.** *AJNR Am J Neuroradiol* 2005;26:2550–59
9. Roth M, Peikert R. *Flow visualization for turbomachinery design.* In: *7th IEEE Visualization Conference (VIS'96).* San Francisco: IEEE Computer Society Press; 1996:381–84
10. Jiang M, Machiraju R, Thompson DS. **Detection and visualization of vortices.** In: Hansen CD and Johnson CR, ed: *Visualization Handbook.* Burlington, Massachusetts: Elsevier Butterworth-Heinemann; 2005:287–301
11. Holmes P, Lumley J, Berkooz G. *Turbulence, Coherent Structures, Dynamical Systems and Symmetry.* Cambridge, UK: Cambridge University Press; 1996
12. Aubry N, Guyonnet R, Lima R. **Spatiotemporal analysis of complex signals: theory and applications.** *J Stat Phys* 1991;64:683–739
13. Cebal JR, Castro MA, Appanaboyina S, et al. **Efficient pipeline for image-based patient-specific analysis of cerebral aneurysm hemodynamics: technique and sensitivity.** *IEEE Trans Med Imaging* 2005;24:457–67
14. Ford MD, Alperin N, Lee SH, et al. **Characterization of volumetric flow rate waveforms in the normal internal carotid and vertebral arteries.** *Physiol Meas* 2005;26:477–88
15. Mut F, Löhner R, Chien A, et al. **Computational hemodynamics framework for the analysis of cerebral aneurysms.** *Int J Numer Method Biomed Eng* 2011;27:822–39
16. Cebal JR, Mut F, Weir J, et al. **Quantitative characterization of the hemodynamic environment in ruptured and unruptured brain aneurysms.** *AJNR Am J Neuroradiol* 2011;32:145–51
17. Sujudi D, Haimes R. *Identification of Swirling Flow in 3D Vector Fields.* Technical Report, Department of Aeronautics and Astronautics, MIT, Cambridge, Massachusetts: 1995

18. Sirovich L. **Turbulence and the dynamics of coherent structures: I, coherent structures; II, symmetry and transformations; III, dynamics and scaling.** *Quart Appl Mathematics* 1987;45:561–90
19. Zweig MH, Campbell G. **Receiver-operating characteristic (ROC) plots: a fundamental evaluation tool in clinical medicine.** *Clin Chem* 1993;39:561–77
20. Ishikawa T, Nakayama N, Yoshimoto T, et al. **How does spontaneous hemostasis occur in ruptured cerebral aneurysms? Preliminary investigation on 247 clipping surgeries.** *Surg Neurol* 2006;66:269–75
21. Biasetti J, Hussain F, Gasser TC. **Blood flow and coherent vortices in the normal and aneurysmatic aortas: a fluid dynamical approach to intraluminal thrombus formation.** *J R Soc Interface* 2011;8:1449–61
22. Arzani A, Shadden SC. **Characterization of the transport topology in patient-specific abdominal aortic aneurysm models.** *Phys Fluids* 2012;24:81901
23. Byrne G, Mut F, Cebal JR. **Vortex Coreline Detection for the Analysis of Blood Flow Patterns in Cerebral Aneurysms.** In: *2nd International Conference on Mathematical and Computational Biomedical Engineering, CMBE. 2011*, Washington, DC. 2011
24. Byrne G, Mut F, Cebal JR. **Using Vortex Detection to Characterize Aneurysmal Flow Activity.** In: *Proceedings of the ASME 2012 Summer Bioengineering Conference*, Fajardo, Puerto Rico. 2012
25. Raschi M, Mut F, Byrne G, et al. **CFD and PIV analysis of hemodynamics in a growing intracranial aneurysm.** *Int J Numer Method Biomed Eng* 2012;28:214–28
26. Gambaruto AM, Joao AJ. **Flow structures in cerebral aneurysms.** *Comp Fluids* 2012;65:56–65
27. Jiang J, Strother CM. **Computational fluid dynamics simulations of intracranial aneurysms at varying heart rates: a “patient-specific” study.** *J Biomech Eng* 2009;131:91–101

Analysis of Complications and Recurrences of Aneurysm Coiling with Special Emphasis on the Stent-Assisted Technique

H. Nishido, M. Piotin, B. Bartolini, S. Pistocchi, H. Redjem, and R. Blanc

ABSTRACT

BACKGROUND AND PURPOSE: Stent-assisted coiling has expanded the treatment of intracranial aneurysms. With the use of continuously compiled data, we reviewed the role and drawbacks of stent-assisted coiling.

MATERIALS AND METHODS: We compiled data from consecutive patients from 2003–2012 who underwent coiling, with or without stent assistance. Clinical and angiographic results were analyzed retrospectively.

RESULTS: Of 1815 saccular aneurysms in 1505 patients, 323 (17.8%) were treated with stents (299 procedures) and 1492 (82.2%) without stents (1400 procedures). Procedure-related complications occurred in 9.4% with stents versus 5.6% without stents ($P = .016$, relative risk 1.5; 95% CI, 1.1–2.7). Ischemic complications were more frequent in the stent group than in the no-stent group (7.0% versus 3.5%; $P = .005$; relative risk, 1.7; 95% CI 1.2–2.5), as were hemorrhagic complications (2.3% versus 1.9%, $P = .64$). Procedure-induced mortality occurred in 2.7% (8/299) with stents versus 1.1% (15/1400) without stents ($P = .029$; relative risk, 2.0; 95% CI, 1.1–3.5). Logistic regression analysis identified wide-neck aneurysms as the most significant independent predictor of complications. A total of 64.1% (207/323) of aneurysms treated with stents and 70.3% (1049/1492) treated without stents have been followed, disclosing angiographic recurrence in 15.5% (32/207) versus 35.5% (372/1049), respectively ($P < .0001$). Logistic regression analysis showed that the presence of a stent was the most important factor for the reduction of angiographic recurrence ($P < .0001$; relative risk, 2.3; 95% CI, 1.6–3.3).

CONCLUSIONS: The stent-assisted coiling technique is associated with a significant decrease in recurrences but a significant increase in complications. The treatment of wide-neck aneurysms remains hazardous.

The stent-assisted coiling technique has broadened the indication for coil embolization, and numerous reports have depicted the value of stents in the treatment of cerebral aneurysms.^{1–6}

We present herein the clinical and angiographic results of a consecutive series of 1815 aneurysms treated over a 9-year period. The aims of this retrospective study were to place the role of stent-assisted coiling into perspective and to determine the factors associated with procedural complications.

MATERIALS AND METHODS

Data Collection

From a prospectively gathered data base of all patients with intracranial saccular aneurysms (with no prior endovascular treat-

ment) who were treated with coils in our institution between January 2003 (when we initiated the use of self-expandable stents) and March 2012, 1505 patients were identified and constituted our study population. The data base included data on the patient (age, sex), the endovascular procedure technique (balloon-assisted, stent-assisted, stand-alone coiling), aneurysm status (ruptured or not), procedure-related morbidity and mortality, immediate and follow-up angiographic results, and the rate of (re-)hemorrhage. All data were reviewed and statistically analyzed. Institutional review board acceptance was obtained for this retrospective study, and the need for informed consent was waived.

Endovascular Procedures

Coiling was performed under general anesthesia and full anticoagulation with heparin in all cases. In all patients with no history of subarachnoid hemorrhage within the previous 4 weeks, 250 mg aspirin was given intravenously. Heparin was discontinued after embolization in most patients. Whenever stent placement was anticipated, patients were given dual antiplatelet therapy before surgery (75–150 mg clopidogrel, 250 mg aspirin daily initiated 15

Received March 1, 2013; accepted after revision May 6.

From the Department of Interventional Neuroradiology, Foundation Rothschild Hospital, Paris, France.

Please address correspondence to Michel Piotin, MD, PhD, Department of Interventional Neuroradiology, Foundation Rothschild Hospital, 25 rue Manin, 75019 Paris, France; e-mail: mpiotin@free.fr

<http://dx.doi.org/10.3174/ajnr.A3658>

Table 1: Baseline demographics and procedures

	Total	Stent-Assisted	No Stent	P
No. of aneurysms	1815	323	1492	—
Age, y, mean ± SD	50.5 ± 12.9	51.8 ± 11.5	50.3 ± 13.1	.009
Ruptured aneurysm, n (%)	767 (42.3)	38 (11.8)	729 (48.9)	<.0001
Female, n (%)	986 (65.5)	196 (68.8)	790 (64.8)	.20
Location, n (%)				
ICA	647 (35.6)	134 (41.5)	513 (34.4)	.015
MCA	489 (26.9)	94 (29.1)	395 (26.5)	.34
AcomA	446 (24.6)	49 (15.2)	397 (26.6)	<.0001
Vertebrobasilar	160 (8.8)	42 (13.0)	118 (7.9)	.003
Pericallosal	59 (3.3)	2 (0.6)	57 (3.8)	.003
PCA	14 (0.8)	2 (0.6)	12 (0.8)	.73
Aneurysm size, mm, mean ± SD	7.1 ± 4.0	8.2 ± 4.7	6.8 ± 3.8	<.0001
Neck size, mm, mean ± SD	3.8 ± 1.9	5.0 ± 2.6	3.6 ± 1.6	<.0001
Multiple, n (%)	1078 (59.4)	147 (45.5)	931 (62.4)	.004
AVM-related, n (%)	36 (2.0)	2 (0.6)	34 (2.3)	.052
No. of procedures	1699	299	1400	—
No. of aneurysms treated in same EVT, n (%)				
1	1591 (93.6)	275 (92.0)	1316 (94.0)	
2	100 (5.9)	24 (8.0)	76 (5.4)	
3	8 (0.5)	0	8 (0.6)	
Balloon-assisted, n (%)	1017 (56.0)	149 (46.1)	868 (58.2)	<.0001
Packing density, %, mean ± SD	26.8 ± 12.3	24.6 ± 11.1	27.3 ± 12.5	<.0001

Note:—AcomA indicates anterior communicating artery; EVT, endovascular treatment; PCA, posterior cerebral artery.

days before the procedure and continued for 6 months). There were no strict exclusion criteria, but a massive subarachnoid hemorrhage potentially requiring ventricular drainage was considered to be a contraindication to stent placement.

Follow-Up Protocol

Our standard follow-up protocol consisted of fixed angiographic follow-up, the first follow-up being performed at 1–6 months after endovascular treatment (depending of the quality of the initial angiographic occlusion and the presentation). The second angiographic follow-up was performed 12 months after the first follow-up, and the third follow-up was performed 24 months after the second follow-up. In the case of angiographic recurrence and/or associated aneurysms left untreated, the follow-up was continued on a yearly basis. A single reader prospectively evaluated all angiograms. The degree of aneurysm occlusion was classified according to the Montreal simplified classification.⁷ Aneurysm recurrence was dichotomized as absent or present. At follow-up, an aneurysm was considered recurrent if a previously totally occluded aneurysm (class 1) had a partial recurrence of the neck (class 2) and/or the sac (class 3). An aneurysm was considered remnant regrowth if a subtotally occluded aneurysm (class 2 or 3) was found to have an increasing neck remnant or residual aneurysm. Aneurysm dimensions were determined on 3D images derived from rotational angiography. Indication for retreatment (class 3 angiographic results) was decided on a case-to-case basis, depending on the patient age and medical history. Aneurysm retreatments were noted.

Statistical Analysis

Data are presented as means for continuous variables and frequencies for categoric variables. Statistical analysis of categoric variables was carried out by use of χ^2 and Wilcoxon tests. Analysis of variance followed by Bonferroni post hoc testing was used to assess differences between the stent-assisted and no-stent groups.

A multivariable logistic regression analysis was carried out to determine predictors of procedural complications and aneurysm recanalization. *P* values of $\leq .05$ were considered statistically significant. Statistical analysis was carried out with R software version 2.15 (<http://www.r-project.org/>).

RESULTS

Baseline Demographics and Procedures

Among 1505 consecutive patients, 1815 intracranial aneurysms were treated by coil embolization in 1699 procedures. A total of 323 aneurysms were treated with the assistance of self-expandable stents in 299 procedures; 1492 aneurysms were treated without stent assistance in 1400 procedures. The baseline demographics of all of the aneurysms according to stent use are shown in Table 1.

In the stent-assisted group, 76.2% (246 aneurysms) had single stent placement and 23.8% (77 aneurysms) had multiple stent placement (Y, X, or straight overlapping configuration). A balloon-assisted technique was used in 46.1% in the stent-assisted group (the stent was deployed after coiling), including 6.8% (22/323) of bailed-out stent placement, versus 58.2% in the no-stent group (*P* < .0001). In 53.3% of aneurysms (172/323), the stents were delivered before coiling (145 trans-cell, 16 jailed-catheter, and 11 stent-jack techniques).

Immediate and Follow-Up Angiographic Results

Immediately, there were more complete obliterations in the no-stent group and more residual aneurysms in the stent-assisted group, but this trend was reversed at last follow-up (Table 2).

Angiographic follow-up was available for 1256 of 1815 aneurysms (69.2%) (Table 3). The no-stent group had a longer mean follow-up (*P* = .0004). The stent-assisted group had fewer angiographic recurrences (*P* < .0001). Of the 1492 aneurysms treated with coils, 140 (9.4%) were retreated, whereas 20 (6.2%) of the 323 stent-assisted coiled aneurysms were retreated (*P* = .084).

Risk Factors for Angiographic Recurrence

In the univariate analysis, the risk factors for angiographic recurrence were ruptured status at presentation, larger aneurysm size, no stent, wider neck, younger age, and lower coil packing attenuation (Table 4). The identified reductive factor for angiographic recurrence was multiple aneurysms. In the logistic regression analysis, the independent variables were ruptured status at presentation, absence of stent, larger aneurysm size, lower packing attenuation, younger age, and wider neck (Table 4). In the univariate analysis, the risk factors for aneurysm retreatment were larger aneurysm, lower packing attenuation, and incomplete initial aneurysm occlusion. In the logistic regression analysis, the independent variables favoring retreatment were larger aneurysm size, absence of stent, hemorrhagic presentation, lower packing attenuation, and initial incomplete occlusion (Table 5).

Table 2: Immediate and follow-up angiographic results

	Total	Stent-Assisted	No Stent	P
Immediate result, n (%)	(n = 1815)	(n = 323)	(n = 1492)	–
Class 1 ^a	1083 (59.7)	165 (51.1)	918 (61.5)	<.001
Class 2 ^b	307 (16.9)	44 (13.6)	263 (17.6)	.08
Class 3 ^c	425 (23.4)	114 (35.3)	311 (20.8)	<.0001
Last follow-up result, n (%)	(n = 1254)	(n = 207)	(n = 1047)	–
Class 1 ^a	718 (57.3)	152 (73.4)	566 (54.1)	<.0001
Class 2 ^b	319 (25.4)	30 (14.5)	289 (27.6)	<.0001
Class 3 ^c	217 (17.4)	25 (12.1)	192 (18.3)	.04

^a Complete obliteration (Reference 7).^b Residual neck (Reference 7).^c Residual aneurysm (Reference 7).**Table 3: Angiographic recurrence**

	Total	Stent-Assisted	No Stent	P
No. of aneurysms followed	1254	207	1047	–
Cumulative follow-up, mo, median (range)	20.0 (1–122)	16.0 (1–69)	21.0 (1–122)	.0004
Recurrence, n (%)	404 (32.2)	32 (15.5)	372 (35.5)	<.0001

Table 4: Risk factors for angiographic recurrence

	Univariate			Logistic Regression
	P	Relative Risk	95% CI	P
Younger age	.004			.008
Location				
ICA	.056	0.84	0.70–1.00	
MCA	.72	1.04	0.86–1.25	
AcomA	.39	1.09	0.90–1.32	
Vertebrobasilar	.82	1.05	0.78–1.37	
Pericallosal	.054	1.50	0.99–2.03	
PCA	.50	0.56	0.10–1.63	
Sac size	<.0001			<.00001
Neck size	.001			.02
Packing density	.013			.005
Cumulative follow-up period	.33			
Balloon-assisted	.82	0.98	0.83–1.16	
SAH	<.0001	1.72	1.46–2.02	<.00001
No stent	<.0001	2.30	1.65–3.28	<.00001

Note:—AcomA indicates anterior communicating artery; PCA, posterior cerebral artery.**Table 5: Risk factors for retreatment**

	Univariate P	Logistic Regression P
Sac size	<.001	<.001
Stent	.084	.0039
SAH	.098	.0024
Packing density	<.001	.019
Initial occlusion	<.001	<.001

Procedure-Related Complications

The procedure-related complications were counted for any intracranial hemorrhages (including a wire perforation or an aneurysm rupture) and any ischemic events (that resulted in patient morbidity or mortality). Hydrocephalus after the treatment of unruptured aneurysms was also counted as a complication. In the no-stent group, procedure-related complications occurred in 5.6% of procedures,

Table 6: Procedure-related complications

	Total	Stent-Assisted	No Stent	χ^2
No. of procedures	1699	299	1400	–
Complications, n (%)	107 (6.3)	28 (9.4)	79 (5.6)	0.016 ^a
Ischemia	70 (4.1)	21 (7.0)	49 (3.5)	0.005 ^a
Hemorrhage	34 (2.0)	7 (2.3)	27 (1.9)	0.64
Hydrocephalus	3 (0.2)	0	3 (0.2)	0.42
Complication-related deaths, n (%)	23 (1.4)	8 (2.7)	15 (1.1)	0.029 ^a

^a Significant value.

including complication-related deaths in 1.1% (Table 6). The 49 ischemic complications resulted in 5 deaths, and the 27 perforations resulted in 10 deaths. There were 3 hydrocephali after treatment of unruptured aneurysms with hydrogel-coated coils.

In the stent-assisted group, complications occurred in 9.4% of procedures and led to 8 deaths (2.7%). The 21 ischemic events led to 5 deaths, and the 7 hemorrhagic events led to 3 deaths. Overall, there were significantly more complications in the stent-assisted group than in the no-stent group (9.4% versus 5.6%; $P = .016$).

In the univariate analysis, the risk factors for procedure-related complications were wider neck, stent-assisted coiling, MCA location, and larger aneurysm. In logistic regression analysis, the independent variable was a wider neck. Stent-assisted coiling and aneurysm size were related to neck width (Table 7).

(Re-)Bleeding After Coiling

Only 21 of 1815 aneurysms (1.2%) bled after endovascular treatment (Table 8). The rates of (re-)bleeding were 0.3% in the stent-assisted group and 1.4% in the no-stent group. In the stent-assisted group, 2 patients bled after treatment of unruptured aneurysms (1 from the aneurysm 12 months after the treatment; the second was readmitted 3 weeks after the treatment with a remote intraparenchymal hematoma). No rebleeding was seen from previously ruptured aneurysms. In the no-stent group, 1 unruptured aneurysm bled 12 months after coiling (modified Rankin Scale 4). Nineteen rebleedings occurred after coil embolization of 729 ruptured aneurysms (2.6%) and led to 13 deaths.

DISCUSSION

Stent-assisted coiling creates a mechanical scaffold to prevent coil protrusion into the parent vessels. Thus, the indication for this technique had mostly been motivated by aneurysm morphology (large neck). Accordingly, our stent-assisted group included aneurysms with wider necks. Ruptured aneurysms were underrepresented to avoid antiplatelet therapy in the setting of subarachnoid hemorrhage. In the stent-assisted group, internal carotid and MCA aneurysms were overrepresented, whereas posterior circulation and pericallosal aneurysms were scarce, explained by a lower incidence of wide-neck aneurysms in these locations. Multiple aneurysms, which were more often treated with coiling alone, tended to have a smaller size, a narrower neck, and fewer ruptured aneurysms compared with the group of single aneurysms.

Immediate and Follow-Up Angiographic Results

Immediate angiographic complete occlusions were obtained less frequently in the stent-assisted than in the no-stent group (51.1% versus 61.5%). This is because larger aneurysms were more frequent in the

stent-assisted group and because dual antiplatelet therapy affected the immediate intra-aneurysmal thrombosis. Catheter kickback out of the stent also affected tight packing. Conversely, at follow-up, complete occlusions increased to 73.4% in the stent-assisted group, whereas these diminished to 54.0% in the no-stent group. For stent-assisted coiling, numerous articles have reported a broad range (13.2–94.4%) of immediate complete occlusion.^{1,2,8-13} However, similar to the present series, most mid-to-long-term follow-up series have reported augmented rates of angiographic complete occlusion at follow-up (range, 54–81%).⁸⁻¹⁴

Angiographic Recurrences

Recurrences were statistically less likely in the stent-assisted group (15.5% versus 35.5%; $P < .0001$). Low rates of recurrence for stent-assisted coiling have also been reported in other recent studies (range, 0–15.2%).^{8,10,11,13-15} In line with our findings, rup-

tured aneurysms, larger size, lower packing attenuation, and wide necks are well-established risk factors for recurrence.^{7,16-20} We also identified younger age to be a risk factor for recurrence. The effect of age is not yet clear, but younger age was one of the predicting factors of late retreatment in the International Subarachnoid Aneurysm Trial.²¹

Multiple aneurysms reduced the likelihood of recurrence, but these aneurysms were generally smaller, had narrower necks, and had fewer ruptured lesions.

In our study, the use of a balloon-assisted technique had no influence on recurrence. Conversely, Shapiro et al²² found both initial and follow-up aneurysm occlusion rates to be higher in balloon-assisted cases. In our study, an absence of a stent was identified as one of the most relevant factors for recurrence. Our results help to confirm the evidence that stent-assisted coiling augments treatment durability and contributes to progressive occlusion.^{10,23,24} This durability can be explained by the combination of biologic, geometric, and hemodynamic mechanisms.²⁵⁻²⁷

Procedural Complications

Our no-stent results show occurrences of complications (5.6%) and mortality (1.1%) similar to various other series without stents.²⁸⁻³¹ Henkes et al²⁸ reported procedural morbidity of 5.0% and mortality of 1.5%. van Rooij et al³⁰ reported procedural complications with a morbidity rate of 3.2% and a mortality rate of 2.6%. A recent meta-analysis for unruptured aneurysms (mainly of studies without the use of stents) found a morbidity rate of 4.8% and a mortality rate of 1.2%.²⁹ Our complication and mortality

Table 7: Risk factors for procedure-related complications

	Univariate <i>P</i>	Relative Risk	95% CI	Logistic Regression <i>P</i>
Age	.16			
Location				
MCA	.01	1.67	1.15–2.43	.058
Vertebrobasilar	.08	0.40	0.15–1.07	–
ICA	.84	0.94	0.64–1.38	–
AcomA	.48	0.83	0.53–1.30	–
Pericallosal	1.00	0.85	0.28–2.50	–
PCA	.71	NA		–
No. of aneurysms in same EVT (multiple vs single)	.98	1.04	0.58–1.79	–
Size	.04			.94
Neck	<.001			.02 ^a
Balloon-assisted	1.00	1.02	0.70–1.47	–
SAH	.98	1.01	0.70–1.47	–
Stent	.016	1.66	1.07–2.55	0.15
Single (vs Y) stenting	.36	1.59	0.73–3.47	–

Note:—AcomA indicates anterior communicating artery; EVT, endovascular treatment; NA, not available for the small sample numbers; PCA, posterior cerebral artery.

^a Significant value.

Table 8: Aneurysm (re)-bleeding summary

Case/Sex/Age	Presentation	Use of Antiplatelet	Initial Aneurysm Occlusion	Stent	(Re)-Bleeding Delay	Outcome (mRS)
1/F/71	SAH	None	1	None	Day 1	6
2/F/68	Fortuitous	None	1	None	12 mo	4
3/M/46	SAH	None	3	None	Day 10	6
4/F/48	SAH	None	3	None	Day 10	6
5/F/65	SAH	8 mg i.a. of abciximab during procedure	1	None	Hour 14	6
6/F/57	SAH	None	1	None	Day 1	4
7/M/35	SAH	None	1	None	Hour 6	6
8/M/48	SAH	None	3	None	Hour 8	6
9/F/55	SAH	None	3	None	89 mo	6
10/F/37	SAH	None	2	None	57 mo	6
11/F/52	SAH	None	1	None	17 mo	1
12/F/81	SAH	None	3	None	Day 4	6
13/F/55	SAH	None	3	None	4 mo	6
14/M/52	Fortuitous	Clopidogrel + aspirin	2	Yes	12 mo	1
15/M/41	SAH	None	1	None	Day 18	6
16/M/52	SAH	4 mg i.a. of abciximab during procedure	1	None	Day 1	6
17/F/51	SAH	4 mg i.a. of abciximab during procedure	1	None	Hour 4	6
18/M/20	SAH	No	1	None	Day 22	1
19/M/69	Fortuitous	Clopidogrel + aspirin	1	Yes	Day 21	6
20/F/56	SAH	No	3	None	Day 1	6
21/F/56	SAH	No	3	None	2 mo	1

Note:—i.a. indicates intra-arterial.

rates in the stent-assisted group were 9.4% and 2.7%, respectively. These are similar to other series of stent-assisted coiling that have reported 2.9–11% morbidity rate and 0–4.8% mortality rate.^{1,3,5,8,32,33} Overall, our complication rate in the stent-assisted group was higher than in the stand-alone coiling series (9.4% versus 5.6%; $P = .016$). The use of a stent was linked to a significantly higher morbidity in our series, but not as an independent factor because stents were generally used in aneurysms with wider necks.

Three cases (0.2%) of hydrocephalus occurred after the treatment of unruptured aneurysms with hydrogel-coated coils, and there were no cases in the smaller stent-assisted group. The HELPS trial also reported that there was no significant difference in the occurrence of hydrocephalus between the hydrogel-coated and bare-platinum coil groups.³⁴

A large aneurysm size was identified as a risk factor for complications but was not identified as an independent value, unlike neck width, which also appeared to be an independent factor. In the CLARITY study, aneurysms >10 mm had a higher risk of thromboembolic events, with higher morbidity-mortality rates compared with smaller lesions.³⁵ Similar results have also been reported in the ATENA study.³³ Moreover, the amount of procedural aneurysmal ruptures was significantly higher for smaller aneurysms.^{33,36} In CLARITY, the morbidity-mortality secondary to thromboembolic events was higher in the group of aneurysms for which the neck was >4 mm.³⁵ In the same study, a neck >4 mm was also identified as an independent risk factor of intraoperative rupture.³⁵

As in our study, age was not identified as a risk factor for complications in the series from van Rooij et al.³⁰ However, Sedat et al¹⁴ reported that thromboembolic events were more frequent among elderly patients, whereas in the CLARITY study, procedural ruptures were more likely to occur in patients <65 years of age.³⁵ As did van Rooij et al,³⁰ we did not find any specific locations to be linked with complications. However, we found that MCA location was a risk factor in the univariate analysis. Similarly, the CLARITY study reported that thromboembolic events were more likely to occur in MCA aneurysms than in aneurysms in other locations, such as intraoperative ruptures.³⁵ The treatment of several aneurysms during the same procedure was not found to result in more complications, as was previously found in the CLARITY study.³⁵ However, only 6.4% of our procedures were multiple aneurysm treatments. The balloon-assisted technique was not identified as a risk factor for complications, unlike in some previous reports.^{28,30,37} However, the ATENA and CLARITY studies showed that the balloon-assisted technique was as safe as conventional coiling.^{33,35} A ruptured aneurysm was not found to be a significant risk factor for complications in the current study. However, this is contrary to various other studies. For example, Ng et al¹⁸ reported that intraprocedural ruptures occurred more frequently for ruptured aneurysms than for unruptured aneurysms. Ishibashi et al³⁸ reported that hyper intensities were seen more frequently on diffusion-weighted MRI after the treatment of ruptured than unruptured aneurysms. Also, Ross and Dhillon³⁹ reported that the risks of vessel or aneurysm rupture or thromboembolic stroke were greater during the treatment of ruptured aneurysms. Similarly, Park et al³⁶ reported that pro-

cedural morbidity and mortality rates were higher for ruptured than unruptured aneurysms. We cannot postulate as to why our results are different from these studies.

(Re-)Bleeding

The (re-)bleeding rates were low for both stented and nonstented aneurysms, which is in line with previous reports.^{40–43} None of the ruptured aneurysms that were treated with stent-assisted coiling rebled. However, no definitive conclusions can be drawn because of the small number of ruptured aneurysms that were treated with stents.

Study Limitations

Our study has the inherent limitations of a retrospective study. The duration of follow-up was shorter for stented aneurysms because most of the stents were implanted during the last 6 years. Moreover, the rate of aneurysms followed by angiography was lower.

CONCLUSIONS

The stent-assisted coiling technique was associated with a significant decrease in recurrences but a significant increase in complications. The treatment of wide-neck aneurysms remains more hazardous.

ACKNOWLEDGMENTS

We thank Thomas Spaety, Arthur Castagnac, and Laurence Salomon from the Department of Clinical Research (data statistical analysis) and Jenny Lloyd (English editing).

Disclosures: Michel Piotin—UNRELATED: Consultancy: Stryker,* Covidien*; Payment for Development of Educational Presentations: Stryker,* Covidien,* Microvention*; Travel/Accommodations/Meeting Expenses Unrelated to Activities Listed: NFocus.* Bruno Bartolini—UNRELATED: Consultancy: Covidien,* Stryker.* Silvia Pistocchi—UNRELATED: Consultancy: Covidien,* Stryker.* Raphaël Blanc—UNRELATED: Consultancy: Stryker,* Covidien* (*money paid to institution).

REFERENCES

1. Akpek S, Arat A, Morsi H, et al. **Self-expandable stent-assisted coiling of wide-necked intracranial aneurysms: a single-center experience.** *AJNR Am J Neuroradiol* 2005;26:1223–31
2. Alfke K, Straube T, Dorner L, et al. **Treatment of intracranial broad-neck aneurysms with a new self-expanding stent and coil embolization.** *AJNR Am J Neuroradiol* 2004;25:584–91
3. Fiorella D, Albuquerque FC, Deshmukh VR, et al. **Usefulness of the Neuroform stent for the treatment of cerebral aneurysms: results at initial (3–6-mo) follow-up.** *Neurosurgery* 2005;56:1191–202
4. Howington JU, Hanel RA, Harrigan MR, et al. **The Neuroform stent, the first microcatheter-delivered stent for use in the intracranial circulation.** *Neurosurgery* 2004;54:2–5
5. Lylyk P, Ferrario A, Pasbon B, et al. **Buenos Aires experience with the Neuroform self-expanding stent for the treatment of intracranial aneurysms.** *J Neurosurg* 2005;102:235–41
6. Wells-Roth D, Biondi A, Janardhan V, et al. **Endovascular procedures for treating wide-necked aneurysms.** *Neurosurg Focus* 2005;18:E7
7. Raymond J, Guilbert F, Weill A, et al. **Long-term angiographic recurrences after selective endovascular treatment of aneurysms with detachable coils.** *Stroke* 2003;34:1398–403
8. Biondi A, Janardhan V, Katz JM, et al. **Neuroform stent-assisted coil embolization of wide-neck intracranial aneurysms: strategies in stent deployment and midterm follow-up.** *Neurosurgery* 2007;61:460–69

9. Fargen KM, Hoh BL, Welch BG, et al. Long-term results of Enterprise stent-assisted coiling of cerebral aneurysms. *Neurosurgery* 2012;71:239–44
10. Lubicz B, Bandeira A, Bruneau M, et al. Stenting is improving and stabilizing anatomical results of coiled intracranial aneurysms. *Neuroradiology* 2009;51:419–25
11. Maldonado IL, Machi P, Costalat V, et al. Neuroform stent-assisted coiling of unruptured intracranial aneurysms: short- and midterm results from a single-center experience with 68 patients. *AJNR Am J Neuroradiol* 2011;32:131–36
12. Mocco J, Fargen KM, Albuquerque FC, et al. Delayed thrombosis or stenosis following Enterprise-assisted stent-coiling: is it safe? Mid-term results of the Interstate Collaboration of Enterprise Stent Coiling. *Neurosurgery* 2011;69:908–14
13. Yahia AM, Latorre JG, Gordon V, et al. Progressive occlusion of aneurysms in Neuroform stent-assisted treatment of intracranial aneurysms. *J Neurol Neurosurg Psychiatry* 2011;82:278–82
14. Sedat J, Chau Y, Mondot L, et al. Endovascular occlusion of intracranial wide-necked aneurysms with stenting (Neuroform) and coiling: mid-term and long-term results. *Neuroradiology* 2009;51:401–09
15. Fiorella D, Albuquerque FC, Woo H, et al. Neuroform stent assisted aneurysm treatment: evolving treatment strategies, complications and results of long term follow-up. *J Neurointerv Surg* 2010;2:16–22
16. Hope JK, Byrne JV, Molyneux AJ. Factors influencing successful angiographic occlusion of aneurysms treated by coil embolization. *AJNR Am J Neuroradiol* 1999;20:391–99
17. Murayama Y, Nien YL, Duckwiler G, et al. Guglielmi detachable coil embolization of cerebral aneurysms: 11 years' experience. *J Neurosurg* 2003;98:959–66
18. Ng P, Khangure MS, Phatouros CC, et al. Endovascular treatment of intracranial aneurysms with Guglielmi detachable coils: analysis of midterm angiographic and clinical outcomes. *Stroke* 2002;33:210–17
19. Nguyen TN, Hoh BL, Amin-Hanjani S, et al. Comparison of ruptured vs unruptured aneurysms in recanalization after coil embolization. *Surg Neurol* 2007;68:19–23
20. Tamatani S, Ito Y, Abe H, et al. Evaluation of the stability of aneurysms after embolization using detachable coils: correlation between stability of aneurysms and embolized volume of aneurysms. *AJNR Am J Neuroradiol* 2002;23:762–67
21. Campi A, Ramzi N, Molyneux AJ, et al. Retreatment of ruptured cerebral aneurysms in patients randomized by coiling or clipping in the International Subarachnoid Aneurysm Trial (ISAT). *Stroke* 2007;38:1538–44
22. Shapiro M, Babb J, Becske T, et al. Safety and efficacy of adjunctive balloon remodeling during endovascular treatment of intracranial aneurysms: a literature review. *AJNR Am J Neuroradiol* 2008;29:1777–81
23. Lawson MF, Newman WC, Chi YY, et al. Stent-associated flow remodeling causes further occlusion of incompletely coiled aneurysms. *Neurosurgery* 2011;69:598–604
24. Piotin M, Blanc R, Spelle L, et al. Stent-assisted coiling of intracranial aneurysms: clinical and angiographic results in 216 consecutive aneurysms. *Stroke* 2010;41:110–15
25. Hirabayashi M, Ohta M, Rufenacht DA, et al. Characterization of flow reduction properties in an aneurysm due to a stent. *Phys Rev E Stat Nonlin Soft Matter Phys* 2003;68:021918
26. Huang QH, Wu YF, Xu Y, et al. Vascular geometry change because of endovascular stent placement for anterior communicating artery aneurysms. *AJNR Am J Neuroradiol* 2011;32:1721–25
27. Lopes D, Sani S. Histological postmortem study of an internal carotid artery aneurysm treated with the Neuroform stent. *Neurosurgery* 2005;56:E416
28. Henkes H, Fischer S, Weber W, et al. Endovascular coil occlusion of 1811 intracranial aneurysms: early angiographic and clinical results. *Neurosurgery* 2004;54:268–85
29. Naggara ON, White PM, Guilbert F, et al. Endovascular treatment of intracranial unruptured aneurysms: systematic review and meta-analysis of the literature on safety and efficacy. *Radiology* 2010;256:887–97
30. van Rooij WJ, Sluzewski M, Beute GN, et al. Procedural complications of coiling of ruptured intracranial aneurysms: incidence and risk factors in a consecutive series of 681 patients. *AJNR Am J Neuroradiol* 2006;27:1498–501
31. Wiebers DO, Whisnant JP, Huston J 3rd, et al. Unruptured intracranial aneurysms: natural history, clinical outcome, and risks of surgical and endovascular treatment. *Lancet* 2003;362:103–10
32. Fiorella D, Albuquerque FC, Han P, et al. Preliminary experience using the Neuroform stent for the treatment of cerebral aneurysms. *Neurosurgery* 2004;54:6–17
33. Pierot L, Spelle L, Vitry F, ATENA Investigators. Immediate clinical outcome of patients harboring unruptured intracranial aneurysms treated by endovascular approach: results of the ATENA study. *Stroke* 2008;39:2497–504
34. White PM, Lewis SC, Nahser H, et al. Hydrocoil endovascular aneurysm occlusion and packing study (HELPS trial): procedural safety and operator-assessed efficacy results. *AJNR Am J Neuroradiol* 2008;29:217–23
35. Pierot L, Cognard C, Anxionnat R, et al. CLARITY Investigators. Ruptured intracranial aneurysms: factors affecting the rate and outcome of endovascular treatment complications in a series of 782 patients (CLARITY study). *Radiology* 2010;256:916–23
36. Park HK, Horowitz M, Jungreis C, et al. Periprocedural morbidity and mortality associated with endovascular treatment of intracranial aneurysms. *AJNR Am J Neuroradiol* 2005;26:506–14
37. Sluzewski M, van Rooij WJ, Beute GN, et al. Balloon-assisted coil embolization of intracranial aneurysms: incidence, complications, and angiography results. *J Neurosurg* 2006;105:396–99
38. Ishibashi T, Murayama Y, Saguchi T, et al. Thromboembolic events during endovascular coil embolization of cerebral aneurysms. *Interv Neuroradiol* 2006;12:112–16
39. Ross IB, Dhillon GS. Complications of endovascular treatment of cerebral aneurysms. *Surg Neurol* 2005;64:12–19
40. Cho YD, Lee JY, Seo JH, et al. Early recurrent hemorrhage after coil embolization in ruptured intracranial aneurysms. *Neuroradiology* 2012;54:719–26
41. Ferns SP, Majoie CB, Sluzewski M, et al. Late adverse events in coiled ruptured aneurysms with incomplete occlusion at 6-month angiographic follow-up. *AJNR Am J Neuroradiol* 2010;31:464–69
42. Lanterna LA, Tredici G, Dimitrov BD, et al. Treatment of unruptured cerebral aneurysms by embolization with Guglielmi detachable coils: case-fatality, morbidity, and effectiveness in preventing bleeding: a systematic review of the literature. *Neurosurgery* 2004;55:767–78
43. Molyneux AJ, Kerr RS, Birks J, et al. Risk of recurrent subarachnoid haemorrhage, death, or dependence and standardised mortality ratios after clipping or coiling of an intracranial aneurysm in the International Subarachnoid Aneurysm Trial (ISAT): long-term follow-up. *Lancet Neurol* 2009;8:427–43

Hyperattenuated Intracerebral Lesions after Mechanical Recanalization in Acute Stroke

N. Lummel, G. Schulte-Altedorneburg, C. Bernau, T. Pfefferkorn, M. Patzig, H. Janssen, C. Opherk, H. Brückmann, and J. Linn



ABSTRACT

BACKGROUND AND PURPOSE: Following mechanical recanalization of an acute intracranial vessel occlusion, hyperattenuated lesions are frequently found on postinterventional cranial CT. They represent either blood or—more frequently—enhancement of contrast agent. Here, we aimed to evaluate the prognostic value of these hyperattenuated intracerebral lesions.

MATERIALS AND METHODS: One hundred one consecutive patients with acute stroke in the anterior circulation who underwent mechanical recanalization were included. Risk factors for hyperattenuated intracerebral lesions were assessed, and lesion volume was compared with the volume of final infarction. Clinical outcome and relative risk of secondary hemorrhage were determined in patients with and without any hyperattenuated lesions and compared.

RESULTS: The frequency of hyperattenuated lesions was 84.2%. Risk factors for hyperattenuated lesions were female sex, higher NIHSS score on admission, and higher amount of contrast agent applied. On follow-up, 3 patients showed no infarction; 53 patients, an ischemic infarction; and 45 patients, a hemorrhagic infarction. In all except 1 case, final volume of infarction (median = 92.4 mL) exceeded the volume of hyperattenuated intracerebral lesions (median = 5.6 mL). Patients with hyperattenuated lesions were at a 4 times higher relative risk for hemorrhagic transformation but had no significantly worse clinical outcome.

CONCLUSIONS: Our data show that the extent of postinterventional hyperattenuated intracerebral lesions underestimates the volume of final infarction. Although hyperattenuated lesions indicate a higher risk of secondary hemorrhagic transformation, their presence seems not to be of any prognostic value regarding clinical outcome.

ABBREVIATIONS: CCT = cranial CT; ECASS = European Cooperative Acute Stroke Study; HI = hemorrhagic infarction; IQR = interquartile range; PH = parenchymal hemorrhage

Hyperattenuated intracerebral lesions are a frequent finding on postinterventional cranial CT following intra-arterial reperfusion therapy in acute ischemic stroke.¹⁻⁵ These hyperattenuated lesions have been documented and described since the 1990s. It has been suggested that hyperattenuated lesions persisting longer than 24 hours correlate with hemorrhagic lesions, whereas hyperattenuated intracerebral lesions that are no longer discernible on the 24-hour follow-up examination correspond to

contrast enhancement.^{6,7} The presence of hyperattenuated intracerebral lesions was considered a risk factor for secondary hemorrhage accompanied by deterioration of neurologic symptoms.³⁻⁵ However, hyperattenuated lesions do not always indicate hemorrhage, and rapid clearance of the contrast medium on postinterventional cranial CT (CCT) has been reported to be a good prognostic sign.^{1,6} A recent small study found no increased risk of symptomatic hemorrhage or negative clinical prognosis in patients with hyperattenuated intracerebral lesions compared with those without.⁸ On the other hand, Costalat et al⁹ recently reported that hyperattenuated intracerebral lesions on postinterventional CCT were significantly associated with poorer clinical outcome. To our knowledge, larger studies on the prognostic value of hyperattenuated intracerebral lesions are lacking to date.

Thus, the aim of this study was to further evaluate the prevalence of hyperattenuated lesions following mechanical recanalization of acute vessel occlusions in the anterior circulation, to identify risk factors for their occurrence, and to assess their prognostic value.

Received March 5, 2013; accepted after revision April 30.

From the Departments of Neuroradiology (N.L., M.P., H.J., H.B., J.L.) and Neurology (T.P., C.O.), and Institute for Stroke and Dementia Research (C.O.), Klinikum Grosshadern, Ludwig-Maximilian-University, Munich, Germany; Institute of Radiology, Neuroradiology, and Nuclear Medicine (G.S.-A.), Klinikum Harlaching, Munich, Germany; and Institute for Medical Information Sciences, Biometry, and Epidemiology (C.B.), Ludwig-Maximilian-University, Munich, Germany.

Please address correspondence to Nina Lummel, MD, Department of Neuroradiology, Ludwig-Maximilian-University Marchioninstr 15, 81377 Munich, Germany; e-mail: nina.lummel@med.uni-muenchen.de

Indicates article with supplemental on-line appendix and tables.

<http://dx.doi.org/10.3174/ajnr.A3656>

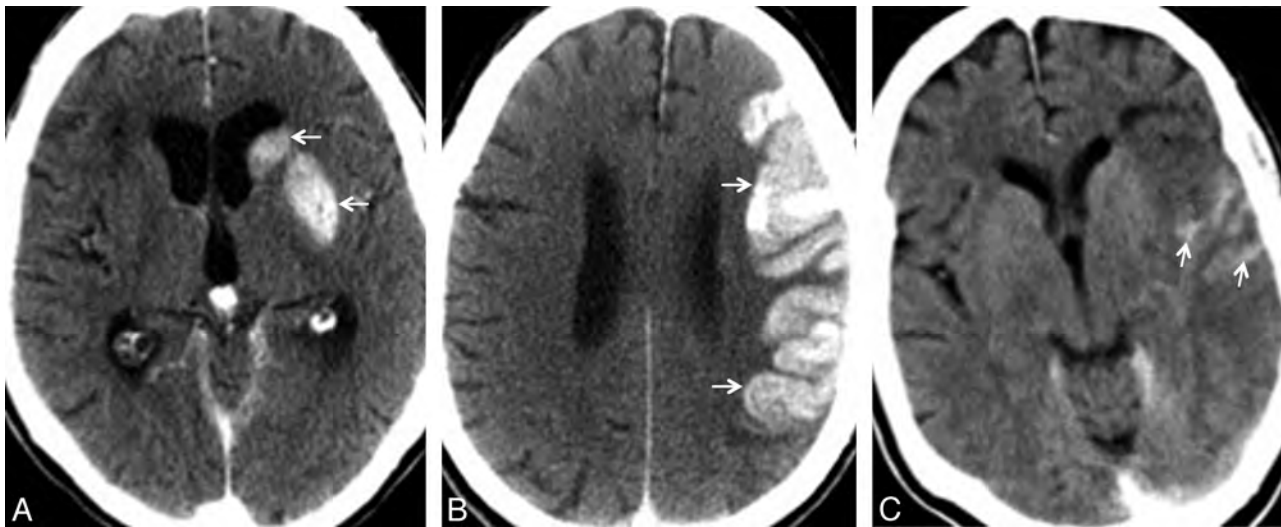


FIG 1. Postinterventional CCT of 3 different patients with hyperattenuated lesions in the basal ganglia (A, arrows), cortex (B, arrows), and cortical sulci (C, arrows).

MATERIALS AND METHODS

The study was approved by our institutional review committee, and subjects or relatives gave their informed consent.

Study Population

All patients with acute stroke who were treated by endovascular mechanical recanalization between February 2007 and February 2012 were identified retrospectively from our in-hospital data base of angiographic records. Details on patient selection for endovascular stroke treatment are given in the On-line Appendix.

Patients were included in the analysis if they fulfilled the following additional inclusion criteria:

- Availability of an initial, complete CT stroke protocol including CCT, CTA, and CTP of evaluable diagnostic quality
- Occlusion of a large intracranial artery of the anterior circulation (common trunk of the MCA or intracranial segment of the ICA)
- Endovascular mechanical recanalization by retriever, suction devices, and/or temporary stent performed
- Availability of a postinterventional CCT performed immediately after endovascular treatment to assess the prevalence of hyperattenuated lesions
- Existence of follow-up CT performed 24 ± 12 hours after treatment (follow-up 1), to distinguish contrast enhancement versus hemorrhagic lesions as detailed below
- Availability of follow-up imaging (MR imaging if available, otherwise CCT) performed >48 hours after treatment (follow-up 2), to determine the final volume of the infarction and to assess secondary hemorrhage
- Periprocedural and clinical parameters were derived from the peri-interventional protocol and the clinical records as detailed in the On-line Appendix. The patient's clinical state on admission was rated by using the NIHSS, and clinical outcome was measured in terms of the mRS 90 days after the event. An mRS of 0–3 was defined as good, and an mRS of 4 or 5 and death were considered poor outcomes.¹⁰

Image Analysis

Image analyses were performed by 2 experienced neuroradiologists in consensus. For details on imaging parameters and image analysis see the On-line Appendix. Briefly, pretherapeutic noncontrast CCT and CT perfusion were analyzed for the presence of early signs of ischemia, according to the ASPECTS; and CT angiography was analyzed for the presence and site of the intracranial vessel occlusion. The presence and topographic distribution of hyperattenuated lesions were determined on the postinterventional CCTs (Fig 1). Hyperattenuated lesions that were no longer discernible on the 24-hour follow-up examination were defined as contrast enhancement; hyperattenuated lesions that persisted on follow-up 1 were considered hemorrhagic lesions.⁶

Final stroke lesion volume and type were determined on follow-up 2 scans on the basis of the ASPECTS, also used for MR imaging,¹¹ and by manual volume measurements as described in the On-line Appendix.

Statistical Analysis

Univariate comparisons between the 2 groups were performed by using the Fisher exact test (categorical variables) and the Mann-Whitney *U* test (continuous variables). For univariate comparison of continuous variables among >2 groups, the Kruskal-Wallis rank sum test was applied. To evaluate risk factors for the incidence of hyperattenuated lesions, we performed logistic regression analyses. The Fisher exact test, ORs, and 95% CIs were determined to evaluate the association of hyperattenuated lesions with the risk of hemorrhagic transformation within the first 3 weeks. Logistic regression analyses with Akaike information criterion-based stepwise variable selection were used to evaluate whether different clinical and/or imaging factors were associated with clinical outcome. The clinical and periprocedural parameters that were tested are detailed in the On-line Appendix. We chose a value of $P = .05$ as a level of statistical significance.

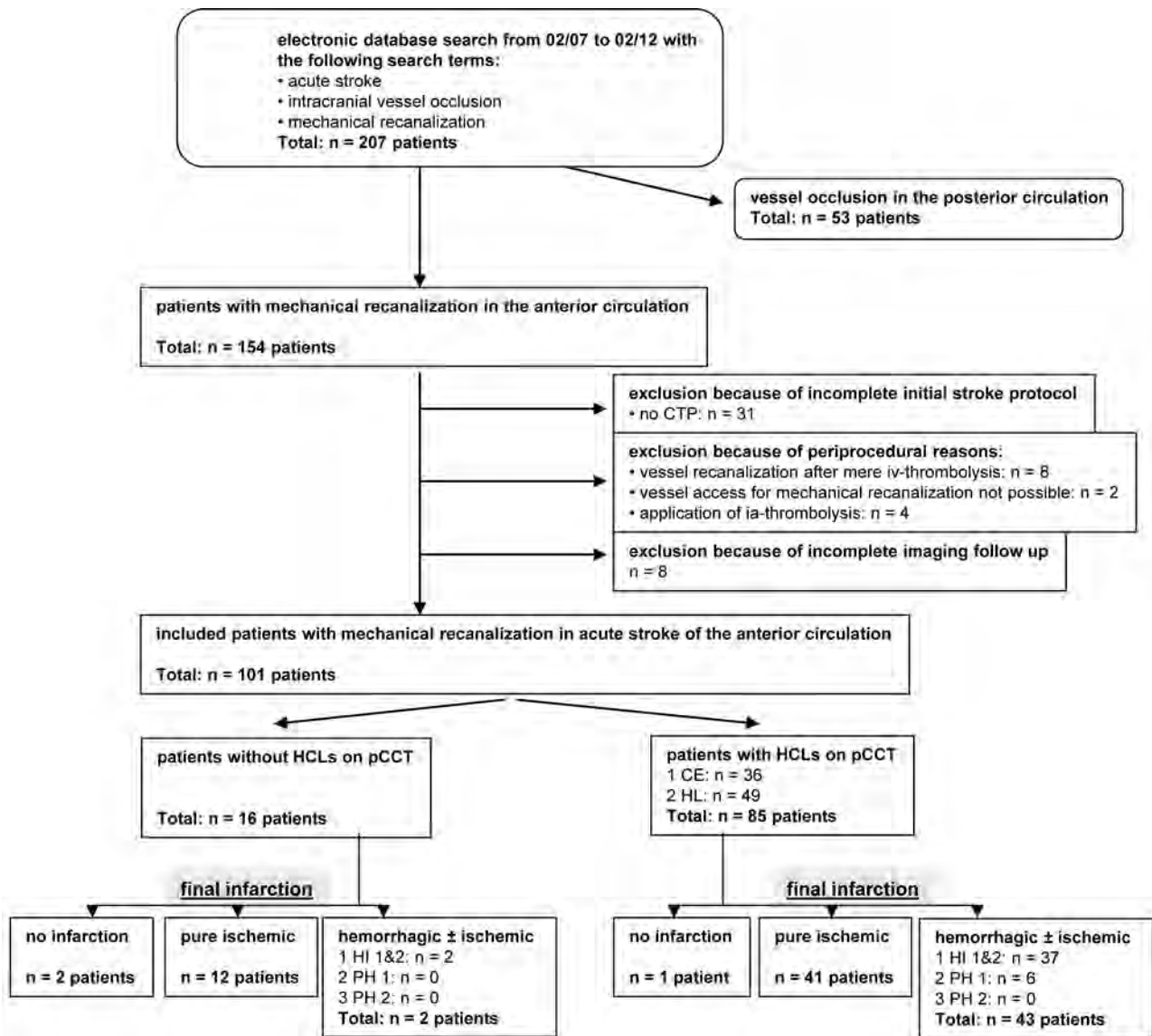


FIG 2. Flow diagram of patient identification and imaging findings. HCLs indicate hyperattenuating intracerebral lesions; pCCT, postinterventional cranial CT; CE, contrast enhancement; HT, hemorrhagic transformation.

RESULTS

One hundred one patients (63 women; median age, 71 years; range, 30–98 years) matched the inclusion criteria and were enrolled in this study (Fig 2). Demographic and clinical patient data, pretherapeutic imaging findings, and treatment details are summarized in Table 1 and On-line Tables 1 and 2.

The overall prevalence of hyperattenuated lesions on postinterventional CCT was 84.2%. Median mean attenuation was 52 HU (interquartile range [IQR], 15 HU) and median maximum attenuation was 94 HU (IQR = 61 HU) (Table 2). The basal ganglia were involved in 72.3%. In 36 cases (35.6%), hyperattenuated intracerebral lesions resolved on follow-up 1, which was performed at a median interval of 17 hours after the postinterventional CCT, and were, therefore, interpreted as contrast enhancement, while hyperattenuated lesions persisted on follow-up 1 in 49 cases (48.5%) and were thus interpreted as hemorrhagic lesions.

In univariate analysis, higher NIHSS scores on admission,

larger amount of contrast agent applied, and longer duration of mechanical recanalization were significantly associated with hyperattenuated lesions (On-line Table 3). There was a tendency for hyperattenuated lesions to be more frequently observed in patients who had not received IV thrombolysis, compared with those with IV thrombolysis ($P = .06$); however, the difference was not statistically significant. The amount of IV thrombolysis showed no significant influence on the occurrence of hyperattenuated lesions ($P = .41$). For details on clinical, imaging, and therapy-related differences between patients with and without hyperattenuated lesions, see On-line Table 3.

The multivariate analysis primarily confirmed results of the univariate analyses. In the multivariate analysis, sex, NIHSS score on admission, and amount of contrast agent applied emerged as relevant influential factors on the occurrence of hyperattenuated lesions, whereby female sex (OR, 5.13; 95% CI, 1.34–19.52), higher NIHSS value (OR, 1.22; 95% CI, 1.02–1.46), and a higher

Table 1: Demographic and clinical characteristics of the study population (N = 101 patients)

	No. ^a	No. (%)	Median	IQR
Age (yr)	101		71	21.5
Sex	101			
Men		38 (37.6%)		
Women		63 (62.4%)		
NIHSS score on admission	98		15	6
No. of CVRFs	81		1	1
Etiology of stroke	101			
TOAST 1		17 (16.8%)		
TOAST 2		63 (62.4%)		
TOAST 3		5 (5%)		
TOAST 4		16 (15.8%)		
Clinical outcome	98		4	2
Good (mRS 0–3)			34 (33.7%)	
mRS 0			5 (5%)	
mRS 1			5 (5%)	
mRS 2			13 (12.9%)	
mRS 3			11 (10.9%)	
Poor (mRS 4–6)			64 (63.4%)	
mRS 4			39 (38.6%)	
mRS 5			14 (13.9%)	
mRS 6			11 (10.9%)	

Note:—CVRF indicates cardiovascular risk factors; Trial of Org 10172 in Acute Stroke Treatment (TOAST) 1, large-artery atherosclerosis; 2, cardioemboly; 3, dissection; 4, unknown etiology.

^aNo. indicates number in which the parameter was available in this retrospective study.

Table 2: Characteristics of hyperattenuated intracerebral lesions regarding Hounsfield units in patients with contrast enhancement versus hemorrhagic lesions on follow-up 1 and patients with final ischemic-versus-hemorrhagic infarction, respectively

	No.	HU Mean			HU Maximum		
		Median	IQR	P Value	Median	IQR	P Value
HCL on pCCT ^a	75	52	15		94	61	
Follow-up 1	75						
CE	29	45	4		72	19.5	
HL	46	58	13.5	<.001	113	59.5	<.001
Final infarction	74 ^b						
Ischemic	35	46	7		80	27	
Hemorrhagic	39	58	11	<.001	109	68	<.001

Note:—HCL indicates hyperattenuated intracerebral lesion; CE, contrast enhancement; HL, hemorrhagic lesion; pCCT, postinterventional cranial CT.

^aAll patients with hyperattenuated intracerebral lesions in the basal ganglia and cortex; patients with pure sulcal hyperattenuating lesions (*n* = 10) are excluded in this calculation because Hounsfield unit values were not evaluated in these patients.

^bOne case with hyperattenuated lesions on postinterventional CCT had no infarction on follow-up 2 and was therefore excluded.

amount of contrast agent (OR, 1.0; 95% CI, 1.0–1.01) led to a higher risk of hyperattenuated lesions (*P* overall = .001).

The median time between follow-ups 1 and 2 was 4 days. MR imaging was available as follow-up 2 in 54 patients. Except for 1 patient, final volume of infarction (median, 92.4 mL; IQR, 177.7 mL) consistently exceeded the volume of hyperattenuated intracerebral lesions (median, 5.6 mL; IQR, 16.2 mL). Of the 36 patients with contrast enhancement on follow-up 1, one patient showed no infarction on follow-up 2, thirty-one patients developed pure ischemic lesions, and 4 cases demonstrated secondary hemorrhagic transformation (HI) (HI1/2 [see On-line Appendix], no parenchymal hemorrhage [PH]1/2). Of the 49 patients with hemorrhagic lesions on follow-up 1, final lesions were pure ischemic in 10 cases and hemorrhagic in 39 cases (HI1/2, *n* = 33;

PH1, *n* = 6; PH2, *n* = 0). In 2 of the hemorrhagic lesion cases with small hematomas on follow-up 2, localization of the bleeding did not accord with localization of hyperattenuated lesions on postinterventional CCT (Fig 3). Patients without any hyperattenuated lesions (*n* = 16) showed no infarction on follow-up 2 in 2 cases, a pure ischemic stroke in 12 cases, and a secondary hemorrhagic transformation in 2 cases (all HI1/2, no PH1/2).

In the univariate analysis, the following factors were significantly associated with poor clinical outcome: older age, higher NIHSS scores on admission, lower ASPECTS on the initial CCT, low degree of mismatch on CTP, longer time between initial CCT and start of the intervention, and unsuccessful recanalization (TICI 0, 1, or 2a) (On-line Table 4).

The multivariate analysis primarily confirmed results of the univariate analyses. In the multivariate analysis, age, NIHSS score on admission, ASPECTS on the initial CCT, degree of mismatch on CTP, and recanalization result emerged as important influential factors on the clinical outcome, whereby older age (OR, 1.07; 95% CI, 1.02–1.12), higher NIHSS values (OR, 1.20; 95% CI, 1.02–1.40), lower ASPECTS values (OR, 0.77; 95% CI, 0.58–1.02), lower degree of mismatch (OR, 0.78; 95% CI, 0.61–1.00), and unsuccessful recanalization (OR, 0.02; 95% CI, 0.00–0.31) led to a higher risk of poor clinical outcome (*P* overall = 1.5×10^{-8}).

DISCUSSION

Hyperattenuated intracerebral lesions are a common finding on CCT following mechanical recanalization in ischemic stroke. Our data show that female sex, a poor clinical condition on admission, and a high amount of contrast agent applied during mechanical thrombectomy correlate with their occurrence. Concerning their prognostic value, we found hyperattenuated lesions significantly more often associated with hemorrhagic transformation of the infarction. However, hyperattenuated lesions seem to be no predictor of poor clinical outcome.

In the 1990s, Wildenhain et al¹ and Komiyama et al² were among the first to document the occurrence of high-attenuation lesions on CT scans immediately after intra-arterial thrombolysis in acute stroke. Currently, hyperattenuated intracerebral lesions on postinterventional CCT are considered a common finding, not only following intra-arterial thrombolysis but also after mechanical thrombectomy.

Compared with previous studies, the incidence of hyperattenuated lesions on postinterventional CCT was fairly high in this study (84% versus 25%–78%^{1,6,8,9,12,13}). However, most earlier studies^{1,6,12,13} evaluated hyperattenuated lesions after IA thrombolysis, while data on hyperattenuated lesions following mechanical recanalization is sparse. In studies with a comparable patient collective, hyperattenuated intracerebral lesions on postinterventional CCT were found in 40% and 54% of cases, respectively,^{8,9} though other factors like a different number of patients, different mechanical retrievers, revascularization rate, and anticoagulation therapy may additionally influence the incidence of hyperattenuated intracerebral lesions. Compared with Parrilla et al,⁸ the percentage of patients who received IV thrombolysis before mechanical recanalization was indeed higher in our collective (46.7%

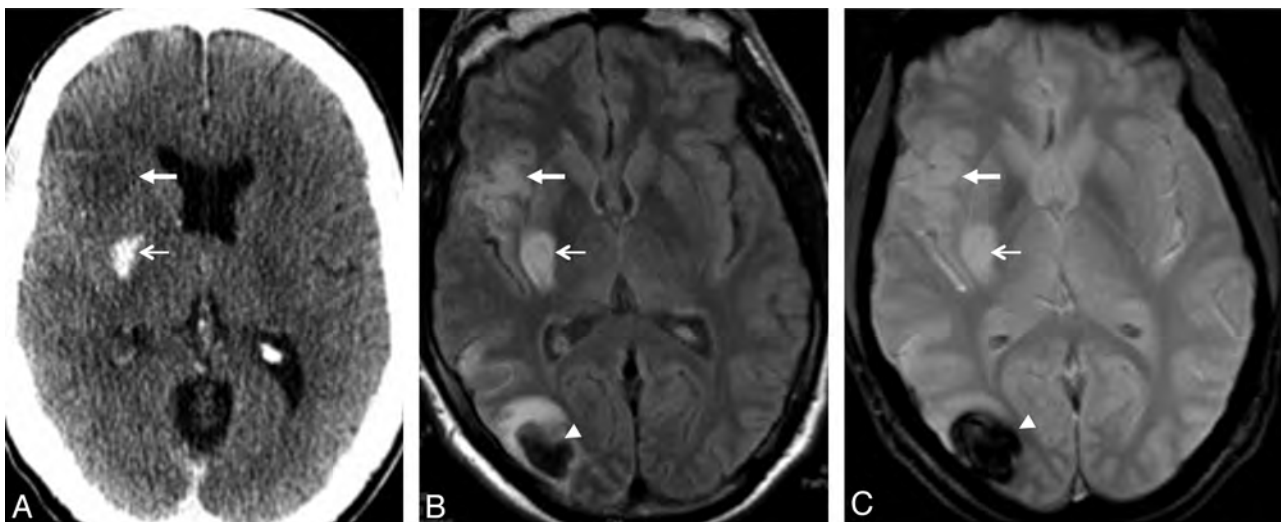


FIG 3. A 47-year-old man with acute occlusion of the right MCA and mechanical recanalization. Postinterventional CCT (A) shows a hyperattenuated intracerebral lesion in the right putamen (*thin arrow*) and early signs of ischemic infarction in the right anterior insula (*thick arrow*). MR imaging (FLAIR in B, and T2* in C) 2 days following the event shows pure ischemic infarction in both localizations (right putamen and anterior insula; *thin* and *thick arrows* in B and C). Furthermore, MR imaging shows an intracerebral hematoma (PHI) in the right parieto-occipital lobe (*arrowheads* on B and C), where no hyperattenuated lesion was evident on postinterventional CCT. Clinical outcome of this patient was good (mRS 1).

versus 73.3%); however, IV lysis was not found to be a risk factor for the occurrence of hyperattenuated lesions.

Hyperattenuated intracerebral lesions do not represent a homogeneous kind of underlying parenchymal change but can reflect different pathologic changes. They correspond either to a primary or secondary parenchymal hemorrhage or to enhancement of contrast medium or a mixture of both. Unfortunately, there is no widely accepted definition for differentiating these phenomena. Referring to Yoon et al (2004),⁴ we distinguished 2 types of hyperattenuated lesions: 1) Hyperattenuated lesions resolving on follow-up 1 were classified as contrast enhancement, identical to those in Yoon et al; 2) hyperattenuated lesions persisting on follow-up 1 were categorized as hemorrhagic lesions in this study. We deliberately used a term different from that of Yoon et al, who classified these lesions as contrast extravasation, to stress that it is not only contrast material but also blood crossing the blood-brain barrier. Using this definition, we found contrast enhancement in 35.6% of patients and hemorrhagic lesions in 48.5% of cases.

In accordance with previous studies, we found the basal ganglia most frequently involved with hyperattenuated intracerebral lesions.^{3,4,6,13} This might be related to the increased vulnerability of the lenticulostriate arteries to ischemia. However, further pathomechanisms seem to be involved in the occurrence of hyperattenuated intracerebral lesions. Regarding the differentiation between contrast enhancement and hemorrhagic lesion, the most widely accepted hypothesis assumes that contrast enhancement is caused by leakage of contrast medium from vessels into the extracellular spaces because of increased permeability of the BBB. On the other hand, hemorrhagic lesions are supposed to be caused by the potential contrast toxicity, which leads to degradation of the basal lamina, associated with disruption of the BBB, and results in cellular blood element extravasation from microvessels.¹⁴ Intravascular injection of iodinated contrast media, especially superselective infusion directly into the site of acute ischemic damage, has been identified as a risk factor for disruption of the BBB.¹³⁻¹⁵

Postulates for the mechanism of contrast neurotoxicity include hyperosmolality, increased pinocytosis, and inherent chemotoxicity of the contrast agents.¹⁴ Additionally, pressure transmission from injections may contribute to BBB disruption and thus contrast extravasation. In our population, the amount of contrast agent applied during mechanical recanalization showed significant influence on the occurrence of hyperattenuated lesions on postinterventional CCT. Furthermore, *in vitro* studies indicate that the type of contrast media applied has an influence on the occurrence and extent of intracerebral hemorrhage.¹⁶ However, our study cannot give further evidence in this regard, because low-osmolar, nonionic contrast was used consistently. Here, additional evaluation is needed.

Furthermore, it might be anticipated that administration of thrombolysis influences the risk of BBB damage. Thrombolytic agents themselves could provoke injury to the microvascular permeability barrier, and exogenous plasminogen activators might accelerate dissolution of the BBB, microvascular basal lamina, and platelet-fibrin plugs, thereby increasing edema formation and the risk of hemorrhage.¹⁷ In this context, the type of administration of thrombolysis seems to play an important role. IA thrombolysis with direct administration of thrombolytics into the core of the infarct has been linked to a higher risk of hemorrhage compared with IV thrombolysis.¹⁸⁻²⁰ In the present study, patients were included only if thrombolysis was given intravenously, and all patients with mere or additional intra-arterial thrombolysis were excluded. Hence, we found no significant association between hyperattenuated intracerebral lesions and IV thrombolysis, in accordance with former investigations.⁸ Neither the application of IV thrombolysis nor the amount of thrombolysis given showed a significant influence on the occurrence of hyperattenuated lesions on postinterventional CCT. Furthermore, other factors with conceivable impact on the occurrence of hyperattenuated intracerebral lesions, like cardiovascular risk factors, ASPECTS on initial CCT, type of retriever, recanalization success,

or different time factors, showed no significant association. Only regarding the NIHSS score on admission did our data deviate from those of Parrilla et al (2012).⁸ In our series, patients who presented with major neurologic deficits were more prone to develop hyperattenuated lesions following recanalization.

In summary, our multivariate analysis highlights the following 3 factors as significant predictors for the occurrence of hyperattenuated lesions: 1) sex, 2) clinical condition on admission (NIHSS score), and 3) the amount of contrast agent applied during mechanical recanalization.

Prognostic Value of Hyperattenuated Intracerebral Lesions

Besides imaging characteristics and etiologic factors of hyperattenuated lesions on postinterventional CCT, their prognostic value was a major objective of this study. Some investigators suggested that hyperattenuated intracerebral lesions are highly associated with the formation of severe hemorrhagic transformation and/or parenchymal hematoma with neurologic deterioration and should thus be considered as a negative prognostic predictor for the procedure.^{3,4,13} In our population also, patients with hyperattenuated lesions demonstrated a clearly higher risk of developing a hemorrhagic infarction compared with patients without hyperattenuated lesions. In patients with hyperattenuated lesions on postinterventional CCT, a hematoma of $\leq 30\%$ of the infarcted area with some mild space-occupying effect (PH1) was evident in 5.9% ($n = 6$) of patients, in whom hemorrhage did not occur in the same localization as hyperattenuated lesions in 2 cases. Despite the increased risk for hemorrhagic transformation in patients with hyperattenuated lesions on postinterventional CCT, we, as well as Parrilla et al (2012),⁸ found no statistically significant influence of hyperattenuated intracerebral lesions on the clinical outcome. Accordingly, the post hoc analysis of the data of the European Cooperative Acute Stroke Study (ECASS) II trial identified only intracerebral hematomas in $>30\%$ of the infarcted area with significant space-occupying effect (PH2) but not hemorrhagic transformation (HI1/2) or PH1 to be significantly associated with clinical deterioration and impaired prognosis.²¹ Even when we considered patients with contrast enhancement separately from patients with hemorrhagic lesions, there was no significant difference regarding clinical outcome in our collective, contrary to Yoon et al (2004),⁴ who suggested that extravasation (like our hemorrhagic lesion) portended poorer outcome than did enhancement.

Generally, occlusion of a proximal intracranial vessel is a serious disease, and our patient collective was severely clinically affected, with a high risk of persisting neurologic deficits (total median NIHSS score on admission = 15 [IQR = 6], total median mRS 90 days after the event = 4 [IQR = 2]). For this reason mRS = 3 was still considered a good outcome when dichotomizing the scale.¹⁰

Among factors for good clinical outcome, time from onset of symptoms to recanalization is considered one of the key factors, with an increasing time span to recanalization decreasing the chances of success for the rescue of tissue at risk.²² In our investigation, various time factors were assessed but, as shown in previous investigations, did not show a statistically significant influ-

ence on clinical outcome.⁹ Only a short time between initial CCT and beginning of the procedure of mechanical thrombectomy was associated with better clinical outcome in the univariate analysis, but it did not sustain multivariate testing. These results emphasize that time alone might not be as essential as suggested because other, more elusive factors, like collateralization, considerably determine the evolution of cerebral infarction.²³

Our data agree with those in previous studies assigning significant influence on clinical outcome to the extent of mismatch in the initial CTP and recanalization success.²³ Furthermore, we likewise found that age seems to play a critical role, implicating that younger patients with stroke might benefit even more from interventional stroke therapy.²³ In our collective, a more favorable outcome was comprehensively evident in patients with lower NIHSS scores⁹ and higher ASPECTS on admission.

In the multivariate analysis, the following 5 factors emerged as significant predictors for clinical outcome after mechanical recanalization of an acute intracranial vessel occlusion in the anterior circulation: 1) age, 2) clinical condition on admission (NIHSS score), 3) extent of early stroke signs (ASPECTS) on the initial CCT, 4) mismatch in initial CTP, and 5) recanalization success of the cerebral artery (TICI).

Limitations

In general, the retrospective design is the major limitation of this study. Due to this approach, only the beginning of the procedure of mechanical thrombectomy, instead of the exact time of recanalization, could be validly ascertained. In addition, time factors were unknown in almost half of the patients, mainly in so-called “wake-up-strokes” or in single patients who were transferred from other hospitals where IV thrombolysis was applied without documentation of time. Another drawback of the current study is the image-based estimation of hemorrhagic transformation without histopathologic correlation. Further experimental and pathologic studies are needed regarding changes in the cerebral microvascular barriers in stroke and mechanical recanalization to clarify underlying mechanisms of hyperattenuated intracerebral lesions, particularly with respect to the differentiation between contrast enhancement and hemorrhagic lesions. Potentially, by using dual-energy CT, accurately differentiating between intracranial hemorrhage and iodinated contrast medium staining might be feasible,²⁴ but currently this technology is not generally available. Furthermore, the lack of detailed information about prior and further anticoagulation therapy is another limitation of this study. An influence of this medication on the occurrence of hyperattenuated lesions and/or hemorrhage might be conceivable, but it was not an objective of this study. Further prospective work is needed regarding this issue.

CONCLUSIONS

In summary, our data show that hyperattenuated intracerebral lesions frequently occur on CCT following mechanical thrombectomy in acute stroke of the anterior circulation. The extent of these lesions underestimates the volume of final infarction; hence, it is of limited predictive value. In our series, hyperattenuated lesions were associated with a higher risk of hemorrhagic transformation, which might be consequential for the postinterven-

tional drug management, and need to be evaluated circumstantially in large, prospective studies. However, hyperattenuated lesions cannot be used to forecast negative clinical outcomes.

Disclosures: Christian Opherk—UNRELATED: Board Membership: Boehringer-Ingelheim, Bristol-Myers-Squibb, Payment for Lectures (including service on Speakers Bureaus): Boehringer-Ingelheim, Bristol-Myers-Squibb, Bayer, Merck & Co.

REFERENCES

1. Wildenhain SL, Jungreis CA, Barr J, et al. **CT after intracranial intraarterial thrombolysis for acute stroke.** *AJNR Am J Neuroradiol* 1994;15:487–92
2. Komiya M, Nishijima Y, Nishio A, et al. **Extravasation of contrast medium from the lenticulostriate artery following local intracarotid fibrinolysis.** *Surg Neurol* 1993;39:315–19
3. Nakano S, Iseda T, Kawano H, et al. **Parenchymal hyperdensity on computed tomography after intra-arterial reperfusion therapy for acute middle cerebral artery occlusion: incidence and clinical significance.** *Stroke* 2001;32:2042–48
4. Yoon W, Seo JJ, Kim JK, et al. **Contrast enhancement and contrast extravasation on computed tomography after intra-arterial thrombolysis in patients with acute ischemic stroke.** *Stroke* 2004;35:876–81
5. Jang YM, Lee DH, Kim HS, et al. **The fate of high-density lesions on the non-contrast CT obtained immediately after intra-arterial thrombolysis in ischemic stroke patients.** *Korean J Radiol* 2006;7:221–28
6. Mericle RA, Lopes DK, Fronckowiak MD, et al. **A grading scale to predict outcomes after intra-arterial thrombolysis for stroke complicated by contrast extravasation.** *Neurosurgery* 2000;46:1307–14, discussion 1314–15
7. Yoon W, Seo JJ, Kang HK. **Bilateral paramedian thalamic contrast enhancement on CT after intra-arterial thrombolysis.** *Korean J Radiol* 2005;6:41–43
8. Parrilla G, Garcia-Villalba B, Espinosa de Rueda M, et al. **Hemorrhage/contrast staining areas after mechanical intra-arterial thrombectomy in acute ischemic stroke: imaging findings and clinical significance.** *AJNR Am J Neuroradiol* 2012;33:1791–96
9. Costalat V, Lobotesis K, Machi P, et al. **Prognostic factors related to clinical outcome following thrombectomy in ischemic stroke (RECOAST Study): 50 patients prospective study.** *Eur J Radiol* 2012;81:4075–82
10. Rittenberger JC, Raina K, Holm MB, et al. **Association between Cerebral Performance Category, Modified Rankin Scale, and discharge disposition after cardiac arrest.** *Resuscitation* 2011;82:1036–40
11. Singer OC, Kurre W, Humpich MC, et al. **Risk assessment of symptomatic intracerebral hemorrhage after thrombolysis using DWI-ASPECTS.** *Stroke* 2009;40:2743–48
12. Urbach H, Bendszus M, Brechtelsbauer D, et al. **Extravasation of contrast medium in local intra-arterial fibrinolysis of the carotid territory [In German].** *Nervenarzt* 1998;69:490–94
13. Yokogami K, Nakano S, Ohta H, et al. **Prediction of hemorrhagic complications after thrombolytic therapy for middle cerebral artery occlusion: value of pre- and post-therapeutic computed tomographic findings and angiographic occlusive site.** *Neurosurgery* 1996;39:1102–07
14. Khatri R, Khatri P, Khoury J, et al. **Microcatheter contrast injections during intra-arterial thrombolysis increase intracranial hemorrhage risk.** *J Neurointerv Surg* 2010;2:115–19
15. Khatri P, Broderick JP, Khoury JC, et al. **Microcatheter contrast injections during intra-arterial thrombolysis may increase intracranial hemorrhage risk.** *Stroke* 2008;39:3283–87
16. Kurosawa Y, Lu A, Khatrri P, et al. **Intra-arterial iodinated radiographic contrast material injection administration in a rat middle cerebral artery occlusion and reperfusion model: possible effects on intracerebral hemorrhage.** *Stroke* 2010;41:1013–17
17. Rudd MA, Johnstone MT, Rabbani LE, et al. **Thrombolytic therapy causes an increase in vascular permeability that is reversed by 1-deamino-8-D-vasopressin.** *Circulation* 1991;84:2568–73
18. Wahlgren N, Ahmed N, Dávalos A, et al. **Thrombolysis with alteplase for acute ischaemic stroke in the Safe Implementation of Thrombolysis in Stroke-Monitoring Study (SITS-MOST): an observational study.** *Lancet* 2007;369:275–82
19. **Tissue plasminogen activator for acute ischemic stroke: the National Institute of Neurological Disorders and Stroke rt-PA Stroke Study Group.** *N Engl J Med* 1995;333:1581–87
20. Nichols C, Khatri P, Tomsick T, et al. **Advantages of a combined approach to recanalization therapy.** *Stroke* 2008;39:e71, author reply e72
21. Berger C, Fiorelli M, Steiner T, et al. **Hemorrhagic transformation of ischemic brain tissue—asymptomatic or symptomatic.** *Stroke* 2001;32:1330–35
22. Jansen O, Schellinger P, Fiebich J, et al. **Early recanalisation in acute ischaemic stroke saves tissue at risk defined by MRI.** *Lancet* 1999;353:2036–37
23. Hesselmann V, Niederstadt T, Dziewas R, et al. **Reperfusion by combined thrombolysis and mechanical thrombectomy in acute stroke: effect of collateralization, mismatch, and time to and grade of recanalization on clinical and tissue outcome.** *AJNR Am J Neuroradiol* 2012;33:336–42
24. Phan CM, Yoo AJ, Hirsch JA, et al. **Differentiation of hemorrhage from iodinated contrast in different intracranial compartments using dual-energy head CT.** *AJNR Am J Neuroradiol* 2012;33:1088–94

Hyperattenuated Intracerebral Lesions after Mechanical Recanalization in Acute Stroke: Contrast and Compare

Lummel et al¹ herein report their observations regarding hyperdense cerebral lesions (HCL) identified after mechanical revascularization in acute ischemic stroke. They construct a nexus between HCL and iodinated radiographic contrast material (IRCM) deposition, which may either disappear within 24 hours (enhancement) or persist as intracerebral hemorrhagic transformation lesions (HL). They analyzed the relationship of HCL to clinical outcome and concluded that HCL indicated a higher risk of secondary HL but that their presence does not seem to be of any prognostic value for clinical outcome.

The latter conclusion seems predicated on a comparison between 16 patients without HCL and 85 with HCL, in which no statistical difference was identified between the 2 groups in the modified Rankin Scale 0–3 outcome. A more convincing conclusion regarding functional outcome might be derived if the sample size of the 2 groups were larger or perhaps the customary mRS 0–2 end points were analyzed. The small group of 16 patients without HCL may well have been favorably predisposed to a 93% revascularization and a 40% mRS 0–3 outcome. The subjects with HCL may have been otherwise predisposed to a poorer 74% revascularization and a 33.7% mRS 0–3 outcome. Lack of adjustment for relevant comorbidities leaves this question unresolved.

Within this HCL group, we are left to wonder about functional outcome differences between the HCL-enhancement group ($n = 41$) and the HCL-HL group ($n = 43$). We are told that there was no significant difference. Due to the lack of specific figures, we can only speculate on what percentage difference and/or P value might be sufficiently hypothesis-generating among those whose HCL disappear within 24 hours versus those in whom they persist and lead to hemorrhagic transformation. A difference of 5% might be large enough to promote further analysis, given sufficient sample sizes.

The authors are to be recognized for the very low PH rate, all PH 1. After all, PH 1 is insignificant, with PH 2 the yardstick of PH significance, according to the European Cooperative Acute Stroke Study (ECASS) experience. But is it? In the Interventional Management of Stroke (IMS) I and II trials, symptomatic intracerebral hemorrhages (ICHs) were composed of

an equal number of PH 1 and PH 2s, and the 2 groups had similar mean lesion (infarct + ICH) volume.² PH 1 and PH 2 status was, therefore, not defined so much by the PH volume, but by lesion volume, in which PH 1s were associated with larger infarcts and a larger denominator from which to determine the PH status as >30% (PH 2) or <30% (PH 1) lesion volume. We hypothesize that endovascular (EV) revascularization studies led to smaller lesions compared with IV treatment of major arterial occlusive lesions, leading to an equal number of symptomatic PH 1 and PH 2 values of equal mean volumes in IMS I and II, as opposed to large infarcts with a large number of PH 2s in ECASS. The presence of all PH 1s and no PH 2s raises the following question: How large were the lesion volumes in the study of Lummel et al?¹ A mean volume of 92 mL is reported in the HCL group. However, this volume is larger than 61.6 mL reported for 109 anterior circulation subjects in the Solitaire Retrospective Trial.³ Surely the 92 mL would be reduced if the 16 non-HCL cases were included.

This speculation leads us to other questions regarding the study. The study population was selected on the basis of good Alberta Stroke Program Early CT scores and CT perfusion, in which patients without mismatch were excluded. They were treated expeditiously with IV rTPA and EV mechanical revascularization. Nevertheless, the reperfusion rates and the percentage mRS 0–2 were relatively low compared with the Solitaire Retrospective Trial, a reasonable comparator for such retrospective analysis, in which 85% modified TICI 2b–3 was achieved for the ICA terminus region and M1 occlusions.⁴ Why should patients with favorable advanced perfusion imaging have relatively low reperfusion, with a relatively low percentage of good outcomes, with an HCL incidence at the upper end of reported ranges? Where there is convergence of numerous HCL, IRCM localization, suboptimal reperfusion rates, and low functional outcome rates, are we missing an elephant in the room?

One possible common denominator to the information above is IRCM. That the HCL incidence correlated with EV low-osmolar IRCM volume in a population that already had IV IRCM infusion for CTA supports an IRCM-ICH hypothesis.

This is consonant with our animal work, in which increased ICH was found in a rat temporary-occlusion model with intra-arterial (IA) low-osmolar iohexol (Omnipaque; GE Healthcare, Piscataway, New Jersey) injection, as opposed to saline injection, despite equal infarct edema.⁵

Supported by the Foundation of the American Society of Neuroradiology and Boston Scientific, Morales et al⁶ studied 3 groups of rats with the same model, with saline, low-osmolar iopamidol (Isovue; Bracco Diagnostics, Monroe Township, New Jersey), or iso-osmolar iodixanol (Visipaque; GE Healthcare) infused IA postocclusion. They performed 3T MR imaging immediately postinfusion and at 24 hours immediately before sacrifice. On MR imaging and postmortem cut sections, the iodixanol rats had not only smaller infarct edema but also less cortical ICH.⁶ ICH and infarct volumes were not significantly different in saline and iopamidol rats.

If IRCM A is associated with smaller infarcts and less ICH than saline or IRCM B in animals, is it too far-fetched to suggest that IRCM may have an adverse effect in human use? Could IRCM A use contribute to a higher percentage of mRS 0–2 than IA IRCM B in humans? IMS III was designed to give insight into the potential clinical effects of IRCM in this respect. Operators recorded contrast type and volume for later analysis. Symptomatic ICH was sufficiently infrequent in IMS III and sufficiently multifactorial that an IRCM-related smoking gun would be impossible to prove, even if it existed. It is not clear that IA IRCM use contributes to symptomatic ICH directly, independent of technical factors.

IMS III showed asymptomatic ICH to be significantly more common when maintaining combined IV rtPA-EV treatment compared with IV rtPA alone; at least it did not negate an IRCM-ICH hypothesis. That Lummel et al¹ found a relationship between procedural IRCM volume and HCL sustains a harmful IRCM hypothesis as well. Analysis of the relationship of ICH and IRCM type and volume in IMS III has been initiated, with interesting preliminary results.

That ICH differences and mRS outcome differences might occur with isomolar-versus-low-osmolar IRCM is consistent with the findings of Morales et al⁶ and, furthermore, is supportive of an IRCM-HCL-ICH functional outcome hypothesis. Unfortunately, IMS III stopped prematurely, and additional opportunities to identify any effect were lost.

Lummel et al¹ briefly discussed potential mechanisms of the harmful effects of IRCM on the basement membrane contributing to HCL and ICH. Effects may, in fact, be additive. Did the IRCM used contribute to blood-brain barrier disruption or apoptosis of initially viable cells? Could IRCM effects be IRCM-specific: Is there a tissue osmotic effect of smaller monomeric IRCM molecules that is reduced or overcome by larger molecular intravascular dimers at the capillary and BBB level? Did a thrombotic effect of IRCM at the precapillary level contribute to reduced perfusion and worse outcomes? Did vasospasm generated by large

guide catheters in the ICA and by devices in the MCA contribute to pressure-flow alterations during IRCM guide-catheter injections, contributing to HCL and potential sequelae? Did IV IRCM prior to EV treatment contribute to these phenomena? Is there a target at the BBB level that can be engaged to reduce or overcome adverse effects of thrombolytic therapy associated with mechanical revascularization?⁷

I have been personally concerned about the relationship of IRCM and outcome for many years during the IA-thrombolysis era. With the advent of mechanical revascularization, I thought this issue would now be relegated to a lower rung on the ladder of stroke-therapy-related concerns. Reported excellent revascularization rates and outcomes would overshadow any small harmful effect that IRCM might add. Identifying a less-harmful effect of one IRCM versus another may be a more reasonable option. Clearly, IRCM is not the primary determinant of EV outcomes. Nevertheless, an effect in 3%–5% of subjects could mean the difference between success and futility in a trial. Lummel et al¹ leave me with the impression that there is still much to understand about IRCM and their use.

REFERENCES

1. Lummel N, Schulte-Altedorneburg G, Bernau C. **Hyperattenuated intracerebral lesions after mechanical recanalization in acute stroke.** *AJNR Am J Neuroradiol* 2014;35:345–51
2. Tao H, Carrozzella J, Broderick J, et al, for the IMS Investigators. **Parenchymal hematoma and total lesion volume in combined IV/IA revascularization stroke therapy.** *J Neurointerv Surg* 2012;4:256–60
3. Javadi A, Carrozzella J, Tomsick T, for the IMS I/II & Solitaire Investigators. **Lesion and ICH volume: IMS I/II vs. Solitaire study.** In: *Proceedings of the Ninth Annual Meeting of the Society of Neurointerventional Surgery*, San Diego, California. July 23–27, 2012
4. Dávalos A, Pereira VM, Chapot R, et al. **Retrospective multicenter study of Solitaire FR for revascularization in the treatment of acute ischemic stroke.** *Stroke* 2012;43:2699–705
5. Kurosawa Y, Lu A, Khatri P, et al. **Intra-arterial iodinated radiographic contrast material injection and intravenous heparin administration in a rat middle cerebral artery occlusion and reperfusion model: possible effects on intracerebral hemorrhage.** *Stroke* 2010;41:1013–17
6. Morales H, Lu A, Kurosawa Y, et al. **Isomolar contrast causes smaller infarcts than low-osmolar contrast.** In: *Proceedings of the 48th American Society of Neuroradiology and Neuroradiology Education and Research Foundation Symposium*, Boston, Massachusetts. May 15–20, 2010
7. Pfefferkorn T, Rosenberg GA. **Closure of the blood-brain barrier by matrix metalloproteinase inhibition reduces rt-PA-mediated mortality in cerebral ischemia with delayed reperfusion.** *Stroke* 2003;34:2025–30

T. Tomsick

University of Cincinnati Medical Center
Cincinnati, Ohio

<http://dx.doi.org/10.3174/ajnr.A3824>

Angioarchitectural Characteristics Associated with Complications of Embolization in Supratentorial Brain Arteriovenous Malformation

J. Pan, H. He, L. Feng, F. Viñuela, Z. Wu, and R. Zhan

ABSTRACT

BACKGROUND AND PURPOSE: Embolization is an important therapeutic technique in brain arteriovenous malformations; however, little has been reported on the factors contributing to complications. We retrospectively reviewed a large series of supratentorial brain AVMs to identify the angioarchitectural characteristics that might be associated with the complications of embolization and poor clinical outcomes.

MATERIALS AND METHODS: The clinical and angiographic features of 130 consecutive patients with supratentorial brain AVMs embolized with ethylene-vinyl alcohol copolymer in our hospital from 2005–2008 were retrospectively reviewed. None of these patients had prior embolization. Complications were classified as transient neurologic deficits, persistent neurologic deficits, and death. Univariate and multivariate analyses were conducted to assess the angiographic features in patients with and without complications.

RESULTS: Twenty-three complications occurred in 130 embolization procedures, 13 (10%) were transient neurologic deficits (9 ischemic and 4 hemorrhagic), 9 (6.92%) were persistent neurologic deficits (7 ischemic and 2 hemorrhagic), and 1 death occurred. By univariate analyses, eloquent cortex (OR, 2.57; 95% CI, 1.08–3.42) and exclusive deep venous drainage (OR, 4.56; 95% CI, 1.28–9.67) were correlated with procedural complications. The impact of eloquent cortical location ($P = .001$) and exclusive deep venous drainage ($P = .035$) on complications were also demonstrated by multivariate analysis. Eloquent cortex mainly resulted in permanent ischemic neurologic deficit; occlusion of drainage vein was significantly correlated with periprocedural hemorrhage in supratentorial brain AVMs with subtotal and partial embolization.

CONCLUSIONS: In a retrospective study on supratentorial brain AVMs with first-time embolization, 6.92% of patients had permanent neurologic deficit or death. Eloquent cortical location and exclusive deep venous drainage were associated with complications.

ABBREVIATIONS: sbAVM = supratentorial brain arteriovenous malformation; EVOH = ethylene-vinyl alcohol copolymer; PVA = polyvinyl alcohol

Embolization is an important adjunctive therapy to microsurgery and radiosurgery in the multidisciplinary management of arteriovenous malformations.^{1–3} Recent advances in endovascular embolization techniques including flow-directed microcatheters and the liquid embolic agents *n*-butyl-cyanoacrylate and ethylene-vinyl

alcohol copolymer (EVOH; Onyx, ev3, Irvine, California)⁴ make it possible to cure AVMs with embolization alone.^{5,6}

Because endovascular treatment might result in hemorrhage and ischemic neurologic dysfunction, embolization of unruptured AVMs remains controversial, particularly in supratentorial brain AVMs (sbAVMs), which have a lower risk of hemorrhage than infratentorial AVMs. The reported complication rates of embolization varied from 3–11%^{2,7–10} and were associated with angiographic features.⁷

In the present study, we retrospectively reviewed 130 patients with sbAVMs to identify angioarchitectural characteristics that might be associated with the complications of embolization and poor clinical outcomes.

MATERIALS AND METHODS

All patients referred to our institution were assessed by a multidisciplinary team of neuroradiologists, neurosurgeons, and neu-

Received March 2, 2013; accepted after revision April 15.

From the Department of Neurosurgery (J.P., R.Z.), The First Affiliated Hospital, School of Medicine, Zhejiang University, Hangzhou, China; Department of Interventional Neuroradiology (H.H., Z.W.), Beijing Tiantan Hospital, Capital Medical University, Beijing, China; Department of Radiology (L.F.), Kaiser Permanente Medical Center, Los Angeles, California; and Department of Radiological Science (F.V.), Division of Interventional Neuroradiology, David Geffen School of Medicine at UCLA, Los Angeles, California.

Please address correspondence to Renya Zhan, Department of Neurosurgery, The First Affiliated Hospital, School of Medicine, Zhejiang University; 79 Qingchun Rd, Hangzhou 310006, China; e-mail: Neurovasword@gmail.com; or Hongwei He, Department of Interventional Neuroradiology, Beijing Tiantan Hospital, Capital Medical University; 6 Tiantan Xili, Beijing 100050, China; e-mail: ttyyhhw@126.com

<http://dx.doi.org/10.3174/ajnr.A3643>

rologists for the therapeutic option on the basis of CT, MR imaging, and DSA. A total of 130 consecutive patients with sbAVMs were diagnosed and embolized with Onyx for the first time during the period January 1, 2005 to December 31, 2008, and their demographic, clinical, and angioarchitectural data were reviewed retrospectively. Patients with prior treatment (surgical removal, embolization, radiosurgery) were excluded from the study.

Initial sbAVM presentation was defined as hemorrhage, ischemic neurologic deficit, headache, seizures, and incidental findings. Angioarchitectural characteristics such as location and size of AVM, arterial feeders and coexisting aneurysms, venous drainage, and venous morphology were retrospectively evaluated.

AVM locations were grouped into eloquent cortex, noneloquent cortex, midline region (ventricle, corpus callosum), and deep region (basal ganglia, internal capsule, and thalamus). Spetzler-Martin grade was assessed in each AVM, and sizes were classified into small (3 cm), medium (3 cm and 6 cm), and large (6 cm). Arterial feeders were categorized as terminal and perforating. Terminal feeding arteries were prominent arteries that connected directly to the nidus, whereas perforating feeders referred to the pattern of several small, short arteries arising from a large parent artery and penetrating brain parenchyma to reach the AVM nidus. The presence of coexisting arterial aneurysms was divided into perinidal and intranidal aneurysms. Remote flow-related or unrelated aneurysms were not taken into account in this study. Venous drainage was noted as deep, superficial, and combined groups. Venous morphology was described according to the presence or absence of ectasia and stenosis. Ectasia was defined as focal dilations that were at least twice the size of the venous diameter. A 50% focal reduction of the venous diameter was considered as a significant stenosis.

Embolization degree was classified into partial (<90%), subtotal (≥90%), and complete (100%) embolization. Neurologic deficits were assessed by a neurosurgeon/neurologist according to NIHSS. CT and MR imaging were performed after embolization to identify postprocedural hemorrhage and ischemia. Postprocedural mRS was assessed, and complications of embolization were categorized as transient (new onset of neurologic deficit that resolved completely within 7 days) and persistent neurologic deficit. Neurologic deficits were further divided into ischemic and hemorrhagic.

The data were managed and analyzed by use of SPSS software (version 13.0; IBM, Armonk, New York). We conducted analyses stratified by each variable (age, sex, nidus size, etc) to evaluate its impact on complications of embolization. Furthermore, multivariate analyses (backward conditional logistic regression) were conducted after the adjustment for some variables that demonstrated and correlated with a significantly increased risk of embolization complications in univariate analyses to assess the effect of modification and interaction among potential risk factors. A probability value of <.05 was considered statistically significant in each analysis.

RESULTS

Of the 130 patients with sbAVM who underwent embolization, there were 78 men and 52 women, ranging from 5–64 years of age (mean, 30.27 ± 12.45 years). Initial presentations included 79

Table 1: Demographic and clinical characteristics of 130 patients with sbAVM embolization

Characteristics	No. (%)
Sex	
Male	78 (60%)
Female	52 (40%)
Age, y	
<18	27 (20.77%)
18–49	100 (76.92%)
≥50	3 (2.31%)
Initial presentation	
Hemorrhage	79 (60.77%)
Ischemia	11 (8.46%)
Headache	13 (10%)
Seizures	20 (15.38%)
No symptoms	7 (5.38%)

Table 2: Preprocedural angioarchitectural characteristics of 130 patients with sbAVM embolization

Angiographic Features	No. (%)
Location	
Eloquent cortex	44 (33.85%)
Noneloquent cortex	62 (47.69%)
Midline	12 (9.23%)
Deep	12 (9.23%)
Size	
≤3 cm	32 (24.62%)
3–6 cm	80 (61.54%)
≥6 cm	18 (13.85%)
No. of feeders	
1	17 (13.08%)
2	28 (21.54%)
≥3	85 (65.38%)
Arterial feeders classification	
Terminal	95 (73.08%)
Perforating	35 (26.92%)
No. of draining veins	
1	55 (42.31%)
2	37 (28.46%)
≥3	38 (29.23%)
Venous drainage classification	
Exclusive superficial	79 (60.77%)
Exclusive deep	16 (12.31%)
Combined	35 (26.92%)
Venous morphology	
Venous reflux	35 (26.92%)
Venous ectasia	29 (22.31%)
Venous stenosis	46 (35.38%)
Coexisting aneurysm	
Intranidal	30 (23.08%)
Perinidal	7 (5.38%)
Spetzler-Martin classification	
I–II	50 (38.46%)
III	36 (27.69%)
IV	30 (23.08%)
V	14 (10.77%)

spontaneous hemorrhages, 11 ischemic manifestations, 13 headaches, 20 seizures, and 7 nonsymptomatic (Table 1).

The preprocedural angioarchitectural characteristics are summarized in Table 2. Most the sbAVMs were medium-sized (61.54%) and located in noneloquent cortices (47.69%). Perforating feeders were found in 35 cases (26.92%), whereas 16 patients (12.31%) had exclusive deep venous drainage. Coexisting aneurysm was noted in 37 cases, of which, 30 (23.08%) were in-

Table 3: Hemorrhagic complications in 38 sbAVMs with obliteration of draining vein

Complication	Embolization	Complete ^a	Subtotal (Near Complete ^a)	Partial
Hemorrhage		0	2 (0)	3
No hemorrhage		8	8 (4)	17

Note:— χ^2 test.

^a $P < .05$, significant difference.

Table 4: Complications of embolization in 130 patients with sbAVMs

Complications	No. (%)
TND	
Ischemic	9 (6.92%)
Hemorrhagic	4 (3.08%)
PND	
Ischemic	7 (5.38%)
Hemorrhagic	2 (1.54%)
Death	
Hemorrhagic	1 (0.77%)

Note:—TND indicates transient neurologic deficit; PND, persistent neurologic deficit.

trianid aneurysms. According to the Spetzler-Martin grading system, the distribution of sbAVMs were 16 in grade I (12.31%); 34 in grade II (26.15%); 36 in grade III (27.69%); 30 in grade IV (23.08%); and 14 in grade V (10.77%).

All patients were embolized with Onyx. The average number of catheterized feeders was 1.26, and the volume of embolic agent was 0.3~9.5 mL (average, 2.5 ± 1.77 mL). Endovascular treatment achieved complete embolization in 28 patients, subtotal in 26 patients, and partial in 76 patients. In the procedure, draining veins were unexpectedly occluded in 38 cases and associated with hemorrhage in 5 cases (Table 3). Among the patients who had subtotal embolization, 4 were nearly complete, with the residual AVMs approximately 1% of their preprocedural volumes.

After embolization, there were 13 transient neurologic deficits (9 were ischemia and 4 were hemorrhage), 9 persistent neurologic deficits (7 ischemia and 2 hemorrhage), and 1 death occurred (hemorrhage) (Table 4). Eloquent cortex location was the main risk factor of symptomatic cerebral ischemia and ischemic persistent neurologic deficit (5/7, 71.4%) after embolization ($P < .05$). The number of catheterized feeders and the volume of embolic agent were not significantly correlated with postprocedural complications ($P > .05$).

By univariate analyses (Table 5), eloquent cortex location (OR, 2.57; 95% CI, 1.08–3.42) and exclusive deep venous drainage (OR, 4.56; 95% CI, 1.28–9.67) were correlated with postprocedural complications ($P < .05$). Eloquent cortical location was associated with persistent ischemic neurologic deficit ($P < .05$); occlusion of the drainage vein was significantly correlated with postprocedural hemorrhage in AVMs with subtotal and partial embolization (Table 3). The impact of eloquent cortical location ($P = .001$) and exclusive deep venous drainage ($P = .035$) on embolization complications were demonstrated by backward conditional logistic regression.

Spetzler-Martin classification of 130 sbAVMs significantly changed after embolization (Table 6), with significantly more patients in grade I than before the procedure (33.33% versus 16.31%, $P < .05$), and patients in other grades decreased. There were significantly more patients with an mRS of 0 and fewer patients with an mRS of 1 after embolization (Table 6), partly attrib-

Table 5: Demographic, clinical, and angioarchitectural characteristics predictive for embolization complications by univariate analysis

Characteristics	OR (95% CI)	P Value
Sex		
Male	0.84 (0.33–2.10)	.75
Age, y		
<18	0.89 (0.31–2.41)	.78
18–49	1.09 (0.37–2.76)	.84
≥ 50	1.16 (0.17–11.36)	1.01
Initial presentation		
Hemorrhage	1.15 (0.59–2.94)	.49
Ischemia	0.65 (0.14–3.27)	1.00
Headache	1.86 (0.93–5.63)	.57
Seizures	0.64 (0.37–2.00)	.55
No symptoms	0.91 (0.17–4.39)	.70
Location		
Eloquent cortex	2.57 (1.08–3.42)	.02
Noneloquent cortex	0.38 (0.24–0.86)	.02
Midline	0.55 (0.19–2.42)	.79
Deep	1.41 (0.29–2.85)	.51
Size		
≤ 3 cm	1.06 (0.42–2.40)	.79
3–6 cm	0.80 (0.33–1.29)	.23
≥ 6 cm	2.45 (0.57–5.32)	.17
No. of feeders		
1	0.39 (0.06–1.54)	.38
2	1.75 (0.76–3.21)	.26
≥ 3	0.85 (0.47–3.84)	.72
Classification of feeders		
Terminal	0.61 (0.35–1.97)	.32
Perforating	1.64 (0.79–4.58)	.25
No. of draining veins		
1	0.73 (0.43–2.96)	.98
2	1.57 (0.58–3.63)	.34
≥ 3	0.62 (0.34–1.89)	.43
Drainage classification		
Exclusive superficial	1.04 (0.77–2.52)	.90
Exclusive deep	4.56 (1.28–9.67)	.00
Combined	0.24 (0.09–0.53)	.03
Venous morphology		
Venous reflux	1.91 (0.51–2.98)	.77
Venous ectasia	2.24 (1.32–9.88)	.26
Venous stenosis	1.50 (0.26–2.34)	.19
Coexisting aneurysm		
Intranidal	0.99 (0.23–3.81)	.22
Perinidal	1.52 (3.72–8.50)	.61
Spetzler-Martin classification		
I–II	2.32 (0.21–9.87)	.48
III	0.58 (0.70–4.05)	.54
IV	1.61 (1.22–4.53)	1.20
V	0.83 (0.06–10.29)	1.00
Embolization degree		
Complete	0.87 (0.27–3.02)	.27
Subtotal	0.71 (0.40–1.60)	.13
Partial	1.92 (1.21–4.07)	.17
Venous occlusion	1.26 (0.94–2.83)	.84

uted to the recovery from their initial hemorrhage or ischemic event.

DISCUSSION

Endovascular embolization is an important part of the multimodality treatment for brain AVMs.^{11–13} Improvements in microcatheter technology and embolic agents, especially *n*-BCA and EVOH, have led to an increased curative rate of brain AVMs.^{5,6,11} Furthermore, embolization can reduce the size and flow of AVMs,

Table 6: Spetzler-Martin classification and mRS score before and after embolization in 130 patients with sbAVMs

Grade	Preprocedural, No. (%)	Postprocedural, No. (%)
Spetzler-Martin classification		
I	16 (16.31%)	34 (33.33%) ^a
II	34 (26.15%)	20 (19.61%)
III	36 (27.69%)	28 (27.45%)
IV	30 (23.08%)	16 (15.69%)
V	14 (10.77%)	4 (3.92%)
mRS		
0	10 (7.69%)	29 (22.31%) ^a
1	79 (60.77%)	54 (41.54%) ^a
2	19 (14.62%)	20 (15.38%)
3	11 (8.46%)	11 (8.46%)
4	5 (3.85%)	12 (9.23%)
5	6 (4.62%)	3 (2.31%)
6	0 (0%)	1 (0.77%)

Note:— χ^2 test.

^a $P < .05$, significant difference.

improving the safety and efficacy of microsurgery and radiosurgical treatment for brain AVMs.¹⁴⁻¹⁸ In this series of 130 sbAVMs that underwent embolization for the first time, there was complete embolization in 28 patients (21.54%) and subtotal embolization in 26 patients (20%). In addition to the cases of complete obliteration of brain AVMs, patients in Spetzler-Martin grade I increased significantly after embolization (preprocedural, 16.31% versus postprocedural, 33.33%; $P < .05$) and the average Spetzler-Martin grade in the series declined (preprocedural, 2.94 versus postprocedural, 1.86; $P < .05$).

Either curative or adjuvant embolization can result in postprocedural hemorrhage and ischemia. Recent studies reported morbidity ranging from 3–11%, and mortality from 0–4%,^{2,4,5,7,8,11,19-26} with associations to angioarchitecture, embolic agents, microcatheters, and the manipulator's skills. Studies on different embolization materials, such as silk,²⁴ polyvinyl alcohol (PVA) and coil,²⁵ Onyx,¹¹ and *n*-BCA,²³ showed 1.4%, 13%, 19.5%, and 50% rates for morbidity and 0%, 0%, 2.9%, and 1.9% for rates of mortality, respectively. Frizzel and Fisher²⁷ reviewed 32 series of brain AVM embolization studies and revealed that permanent neurologic deficit and mortality were 9% and 2% before 1990, decreasing to 8% and 1% after 1990. Because some embolic agents such as PVA and isobutyl cyanoacrylate are no longer in use and new materials such as Onyx have been widely adopted, the complications of embolization should be reassessed. Moreover, the statistical bias caused by different embolic materials, different locations of AVMs, and technical-related complications need to be evaluated. We reviewed 11 series of embolization by use of *n*-BCA and Onyx (Table 7)^{2,4,5,7,8,11,19-22} and retrospectively studied sbAVMs treated by flow-directed microcatheters and liquid embolic agents in 5 recent years. We found a complication rate of 6.4–21%, permanent neurologic deficit of 1.6–12.2%, and mortality rate of 0–2.9%.

Complications of embolization can be categorized into technical-related and non-technical-related. Technical-related complications included vascular perforation, normal branch occlusion, and bleeding caused by catheter removal. Recent improvement in flow-directed microcatheter and nonadhesive embolic agents has reduced the risk of microcatheter delivery and removal. In our

Table 7: Embolization complications by *n*-BCA and/or Onyx according to the literature (11 series)

Series [Reference]	Patients	Materials	Complication, %	PND, %	Mortality, %
Taylor et al [2]	201	<i>n</i> -BCA/Onyx	21	11	2
Van Rooij et al [4]	44	Onyx	13.8	4.6	2.3
Katsaridis et al [5]	101	Onyx	14.9	7.9	2.9
Ledezma et al [7]	168	<i>n</i> -BCA	16.1	6.5	1.2
Haw et al [8]	306	<i>n</i> -BCA	6.4	3.9	0
Panagiotopoulos et al [11]	82	Onyx	19.5	3.8	2.4
Jayaraman et al [19]	192	<i>n</i> -BCA/Onyx	15.7	1.6	0
Starke et al [20]	275	<i>n</i> -BCA	14	2.5	0
Hauck et al [21]	107	Onyx	17	12.2	0
Velat et al [22]	88	<i>n</i> -BCA/Onyx	13.6	4.5	2.2
Present study	130	Onyx	17.7	6.9	0.8

Note:—PND indicates persistent neurologic deficit.

series with sbAVM embolization, contrast extravasation was noted in 3 cases during the procedure. None of these 3 patients ended with persistent neurologic deficit because of timely occlusion of microperforation sites. The technical-related complication rate in the present study was 2.31%, less than the results of Ledezma et al⁷ and less than our non-technical-related complications (21/130, 16.15%).

Non-technical-related complications are mainly associated with angioarchitectural characteristics of brain AVMs. Periprocedural hemorrhage rate was 3–15%,²⁸⁻³⁰ probably related to hemodynamic changes and alteration in nidus pressure.^{30,31} Picard et al²⁸ demonstrated that venous outflow obstruction was correlated with hemorrhagic presentation after embolization. Furthermore, by progressively blocking draining veins in an AVM model, Hademenos and Massoud³² revealed that venous stenosis or occlusion would result in redistribution of blood flow in the nidus and cause intranidal hypertension. Nonetheless, not all venous occlusion resulted in hemorrhage; the extent and severity of outflow obstruction matter as well. In the present study, venous occlusion occurred in 29.23% of all 130 cases and did not correlate with embolization complications in the univariate model. In the 38 patients with venous occlusion, no postprocedural hemorrhagic presentation occurred when the AVM was completely or nearly completely embolized, whereas a significantly higher hemorrhage rate was seen in the subtotal and partial embolization group (0% versus 23.81%, $P < .05$). This result suggested that imbalance between inflow and outflow could be a predictive factor of postprocedural hemorrhage and that to avoid rupture of the residual AVM, sbAVMs should be completely or nearly completely embolized as soon as possible when venous outflow obstruction is identified.

Normal perfusion pressure breakthrough related to disruption of cerebral vascular autoregulation³³ and delayed venous thrombosis have been postulated as the etiologies of periprocedural hemorrhage. There was no normal perfusion pressure breakthrough in our series because blood pressure was tightly controlled in all patients immediately after embolization. One patient with subtotal embolization (and reserved draining veins) had severe brain edema, which could be attributed to delayed venous thrombosis and stagnation. Purdy et al³⁰ suggested that delayed venous outflow obstruction might occur because of sluggish blood flow rather than direct venous occlusion by embolic agents.

Although hemorrhage results in poorer outcome, ischemic events were the most common complications of AVM embolization.^{2,4,5,7,8,11,19-22} Sixteen patients (12.31%) in our series had cerebral infarction after embolization, with persistent neurologic deficits in 7 patients. Because of rapid shunting and complex angioarchitecture, perinidal or intranidal normal arteries were very difficult to identify, and neurologic deficits could result from occlusion of these arteries. The present study revealed that sbAVMs located in eloquent cortices had a significantly higher rate of postprocedural persistent ischemic neurologic dysfunction.

In addition to AVM location, other angioarchitectural characteristics that contribute to nonmanipulated complications of embolization remain controversial.^{2,7,8,19,20,34-37} Haw et al⁸ reviewed 306 consecutive patients and 513 embolization sessions from 1984–2002 at the University of Toronto and suggested that the factors associated with complications included the presence of a high-flow fistula or fistulous component to the nidus, eloquent cortex involvement, or venous glue embolization. The long interval of data collection (1984–2002) could have undermined the validity of these conclusions because significant advancement in the embolization technique occurred during this time period. Among all angiographic parameters investigated in 168 consecutive patients and 295 embolization sessions, Ledezma et al⁷ found that Spetzler-Martin grades III–V were significantly associated with unfavorable outcomes and embolization complications. Gobin et al³⁸ revealed that embolization complications were 0% (grade II), 5% (grade III), 15% (grade IV), and 22% (grade V) in their 125 patients studied on Spetzler-Martin classification. On the other hand, studies of Hartmann et al³⁶ and Kim et al¹⁰ failed to demonstrate the correlation between Spetzler-Martin grade and embolization complication and found that embolization sessions were the primary factor for postprocedural complications.

To eliminate the statistical bias caused by embolization sessions, we studied the complications of first-time embolization of 130 sbAVMs and demonstrated that postprocedural complications were associated with eloquent cortical location (OR, 2.57; 95% CI, 1.08–3.42) and exclusive deep venous drainage (OR, 4.56; 95% CI, 1.28–9.67) but not with Spetzler-Martin classification in univariate and multivariate models. The result suggested that the required multiple sessions in large AVMs but not the AVM size itself might be associated with procedural complications.^{10,36} The higher complication rate in sbAVMs with exclusive deep venous drainage could be related to the relative lack of a collateral drainage pathway, making them prone to venous outflow obstruction by embolic agents. This observation may also be confounded by the deep location of these AVMs. Thus, sbAVMs with functional cortex and exclusive deep venous drainage would be more difficult to treat and would be at greater risk for embolization complications than the other types of sbAVMs.

CONCLUSIONS

Embolization is a safe treatment technique for supratentorial AVM, with the development of flow-directed microcatheters and liquid embolic agents. Eloquent cortical location and exclusive deep venous drainage were significantly associated with embolization complications, and venous outflow occlusion in cases with

subtotal and partial embolization might be a predictive factor for periprocedural hemorrhage.

REFERENCES

1. Chang SD, Marcellus ML, Marks MP, et al. **Multimodality treatment of giant intracranial arteriovenous malformations.** *Neurosurgery* 2003;53:1–11
2. Taylor CL, Dutton K, Rappard G, et al. **Complications of preoperative embolization of cerebral arteriovenous malformations.** *J Neurosurg* 2004;100:810–12
3. Izawa M, Chernov M, Hayashi M, et al. **Combined management of intracranial arteriovenous malformations with embolization and gamma knife radiosurgery: comparative evaluation of the long-term results.** *Surg Neurol* 2009;71:43–53
4. Van Rooij WJ, Sluzewski M, Beute GN. **Brain AVM embolization with Onyx.** *AJNR Am J Neuroradiol* 2007;28:172–77
5. Katsaridis V, Papagiannaki C, Aimar E. **Curative embolization of cerebral arteriovenous malformations (AVMs) with Onyx in 101 patients.** *Neuroradiology* 2008;50:589–97
6. Pan JW, Zhou HJ, Zhan RY, et al. **Supratentorial brain AVM embolization with Onyx-18 and post-embolization management: a single-center experience.** *Intervent Neuroradiol* 2009;15:275–82
7. Ledezma CJ, Hoh BL, Carter BS, et al. **Complications of cerebral arteriovenous malformation embolization: multivariate analysis of predictive factors.** *Neurosurgery* 2006;58:602–11
8. Haw CS, terBrugge K, Willinsky R, et al. **Complications of embolization of arteriovenous malformations of the brain.** *J Neurosurg* 2006;104:226–32
9. Cockroft KM, Hwang SK, Rosenwasser RH. **Endovascular treatment of cerebral arteriovenous malformations: indications, techniques, outcome, and complications.** *Neurosurg Clin North Am* 2005;16:367–80
10. Kim LJ, Albuquerque FC, Spetzler RF, et al. **Postembolization neurological deficits in cerebral arteriovenous malformations: stratification by arteriovenous malformation grade.** *Neurosurgery* 2006;58:53–59
11. Panagiotopoulos V, Gizewski E, Asgari S, et al. **Embolization of intracranial arteriovenous malformations with ethylene-vinyl alcohol copolymer (Onyx).** *AJNR Am J Neuroradiol* 2009;30:99–106
12. Ogilvy CS, Stieg PE, Awad I, et al. **AHA Scientific Statement: recommendations for the management of intracranial arteriovenous malformations: a statement for healthcare professionals from a special writing group of the Stroke Council.** *Stroke* 2001;32:1458–71
13. Viñuela F, Duckwiler G, Guglielmi G. **Contribution of interventional neuroradiology in the therapeutic management of brain arteriovenous malformations.** *J Stroke Cerebrovasc Dis* 1997;6:268–71
14. Hartmann A, Mast H, Mohr JP, et al. **Determinants of staged endovascular and surgical treatment outcome of brain arteriovenous malformations.** *Stroke* 2005;36:2431–35
15. Morgan MK, Zurin AA, Harrington T, et al. **Changing role for preoperative embolisation in the management of arteriovenous malformations of the brain.** *J Clin Neurosci* 2000;7:527–30
16. Martin NA, Khanna R, Doberstein C, et al. **Therapeutic embolization of arteriovenous malformations: the case for and against.** *Clin Neurosurg* 2000;46:295–318
17. Viñuela F, Dion JE, Duckwiler G, et al. **Combined endovascular embolization and surgery in the management of cerebral arteriovenous malformations: experience with 101 cases.** *J Neurosurg* 1991;75:856–64
18. Weber W, Kis B, Siekmann R, et al. **Preoperative embolization of intracranial arteriovenous malformations with Onyx.** *Neurosurgery* 2007;61:244–52
19. Jayaraman MV, Marcellus ML, Hamilton S, et al. **Neurologic com-**

- plications of arteriovenous malformation embolization using liquid embolic agents. *AJNR Am J Neuroradiol* 2008;29:242–46
20. Starke RM, Komotar RJ, Otten ML, et al. **Adjuvant embolization with N-butyl cyanoacrylate in the treatment of cerebral arteriovenous malformations: outcomes, complications, and predictors of neurologic deficits.** *Stroke* 2009;40:2783–90
 21. Hauck EF, Welch BG, White JA, et al. **Preoperative embolization of cerebral arteriovenous malformations with Onyx.** *AJNR Am J Neuroradiol* 2009;30:492–95
 22. Velat GJ, Reavey-Cantwell JF, Siström C, et al. **Comparison of N-butyl cyanoacrylate and Onyx for the embolization of intracranial arteriovenous malformations: analysis of fluoroscopy and procedure times.** *Neurosurgery* 2008;63:ONS73–78
 23. NBCA Trial Investigators. **N-butyl cyanoacrylate embolization of cerebral arteriovenous malformations: results of a prospective, randomized, multi-center trial.** *AJNR Am J Neuroradiol* 2002;23:748–55
 24. Schmutz F, McAuliffe W, Anderson DM, et al. **Embolization of cerebral arteriovenous malformations with silk: histopathologic changes and hemorrhagic complications.** *AJNR Am J Neuroradiol* 1997;18:1233–37
 25. Mathis JA, Barr JD, Horton JA, et al. **The efficacy of particulate embolization combined with stereotactic radiosurgery for treatment of large arteriovenous malformations of the brain.** *AJNR Am J Neuroradiol* 1995;16:299–306
 26. Deruty R, Pelissou-Guyotat I, Amat D, et al. **Complications after multidisciplinary treatment of cerebral arteriovenous malformations.** *Acta Neurochir (Wien)* 1996;138:119–31
 27. Frizzel RT, Fisher WS 3rd. **Cure, morbidity, and mortality associated with embolization of brain arteriovenous malformations: a review of 1246 patients in 32 series over a 35-year period.** *Neurosurgery* 1995;37:1031–39
 28. Picard L, DaCosta E, Anxionnat R, et al. **Acute spontaneous hemorrhage after embolization of brain arteriovenous malformation with N-butyl cyanoacrylate.** *J Neuroradiol* 2001;28:147–65
 29. Jafar JJ, Davis AJ, Berenstein A, et al. **The effect of embolization with N-butyl cyanoacrylate prior to surgical resection of cerebral arteriovenous malformations.** *J Neurosurg* 1993;78:60–69
 30. Purdy PD, Batjer HH, Samson DS. **Management of hemorrhagic complications from preoperative embolization of arteriovenous malformations.** *J Neurosurg* 1991;74:205–11
 31. Massoud TF, Hademenos GJ, Young WL, et al. **Can induction of systemic hypotension help prevent nidus rupture complicating arteriovenous malformation embolization? Analysis of underlying mechanism achieved using a theoretical model.** *AJNR Am J Neuroradiol* 2000;21:1255–67
 32. Hademenos GJ, Massoud TF. **Risk of intracranial arteriovenous malformation rupture due to venous drainage impairment: a theoretical analysis.** *Stroke* 1996;27:1072–83
 33. Spetzler RF, Wilson CB, Weinstein P, et al. **Normal perfusion pressure breakthrough theory.** *Clin Neurosurg* 1978;25:651–72
 34. Heidenreich JO, Hartlieb S, Stendel R, et al. **Bleeding complications after endovascular therapy of cerebral arteriovenous malformations.** *AJNR Am J Neuroradiol* 2006;27:313–16
 35. Debrun GM, Aletich V, Ausman JI, et al. **Embolization of the nidus of brain arteriovenous malformations with n-butyl cyanoacrylate.** *Neurosurgery* 1997;40:112–20
 36. Hartmann A, Pile-Spellman J, Stapf C, et al. **Risk of endovascular treatment of brain arteriovenous malformations.** *Stroke* 2002;33:1816–20
 37. Lawton MT. **Spetzler-Martin grade III arteriovenous malformations: surgical results and a modification of the grading scale.** *Neurosurgery* 2003;52:740–48
 38. Gobin YP, Laurent A, Merienne L, et al. **Treatment of brain arteriovenous malformations by embolization and radiosurgery.** *J Neurosurg* 1996;85:19–28

Acute Bleeding in the Head and Neck: Angiographic Findings and Endovascular Management

L.-B. Zhao, H.B. Shi, S. Park, D.g. Lee, J.H. Shim, D.H. Lee, and D.C. Suh



ABSTRACT

BACKGROUND AND PURPOSE: Life-threatening bleeding in the head and neck requires urgent management. This study evaluated the angiographic findings related to head and neck bleeding and presents endovascular management techniques.

MATERIAL AND METHODS: Sixty-one consecutive patients who presented with acute bleeding in the head and neck areas and subsequently underwent endovascular therapy between January 2002 and October 2012 were included in our study. We evaluated the angiographic findings, techniques, and results of endovascular management.

RESULTS: Contrast leakage ($n = 10$), pseudoaneurysm ($n = 20$), or both ($n = 10$) were the most common life-threatening angiographic findings (66%) and were the foci of immediate embolization or endoluminal vessel reconstruction. Seventeen patients (28%) had hypervascular staining of the tumor or mucosa, and 4 patients (6%) did not have any abnormal findings. The acute bleeding was successfully controlled by endovascular management according to the bleeding foci. Carotid arterial lesions, so-called "carotid blowout," required reconstructive or deconstructive therapy. Bleeding of the external carotid artery required specific branch embolization by a combination of various embolic materials. No procedure-related complications occurred except in 1 patient who experienced acute infarction caused by thromboemboli from the covered stent. Seventeen patients (28%) were retreated due to rebleeding after the mean 20-month follow-up.

CONCLUSIONS: Contrast leakage or a pseudoaneurysm or both seen on angiography are active bleeding foci and targets for therapy in patients with acute bleeding in the head and neck area. Despite different bleeding-control strategies according to vessel involvement, endovascular treatment is safe and effective for controlling hemorrhage.

ABBREVIATIONS: CBS = carotid blowout syndrome; ECA = external carotid artery

Acute bleeding in the head and neck area occurs due to various causes and often is a life-threatening situation. If conservative management is unsuccessful, conventional angiography followed by endovascular treatment can have a major role in localizing the source of the bleeding and obliterating bleeding foci, thus leading to immediate and complete hemostasis.

Head and neck cancers are the main cause of intractable hemorrhage from local tumor irradiation or spontaneous tumor bleeding.¹⁻⁵ Acute rupture of irradiated, large vessels is a rare but

life-threatening therapy complication.⁶ In addition to tumor-related bleeding, there is also iatrogenic bleeding related to surgical procedures or craniomaxillofacial trauma, which can also lead to intractable, life-threatening bleeding.

The distribution of bleeding foci is diverse and can range from large vessels, such as the internal or common carotid arteries, to small branches of the external carotid artery (ECA). Identification of the lesion location is mandatory when performing an angiographic procedure and analyzing the angiographic findings because the exact localization of the bleeding site is associated with immediate bleeding control.

The endovascular management of bleeding arising from the extracranial carotid arteries, the so-called "carotid blowout syndrome," has been extensively reported.⁷⁻¹⁴ However, to our knowledge, the exact extent of the carotid blowout syndrome (CBS) in patients with acute bleeding has not been evaluated or compared with that of patients without CBS, despite the completely different application of endovascular hemostatic techniques for CBS versus non-CBS lesions. Therefore, we present our

Received March 14, 2013; accepted after revision May 20.

From the Departments of Radiology and Research Institute of Radiology (L.-B.Z., H.B.S., S.P., D.-g.L., J.H.S., D.H.L., D.C.S.), University of Ulsan, College of Medicine, Asan Medical Center, Seoul, Korea; and Department of Radiology (L.-B.Z., H.B.S.), First Affiliated Hospital of Nanjing Medical University, Nanjing, Nanjing, China.

H.B.S. and D.C.S. contributed equally as corresponding authors.

Please address correspondence to Dae Chul Suh, MD, PhD, Department of Radiology, Asan Medical Center, University of Ulsan, College of Medicine, 86 Asanbyeongwon-Gil, Songpa-Gu, Seoul 138-736, Korea; e-mail: dcsuh@amc.seoul.kr

Indicates article with supplemental on-line table.

<http://dx.doi.org/10.3174/ajnr.A3761>

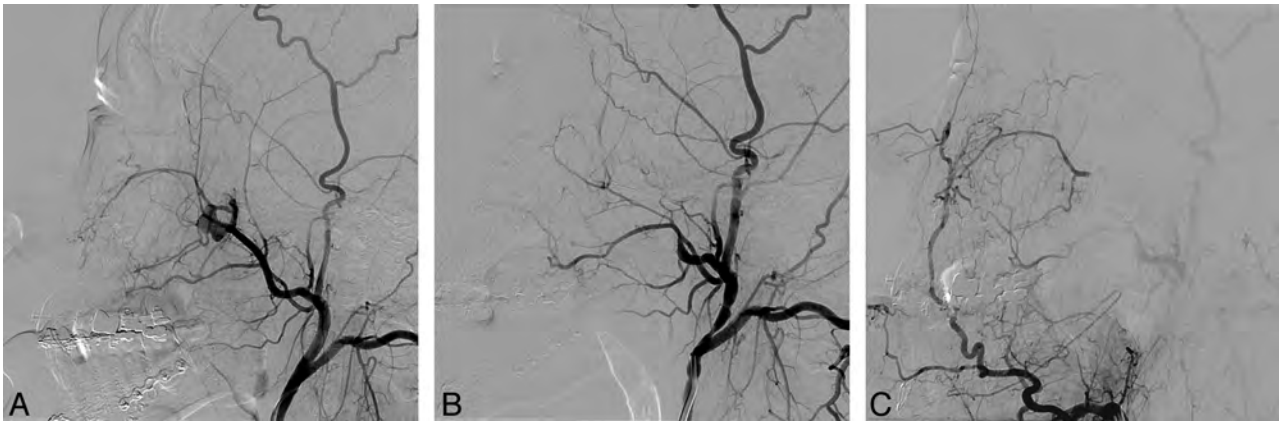


FIG 1. A 24-year-old male patient who presented with intractable epistaxis after sagittal split ramus osteotomy. *A*, Lateral left ECA arteriogram shows a pseudoaneurysm at the internal maxillary artery segment at the pterygopalatine fossa. *B*, A microcatheter was advanced to the distal maxillary artery beyond the pseudoaneurysm that was embolized by using a coil. *C*, Selective injection of the left facial artery shows collaterals from the ascending artery to the distal maxillary artery via the infraorbital artery. Note the absence of filling of the pseudoaneurysm from retrograde flow of the distal maxillary artery.

experience of endovascular management of 61 patients with acute head and neck bleeding from a variety of causes, with an emphasis on the angiographic results and the subsequent endovascular management according to the angiographic findings. We also compared the differences between patients with and without tumors related to the causative angiographic features, treatment outcome, and rate of endovascular retreatment.

MATERIALS AND METHODS

Patients

Sixty-one consecutive patients (49 men and 12 women; 17–79 years of age [mean age, 53 years]) who presented with acute hemorrhage in the head and neck and were subsequently treated by endovascular therapy between January 2002 and October 2012 were included from the neurointerventional data base of our institution. Three bleeding sites were classified according to the lesion location with or without an open wound in the mucosa or skin: bleeding or hematoma in the oral cavity ($n = 32$), nasal cavity ($n = 20$), or head and neck area ($n = 9$). The estimated causes of bleeding were head and neck cancers ($n = 36$) associated with prior radiation treatment ($n = 33$) or tumor bleeding itself ($n = 3$). Non-tumor-related bleeding ($n = 25$) included iatrogenic complications ($n = 13$), trauma ($n = 5$), refractory idiopathic epistaxis ($n = 3$), intraosseous mandibular arteriovenous malformation ($n = 1$), invasive fungal sinusitis ($n = 1$), a history of antiplatelet medication ($n = 1$), or history of liver transplantation ($n = 1$). Iatrogenic bleeding ($n = 13$) included postsurgery ($n = 8$), postbiopsy ($n = 4$), and post-C-line insertion ($n = 1$). Regarding the 8 patients with postsurgical bleeding, in 3, it occurred after maxillofacial plastic surgery; in 3, after endoscopic sinus surgery; in 1, after posterior cervical fusion; and in 1, after wide excision of recurrent left tonsillar cancer.

There was no commercial involvement in the design, conduct, or analyses of this study. The institutional review board of the Asan Medical Center approved both the study design and use of clinical data, and all patients provided written informed consent.

Procedures

All procedures were performed with the patient under local anesthesia. High-resolution digital fluoroscopy with biplane road-mapping capability and subtraction techniques was used. Angiography usually began by using a 4F angiocatheter with a 0.035-inch inner diameter, which can also be used as a guiding catheter for a microcatheter. If further procedures using a covered stent were required, a 9F guiding catheter was introduced.

Bilateral selective angiography of the common, internal, and external carotid arteries was performed. Regarding patients with neck bleeding or hematoma, both sides of the thyrocervical or costocervical trunks were also investigated. If the patients presented with massive bleeding or hemodynamic instability, the most likely injured vessels were first evaluated to manage the bleeding immediately, and the remaining vessels were studied if indicated.

Angiographic findings of pathologic vascular lesions were recorded as being caused by contrast leakage, pseudoaneurysms combined with contrast leakage, pseudoaneurysms, fistula, tumor, or hypervascular mucosal staining or as negative (without abnormal findings). Lesion locations were recorded as branches of the ECA, the carotid arteries including the internal carotid artery, the common carotid artery, and the carotid artery bulb or the thyrocervical or costocervical trunks.

If bleeding was localized to the ECA or its branches, they were occluded by using polyvinyl alcohol particles (150–250 μm), Gelfoam (Phadia, Uppsala, Sweden), glue, fibered platinum or detachable coils, or a combination of these embolic materials. Collateral cerebral circulation via the circle of Willis, leptomeningeal vessels, or the ophthalmic artery was evaluated by using compression angiographic studies if bleeding originated from the internal or common carotid artery. The covered nitinol stent (NITI-S Stent; Taewoong Medical, Seoul, Korea), composed of a self-expanding nitinol wire covered with polytetrafluoroethylene, was used in patients with incomplete collaterals determined on a compression test performed during the procedure or if there was

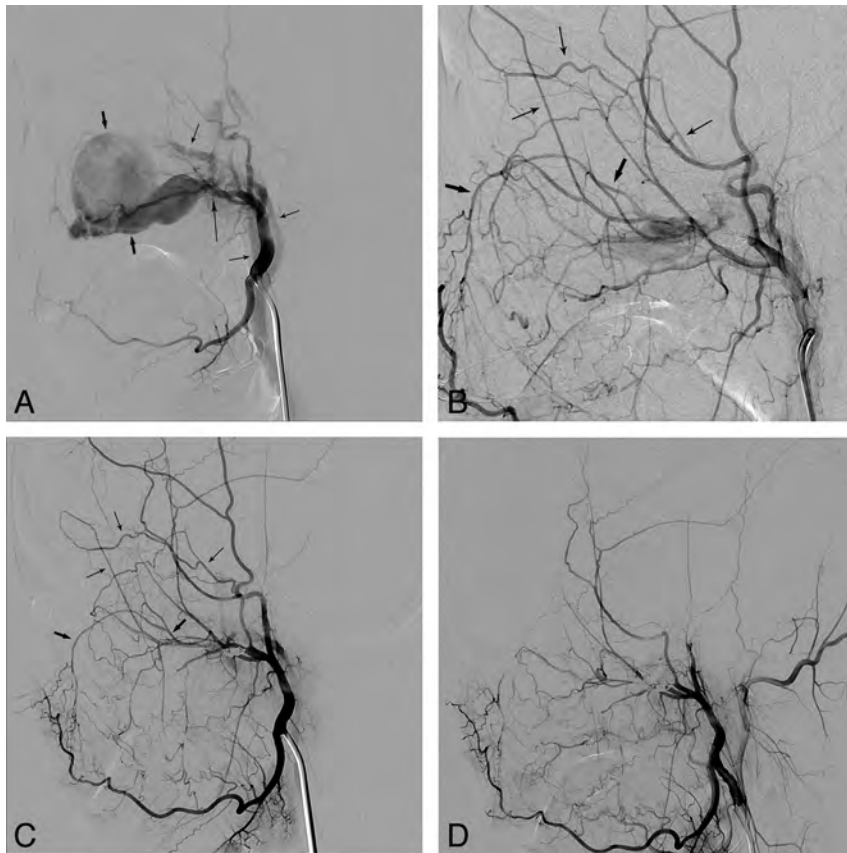


FIG 2. A 19-year-old female patient who presented with intractable epistaxis after maxillofacial plastic surgery. *A*, An external carotid angiogram shows a large pseudoaneurysm (*short thick arrows*) and a fistula (*long thin arrow*) with an arteriovenous shunt. Note the early filling veins (*short thin arrows*). *B*, An angiogram obtained following coil embolization of the maxillary artery at the aneurysm site shows retrograde filling of the remaining shunt through the infraorbital artery (*short thick arrows*) via the facial artery and the zygomatico-orbital branch (*short thin arrows*) of the superficial temporal artery. *C*, An angiogram obtained the following day revealed a slightly smaller but still remaining fistula with persistent bleeding. Note the retrograde filling as indicated on *B* by the same arrows. *D*, The bleeding was finally controlled after additional coil embolization via the zygomatico-orbital branch (*short thin arrows, B*) into the fistula.

no time to perform occlusion or a compression test due to unstable vital signs due to massive bleeding.⁷ The diameters and lengths of the stents were 10 × 70 mm or 10 × 50 mm. Because the stent adheres to the polytetrafluoroethylene graft by using polyurethane, it is composed of polyurethane on its outer surface and the polytetrafluoroethylene sheet on its inner surface.⁸ Antiplatelet medication with 200 mg of aspirin and a loading dose of 300 mg of clopidogrel was administered immediately after stent placement if patients were not already taking these medications. After the revascularization procedure, maintenance doses of 100 mg of aspirin and 75 mg of clopidogrel were given; 75 mg of clopidogrel for at least 6 months and 100 mg of aspirin as a permanent medication were also given. The common carotid artery or ICA was completely occluded in patients with uncontrolled massive carotid hemorrhage if good collateral cerebral circulation was seen on the compression test.

We collected data on the procedural and clinical outcomes, complications resulting from the procedures, additional repeated treatments, and survival data from the patients' medical records.

RESULTS

Angiographic Findings

The On-line Table summarizes the patients' angiographic findings and the baseline characteristics. Forty patients (66%) presented with bleeding signs at the time of their angiographic procedure, including 20 cases of pseudoaneurysm (Fig 1), 10 cases of contrast leakage, and 10 cases of pseudoaneurysm combined with contrast leakage. A fistula was present in a patient with a large pseudoaneurysm caused by postoperative injury of the maxillary artery in the pterygopalatine fossa (Fig 2). No bleeding sign was seen in 21 patients (34%), including 17 with hypervascular tumor or mucosal staining (28%) and 4 with negative findings (6%). Angiographic bleeding foci were identified as CBS in 25% (15/61) and non-CBS in 75% (46/61) of our patients. CBS involved the internal ($n = 6$) or common ($n = 8$) carotid artery or the carotid artery bulb ($n = 1$). There was non-CBS in the ECAs in 40 patients, in the thyrocervical trunks in 2 patients, and in 4 patients with negative angiographic findings. Thirty-six patients (36/61, 59%) were identified as having tumor-related bleeding versus 25 patients (25/61, 41%) with non-tumor-related bleeding.

Procedural Outcome

Forty-six patients underwent transarterial embolization treatment: The lesions were located in the ECAs in 40 patients, at the thyrocervical trunks in 2, and neg-

ative angiographic findings existed in 4 patients. For these patients with negative findings, embolization of the ipsilateral ECA branches with polyvinyl alcohol particles on the bleeding side was performed in 3 for prevention of rebleeding, while the other patient was embolized on both sides of the ECA branches. As to the 15 patients with bleeding lesions located on the ICA, common carotid artery, or bulb, 10 underwent covered stent insertion and the other 5 underwent ICA or common carotid artery occlusion by embolization.

Clinical Outcome and Recurrent Bleeding

Initial hemostasis was achieved in all patients. There were 17 (28%, 17/61) patients who underwent repeated endovascular management due to rebleeding. Seven of these patients experienced recurrent bleeding during the same hospital stay; 4 had rebleeding in the same vascular locations, and 3, in different locations. Five of these 7 patients had head and neck cancers, and 3 presented with CBS. Ten patients were readmitted due to rebleeding after discharge (Fig 3), and they subsequently underwent endovascular retreatment at a mean interval of 2 months (range,

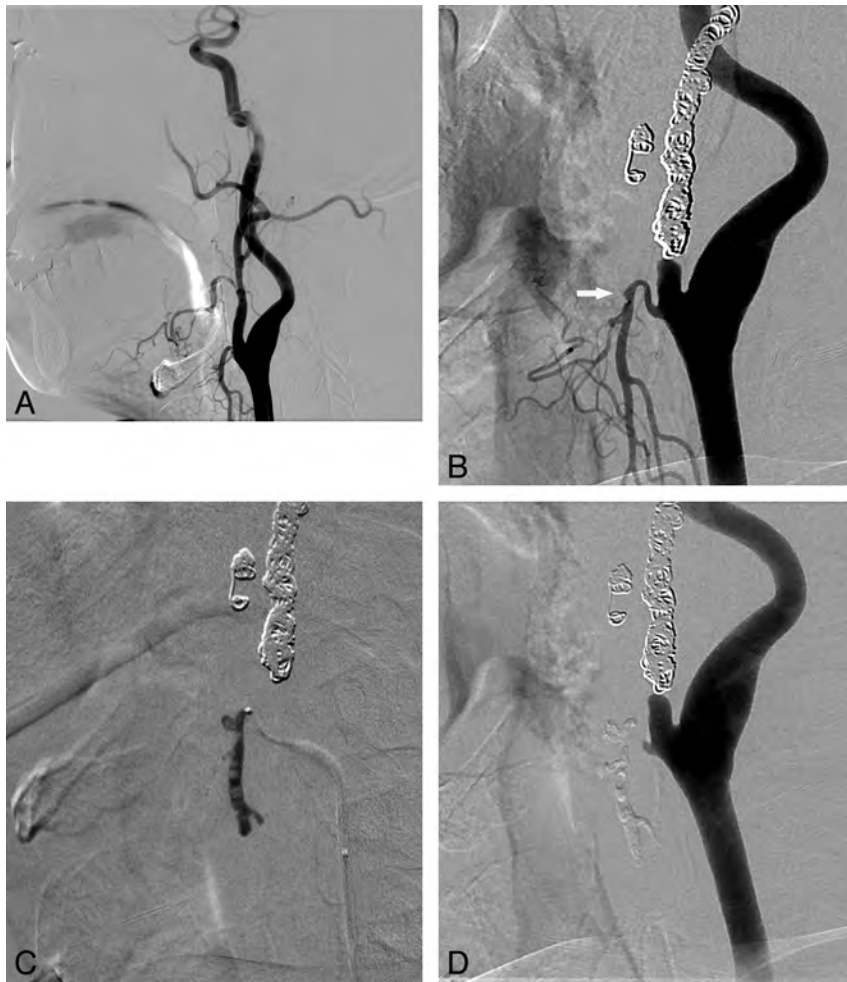


FIG 3. Endovascular treatment for recurrent bleeding approximately 2 months and 15 days after the initial embolization of the left ECA in a 45-year-old male patient with tonsil cancer. *A*, At the time of the first bleeding, the right facial and nearby maxillary arteries showing irregularities were regarded as the origin of the initial bleeding site and were embolized with coils as shown in *B*. *B*, Left common carotid arteriogram obtained at the time of the second bleeding reveals a tiny pseudoaneurysm (*white arrow*) in the proximal segment of the left superior thyroidal artery. Note the coils used in the previous embolization. *C*, Glue was used for embolization of the left superior thyroidal artery, and the final angiogram shows no residual pseudoaneurysm filling. The patient's bleeding was controlled thereafter.

1–6 months) after their initial endovascular treatment: 8 patients had head and neck cancers (5 of these 8 patients presented with CBS), 1 had juvenile angiofibroma, and 1 had an intraosseous mandibular arteriovenous malformation.

Complications and Follow-Up

One patient experienced occlusion of the ipsilateral middle cerebral artery branches during the covered stent placement and acute infarction in the corresponding vascular territory, probably due to no premedication with an antiplatelet agent. This patient presented with massive neck bleeding and had a history of radiation therapy for supraglottic cancer. The bleeding originated from rupture of the exposed carotid artery through the ulcerated mucosa. When he was brought to the angiography suite with manual compression of the bleeding site, his vital signs were unstable due to the uncontrollable massive bleeding, despite an urgent transfusion. The angiogram showed a common carotid artery blowout with massive, active, contrast leakage. Covered stent placement

was immediately introduced to control the active bleeding. An angiogram obtained after stent-graft placement showed successful hemostasis and multiple embolic occlusions of the MCA branches. MR imaging performed the following day showed acute right MCA territorial infarction. The patient's neurologic status subsequently improved and became stable (modified Rankin Scale = 2) for 17 months; then the patient was lost to follow-up (Fig 4).

Delayed cerebral infarcts were present 3 or 4 months after endovascular treatment, respectively, in 2 patients who underwent stent placement for CBS. The deficit seen in the first patient resulted from embolization or ligation of the internal carotid artery performed to control recurrent CBS after stent placement. In the second patient, it resulted from occlusion of the covered stent or local progression of nasopharyngeal carcinoma. No neurologic deficits were found in the patients who initially underwent obliteration of the entire involved carotid artery by using coil embolization.

Extrusion of the coils previously placed for embolization was observed in 4 patients in whom the carotid arteries had been exposed to the infected wound cavity. These patients subsequently underwent ligation ($n = 3$) or re-embolization ($n = 1$) of the involved carotid artery. No brain abscess developed in our series, and no complications were seen in patients who underwent embolization of the ECA or its branches.

Of the 36 patients with head and neck cancers, 8 did not experience any further bleeding events during the mean follow-up time of 27 months (range, 12–59 months). Twenty-four of these patients with cancer died due to recurrent or progressive tumor growth–related problems, with a mean survival time of 3 months (range, 1–10 months). As for the other 4 patients with cancer, 3 were lost to follow-up 1 month after the initial endovascular treatment, and the other was lost after 3 months.

Among the 10 patients who presented with CBS and underwent covered stent placement, 7 died within 1–10 months (median, 2 months). The exact cause of death could not be determined in these patients because they were regarded as having terminal-stage cancer. Two patients were lost to follow-up after 1 month. One patient with an infarct in the right middle cerebral artery territory was followed for 17 months (Fig 4).

Two patients without tumor died of traumatic intracranial hemorrhage: One patient died from a car collision 1 week follow-

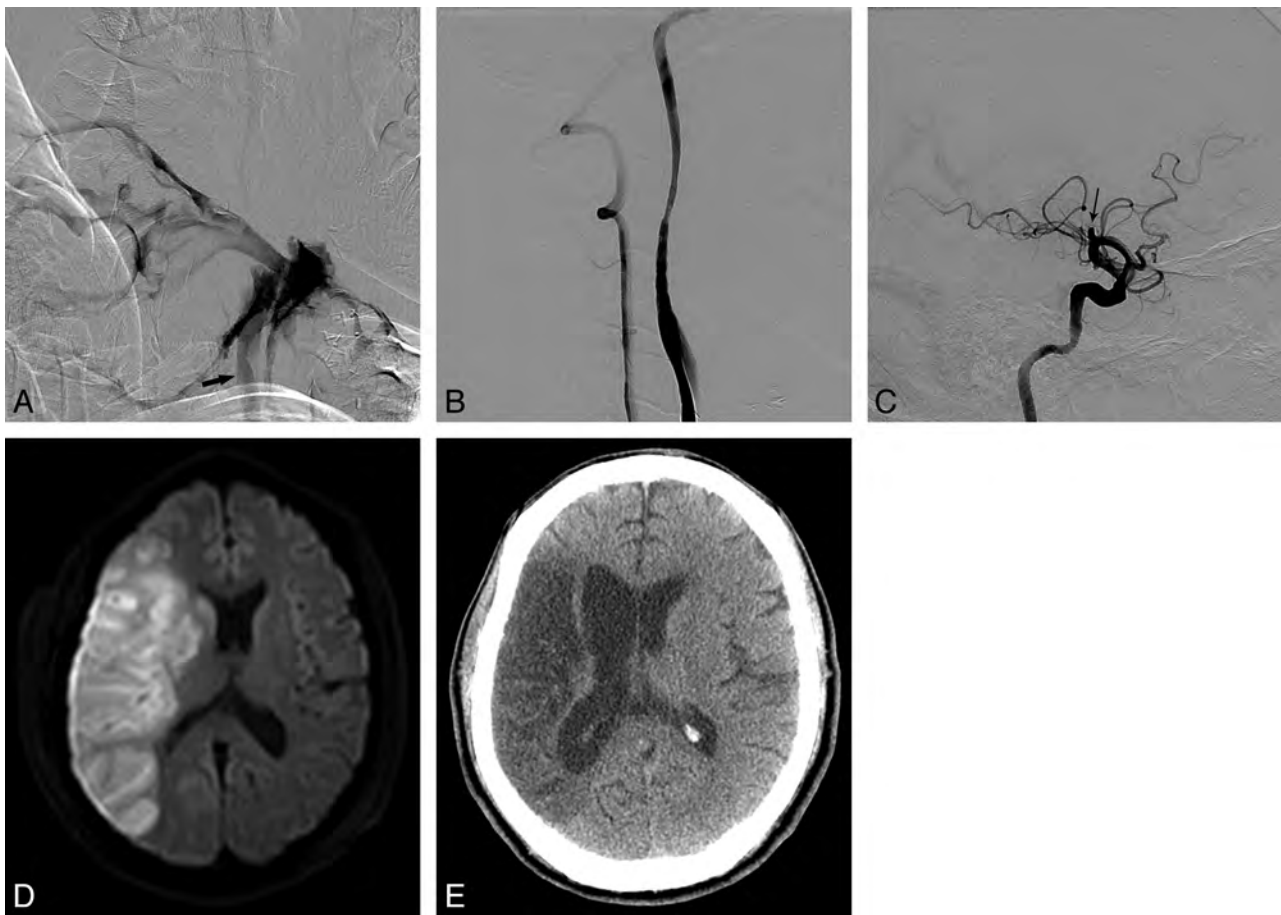


FIG 4. A 51-year-old male patient with a history of supraglottic cancer who presented with massive bleeding at the ulcerative wound site in the right neck. After tracheostomy, he became drowsy and developed left-sided weakness in both the upper and lower extremities. *A*, A common carotid arteriogram shows extensive contrast leakage due to massive bleeding. No filling of the internal carotid artery from the common carotid artery (*arrow*) was seen. *B*, Bleeding was stopped following deployment of a covered stent. *C*, There is an occlusion of the right middle cerebral artery at the proximal M2 segment (*arrow*). *D*, Diffusion-weighted image obtained the next day shows a territorial infarct in the right MCA territory. *E*, CT scan obtained 17 months later shows the old infarction in the right middle cerebral artery territory, though the patient's weakness had improved and he walked without assistance.

ing endovascular treatment, and the other died of an event related to liver transplantation 7 months after embolization.

DISCUSSION

Our study revealed that angiographically detected active bleeding signs, such as contrast leakage and/or pseudoaneurysm requiring urgent endovascular treatment, were noted in 66% of our patients. As to the patients in whom a pseudoaneurysm was only identified at the time of the angiography, management similar to that of the patients with active bleeding was also required because the risk of delayed or repetitive massive hemorrhage is very high, even though these patients may not present with active bleeding when brought to the angiography suite. Nonselective particle embolization in the external carotid arterial branches was sufficient as a preventive measure in those patients who showed only hypervascular staining (28%) or normal angiographic findings (6%).

When we categorized our patients as CBS versus non-CBS according to the lesion involvement, 25% were CBS and immediately required either reconstructive or deconstructive management of the carotid artery to control life-threatening bleeding, as we previously reported.⁷⁻⁹ Non-CBS, in 75% of our patients, included those with lesions located at the branches of the ECA or the

thyrocervical trunks. An active angiographic bleeding sign of contrast leakage and/or a pseudoaneurysm was seen in 56% of patients who presented with non-CBS, thus indicating direct injury to the arterial branches. When one treats injured vessels as a bleeding focus in branches of the ECA, the stumps proximal and distal to the lesions should be identified and embolized together, as shown in Fig 1. For example, when there is a pseudoaneurysm or fistula in the maxillary artery, the distal maxillary artery beyond the bleeding focus of the injured vessel should be identified by selective angiography of the ipsilateral facial artery. If only the proximal segment is embolized, as shown in Fig 2, a collateral to the distal maxillary artery, such as the facial artery, can flow into the injured vessel in retrograde fashion. Therefore, a collateral through the other side of a stump may cause bleeding recurrence due to incomplete embolization.

When we divided our patients into tumor-versus-nontumor groups, we found that head and neck cancer was the main cause of acute bleeding in our series and was present in 59% of the patients. Previous radiation therapy, recurrent carcinoma, and surgical complications such as infection and fistula formation may all contribute to the onset of such bleeding and may make

controlling it more difficult.^{13,15,16} Repeated bleeding in such patients is also a common and troublesome problem.¹⁷ In our series, the rate of endovascular retreatment for rebleeding in patients with cancers (36%) was higher compared with that for patients without tumor (16%), which can be attributed to carcinoma recurrence, radiation therapy, or surgical complications (Fig 3).

Iatrogenic acute bleeding was found in 21% (13 patients) of our patients and included those who had undergone surgery ($n = 8$), biopsy ($n = 4$), and C-line-insertion-associated bleeding complications ($n = 1$). Among the 8 patients who presented with uncontrolled oronasal hemorrhage after surgeries, 5 showed active contrast leakage or pseudoaneurysm on angiography. Maxillofacial surgical procedures, such as orthognathic surgery, may be associated with significant blood loss and, infrequently, life-threatening hemorrhage caused by injury to the vascular structures in the pterygopalatine fossa, such as the pterygoid venous plexus, the descending palatine arteries, the sphenopalatine arteries, or the maxillary artery itself, leading to acute epistaxis.¹⁸ Pooled data revealed that in 72% of the Le Fort osteotomies, an arterial source was the culprit, whereas in almost 19% of the cases, the source of hemorrhage was venous. In the remaining cases, the exact source was unidentifiable. In mandibular sagittal split osteotomies, an arterial source was the cause of hemorrhage in 48.2%, and a venous source, in 20.6% of the cases.¹⁹ In cases in which damage to the inferior alveolar artery, internal maxillary artery, or facial artery was suspected, blood loss ranged from 1500 to 3000 mL.²⁰ In these cases, obvious bleeding signs will be more likely on angiograms compared with those with lesions located in veins or with unidentifiable sources.

There were 5 trauma patients (8%) in our series, and all presented with massive bleeding. Trauma is the ninth leading cause of death worldwide, and traumatic injury of a vessel is a relatively common occurrence in the emergency department.²¹ With injury caused by either blunt or penetrating forces, these patients presented with acute bleeding due to laceration or fistula of vessels as a result of penetrating injury or bone fractures. For these patients, anterior and posterior nasal packing as the initial measure used to manage massive oronasal hemorrhage is supported by the published medical literature.²² Other conventional techniques, such as cauterization or ligation of the ECA and reduction and fixation of a facial fracture, can secure hemostasis in most remaining cases. Infrequently, the bleeding may become intractable and thus life-threatening.^{23,24} If conventional techniques fail to stop the bleeding, transarterial embolization of relevant vessels may be effective as it was in our patients in whom all the bleeding foci were identified at the branches of the ECA, which were successfully embolized without rebleeding or complications after transarterial embolization.

Although endovascular management for acute head and neck bleeding has been extensively reported, especially regarding the management of CBS and bleeding with head and neck cancers, little emphasis has been placed on studying the angiographic findings or on the differences in treatment outcome and the rate of endovascular retreatment between patients with and without tumors. In this study, we present our 11 years of clinical experience with endovascular management of head and neck acute bleeding caused by various pathologic etiologies. We studied the angio-

graphic findings and compared the differences in the angiographic findings, endovascular techniques, clinical outcomes, and the rate of endovascular retreatment among patients with and without tumors.

There are several limitations to our study. Because our series was a retrospective analysis, comparative application of different endovascular methodologies used to control the bleeding was not tested. Even though our series is rather large, the incidence and comparison of CBS versus non-CBS or tumor-related versus non-tumor-related bleeding can be more accurately evaluated or compared by performing a multicenter registry.

CONCLUSIONS

Acute bleeding in the head and neck is a common life-threatening situation. If conventional techniques fail to stop the hemorrhaging, conventional angiography can have an important role in localizing the bleeding foci and controlling the bleeding by endovascular treatment, which is a safe and effective therapy for the management of hemorrhage.

REFERENCES

1. Pereira J, Phan T. **Management of bleeding in patients with advanced cancer.** *Oncologist* 2004;9:561–70
2. Dhiwakar M, Khan NA, McClymont LG. **Surgical resection of cutaneous head and neck lesions: does aspirin use increase hemorrhagic risk?** *Arch Otolaryngol Head Neck Surg* 2006;132:1237–41
3. Bachar G, Esmat N, Stern S, et al. **Transarterial embolization for acute head and neck bleeding: eight-year experience with emphasis on rebleeding risk in cancer patients.** *Laryngoscope* 2013;123:1220–26
4. Sesterhenn AM, Iwinska-Zelder J, Dalchow CV, et al. **Acute haemorrhage in patients with advanced head and neck cancer: value of endovascular therapy as palliative treatment option.** *J Laryngol Otol* 2006;120:117–24
5. Remonda L, Schroth G, Caversaccio M, et al. **Endovascular treatment of acute and subacute hemorrhage in the head and neck.** *Arch Otolaryngol Head Neck Surg* 2000;126:1255–62
6. Toyoda T, Sawatari K, Yamada T, et al. **Endovascular therapeutic occlusion following bilateral carotid artery bypass for radiation-induced carotid artery blowout: case report.** *Radiat Med* 2000;18:315–17
7. Pyun HW, Lee DH, Yoo HM, et al. **Placement of covered stents for carotid blowout in patients with head and neck cancer: follow-up results after rescue treatments.** *AJNR Am J Neuroradiol* 2007;28:1594–98
8. Kim HS, Lee DH, Kim HJ, et al. **Life-threatening common carotid artery blowout: rescue treatment with a newly designed self-expanding covered nitinol stent.** *Br J Radiol* 2006;79:226–31
9. Roh JL, Suh DC, Kim MR, et al. **Endovascular management of carotid blowout syndrome in patients with head and neck cancers.** *Oral Oncol* 2008;44:844–50
10. Chang FC, Lirng JF, Luo CB, et al. **Patients with head and neck cancers and associated postirradiated carotid blowout syndrome: endovascular therapeutic methods and outcomes.** *J Vasc Surg* 2008;47:936–45
11. Chang FC, Lirng JF, Luo CB, et al. **Carotid blowout syndrome in patients with head-and-neck cancers: reconstructive management by self-expandable stent-grafts.** *AJNR Am J Neuroradiol* 2007;28:181–88
12. Warren FM, Cohen JI, Nesbit GM, et al. **Management of carotid 'blowout' with endovascular stent grafts.** *Laryngoscope* 2002;112:428–33
13. Chaloupka JC, Putman CM, Citardi MJ, et al. **Endovascular therapy for the carotid blowout syndrome in head and neck surgical**

- patients: diagnostic and managerial considerations. *AJNR Am J Neuroradiol* 1996;17:843–52
14. Ketcham AS, Hoyer RC. **Spontaneous carotid artery hemorrhage after head and neck surgery.** *Am J Surg* 1965;110:649–55
 15. Wong SJ, Machtay M, Li Y. **Locally recurrent, previously irradiated head and neck cancer: concurrent re-irradiation and chemotherapy, or chemotherapy alone?** *J Clin Oncol* 2006;24:2653–58
 16. Macdonald S, Gan J, McKay AJ, et al. **Endovascular treatment of acute carotid blow-out syndrome.** *J Vasc Interv Radiol* 2000;11:1184–88
 17. Chen YF, Lo YC, Lin WC, et al. **Transarterial embolization for control of bleeding in patients with head and neck cancer.** *Otolaryngol Head Neck Surg* 2010;142:90–94
 18. Lanigan DT, Hey JH, West RA. **Major vascular complications of orthognathic surgery: hemorrhage associated with Le Fort I osteotomies.** *J Oral Maxillofac Surg* 1990;48:561–73
 19. Khanna S, Dagum AB. **A critical review of the literature and an evidence-based approach for life-threatening hemorrhage in maxillofacial surgery.** *Ann Plast Surg* 2012;69:474–78
 20. Lanigan DT, Hey J, West RA. **Hemorrhage following mandibular osteotomies: a report of 21 cases.** *J Oral Maxillofac Surg* 1991;49:713–24
 21. Radvany MG, Gailloud P. **Endovascular management of neurovascular arterial injuries in the face and neck.** *Semin Intervent Radiol* 2010;27:44–54
 22. Cogbill TH, Cothren CC, Ahearn MK, et al. **Management of maxillofacial injuries with severe oronasal hemorrhage: a multicenter perspective.** *J Trauma* 2008;65:994–99
 23. Ardekian L, Samet N, Shoshani Y, et al. **Life-threatening bleeding following maxillofacial trauma.** *J Craniomaxillofac Surg* 1993;21:336–38
 24. Tung TC, Tseng WS, Chen CT, et al. **Acute life-threatening injuries in facial fracture patients: a review of 1,025 patients.** *J Trauma* 2000;49:420–24

Recanalization of Symptomatic Vertebral Ostial Occlusion in Patients with Acute or Subacute Stroke

S. Park, D.-G. Lee, J.H. Shim, D.H. Lee, and D.C. Suh



SUMMARY: Vertebral artery recanalization in symptomatic stenosis/occlusion remains controversial, as no definite evidence exists regarding this topic. There are only a few reports regarding the feasibility and safety of recanalization in the first segment of the vertebral artery with atherosclerotic vertebral ostial occlusion. We report our experience treating first segment occlusion in 8 patients and present a balloon protection technique used to reduce the thromboembolic burden during the stent placement procedure. The outcome at 3 months showed an mRS ≤ 2 except for a patient with a poor initial status with basilar artery occlusion. Revascularization of a rather long first segment occlusion is technically feasible and can be safely performed by use of embolic protection methods.

ABBREVIATIONS: BA = basilar artery; DUS = Doppler ultrasonography; NIHSS_o = National Institutes of Health Stroke Scale on admission; PcomA = posterior communicating artery; VA = vertebral artery; V1 = first segment of the vertebral artery.

Atherosclerotic lesions of the vertebral artery (VA) origin are a potential cause of posterior circulation ischemia, which has approximately a 20% to 50% risk for vertebrobasilar TIA or stroke.¹ The VA ostium is known to be the most common site for atherosclerosis of the posterior circulation.² Patients with symptomatic severe (> 70%) ostial VA stenosis face an 11% annual risk for recurrent stroke or TIA while receiving medical treatment.³

Early understanding of the stroke mechanism of VA ostial lesions was focused on their hemodynamic nature, which commonly presents with TIA including dizziness.⁴ After a few case series that described an embolic infarct originating from vertebral ostial occlusive disease,⁵ artery-to-artery embolism was also considered as an important cause of the stroke mechanism in lesions in the first segment of the VA (V1).⁶ A large series of patients revealed that half of the artery-to-artery embolic strokes in the posterior circulation were the result of VA ostial lesions.⁷ The presence of a clot in the vertebral ostial plaque provides the cause-and-effect relationship between vertebral arterial ostial lesions and posterior circulation stroke.⁸ Even a large ulcer in the verte-

bral arterial ostium has been described as adding to the possibility of the vertebral arterial ostium as a source of emboli.⁹

The optimal treatment of patients with symptomatic severe ostial VA stenosis is still unclear.³ The only randomized trial comparing endovascular with medical treatment is the Carotid and VA Transluminal Angioplasty Study.¹⁰ This study did not show a separate result for the small number of its patients ($n=16$) with VA stenosis, though it failed to demonstrate the benefit of angioplasty of carotid and vertebral stenosis.

Although several articles have dealt with revascularization of vertebral ostial lesions, they mostly have described revascularization of vertebral arterial stenosis.¹¹ To our knowledge, only a few case reports have demonstrated anecdotal evidence of revascularization for vertebral ostial occlusion.¹² Therefore, we present the revascularization procedure and the outcome of vertebral ostial occlusion in strokes related to artery-to-artery embolism.

MATERIALS AND METHODS

Case Series

Eight consecutive patients (12%) were identified among 68 consecutive patients who were treated by angioplasty and/or stent placement for atherosclerotic stenosis or occlusion in the V1 segment between January 2002 and October 2012. There were 7 men and 1 woman with a median age of 67 years (age range, 54–75 years). Informed consent was obtained from each patient or their relative. This study was approved by our institutional review board.

The patients' baseline characteristics are listed in the On-line Table. Patients with acute stroke who were within 6 hours of symptom presentation ($n=1$) were treated according to our insti-

Received April 11, 2013; accepted after revision May 31.

From the Department of Radiology and Research Institute of Radiology (S.P., D.-G.L., J.H.S., D.H.L., D.C.S.), University of Ulsan, College of Medicine, Asan Medical Center, Seoul, Korea; and Department of Radiology (S.P.), Korea University Anam Hospital, Seoul, Korea.

Please address correspondence to Dae Chul Suh, MD, Department of Radiology, University of Ulsan, College of Medicine, Asan Medical Center, 88, Olympic-ro 43-gil, Songpa-Gu, Seoul 138–736, Korea; e-mail: dcsuh@amc.seoul.kr

Indicates article with supplemental on-line table.

<http://dx.doi.org/10.3174/ajnr.A3681>

tution's inclusion criteria, which had been modified after other previously reported IV or intra-arterial thrombolytics.¹³ Patients with vertebrobasilar insufficiency or lacunar syndromes where vascular imaging results did not show any corresponding ischemic lesion were excluded from the analysis. All patients underwent a standard etiologic work-up, including blood tests (hemoglobin, white cell and platelet counts, prothrombin time, activated partial thromboplastin time, serum electrolytes, glucose, urea, creatinine, transaminases, and cholesterol levels); 12-lead electrocardiography; cranial CT and/or MR imaging (axial T2, intermediate-weighted images, fluid-attenuated inversion recovery, time-of-flight MR angiography, DWI, and contrast-enhanced MRA of the cervical vessels at 1.5T or 3T). The following ancillary investigations were carried out at the discretion of the neurologist treating the patient with stroke: neurovascular sonography, perfusion-weighted images, CTA, transthoracic echocardiography, and 24-hour electrocardiographic monitoring. The severity of the neurologic deficit was assessed on admission by a neurologist by use of the National Institutes of Health Stroke Scale on admission (NIHSS_o) and is shown in the On-line Table. The study patients did not have cardiogenic problems suggesting the possibility of cardioembolism. The patient symptoms and signs varied at the time of presentation according to the time from the onset or the extent and degree of the acute ischemic lesion seen on DWI. Although there was only dizziness experienced by 2 patients at the time of hospital admission, both of these patients had a history of fluctuating neurologic deficits including dysarthria or sensory changes in the upper extremity.

Two patients (patients 5 and 6) had taken oral antiplatelet agents (ie, aspirin and/or clopidogrel) and a statin for 1 month when the severe VA ostial stenosis related to dizziness was detected. One patient (patient 8) had taken aspirin for 1 month for stroke prevention and without undergoing any vascular imaging. The remaining patients did not take any antiplatelet medication, probably because they did not have any symptoms until an acute stroke developed because of VA occlusion.

Cerebral Angiography and Revascularization Procedures

The lesion characteristics were then further studied by DSA. The contralateral VA, the posterior communicating artery (PcomA) from the anterior circulation, and the thyrocervical and costocervical trunks were evaluated to determine the collateral supply distal to the occluded vertebral segment. The PcomA size was designated as normal if it was visible on MRA without any hypoplasia of the ipsilateral P1 segment of the posterior cerebral artery.

The procedures were performed via the transfemoral route with the patient under local anesthesia. Cerebral angiography, which was performed with a 4F angiocatheter, included examination of both internal carotid arteries and both subclavian arteries, including both VAs. An optimal subclavian arteriogram was obtained to reveal the entire segment of the occluded VA by demonstration of collateral channels via the thyrocervical or costocervical trunks, as well as the presence of the anterior spinal artery and the status of the intracranial posterior circulation including the basilar artery (BA). The angiographic assessment of the external carotid artery-VA anastomosis via the occipital artery and the

ascending pharyngeal artery, both of which are known to be effective collateral pathways in proximal VA stenosis, was also performed unless collateral filling of the VA was demonstrated via the ascending or deep cervical artery from the subclavian artery.^{14,15}

After analysis of the complete angiogram, we inserted a 6–9F guiding catheter in the subclavian artery. After placement of the guiding catheter, a 4F catheter was then passed along a 0.035-inch guidewire through the occluded segment and a distal balloon (ie, PercuSurge; Medtronic, Minneapolis, Minnesota), was then introduced via the 4F angiocatheter, as shown in Figs 1 and 2. The location of the 4F catheter tip in the free lumen was identified by the suctioning of thrombotic debris in the distal segment beyond the occlusion and the regurgitation of blood. Once protective distal occlusion was achieved, suction of the proximal ICA segment was followed by angioplasty and/or stent placement.

If the position of the guiding catheter was unstable, we inserted an additional sturdy guidewire as a supportive wire into the ipsilateral brachial artery. The occluded segment was probed by using a 0.014–0.035-inch guidewire.^{16–18} In 3 patients, we used the exchange technique after passing the occluded V1 segment by using a combination of a 4F angiocatheter and a 0.035-inch guidewire (Figs 1 and 2). Once the guidewire was introduced, subsequent angioplasty by use of a 2–4-mm diameter angioplasty balloon was followed by stent placement. The degree and occlusion length were measured with clear delineation of the vertebral ostium with pixel shift on DSA. A self-expandable stent was placed with minimal protrusion to the subclavian artery to minimize distal migration of the stent and to properly cover the atherosclerotic lesion in the occluded segment. Poststenting angioplasty was performed if there was residual stenosis. In 2 patients with vertebral ostial occlusion with concomitant embolic occlusion of the basilar artery demonstrated on MRA and DSA, we revascularized the BA by using a self-expandable stent because mechanical thrombolysis or the introduction of urokinase to reduce the clot burden was not effective.

Preprocedural antiplatelet conditioning with 200 mg of aspirin and a loading dose of 300 mg of clopidogrel was given if the patients were not already taking these medications. The heparin was adjusted to achieve an activated clotting time of 2–2.5 times that of the baseline. After the revascularization procedure, maintenance doses of 100 mg of aspirin and 75 mg of clopidogrel were given. Also given were 75 mg of clopidogrel for at least 6 months and 100 mg of aspirin as a permanent medication.

Immediate results were evaluated according to the angiographic patency of the stented segment. Postprocedural precontrast CT or MR imaging scanning was then performed within 24 hours to identify any new infarction or hemorrhage. The NIHSS_o and a 3-month mRS were compared to assess the clinical results of the procedures. Follow-up imaging was obtained in 4 patients with Doppler ultrasonography (DUS) ($n=2$) or CTA ($n=2$). For all patients treated with stent placement, routine angiographic follow-up was recommended 6–12 months after the procedure. However, patients who were at high risk for procedural complications during angiography and who had no symptoms or signs of ischemia, as well as patients who declined the recommendation, did not undergo routine follow-up angiography and, instead, underwent CTA or transcranial DUS which are noninvasive diagnostic tools used for follow-up in patients who have undergone

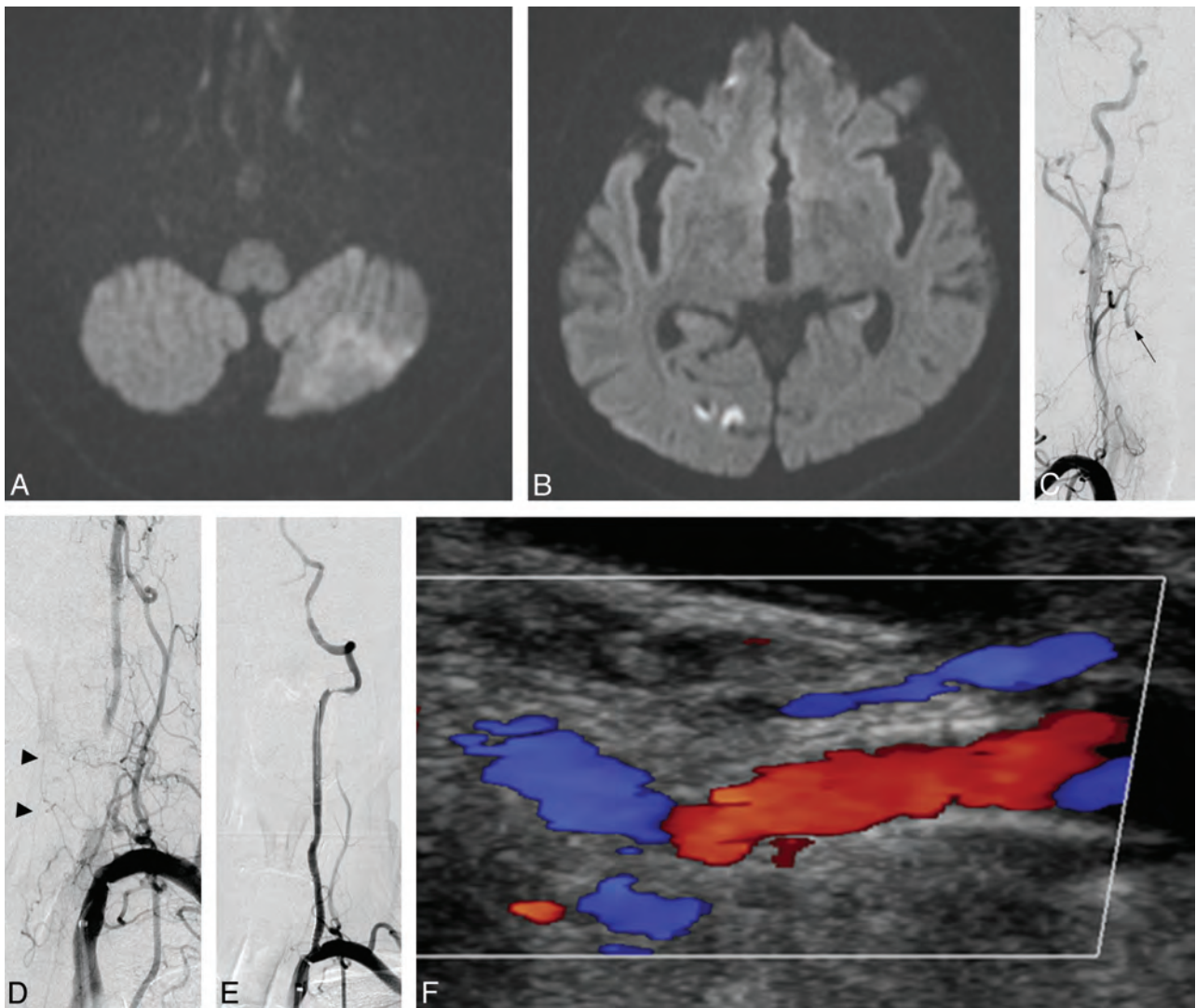


FIG 1. A 70-year-old man presented with severe dizziness and ataxia. DWI showed a wedge-shaped infarct in the left cerebellar hemisphere (A) and multifocal infarcts in the right occipital lobe (B). C, An angiogram of the right subclavian artery showed occlusion of the hypoplastic right VA at the C4 level (arrow). Both internal carotid arteriograms showed poor development of both PcomAs (not shown). D, An arteriogram of the left subclavian artery shows occlusion of the V1 segment. Note the filling of the anterior spinal artery arising from the costocervical trunk in the late phase of the angiogram (arrowheads). E, Final angiogram after stent placement shows good patency of the occluded VA and good filling of the posterior circulation. F, Good patency of the stented lumen was seen on follow-up DUS 4 months later and without any neurologic deficit (mRS=0).

V1 stent placement, as we already reported.¹⁹ We evaluate the mobile V1 segment with DUS because, in most patients, the stented segment can be seen without difficulty. The implanted stent is also a good anatomic landmark for clear visualization of the lumen. Restenosis on CTA was determined by reconstituted delineation of traced-stented vessel segments by Advanced Vessel Analysis (Siemens, Erlangen, Germany) along the stented vessel.

RESULTS

Angiographic and Imaging Findings

Angiographic analysis revealed that all vertebral occlusions occurred in the dominant VA. The mean length of the occlusions was 43 mm (range, 10–69 mm). The contralateral VA was hypoplastic in all patients; it barely filled the BA ($n=4$), only filled the posteroinferior cerebellar artery ($n=2$), and was occluded in the proximal segment ($n=2$). The PcomA filled the distal aspect of the BA in 2 cases. Other patients showed no PcomA contribution

to the BA flow. The PcomA was not well developed in any of these patients, thus suggesting that hypoperfusion-associated stump embolism was the primary stroke mechanism in these patients. The proximal stump of the V1 occlusion in the subclavian artery was barely able to be identified, thus suggesting that the occlusion was related to an atherosclerotic ostial plaque lesion leading to a tight occlusion. The deep cervical artery contribution was the primary angiographic collateral at the C3–4 levels of the VA distal to the occluded segment, as seen on DSA. The anterior spinal artery filling from the costocervical trunk was identified in 2 patients. There was no collateral development via the anterior spinal artery in our study patients.

Results revealed acute infarct in the cerebellum, brain stem, thalami, and occipital lobes in all 8 patients. The infarct lesions seen on DWI varied in size from focal or localized to territorial. Two patients had focal ischemic lesions in the middle cerebral

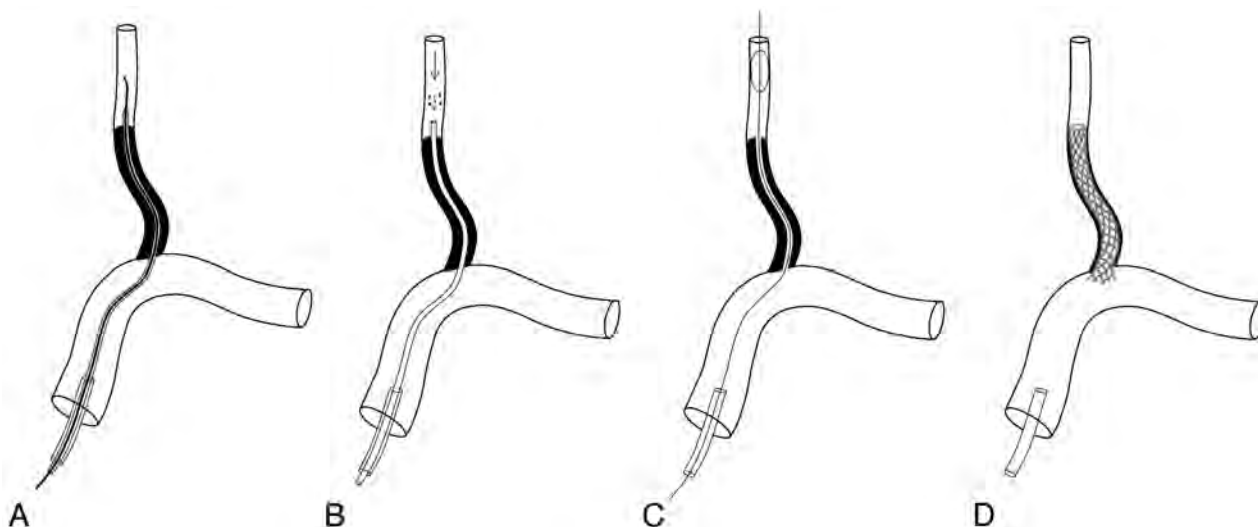


FIG 2. Diagram showing the recanalization process in patients with V1 segment occlusion. A, Smooth probing and traversing of the occluded segment by a 0.035-inch guidewire are followed by the introduction of a 4F angiocatheter (or a guiding catheter), which can also allow the passage of a PercuSurge protective balloon guidewire. B, Passage of the occluded segment can be identified by free regurgitation of blood as well as suction of debris beyond the occluded segment. Under distal balloon protection (C), angioplasty is followed by stent placement (D).

artery territory, probably caused by concomitant perforator infarcts.

Recanalization Outcome

Endovascular revascularization was successful in 7 of 8 patients. Revascularization failed in 1 patient because of failed guidewire passage through the occluded vertebral ostium. Each patient's data are summarized in the On-line Table. Poststenting angioplasty was required in all patients because of elastic recoiling of the vertebral ostial lesion after angioplasty and stent placement. After postdilatation, there was no significant residual stenosis. In 2 patients with concomitant BA occlusion that was identified as a thromboembolism on both MRA and DSA, we deployed a self-expanding stent in the BA in 1 patient and thrombolysis with 100,000 U of urokinase followed by a self-expanding stent in the BA in the other patient.

There were neither immediate (<24 hours) nor delayed (≥ 24 hours) complications except for 1 complication in a patient in whom a microguidewire remained in the BA and detached in the femoral artery because of inadvertent anchoring to the stent strut while advancing the microguidewire beyond the deployed stent in the mid-BA to the remaining basilar top occlusion. CT perfusion the next day showed good patency of the stented vessels, and DWI 5 days later showed localized infarcts in the cerebellum and the left temporal lobe, but without any symptom aggravation. This patient improved to NIHSS₀ 6 from NIHSS₀ 9, had an mRS score of 1 at the 3-month follow-up, and showed good patency of the stented lumen on CTA without any symptom recurrence during the 2.5-year follow-up period. Therefore, the rate of technical complications was 12.5% (95% CI, 2.24%–47.10%). However, there were no clinical complications in all 8 patients (95% CI, 0.00%–32.44%).

No hemorrhage or aggravation was seen in any patients, based on images taken during the following 24 hours after the procedure ($n=5$). Three patients did not undergo an imaging study because there was no clinical symptom aggravation and these patients had

relief of their symptoms. Seven patients scored ≤ 2 in the mRS at 3 months. A patient with BA occlusion presented with a poor clinical condition (NIHSS₀ = 17), resulting in a poor outcome at 3 months (mRS = 5). There was good patency and no in-stent restenosis in 2 patients, as seen on DUS ($n=2$) after 4 months and 10 months, respectively. Another patient (patient 6) monitored with CTA at 5 months after the procedure showed 40% restenosis at the ostium but without symptom recurrence. Other study patients did not undergo imaging follow-up and had no symptom recurrence.

DISCUSSION

Approximately 7.6% of patients who clinically manifest atherosclerotic disease have an asymptomatic VA stenosis or occlusion visible on DUS.²⁰ However, to our knowledge the incidence of stroke caused by V1 occlusion has not been reported in the general population. Our study showed that stroke caused by V1 segmental occlusion was responsible for 12% of the recanalization procedures performed in the V1 segment. Our patients revealed dominant VA occlusion with insufficient or occluded flow through the contralateral VA.

Large-artery disease, especially in the V1 segment of the VA, is known to demonstrate topographic heterogeneity of the cerebellar infarcts, as seen in our study, which revealed a wide range of posterior circulation infarcts related to vertebral ostial occlusion strokes.²¹ Artery-to-artery embolism from the stump of the occluded V1 segment seems to be involved more often in large arterial embolic stroke than in hemodynamic stroke.²² The prevalence of the so-called "VA stump syndrome" is 1.4% in patients with posterior circulation stroke, the rate of recurrence of ischemic stroke is 25%, and it shows unfavorable outcomes in 25% of patients with posterior circulation stroke.²³ A low-flow state in the stump might cause thrombus formation that can lead to distal embolism.²⁴ Retrograde filling of the blood flow via the C3–4 collaterals through thyrocervical or costocervical trunks, or C1–2

anastomosis via the occipital artery or the ascending pharyngeal artery, slowly fills the occluded segment, and sluggish blood flow forms a clot as a source of emboli to the posterior circulation.²⁵ Although the number and distribution of acute ischemic lesions in our patients were too varied to categorize them into a specific stroke pattern, such findings may suggest rather remote artery-to-artery embolism from the VA ostial stump in a relatively hypoperfused posterior circulation. However, the association of a perforator infarct cannot be excluded in this small number of patients.

Several studies have shown that thromboembolism caused by erosion of the plaque surface, or plaque rupture, can contribute to posterior circulation infarcts.²³⁻²⁵ As VA-origin plaques are hard, smooth, and concentric and are less prone to ulceration or intramural hemorrhage, they are therefore known to have less risk for embolism than carotid bifurcation plaques.²⁶ However, acute thrombus formation at the stump or due to plaque rupture can cause sudden occlusion of the V1 segment as well as a large thrombus burden.^{27,28}

The endovascular treatment of VA atheromatous disease remains controversial, as its natural history is poorly understood and no randomized trials have assessed the effectiveness and long-term outcome of this therapy.²⁹ There were a few anecdotal case reports regarding the protection technique in recanalization of a V1 occlusion by use of a flow-reversal technique^{30,31} or a distal filter protection device.³² Our clinical experience has shown that smooth passage of a 0.035-inch guidewire could be followed by the introduction of a 4F angiocatheter, which allows clot aspiration and also accepts a distal balloon system with a 0.014-inch outer diameter. A more rigid microguidewire can also be used for probing the occluded segment. We performed vertebral ostial stent placement by using a self-expandable stent¹⁹ because of its long lesion coverage, radial flexibility, and conformability to the tortuousness and longitudinal flexibility of a nitinol stent.³³

Endovascular recanalization of the occluded V1 can be warranted for patients in whom stroke has developed despite medical treatment or for patients with tandem lesions. The timing of recanalization therapy must be at least in the subacute stage because recanalization 2 months after the onset of symptoms failed in one of our study patients. In addition to medical treatment of acute or subacute occlusion of the V1 segment, a recanalization procedure, if required, must be done in the acute or subacute stage of occlusion because successful recanalization may not be achieved in chronic occlusion or may not be necessary when there is good development of collaterals.^{16,17} In acute stroke with poor clinical status, recanalization should not be hesitated as a first-line of treatment. In patients with subacute stroke without alleviation of symptoms, recanalization could be an option to improve clinical status and to prevent further embolic stroke. Although surgical bypass can be performed for vertebral ostial occlusion, surgical morbidity seems to be significant and these procedures require shunt appliances.³⁴ If a lesion is not accessible via the endovascular route, surgical treatment may be considered if there is no response to maximal medical therapy or if there is enough of a distal stump in the occluded V1 segment.³⁵

Study Limitations

There were several limitations to our study. For example, the sample size of the study was relatively small, and the number of imaging follow-ups was limited in this patient cohort, thus making us unable to evaluate the rate of restenosis. Our series was based on a retrospective analysis, which can create bias for this recanalization procedure and which cannot predict the final outcome of patients with V1 ostial occlusion without performing a randomized controlled comparison. Therefore, recanalization should be used with caution in patients with symptomatic V1 occlusion. Other possibilities, such as dissection or vasculitis, could not be completely excluded. However, a small stump caused by tight stenotic atherosclerotic plaque differs from a normal-looking stump caliber, as shown in dissection.³⁶ Intravascular DUS can be helpful in making the differential diagnosis.³⁷ Lastly, because the follow-up period of our study was short and the long-term clinical benefits of recanalization treatment still remain unclear, such benefits should be more thoroughly evaluated in future studies.

CONCLUSIONS

The thrombus burden of an occluded V1 segment is variable and can cause a serious embolic infarct in the posterior circulation. Revascularization of a vertebral ostial occlusion can be achieved with good clinical results by use of strategic revascularization based on the V1 occlusion stroke mechanism. In some patients, passage of the occluded segment can be performed safely by gentle probing with use of a guidewire followed by introduction of an angiocatheter. Subsequent recanalization by angioplasty and stent placement can be successfully performed under balloon protection in some patients. Re-establishment of the antegrade vertebral blood flow via endovascular recanalization might be an option used to decrease stroke recurrence in selected patients with acute posterior circulation stroke caused by an ostial V1 segment occlusion.

REFERENCES

1. Dabus G, Gerstle RJ, Derdeyn CP, et al. **Endovascular treatment of the vertebral artery origin in patients with symptoms of vertebrobasilar ischemia.** *Neuroradiology* 2006;48:917-23
2. Zavala-Alarcon E, Emmans L, Little R, et al. **Percutaneous intervention for posterior fossa ischemia. A single center experience and review of the literature.** *Int J Cardiol* 2008;127:70-77
3. Karameshev A, Schroth G, Mordasini P, et al. **Long-term outcome of symptomatic severe ostial vertebral artery stenosis (OVAS).** *Neuroradiology* 2010;52:371-79
4. Glass TA, Hennessey PM, Pazdera L, et al. **Outcome at 30 days in the New England Medical Center Posterior Circulation Registry.** *Arch Neurol* 2002;59:369-76
5. Caplan LR, Amarenco P, Rosengart A, et al. **Embolism from vertebral artery origin occlusive disease.** *Neurology* 1992;42:1505-12
6. Wityk RJ, Chang HM, Rosengart A, et al. **Proximal extracranial vertebral artery disease in the New England Medical Center Posterior Circulation Registry.** *Arch Neurol* 1998;55:470-78
7. Caplan LR, Wityk RJ, Glass TA, et al. **New England Medical Center Posterior Circulation Registry.** *Annals of neurology* 2004;56:389-98
8. Al-Ali F, Barrow T, Duan L, et al. **Vertebral artery ostium atherosclerotic plaque as a potential source of posterior circulation ischemic stroke: result from Borgess Medical Center Vertebral Artery Ostium Stenting Registry.** *Stroke* 2011;42:2544-49
9. Pelouze GA. **[Emboligenic ulcerated plaque of the foramen of the vertebral artery].** *Rev Neurol (Paris)* 1989;145:478-81

10. Endovascular versus surgical treatment in patients with carotid stenosis in the Carotid and Vertebral Artery Transluminal Angioplasty Study (CAVATAS): a randomised trial. *Lancet* 2001;357:1729–37
11. Qureshi AI, Kirmani JF, Harris-Lane P, et al. Vertebral artery origin stent placement with distal protection: technical and clinical results. *AJNR Am J Neuroradiol* 2006;27:1140–45
12. Gupta R, Sivapatham T, Moskowitz SI, et al. Stenting of a symptomatic long-segment extracranial vertebral artery occlusion. *J Neurointerv Surg* 2011;3:54–56
13. Furlan A, Higashida R, Wechsler L, et al. Intra-arterial prourokinase for acute ischemic stroke. The PROACT II study: a randomized controlled trial. *JAMA* 1999;282:2003–11
14. Geibprasert S, Pongpech S, Armstrong D, et al. Dangerous extracranial-intracranial anastomoses and supply to the cranial nerves: vessels the neurointerventionalist needs to know. *AJNR Am J Neuroradiol* 2009;30:1459–68
15. Lasjaunias P, Berenstein A, Ter Brugge KG. *Surgical Neuroangiography: Craniocervical Junction*. Berlin: Springer-Verlag; 2001:165–259
16. Lu PH, Park JW, Park S, et al. Intracranial stenting of subacute symptomatic atherosclerotic occlusion versus stenosis. *Stroke* 2011;42:3470–76
17. Liu S, Hee Jung J, Kwon HJ, et al. Landmark-wire technique of symptomatic subclavian artery occlusion. *Interv Neuroradiol* 2009;15:401–05
18. Park S, Kwak JH, Baek HJ, et al. The use of protection device in landmark-wire technique of symptomatic subclavian artery occlusion with combined approach via trans-femoral vs. trans-brachial arteries: technical note. *Neurointervention* 2011;6:89–94
19. Chung SY, Lee DH, Choi JW, et al. Use of self-expanding stents for the treatment of vertebral artery ostial stenosis: a single center experience. *Korean J Radiol* 2010;11:156–63
20. Compter A, van der Worp HB, Algra A, et al. Prevalence and prognosis of asymptomatic vertebral artery origin stenosis in patients with clinically manifest arterial disease. *Stroke* 2011;42:2795–800
21. Min WK, Kim YS, Kim JY, et al. Atherothrombotic cerebellar infarction: vascular lesion-MRI correlation of 31 cases. *Stroke* 1999;30:2376–81
22. Caplan L, Chung CS, Wityk R, et al. New England Medical Center Posterior Circulation Stroke Registry: I. Methods, data base, distribution of brain lesions, stroke mechanisms, and outcomes. *J Clin Neurol* 2005;1:14–30
23. Kawano H, Inatomi Y, Hirano T, et al. Vertebral artery stump syndrome in acute ischemic stroke. *J Neurol Sci* 2013;324:74–79
24. Kyrle PA, Eichinger S. Is Virchow's triad complete? *Blood* 2009;114:1138–39
25. Nguyen TN, Raymond J, Mahmoud M, et al. Vertebral artery stump syndrome. *J Neurol Neurosurg Psychiatry* 2008;79:91–92
26. Moufarrij NA, Little JR, Furlan AJ, et al. Vertebral artery stenosis: long-term follow-up. *Stroke* 1984;15:260–63
27. Divani AA, Berezina TL, Zhou J, et al. Microscopic and macroscopic evaluation of emboli captured during angioplasty and stent procedures in extracranial vertebral and internal carotid arteries. *J Endovasc Ther* 2008;15:263–69
28. Spetzler RF, Hadley MN, Martin NA, et al. Vertebrobasilar insufficiency. Part I: microsurgical treatment of extracranial vertebrobasilar disease. *J Neurosurg* 1987;66:648–61
29. Stayman AN, Nogueira RG, Gupta R. A systematic review of stenting and angioplasty of symptomatic extracranial vertebral artery stenosis. *Stroke* 2011;42:2212–16
30. Mayer TE, Hamann GF, Brueckmann HJ. Treatment of basilar artery embolism with a mechanical extraction device: necessity of flow reversal. *Stroke* 2002;33:2232–35
31. Iwata T, Mori T, Tajiri H, et al. Successful stenting by combination technique of reverse flow and downstream filtering for long chronic total occlusion of the cervical vertebral artery: technical case report. *Neurosurgery* 2009;65:E378–79; discussion E379
32. Mintz EP, Gruberg L, Kouperberg E, et al. Vertebral artery stenting using distal emboli protection and transcranial Doppler. *Catheter Cardiovasc Interv* 2004;61:12–15
33. Vos AW, Linsen MA, Diks J, et al. Carotid stent mobility with regard to head movements: in vitro analysis. *Vascular* 2004;12:369–73
34. Kakino S, Ogasawara K, Kubo Y, et al. Symptomatic occlusion at the origin of the vertebral artery treated using external carotid artery-cervical vertebral artery bypass with interposed saphenous vein graft. *Surg Neurol* 2008;69:164–68; discussion 168
35. da Costa LB, Tymianski M. Symptomatic non-atherosclerotic bilateral extracranial vertebral artery occlusion treated with extracranial to intracranial bypass: case report. *Arq Neuropsiquiatr* 2006;64:664–67
36. Fava M, Meneses L, Loyola S, et al. Carotid artery dissection: endovascular treatment. Report of 12 patients. *Catheter Cardiovasc Interv* 2008;71:694–700
37. Liu X, Tsujita K, Maehara A, et al. Intravascular ultrasound assessment of the incidence and predictors of edge dissections after drug-eluting stent implantation. *JACC Cardiovasc Interv* 2009;2:997–1004

Imaging Findings of Head and Neck Dermatofibrosarcoma Protuberans

G.G. Millare, N. Guha-Thakurta, E.M. Sturgis, A.K. El-Naggar, and J.M. Debnam

ABSTRACT

BACKGROUND AND PURPOSE: Dermatofibrosarcoma protuberans is a rare, locally aggressive sarcoma of the skin in children and adults, usually involving the trunk and extremities and less commonly the head and neck. Despite clinical reports in the literature on the management of dermatofibrosarcoma protuberans, there are limited articles describing its imaging features.

MATERIALS AND METHODS: We retrospectively reviewed the demographics and imaging findings in all 24 patients with pathologically proven dermatofibrosarcoma protuberans of the head and neck seen at a tertiary cancer center between 2001 and 2010.

RESULTS: Twenty-two of the 24 lesions were nodular and well circumscribed; 19 of the 24 were located on the scalp. On imaging, all 24 lesions involved subcutaneous tissues. The lesions ranged in size from 0.6–9.5 cm (mean, 3.7 cm; standard deviation, 2.3 cm). Twelve lesions involved the soft tissues either at or extending directly to the midline. Thirteen lesions were associated with bulging of the skin surface. Fourteen lesions were imaged with CT and 14 with MR imaging. Whereas variable enhancement patterns were noted on CT and MR imaging, dermatofibrosarcoma protuberans was usually T2-hyperintense and demonstrated marked enhancement. None of the lesions was associated with bone invasion, perineural spread, or nodal/distant metastasis.

CONCLUSIONS: Knowledge of the imaging characteristics of dermatofibrosarcoma protuberans may alert neuroradiologists to include dermatofibrosarcoma protuberans in the differential diagnosis of lesions about the head and neck with similar imaging characteristics.

ABBREVIATIONS: DFSP = dermatofibrosarcoma protuberans; PDGFB = platelet-derived growth factor β -chain; PDGF-R = platelet-derived growth factor receptor tyrosine kinase

Dermatofibrosarcoma protuberans (DFSP) is a rare, locally aggressive sarcoma of the dermis with a high cure rate.^{1,2} DFSP often presents in the third or fourth decade of life, most commonly involving the trunk (50–60%) or proximal extremities (20–30%) and less commonly involving the head and neck (10–15%).^{3,4} DFSP grows in an infiltrative manner and has the capacity for local recurrence, though it rarely metastasizes.^{5,6}

The imaging features of DFSP of the trunk and extremities are

nonspecific, including low signal on T1 and high on T2 on MR imaging, with uniform enhancement after contrast administration.^{7,8} CT findings include isoattenuated to hypoattenuated lesions without calcifications and uniform (small lesions) to heterogeneous (large lesions) enhancement after contrast administration.⁹ Previously published reports on DFSP have highlighted its clinical features, but only a few small series have outlined its imaging features.^{7,8,10} The purpose of this study was to more comprehensively define the CT and MR imaging appearance of DFSP of the head and neck.

MATERIALS AND METHODS

This study was approved by the Institutional Review Board of The University of Texas MD Anderson Cancer Center, which waived the requirement for informed consent. We retrospectively reviewed the demographics and radiologic images of 24 patients with pathologically proven DFSP of the head and neck seen at our institution between 2001–2010.

Fourteen patients underwent CT of the head and neck, and 14 patients underwent MR imaging of the head and neck. The CT examinations were performed after intravenous administration

Received February 10, 2013; accepted after revision April 19.

From the Department of Diagnostic Radiology (G.G.M.), Baylor College of Medicine, Houston, Texas; and Department of Diagnostic Radiology (N.G.-T., J.M.D.), Section of Neuroradiology, and Departments of Head and Neck Surgery (E.M.S.), Epidemiology (E.M.S.), and Pathology (A.K.E.-N.), The University of Texas MD Anderson Cancer Center, Houston, Texas.

Paper previously presented as a poster at: Annual Meeting of the American Society of Head and Neck Radiology, October 3–7, 2012; Miami Beach, Florida.

Please address correspondence to Giovanni G. Millare, MD, Diagnostic Radiology, Baylor College of Medicine, One Baylor Plaza, Houston, TX 77030; e-mail: gmill2003@sbcglobal.net

The University of Texas MD Anderson Cancer Center is supported in part by the National Institutes of Health through Cancer Center Support Grant CA016672.

<http://dx.doi.org/10.3174/ajnr.A3650>

Patient demographics and image appearance

Patient	Age, Years/Sex	Location	CT Enhancement Pattern	MR Appearance (T2)	MR T1 Enhancement
1	31/M	Parietal midline scalp	NA	Hyperintense	Marked homogeneous
2	68/M	Right cheek	Homogeneous	NA	NA
3	37/M	Frontal paramedian scalp	Homogeneous	NA	NA
4	66/M	Frontal midline scalp	Heterogeneous	Hyperintense	Marked homogeneous
5	39/F	Frontal midline scalp	NA	Hyperintense	Mild
6	46/F	Frontal midline scalp	NA	Hyperintense	Marked homogeneous
7	25/F	Right parietal paramedian scalp	Minimal	NA	NA
8	29/F	Right pre-auricular region	Homogeneous	NA	NA
9	58/F	Frontal midline scalp	NA	Hyperintense	Marked homogeneous
10	31/F	Right parietal scalp near midline	Heterogeneous	Hyperintense	Marked heterogeneous
11	45/M	Left parietal paramedian scalp	Minimal	NA	NA
12	42/M	Parietal scalp near midline	NA	Hyperintense	Marked heterogeneous
13	48/F	Parietal midline scalp	Homogeneous	NA	NA
14	15/F	Frontal paramedian scalp	NA	Iso-/hypointense	Marked homogeneous
15	40/M	Frontal paramedian scalp	Homogeneous	NA	NA
16	25/M	Parietal scalp to midline	Heterogeneous	NA	NA
17	64/F	Midline chin	Minimal	NA	NA
18	36/M	Midline occipital scalp	NA	Hyperintense	Marked heterogeneous
19	34/M	Right frontal scalp	NA	Hypointense	Marked homogeneous
20	72/F	Right posterior neck	Homogeneous	Hyperintense	Marked heterogeneous
21	55/M	Left face to midline	NA	Iso-/hypointense	Marked homogeneous
22	42/M	Parieto-occipital scalp	Homogeneous	Hypointense	Marked homogeneous
23	31/F	Parietal scalp to midline	Homogeneous	NA	NA
24	40/F	Parietal scalp	NA	Hyperintense	Marked homogeneous

Note:—NA indicates not applicable.

of contrast material. Soft tissue and bone windows were evaluated in all patients. MR imaging sequences included axial T1 precontrast, orthogonal T1 postcontrast, and T2-weighted sequences (Table).

The following imaging features were documented: lesion size, location, enhancement pattern, calcification, and perineural spread; associated osseous abnormality; and presence of nodal or distant metastasis.

RESULTS

Clinical Features

The patients ranged in age from 15–72 years (mean, 42.5 years; median, 40 years) and included 12 women and 12 men. Seventeen patients presented with a primary, untreated tumor, and 7 patients presented with recurrent disease. The most common presenting symptom was a slowly enlarging mass ($n = 18$). Six patients described a history of trauma before development of a slowly growing mass at the same site as the trauma. The trauma occurred 2 years before presentation in 2 patients, 6–11 years before presentation in 3 patients, and as a child in 1 patient. DFSP was diagnosed through biopsy in all 24 patients.

Imaging Findings

On imaging, 19 lesions involved the scalp; other locations included the posterior neck ($n = 1$), left face to midline ($n = 1$), pre-auricular region ($n = 1$), chin ($n = 1$), and cheek ($n = 1$). All 24 lesions involved the subcutaneous soft tissues. Eighteen lesions extended up to the skin surface, and, of these, 13 were associated with bulging of the skin, 2 were associated with an exophytic fungating component, and 2 were associated with skin retraction; 1 was associated with none of these findings. Twelve of the lesions involved the soft tissues either at ($n = 6$) or near the midline ($n = 6$). The lesions ranged in size from 0.6–9.5 cm (mean, 3.7 cm;

standard deviation, 2.3 cm). Twenty-two of the 24 lesions were nodular and well-circumscribed; the nodules were singular in 13 cases, coalescent in 6 cases, and multiple but separated in 3 cases. Two lesions had an infiltrative pattern; both manifested as recurrences in the operative field. None of the patients had evidence of osseous destruction, cervical lymph node, or distant metastasis.

CT Findings

The 14 lesions imaged with CT demonstrated enhancement that was either minimal ($n = 3$), heterogeneous ($n = 3$) (Fig 1A), or homogeneous ($n = 8$). There was no evidence of calcification, and none of the lesions demonstrated CT evidence of perineural spread. Osseous destruction was absent; however, thinning of the underlying calvaria (Fig 1B) was seen in 2 patients (patients 10 and 16).

MR Imaging Findings

All 14 lesions imaged with MR were T1-isointense to muscle (Fig 2A); 10 lesions were T2-hyperintense (Fig 2B) and 4 were iso-intense to hypointense to muscle. T1 postcontrast enhancement patterns ranged from mild ($n = 1$) to markedly heterogeneous ($n = 4$) or markedly homogeneous ($n = 9$) (Fig 2C,-D). Neither perineural spread nor bone involvement was present in any case.

Pathologic Findings

Most the lesions were found in the lower dermis and the subcutaneous tissue. All tumors manifested spindle cell proliferation arranged in light storiform patterns. Although infiltrative with ill-defined boundaries, the cells were bland and lacking mitotic activity and nuclear pleomorphism.

Seven patients presented to our institution with recurrent disease after having undergone resection at other centers. In 6 of the 7 patients, the pathologic specimens from the initial resection

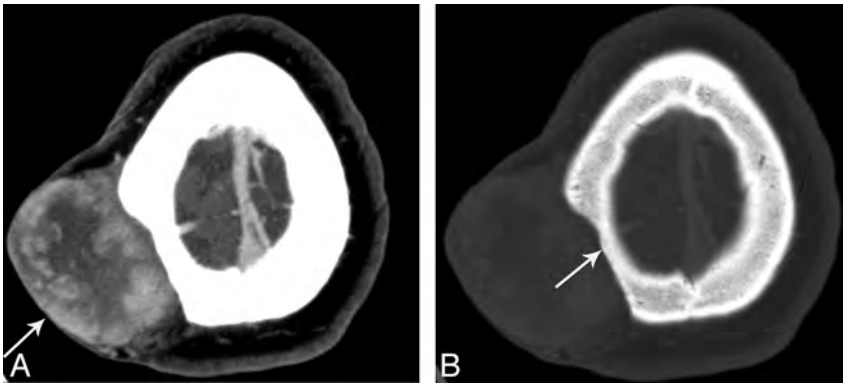


FIG 1. A 31-year-old woman (patient 10) with DFSP of the right parietal scalp. Contrast-enhanced axial CT in soft tissue (A) and bone window (B) shows a 6.1×4.8 -cm heterogeneously enhancing mass (A, arrow) that bulges the skin surface outward and thins underlying calvaria (B, arrow).

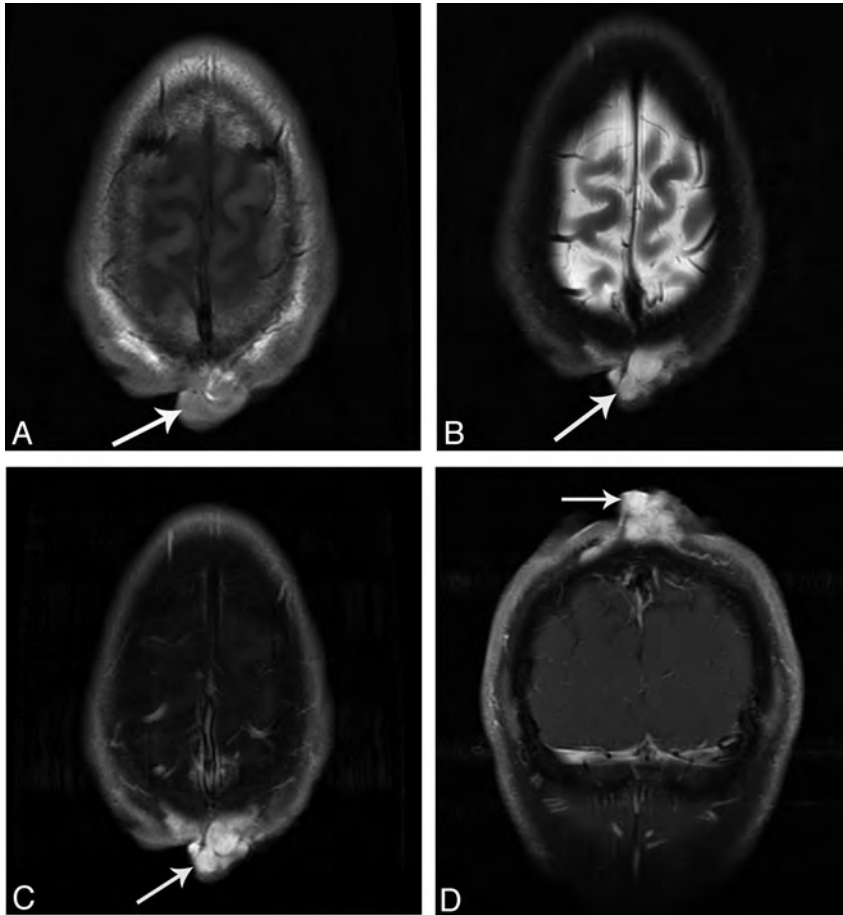


FIG 2. A 31-year-old man (patient 1) with DFSP of the parietal midline scalp. MR imaging shows a 3.5×1.8 -cm T1-isointense, T2-hyperintense, coalescing nodular mass with marked homogeneous enhancement in the parietal midline scalp (arrows). A, Axial noncontrast T1. B, Fast spin-echo T2 with fat saturation. C, T1 postcontrast axial with fat saturation. D, T1 postcontrast coronal with fat saturation.

were submitted and reviewed by our pathology department. In all 6 patients, DFSP was present at the surgical margins.

Treatment

The lesions were treated with surgical excision ($n = 9$), excision and radiation ($n = 8$), excision and chemotherapy ($n = 3$), chemotherapy ($n = 3$), or all 3 treatments ($n = 1$). All of the patients were still alive at the time of this report.

DISCUSSION

DFSP typically presents as a slow-growing, painless, and firm subcutaneous nodule.¹¹ The lesions can be multiple and may coalesce to form an indurated plaque (Fig 3), which on clinical examination is often violaceous.^{12,13} The growth rate is variable; some lesions remain stable in size for many years, whereas others demonstrate slow progressive growth.¹⁴ DFSP can arise in healthy skin or in areas of repeated trauma, vaccination sites, irradiated skin, or scars.¹⁵ Six patients in our series had a history of local trauma before the development of DFSP, and the interval between the trauma and development of DFSP varied. Tattoo sites also show a predilection for benign and malignant changes and should be evaluated during regular skin examinations; DFSP should be considered in the differential diagnosis of neoplasms arising within areas of tattoos.¹⁶

In our series, DFSP lesions ranged in size from 0.6–9.5 cm, and half were located at or extended to the midline. Variable enhancement was noted on CT (Fig 1A), similar to prior reports.^{8,9} On MR imaging, almost all of the cases showed marked enhancement (Fig 2C, D), which has not previously been reported.^{7,8} None of the lesions was associated with perineural spread, nodal, or distant metastases. No osseous destruction was demonstrated; however, calvarial thinning was seen in 2 patients. These 2 patients (patients 10 and 16) had the largest lesions, which suggests that the thinning could be related to a pressure effect. Although none of the lesions in our series showed intracranial extension, this has been described in 2 case reports.^{10,17}

None of the patients in our series had local or nodal metastasis, perineural spread, or bone destruction. In contrast, 2–3% of all patients with squamous cell carcinoma of the skin have metastasis, which occurs almost exclusively through lymphatic channels and only rarely through hematogenous spread.¹⁸ Perineural spread

occurs in basal cell carcinoma, squamous cell carcinoma, and melanoma (desmoplastic), usually involving cranial nerves V and VII.^{19,20}

Bony destruction is uncommon with skin tumors, but when bone destruction is noted on imaging, malignant melanoma and squamous cell carcinoma should be considered.^{21–23}

Histologically, DFSP is an infiltrative soft tissue neoplasm of the dermis and subcutaneous tissues. DFSP is composed of bland,



FIG 3. Photographs of 2 patients with DFSP. A, Patient 16, a 25-year-old man with a large DFSP of the scalp extending from the midline near the vertex down to the left lower parietal region with subcutaneous infiltration. B, Patient 10, a 31-year-old woman with a large DFSP of the right paramechan posterior parietal scalp.

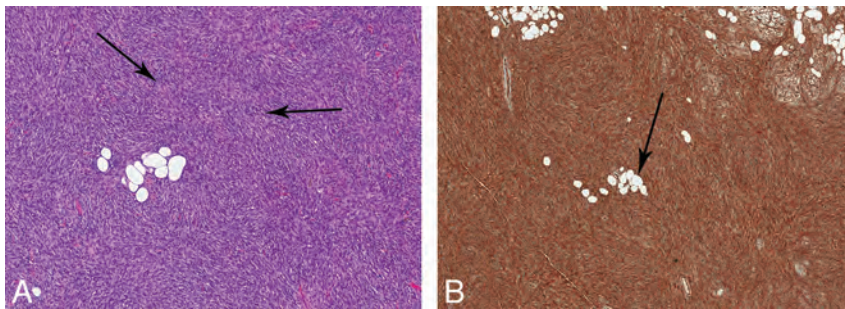


FIG 4. Pathologic specimen of DFSP. A, Hematoxylin and eosin stain. Elongated spindle cells with a storiform (whorled) pattern arranged around foci of collagen or vascular spaces, radiating outward (arrows). B, CD34 stain. The specimen is positive for CD34 staining. Fat entrapment is noted with a honeycomb pattern (arrow).

elongated spindle cells with a storiform, or whorled, pattern arranged around foci of collagen or vascular spaces, radiating outward like the spokes of a wheel (Fig 4A).²⁴ Infiltration around fat cells may produce a honeycomb appearance of the fat (Fig 4B).²⁵ Immunohistochemical analysis may assist if the diagnosis as DFSP is positive for CD34 staining (Fig 4B), with a reported sensitivity of 84–100%.^{26–28} Because other skin lesions are also positive for CD34 staining, CD34 is not specific for DFSP; however, CD34 positivity in combination with the histologic features makes the diagnosis.

At the genetic level, the critical initiating event in DFSP development is rearrangement of chromosomes 17 and 22 in the form of a supernumerary ring chromosome [r (17; 22)] or a reciprocal translocation [t (17; 22)]. Either of these rearrangements results in chimeric fusion of the genes encoding the platelet-derived growth factor β -chain (PDGFB) and the collagen type 1 α_1 -chain, which in turn results in autocrine activation of the platelet-de-

rived growth factor receptor tyrosine kinase (PDGF-R), which triggers the proliferation of DFSP tumor cells.^{29,30}

Treatment options include complete surgical excision, including wide excision and Mohs micrographic surgery, radiation, and imatinib mesylate.^{2,11,31} Imatinib, a competitive tyrosine kinase inhibitor, is currently approved by the Food and Drug Administration for the treatment of adult patients with unresectable, recurrent, and/or metastatic DFSP, and this may in turn facilitate tumor resection and/or decrease disfigurement.³² After local resection, the 5-year survival rate is 93–100%.^{33,34} In agreement with these previously reported findings, none of the patients in our series had died of disease at the time of this report. Local recurrence occurs in 20–55% of cases.^{12–14,35} Most local recurrences occur within 3 years^{11,12,35}; only 30% occur after 5 years.³² The lungs are the most common site of distant metastasis,^{12,30,36,37} and metastasis has been reported to occur in 5–6% of cases.^{13,14,34,35,38,39}

Differential diagnoses of other cutaneous neoplasms that could be confused with DFSP include dermatofibroma, epidermal cyst, peripheral nerve sheath tumor, nodular fasciitis, cavernous hemangioma, liposarcoma, nodular type of melanoma, and mycosis fungoides.^{21,40,41} Dermatofibroma can have imaging findings similar to DFSP on CT and MR imaging but is most frequently seen in the extremities, whereas DFSP is most commonly seen in the trunk.^{42,43} Epidermal cyst, most commonly an incidental finding, does not enhance on both CT and

MR, unless infected, whereas DFSP shows variable enhancement on CT and MR imaging.^{44,45} Peripheral nerve sheath tumors are usually close to a major nerve, with certain signs such as split fat or fascicular or target sign, which are absent in DFSP.^{45,46} Plexiform neurofibromas tend to be asymmetric and diffuse, whereas DFSP most commonly is nodular.^{47,48} Clinically, patients with plexiform neurofibromas have neurofibromatosis type 1. Nodular fasciitis can be indistinguishable from DFSP by imaging. However, on MRI, one may see fascial tail sign, which is the linear extension of the lesion along the fascia, which also may appear to be enhanced. Nodular fasciitis favors the upper extremity, whereas DFSP favors the trunk.^{40,41,49} Cavernous hemangioma has low attenuation on CT, and calcifications are common, features not seen in DFSP.^{49,50} Liposarcoma contains fat, which is not present on DFSP.⁴⁵ The nodular type of melanoma is mostly clinically blue to black, and DFSP is often violaceous. Melanotic melanoma is hyperintense on T1-weighted images and hypointense on T2-

weighted images. Melanomas can have associated lymphadenopathy and osseous destruction not usually found in DFSP.^{44,51,52} Mycosis fungoides is the most common type of cutaneous T-cell lymphoma. CT findings include skin thickening, edema, soft tissue infiltration, lymphadenopathy, and systemic manifestations, not typically found in DFSP.^{45,53} The imaging findings of DFSP are nonspecific, but the combination of imaging findings, location of the lesion, and clinical features of the lesion help narrow the differential diagnosis of these cutaneous lesions mimicking DFSP.

Limitations of the study include the retrospective nature of the review. Similar imaging studies were not available for each patient, and, for the 7 patients presenting to our center with recurrent disease, the initial imaging of the primary lesion was not submitted for interpretation. However, the pathologic specimens for 6 of the 7 patients with recurrent DFSP were reviewed by our pathology department. DFSP was present at the surgical margins in all 6 specimens, which suggests that recurrent disease may be associated with incomplete surgical resection. This is in keeping with published reports of high recurrence rates in patients with positive surgical margins.⁵⁴ The most significant prognostic factor in patients with DFSP has been the extent of surgical resection.²

CONCLUSIONS

DFSP of the head and neck region typically involves the dermis of the scalp, is often well-circumscribed with a nodular appearance, presents as a subcutaneous mass of variable size, often occurs near the midline, and is associated with bulging of the skin surface. Variable enhancement patterns are noted on CT, but, on MR imaging, DFSP is usually T2-hyperintense with marked enhancement. There is a high propensity for local recurrence but a low incidence of bone invasion, perineural spread, and nodal or distant metastasis. Neuroradiologists should be familiar with the imaging appearance of DFSP and include DFSP in the differential diagnosis of head and neck dermal tumors with similar imaging characteristics.

ACKNOWLEDGMENTS

We wish to thank Stephanie Deming for editorial assistance.

Disclosures: Adel K. El-Naggar—UNRELATED: Grants/Grants Pending: NIH,* NCI,* NIDCR*; Other: Salivary Gland Tissue Biorepository.* Comments: Contract with NIH to collect extremely rare cancers of the head and neck and distribute to researchers conducting relevant research (*money paid to institution).

REFERENCES

- Snow SN, Gordon EM, Larson PO, et al. **Dermatofibrosarcoma protuberans: a report on 29 patients treated by Mohs micrographic surgery with long-term follow-up and review of the literature.** *Cancer* 2004;101:28–38
- Doreen L, Mügge O, Mentzel T, et al. **Current treatment options in dermatofibrosarcoma.** *J Cancer Res Clin Oncol* 2009;135:653–65
- Gloster HM. **Dermatofibrosarcoma protuberans.** *J Am Acad Dermatol* 1996;35:355–74
- Maggoudi D, Vahntsevanos K, Psomaderi K, et al. **Dermatofibrosarcoma protuberans of the face: report of 2 cases and an overview of the recent literature.** *J Oral Maxillofac Surg* 2006;64:140–44
- Gatlin JL, Hosch R, Khan M. **Dermatofibrosarcoma protuberans of the scalp with fibrosarcomatous degeneration and pulmonary metastasis.** *J Clin Imaging Sci* 2011;1:55
- Lal P, Goel A, Mandal AK. **Dermatofibrosarcoma of the scalp with cervical lymph node metastasis.** *Sarcoma* 2004;8:43–45
- Torreggiani WC, Al-Ismail K, Munk PL, et al. **Dermatofibrosarcoma protuberans: MR imaging features.** *AJR Am J Roentgenol* 2002;178:989–93
- Kransdorf MJ, Meis-Kindblom JM. **Dermatofibrosarcoma protuberans: radiologic appearance.** *AJR Am J Roentgenol* 1994;163:391–94
- Li X, Zhang W, Xiao L, et al. **Computed tomographic and pathological findings of dermatofibrosarcoma protuberans.** *J Comput Assist Tomogr* 2012;36:462–68
- Das L, Grover SB, Chand K. **Intracranial extension of a dermatofibrosarcoma protuberans of the scalp: a case report with brief review of literature.** *Surg Neurol* 2000;54:452–54
- Stojadinovic A, Karpoff HM, Antonescu CR, et al. **Dermatofibrosarcoma protuberans of the head and neck.** *Ann Surg Oncol* 2000;7:696–704
- Brenner W, Schaefer K, Chhabra H, et al. **Dermatofibrosarcoma protuberans metastatic to a regional lymph node: report of a case and review.** *Cancer* 1975;36:1897–902
- Simstein NL, Tuthill RJ, Sperber EE, et al. **Dermatofibrosarcoma protuberans: case reports and review of literature.** *South Med J* 1977;70:487–89
- Phelan JT, Juargo J. **Dermatofibrosarcoma protuberans.** *Am J Surg* 1963;106:943–48
- McGuire JF, Ge NN, Dyson S, et al. **Nonmelanoma skin cancer of the head and neck: histopathology and clinical behavior.** *Am J Otolaryngology* 2009;30:121–33
- Baker PA, Dowd GJ, Khan IU. **Dermatofibrosarcoma protuberans arising in a decorative tattoo.** *Sarcoma* 2005;9:37–41
- Marakovic J, Vilendecic M, Marinovic T, et al. **Intracranial recurrence and distant metastasis of scalp dermatofibrosarcoma protuberans.** *J Neurooncol* 2008;88:305–08
- Vargo NL. **Basal and squamous cell carcinomas: an overview.** *Semin Oncol Nurs* 1991;7:13–25
- Williams LS, Mancuso AA, Mendenhall WM. **Perineural spread of cutaneous squamous and basal cell carcinoma: CT and MR detection and its impact on patient management and prognosis.** *Int J Radiat Oncol Biol Phys* 2001;49:1061–69
- Chang PC, Fischbein NJ, McCalmont TH. **Perineural spread of malignant melanoma of the head and neck: clinical and imaging features.** *AJNR Am J Neuroradiol* 2004;25:5–11
- Kim JH, Kim JY, Chun KA, et al. **MR imaging manifestations of skin tumors.** *Eur Radiol* 2008;18:2652–61
- Tsao SW, Burman JF, Pittam MR. **Further observations on mechanisms of bone destruction by squamous carcinomas of the head and neck: the role of host stroma.** *Br J Cancer* 1983;48:697–704
- Schwarze HP, Loche F, Gorguet MC. **Invasive cutaneous squamous cell carcinoma associated with actinic keratosis: a case with orbital invasion and meningeal infiltration.** *Dermatol Surg* 1999;25:587–89
- Taylor HB, Hewlwig EB. **Dermatofibrosarcoma protuberans: a study of 115 cases.** *Cancer* 1962;15:717–25
- Reimann JD, Fletcher CD. **Myxoid dermatofibrosarcoma protuberans: a rare variant analyzed in a series of 23 cases.** *Am J Surg Pathol* 2007;31:1371–77
- Haycox CL, Odland PB, Olbricht SM, et al. **Immunohistochemical characterization of dermatofibrosarcoma protuberans with practical applications for diagnosis and treatment.** *J Am Acad Dermatol* 1997;37:438–44
- Abenzoza P, Lillemoe T. **CD34 and factor XIIIa in the differential diagnosis of dermatofibroma and dermatofibrosarcoma protuberans.** *Am J Dermatopathol* 1993;15:429–34
- McArthur GA, Demetri GD, van Oosterom A, et al. **Molecular and clinical analysis of locally advanced dermatofibrosarcoma protuberans treated with imatinib: Imatinib Target Exploration Consortium Study B2225.** *J Clin Oncol* 2005;23:866–73
- Nikolaos A, Panagiotis K, Waseem J, et al. **Dermatofibrosarcoma**

- protuberans with fibrosarcomatous transformation of the head and neck. *Head Neck Oncology* 2011;3:5
30. Shimizu A, O'Brien KP, Sjöblom T, et al. **The dermatofibrosarcoma protuberans-associated collagen type I α 1/platelet-derived growth factor (PDGF) B-chain fusion gene generates a transforming protein that is processed to functional PDGF-BB.** *Cancer Res* 1999;59:3719–23
 31. DuBay D, Cimmino V, Lowe L, et al. **Low recurrence rate after surgery for dermatofibrosarcoma protuberans: a multidisciplinary approach from a single institution.** *Cancer* 2004;100:1008–16
 32. Rutkowski P, Debiec-Rychter M, Nowecki ZI, et al. **Treatment of advanced dermatofibrosarcoma protuberans with imatinib mesylate with or without surgical resection.** *J Eur Acad Dermatol Venereol* 2011;25:264–70
 33. Mark RJ, Bailet JW, Tran LM, et al. **Dermatofibrosarcoma protuberans of the head and neck: a report of 16 cases.** *Arch Otolaryngol Head Neck Surg* 1993;119:891–96
 34. Hashimoto K, Brownstein MH, Jakobiec FA. **Dermatofibrosarcoma protuberans.** *Arch Dermatol* 1974;110:874–85
 35. Batsakis JG, Manning JT. **Soft tissue tumors: unusual forms.** *Otolaryngology Clin North Am* 1986;19:659–83
 36. Rockley PF, Robinson JK, Magid M, et al. **Dermatofibrosarcoma protuberans of the scalp: a series of cases.** *J Am Acad Dermatol* 1989;21:278–82
 37. Voth H, Landsberg J, Hinz T, et al. **Management of dermatofibrosarcoma protuberans with fibrosarcomatous transformation: an evidence-based review of the literature.** *J Eur Acad Dermatol Venereol* 2011;25:1385–91
 38. Mendenhall WM, Zlotecki RA, Scarborough MT. **Dermatofibrosarcoma protuberans.** *Cancer* 2004;101:2503–08
 39. Nakra T, Cook T, Douglas RS, et al. **Dermatofibrosarcoma protuberans metastatic to the orbit.** *Arch Ophthalmol* 2004;122:1240–01
 40. Dinauer PA, Brixey CJ, Moncur JT, et al. **Pathologic and MR imaging features of benign fibrous soft-tissue tumors in adults.** *RadioGraphics* 2007;27:173–87
 41. Beaman FD, Kransdorf MJ, Andrews TR, et al. **Superficial soft-tissue masses: analysis, diagnosis, and differential considerations.** *RadioGraphics* 2007;27:509–23
 42. Skoulakis CE, Papadakis CE, Datsaris GE, et al. **Subcutaneous benign fibrous histiocytoma of the cheek: case report and review of the literature.** *Acta Otorhinolaryngol Ital* 2007;27:90–93
 43. Ito T, Yoshida Y, Masutaka F, et al. **Subcutaneous benign fibrous histiocytoma showing nerve involvement on the eyebrow region.** *Acta Derm Venereol* 2013;93:1–2
 44. Kim HK, Kim SM, Lee SH, et al. **Subcutaneous epidermal inclusion cysts: ultrasound (US) and MR imaging findings.** *Skelet Radiol* 2011;40:1415–19
 45. Beaman FD, Kransdorf MJ, Menke DM. **Schwannoma: radiologic-pathologic correlation.** *RadioGraphics* 2004;24:1477–81
 46. Lin J, Martel W. **Cross-sectional imaging of peripheral nerve sheath tumors: characteristic signs on CT, MR imaging, and sonography.** *AJR* 2001;176:75–82
 47. Lim R, Jaramillo D, Poussaint TY, et al. **Superficial neurofibroma: a lesion with unique MRI characteristics in patients with neurofibromatosis type 1.** *AJR* 2005;184:962–68
 48. Hassell DS, Bancroft LW, Kransdorf MJ, et al. **Imaging appearance of diffuse neurofibroma.** *AJR* 2008;190:582–88
 49. Walker EA, Fenton ME, Salesky JS, et al. **Magnetic resonance imaging of benign soft tissue neoplasms in adults.** *Radiol Clin North Am* 2011; 1197–217
 50. Dubois J, Soulez G, Oliva VL, et al. **Soft-tissue venous malformations in adult patients: imaging and therapeutic issues.** *RadioGraphics* 2001;21:1519–31
 51. Bolognia JL, Jorizzo JL, Schaffer JV, et al. *Dermatology.* Tampa, Florida: Elsevier, Saunders; 2012:1892
 52. Kienstra MA, Padhya TA. **Head and neck melanoma.** *Cancer Control* 2005;12:242–47
 53. Shapeero LG, Young SW. **Mycosis fungoides: manifestations on computed tomography.** *Radiology* 1983;148:202
 54. Bowne WB, Antonescu CR, Leung DH, et al. **Dermatofibrosarcoma protuberans a clinicopathologic analysis of patients treated and followed at a single institution.** *Cancer* 2000;88:2711–20

Fractional Change in Apparent Diffusion Coefficient as an Imaging Biomarker for Predicting Treatment Response in Head and Neck Cancer Treated with Chemoradiotherapy

M. Matoba, H. Tuji, Y. Shimode, I. Toyoda, Y. Kuginuki, K. Miwa, and H. Tonami

ABSTRACT

BACKGROUND AND PURPOSE: ADC provides a measure of water molecule diffusion in tissue. The aim of this study was to evaluate whether the fractional change in ADC during therapy can be used as a valid predictive indicator of treatment response in head and neck squamous cell carcinoma treated with chemoradiotherapy.

MATERIALS AND METHODS: Forty patients underwent DWI at pretreatment and 3 weeks after the start of treatment. The pretreatment ADC, fractional change in ADC, tumor regression rate, and other clinical variables were compared with locoregional control and locoregional failure and were analyzed by using logistic regression analysis and receiver operating characteristic analysis. Furthermore, progression-free survival curves divided by the corresponding threshold value were compared by means of the log-rank test.

RESULTS: The fractional change in ADC_{primary}, the fractional change in ADC_{node}, primary tumor volume, nodal volume, tumor regression rate_{node}, N stage, and tumor location revealed significant differences between locoregional failure and locoregional control ($P < .05$). In univariate analysis, the fractional change in ADC_{primary}, fractional change in ADC_{node}, tumor regression rate_{node}, N stage, and tumor location showed significant association with locoregional control ($P < .05$). In multivariate analysis, however, only the fractional change in ADC_{primary} was identified as a significant and independent predictor of locoregional control ($P = .04$). A threshold fractional change in ADC_{primary} of 0.24 revealed a sensitivity of 100%, specificity of 78.7%, and overall accuracy of 84.8% for the prediction of locoregional control. Progression-free survival of the 2 groups divided by the fractional change in ADC_{primary} at 0.24 showed a significant difference ($P < .05$).

CONCLUSIONS: The results suggest that the fractional change in ADC_{primary} is a valid imaging biomarker for predicting treatment response in head and neck squamous cell carcinoma treated with chemoradiotherapy.

ABBREVIATIONS: Δ ADC = fractional change in ADC; HNSCC = head and neck squamous cell carcinoma; Δ TV = tumor regression rate; LRC = locoregional control; LRF = locoregional failure

Approximately two-thirds of patients with head and neck squamous cell carcinoma (HNSCC) present with advanced-stage disease, and regional lymph node involvement is common.¹ Surgery with or without adjuvant chemotherapy and/or radiation therapy remains a mainstay of treatment in advanced HNSCC, but radical radiation therapy alone or concurrent chemoradiotherapy as a definitive treatment has become a standard management option for many patients with HNSCC to improve the pa-

tient's quality of life via organ preservation. Despite these rigorous treatment methods, however, locoregional disease failure occurs in as many as 30%–40% of cases.^{2,3} Therefore, if a reliable indicator of response to radiation therapy or chemoradiotherapy before or at an early stage of treatment could be found, patients whose prognoses are likely to be unfavorable with current approaches might be selected for alternative strategies, improving their chances of success and sparing them from ineffective treatment with unnecessary toxicity. It has been impossible, however, to reliably predict early individual treatment response despite careful evaluation by using traditional clinical predictors such as tumor size, clinical stage, tumor location, and lymph node involvement.⁴

DWI extracts information from the diffusion of water molecules in tissue. Water molecule diffusion motion can be quantified by using the ADC. In general, highly cellular cancers have more restricted diffusion, resulting in lower ADC values, while

Received February 17, 2013; accepted after revision May 17.

From the Departments of Radiology (M.M., I.T., Y.K., H. Tonami) and Otorhinolaryngology (H. Tuji, Y.S., K.M.), Kanazawa Medical University, Ishikawa, Japan.

Please address correspondence to Munetaka Matoba, MD, Department of Radiology, Kanazawa Medical University, Daigaku 1-one, Uchinada, Kahoku, Ishikawa, 920-0293, Japan; e-mail: m-matoba@kanazawa-med.ac.jp

<http://dx.doi.org/10.3174/ajnr.A3706>

Histologically confirmed HNSCC between January 2008 and September 2012

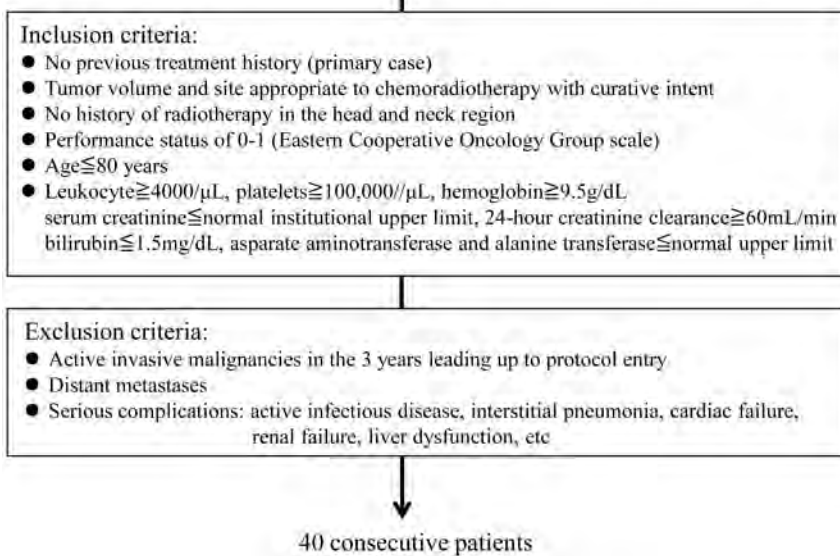


FIG 1. Patient selection criteria.

Table 1: Patient characteristics

Characteristics	No. of Patients (n = 35)
Age (yr)	
Median	66.2
Range	33–79
Male/female	30:5
Tumor location	
Supraglottis	3
Oropharynx	9
Hypopharynx	9
Larynx	10
Oral cavity	4
T stage (UICC 2002)	
T1	1
T2	14
T3	8
T4	12
N stage (UICC 2002)	
N0	3
N1	7
N2	20
N3	5

Note:—UICC indicates Union for International Cancer Control.

cancer treatments causing cell death increase water diffusion and lead to a rise in ADC.⁵

In HNSCC, recent clinical studies have applied DWI to the prediction of treatment response to neoadjuvant chemotherapy, radiation therapy, or chemoradiotherapy before or at an early stage of treatment, revealing that pretreatment ADC correlates with treatment response and that ADC changes at 1, 2, and 4 weeks after the start of treatment can predict treatment response.^{6–9} In addition, it has been reported that ADC changes at 3 weeks posttreatment can predict treatment response with higher accuracy than morphologic imaging assessment.¹⁰ Studies evaluating the predictive value of DWI for treatment response post-radiation therapy and/or chemotherapy are limited, however, and the optimal timing of the evaluation of the DWI and ADC analysis method

for predicting the treatment response has not been established, to our knowledge.

The aim of this study was to evaluate the usefulness of the fractional change in ADC (Δ ADC) during therapy for prediction of treatment response in patients with HNSCC treated with chemoradiotherapy compared with the other clinical variables and to identify whether the Δ ADC during therapy can be used as a valid imaging biomarker for prediction of treatment response.

MATERIALS AND METHODS

Patient Population

This prospective study was approved by the Committee on Clinical Study at our institution, and written informed consent was obtained from all patients. The study population consisted of patients with histologically confirmed primary HNSCC who were treated with chemoradiotherapy between January 2008 and September

2012 at our institution. Patient selection was performed according to the inclusion and exclusion criteria for this study, summarized in Fig 1. Forty patients who met these criteria were enrolled in this study. Five patients were excluded from the data analysis: 2 who refused the proposed treatment, 2 for whom the MR image quality was poor due to a low signal-to-noise ratio or artifacts, and 1 who died within 3 months after therapy with unknown disease status. Eventually, 35 patients were eligible for the present analysis. Patient characteristics are displayed in Table 1. All tumors were staged according to the 2002 Union for International Cancer Control Tumor, Node, Metastasis staging system.

Treatment and Follow-Up

All patients underwent concurrent chemoradiotherapy. External radiation therapy was administered in 2-Gy daily standard fractions by using 4-MV x-ray, and CT-based 3D conformal radiation therapy was mandatory. The gross tumor volume and the bulky lymph nodes were treated with up to 60–70 Gy (median, 68.4 Gy). A prophylactic nodal area was irradiated with up to 40–50 Gy (median, 44.6 Gy). Patients received concurrent chemotherapy by using S-1 and cisplatin: S-1 at the dose of 60 mg/m² for 3 weeks followed by 1 week of rest plus weekly cisplatin at the dose of 30 mg/m² for 3 weeks followed by 1 week of rest (n = 25) or cisplatin, 100 mg/m², at weeks 1 and 4 (n = 10). Chemotherapy was repeated every 4 weeks for 2 courses.

Pretreatment diagnostic examinations included contrast-enhanced CT in all patients, [¹⁸F]FDG-PET/CT in 20 patients, and panendoscopy with biopsy in all patients. For routine pretreatment examinations, MR imaging with DWI was performed in all patients. Pretreatment MR imaging with DWI was performed from 1 to 10 days before the start of treatment, and a second MR imaging with DWI was performed at 3 weeks after the start of treatment. In the previous study of the usefulness of DWI in predicting the response to neoadjuvant chemoradiotherapy for

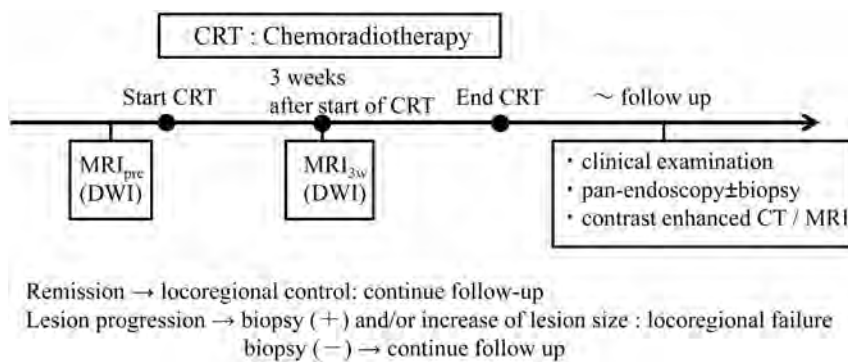


FIG 2. Time line illustrating the consecutive methodologic steps in this study.

HNSCC, a significant ADC change to predict the treatment response was obtained at a cumulative dose of 30 Gy.¹¹ Therefore, in this study, the second MR imaging with DWI was performed at 3 weeks after the start of treatment, reaching a cumulative dose of 30 Gy to the primary tumors and metastatic nodes. After the treatment, patients were followed to evaluate locoregional control (LRC) by clinical examination and a panendoscopy, followed by biopsy in cases of suspected residual disease.

In addition, routine follow-up contrast-enhanced CT and MR imaging were performed every 6 months during the follow-up period. The follow-up period was designated as the total time of follow-up starting at treatment completion and ending with either tumor recurrence or at the last patient contact without tumor recurrence. Tumor recurrence was defined at primary and nodal sites by a persistent or recurrent mass with either histopathologic proof or an increase in lesion size on serial CT or MR imaging examinations. A time line describing the consecutive methodologic steps in this study is shown in Fig 2. The progression-free survival period was defined as the time between assignment and disease progression, death, or last known follow-up. The median follow-up period for all patients was 30.8 months (range, 7–56 months); the median follow-up in survivors (no evidence of disease) was 37.6 months (range, 24–56 months).

MR Imaging and Imaging Analysis

Diffusion-Weighted MR Imaging. MR imaging was performed by using a 1.5T system (Avanto; Siemens, Erlangen, Germany) with a neck coil or a neurovascular coil. All sequences extended from the skull base to the thoracic outlet. The imaging protocol consisted of the following: T2-weighted axial and coronal images acquired by using a turbo spin-echo sequence (TR/TE = 4000/90 ms, 512 × 256 matrix), and T1-weighted axial images acquired by using a gradient recalled-echo sequence (TR/TE = 630/12 ms, 512 × 256 matrix). DWI was performed with a single-shot spin-echo echo-planar imaging sequence by using a short inversion recovery time for fat suppression (TR/TE/TI = 4000/68/180 ms, 512 × 256 matrix). The sequence was repeated for 3 values of the motion-probing gradients ($b=0, 90, \text{ and } 800 \text{ s/mm}^2$). The motion-probing gradients were placed on the 3 directions with the same strength. The FOV was 25 cm, and the section thickness was 6 mm with an intersection gap of 3 mm. The ADC map was reconstructed for each pixel by the b-values of 90 and 800 s/mm^2 by using the standard software on the console (syngo; Siemens).

Imaging Analysis. All primary tumors and lymph nodes diagnosed as metastatic nodes on pretreatment clinical and imaging assessment were evaluated on MR imaging with DWI performed from 1 to 10 days before the start of treatment and MR imaging with DWI performed at 3 weeks after the start of treatment, respectively. Because the images of HNSCC are subject to artifacts induced by continuous physiologic motion such as breathing and swallowing as well as susceptibility artifacts, automated evaluation of serial changes in ADC, such as a histogram-based or voxel-

wise approach incorporating registered image datasets between treatment interval examinations, may be needed to decrease interpretation error. Therefore, in this study, the mean value of ADC of the whole tumor and the mean change in ADC during treatment were used. ROIs were independently placed over all targeted lesions on every section of the ADC map, and the ADC values for the sections were averaged to obtain the mean value of ADC of the whole tumor for each of the patients at each measurement time point. For region-of-interest placements in the lesions, care was taken to include the solid portions of the lesions and to exclude any obviously cystic or necrotic areas in reference to the T2WI. In addition, these ROIs were used to measure the whole tumor volume. In each primary tumor and metastatic node, whole tumor volume was calculated by multiplying each cross-sectional area by the section thickness. These procedures were performed separately and independently by 2 observers (M.M. and Y.K., with 15 and 20 years of experience in head and neck MR imaging, respectively) who were blinded to the information regarding local failure or control. All ADC and tumor volume measurements were performed twice by each observer.

The ΔADC at 3 weeks for each primary tumor and metastatic node was calculated on the basis of the ADC values at pretreatment and 3 weeks after the start of treatment by using the formula

$$\Delta\text{ADC} = (\text{ADC}_{3\text{W}} \cdot \Delta\text{ADC}_{\text{pre}}) / \text{ADC}_{\text{pre}}$$

where ADC_{pre} represents the pretreatment ADC values and $\text{ADC}_{3\text{W}}$ represents the ADC values at 3 weeks after the start of treatment.

In addition, the tumor regression rate (ΔTV) for each primary tumor and metastatic node was calculated on the basis of the tumor volume at pretreatment and 3 weeks after the start of treatment by using the formula

$$\Delta\text{TV} = (\text{TV}_{\text{pre}} - \text{TV}_{3\text{W}}) / \text{TV}_{\text{pre}}$$

where TV_{pre} represents the pretreatment tumor volume and $\text{TV}_{3\text{W}}$ represents the tumor volume at 3 weeks after the start of treatment.

Statistical Analysis

The intraobserver and interobserver variability of region-of-interest placement for the measurement of ADC and tumor volume of primary tumors and metastatic nodes was analyzed by calculating the interclass correlation coefficient for single measurements (0–0.20 is considered poor; 0.21–0.40, as fair; 0.41–0.60,

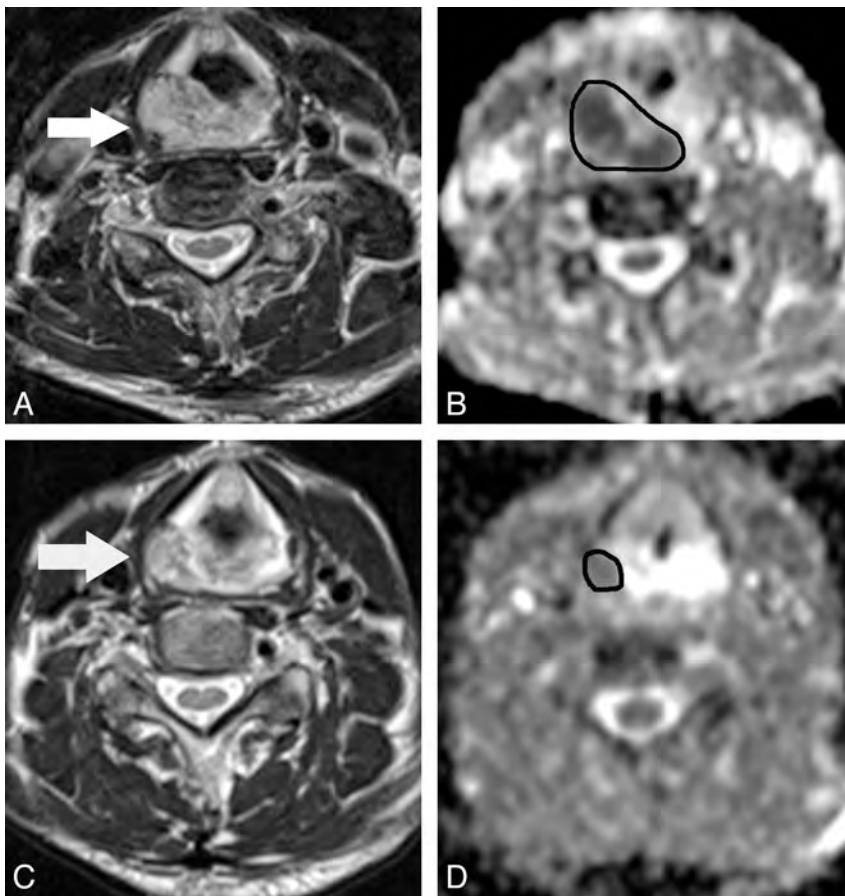


FIG 3. A 68-year-old man with hypopharyngeal cancer (poorly differentiated squamous cell carcinoma). *A*, Pretreatment transverse T2-weighted MR image shows a primary hypopharyngeal cancer (arrow). *B*, The pretreatment ADC map derived from the DWI shows that the corresponding ADC value was $1.11 \times 10^{-3} \text{ mm}^2/\text{s}$ for the manually placed region of interest covering the tumor. *C*, At 3 weeks after the start of treatment, the T2-weighted MR image shows a mass with marked regression (arrow). *D*, The $\Delta\text{ADC}_{\text{primary}}$ at 3 weeks of treatment is 0.69.

as moderate; 0.61–0.80, as good; and 0.81–1.00, as excellent correlation). The pretreatment ADC; ΔADC ; primary tumor volume; primary nodal volume; ΔTV ; and the other clinical variables such as age, T stage (T1–2 versus T3–4), N stage (N0–1 versus N2–3), and tumor location (hypopharynx or oral cavity versus others) were compared with LRC and locoregional failure (LRF) by using a Mann-Whitney *U* test. The univariate/multivariate nominal logistic analysis was used to assess the correlation between LRC and the same variables described above. Then, a receiver operating characteristic analysis with the area under the curve was used to investigate the discriminatory capability of the significant predictive value of LRC. For calculation of the sensitivity, specificity, and accuracy of the significant predictive value of LRC, the optimal threshold was determined by giving equal weighting to sensitivity and specificity on the receiver operating characteristic curve.

Finally, to determine the usefulness of ΔADC for the prediction of prognosis after chemoradiotherapy, we compared progression-free survival for the 2 groups divided by the optimal threshold value by using the Kaplan-Meier method followed by the log-rank test.

Statistical calculations were performed by using statistical analysis software (Statistical Package for the Social Sciences, Version 15.0; IBM, Armonk, New York), and *P* values < .05 were considered statistically significant.

RESULTS

Treatment Outcome

During the follow-up period, complete LRC was achieved in 21 of 35 patients (60%). Four of 35 patients (11.4%) developed an isolated local recurrence. Five of 35 patients (14.3%) developed a regional recurrence without primary tumor recurrence. Five of 35 patients (14.3%) developed a simultaneous locoregional tumor recurrence. Patients with locoregional recurrence were treated with salvage surgery and/or neck dissection with or without adjuvant chemotherapy. In patients whose tumors were inoperable, only chemotherapy was performed. Three of 35 patients (8.6%) died during the follow-up period because of the extent of local recurrent tumor.

Observer Agreement

The intraobserver and interobserver agreement for the ADC measurement was 0.81 and 0.73 on primary tumors and 0.91 and 0.82 on metastatic nodes, respectively. The intraobserver and interobserver agreement for the tumor volume measurement was 0.80 and 0.70 on primary tumors and 0.92 and 0.83 on metastatic nodes, respectively.

Analysis of Variables for Treatment Response

All DWI examinations of eligible patients for the present analysis were performed successfully. A representative case is shown in Fig 3.

Comparison of variables in LRC and LRF and univariate and multivariate analysis of variables in association with LRC are summarized in Table 2. The $\Delta\text{ADC}_{\text{primary}}$, $\Delta\text{ADC}_{\text{node}}$, primary tumor volume, primary nodal volume, $\Delta\text{TV}_{\text{node}}$, N stage, and tumor location revealed significant differences between LRC and LRF; however, there was no significant difference in $\text{ADC}_{\text{primary}}$, ADC_{node} , $\Delta\text{TV}_{\text{primary}}$, age, and T stage. In univariate logistic analysis, $\Delta\text{ADC}_{\text{primary}}$, $\Delta\text{ADC}_{\text{node}}$, $\Delta\text{TV}_{\text{node}}$, N stage, and tumor location showed significant association with LRC. Primary tumor volume and primary nodal volume showed no significant association. In multivariate logistic analysis after variable selection with the use of the forward stepwise method, only $\Delta\text{ADC}_{\text{primary}}$ was identified as a significant and independent predictor of LRC.

The receiver operating characteristic analysis resulted in a threshold $\Delta\text{ADC}_{\text{primary}}$ of 0.24 and an area under the curve of 0.9.

Table 2: Comparison of variables in LRC and LRF/univariate and multivariate analysis of variables in association with LRC

	Comparison of Variables			Univariate Analysis		Multivariate Analysis			
	LRC	LRF	P Value	P Value	OR	95% CI	P Value	OR	95% CI
ADC _{primary}	1.18 ± 0.29	1.24 ± 0.3	NS	NS					
ADC _{node}	1.09 ± 0.05	1.15 ± 0.03	NS	NS					
ΔADC _{primary}	0.6 ± 0.31	0.23 ± 0.23	.0003	.004	6.85 × 10 ⁻⁴	0.48 × 10 ⁻⁵ –0.1	.04	1.42 × 10 ⁻³	0.21 × 10 ⁻⁵ –0.94
ΔADC _{node}	0.47 ± 0.11	0.32 ± 0.04	.01	.03	1.78 × 10 ⁻²	0.46 × 10 ⁻³ –0.69	NS		
Primary tumor volume (mm ³)	9,612 ± 18,886	32,122 ± 65,012	.03	NS					
Primary nodal volume (mm ³)	7,106 ± 11,048	4,788 ± 6,999	.01	NS					
ΔTV _{primary}	0.72 ± 0.14	0.69 ± 0.13	NS	NS					
ΔTV _{node}	0.71 ± 0.19	0.56 ± 0.19	.02	.002	1.23 × 10 ⁻³	0.52 × 10 ⁻⁵ –0.29	NS		
Age (yr)	69.3 ± 9.67	66.9 ± 12.6	NS	NS					
T (T1–2 vs T3–4)	7/14	8/6	NS	NS					
N (0–1 vs 2–3)	7/14	3/11	.02	.02	4.16	1.23–21.55	NS		
Tumor location (hypopharynx or oral cavity vs others)	4/17	9/5	.003	.03	0.22	0.05–0.88	NS		

Note:—NS indicates a P value >.05.

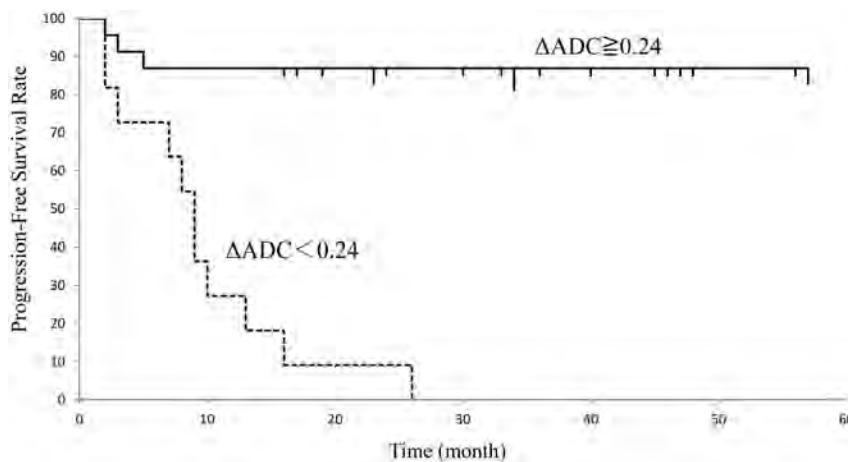


FIG 4. Progression-free survival of patients with head and neck squamous cell carcinoma assessed by ΔADC. The graph shows that the median progression-free survival period of patients with ΔADC ≥ 0.24 was significantly longer than that of patients with ΔADC < 0.24 (*P* < .05).

The 2-by-2 contingency table based on a ΔADC_{primary} of 0.24 revealed a sensitivity of 100%, specificity of 78.7%, positive predictive value of 76.7%, negative predictive value of 100%, and overall accuracy of 84.8% for the prediction of LRC.

The progression-free survival curves in patients with ΔADC_{primary} ≥ 0.24 and ΔADC_{primary} < 0.24 are shown in Fig 4. The median progression-free survival period of patients with ΔADC_{primary} < 0.24 was 11.5 ± 7.6 and that of patients with ΔADC_{primary} ≥ 0.24 was 32.8 ± 8.2. The difference in progression-free survival between the 2 groups divided by the threshold value of ΔADC_{primary} was significant (*P* < .05).

DISCUSSION

In previous clinical studies evaluating the use of DWI to predict treatment response to radiation therapy or chemoradiotherapy in HNSCC, 2 ADC parameters—namely, pretreatment ADC and the change in ADC during or early after treatment—have been shown to be useful. Kim et al⁶ reported the usefulness of pretreatment ADC for predicting the treatment response of neck lymph nodes at the end of treatment. In addition, Hatakenaka et al⁷ reported the usefulness of pretreatment ADC for predicting local failure during follow-up after chemoradiotherapy or radiation therapy. On the other hand, Vandecaveye et al⁸ reported that the change in ADC at 2 and 4 weeks of treatment correlated signifi-

cantly with the LRC and was more accurate than volumetric changes for the prediction of treatment outcome. In addition, King et al⁹ reported that a strong significant correlation was found between LRF and serial change in ADC. Thus, the optimal timing of the evaluation of ADC and its analysis method for predicting the treatment response to chemotherapy or chemoradiotherapy in HNSCC have not been established.

In the current study, the ΔADC_{primary} at 3 weeks of treatment was significantly lower for lesions with LRF than for those with LRC, and in the multivariate analysis, only ΔADC_{primary} revealed a significant association with LRC. By contrast, pretreatment ADC_{primary} was not statistically correlated with LRC. In addition, the ΔADC_{primary} threshold value of 0.24 resulted in 100% sensitivity and 100% negative predictive value for the prediction of LRC. The high negative predictive value of ΔADC_{primary} may help to predict patients with LRF of chemoradiotherapy at the early phase of treatment. Furthermore, in comparison of progression-free survival by using the ΔADC_{primary} threshold value of 0.24 for distinguishing the LRC group from the LRF group, the patients with ΔADC_{primary} ≥ 0.24 showed better prognosis than those with ΔADC_{primary} < 0.24. Therefore, our results indicate that ΔADC_{primary} is a potential predictive indicator of treatment response to chemoradiotherapy but that pretreatment ADC_{primary} is not. However, further studies that prospectively use the thresholds obtained in this study are necessary to determine the real significance of ΔADC_{primary} for prediction and management of patients with HNSCC treated with chemoradiotherapy.

In many previous clinical and animal model studies, tumors showing a rise in the ADC at an early phase of treatment showed a better treatment response than those with little or no ADC rise.^{12,13} Although the mechanism of rise in the ADC at an early phase of treatment following cytotoxic and radiation treatment in experimental and human tumors is not fully understood, it has been speculated that a rise in ADC might be attributed to an increase in the fractional volume and diffusion of water molecules in the extracellular space that occurs with the disorganized micro-

structure in necrosis and apoptosis in response to treatment.¹⁴ Therefore, ΔADC at an early phase of treatment seems to reflect the degree of tumor cell damage resulting from the treatment. However, because the treatment response may be attributed to differences in tumor aggressiveness, the treatment method, or the intensity of treatment, the use of only a single ADC measurement at pretreatment appears to be inadequate for the prediction of treatment response. Therefore, evaluating the ΔADC may be necessary for the prediction of treatment response.

The induction of tiny regions of liquefaction necrosis at the early phase of treatment may interfere with ADC measurement.¹⁵ For this reason, there may be a misleading and misrepresentative rise in ADC despite the persistence of viable tumor components. In the ADC measurement in our study, it may have been difficult to distinguish tiny liquefaction necrosis from lesions at 3 weeks of treatment because the lesions were visually associated on the ADC map in reference to T2WI for tumor heterogeneity. Therefore, we used the mean value of ADC of the whole tumor and the mean change in ADC during treatment. The use of the mean change in ADC may be explained by the fact that the specificity and positive predictive value of ΔADC were low in the current study. In brain tumor, quantification of diffusion changes has evolved from the mean change in ADC to a voxel-by-voxel approach, termed the “functional diffusion map,” as a biomarker for treatment response.¹⁶ In the functional diffusion map, treatment response is evaluated on the basis of the fractional volume of significantly increased ADC within tumor. In the study by Galbán et al¹⁷ of the functional diffusion map of HNSCC, the change in ADC assessed by the functional diffusion map was superior to the percentage change of the mean ADC in prediction of disease control after chemoradiotherapy. Therefore, in the future, more automated evaluations, such as a voxel-by-voxel approach, may be needed to estimate the change in ADC during treatment more accurately. However, it may be difficult to implement it in routine examinations for organs outside the brain due to differences in the orientation of images and artifacts induced by continuous physiologic motion.

In many previous studies that used DWI to examine the treatment response in HNSCC, a maximum b-value of 1000 s/mm² was used.⁶⁻¹⁰ Preferentially, a standardized ADC calculation by using at least 3 b-values, including a maximum b-value exceeding 500 s/mm², should be performed.¹⁸ In the current study, a maximum b-value of 800 s/mm² was used to limit the possible effects of distortion due to susceptibility artifacts and to reduce the signal-to-noise ratio on the ADC value; such factors are problems at high b-values. In this study, only 2 patients were excluded from this study due to a low signal-to-noise ratio or artifacts of DWI. The merit of ADC values differs with b-values because they are influenced by tissue perfusion and T2 time, and it may be desirable for accurate ADC measurement that 1 of the b values not be zero. Therefore, in this study, ADC values were calculated from b-values of 90 and 800 s/mm², and DWI with a b-value of zero was used for image registration.

With regard to the relationship between the ADC of metastatic nodes and treatment response, Kim et al⁶ reported that the change in ADC of metastatic nodes within the first week of chemoradiotherapy was more useful for predicting treatment response than

pretreatment ADC. In addition, Vandecaveye et al⁸ reported that the change in the ADC of metastatic nodes at 2 and 4 weeks after the start of treatment correlated significantly with 2-year LRC. In this study, $\Delta\text{ADC}_{\text{node}}$ revealed a significant difference between LRC and LRF and showed a significant association with LRC in univariate analysis. Therefore, our results were comparable with theirs, and it was suggested that the change in ADC of metastatic nodes during treatment may be useful for the prediction of treatment response and/or LRC. The primary sites of HNSCC are generally located at the air-tissue interface and in areas prone to motion artifacts induced by physiologic motion such as breathing and swallowing. Therefore, in DWI, the primary sites seem to be more influenced by physiologic motion and susceptibility artifacts than cervical lymph nodes. In addition, in variability analysis of region-of-interest placement for measurements of ADC, intraobserver and interobserver agreement of the metastatic nodes tended to be higher than those of the primary tumors in this study. Therefore, although only the $\Delta\text{ADC}_{\text{primary}}$ was identified as a significant and independent predictor of LRC in this study, the possibility that ADC values from the metastatic nodes may predict LRC in patients with HNSCC treated with chemoradiotherapy was thought to have great clinical significance.

The value of the primary tumor volume and T stage as a prognostic factor in HNSCC has been reported in published studies for multiple subsites and different treatment modalities.^{7,19} However, in the current study, primary tumor volume and T stage did not show a significant correlation with LRC. Most previously published studies included patients treated with single-technique therapy (radiation therapy or surgery alone). However, in this study, all patients were treated with definitive concurrent chemoradiotherapy. There have been many reports that definitive concurrent chemoradiotherapy leads to better clinical outcome than single-technique therapy in HNSCC.²⁰ Therefore, it was speculated that clinical outcome after definitive concurrent chemoradiotherapy might not be significantly influenced by primary tumor volume or T stage.

In patients with HNSCC treated with chemoradiotherapy, controversies remain concerning the role of neck dissection for the management of the neck with bulky lymph node involvement.²¹ There is no consensus on the treatment of patients with a complete regional response after treatment. With regard to the regional recurrence after chemoradiotherapy, it has been reported that lymph node residual size and the regression rate of nodal maximal diameter or nodal volume after treatment might be useful for the prediction of regional recurrence.^{22,23} In this study, we evaluated the usefulness of the tumor regression ratio at 3 weeks after the start of chemoradiotherapy for prediction of LRC. As a result, $\Delta\text{TV}_{\text{node}}$ revealed a significant difference between LRC and LRF and showed significant association with LRC in univariate analysis. Therefore, if prediction of regional recurrence is possible by the tumor regression rate of metastatic nodes during treatment, it has great clinical significance. In the future, it would be interesting to evaluate whether $\Delta\text{TV}_{\text{node}}$ may be a useful criterion to guide clinical decisions regarding neck dissection after chemoradiotherapy.

There are limitations to our study. First, the patient population was relatively small and heterogeneous, including those with

tumors from various head and neck sites. Also in this study, patients with oral cavity cancer were included. Surgery is usually the preferred treatment option in patients with oral cavity carcinoma, but these patients whose disease was considered inoperable because of tumor extent and/or medical reasons were enrolled in this study. Therefore, further studies with a large number of patients without potential selection bias are needed because direct comparison among DWI and other predictive or prognostic factors is necessary to show the actual clinical significance of our findings. Second, the biologic differences in squamous cell carcinomas due to differences in smoking and alcohol use as well as molecular markers such as epidermal growth factor receptor expression and human papillomavirus infection have been suggested as prognostic factors.²⁴ In particular, human papillomavirus-positive oropharyngeal carcinoma has emerged as a new entity with an excellent overall survival rate, but the patients in this study were not tested for human papillomavirus infection.

CONCLUSIONS

DWI provides information that may be used as a predictive imaging biomarker of LRC in patients with HNSCC treated by chemoradiotherapy. The $\Delta\text{ADC}_{\text{primary}}$ at 3 weeks during treatment is a valid predictive clinical factor, showing a significant association with LRC. Thus, sequential DWI may help to avoid ineffective treatment and unnecessary toxicity, allowing chemoradiotherapy to be selectively used for appropriate patients.

REFERENCES

- Argiris A, Karamouzis MV, Raben D, et al. **Head and neck cancer.** *Lancet* 2008;371:1695–709
- Horiot JC, Bontemps P, van den Bogaert W, et al. **Accelerated fractionation (AF) compared with conventional fractionation (CF) improves locoregional control in the radiotherapy of advanced head and neck cancers: results of the EORTC 22851 randomized trial.** *Radiother Oncol* 1997;44:111–21
- Ang KK, Torti A, Brown BW, et al. **Randomized trial addressing risk feature and time factors of surgery plus radiotherapy in advanced head-and-neck cancer.** *Int J Radiat Oncol Biol Phys* 2001;51:571–78
- Chiesa F, Mauri S, Tradati N, et al. **Surfing prognostic factors in head and neck cancer at the millennium.** *Oral Oncol* 1999;35:590–96
- Chenevert TL, Stegman LD, Taylor JM, et al. **Diffusion magnetic resonance imaging: an early surrogate marker of therapeutic efficacy in brain tumors.** *J Natl Cancer Inst* 2000;92:2029–36
- Kim S, Loevner L, Quon H, et al. **Diffusion-weighted magnetic resonance imaging for predicting and detecting early response to chemoradiation therapy of squamous cell carcinomas of the head and neck.** *Clin Cancer Res* 2009;15:986–94
- Hatakenaka M, Nakamura K, Yabuuchi H, et al. **Pretreatment apparent diffusion coefficient of the primary lesion correlates with local failure in head-and-neck cancer treated with chemoradiotherapy or radiotherapy.** *Int J Radiat Oncol Biol Phys* 2011;81:339–45
- Vandecaveye V, Dirix P, De Keyser F, et al. **Predictive value of diffusion-weighted magnetic resonance imaging during chemoradiotherapy for head and neck squamous cell carcinoma.** *Eur Radiol* 2010;20:1703–14
- King AD, Mo FK, Yu KH, et al. **Squamous cell carcinoma of the head and neck: diffusion-weighted MR imaging for prediction and monitoring of treatment response.** *Eur Radiol* 2010;20:2213–20
- Vandecaveye V, Dirix P, Keyzer FD, et al. **Diffusion-weighted magnetic resonance imaging early after chemoradiotherapy to monitor treatment response in head-and-neck squamous cell carcinoma.** *Int J Radiat Oncol Biol Phys* 2012;82:1098–107
- Kato H, Kanematsu M, Tanaka O, et al. **Head and neck squamous cell carcinoma: usefulness of diffusion-weighted MR imaging in the prediction of a neoadjuvant therapeutic effect.** *Eur Radiol* 2009;19:103–09
- Hamstra DA, Rehemtulla A, Ross BD. **Diffusion magnetic resonance imaging: a biomarker for treatment response in oncology.** *J Clin Oncol* 2007;25:4104–09
- Roth Y, Tichler T, Kostenich G, et al. **High-b-value diffusion-weighted MR imaging for pretreatment prediction and early monitoring of tumor response to therapy in mice.** *Radiology* 2004;232:685–92
- Hamstra DA, Lee KC, Moffat BA, et al. **Diffusion magnetic resonance imaging: an imaging treatment response biomarker to chemoradiotherapy in a mouse model of squamous cell cancer of head and neck.** *Transl Oncol* 2008;1:187–94
- Padhani AR, Liu G, Koh DM, et al. **Diffusion-weighted magnetic resonance imaging as a cancer biomarker: consensus and recommendations.** *Neoplasia* 2009;11:102–25
- Moffat BA, Chenevert TL, Lawrence TS, et al. **Functional diffusion map: a noninvasive MRI biomarker for early stratification of clinical brain tumor response.** *Proc Natl Acad Sci U S A* 2005;102:5524–29
- Galbán CJ, Mukherji SK, Chenevert TL, et al. **A feasibility study of parametric response map analysis of diffusion-weighted magnetic resonance imaging scans of head and neck cancer patients for providing early detection of therapeutic efficacy.** *Transl Oncol* 2009;2:184–90
- Koh DM, Collins DJ. **Diffusion-weighted MRI in the body: applications and challenges in oncology.** *AJR Am J Roentgenol* 2007;188:1622–35
- Chung EJ, Lee NJ, Baek SK, et al. **Clinical efficacy of primary tumor volume measurements: comparison of different primary sites.** *Clin Exp Otorhinolaryngol* 2009;2:78–84
- Pignon JP, Bourhis J, Designe L. **Chemotherapy added to locoregional treatment for head and neck squamous-cell carcinoma: three meta-analyses of updated individual data.** *Lancet* 2000;355:949–55
- Lango MN, Myers JN, Garden AS. **Controversies in surgical management of the node-positive neck after chemoradiation.** *Semin Radiat Oncol* 2009;19:24–28
- Labadie RF, Yarbrough WG, Weissler MC, et al. **Nodal volume reduction after concurrent chemo- and radiotherapy: correlation between initial CT and histopathologic findings.** *AJNR Am J Neuroradiol* 2000;21:310–14
- Clavel S, Charron MP, Belair M, et al. **The role of computed tomography in the management of the neck after chemoradiotherapy in patients with head-and-neck cancer.** *Int J Radiat Oncol Biol Phys* 2012;82:567–73
- Fakhry C, Westra WH, Li S, et al. **Improved survival of patients with human papillomavirus: positive head and neck squamous cell carcinoma in a prospective clinical trial.** *J Natl Cancer Inst* 2008;100:261–69

Yield of Neck CT and Barium Esophagram in Patients with Globus Sensation

L. Alhilali, S.-h. Seo, B.F. Branstetter IV, and S. Fakhran

ABSTRACT

BACKGROUND AND PURPOSE: Globus sensation is common and difficult to treat. The purpose of our study was to compare the diagnostic and therapeutic efficacy of barium esophagram and neck CT in patients with isolated globus sensation, to determine which of these modalities should be preferred in the evaluation of this condition.

MATERIALS AND METHODS: We retrospectively identified patients presenting with isolated globus sensation from January 1, 2005, to December 31, 2012, who underwent neck CT or barium esophagram. We calculated the proportion of patients with abnormal findings, tabulated the nature of the abnormality, and reviewed the medical records to determine whether imaging changed management.

RESULTS: One hundred forty-eight neck CTs and 104 barium esophagrams were included. Five (3.4%) patients with neck CTs and 4 (3.9%) with barium esophagrams demonstrated significant findings related to the history of globus sensation. Of these, 1 (0.7%) neck CT and 1 (1.0%) barium esophagram resulted in a change in clinical management.

CONCLUSIONS: Imaging evaluation of the patient with uncomplicated globus sensation is unlikely to identify clinically significant imaging findings and is very unlikely to result in a change in clinical management, with a combined therapeutic efficacy of 0.8%. Thus, the routine use of imaging in the evaluation of patients with globus sensation cannot be recommended.

ABBREVIATIONS: DE = diagnostic efficacy; GS = globus sensation; TE = therapeutic efficacy

Globus sensation (GS), an intermittent or persistent painless sensation of a foreign body or lump in the throat, is a long-lasting and often frustratingly difficult-to-treat clinical entity.¹ It is a relatively common condition, accounting for up to 4% of new referrals to otolaryngology clinics, with a prevalence of up to 35% in males and over 50% in females, with a relative peak in middle age.²⁻⁴ A range of etiologies has been suggested and described, including lingual and tonsillar hypertrophy, psychogenic factors, cervical osteophytes, upper aerodigestive tract malignancy, thyroid disease, and esophageal motor disorders.⁵⁻⁸ More recently, there has been increasing focus on gastroesophageal reflux disease as a cause of GS.⁹⁻¹³ The myriad potential etiologies of GS have made it difficult to establish standard treatment and imaging strategies for affected patients.

The imaging approach to the patient with GS varies widely in clinical practice. A neck CT, usually ordered with contrast, is well-suited to detect many structural causes of GS and is a useful tool to exclude a large upper aerodigestive tract malignancy, while a barium esophagram is well-suited for detailed evaluation of esophageal motility and mucosal and submucosal lesions of the esophagus. While a barium esophagram may also detect (but cannot exclude) intermittent esophageal reflux, if evaluation for esophageal reflux is of primary concern, then esophageal manometry, endoscopy, esophageal pH monitoring, or a trial of empiric therapy is the preferred diagnostic test.¹⁴⁻¹⁶

The imaging approach to the patient with GS varies widely in clinical practice. Because an evidence-based approach to imaging GS is lacking in current clinical practice, practitioner and locoregional biases strongly influence the decision to use neck CT or barium esophagram. This may adversely impact the clinical value of these studies because the value of a diagnostic test is largely dependent on the prevalence (or the clinician's estimate of the pretest probability) of the target disorder, and abnormalities detectable on neck CT and barium esophagram are statistically unlikely etiologies in a general sample of patients with GS. Because overuse of diagnostic tests contributes to both the rising cost and

Received April 22, 2013; accepted after revision May 31.

From the Departments of Radiology (L.A., S.-h.S., B.F.B., S.F.) and Otolaryngology (B.F.B.), University of Pittsburgh School of Medicine, Pittsburgh, Pennsylvania.

Paper previously presented at: Annual Meeting of the American Society of Neuroradiology and the Foundation of the ASNR Symposium, May 18-23, 2013; San Diego, California.

Please address correspondence to Saeed Fakhran, MD, 200 Lothrop St, Presby South Tower, 8th Floor, 8 North, Pittsburgh, PA 15213; fakhrans@upmc.edu

<http://dx.doi.org/10.3174/ajnr.A3683>

the overall quality of health care, defining the value of diagnostic tests has become an important goal of health care reform. We conducted the present study to determine the incidence and nature of abnormalities on neck CT and barium esophagram examinations performed in the work-up of patients with isolated GS and to assess which imaging technique contributed most effectively to the clinical management of these patients.

MATERIALS AND METHODS

Patient Selection and Image Acquisition

Our institutional review board approved this study with a waiver of informed consent. All neck CT and barium esophagram examinations included in this study were performed as part of routine clinical care, and the results were retrospectively reviewed.

We searched our enterprise-wide medical records, encompassing 20 academic and community hospitals, in an effort to identify patients with neck CT or barium esophagram studies performed for the evaluation of GS. Radiology reports from January 1, 2005, to December 1, 2012, were searched by using the key words “globus,” “lump in throat,” and “globus sensation.” Neck CT or barium esophagram studies were excluded if performed on patients with a known history of upper aerodigestive or esophageal malignancy (either primary or secondary), lymphoma, prior history of neck, esophageal, or gastric surgery, or palpable abnormality on clinical examination. Demographic data collected included age and sex. Clinical data collected from a retrospective review of the electronic medical record and radiology report included presenting symptom, presentation to the emergency department versus outpatient clinic, specialty of ordering clinician, imaging results, and postimaging clinical management.

Neck CT was performed with 16- or 64-section multidetector row CT scanners (Lightspeed VCT; GE Healthcare, Milwaukee, Wisconsin). CT acquisitions were performed according to standard protocols by scanning from the thoracic inlet to the skull base by using a helical technique with 1.0 pitch, 2.50-mm collimation, 160 maximal mA, 120 kV(peak), and 22-cm FOV. In patients who received contrast, 100 mL of iopamidol (Isovue 370; Bracco, Princeton, New Jersey) contrast material was typically administered by power injector at 1–2 mL per second into an antecubital vein with an 80-second delay before postcontrast imaging commenced (minor variations in the rate and time delay of contrast injection between various sites during the time period of this study were present).

Barium esophagrams were obtained by using a double-contrast technique as biphasic examinations. The studies included upright left posterior oblique double-contrast views of the esophagus obtained with an effervescent agent, sodium bicarbonate/tartaric acid (Baros; Lafayette Pharmaceuticals, Lafayette, Indiana) and a 250% weight/volume high-attenuation barium suspension (E-Z-HD; Bracco Diagnostics, Monroe Township, New Jersey) and prone right anterior oblique single-contrast views with a 50% weight/volume low-attenuation barium suspension (Entrobar; Lafayette Pharmaceuticals). Pharyngeal anatomy was assessed with sequential swallows of low-attenuation barium suspension with the patient in a standing position from multiple projections, by using both video fluoroscopy and cine fluoroscopy, typically set to 4 frames/second.

Esophageal motility was evaluated by having the patient take

multiple (usually 2–5) separate swallows of low-attenuation barium while in the prone right anterior oblique position, with the radiologist evaluating the progression of primary esophageal peristalsis from the thoracic esophagus through the gastroesophageal junction during the real-time examination. At the end of the study, the patient was rotated to the supine and right lateral positions for assessment of spontaneous gastroesophageal reflux; provocative techniques including the Valsalva maneuver were performed at the discretion of the radiologist.

Diagnostic and Therapeutic Efficacy

To determine the value of neck CT and barium esophagram in the work-up of GS, we used the 2 categories of efficacy as defined by the American College of Radiology Committee on Efficacy.¹⁷ Diagnostic efficacy (DE) is the number of studies with a new or progressive major finding divided by the total number of studies and is an indicator of the value of the study in assisting in a diagnosis. Therapeutic efficacy (TE) is the number of studies resulting in a change in clinical management divided by the total number of studies and is an indicator of the influence on patient clinical management.

Data Analysis

Confidence intervals for proportions in the demographic data and for therapeutic and diagnostic efficacy were calculated for pertinent imaging findings by using a continuity correction.¹⁸

RESULTS

Patient Selection and Image Acquisition

One hundred fifty-nine neck CTs and 110 barium esophagrams performed for GS were initially evaluated. Among patients with neck CT studies, 5 were excluded for a palpable abnormality on clinical examination, 1 was excluded due to a history of Burkitt lymphoma involving the neck, 1 was excluded due to a history of prior lung cancer with esophageal invasion and erosion, and 4 were excluded due to prior surgery involving the neck (thyroglossal duct cyst removal and vocal cord polyp removal) or esophagus (prior Nissen fundoplication in 2 patients). Among patients with esophagrams, 5 were excluded due to a history of neck (thymoma), esophageal (Nissen fundoplication, repair of paraesophageal hernia, prior esophageal web with multiple dilations), or gastric (prior gastrojejunostomy) surgery, and 1 was excluded due to a history of tonsillar carcinoma. The remaining 148 neck CTs, of which 140 (94.6%) were contrast-enhanced, and 104 barium esophagrams were included in our study. Five patients had both a neck CT and barium esophagram in the timeframe of the study and were included within both groups. Demographic and clinical characteristics are summarized in Table 1.

Slightly less than half of the neck CTs were ordered by otolaryngologists. Slightly more than half of the esophagrams were ordered by primary care physicians. The specialties of ordering physicians are shown in Table 2.

Diagnostic and Therapeutic Efficacy

Four of the 104 barium esophagrams (DE, 3.9%; 95% CI, 1.5%–9.5%) demonstrated previously unknown clinically important findings in the evaluation of GS. Two revealed mild indentation of

Table 1: Patient demographics and clinical characteristics

	Barium		
	Neck CT	Esophagram	Total
No. of patients	148	104	252
No. of males (%)	55 (37)	63 (61)	118 (47)
Age (yr) (mean, range)	55 (18–91)	55 (17–91)	55 (17–91)
Emergency setting (%)	22 (15%)	3 (3%)	25 (10%)
Diagnostic efficacy	5 (3.4%)	4 (3.9%)	9 (3.6%)
Therapeutic efficacy	1 (0.7%)	1 (1.0%)	2 (0.8%)

Table 2: Ordering clinicians by specialty

	Barium		
	Neck CT (%)	Esophagram (No.) (%)	Total (%)
Otolaryngology	70 (47)	31 (30)	101 (40)
Gastroenterology	10 (7)	11 (11)	21 (8)
Internal medicine/primary care	40 (27)	58 (56)	98 (39)
Emergency department	22 (15)	3 (3)	25 (10)
Other ^a	6 (5)	1 (0.9)	7 (3)

^a Each ordering 3 or fewer studies: General Surgery, Orthopedic Surgery, Geriatrics, Hematology-Oncology, Rheumatology.

the posterior esophagus from cervical spondylosis, 1 revealed minimal narrowing of the distal esophagus, and 1 revealed marked esophageal dysmotility with a suggestion of a distal esophageal stricture. Only the study revealing minimal narrowing of the distal esophagus was documented to have changed clinical management (TE, 1.0%; 95% CI, 0.2%–5.2%), with the patient eventually receiving pneumatic dilation of a benign esophageal stricture on subsequent endoscopy, with resulting resolution of his or her GS. The patient with marked dysmotility and suggestion of a distal esophageal stricture had normal endoscopic examination findings.

Five of the 148 neck CTs (DE, 3.4%; 95% CI, 1.5%–7.7%) demonstrated previously unknown major findings in the setting of a GS work-up. One demonstrated thickening of the upper third of the esophagus, 1 revealed questionable abnormal enhancement of the larynx, 1 showed an infected thyroglossal duct cyst, and 2 demonstrated hypertrophy of the lymphoid tissue of the Waldeyer ring. Of all neck CT studies, only the study demonstrating an infected thyroglossal duct cyst was documented to have changed clinical management (TE, 0.7%; 95% CI, 0.1%–3.7%). The 2 patients with hypertrophy of the lymphoid tissue of the Waldeyer ring on CT had negative flexible laryngoscopic examination findings, while the patient with thickening of the upper third of the esophagus had negative flexible laryngoscopic and esophagogastroduodenoscopy study findings. This last patient's GS was thought to be secondary to depression and resolved approximately 1 year after the abnormal CT finding. The patient with questioned abnormal enhancement of the larynx had a flexible laryngoscopic examination that revealed mild interarytenoid erythema and edema attributed to laryngeoesophageal reflux, for which the patient had already started treatment.

When we considered both types of imaging studies together, the overall diagnostic efficacy of imaging in patients with GS was 3.6% (95% CI, 1.9%–6.7%), while the overall therapeutic efficacy was 0.8% (95% CI, 0.2%–2.8%).

Of the studies with previously unknown major findings, 4 were ordered by otolaryngologists (DE, 0.040; 95% CI, 0.016–0.097), 4 were ordered by primary care physicians (DE, 0.041;

95% CI, 0.016–0.100), and 1 was ordered by an emergency department physician (DE, 0.040; 95% CI, 0.007–0.195). Of the studies that changed management, 1 was ordered by an otolaryngologist (TE, 0.010; 95% CI, 0.002–0.054) and 1 was ordered by a primary care physician (TE, 0.010; 95% CI, 0.002–0.056).

DISCUSSION

The purpose of this study was to compare the diagnostic and therapeutic efficacies of barium esophagrams and neck CTs in the evaluation of GS. Our results indicate that the diagnostic and therapeutic efficacy of imaging GS with either of the 2 modalities is extremely low. Unsuspected abnormalities were found in <4% of patients, and less than half of those induced a change in clinical management.

Imaging plays a role in the evaluation of GS in those patients with a known history of upper aerodigestive or esophageal malignancy (either primary or secondary); lymphoma; history of neck, esophageal, or gastric surgery; or palpable abnormality on clinical examination; thus, the importance of a careful and detailed history and physical examination cannot be overstated. On the basis of the findings of this study, however, we cannot endorse the routine use of imaging—with barium esophagram or neck CT—in the evaluation of the patient with GS without these modifying risk factors.

There is no consensus on the diagnostic approach to the patient with GS. Most practitioners will combine a detailed history and physical examination, with special attention to symptoms suggestive of upper aerodigestive tract malignancy—such as dysphagia, odynophagia, weight loss, and hoarseness—gastroesophageal reflux, or potential psychological history, and physical examination of the neck.^{6,7} Some authors advocate routinely prescribing antireflux medications,¹⁹ while others favor the routine use of nasolaryngoscopy²⁰; still others advocate the use of various radiologic modalities to evaluate GS.^{21,22}

In the past, many otolaryngologists advocated the routine use of rigid endoscopy in patients presenting with GS. Endoscopy for GS accounted for >7% of all endoscopy cases during a 12-month period in 1 review²³; however, recent articles have questioned the limited added value provided by rigid endoscopy in light of its associated risks (both of the procedure and accompanying anesthesia), costs, and patient discomfort and have suggested that an outpatient transnasal fiberoptic flexible endoscopic examination be used instead.^{7,20,23,24}

Reliance on imaging may be, at least in part, driven by a fear of missing a potentially treatable aerodigestive tract malignancy. Despite concern that this potentially life-threatening disease may at times present with isolated GS, our results confirm those of multiple prior studies in which no pharyngeal or esophageal malignancy was found in patients presenting with GS and undergoing a barium esophagram.^{20,25–27} Furthermore, our study identified no cases of pharyngeal or esophageal malignancy in patients presenting with isolated GS and undergoing neck CT.

Given the potential psychosocial component underlying GS, it may be argued that a negative finding on an imaging study could be reassuring to the patient and play a role in improvement or resolution of clinical symptoms. While it would be difficult to undertake an evidence-based assessment of such a treatment

model, given the current focus on efficient and economic use of limited health care resources, we cannot endorse the routine use of a study that will almost never yield positive findings.

We would also caution that overuse of imaging for clinical symptoms such as GS that lacks correlation with an identifiable radiographic finding will inevitably lead to discovery of incidental findings with a high prevalence in the general population and without a strong link to the clinical entity that led to imaging. In the setting of a symptom such as GS whose underlying mechanism is poorly understood, such incidental findings are of unknown clinical significance and, once demonstrated on imaging, may lead to overtreatment of patients. In our study, as in previous studies,^{26,27} many otherwise asymptomatic abnormalities such as small hiatal hernias, mild gastroesophageal reflux, and esophageal dysmotility, with a high prevalence in the general population and without a strong link to GS, were demonstrated.

The principal limitation to our study is the relatively large number of exclusion criteria used. Given that patients presenting with GS may have a history of prior head and neck or gastric conditions, one may argue that our results are applicable to only a small subset of patients presenting with GS. However, our exclusion rate of <7% does not suggest that this would affect our overall conclusion. A second limitation is the relatively small number of patients in our study, especially given the 7-year timeframe during which the study was conducted. If anything, this would suggest that clinicians in our academic hospital system are more selective than average when requesting imaging, lending more credence to our findings. Additionally, our study is retrospective in nature. While we may infer that studies with no significant findings did not affect clinical management, it is impossible to know whether clinical management would have been the same in the absence of a negative imaging study or a different work-up pathway would have been followed without the reassurance that a negative imaging report brings.

CONCLUSIONS

Imaging evaluation of patients with uncomplicated GS is unlikely to identify a clinically significant imaging finding and is very unlikely to result in a change in clinical management, with an overall therapeutic efficacy of 0.8%. Thus, the routine use of imaging in the evaluation of patients with uncomplicated GS cannot be recommended.

REFERENCES

1. Galmiche JP, Clouse RE, Bálint A, et al. **Functional esophageal disorders.** *Gastroenterology* 2006;130:1459–65
2. Thompson WC, Heaton KW. **Heartburn and globus in apparently healthy people.** *Can Med J* 1982;126:46–48
3. Moloy PJ, Charter R. **The globus symptom.** *Arch Otolaryngol* 1982;108:740–44
4. Drossman DA, Li Z, Andruzzi E, et al. **US householder survey of functional gastrointestinal disorders: prevalence, sociodemography, and health impact.** *Dig Dis Sci* 1993;38:1569–80
5. Färkkilä MA, Ertama L, Katila H, et al. **Globus pharyngitis, commonly associated with esophageal motility disorders.** *Am J Gastroenterol* 1994;89:503–08
6. Burns P, O'Neil J. **The diagnosis and management of globus: a perspective from Ireland.** *Curr Opin Otolaryngol Head Neck Surg* 2008;16:503–06
7. Lee B, Kim G. **Globus pharyngeus: a review of its etiology, diagnosis, and treatment.** *World J Gastroenterol* 2012;18:2462–71
8. Mabry L, Ross M, Martin P, et al. **Globus sensation associated with cervical spondylolisthesis.** *Am J Phys Med Rehabil* 2011;90:615
9. Hill J, Stuart RC, Fung HK, et al. **Gastroesophageal reflux, motility disorders, and psychological profiles in the etiology of globus pharyngitis.** *Laryngoscope* 1997;107:1373–77
10. Chevalier JM, Brossard E, Monnier P. **Globus sensation and gastroesophageal reflux.** *Eur Arch Otorhinolaryngol* 2003;260:273–76
11. Oridate N, Nishizawa N, Fukuda S. **The diagnosis and management of globus: a perspective from Japan.** *Curr Opin Otolaryngol Head Neck Surg* 2008;16:498–502
12. Park KH, Choi SM, Kwon SU, et al. **Diagnosis of laryngoesophageal reflux among globus patients.** *Otolaryngol Head Neck Surg* 2006;134:81–85
13. Tokashiki R, Funato N, Suzuki M. **Globus sensation and increased upper esophageal sphincter pressure with distal esophageal acid perfusion.** *Eur Arch Otorhinolaryngol* 2010;267:737–41
14. Pace F, Pace M. **The proton pump inhibitor test and the diagnosis of gastroesophageal reflux disease.** *Expert Rev Gastroenterol Hepatol* 2010;4:423–27
15. Fock KM, Poh CH. **Gastroesophageal reflux disease.** *J Gastroenterol* 2010;45:808–15
16. Soll AH, Fass R. **Gastroesophageal reflux disease: presentation and assessment of a common, challenging disorder.** *Clin Cornerstone* 2003;5:2–14
17. Loop JW, Lusted LE. **American College of Radiology diagnostic efficacy studies.** *AJR Am J Roentgenol* 1978;131:173–79
18. Newcombe RG. **Two-sided confidence intervals for the single proportion: comparison of seven methods.** *Stat Med* 1998;17:857–72
19. Webb CJ, Makura ZG, Fenton JE, et al. **Globus pharyngeus: a postal questionnaire of UK ENT consultants.** *Clin Otolaryngol Allied Sci* 2000;25:566–69
20. Harar RP, Kumar S, Saeed MA, et al. **Management of globus pharyngeus: review of 699 cases.** *J Laryngol Otol* 2004;118:522–27
21. Koufmann JA. **Gastroesophageal reflux disease.** In: Cummings CW, Harker LA, and Krause, CJ, eds. *Otolaryngology Head Neck Surgery*. 3rd ed. St. Louis; Mosby-Year-Book; 1998
22. Caylakli F, Yavuz H, Erkan AN, et al. **Evaluation of patients with globus pharyngeus with barium swallow pharyngoesophagography.** *Laryngoscope* 2006;116:37–39
23. Takwoingi YM, Kale US, Morgan DW. **Rigid endoscopy in globus pharyngeus: how valuable is it?** *J Laryngol Otol* 2006;120:42–46
24. Karkos PD, Wilson JA. **The diagnosis and management of globus pharyngeus: our perspective from the United Kingdom.** *Curr Opin Otolaryngol Head Neck Surg* 2008;16:521–24
25. Alaani A, Vengala S, Johnston MN. **The role of barium swallow in the management of globus pharyngeus.** *Eur Arch Otorhinolaryngol* 2007;264:1095–97
26. Back GW, Leong P, Kumar R, et al. **Value of barium swallow in investigation of globus pharyngeus.** *J Laryngol Otol* 2000;114:951–54
27. Mahrous AK, Kaoutzanis C, Amin K, et al. **Positive findings on barium swallow in patients presenting with a “sensation of a lump in the throat.”** *Eur Arch Otorhinolaryngol* 2012;269:1047–10

Actinomycosis in the Mandible: CT and MR Findings

Y. Sasaki, T. Kaneda, J.W. Uyeda, H. Okada, K. Sekiya, M. Suemitsu, and O. Sakai

ABSTRACT

SUMMARY: Mandibular actinomycosis is an uncommon disease. We retrospectively reviewed 6 patients with pathologically proven mandibular actinomycosis who underwent both CT and MR imaging to evaluate the characteristic imaging findings. CT results showed an irregularly marginated lesion with increased bone marrow attenuation, osteolysis, and involvement of the skin in all patients. Periosteal reaction and intralesional gas were seen in 4 patients. MR imaging results revealed low signal on T1-weighted and high signal on T2-weighted images of the mandible, and moderate heterogeneous enhancement was seen in all patients who received intravenous contrast. Cervical lymphadenopathy was not observed. Involvement of the masseter, lateral pterygoid, and medial pterygoid muscles was seen in 4 patients, whereas parotid gland and submandibular gland as well as parapharyngeal space involvement were seen in 3 patients. Familiarity with the imaging findings of mandibular actinomycosis may help to diagnosis this entity.

ABBREVIATION: MA = mandibular actinomycosis

Mandibular actinomycosis (MA) is an uncommon disease caused by *Actinomyces israelii*.¹ Actinomycosis infection typically manifests as a chronic disease resulting in multiple abscesses, firm soft tissue masses, and the presence of sulfur granules in exudates or tissues.² When the infection involves bone, osteolysis is likely to occur.³ In the maxillofacial region, infection is frequently of odontogenic origin, the result of oromaxillofacial trauma, dental manipulation, or dental caries.¹⁻¹⁰

Intraoral and panoramic radiographs are often used to assess various diseases and conditions of the maxilla and mandible in the dental clinic,³ but the imaging findings are often nonspecific, and differentiating actinomycosis from other inflammatory or infectious conditions or from neoplastic processes is difficult and often necessitates additional imaging.^{2,4} A few reports have described imaging findings of actinomycosis in the head and neck,^{2-4,6,8,11} but the CT and MR imaging characteristics of MA have not been fully described. The purpose of this study was to evaluate the characteristic CT and MR imaging findings of MA.

Received March 25, 2013; accepted after revision April 13.

From the Departments of Radiology (Y.S., T.K., K.S.), Histology (H.O.), and Pathology (M.S.), Nihon University School of Dentistry at Matsudo, Chiba, Japan; and Department of Radiology (J.W.U., O.S.) Boston Medical Center, Boston University School of Medicine, Boston, Massachusetts.

Paper previously presented at: Annual Meeting of the American Society of Neuroradiology; April 21–26, 2012, New York, New York.

Please send correspondence to Yusuke Sasaki, DDS, PhD, Department of Radiology, Nihon University School of Dentistry at Matsudo, 2-870-1, Sakaecho-Nishi, Matsudo, Chiba 271-8587, Japan; e-mail: sasaki.yusuke@nihon-u.ac.jp

<http://dx.doi.org/10.3174/ajnr.A3673>

CASE SERIES

Patients

After institutional review board approval, a retrospective review of our imaging data base was performed to identify patients with pathologically proven MA between April 2006 and November 2008. Both the dental history and the chief presenting complaint were evaluated, and the preoperative initial imaging diagnosis was reviewed. Histologic diagnosis was established after surgical excision in all patients.

Imaging Analysis

CT studies were performed with a 64-row multidetector CT scanner (Aquilion 64; Toshiba Medical Systems, Tokyo, Japan) with the following parameters: reconstruction thickness, 0.5 mm; tube voltage, 120 kV; tube current, 100 mA; and field of view, 240 mm × 240 mm. In all cases, multiplanar reformations in the coronal and sagittal planes were provided (1.0 mm × 3.0 mm). All images were reconstructed by use of bone and soft tissue algorithms and evaluated in bone and soft tissue windows, respectively (bone window, level: 500, width: 2800; soft tissue window, level: 30, width: 300). MR imaging was performed by use of a 1.5T MR scanner (Intera Achieva 1.5T; Philips Healthcare, Best, the Netherlands) with a head coil. Axial and coronal spin-echo T1-weighted images (TR, 500–600 ms; TE, 9.0 ms; section thickness, 6 mm), turbo spin-echo T2-weighted images (TR, 6000–8000 ms; TE, 130 ms; section thickness, 6 mm), and STIR (TR, 2500 ms; TE, 50 ms; TI, 180 ms; and section thickness, 6 mm) images were obtained in all patients. Contrast was administered in 1

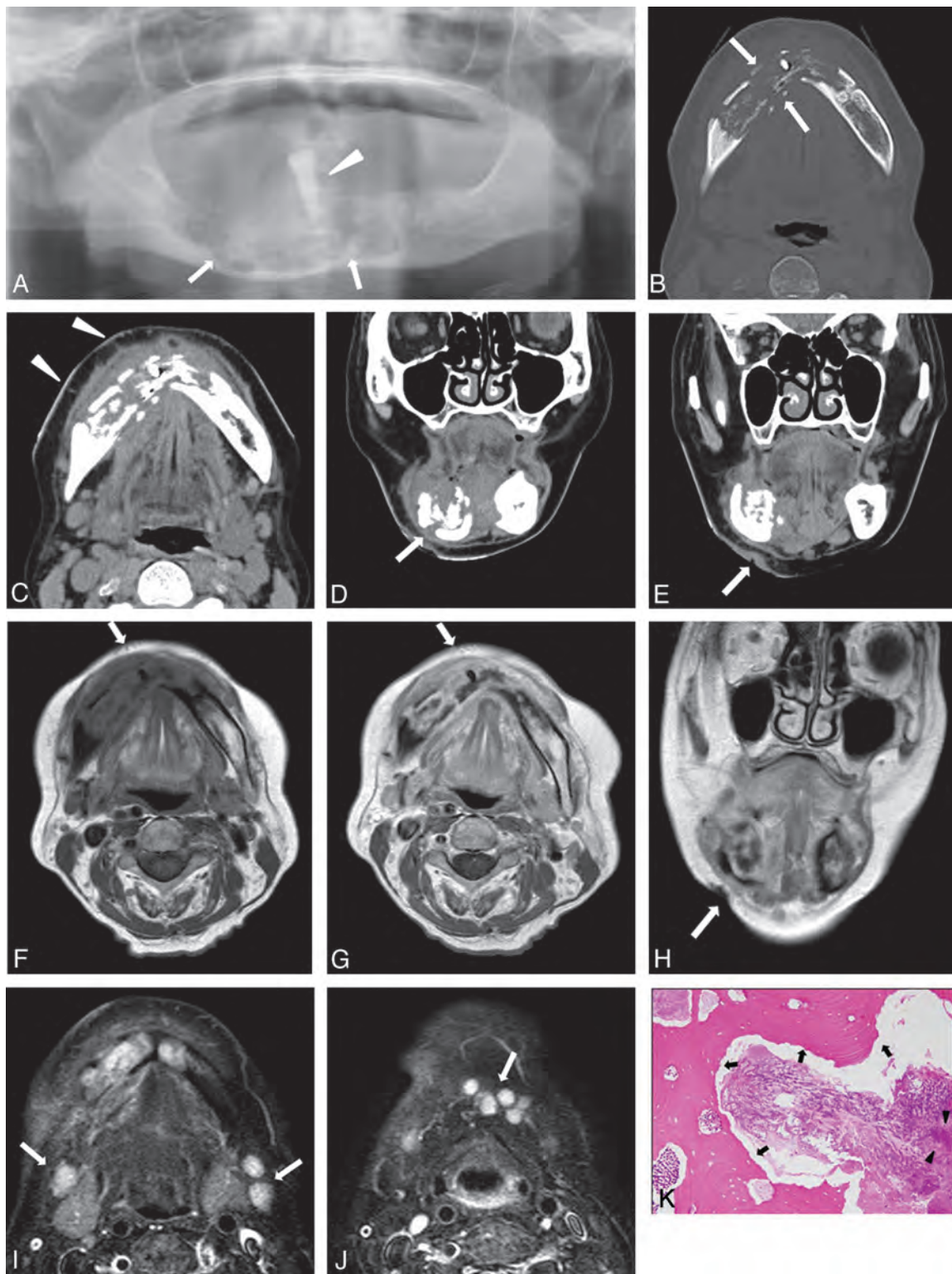


FIG 1. A 68-year-old woman with discharge of pus on the right side of the face. *A*, Panoramic radiograph reveals a large osteolytic region (arrows), with a floating tooth (arrowhead), in the right mandibular body crossing the midline. Axial CT in bone (*B*) and soft tissue (*C*) windows reveals an ill-defined osteolytic lesion in the right mandibular body crossing the midline (arrows). Note extensive demineralization of the buccal and lingual cortices and extensive soft tissue infiltrative change extending to the skin (arrowheads). *D* and *E*, Coronal CT in soft tissue window shows bone destruction and fistula from the mandible to the skin (arrows). *F*, Axial T1-weighted MR image shows heterogeneous, low signal intensity in the lesion involving the mandible and surrounding soft tissues (arrow). *G*, Contrast-enhanced axial T1-weighted MR image shows heterogeneous mass with moderate contrast enhancement in the lesion involving the mandible and surrounding soft tissues (arrow). *H*, Coronal T2-weighted MR image shows a fistula (arrow). *I* and *J*, Axial STIR MR images shows multiple mildly reactive nodes with increased signal intensity in levels IA and IB (arrows). *K*, Photomicrograph of a specimen shows actinomycotic granules (arrowheads) and presence of sequestra (arrows) (hematoxylin-eosin stain, original magnification $\times 200$).

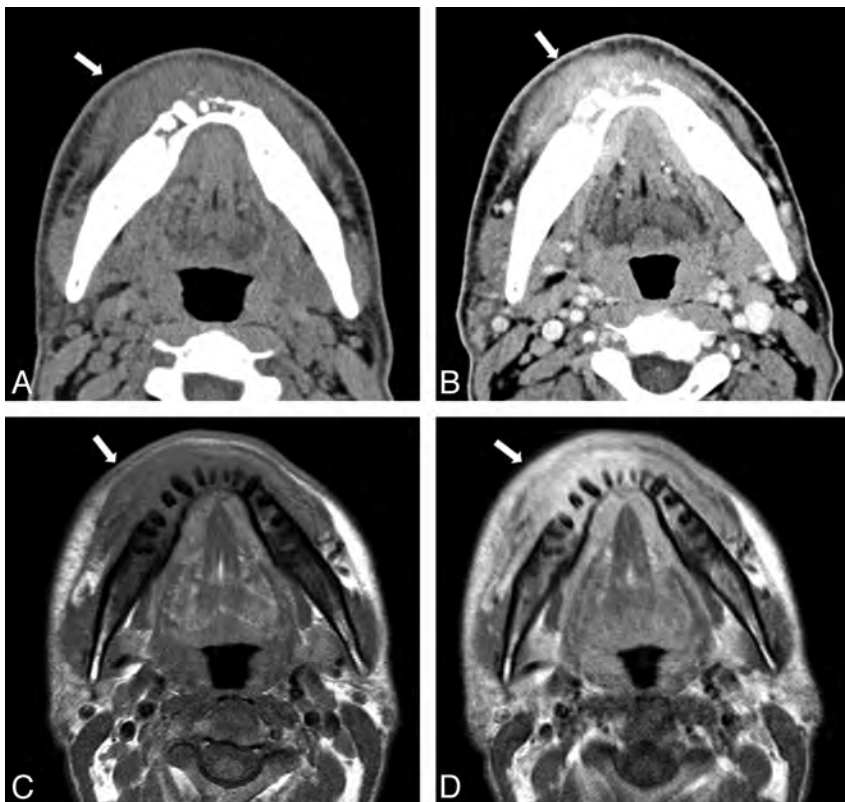


FIG 2. A 40-year-old man with discharge of pus on the right side of the face. *A*, Axial CT in soft tissue window reveals extensive soft tissue (outer layer fat around mandible) infiltrative change extending to the skin (*arrow*). *B*, Contrast-enhanced axial CT scan in soft tissue window reveals a heterogeneous, moderately enhancing mass in the lesion and extensive soft tissue (outer layer fat around mandible) infiltrative change extending to the skin (*arrow*). Axial T1-weighted (*C*) and contrast-enhanced axial T1-weighted (*D*) MR imaging reveals heterogeneous, low signal intensity in the lesion involving the mandible and surrounding soft tissues (*arrow*). Note this lesion shows diffuse and moderate contrast enhancement of the soft tissue and marrow space.

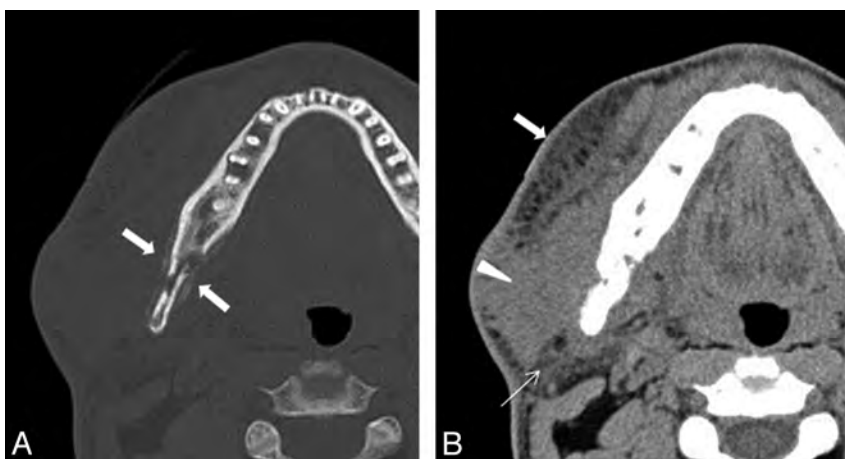


FIG 3. A 28-year-old man with swelling of the right mandibular region. *A*, Axial CT in bone window shows a heterogeneous osteolytic lesion with periosteal reaction in the posterior body to ramus of the right mandible (*arrows*). *B*, Axial CT in soft tissue window shows extensive soft tissue infiltrative change extending to the skin (*arrow*), masseter muscle (*arrowhead*), and parotid gland (*thin arrow*).

patient who underwent CT scanning and 2 patients who underwent MR imaging. Two radiologists (Y.S. and T.K.) independently reviewed the CT and MR images, and any discrepancy was solved by consensus of the 2 radiologists. The location, extension,

margin, attenuation or signal intensity of the lesions, associated osteolysis or sclerosis, periosteal reaction, intralesional gas, fistula formation, enhancement pattern of the lesions, and presence of cervical lymphadenopathy in levels I and II were recorded. The margins of the lesions were classified as either well- or ill-defined. Lymphadenopathy was defined as a lymph node > 10 mm in the short axis or by the presence of an intranodal abscess. A lymph node measuring < 10 mm in the short axis with increased signal intensity on STIR images but without intranodal abscess was considered to be a reactive node.

Imaging Findings

Review of our imaging data base revealed 6 patients with pathologically proven MA (3 men and 3 women; mean age, 51 years; age range, 28–68 years). A history of extraction of the third molar was seen in 3 patients. On physical examination, all patients had pain and swelling of the affected areas suggestive of chronic inflammation or infection, but a neoplastic process could not be completely excluded. Therefore, these patients underwent CT and MR imaging studies. Some patients had multiple findings involving muscles and/or parotid and submandibular glands. The number of various organs involved is more than the number of patients.

All 6 patients underwent unenhanced CT scanning, and 1 of 6 patients subsequently received an additional contrast-enhanced CT scan. The lesions demonstrated irregular margins with soft tissue inflammatory changes, which extended to the surface of the skin in all cases (Figs 1 and 2), and a soft tissue fistula was seen in 4 patients (Fig 1). Periosteal reaction was observed in 4 patients (Fig 3). Moderate heterogeneous contrast enhancement was seen in a patient who received intravenous contrast administration (Fig 2). Intralesional gas was seen in 4 patients (Fig 4) (Table 1).

On MR imaging scans, the lesions demonstrated signal intensity similar to muscle on T1-weighted images (Figs 1 and 2), and intermediate to high signal intensity on T2-weighted images. Heterogeneous, moderate enhancement was seen within the lesions, bone marrow, and affected soft tissues in 2 patients who received intravenous contrast (Figs 1 and 3). Ad-

Adjacent soft tissue involvement was seen in all patients on MR imaging. Involvement with inflammatory change of the masseter muscle was seen in 4 patients. Four patients had involvement of the masseter, lateral pterygoid, and medial pterygoid muscles (Fig 4). Three patients had involvement of the parotid and submandibular glands. The parapharyngeal space was affected in 3 patients (Figs 1 and 2) (Table 2).

Pathologic cervical lymphadenopathy was not seen in any patients, but reactive-appearing nodes were visualized in levels I and II in all patients (Fig 1).

DISCUSSION

Actinomycosis is an unusual chronic suppurative bacterial infection usually caused by *A israelii* that most often affects the cervicofacial region, accounting for approximately 50% of all patients.⁵ Most reports note a predilection for male patients with a male-to-female ratio of 3:1–4:1.¹¹

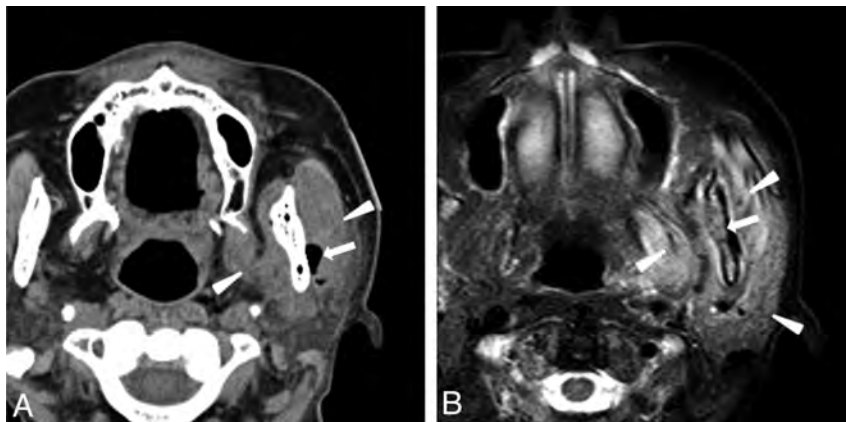


FIG 4. A 66-year-old woman with swelling of left mandibular region. A, Axial CT in soft tissue window demonstrates foci of air adjacent to the left mandible (arrow) and swelling of masseter and medial pterygoid muscle (arrowheads). B, Axial STIR MR image shows extensive inflammation in the left masseter muscle, medial pterygoid muscles, parotid gland (arrowheads), and mandibular bone marrow (arrow).

The clinical diagnosis of actinomycosis is difficult, as it may mimic a neoplasm.^{2,4} The most common clinical finding of actinomycosis is a firm palpable mass with a subacute clinical course.⁴ Approximately half of patients present with a low-grade fever.⁷ Because actinomycosis species are anaerobic bacteria that cannot penetrate healthy tissue, mucosal breakdown is a prerequisite for infection.⁵ Roughly half of patients have a history of local trauma resulting in mucosal breakdown, with poor dental hygiene, caries, oral trauma, dental extraction, and an immunocompromised status being important predisposing factors.⁵ A presumptive diagnosis of actinomycosis can be made by identification of sulfur granules in an abscess or in the secretions from a sinus tract,⁶ but only 10% of actinomycotic infections are correctly diagnosed at the time of initial presentation.⁷ The diagnosis of actinomycosis is made most accurately by isolation of *Actinomyces* species in cultures of clinical specimens.⁶ The visualization of actinomycotic granules in exudates or in histopathologic tissue sections is strongly supportive of the diagnosis.⁷

In the literature, an enhancing soft tissue mass with invasion in the cervicofacial region and rarefying osteomyelitis in MA have been described.² In our study, all lesions had ill-defined, infiltrative margins with surrounding soft tissue inflammatory response that extended to the skin. Soft tissue fistula/sinus tract formation and intralesional gas were seen in 4 of 6 patients; these findings are useful to differentiate actinomycosis from other infection. Osteomyelitis caused by actinomycosis demonstrates intralesional gas from anaerobic breakdown or fistulas within the mouth, whereas mandibular osteomyelitis caused by other organisms does not typically result in fistulas or intral-

Table 1: CT imaging features of MA

Patient No/ Age (y)/Sex	CT Imaging Findings								
	Contrast Enhancement	Margin	Density	Intralesional Gas	Fistula	Osteolysis	Periosteal Reaction	Sequestra	Lymphadenopathy
1/40/M	Mod. heterog.	Irregular	Low-intermed.	—	+	+	+	+	—
2/34/M	Not done	Irregular	Low-intermed.	+	+	+	—	—	—
3/66/F	Not done	Irregular	Low-intermed.	+	—	+	+	+	—
4/28/M	Not done	Irregular	Low-intermed.	—	+	+	+	+	—
5/78/F	Not done	Irregular	Low-intermed.	+	+	+	+	+	—
6/68/F	Not done	Irregular	Low-intermed.	+	—	+	—	—	—

Note:—F indicates female; M, male; Low-intermed., low to intermediate; Mod. heterog., moderate heterogeneous.

Table 2: MR imaging features of actinomycosis in the mandible

Patient No	MRI Findings				
	Gadolinium Enhancement	Cellulitis Adjacent to the Facial Skin	Inflammation of Masseter Muscle	Inflammation of Pterygoid Muscle	Lymph Adenopathy
1	Moderate heterogeneous	+	—	—	—
2	Not done	+	+	—	—
3	Not done	+	+	+	—
4	Not done	+	+	+	—
5	Not done	+	+	+	—
6	Moderate heterogeneous	+	+	+	—

Note:—+ indicates findings present; —, findings absent.

esional gas.¹² MR imaging has higher accuracy in the detection of inflammatory and infiltrative changes in the surrounding soft tissue extending to the skin,¹³ particularly in the muscles of mastication, though visualization of gas is challenging. Although bone marrow signal changes of MA were similar to osteomyelitis secondary to other causes,¹³ very extensive soft tissue inflammatory and infiltrative changes in the surrounding soft tissues extending to the skin may be useful in the differentiation of actinomycosis from osteomyelitis due to other causes. In particular, extensive soft tissue inflammation extending to the skin surface and forming fistulas appeared to be characteristic for actinomycosis.

Lymphadenopathy is thought to be a relatively uncommon finding in actinomycosis because the organism does not spread via the lymphatic system secondary to the size of the bacterium.^{1,2} None of our patients showed lymphadenopathy measuring more than 10 mm in the short axis, though mildly reactive nodes with increased signal intensity on STIR images but without intranodal abscess were seen in all patients. An et al¹⁴ reported that cervical lymphadenopathy was present in approximately 40% of mandibular osteomyelitis cases from ordinal bacterial infection. Therefore, absence of lymphadenopathy may be suggestive of MA rather than other acute or chronic infections or malignant tumors, particularly in patients with extensive soft tissue changes with fistula formation.

CONCLUSIONS

CT and MR imaging findings of MA were reviewed. Characteristics imaging findings including the presence of intralesional gas, osteolytic changes with extensive inflammatory changes in the surrounding soft tissue extending to the skin surface, fistula formation, and absence of lymphadenopathy were frequently seen and are helpful in narrowing the differential diagnosis.

Disclosures: Osamu Sakai—UNRELATED: Royalties: Sakai O. *Head and neck imaging cases*. McGraw-Hill Companies.

REFERENCES

1. Hansen T, Kunkel M, Springer E, et al. **Actinomycosis of the jaws—histopathological study of 45 patients shows significant involvement in bisphosphonate-associated osteonecrosis and infected osteoradionecrosis.** *Virchows Arch* 2007;451:1009–17
2. Park JK, Lee HK, Ha HK, et al. **Cervicofacial actinomycosis: CT and MR imaging findings in seven patients.** *AJNR Am J Neuroradiol* 2003;24:331–35
3. Smith MH, Harms PW, Newton DW, et al. **Mandibular actinomycosis osteomyelitis complicating florid cemento-osseous dysplasia: case report.** *BMC Oral Health* 2011;11:21
4. Sa'do B, Yoshiura K, Yuasa K, et al. **Multimodality imaging of cervicofacial actinomycosis.** *Oral Surg Oral Med Oral Pathol* 1993;76:772–82
5. Belmont MJ, Behar PM, Wax MK. **Atypical presentations of actinomycosis.** *Head Neck* 1999;21:264–68
6. Nagler R, Peled, Laufer D. **Cervicofacial actinomycosis: a diagnostic challenge.** *Oral Surg Oral Med Oral Pathol Oral Radiol Endod* 1997;83:652–56
7. Oostman O, Smego RA. **Cervicofacial actinomycosis: diagnosis and management.** *Curr Infect Dis Rep* 2005;7:170–74
8. Kemp FH, Vollum L. **Anaerobic cellulitis due to actinomycetes, associated with gas production.** *Br J Radiol* 1946;19:248
9. Nielsen PM, Novak A. **Acute cervico-facial actinomycosis.** *Int J Oral Maxillofac Surg* 1987;16:440–44
10. Bennhoff DF. **Actinomycosis: diagnostic and therapeutic considerations and a review of 32 cases.** *Laryngoscope* 1984;94:1198–217
11. Miller M, Haddad AJ. **Cervicofacial actinomycosis.** *Oral Surg Oral Med Oral Pathol Oral Radiol Endod* 1998;85:496–508
12. Adekeye EO, Cornah J. **Osteomyelitis of the jaws: a review of 141 cases.** *Br J Oral Maxillofac Surg* 1985;23:24–35
13. Lee K, Kaneda T, Mori S, et al. **Magnetic resonance imaging of normal and osteomyelitis in the mandible: assessment of short inversion time inversion recovery sequence.** *Oral Surg Oral Med Oral Pathol Oral Radiol Endod* 2003;96:499–507
14. An CH, An SY, Choi BR, et al. **Hard and soft tissue changes of osteomyelitis of the jaws on CT images.** *Oral Surg Oral Med Oral Pathol Oral Radiol* 2012;114:118–26

Arterial Spin-Labeled Perfusion of Pediatric Brain Tumors

K.W. Yeom, L.A. Mitchell, R.M. Lober, P.D. Barnes, H. Vogel, P.G. Fisher, and M.S. Edwards



ABSTRACT

BACKGROUND AND PURPOSE: Pediatric brain tumors have diverse pathologic features, which poses diagnostic challenges. Although perfusion evaluation of adult tumors is well established, hemodynamic properties are not well characterized in children. Our goal was to apply arterial spin-labeling perfusion for various pathologic types of pediatric brain tumors and evaluate the role of arterial spin-labeling in the prediction of tumor grade.

MATERIALS AND METHODS: Arterial spin-labeling perfusion of 54 children (mean age, 7.5 years; 33 boys and 21 girls) with treatment-naive brain tumors was retrospectively evaluated. The 3D pseudocontinuous spin-echo arterial spin-labeling technique was acquired at 3T MR imaging. Maximal relative tumor blood flow was obtained by use of the ROI method and was compared with tumor histologic features and grade.

RESULTS: Tumors consisted of astrocytic (20), embryonal (11), ependymal (3), mixed neuronal-glial (8), choroid plexus (5), craniopharyngioma (4), and other pathologic types (3). The maximal relative tumor blood flow of high-grade tumors (grades III and IV) was significantly higher than that of low-grade tumors (grades I and II) ($P < .001$). There was a wider relative tumor blood flow range among high-grade tumors (2.14 ± 1.78) compared with low-grade tumors (0.60 ± 0.29) ($P < .001$). Across the cohort, relative tumor blood flow did not distinguish individual histology; however, among posterior fossa tumors, relative tumor blood flow was significantly higher for medulloblastoma compared with pilocytic astrocytoma ($P = .014$).

CONCLUSIONS: Characteristic arterial spin-labeling perfusion patterns were seen among diverse pathologic types of brain tumors in children. Arterial spin-labeling perfusion can be used to distinguish high-grade and low-grade tumors.

ABBREVIATIONS: ASL = arterial spin-labeling; DIPG = diffuse intrinsic pontine glioma; DNT = dysembryoplastic tumor; OPG = optic pathway glioma; rTBF = relative tumor blood flow; WHO = World Health Organization

Brain tumors are the most common solid tumors of childhood and are a leading cause of cancer deaths in children.¹ Unlike in adults, these tumors predominate in the posterior fossa and have more heterogeneous pathologic features, including embryonal and mixed neuronal-glial types.² Because of their diverse histologic presentation and biologic behavior, evaluation and treatment of pediatric brain tumors remain complex.

MR imaging is important in tumor diagnosis, surgical guidance, and therapeutic monitoring of brain tumors. Various PWI methods have shown clinical usefulness in adult glioma, including the use of relative maximal CBV and relative CBF from DSC-PWI to predict tumor grade and behavior.³⁻¹⁰ Despite abundant literature on adult brain tumors, few perfusion reports exist for pediatric brain tumors,¹¹⁻¹⁴ potentially because of technical challenges. For example, the most widely available T2*-weighted DSC imaging often requires constant, high-flow contrast injection by power injectors, double-dosing, and large-bore intravenous access, which pose challenges in young children and infants.

Recent studies have shown that arterial spin-labeling (ASL) may be a reliable alternative to DSC-PWI in the evaluation of tumor perfusion¹⁵⁻²⁰ and can predict adult glioma grade.¹⁶ ASL has distinct advantages in children because of lack of contrast requirement, high SNR, labeling efficiency, and the potential for CBF quantification. Also, ASL can be repeated in cases of failed sedation or patient motion, a frequent problem in children with brain tumors.

Received April 4, 2013; accepted after revision May 15.

Abstract previously presented at: Annual Meeting of the American Society of Neuroradiology, April 2012; New York, New York.

From the Departments of Radiology (K.W.Y., L.A.M., P.D.B.) Neurosurgery (R.M.L., M.S.E.), Pathology (H.V.), and Neurology (P.G.F.), Lucile Packard Children's Hospital, Stanford University, Palo Alto, California.

Please address correspondence to Kristen W. Yeom, MD, Lucile Packard Children's Hospital, Stanford University, Department of Radiology, Pediatric MRI & CT, Room 0511, 725 Welch Rd, Palo Alto, CA 94304; e-mail: kyeom@stanford.edu

 Indicates article with supplemental on-line figures.

<http://dx.doi.org/10.3174/ajnr.A3670>

Although ASL has become increasingly available clinically, no ASL data exist on pediatric brain tumors. Our goal was to apply ASL perfusion for diverse pathologic types of pediatric brain tumors and evaluate the use of ASL perfusion for the prediction of tumor grade in children.

MATERIALS AND METHODS

Patients

A total of 54 consecutive patients younger than 19 years old with new primary brain tumors at our children's hospital were retrospectively reviewed after approval by the institutional review board (IRB-23336). The following inclusion criteria were used: patients obtained ASL at 3T as part of routine MR imaging; had no prior surgical resection, biopsy, or treatment of the tumor; underwent subsequent resection or biopsy of the tumor except in cases of optic pathway glioma (OPG) and diffuse intrinsic pontine glioma (DIPG), where tissue sampling was not used for diagnosis as part of standard care; and the solid component of the tumor exclusive of cyst, hemorrhage, or necrosis was greater than 1 mL. Patients with underlying cardiac disease, hypertension, or vasculopathy that could alter ASL perfusion, as well as patients with motion artifacts or dental braces or hardware that degrade ASL imaging were excluded.

Imaging Methods

All patients were examined at 3T MR imaging (Discovery 750; GE Healthcare, Milwaukee, Wisconsin) by use of an 8-channel head coil. The technique used to perform perfusion ASL has been detailed elsewhere.²¹ In brief, ASL was performed by use of a pseudocontinuous labeling period of 1500 ms, followed by a 1500-ms postlabel delay. Whole-brain images were obtained with a 3D background-suppressed FSE stack-of-spirals method, with a TR of approximately 5 seconds. Multiarm spiral imaging was used, with 8 arms and 512 points acquired on each arm (bandwidth, 62.5 kHz), yielding in-plane and through-plane spatial resolution of 3 and 4 mm, respectively. A high level of background suppression was achieved by use of 4 separate inversion pulses spaced around the pseudocontinuous labeling pulse. The sequence required 5 minutes to acquire, including proton attenuation images for CBF quantitation. An effort was made to position the patients' heads in the exact same position to minimize any head tilting; all scans were performed in the axial plane. For graphic prescription of the ASL, the sagittal image following the 3-plane localizer was used for alignment. Using the microsphere methodology described by Buxton et al,²² we performed postprocessing by using an automated reconstruction script that returned CBF images directly to the scanner console. Other ASL parameters were TR, 4632 ms; TE, 10.5 ms; FOV, 24 cm x 24 cm; matrix, 512 x 8; and NEX, 3.

Imaging Analysis

For each tumor, ROIs were drawn around both the enhancing and nonenhancing solid portions of the tumor at all available axial levels of the ASL tumor blood flow map. Conventional MR imaging, including T2WI and contrast-enhanced T1WI, was used to cross-reference solid portions of the tumor to the ASL tumor blood flow maps. Areas of cyst, necrosis, and gross hemorrhage

(detected by the T2* gradient-recalled echo and noncontrast T1WI) were avoided. A board-certified neuroradiologist (K.W.Y.) with a Certificate of Added Qualification (7 years of experience) selected ROIs blinded to clinical and pathologic data. A second blinded board-certified neuroradiologist (P.D.B.) with a Certificate of Added Qualification (30 years of experience) independently confirmed the appropriate ROI placement.

The maximal ASL signal was recorded for each ROI of the tumor, and the 2 highest values were averaged. Maximal, rather than mean, tumor blood flow was assessed, as prior studies have used maximal blood volume or flow values to correlate glioma grade and vascularity^{4-7,9,16,23} and have shown that maximal relative tumor blood flow (rTBF) may be most sensitive for tumor grade.²⁴ To correct for age-dependent and patient-dependent variations of mean cerebral perfusion,²⁵ maximal tumor blood flow was normalized to a 150-mm² ROI in the contralateral gray matter to produce the maximal rTBF. Prior tumor perfusion studies have used various brain regions, including contralateral white matter,^{6,8,9} gray matter,^{10,17,20,26} or the cerebellum¹⁷ as an internal standard. For this study, contralateral gray matter, which has a higher SNR than white matter, was chosen as a reference, similar to the technique by Noguchi et al,²³ because a longer arterial transit time of the white matter underestimates the ASL signal.^{27,28} The control ROI in healthy gray matter was placed independently by a blinded board-certified second-year neuroradiology fellow (L.A.M.), also independently confirmed by a blinded neuroradiologist (K.W.Y.). Sample ROI placement is shown in Fig 1.

Enhancement of each tumor was graded by a blinded neuro-radiologist (K.W.Y.) with the following scoring system: 0 = no enhancement, 1 = < 50% enhancement of the solid tissue, 2 = ≥ 50% enhancement of the solid tissue.

Pathology Findings

All surgical specimens were reviewed by a board-certified pediatric neuropathologist (H.V.; 30 years of experience). Tumors were categorized according to the 2007 *World Health Organization (WHO) Classification of Tumors of the Central Nervous System*.²⁹ For this study, WHO grade III and IV tumors were considered high grade; WHO grades I and II were considered low grade.

Statistics

We performed statistical analyses by using SPSS version 21 (IBM, Armonk, New York) with an a priori significance level $\alpha = .05$. The Kruskal-Wallis test for independent samples was used for comparison of the distribution of maximal rTBF and range between multiple tumor grades (low, high, or unspecified), specific histologic types within those grades, different posterior fossa tumors, and different locations for a given tumor type. A separate analysis of posterior fossa tumors was performed to compare perfusion differences among medulloblastoma, pilocytic astrocytomas, and ependymoma (grades II and III). Comparison of values between 2 groups, such as medulloblastoma and pilocytic astrocytoma, was performed with the Mann-Whitney *U* test for independent samples. DIPGs were excluded from the analysis because these tumors are graded as WHO II-IV and typically do not have available pathologic

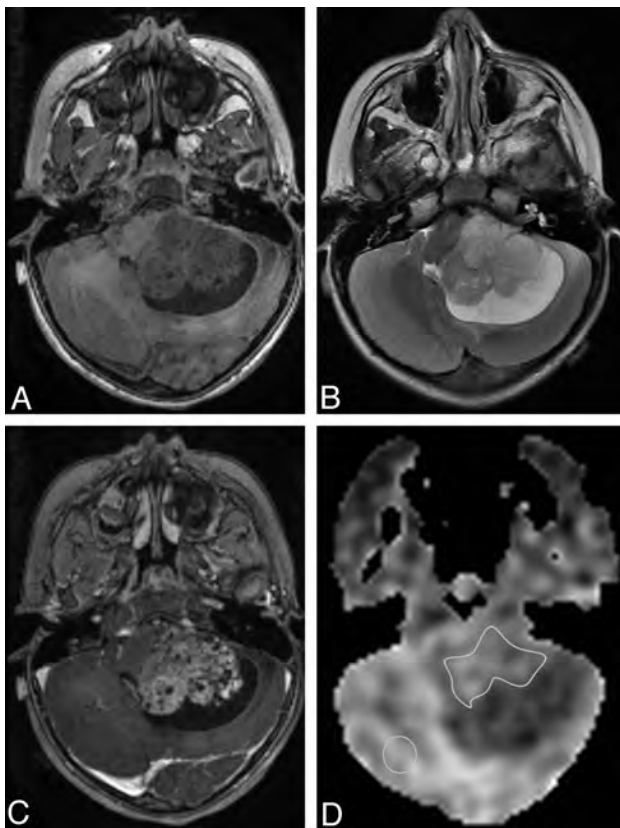


FIG 1. Example of ROI placement is shown in a 2-year-old girl with a posterior fossa atypical choroid plexus papilloma. *A*, Axial T1-spoiled gradient-recalled MR image. *B*, Axial T2-weighted MR image. *C*, Contrast-enhanced axial T1-spoiled gradient-recalled MR image shows enhancing mass with a cystic component. *D*, ASL perfusion map shows ROI placement over the solid tumor and in the contralateral brain not affected by the tumor.

specimens. The relationship between tumor volume and rTBF was tested by Pearson correlation.

RESULTS

Patients

The mean age of the 54 participants was 7.5 years (median age, 6 years; age range, 2 months to 18 years). There were 33 boys and 21 girls. Surgical specimens were available in 49 of these patients. Diagnoses in 4 patients with OPG and 1 patient with DIPG were based on characteristic MR imaging and clinical presentation, as these typically are not resected.

Tumor Pathologic Features

The tumors included 21 high-grade tumors (WHO III and IV), 32 low-grade tumors (WHO I and II), and 1 DIPG with unspecified grade. Tumor pathologic features by WHO grade, age, location, and rTBF are shown in the Table. Although OPGs are not typically surgically sampled, prior studies have shown that they usually represent grade I pilocytic astrocytoma³⁰ and are therefore considered low grade.

Comparison of High-Grade vs Low-Grade Tumors

The values of averaged maximal rTBF by tumor pathologic specimen are shown in the Table. Both the maximal and averaged

maximal rTBF of the high-grade tumors (grades III and IV) were significantly higher vs low-grade tumors (grades I and II) ($P < .001$) (Fig 2). There was a wider range of rTBF (minimal to maximal rTBF) among high-grade tumors (2.14 ± 1.78 ; median, 1.23; range, 0.55–6.96) compared with low-grade tumors (0.60 ± 0.29 ; median, 0.54; range, 0.32–1.66) ($P < .001$).

High-Grade Tumors

Among high-grade tumors, individual histologic features were not distinguished by rTBF ($P = .377$). The rTBF of glioblastoma (3.70 ± 1.89) was not distinguished from medulloblastoma (2.87 ± 1.74) or combined embryonal tumors (medulloblastoma, primitive neuroectodermal tumor, atypical teratoid rhabdoid tumor) (2.62 ± 1.66) ($P = .283$ and $P = .142$, respectively). The averaged maximal rTBF ranged from 2.43–6.49 for pediatric glioblastoma and 0.98–4.97 for medulloblastoma. Perfusion examples are shown in Fig 3.

Low-Grade Tumors

Among low-grade tumors, individual histologic features were not distinguished by rTBF ($P = .179$). Their maximal rTBF was similar to contralateral gray matter (range, 0.89–1.12). Pilocytic astrocytoma (1.05 ± 0.18) most closely approximated contralateral normal brain CBF, whereas dysembryoplastic tumors (DNTs) (0.89 ± 0.13) and OPG (0.80 ± 0.09) were hypoperfused. There was no difference in rTBF among pilocytic astrocytomas by location (cerebrum, brain stem, cerebellum) ($P = .670$). Perfusion examples are shown in Fig 4.

Posterior Fossa Tumors

There were 22 tumors after exclusion of DIPG, consisting of medulloblastoma,⁸ pilocytic astrocytoma,⁷ ependymoma,³ choroid plexus papilloma,³ and ganglioglioma.¹ Perfusion examples are shown in On-line Fig 1. Among all posterior fossa tumors, rTBF did not reliably distinguish individual histologic features ($P = .202$). However, there was a significant difference in rTBF between medulloblastoma and pilocytic astrocytoma when compared without consideration of other tumor types (independent-sampled Mann-Whitney U test; $P = .014$). There was also a wider range of rTBF variability among medulloblastoma compared with pilocytic tumors ($P = .025$) (On-line Fig 2).

Tumor Volume and Enhancement

There was no correlation between tumor volume and rTBF ($P = .459$). The rTBF values were not different based on patterns of contrast enhancement ($P = .245$).

DISCUSSION

Although abundant perfusion data exist in adult glioma regarding tumor detection, pathologic correlates, and therapeutic response, few studies have examined tumor perfusion in children. However, it may not always be feasible or appropriate to apply adult glioma data in the evaluation of pediatric tumors because of features unique to the pediatric population.^{31–33} For example, embryonal tumors, such as medulloblastoma and primitive neuroectodermal tumor, are rarely seen in adults; epidermal growth factor receptor amplification and deletion of phosphate and tensin homolog

Tumor pathologic features by WHO grade, age, location, and rTBF

Tumor Pathologic Feature	WHO Grade	Mean Age ^a	Tumor Location	rTBF ^b
High-grade tumors (III and IV) (n=21)				
Glioblastoma (4)	IV	13 ± 8.5	Cerebrum	3.70 ± 1.89
Anaplastic astrocytoma (1)	III	11	Cerebrum	3.60
CNS PNET (1)	IV	9	Thalamus	1.32
Medulloblastoma (9)	IV	6.1 ± 3.7	PF	2.87 ± 1.74
Primary malignant melanoma (1)	IV	12	Cerebrum	1.70
Anaplastic ependymoma (2)	III	3 ± 2.8	PF	1.99 ± 0.39
CNS ATRT (1)	IV	4	Cerebrum	1.67
Choroid plexus carcinoma (1)	III	3 months	Lateral ventricle	7.96
DIPG (1)	III	7	Pons	1.70
Low-grade tumors (I and II) (n=32)				
Pilocytic astrocytoma (8)	I	9.4 ± 6.1	Cerebrum (1), cerebellum (3), brain stem (4)	1.05 ± 0.19
Hypothalamic astrocytoma (1)	II	10	Hypothalamus–third ventricle	0.99
Angiocentric glioma (1)	I	15	Cerebrum	0.94
DNT (2)	I	5.5 ± 4.9	Cerebrum	0.89 ± 0.13
OPG (4)	I	4.8 ± 1.5	Optic chiasm	0.80 ± 0.09
Choroid plexus papilloma (3)	I	5.6 ± 3.5	PF (2), lateral ventricle (1)	1.13 ± 0.15
Atypical choroid plexus papilloma (1)	II	2	PF	1.34
Ganglioglioma (6)	I	6.2 ± 6.6	Cerebrum (5), brain stem (1)	1.45 ± 0.54
Craniopharyngioma (4)	I	12.8 ± 4.3	Suprasellar cistern	0.99 ± 0.13
Atypical meningioma (1)	II	8 months	Cerebrum	1.60
Ependymoma (1)	II	3	PF	1.82
Unspecified grade (n=1)				
DIPG (1)	II–IV	6	Pons	1.35

Note:—ATRT indicates atypical teratoid rhabdoid tumor; PF, posterior fossa; PNET, primitive neuroectodermal tumor.

^a Age in years, unless otherwise specified.

^b rTBF equals the averaged maximal rTBF values from 2 different ROIs within the solid tumor.

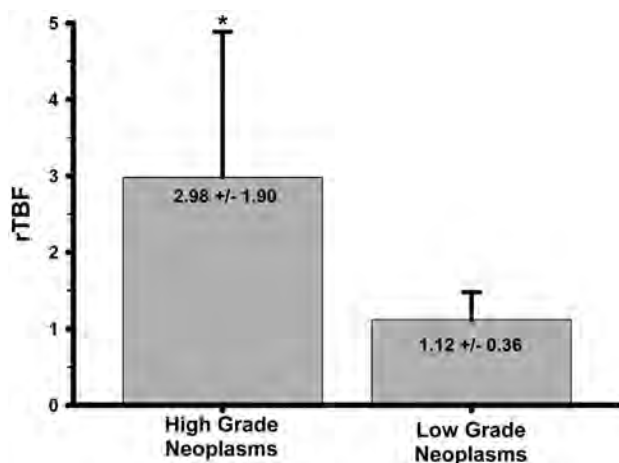


FIG 2. A bar graph showing comparison of high-grade and low-grade neoplasms. Significantly higher mean rTBF (*) is seen in high-grade compared with low-grade tumors. The error bars represent standard deviation.

gene, commonly found in adult primary glioblastoma, are rarely detected in pediatric glioblastoma.^{31,33} With increased use of antiangiogenic therapies, including treatment of pediatric high-grade astrocytomas and treatment-resistant medulloblastoma and pilocytic astrocytoma, PWI may be a key to tumor surveillance and identification of treatment-responsive tumor subtypes.

The benefits of ASL perfusion in children are well known, including high labeling efficiency, SNR, and lack of contrast requirement.³⁴ Immature paranasal sinuses also likely contribute to improved image quality of ASL, with reduced distortion artifacts in the frontal and inferior brain regions in young children.³⁵ Here, we used spin-echo ASL that incorporates high-field parallel imaging, pseudocontinuous labeling, and 3D imaging with back-

ground suppression, which has previously been shown to increase sensitivity for CBF imaging.³⁶ To our knowledge, our study is the first to report ASL parameters of various pathologic types of pediatric brain tumors and its use in correlating tumor grade in children.

Our results for neuronal-glia and astrocytic tumors are similar to nuclear medicine and adult perfusion studies. Similar to a prior report by Kumabe et al³⁷ that showed high uptake in their 3 cases of ganglioglioma by use of thallium-201 SPECT, tumor blood flow was elevated compared with gray matter in 5 of 6 gangliogliomas in our study. In contrast, DNTs, which generally have low growth potential,³⁸ showed lower rTBF, similar to hypoperfusion pattern by use of iodine 123 *N*-isopropyl-*p*-iodoamphetamine or technetium Tc99m hexamethylpropyleneamine oxime methods.³⁹ In our study, rTBF for glioblastoma ranged from 2.43–6.49, similar to the wide range of 1.18–5.86 reported for adult high-grade gliomas.^{16,24} Also, rTBF of 0.78–1.37 for grade I/II glioma was similar to the 0.59–0.96 range reported for adult low-grade gliomas.^{16,24} Different ASL techniques and reference brain regions may account for some variations. A wide rTBF range for high-grade neoplasms suggests vascular heterogeneity, which also has been noted for adult glioblastoma by use of DSC perfusion.⁹ The ability of ASL maps to depict tumor vascular heterogeneity and indicate higher tumor blood flow regions offers a useful parameter, which could help direct biopsy of higher vascular density or more malignant regions.

Pilocytic astrocytomas are typically considered vascular with characteristic hyalinized and glomerular vessel formation along the cyst wall.⁴⁰ In our study, rTBF of pilocytic astrocytoma was not elevated and was similar to contralateral gray matter. This finding may be attributed to the characteristic capillary exchange rate within the pilocytic tumor tissues, vessel density, and micro-

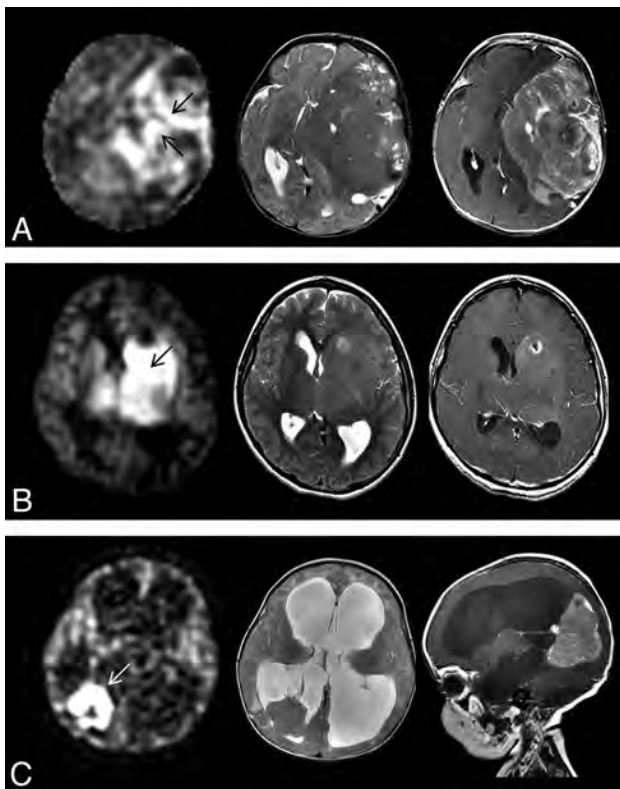


FIG 3. ASL perfusion (*left*) of various high-grade tumors and correlative axial T2-weighted MR image (*middle*) and axial contrast-enhanced T1-weighted MR image (*right*). A, Heterogeneous signal with regions of high rTBF (*arrows*) is seen in a 2-month-old girl with a large hemispheric glioblastoma. B, High rTBF signal (*arrow*) is seen in an 11-year-old girl. Biopsy of tumor just posterior to the necrosis showed anaplastic astrocytoma histology. Given the presence of necrosis, this was considered mixed anaplastic astrocytoma-glioblastoma. C, Markedly high rTBF (*arrow*) is seen within choroid plexus carcinoma in a 3-month-old girl.

vascular architecture or integrity.^{41,42} Although not statistically different, OPG consistently showed slightly lower perfusion than other pilocytic astrocytomas. Given reports of increased microvessel density in OPG with more aggressive behavior,⁴³ exclusion of OPG that required therapy could have biased toward a subset of less vascular, or biologically less aggressive, OPG in our cohort.

Although posterior fossa tumors comprise approximately 50% of pediatric brain tumors,⁴⁴ perfusion parameters of these tumors are relatively unknown, in part, because of general technical challenges of DSC perfusion requiring large intravenous access or power injection and posterior fossa susceptibility artifacts when using the gradient-echo technique. Here, we showed higher perfusion in medulloblastoma compared with pilocytic astrocytoma, which may complement DWI in distinguishing these tumors, as previously described by Rumboldt et al.⁴⁵ Although medulloblastoma, on average, showed higher rTBF than ependymoma, overlap between these 2 tumors was seen because of wide perfusion variability of medulloblastoma.

Such heterogeneous perfusion among medulloblastoma is noteworthy. Although medulloblastomas are classically categorized based on the presence of densely packed round cells, pathologic “variants” (large-cell or anaplastic medulloblastoma,

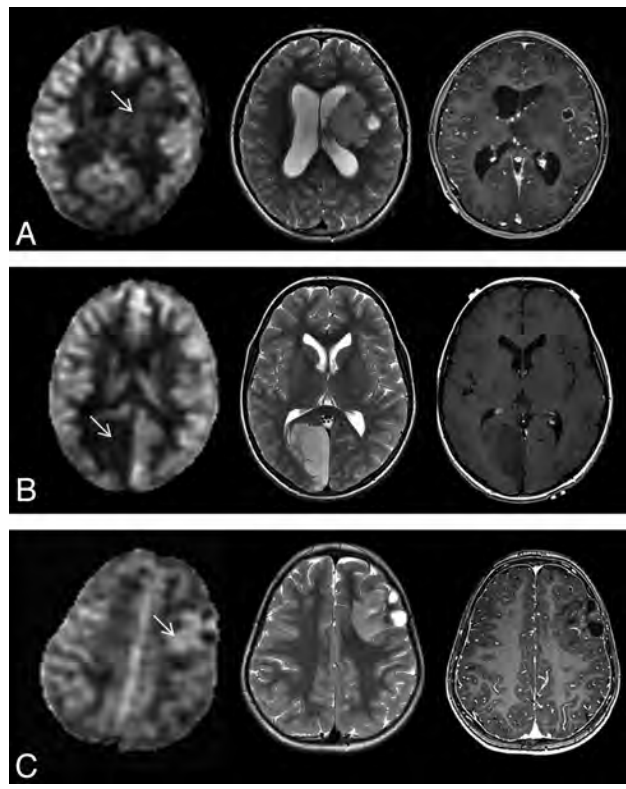


FIG 4. ASL perfusion (*left*) of various low-grade tumors and correlative axial T2-weighted MR image (*middle*) and axial contrast-enhanced T1-weighted MR image (*right*). A, Low rTBF is seen within the pilocytic astrocytoma (*arrow*) with some tumor regions that show ASL signal similar to the contralateral gray matter in a 9-year-old boy. B, DNT shows low ASL signal (*arrow*) in a 9-year-old boy. C, Higher rTBF (*arrow*) compared with DNT (B) is seen in a 3-year-old girl with left frontal ganglioglioma.

desmoplastic medulloblastoma, and medulloblastoma with extensive nodularity) with unique histologic features and biologic or clinical behavior are now recognized and incorporated in the 2007 WHO classification. Investigators have further shown heterogeneous imaging features⁴⁶ and marked genetic diversity of medulloblastoma with at least 4 unique molecular subgroups (WNT, SHH, group C, and group D) having distinct transcription profiles, chromosomal aberrations, and clinical behavior.^{47,48} Of note, 4 of the 8 medulloblastomas with the highest rTBF (range, 2.16–4.97) demonstrated the most aggressive behavior, with death occurring within 11 months of tumor diagnosis in 3 patients and the remaining patient classified as having high-risk disease at the time of the study because of leptomeningeal seeding. Further studies are needed to determine perfusion and genomic correlates and the potential prognostic role of perfusion imaging in pediatric medulloblastoma.

We observed no significant difference in rTBF values on the basis of the degree of contrast enhancement. Perfusion measurements of tumors by ASL are much less sensitive to permeability changes than the DSC methods, which are more affected by impaired blood-brain barrier function.^{24,49} It is likely that the ASL signal of our tumors represented tumor perfusion on the basis of vascular density as previously described by Noguchi et al.²³

We recognized a few limitations in our study. Although most of the patients presented with headaches, nausea or vomiting, and

focal neurologic deficits, a small number of those with seizures, specifically those with ganglioglioma or DNTs, could have presented with altered brain hemodynamics.⁵⁰ Elevated intracranial pressure from brain tumor could potentially reduce global cerebral perfusion and thereby decrease SNR and accuracy of the CBF and tumor blood flow measurements. To mitigate this problem, as well as age and other patient-dependent factors that could affect cerebral perfusion, tumor blood flow was referenced to normal brain as an internal control. Also, given general unknown effects of sedatives on ASL imaging, sedation status remains an important consideration in pediatric imaging.⁴⁹ However, for relative ASL tumor blood flow measures, its effect is likely small because of its focus on regional hemodynamic change, similar to presumed insignificant effect on relative calculations obtained by the DSC method.⁴⁹ Prior investigators have shown that ASL underestimates CBF in brain regions with delayed flow, such as the white matter.²⁷ It is possible that ASL could underestimate tumor blood flow in cases of tortuous vasculature from angiogenesis because of delay in signal arrival, and alternatively, overestimate tumor blood flow in cases of vascular shunting. Despite reports of fewer susceptibility artifacts compared with gradient-echo PWI,¹⁷ many patients were excluded from our study because of dental braces, which rendered the ASL nondiagnostic, an important factor in clinical implementation.

CONCLUSIONS

Characteristic ASL perfusion patterns were seen among diverse pathologic types of brain tumors in children and can be used to distinguish high-grade and low-grade tumors.

ICMJE Disclosures: Michael Edwards—UNRELATED: Grants/Grants Pending: Stanford University,* Comments: Private funding from donors as well as National Institutes of Health and Brain Tumor Funding Grant Associations.

REFERENCES

- Gurney JG, Smith MA, Bunin GR. **CNS and miscellaneous intracranial and intraspinal neoplasms.** In: Ries L, Smith M, Gurney J, eds. *Cancer Incidence and Survival Among Children and Adolescents: United States SEER Program 1965–1995.* NIH Publication No. 99–4649. Bethesda, Maryland: National Cancer Institute SEER Program;1999:51–63
- Pollack IF. **Brain tumors in children.** *N Engl J Med* 1994; 331:1500–07
- Sugahara T, Korogi Y, Kochi M, et al. **Correlation of MR imaging-determined cerebral blood volume maps with histologic and angiographic determination of vascularity of gliomas.** *AJR Am J Roentgenol* 1998;171:1479–86
- Knopp EA, Cha S, Johnson G, et al. **Glial neoplasms: dynamic contrast-enhanced T2*-weighted MR imaging.** *Radiology* 1999;211:791–98
- Sugahara T, Korogi Y, Kochi M, et al. **Perfusion-sensitive MR imaging of gliomas: comparison between gradient-echo and spin-echo echo-planar imaging techniques.** *AJNR Am J Neuroradiol* 2001; 22:1306–15
- Shin JH, Lee HK, Kwun BD, et al. **Using relative cerebral blood flow and volume to evaluate the histopathologic grade of cerebral gliomas: preliminary results.** *AJR Am J Roentgenol* 2002;179:783–89
- Law M, Yang S, Wang H, et al. **Glioma grading: sensitivity, specificity, and predictive values of perfusion MR imaging and proton MR spectroscopic imaging compared with conventional MR imaging.** *AJNR Am J Neuroradiol* 2003;24:1989–98
- Law M, Yang S, Babb JS, et al. **Comparison of cerebral blood volume and vascular permeability from dynamic susceptibility contrast-enhanced perfusion MR imaging with glioma grade.** *AJNR Am J Neuroradiol* 2004;25:746–55
- Aronen HJ, Gazit IE, Louis DN, et al. **Cerebral blood volume maps of gliomas: comparison with tumor grade and histologic findings.** *Radiology* 1994;191:41–51
- Law M, Oh S, Babb JS, et al. **Low-grade gliomas: dynamic susceptibility-weighted contrast-enhanced perfusion MR imaging—prediction of patient clinical response.** *Radiology* 2006;238:658–67
- Tzika AA, Astrakas LG, Zarifi MK, et al. **Spectroscopic and perfusion magnetic resonance imaging predictors of progression in pediatric brain tumors.** *Cancer* 2004;100:1246–56
- Cha S. **Dynamic susceptibility-weighted contrast-enhanced perfusion MR imaging in pediatric patients.** *Neuroimaging Clin N Am* 2006;16:137–47, ix
- Thompson EM, Guillaume DJ, Dósa E, et al. **Dual contrast perfusion MRI in a single imaging session for assessment of pediatric brain tumors.** *J Neurooncol* 2012;109:105–14
- Löbel U, Sedlacik J, Reddick WE, et al. **Quantitative diffusion-weighted and dynamic susceptibility-weighted contrast-enhanced perfusion MR imaging analysis of T2 hypointense lesion components in pediatric diffuse intrinsic pontine glioma.** *AJNR Am J Neuroradiol* 2011;32:315–22
- Kimura H, Takeuchi H, Koshimoto Y, et al. **Perfusion imaging of meningioma by using continuous arterial spin labeling: comparison with dynamic susceptibility-weighted contrast-enhanced MR images and histopathologic features.** *AJNR Am J Neuroradiol* 2006;27:85–93
- Warmuth C, Gunther M, Zimmer C. **Quantification of blood flow in brain tumors: comparison of arterial spin labeling and dynamic susceptibility-weighted contrast-enhanced MR imaging.** *Radiology* 2003;228:523–32
- Järnum H, Steffensen EG, Knutsson L, et al. **Perfusion MRI of brain tumors: a comparative study of pseudo-continuous arterial spin labeling and dynamic susceptibility contrast imaging.** *Neuroradiology* 2010;52:307–17
- White CM, Pope WB, Zaw T, et al. **Regional and voxel-wise comparisons of blood flow measurements between DSC magnetic resonance imaging (DSC-MRI) and arterial spin labeling (ASL) in brain tumors.** *J Neuroimaging* 2014;24:23–30
- van Westen D, Petersen ET, Wirestam R, et al. **Correlation between arterial blood volume obtained by arterial spin labeling and cerebral blood volume in intracranial tumours.** *MAGMA* 2011;24:211–23
- Hirai T, Kitajima M, Nakamura H., et al. **Quantitative blood flow measurements in gliomas using arterial spin labeling at 3T: intermodality agreement and inter- and intraobserver reproducibility study.** *AJNR Am J Neuroradiol* 2011;32:2073–79
- Dai W, Garcia D, Bazelaire C, et al. **Continuous flow-driven inversion for arterial spin labeling using pulsed radio frequency and gradient fields.** *Magn Reson Med* 2008;60:1488–97
- Buxton RB, Frank LR, Wong EC, et al. **A general kinetic model for quantitative perfusion imaging with arterial spin labeling.** *Magn Reson Med* 1998;40:383–96
- Noguchi T, Yshiura T, Hiwatashi A. **Perfusion imaging of brain tumors using arterial spin labeling: correlation with histopathologic vascular density.** *AJNR Am J Neuroradiol* 2008;29:688–93
- Wolf RL, Wang J, Wang S, et al. **Grading of CNS neoplasms using continuous arterial spin labeled perfusion MR imaging at 3 Tesla.** *J Magn Reson Imaging* 2005;22:475–82
- Parke LM, Rashid W, Chard DT, et al. **Normal cerebral perfusion measurements using arterial spin labeling: reproducibility, stability, and age and gender effects.** *Magn Reson Med* 2004;51:736–43
- Ulmer S, Helle M, Jansen O, et al. **Intraoperative dynamic susceptibility contrast weighed magnetic resonance imaging (iDSC-MRI)—technical considerations and feasibility.** *Neuroimage* 2009;45:38–43
- van Gelderen P, de Awtart JA, Duyn JH. **Pitfalls of MRI measure-**

- ments of white matter perfusion based on arterial spin labeling. *Magn Reson Med* 2008;59:788–95
28. Ye FQ, Berman KF, Ellmore T, et al. **H2 15O PET validation of steady-state arterial spin tagging cerebral blood flow measurements in humans.** *Magn Reson Med* 2000;44:450–56
 29. Louis DN, Ohgaki H, Wiestler OD, et al, eds. *WHO Classification of Tumours of the Central Nervous System, Fourth Edition.* Lyon, France: International Agency for Research on Cancer; 2007
 30. Kleihues P, Cavenee WK, eds. *World Health Organization Classification of Tumours: Pathology and Genetics of Tumours of the Nervous System.* Lyon, France: International Agency for Research on Cancer; 2000
 31. Bredel M, Pollack IF, Hamilton RL, et al. **Epidermal growth factor receptor (EGFR) expression and gene amplification in high grade non-brainstem gliomas of childhood.** *Clin Cancer Res* 1999;5:1786–92
 32. Rickert CH, Strater R, Kaatsch P, et al. **Pediatric high-grade astrocytomas show chromosomal imbalances distinct from adult cases.** *Am J Pathol* 2001;158:1525–32
 33. Suri V, Das P, Jain A, et al. **Pediatric glioblastoma: a histopathological and molecular genetic study.** *Neuro Oncol* 2009;11:274–80
 34. Wang J, Licht DJ, Jahng GH, et al. **Pediatric perfusion imaging using pulsed arterial spin labeling.** *J Magn Reson Imaging* 2003;18:404–13
 35. Deibler AR, Pollock JM, Kraft RA, et al. **Arterial spin-labeling in routine clinical practice, part 1: technique and artifacts.** *AJNR Am J Neuroradiol* 2008;29:1228–34
 36. Wolf RL, Detre JA. **Clinical neuroimaging using arterial spin-labeled perfusion magnetic resonance imaging.** *Neurotherapeutics* 2007;4:346–59
 37. Kumabe T, Shimazu H, Sonoda Y, et al. **Thallium-201 single-photon emission computed tomographic and proton magnetic resonance spectroscopic characteristics of intracranial ganglioglioma: three technical case reports.** *Neurosurgery* 1999;45:183–187; discussion 187
 38. Daumas-Duport C, Pietsch T, Lantos PL. **Dysembryoplastic neuroepithelial tumour.** In: Kleihues P, Cavenee WK, eds. *World Health Organization Classification of Tumours: Pathology and Genetics of Tumours of the Nervous System.* Lyon, France: International Agency for Research on Cancer; 2000:103–106
 39. Abe M, Tabuchi K, Tsuji T, et al. **Dysembryoplastic neuroepithelial tumor: report of three cases.** *Surg Neurol* 1995;43:240–245
 40. Burger PC, Scheithauer BW, Paulus W, et al. **Pilocytic astrocytoma.** In: Kleihues P, Cavenee W, eds. *World Health Organization Classification of Tumours: Pathology and Genetics of Tumours of the Nervous System.* Lyon, France: International Agency for Research on Cancer; 2000:45–51
 41. Birluk, Canda S, Ozer E. **Tumour vascularity is of prognostic significance in adult, but not paediatric astrocytomas.** *Neuropathol Appl Neurobiol* 2006;32: 532–38
 42. Sie M, de Bont ES, Scherpen FJ, et al. **Tumour vasculature and angiogenic profile of paediatric pilocytic astrocytoma; is it much different from glioblastoma?** *Neuropathol Appl Neurobiol* 2010;36: 636–47
 43. Bartels U, Hawkins C, Jing M, et al. **Vascularity and angiogenesis as predictors of growth in optic pathway/hypothalamic gliomas.** *J Neurosurg* 2006;104:314–20
 44. Centers for Disease Control and Prevention. *Data Collection of Primary Central Nervous System Tumors. National Program of Cancer Registries Training Materials.* Atlanta, Georgia: Department of Health and Human Services, Centers for Disease Control and Prevention; 2004
 45. Rumboldt Z, Camacho DL, Lake D, et al. **Apparent diffusion coefficients for differentiation of cerebellar tumors in children.** *AJNR Am J Neuroradiol* 2006;27:1362–69
 46. Yeom KW, Mobley BC, Lober RM, et al. **Distinctive MRI features of pediatric medulloblastoma subtypes.** *AJR Am J Roentgenol* 2013;200:895–903
 47. Northcott PA, Korshunov A, Witt H, et al. **Medulloblastoma comprises four distinct molecular variants.** *J Clin Oncol* 2011;29: 1408–14
 48. Cho YJ, Tsherniak A, Tamayo P, et al. **Integrative genomic analysis of medulloblastoma identifies a molecular subgroup that derives poor clinical outcome.** *J Clin Oncol* 2011;29:1424–30
 49. Wang J, Licht DJ. **Pediatric perfusion MR imaging using arterial spin labeling.** *Neuroimaging Clin N Am* 2006;16:149–67, ix
 50. Toledo M, Munuera J, Salas-Puig X, et al. **Localisation value of ictal arterial spin-labelled sequences in partial seizures.** *Epileptic Disord* 2011;13:336–39

Bannayan-Riley-Ruvalcaba Syndrome: MRI Neuroimaging Features in a Series of 7 Patients

R. Bhargava, K.J. Au Yong, and N. Leonard

ABSTRACT

SUMMARY: Bannayan-Riley-Ruvalcaba syndrome is a congenital disorder characterized by macrocephaly, intestinal polyposis, lipomas, and pigmented macules of the penis. There is limited published radiologic literature on the syndrome. The purpose of this study was to review the brain MR imaging findings in Bannayan-Riley-Ruvalcaba syndrome as well as to compare and contrast the findings with other brain disorders that also have brain cysts and white matter lesions. All brain MR imaging studies were reviewed in patients with a diagnosis of Bannayan-Riley-Ruvalcaba syndrome from our hospital. All 7 patients were evaluated with brain MR imaging. MR imaging results showed white matter cysts in the parietal lobe (7/7), frontal lobe (3/7), and temporal lobe (1/7). These were predominantly surrounded by white matter T2 hyperintensities associated with macrocephaly. Cystic lesions on MR imaging in Bannayan-Riley-Ruvalcaba syndrome are prevalent, and knowledge of this differential diagnosis can allow the radiologist to suggest a diagnosis of this condition in a child with macrocephaly.

ABBREVIATIONS: BRRS = Bannayan-Riley-Ruvalcaba syndrome; CS = Cowden syndrome; LDD = Lhermitte-Duclos disease; *PTEN* = phosphatase and tensin homolog; VR = Virchow-Robin

Bannayan-Riley-Ruvalcaba syndrome (BRRS) classically presents with macrocephaly, subcutaneous and visceral lipomata, hemangiomas, hamartomatous intestinal polyps, and pigmented macules involving the genitalia.

This autosomal dominant disorder is linked to germline mutations of the phosphatase and tensin homolog gene (*PTEN*), a tumor suppressor gene localized to 10q23 that has a significant role in the molecular pathway of cellular proliferation, migration, and apoptosis. In 1996, it was recognized that BRRS shared features with Cowden syndrome (CS), another autosomal dominant condition with multiple hamartomas.¹

An estimated 65% of patients with a clinical diagnosis of BRRS have a detectable *PTEN* mutation. When BRRS is not caused by mutations or deletions of the *PTEN* gene, the cause of the condition is unknown.

Other features would include high birth weight, developmental delay, and intellectual disability (50%); a myopathic process in

proximal muscles (60%); and joint hyperextensibility, pectus excavatum, and scoliosis (50%).² Abnormal facial features include frontal bossing, hypertelorism, down-slanting palpebral fissures, depressed nasal bridge, strabismus, epicanthus inversus, small beaked nose, long philtrum, thin upper lip, broad mouth, and relative micrognathia.³

There are no agreed international criteria for the diagnosis of BRRS. The criteria suggested by Marsh et al⁴ should include at least the following 4 features: macrocephaly, lipomatosis, hemangiomas, and speckled penis in boys. The other criteria suggested by Parisi et al⁵ should include at least 2 of the following characteristics: macrocephaly, hamartomas (including at least 1 lipoma, hemangioma, or intestinal polyp), and penile macules in boys. Although cancer was initially not believed to be a component of the syndrome, people with BRRS and a *PTEN* mutation are currently thought to have the same cancer risks as those with CS.⁴

PTEN, on 10q23.3, encodes a major lipid phosphatase that signals down the phosphoinositol-3-kinase/Akt pathway and effects G1 cell cycle arrest and apoptosis. Germline *PTEN* mutations have been found to occur in 80% of classic CS, 60% of BRRS, up to 20% of Proteus syndrome, and approximately 50% of a Proteus-like syndrome.⁶ *PTEN* hamartoma tumor syndrome now encompasses 4 major clinically distinct syndromes associated with germline mutations in the tumor suppressor *PTEN*.⁷ CS is rarely diagnosed before adolescence; BRRS is generally reported with a childhood onset, often with delayed motor and intellectual devel-

Received April 14, 2013; accepted after revision May 27.

From the Departments of Radiology and Diagnostic Imaging (R.B.), and Medical Genetics (N.L.), University of Alberta Hospital, Edmonton, Alberta, Canada; and Department of Radiology and Diagnostic Imaging (K.J.A.), McMaster University Medical Centre, McMaster Children's Hospital, Hamilton, Ontario, Canada.

Please address correspondence to Kong Jung Au Yong, MB ChB, MRCS, FRCS, MBA, Department of Radiology and Diagnostic Imaging, McMaster University Medical Centre, McMaster Children's Hospital, 1280 Main St West, Hamilton, ON L8S 4L8, Canada; e-mail: kong.auyong@gmail.com

<http://dx.doi.org/10.3174/ajnr.A3680>

Summary of MRI and clinical characteristic of 7 patients diagnosed with BRRS

Patient No.	Sex	Age at MRI (y)		Mutation		Physical Features	WM Cyst	Cyst Location
		Macrocephaly		<i>PTEN</i>	Development			
1	M	4	Yes	Yes	Autistic	Abdominal hemangioma	Yes	f,p,t
2	M	0.65	Yes	Yes	Delay	Café au lait spot, thyroid nodules, testicular hamartomas, rectal and gastric polyps	Yes	p
3	M	2.7	Yes	No protein	Autistic	Motor speech disorder	Yes	f,p
4	M	3.5	90th centile	No protein	Delay	Café au lait spot	Yes	p
5	M	2.6	Yes	No protein	Delay	Moles, thyroid nodules, intestinal polyps	Yes	p
6	M	7.7	Yes	No protein	Delay	Moles, thyroid nodules, intestinal polyps	Yes	p
7	M	7.7	Yes	Yes	Delay	Pigmentation of the glans penis, multiple thyroid nodules, and carcinoma	Yes	f,p

Note:—f indicates frontal; p, parietal; t, temporal.

opment. Most studies have failed to demonstrate a consistent genotype–phenotype relationship between CS and BRRS, but recently, studies have suggested that the unique features in the 2 syndromes may actually represent age-related penetrance of the same condition.⁸ People with CS and BRRS within the same family (CS/BRRS overlap families) have been reported.⁹ Therefore, early diagnosis of BRRS at a young age may allow patients to be monitored for the onset of malignant disease.

With increased recognition of the syndrome, neuroimaging signs such as AVMs and increased perivascular spaces have been recently described.^{10,11} Therefore, it is important for radiologists to be aware of the neuroimaging abnormalities found in patients with BRRS to allow accurate diagnosis and provide preventive care. We have reviewed the neuroimaging features of 7 patients with BRRS.

MATERIALS AND METHODS

Local Human Research Ethics board approval was obtained to review the clinical and imaging records of patients with BRRS without patient consent. We searched the genetic disorder data base at our institution for all cases of BRRS diagnosed since 1994. All available MR imaging studies and clinical records were reviewed in patients with a diagnosis of BRRS.

All patients had a review by geneticists and were tested for the *PTEN* gene mutation. To our knowledge, no diagnostic criteria for BRRS have been set. We based our diagnosis heavily on the presence of cardinal features of macrocephaly, developmental delay/autism, characteristic triangular facial feature, prominent forehead, malar hypoplasia, down-slanting palpebral fissures, myopathic features, and pigmented macules of the glans penis associated with the *PTEN* mutation.

All MR imaging was performed in routine clinical care by use of 1.5T scanning. Standard 3D MPRAGE T1-weighted, fast spin-echo T2-weighted, and FLAIR images were available for all patients. The MR imaging results in each patient were reviewed separately and then jointly by 2 pediatric neuroradiologists. Systematic chart review was used to document the clinical details, mode of presentation, patient demographics, clinical features, and MR imaging brain features.

RESULTS

Since 1994, a total of 7 patients (all boys) have been diagnosed with BRRS at the University of Alberta Hospital (Edmonton, Alberta, Canada), and all 7 were evaluated with brain MR imaging. The accompanying table summarizes the neuroimaging and clinical findings of these 7 patients.

Patient Demographics

The age at presentation ranged from 8 months–7.7 years. Patients 5 and 6 were siblings.

PTEN Gene

Three patients had the *PTEN* mutation and 4 had absence of the *PTEN* protein, indicating an abnormality of *PTEN*.

Clinical Presentation

All 7 of our patients presented with developmental delay or autism spectrum disorder. Skin pigmentation, nevi, or café au lait spots were seen in 5 of 7 patients. Three patients had intestinal polyps, and 4 had thyroid nodules. One patient had testicular hamartomas. Thyroid carcinoma developed in another patient at age 16 years.

The distinctive finding of penile macules in boys (seen in 67% of patients with BRRS) is a major criterion in BRRS but may not appear until mid-childhood and was only seen in 2 of our patients at presentation. *PTEN* mutations can have many different phenotypes; therefore, our diagnosis of BRRS was guided more specifically by the facial features; pigmented macules of the glans; myopathy; and subsequent determination of intestinal hamartomatous polyps, which separates them from Cowden and Proteus. The features of Cowden and Proteus, which are also associated with *PTEN* mutations, were not seen in our patients.

MR Imaging Brain Features

All of our 7 patients had MR imaging of the brain, as shown in the accompanying figures (Fig 1). The imaging findings include CSF signal intensity (hyperintense on T2 and hypointense on FLAIR) and white matter cysts in the parietal lobes (7/7), frontal lobes (3/7), and temporal lobes (1/7). These were associated with white matter T2 hyperintensities predominantly around the cysts (7/7). Additional findings in 1 patient included a cavum velum interpositum arachnoid cyst. All but 1 patient (above the 90th centile) had extreme macrocephaly.

DISCUSSION

BRRS has been shown to affect the skin and central nervous system. However, descriptions of neuroimaging studies are uncommon in the literature. To our knowledge, no similar case series has specifically studied the neuroimaging findings of BRRS.

In a recent study of 181 patients with pathogenic germline *PTEN* mutations, 152 (94.4%) had macrocephaly as defined by a

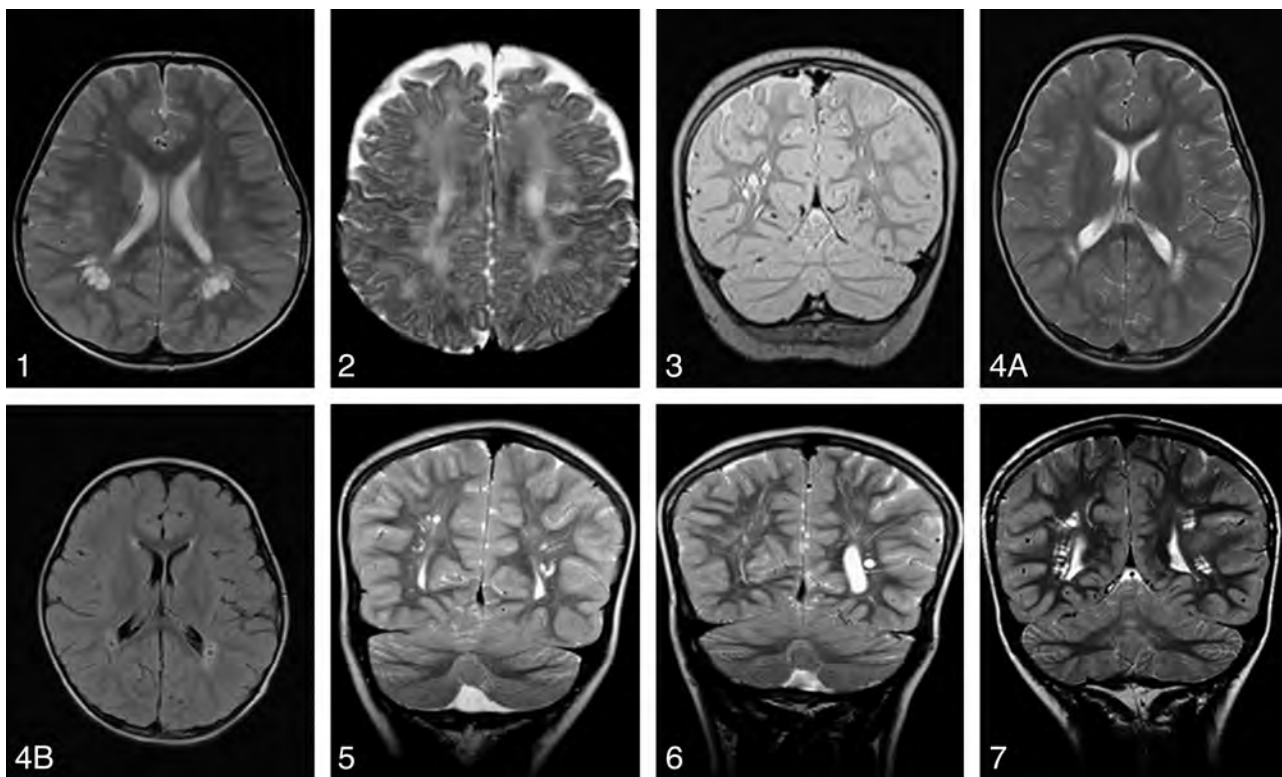


FIG 1. 1, Axial T2 image in patient 1 demonstrates bilateral cystic spaces in the biparietal periventricular white matter. 2, Axial T2 image in patient 2 demonstrating small cystic spaces in the parietal white matter associated with increased T2 signal of the periventricular white matter. 3, Coronal T2 image in patient 3 demonstrates cystic spaces in the periventricular white matter of the parietal lobes. 4A, Axial T2 image in patient 4 demonstrates bilateral small parietal periventricular cyst associated with white matter T2 hyperintensities predominantly around the cysts. 4B, An axial FLAIR image in patient 4 demonstrates pericyst hyperintensities and suppression of the VR space fluid. 5, Coronal T2 image of patient 5 demonstrates a well-defined small periventricular cyst in the parietal region. 6, Coronal T2 image in patient 6 demonstrates a well-defined small periventricular cyst in the left parietal region. 7, Coronal T2 image in patient 7 demonstrates small periventricular cysts in the biparietal region.

head circumference of 2 SD over the mean. There was no significant difference in age or sex. Macrocephaly was observed in all but one of our patients. Studies on mice specimens with *PTEN* mutations have shown megalencephaly.¹² The size of the ventricles and the extra-axial spaces in all of our patients were within normal limits in keeping with megalencephaly.

Megalencephaly in BRRS is often associated with overgrowth features but can be distinguished from other causes of megalencephaly with overgrowth such as Soto syndrome, neurofibromatosis type 1, Simpson-Golabi-Behmel, Fragile X, Weaver, and macrocephaly-cutis marmorata telangiectatica congenita by use of a combination of dysmorphic features, associated malformations, family history, and specific growth patterns.¹³

All of our patients were referred for neuroimaging because of developmental delay or autism. Cognitive impairment is reported to be between 20%–50% in patients with BRRS, which is higher than in those with CS at 10%.¹⁴ In a study of 18 patients with autism with a head circumference range from 2.5–8.0 SD above the mean and with autism spectrum disorder, 3 boys (17%) carried germline *PTEN* mutations. Two of 7 patients in our study have autistic spectrum disorder.¹⁵ A total of 24 patients with *PTEN* mutation, autism, macrocephaly, and some clinical findings described in *PTEN* syndromes have been reported in the literature.¹⁶ Approximately 25% of patients with BRRS have seizures.¹⁷ Cortical malformation is considered rare in BRRS, with only 3 cases associated with *PTEN* mutation reported in the liter-

ature.¹⁸ None of our patients demonstrated any cortical malformation or midline defects. A small cavum velum interpositum arachnoid cyst was found in 1 patient.

The *PTEN* gene, a tumor suppressor, contains a phosphatase domain, and its protein product has phosphatase activity. Mutations of this gene have been detected in glioblastoma cell lines and tumors. In a large series, 74% (25/34) of glioblastomas demonstrated loss of heterozygosity at the *PTEN* locus, and 60% (15/25) of these cases contained somatic *PTEN* mutations of both alleles, implicating the *PTEN* gene in tumor development.¹⁹

Published case reports have described rare cases of meningiomas, frontal vascular hamartoma, intracranial lipomatous hamartoma, and malignant intracranial human chorionic gonadotropin-secreting tumor in patients with BRRS.^{14,20}

The *PTEN*/*PI3K* pathway governs normal vascular development and tumor angiogenesis.²¹ High-flow vascular malformations,¹ including dural AVM,¹⁰ hemangiomas, and vertebral angiomas,²² may exist in patients with BRRS.

In a study of 26 patients with *PTEN* mutation²³, vascular anomalies were found in 14 (54%) patients. Intracranial developmental venous anomalies were found in 8 (89%) of 9 patients who had brain MR imaging with contrast.²³ High frequency of vascular malformations was noted in a study of 20 patients with CS, where 5 patients had venous angiomas (3 associated with Lhermitte-Duclos disease [LDD]) and 2 patients had cavernous angi-

omas (1 associated with LDD) with a significant proportion related to LDD.¹⁴

No vascular anomalies were found in our 7 patients, but this probably is an underestimate because none of our patients received contrast material. More recently, congenitally enlarged VR spaces have been described in a case of BRRS.¹¹

Our 7 patients demonstrated cystic dilation of the VR spaces at the white matter of the centrum semiovale and parietal region. There were round, oval, or curvilinear well-defined cystic lesions with smooth margins and isointense to CSF. On FLAIR imaging, there was suppression of the VR space fluid. One follow-up MR imaging study was available for comparison, and the cystic dilation of the VR spaces appeared nonprogressive. Lok et al¹⁴ reported cystic dilation of the VR spaces in 3 (15%) of 20 patients (ages 34–56 years) with CS. Merks et al²⁴ described a mother and 3 sons with CS/BRRS and variable phenotype: 1 family member having macrocephaly, normal intelligence, and minimal pigmentation abnormalities; another member with macrocephaly with developmental delay; another with macrocephaly, delay and lipoma; and the last family member having hemimegalencephaly, Jadassohn naevus sebaceous, and neonatal demise. Two of the 3 sons have periventricular cyst or dilated perivascular spaces.

It is unknown if the cystic VR space dilations in our patients constitute a physiopathologic marker, but the extent encountered in our patients has not been described in unaffected children; therefore, a causal relationship with the presenting signs is probable.

The cystic dilation of VR spaces discussed above is nonspecific and does not distinguish it from other diseases that cause white matter brain cysts such as Soto syndrome, Lowe syndrome, mucopolysaccharidosis, and Van der Knaap syndrome; however, ancillary imaging findings allow for diagnosis of these conditions. Soto syndrome is frequently associated with large ventricles, increased extracerebral fluid, and midline anomalies.²⁵ In Lowe syndrome, hyperintensities on T2-weighted images and periventricular cystic lesions have been described; however, the brain size is usually below normal and is associated with white matter gliosis (increased myo-inositol peak) mainly in the centrum semiovale, atrophy, ventricular enlargement, and thinning of the corpus callosum.²⁶ The disease is also associated with bilateral congenital cataracts, glaucoma, hypotonia, severe psychomotor retardation, seizures, and disturbances of renal tubular function.²⁷ Neuroimaging findings such as hydrocephalus, white matter lesions, brain atrophy, MR spectroscopy changes (a low NAA/Cr and elevated mIns/Cr), and clinical phenotype can easily distinguish mucopolysaccharidosis from BRRS. Thickening of the diploic space, sellar abnormalities, or vertebral body changes seen on head MR imaging can also allow for differentiation of a mucopolysaccharidosis from BRRS. Finally, Van der Knaap syndrome is associated with extensive white matter changes, and the cysts are usually subcortical in position, sparing the deeper structures.²⁸

Our small retrospective study had some limitations. This frequency of cerebral abnormalities in patients with BRRS was surely an underestimate, as serial neuroimaging or contrast imaging has not been performed. Because our study was small, we found it difficult to draw statistically significant conclusions. All of the patients in our study had been referred for a pediatric medical

opinion because of concerns about early motor development or learning difficulties, and this ascertainment bias may have led to an overestimate of the risk of learning difficulties in children diagnosed with BRRS.

CONCLUSIONS

Although a rare syndrome, the cystic lesions seen on brain imaging findings in BRRS are quite prevalent. Future studies of larger populations and long-term follow-up are needed to confirm our preliminary MR imaging findings. Knowledge of the differential diagnosis of macrocephaly and brain cystic lesions in the setting of a white matter disorder can allow the radiologist to suggest a diagnosis of BRRS on brain MR imaging. Macrocephaly, together with cystic VR spaces on MR imaging, may be a useful diagnostic pointer, particularly when deciding which patients to test for *PTEN* mutation.

Disclosures: Norma Leonard—RELATED: Payment for Writing or Reviewing the Manuscript: University of Alberta (clarify).

REFERENCES

1. Fargnoli MC, Orlow SJ, Semel-Concepcion J, et al. **Clinicopathologic findings in the Bannayan-Riley-Ruvalcaba syndrome.** *Arch Dermatol* 1996;132:1214–18
2. Zbuk KM, Eng C. **Cancer phenomics: RET and PTEN as illustrative models.** *Nat Rev Cancer* 2007;7:35–45
3. Hendriks YM, Verhallen JT, van der Smagt JJ, et al. **Bannayan-Riley-Ruvalcaba syndrome: further delineation of the phenotype and management of PTEN mutation-positive cases.** *Fam Cancer* 2003;2:79–85
4. Marsh DJ, Kum JB, Lunetta KL, et al. **PTEN mutation spectrum and genotype-phenotype correlations in Bannayan-Riley-Ruvalcaba syndrome suggest a single entity with Cowden syndrome.** *Hum Mol Genet* 1999;8:1461–72
5. Parisi MA, Dinulos MB, Leppig KA, et al. **The spectrum and evolution of phenotypic findings in PTEN mutation positive cases of Bannayan-Riley-Ruvalcaba syndrome.** *J Med Genet* 2001;38:52–58
6. Eng C. **PTEN: one gene, many syndromes.** *Hum Mutat* 2003;22:183–98
7. Hobert JA, Eng C. **PTEN hamartoma tumor syndrome: an overview.** *Genet Med* 2009;11:687–94
8. Lachlan KL, Lucassen AM, Bunyan D, et al. **Cowden syndrome and Bannayan Riley Ruvalcaba syndrome represent one condition with variable expression and age-related penetrance: results of a clinical study of PTEN mutation carriers.** *J Med Genet* 2007;44:579–85
9. Wanner M, Celebi JT, Peacocke M. **Identification of a PTEN mutation in a family with Cowden syndrome and Bannayan-Zonana syndrome.** *J Am Acad Dermatol* 2001;44:183–87
10. Srinivasa RN, Burrows PE. **Dural arteriovenous malformation in a child with Bannayan-Riley-Ruvalcaba syndrome.** *AJNR Am J Neuroradiol* 2006;27:1927–29
11. Nebgen S, Zerres K, Deutz U, et al. **Bannayan-Riley-Ruvalcaba syndrome—an unusual differential diagnosis of dilated Virchow-Robin spaces.** *Neuropediatrics* 2012;43 – PS13_06
12. Mester JL, Tilot AK, Rybicki LA, et al. **Analysis of prevalence and degree of macrocephaly in patients with germline PTEN mutations and of brain weight in PTEN knock-in murine model.** *Eur J Hum Genet* 2011;19:763–68
13. Olney AH. **Macrocephaly syndromes.** *Semin Pediatr Neurol* 2007;14:128–35
14. Lok C, Viseux V, Avril MF, et al. **Brain magnetic resonance imaging in patients with Cowden syndrome.** *Medicine (Baltimore)* 2005;84:129–36
15. Butler MG, Dasouki MJ, Zhou XP, et al. **Subset of individuals with autism spectrum disorders and extreme macrocephaly associated with germline PTEN tumour suppressor gene mutations.** *J Med Genet* 2005;42:318–21

16. Conti S, Condò M, Posar A, et al. **Phosphatase and tensin homolog (PTEN) gene mutations and autism: literature review and a case report of a patient with Cowden syndrome, autistic disorder, and epilepsy.** *J Child Neurol* 2012;27:392–97
17. DiLiberti JH, D'Agostino AN, Ruvalcaba RH, et al. **A new lipid storage myopathy observed in individuals with the Ruvalcaba-Myhre-Smith syndrome.** *Am J Med Genet* 1984;18:163–67
18. O'Rourke DJ, Twomey E, Lynch SA, et al. **Cortical dysplasia associated with the PTEN mutation in Bannayan Riley Ruvalcaba syndrome: a rare finding.** *Clin Dysmorphol* 2012;21:91–92
19. Wang SI, Puc J, Li J, et al. **Somatic mutations of PTEN in glioblastoma multiforme.** *Cancer Res* 1997;57:4183–86
20. Faisal Ahmed S, Marsh DJ, Weremowicz S, et al. **Balanced translocation of 10q and 13q, including the PTEN gene, in a boy with a human chorionic gonadotropin-secreting tumor and the Bannayan-Riley-Ruvalcaba syndrome.** *J Clin Endocrinol Metab* 1999;84:4665–70
21. Hamada K, Sasaki T, Koni PA, et al. **The PTEN/PI3K pathway governs normal vascular development and tumor angiogenesis.** *Genes Dev* 2005;19:2054–65
22. Pancaro C, Miller T, Dingeman RS. **Anesthetic management of a child with Bannayan-Riley-Ruvalcaba syndrome.** *Anesth Analg* 2008;106:1928–29
23. Tan WH, Baris HN, Burrows PE, et al. **The spectrum of vascular anomalies in patients with PTEN mutations: implications for diagnosis and management.** *J Med Genet* 2007;44:594–602
24. Merks JH, de Vries LS, Zhou XP, et al. **PTEN hamartoma tumour syndrome: variability of an entity.** *J Med Genet* 2003;40:e111
25. Schaefer GB, Bodensteiner JB, Buehler BA, et al. **The neuroimaging findings in Sotos syndrome.** *Am J Med Genet* 1997;68:462–65
26. Carvalho-Neto A, Ono SE, Cardoso Gde M, et al. **Oculocerebrorenal syndrome of Lowe: Magnetic resonance imaging findings in the first six years of life.** *Arq Neuropsiquiatr* 2009;67:305–07
27. Demmer LA, Wippold FJ 2nd, Downton SB. **Periventricular white matter cystic lesions in Lowe (oculocerebrorenal) syndrome. A new MR finding.** *Pediatr Radiol* 1992;22:76–77
28. Batla A, Pandey S, Nehru R. **Megalencephalic leukoencephalopathy with subcortical cysts: A report of four cases.** *J Pediatr Neurosci* 2011;6:74–77

Comparison of Dynamic Contrast-Enhanced 3T MR and 64-Row Multidetector CT Angiography for the Localization of Spinal Dural Arteriovenous Fistulas

S. Oda, D. Utsunomiya, T. Hirai, Y. Kai, Y. Ohmori, Y. Shigematsu, Y. Iryo, H. Uetani, M. Azuma, and Y. Yamashita

ABSTRACT

BACKGROUND AND PURPOSE: For the localization of spinal dural arteriovenous fistulas, it is not determined whether dynamic contrast-enhanced MRA is more reliable than multidetector CTA. The aim of this study was to compare the agreement between intra-arterial DSA, dynamic contrast-enhanced MRA at 3T, and 64-row multidetector CTA for the localization of spinal dural arteriovenous fistulas.

MATERIALS AND METHODS: We enrolled 12 consecutive patients (11 men, 1 woman; age range, 46–83 years; mean, 65 years) who underwent preoperative dynamic contrast-enhanced MRA at 3T and 64-row multidetector CTA. The spinal dural arteriovenous fistula location was confirmed by intra-arterial DSA as the reference standard. Two reviewers independently evaluated the level of the artery feeding the spinal dural arteriovenous fistula on the basis of continuity between the feeder and abnormal spinal vessels on 3T dynamic contrast-enhanced MRA and 64-row multidetector CTA images. Interobserver and intermodality agreement was determined by calculation of the κ coefficient.

RESULTS: On DSA, the vessel feeding the spinal dural arteriovenous fistula was the intercostal artery (7 cases), the lumbar artery (3 cases), and the internal iliac artery or the ascending pharyngeal artery (1 case each). For the fistula level, interobserver agreement was excellent for 3T dynamic contrast-enhanced MRA ($\kappa = 0.97$; 95% CI, 0.92–1.00) and very good for 64-row multidetector CTA ($\kappa = 0.84$; 95% CI, 0.72–0.96). Intermodality agreement with DSA was good for 3T dynamic contrast-enhanced MRA ($\kappa = 0.78$; 95% CI, 0.49–1.00) and moderate for 64-row multidetector CTA ($\kappa = 0.41$; 95% CI, 0.020–0.84).

CONCLUSIONS: For the localization of spinal dural arteriovenous fistulas, 3T dynamic contrast-enhanced MRA may be more reliable than 64-row multidetector CTA.

ABBREVIATIONS: DCE = dynamic contrast-enhanced; SDAVF = spinal dural arteriovenous fistulas; VR = volume-rendering; 64-CTA = 64-row multidetector CTA

Spinal dural arteriovenous fistulas (SDAVF) are the most commonly encountered spinal vascular shunt lesions and a treatable cause of myelopathy.¹ The arteriovenous shunt is located inside the dura mater close to the spinal nerve root, where the arterial blood from a radiculomeningeal artery enters a radicular vein. Shunt interruption by either neurosurgery or superselective embolization is the basic treatment strategy,^{1–3} and pretreatment localization of SDAVF is important for their adequate treatment. Catheter spinal DSA is the standard technique that accurately

detects the location of SDAVF and their feeders. However, an exhaustive search for the lesion by selective catheterization is time-consuming and increases the amount of radiation exposure and contrast material and is accompanied by risks for neurologic complications.^{4,5}

Noninvasive imaging modalities such as multidetector CTA and dynamic contrast-enhanced (DCE)-MRA reliably detect SDAVF and may predict the level of their location.^{5–11} However, the noninvasive technique more reliable for the localization of SDAVF remains to be identified, and interobserver and intermodality agreement for the location of SDAVF on CTA and DCE-MRA studies has not been fully investigated.

In multidetector CTA, scanner performance can be improved by adding detector rows,¹² and, in DCE-MRA, higher magnetic fields improve the image quality while reducing the acquisition time.¹³ In the present study, we compared the agreement between DSA, DCE-MRA at 3T, and 64-row multidetector CTA (64-CTA) for the localization of SDAVF.

Received March 20, 2013; accepted April 18.

From the Departments of Diagnostic Radiology (S.O., D.U., T.H., Y.S., Y.I., H.U., M.A., Y.Y.) and Neurosurgery (Y.K., Y.O.), Graduate School of Medical Sciences, Kumamoto University, Kumamoto, Japan.

Please address correspondence to Toshinori Hirai, MD, Department of Diagnostic Radiology, Graduate School of Medical Sciences, Kumamoto University, 1–1–1 Honjo, Kumamoto 860-8556, Japan; e-mail: t-hirai@kumamoto-u.ac.jp

<http://dx.doi.org/10.3174/ajnr.A3660>

Table 1: Summary of patients and SDAVF

Case No.	Age, y	Sex	Clinical Manifestation	Extent of Cord Signal Abnormality	Feeder	Fistula Level
1	46	M	Paraparesis	C2–C7	L, APHA	FM
2	58	M	Paraplegia	T3–CM	L, IA	T5
3	75	M	Paraparesis	T7–CM	R, IA	T6
4	60	M	Paraplegia	T8–CM	R, IA	T7
5	58	M	Paraparesis	T5–CM	R, IA	T7
6	78	M	Paraplegia	T7–T11	L, IA	T7
7	62	M	Paraplegia	T5–CM	R, IA	T8
8	75	F	Quadriparesis	C5–C6	R, IA	T9
9	76	M	Paraplegia	T6–CM	R, LA	L2
10	83	M	Paraplegia	T3–CM	R, LA	L2
11	58	M	Paraplegia	T5–CM	L, LA	L3
12	52	M	Paraplegia	T3–CM	L, IIA	S1

Note:—L indicates left; R, right; T, thoracic spine; L, lumbar spine; S, sacral spine; CM, conus medularis; APHA, ascending pharyngeal artery; IA, intercostal artery; LA, lumbar artery; IIA, internal iliac artery; FM, foramen magnum.

MATERIALS AND METHODS

Study Population

Our study was approved by our institutional review board. Prior informed consent for imaging examinations was obtained from all patients or their relatives. Between October 2008 and December 2012, 23 patients were referred for spinal 64-CTA and DCE-MRA at 3T and for the evaluation of possible SDAVF suspected on the basis of combined spinal MR imaging and clinical findings. Our inclusion criteria were a diagnosis of SDAVF on the basis of spinal DSA scans and verified at surgery after spinal 3T DCE-MRA and 64-CTA examinations. Exclusion criteria were renal dysfunction (estimated glomerular filtration rate <30 mL/min per 1.73 m²) and allergy to iodinated and gadolinium-based contrast materials. On the basis of these criteria, we enrolled 12 consecutive patients (11 men and 1 woman ranging in age from 46–83 years; mean age, 65 years). All patients presented with congestive myelopathy and a diffuse, continuous hyperintense cord lesion in various cord regions (Table 1), and all underwent spinal CTA, MRA, and intra-arterial DSA. The interval between CTA, MRA, and DSA studies ranged from 3–20 days (mean, 10 days).

DSA Technique

Diagnostic intra-arterial DSA through a femoral arterial approach was performed in a biplane angiography suite (Allura Xper FD; Philips Healthcare, Best, the Netherlands) by a trained neuroradiologist and/or a neurosurgeon. The angiographic technique included the selective manual injection of 3–5 mL of a 300-mg/mL iodinated nonionic contrast agent into the intended arteries and anteroposterior imaging at a rate of 3 frames/s. Images were obtained with a 2048 × 2048 matrix; the FOV was 42 cm.

When DCE-MRA and CTA findings suggested the location of the fistula, we first delivered a selective manual injection at the anticipated level. If the fistula was identified, the contralateral segmental artery and the segmental arteries ranging from 2 levels above to 2 levels below the fistula were studied to ensure complete evaluation of the fistula and the adjacent vasculature. If the fistula site was not identified, additional injections were delivered into segmental arteries from the supreme intercostal artery to the median sacral arteries, the bilateral internal iliac arteries, and the bilateral vertebral, subclavian, costocervical, thyrocervical, and external carotid arteries.

To obtain 3D images of the vessels injected from the feeder and of the bony structures, we acquired 3D rotational angiographs by use of the same angiography system. The parameters were 4.1-second rotation; rotation angle, 240° with 2° increments, resulting in 120 projections; rotation speed, 55°/s, acquisition matrix, 1024 × 1024; frame rate, 30 frames/s. The volume and the injection rate of the non-ionic iodinated contrast agent were 15 mL and 1.5 mL/s respectively. We then reconstructed and analyzed the filling run-volume by use of a dedicated commercially available workstation (Philips Healthcare). The 3D images were reconstructed in a 512 × 512 × 512 matrix with an isotropic voxel size.

CT Data Acquisition

All CT studies were performed on a 64-detector CT system (Brilliance-64, Philips Healthcare) with a 0.5-second gantry rotation speed, an x-ray tube voltage of 120 kV, and an x-ray tube current of 412 mA. The collimation was 64 × 0.625 mm, the beam pitch was 0.515, and the table speed was 20.6 mm per rotation. A double-head power injector (Dual Shot-Type GX; Nemoto Kyorindo, Tokyo, Japan) was used to administer a bolus of 350 mgI/mL contrast medium (135 mL of iomeprol, Iomeron; Bracco, Milan, Italy) at 5.0 mL/s through a 20-gauge IV catheter in an antecubital vein; the contrast agent was followed by a 40-mL bolus of saline solution at the same rate.

Synchronization between the flow of contrast material and CT acquisition was achieved by use of a computer-assisted bolus tracking system. The CT attenuation value was monitored by a radiology technologist. The anatomic level for monitoring was set in the descending aorta at the T10 level on the scout CT image. The trigger threshold was set at 250 HU for the aortic ROI. CT data acquisition was started 10 seconds after triggering. Data were acquired during a single breath-hold in the head-to-foot direction. The CT scan was from the level of the foramen magnum to the groin.

The helical data were reconstructed in the axial plane with a 0.5-mm section thickness at 0.3-mm intervals before storage and transfer to a workstation (M900QUADRA; Amin, Tokyo, Japan). The multiplanar reformation images, including oblique coronal images with craniocaudal angulations and curved planar reformation images, were reconstructed at a voxel size of 0.4 × 0.4 × 0.7 mm to confer the greatest possible likelihood that the spinal vessels were included in the scan. Volume-rendering (VR) CTA images were also reconstructed for image interpretation.

MR Data Acquisition

All MR studies were performed on a 3T MR imaging system (Magnetom Trio, Siemens, Erlangen, Germany) equipped with a phased-array spine coil. The patients were imaged in the supine

position with a 20-gauge intravenous catheter inserted into the antecubital vein. Conventional MR imaging was with sagittal and axial T1- and T2-weighted sequences.

A test bolus was delivered to determine the arrival time of the contrast agent in the arteries feeding the spine. The intravenous injection of 0.2 mL gadopentetate dimeglumine (Magnevist; Bayer HealthCare Pharmaceuticals, Wayne, New Jersey) per kilogram of body weight, delivered at a flow rate of 3 mL/s, was followed by a 30-mL saline flush administered with an automated power injector. On the basis of test bolus results, we injected the contrast agent and started dynamic 3-phase DCE-MRA with a 3D FLASH sequence in the coronal plane. To facilitate subtraction DCE-MRA, 1 precontrast phase, composed of the exact same pulse sequence parameters as the DCE-MRA sequence, was acquired. The imaging data were acquired during breath-holding. The FOV of contrast-enhanced MRA was positioned to cover the entire T2 hyperintense cord and dilated vessels. If previous contrast-enhanced MR images were available, they were also used for determining the positioning of the FOV. The acquisition parameters for the contrast-enhanced MRA sequence were TR/TE, 3.1 ms/1.1 ms; flip angle, 15°; image matrix, 280 × 390; FOV, 400 mm; slab thickness, 78 mm; generalized autocalibrating partially parallel acquisition, 2. The reconstructed voxel size and temporal resolution were 1.4 × 1.2 × 1.5 mm and 17 seconds, respectively. Subtracted maximum-intensity projection, partial MIP, and VR DCE-MRA images in arterial and venous phases and their MPR images were reconstructed for image interpretation.

Image Evaluation

Two independent readers (Y.K. and Y.O., with 23 and 14 years of experience in neuroangiography, respectively) qualitatively evaluated the entire series of DSA images on a PACS workstation. Disagreements were resolved by consensus. Two other readers (T.H. and Y.I., with 21 and 8 years of experience in diagnostic neuro-MR imaging, respectively), blinded to the clinical, CTA, and DSA results, independently evaluated the DCE-MRA data on a PACS workstation. In each case, the subtracted source, MPR, MIP, partial MIP, and VR DCE-MRA images and conventional MR imaging data were displayed with all regions visible. Two other readers (D.U. and S.O., with 16 and 8 years of experience in CTA, respectively), blinded to the clinical, DCE-MRA, and DSA results, independently evaluated the CTA data on a PACS workstation. In each case, the source, MPR, and VR CTA images were displayed with all regions visible. Our software allowed the enlargement of regions of special interest in any given spatial orientation.

Each reviewer for DSA, DCE-MRA, and CTA recorded the shunt level of the SDAVF on the basis of continuity between the feeding artery and abnormal spinal vessels. When the 2 reviewers disagreed, final determinations were based on consensus readings.

After the blinded study, the observers consensually reviewed the reasons of incorrect interpretation for the fistula location with the DSA findings. The observers also determined whether CTA provided additional information to DCE-MRA with regard to the fistula location of SDAVF.

Table 2: Summary of localization of SDAVF on DCE-MRA and DSA

Case No.	DCE-MRA		Interobserver Agreement ^a	DCE-MRA ^b	DSA	Intermodality Agreement ^c
	Reader 1	Reader 2				
1	FM	FM		FM	FM	
2	T5	T5		T5	T5	
3	T6	T6		T6	T6	
4	T7	T7		T7	T7	
5	T7	T7		T7	T7	
6	T10	T10	11 (92%)	T10	T7	10 (83%)
7	T8	T8	$\kappa = 0.97$	T8	T8	$\kappa = 0.78$
8	L2	L3	[0.92–1.00]	L2	T9	[0.49–1.00]
9	L2	L2		L2	L2	
10	L2	L2		L2	L2	
11	L3	L3		L3	L3	
12	S1	S1		S1	S1	

Note:—Data are number of cases. Data in parentheses are the percentage of times that results were concordant; data in brackets are 95% CIs.

FM indicates foramen magnum; T, thoracic spine; L, lumbar spine; S, sacral spine.

^a Agreement of DCE-MRA between reader 1 and reader 2.

^b Consensus reading of DCE-MRA of reader 1 and reader 2.

^c Agreement between the consensus reading of DCE-MRA of reader 1 and reader 2 and DSA.

Statistical Analysis

The level of interobserver agreement (between readers 1 and 2 for DSA, DCE-MRA, and CTA) and of intermodality agreement (between consensus readings of DCE-MRA/CTA and DSA images) with respect to the location of the SDAVF was determined by calculating the κ coefficient ($\kappa < 0.20$, poor; $\kappa = 0.21$ –0.40, fair; $\kappa = 0.41$ –0.60, moderate; $\kappa = 0.61$ –0.80, good; $\kappa = 0.81$ –0.90, very good; and $\kappa > 0.90$, excellent agreement) with a 95% CI. The laterality of the fistula site was not put into the statistical analyses. We also recorded the exact number and percentage of times when the results from both readers and both modalities were in exact agreement. MedCalc for Windows (MedCalc Software, Mariakerke, Belgium) was used for all analyses.

RESULTS

DCE-MRA, 64-CTA, and intra-arterial DSA were performed successfully in all 12 patients. At qualitative evaluation of DSA, interobserver agreement for the fistula location was excellent ($\kappa = 1.0$; 95% CI, 1.0–1.0). In 7 cases, the location of the SDAVF was the thoracic spine (T5, T6, T8, T9, $n = 1$ each; T7, $n = 3$); in 3 it was the lumbar spine (L2, $n = 2$; L3, $n = 1$). In the other 2 cases, the SDAVF was located at the sacral (S1) or the cervical spine (foramen magnum). The locations of the feeders and fistulas identified on DSA images are shown in Table 1.

Table 2 is a summary of DCE-MRA and DSA findings. In 11 of 12 cases (92%), both readers agreed on the fistula location on DCE-MRA images, and interobserver agreement was excellent ($\kappa = 0.97$; 95% CI, 0.92–1.00; Figs 1, 2, and 3). In 10 of 12 studies (83%), the DCE-MRA (consensus reading) and DSA findings of both readers coincided with respect to the fistula location. Intermodality agreement (DCE-MRA versus DSA findings) was good ($\kappa = 0.78$; 95% CI, 0.49–1.00).

As shown in Table 3, both readers reviewing CTA images agreed on the fistula location in 7 of 12 studies (58%); interobserver agreement was very good ($\kappa = 0.84$; 95% CI, 0.72–0.96; Figs 1–3). In 7 of 12 studies (58%), the CTA (consensus reading) and DSA findings of both readers coincided with respect to the fistula location. Intermodality agreement (CTA versus DSA findings) was moderate ($\kappa = 0.41$; 95% CI, 0.020–0.84).

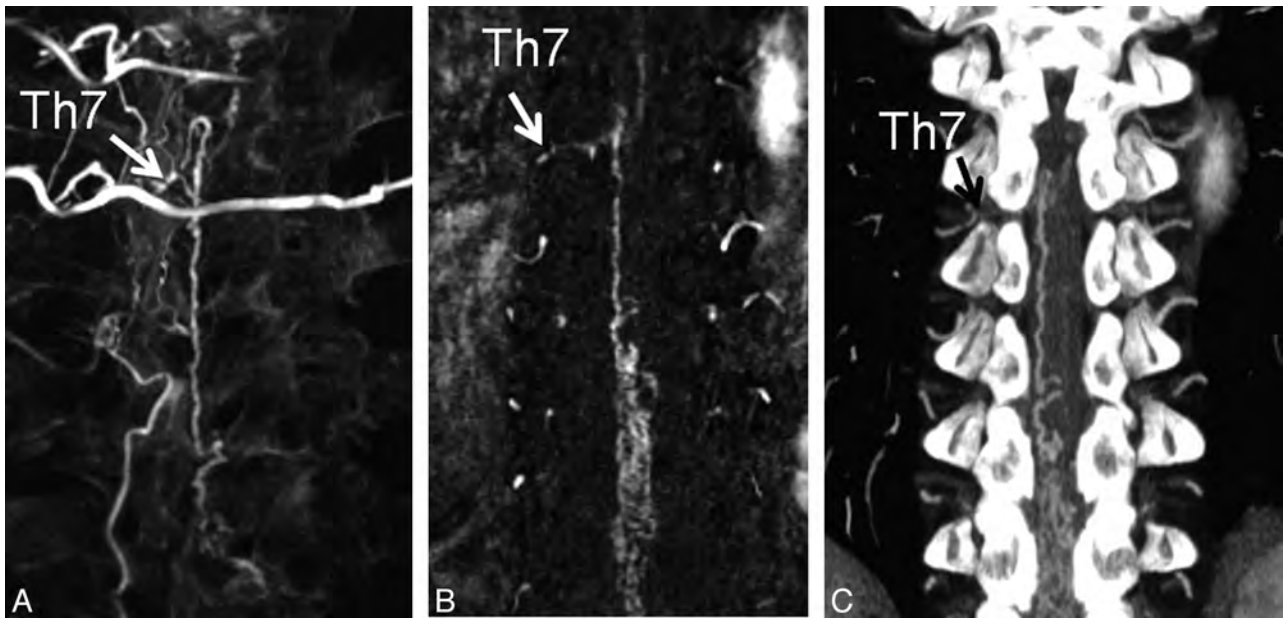


FIG 1. A 58-year-old man (case 5) with SDAVF at the T7 level. *A*, Reconstructed coronal MPR 3D angiogram demonstrates the fistula site at the level of T7 on the right side (*arrow*) and the surrounding vertebrae. *B*, Subtracted coronal partial-MIP DCE-MRA image shows the fistula site at the level of T7 on the right side (*arrow*). Two readers judged the fistula location as T7. *C*, On the coronal partial-MIP CTA image, the feeding artery of the SDAVF is depicted to derive from the 7th thoracic level (T7) on the right side (*arrow*). Two readers judged the fistula location as T7.

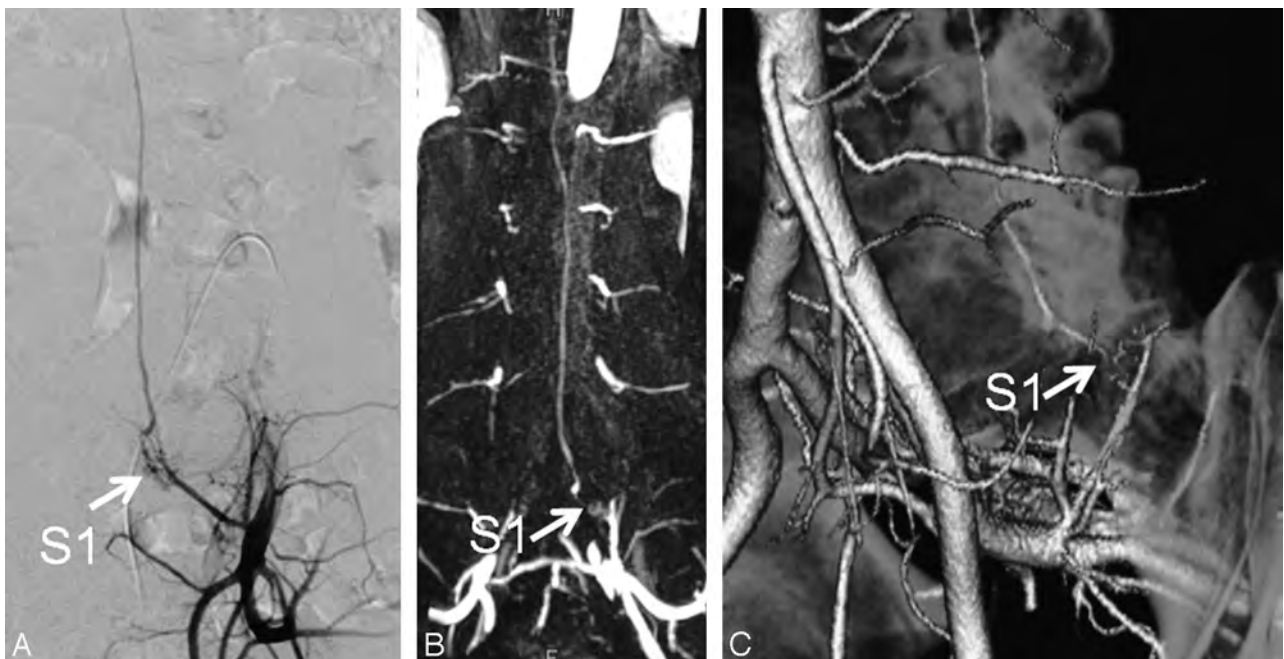


FIG 2. A 52-year-old man (case 12) with SDAVF at the S1 level. *A*, Catheter angiogram from the left internal iliac artery depicts the fistula site at the level of S1 (*arrow*). *B*, Subtracted coronal partial-MIP DCE-MRA image shows the fistula site at the S1 level (*arrow*). Two readers judged the fistula location as S1. *C*, On the oblique VR CTA image, 2 readers judged the fistula level to be at S1 (*arrows*). In the retrospective consensus review, additional use of CTA images increased the observers' confidence level of the diagnosis.

In the retrospective consensus reviews, the incorrect interpretation on DCE-MRA and CTA was found in 2 of 12 (17%) and 5 of 12 (42%), respectively. The reasons for the incorrect interpretation on DCE-MRA in the 2 cases were considered to be small caliber of the feeder and the radicular vein at the spinal nerve root. In the 5 cases on CTA, the incorrect interpretation was caused by the overlap of bony structures and the vessels at the spinal nerve

root in 3 cases, the scanning of inappropriate arterial phase in 1 case (Fig 3), and the presence of slight venous contamination in 1 case. Although there were no cases in which the observer's judgment for diagnosing the fistula location of SDAVF was changed by CTA information, their confidence level in the diagnosis was further increased by use of combined DCE-MRA and CTA images in 3 cases.

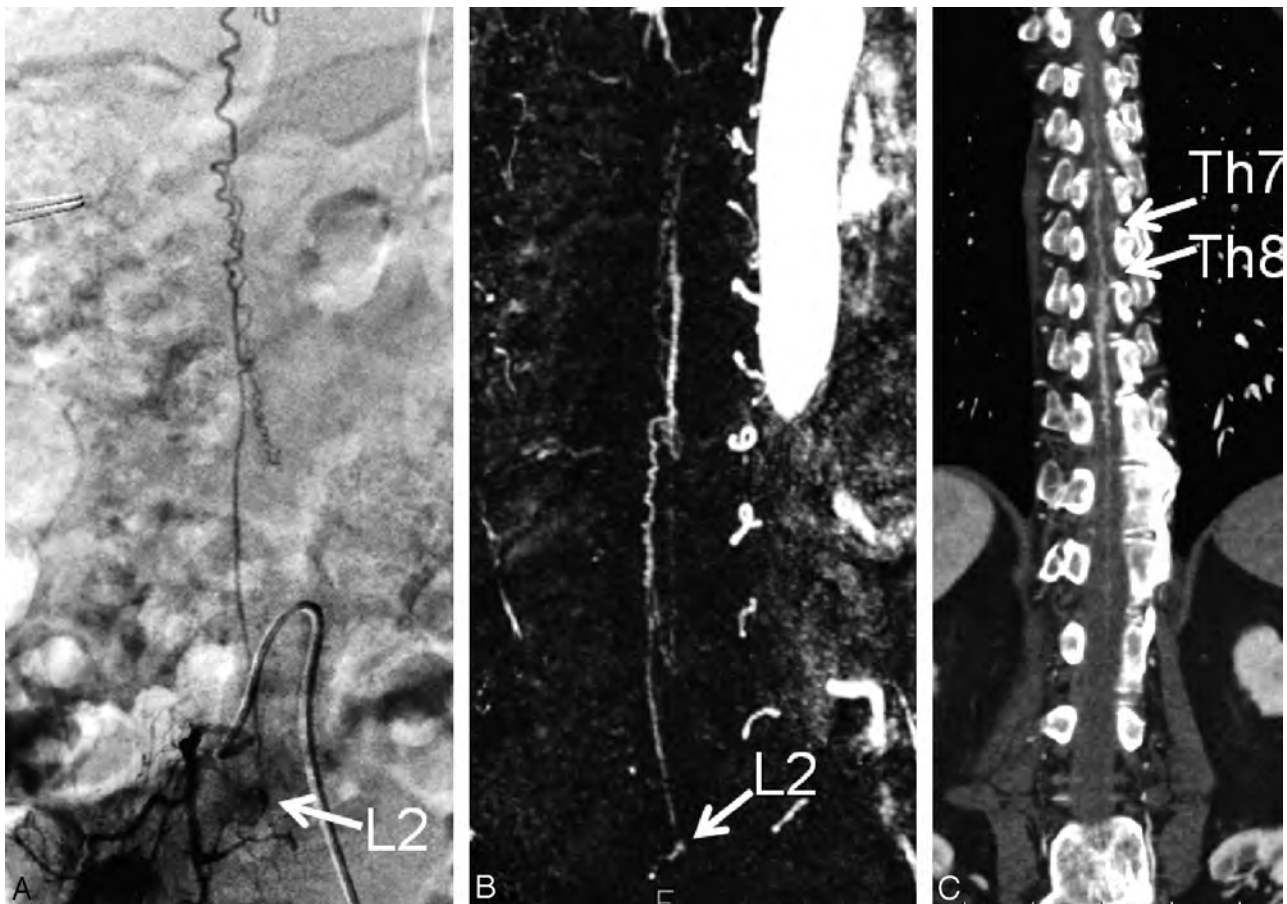


FIG 3. A 76-year-old man (case 9) with SDAVF at the L2 level. *A*, Catheter angiogram from the right lumbar artery demonstrates the fistula site at the level of L2 on the right side (arrow). *B*, Subtracted coronal partial-MIP DCE-MRA image shows the fistula site at the L2 level (arrow). Two readers judged the fistula location as L2. *C*, On the coronal partial-MIP CTA image, 2 readers judged the fistula level to be at T7 and T8, respectively (arrows). In the retrospective consensus review, the reason for their incorrect interpretation was considered to be scanning of inappropriate arterial phase of CTA.

Table 3: Summary of localization of SDAVF at CTA and DSA

Case No.	CTA		Interobserver Agreement ^a	CTA ^b	DSA	Intermodality Agreement ^c
	Reader 1	Reader 2				
1	FM	FM		FM	FM	
2	T5	T5		T5	T5	
3	T6	T6		T6	T6	
4	T8	T9		T9	T7	
5	T7	T7		T7	T7	
6	T10	T12	7 (58%)	T12	T7	7 (58%)
7	T8	T8	$\kappa = 0.84$	T8	T8	$\kappa = 0.41$
8	L2	L3	[0.72–0.96]	L2	T9	[0.02–0.84]
9	T8	T7		T8	L2	
10	T9	T8		T9	L2	
11	L3	L3		L3	L3	
12	S1	S1		S1	S1	

Note:—Data are number of cases. Data in parentheses are the percentage of times that results were concordant; data in brackets are 95% CIs.

FM indicates foramen magnum; T, thoracic spine; L, lumbar spine; S, sacral spine.

^a Agreement of CTA between reader 1 and reader 2.

^b Consensus reading at CTA of reader 1 and reader 2.

^c Agreement between the consensus reading at CTA of reader 1 and reader 2 and DSA.

DISCUSSION

Our study showed that for the characterization of SDAVF, DCE-MRA at 3T was more reliable than 64-CTA. We attribute the good interobserver and intermodality agreement for DCE-MRA to 3 factors. First, we performed dynamic 3-phase contrast-enhanced MRA with a parallel imaging technique. The DCE-MRA images

were acquired with the patients holding their breath, and this allowed data acquisition with a temporal resolution of 17 s/volume, at which it was possible to differentiate the arterial and venous phases. Second, because we used a high-field 3T MR imaging unit, our DCE-MRA studies benefited from 2 key conditions. Namely, the theoretic signal-to-noise ratio at 3T is twice that at 1.5T, thus allowing for increased spatial resolution. The longer T1 values of tissues at 3T yield better background suppression and contrast-to-noise ratios.^{13–15} Third, the DCE-MRA images that we used provided a uniform background from the subtraction technique, and this rendered the detection of subtle vascular lesions easier.

The spatial resolution was higher on 64-CTA than on 3T DCE-MRA studies; however, intermodality agreement for the identification of the location of the SDAVF was insufficient. In our study, adequate arterial phase on CTA was not obtained in 2 (17%) of 12 cases. In our protocol, CT acquisition was performed by use of a computer-assisted bolus tracking system, and its monitoring was set in the descending aorta at the T10 level. However, the level of feeders of SDAVF was variable: cervical to sacral vertebrae. Therefore, adequate arterial phase on CTA may not always have been obtained. The identification of feeding arteries and radicular veins adjacent to the bones may have been hampered because of the

similar attenuation of these structures. In our retrospective reviews, the incorrect interpretation from this effect was found in 3 (25%) of 12 cases. Background suppression of bones can be achieved on CTA scans by first acquiring a precontrast scan followed by subtraction from the contrast-enhanced scan. However, this would further increase radiation exposure and the noise level.

Zampakis et al⁷ reported that the sensitivity of MRA and CTA for determining the level of SDAVF was 40% and 90%, respectively. Their results differ from ours. They used 2 different contrast-enhanced MRA techniques at 1.5T, that is, a first-pass elliptical centric contrast-enhanced MRA technique in 7 patients and an elliptical centric time-resolved imaging in constant kinetics technique in 2 patients. They obtained single 3D volume data at an acquisition time of 52 seconds with the former and 20 3D volume datasets at 1.7 seconds of temporal resolution with the latter technique, and they did not use subtraction. Under these imaging conditions for contrast-enhanced MRA, they may not have used the appropriate arterial phase for spinal MRA scans, and this may have rendered difficult the interpretation of their unsubtracted MRA images.

Compared with DCE-MRA, multidetector CTA generally provides for a shorter scan time, larger scan coverage, and higher spatial resolution and facilitates the observation of enhanced vessels with the surrounding bony structures. In our study, the observer's confidence level of the diagnosis was furthermore increased by additional use of CTA in 3 (25%) of 12 cases. This is thought to be a benefit for planning of diagnostic and interventional spinal angiography. For surgical planning, the visualization on CTA images of both vessels and bones may be advantageous. On the other hand, a distinct disadvantage of CTA is the patient exposure to ionizing radiation. A CT scan of the entire spinal cord delivers an effective dose of approximately 20 mSv.¹⁶ To achieve a radiation dose reduction, CT scanners with more detectors (eg, 256- or 320-detector CT scanners) and iterative reconstruction algorithms might be useful.¹⁷ Further experimental and clinical studies are required to clarify this issue.

Our study has some limitations. First, we did not compare different 3D reconstructing techniques (eg, VR, MIP) for the display of SDAVF on DCE-MRA and CTA images. Although the most suitable display method for evaluating SDAVF on DCE-MRA and CTA scans remains to be identified, we used source, MPR, MIP, and partial MIP images with or without VR images. These are widely used in the clinical setting to evaluate MRA and CTA studies. Second, our study population was relatively small. Further studies with a larger number of patients with SDAVF are needed to clarify the role of these techniques in the clinical setting.

CONCLUSIONS

In the localization of SDAVF, 3T DCE-MRA was more reliable than 64-CTA. Thus, 3T DCE-MRA may be the first technique for

evaluating localization of SDAVF. Additional use of 64-CTA might increase the observer confidence level of the diagnosis.

REFERENCES

1. Krings T, Geibprasert S. **Spinal dural arteriovenous fistulas.** *AJNR Am J Neuroradiol* 2009;30:639–48
2. Van Dijk JM, TerBrugge KG, Willinsky RA, et al. **Multidisciplinary management of spinal dural arteriovenous fistulas: clinical presentation and long-term follow-up in 49 patients.** *Stroke* 2002; 33:1578–83
3. Narvid J, Hetts SW, Larsen D, et al. **Spinal dural arteriovenous fistulae: clinical features and long-term results.** *Neurosurgery* 2008;62:159–66
4. Rodesch G, Lasjaunias P. **Spinal cord arteriovenous shunts: from imaging to management.** *Eur J Radiol* 2003;46:221–32
5. Luetmer PH, Lane JJ, Gilbertson JR, et al. **Preangiographic evaluation of spinal dural arteriovenous fistulas with elliptical centric contrast-enhanced MR angiography and effect on radiation dose and volume of iodinated contrast material.** *AJNR Am J Neuroradiol* 2005;26:711–18
6. Lai PH, Pan HB, Yang CF, et al. **Multi-detector row computed tomography angiography in diagnosing spinal dural arteriovenous fistulae: initial experience.** *Stroke* 2005;36:1562–64
7. Zampakis P, Santosh C, Taylor W, et al. **The role of non-invasive computed tomography in patients with suspected dural fistulas with spinal drainage.** *Neurosurgery* 2006;58:686–94
8. Yamaguchi S, Nagayama T, Eguchi K, et al. **Accuracy and pitfalls of multidetector-row computed tomography in detecting spinal dural arteriovenous fistulas.** *J Neurosurg Spine* 2010;12:243–48
9. Farb RI, Kim JK, Willinsky RA, et al. **Spinal dural arteriovenous fistula localization with a technique of first-pass gadolinium-enhanced MR angiography: initial experience.** *Radiology* 2002; 222:843–50
10. Saraf-Lavi E, Bowen BC, Quencer RM, et al. **Detection of spinal dural arteriovenous fistulae with MR imaging and contrast-enhanced MR angiography: sensitivity, specificity, and prediction of vertebral level.** *AJNR Am J Neuroradiol* 2002;23:858–67
11. Mull M, Nijenhuis RJ, Backes WH, et al. **Value and limitations of contrast-enhanced MR angiography in spinal arteriovenous malformations and dural arteriovenous fistulas.** *AJNR Am J Neuroradiol* 2007;28:1249–58
12. Flohr TG, Schaller S, Stierstorfer K, et al. **Multi-detector row CT systems and image-reconstruction techniques.** *Radiology* 2005; 235:756–73
13. Vargas MI, Nguyen D, Viallon M, et al. **Dynamic MR angiography (MRA) of spinal vascular diseases at 3T.** *Eur Radiol* 2010;20:2491–95
14. Schmitz BL, Aschoff AJ, Hoffmann MH, et al. **Advantages and pitfalls in 3T MR brain imaging: a pictorial review.** *AJNR Am J Neuroradiol* 2005;26:2229–37
15. DeLano MC, DeMarco JK. **3.0 T versus 1.5 TMR angiography of the head and neck.** *Neuroimaging Clin North Am* 2006;16:321–41
16. Jones DG, Shrimpton PC. *Survey of CT Practice in the UK: Normalised Organ Doses for X-Ray Computed Tomography Calculated Using Monte Carlo Techniques.* Harwell, United Kingdom: National Radiological Protection Board; 1991
17. Nakaura T, Nakamura S, Maruyama N, et al. **Low contrast agent and radiation dose protocol for hepatic dynamic CT of thin adults at 256-detector row CT: effect of low tube voltage and hybrid iterative reconstruction algorithm on image quality.** *Radiology* 2012;264: 445–54

DOTAREM® (gadoterate meglumine) injection, for intravenous use
Initial U.S. Approval: 2013

BRIEF SUMMARY OF PRESCRIBING INFORMATION
CONSULT PACKAGE INSERT FOR FULL PRESCRIBING INFORMATION

WARNING: NEPHROGENIC SYSTEMIC FIBROSIS (NSF)

Gadolinium-based contrast agents (GBCAs) increase the risk for NSF among patients with impaired elimination of the drugs. Avoid use of GBCAs in these patients unless the diagnostic information is essential and not available with non-contrast MRI or other modalities. NSF may result in fatal or debilitating fibrosis affecting the skin, muscle and internal organs.

- The risk for NSF appears highest among patients with:
 - Chronic, severe kidney disease (GFR < 30 mL/min/1.73m²), or
 - Acute kidney injury.
- Screen patients for acute kidney injury and other conditions that may reduce renal function. For patients at risk for chronically reduced renal function (e.g. age > 60 years, hypertension, diabetes), estimate the glomerular filtration rate (GFR) through laboratory testing (5.1).
- For patients at highest risk for NSF, do not exceed the recommended DOTAREM dose and allow a sufficient period of time for elimination of the drug from the body prior to any re-administration [see *Warnings and Precautions (5.1)*].

1 INDICATIONS AND USAGE

DOTAREM is a gadolinium-based contrast agent indicated for intravenous use with magnetic resonance imaging (MRI) in brain (intracranial), spine and associated tissues in adult and pediatric patients (2 years of age and older) to detect and visualize areas with disruption of the blood brain barrier (BBB) and/or abnormal vascularity. (1)

4 CONTRAINDICATIONS

History of clinically important hypersensitivity reactions to DOTAREM. (4)

5 WARNINGS AND PRECAUTIONS

5.1 Nephrogenic Systemic Fibrosis

Gadolinium-based contrast agents (GBCAs) increase the risk for nephrogenic systemic fibrosis (NSF) among patients with impaired elimination of the drugs. Avoid use of GBCAs among these patients unless the diagnostic information is essential and not available with non-contrast MRI or other modalities. The GBCA-associated NSF risk appears highest for patients with chronic, severe kidney disease (GFR < 30 mL/min/1.73m²) as well as patients with acute kidney injury. The risk appears lower for patients with chronic, moderate kidney disease (GFR 30 - 59 mL/min/1.73m²) and little, if any, for patients with chronic, mild kidney disease (GFR 60 - 89 mL/min/1.73m²). NSF may result in fatal or debilitating fibrosis affecting the skin, muscle and internal organs. Report any diagnosis of NSF following DOTAREM administration to Guerbet LLC (1-877-729-6679) or FDA (1-800-FDA-1088 or www.fda.gov/medwatch).

Screen patients for acute kidney injury and other conditions that may reduce renal function. Features of acute kidney injury consist of rapid (over hours to days) and usually reversible decrease in kidney function, commonly in the setting of surgery, severe infection, injury or drug-induced kidney toxicity. Serum creatinine levels and estimated GFR may not reliably assess renal function in the setting of acute kidney injury. For patients at risk for chronically reduced renal function (e.g., age > 60 years, diabetes mellitus or chronic hypertension), estimate the GFR through laboratory testing.

Among the factors that may increase the risk for NSF are repeated or higher than recommended doses of a GBCA and the degree of renal impairment at the time of exposure. Record the specific GBCA and the dose administered to a patient. For patients at highest risk for NSF, do not exceed the recommended DOTAREM dose and allow a sufficient period of time for elimination of the drug prior to re-administration. For patients receiving hemodialysis, physicians may consider the prompt initiation of hemodialysis following the administration of a GBCA in order to enhance the contrast agent's elimination. The usefulness of hemodialysis in the prevention of NSF is unknown [see *Dosage and Administration (2)* and *Clinical Pharmacology (12)*].

5.2 Hypersensitivity Reactions

Anaphylactic and anaphylactoid reactions have been reported with DOTAREM, involving cardiovascular, respiratory, and/or cutaneous manifestations. Some patients experienced circulatory collapse and died. In most cases, initial symptoms occurred within minutes of DOTAREM administration and resolved with prompt emergency treatment [see *Adverse Reactions (6)*].

- Before DOTAREM administration, assess all patients for any history of a reaction to contrast media, bronchial asthma and/or allergic disorders. These patients may have an increased risk for a hypersensitivity reaction to DOTAREM.
- Administer DOTAREM only in situations where trained personnel and therapies are promptly available for the treatment of hypersensitivity reactions, including personnel trained in resuscitation.
- During and following DOTAREM administration, observe patients for signs and symptoms of hypersensitivity reactions.

5.3 Acute Kidney Injury

In patients with chronically reduced renal function, acute kidney injury requiring dialysis has occurred with the use of GBCAs. The risk of acute kidney injury may increase with increasing dose of the contrast agent; administer the lowest dose necessary for adequate imaging. Screen all patients for renal impairment by obtaining a history and/or laboratory tests. Consider follow-up renal function assessments for patients with a history of renal dysfunction.

5.4 Extravasation and Injection Site Reactions

Ensure catheter and venous patency before the injection of DOTAREM. Extravasation into tissues during DOTAREM administration may result in tissue irritation [see *Nonclinical Toxicology (13.2)*].

6 ADVERSE REACTIONS

GBCAs have been associated with a risk for NSF [see *Warnings and Precautions (5.1)*]. NSF has not been reported in patients with a clear history of exposure to DOTAREM alone. For hypersensitivity reactions and acute kidney injury see *Warnings and Precautions (5.2)* and (5.3).

6.1 Clinical Studies Experience

Because clinical trials are conducted under widely varying conditions, adverse reaction rates observed in the clinical trials of a drug cannot be directly compared to rates in the clinical trials of another drug and may not reflect the rates observed in clinical practice.

The data described below reflect DOTAREM exposure in 2813 patients, representing 2672 adults and 141 pediatric patients. Overall, 55% of the patients were men. In clinical trials where ethnicity was recorded the ethnic distribution was 74% Caucasian, 12% Asian, 4% Black, and 10% others. The average age was 53 years (range from 0.1 to 97 years).

Overall, 3.9% of patients reported at least one adverse reaction, primarily occurring immediately or several days following DOTAREM administration. Most adverse reactions were mild or moderate in severity and transient in nature.

Table 1 lists adverse reactions that occurred in ≥ 0.2% patients who received DOTAREM.

Table 1: Adverse Reactions in Clinical Trials

Reaction	Rate (%) n = 2813
Nausea	0.6%
Headache	0.5%
Injection Site Pain	0.4%
Injection Site Coldness	0.2%
Burning Sensation	0.2%

Adverse reactions that occurred with a frequency < 0.2% in patients who received DOTAREM include: feeling cold, rash, somnolence, fatigue, dizziness, vomiting, pruritus, paresthesia, dysgeusia, pain in extremity, anxiety, hypertension, palpitations, oropharyngeal discomfort, serum creatinine increased and injection site reactions, including site inflammation, extravasation, pruritus, and warmth.

Adverse Reactions in Pediatric Patients

During clinical trials, 141 pediatric patients (7 aged < 24 months, 33 aged 2 - 5 years, 58 aged 6 - 11 years and 43 aged 12 - 17) received DOTAREM. Overall, 6 pediatric patients (4.3%) reported at least one adverse reaction following DOTAREM administration. The most frequently reported adverse reaction was headache (1.5%). Most adverse events were mild in severity and transient in nature, and all patients recovered without treatment.

6.2 Postmarketing Experience

The following additional adverse reactions have been identified during postmarketing use of DOTAREM. Because these reactions are reported voluntarily from a population of uncertain size, it is not always possible to reliably estimate their frequency or establish a causal relationship to drug exposure.

- bradycardia, tachycardia, arrhythmia
- hypersensitivity / anaphylactoid reactions including cardiac arrest, respiratory arrest, cyanosis, pharyngeal edema, laryngospasm, bronchospasm, angioedema, conjunctivitis, ocular hyperemia, eyelid edema, lacrimation increased, hyperhidrosis, urticaria

- coma, convulsion, syncope, presyncope, parosmia, tremor
- muscle contracture, muscle weakness
- diarrhea, salivary hypersecretion
- malaise, fever
- NSF, in patients whose reports were confounded by the receipt of other GBCAs or in situations where receipt of other GBCAs could not be ruled out. No unconfounded cases of NSF have been reported with DOTAREM.
- superficial phlebitis

7 DRUG INTERACTIONS

DOTAREM does not interfere with serum and plasma calcium measurements determined by colorimetric assays. Specific drug interaction studies with DOTAREM have not been conducted.

8 USE IN SPECIFIC POPULATIONS

8.1 Pregnancy

Pregnancy Category C

There are no adequate and well-controlled studies with DOTAREM conducted in pregnant women. Limited published human data on exposure to other GBCAs during pregnancy did not show adverse effects in exposed neonates. No effects on embryo fetal development were observed in rats or rabbits at doses up to 10 mmol/kg/day in rats or 3 mmol/kg/day in rabbits. The doses in rats and rabbits were respectively 16 and 10 times the recommended human dose based on body surface area. DOTAREM should be used during pregnancy only if the potential benefit justifies the potential risk to the fetus. While it is unknown if DOTAREM crosses the human placenta, other GBCAs do cross the placenta in humans and result in fetal exposure.

Reproductive and developmental toxicity studies were conducted with gadoterate meglumine in rats and rabbits. Gadoterate meglumine was administered intravenously in doses of 0, 2, 4 and 10 mmol/kg/day (or 3.2, 6.5 and 16.2 times the recommended human dose based on body surface area) to female rats for 14 days before mating throughout the mating period and until gestation day (GD) 17. Pregnant rabbits were intravenously administered gadoterate meglumine at the dose levels of 0, 1, 3 and 7 mmol/kg/day (or 3.3, 10 and 23 times the human doses based on body surface area) from GD6 to GD19. No effects on embryo fetal development were observed in rats or rabbits at doses up to 10 mmol/kg/day in rats or 3 mmol/kg/day in rabbits. Maternal toxicity was observed in rats at 10 mmol/kg/day (or 16 times the human dose based on body surface area) and in rabbits at 7 mmol/kg/day (23 times the human dose based on body surface area).

8.3 Nursing Mothers

It is not known whether DOTAREM is excreted in human milk. Limited case reports on use of GBCAs in nursing mothers indicate that 0.01 to 0.04% of the maternal gadolinium dose is excreted in human breast milk. Because many drugs are excreted in human milk, exercise caution when DOTAREM is administered to a nursing woman. Nonclinical data show that gadoterate meglumine is excreted into breast milk in very small amounts (< 0.1% of the dose intravenously administered) and absorption via the gastrointestinal tract is poor.

8.4 Pediatric Use

The safety and efficacy of DOTAREM at a single dose of 0.1 mmol/kg have been established in pediatric patients from 2 to 17 years of age. No dosage adjustment according to age is necessary in this population [See *Dosage and Administration (2)* and *Clinical Studies (14)*]. The safety and efficacy of DOTAREM have not been established in pediatric patients below 2 years of age. GFR does not reach adult levels until 1 year of age [see *Warnings and Precautions (5.1)*].

8.5 Geriatric Use

In clinical studies of DOTAREM, 900 patients were 65 years of age and over, and 312 patients were 75 years of age and over. No overall differences in safety or efficacy were observed between these subjects and younger subjects. In general, use of DOTAREM in elderly patients should be cautious, reflecting the greater frequency of impaired renal function and concomitant disease or other drug therapy. No age-related dosage adjustment is necessary.

8.6 Renal Impairment

No DOTAREM dosage adjustment is recommended for patients with renal impairment. Gadoterate meglumine can be removed from the body by hemodialysis [see *Warnings and Precautions (5.1)* and *Clinical Pharmacology (12.3)*].

10 OVERDOSAGE

DOTAREM administered to healthy volunteers and to patients at cumulative doses up to 0.3 mmol/kg was tolerated in a manner similar to lower doses. Adverse reactions to overdosage with DOTAREM have not been reported. Gadoterate meglumine can be removed from the body by hemodialysis [see *Clinical Pharmacology (12.3)*].

13 NONCLINICAL TOXICOLOGY

13.1 Carcinogenesis, Mutagenesis, Impairment of Fertility

Long-term animal studies have not been performed to evaluate the carcinogenic potential of gadoterate meglumine. Gadoterate meglumine did not demonstrate mutagenic potential in *in vitro* bacterial reverse mutation assays (Ames test) using *Salmonella typhimurium*, in an *in vitro* chromosome aberration assay in Chinese hamster ovary cells, in an *in vitro* gene mutation assay in Chinese hamster lung cells, nor in an *in vivo* mouse micronucleus assay.

No impairment of male or female fertility and reproductive performance was observed in rats after intravenous administration of gadoterate meglumine at the maximum tested dose of 10 mmol/kg/day (16 times the maximum human dose based on surface area), given during more than 9 weeks in males and more than 4 weeks in females. Sperm counts and sperm motility were not adversely affected by treatment with the drug.

13.2 Animal Toxicology and/or Pharmacology

Local intolerance reactions, including moderate irritation associated with infiltration of inflammatory cells were observed after perivenous injection in rabbits suggesting the possibility of local irritation if the contrast medium leaks around the veins in a clinical setting [see *Warnings and Precautions (5.4)*].

17 PATIENT COUNSELING INFORMATION

17.1 Nephrogenic Systemic Fibrosis

Instruct patients to inform their healthcare provider if they:

- have a history of kidney disease, or
 - have recently received a GBCA.
- GBCAs increase the risk for NSF among patients with impaired elimination of the drugs. To counsel patients at risk for NSF:
- Describe the clinical manifestations of NSF.
 - Describe procedures to screen for the detection of renal impairment.
- Instruct the patients to contact their physician if they develop signs or symptoms of NSF following DOTAREM administration, such as burning, itching, swelling, scaling, hardening and tightening of the skin; red or dark patches on the skin; stiffness in joints with trouble moving, bending or straightening the arms, hands, legs or feet; pain in the hip bones or ribs; or muscle weakness.

17.2 Common Adverse Reactions

Inform patients that they may experience:

- Reactions along the venous injection site, such as mild and transient burning or pain or feeling of warmth or coldness at the injection site.
- Side effects of headache, nausea, abnormal taste and feeling hot.

17.3 General Precautions

Instruct patients receiving DOTAREM to inform their physician if they:

- Are pregnant or breastfeeding.
- Have a history of allergic reaction to contrast media, bronchial asthma or allergy.
- Are taking any medications.

Rx Only



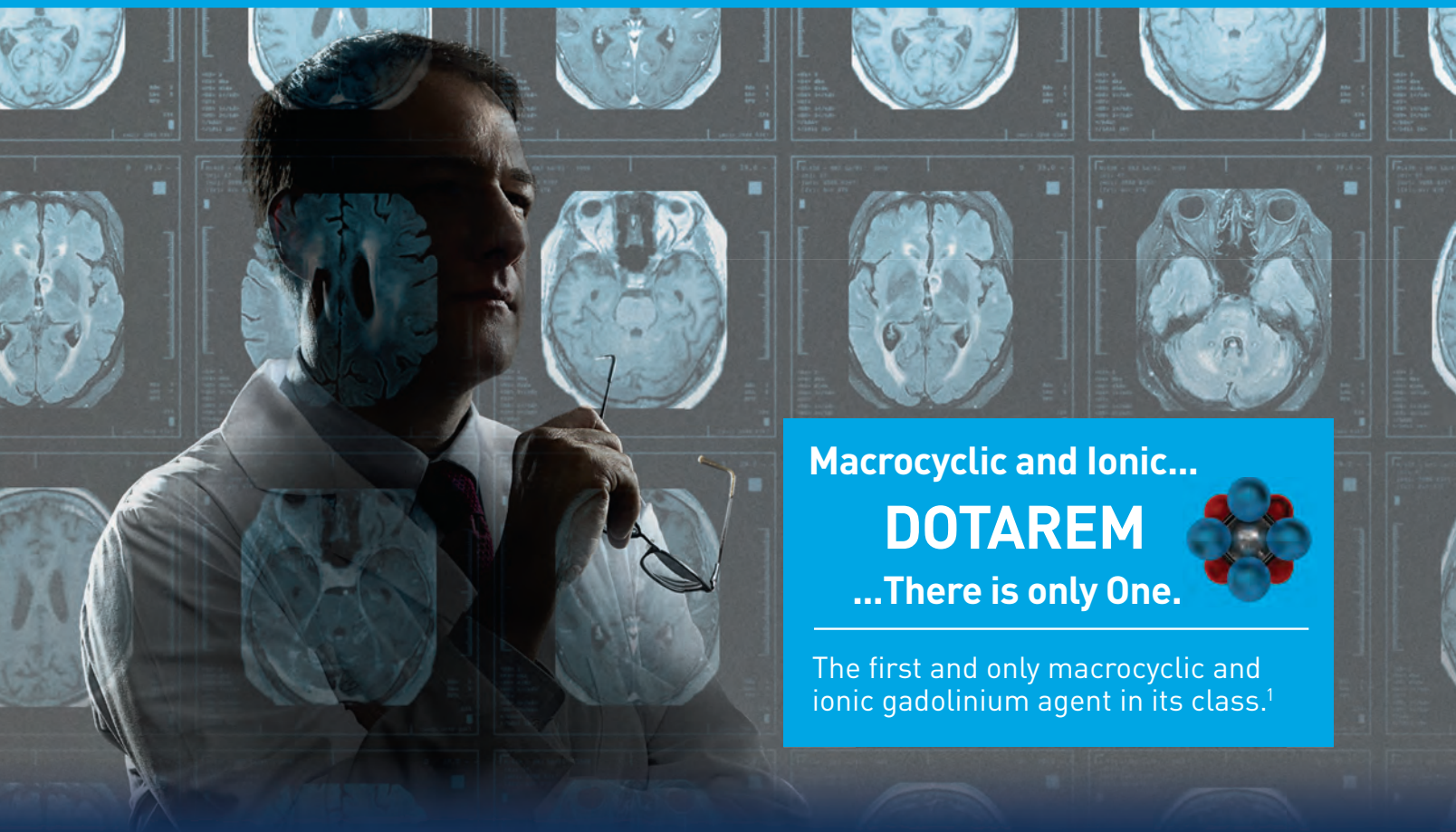
Pre-filled syringes manufactured by Catalent, Belgium for Guerbet
Vials manufactured by Recipharm, France for Guerbet

GU06131043
Revised 06/2013



DOTAREM[®]

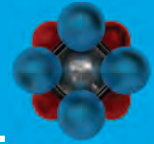
(gadoterate meglumine) Injection



Macrocyclic and Ionic...

DOTAREM

...There is only One.



The first and only macrocyclic and ionic gadolinium agent in its class.¹

Global clinical experience with over **37 million doses** administered outside the US.²

INDICATION¹

DOTAREM is a gadolinium-based contrast agent indicated for intravenous use with magnetic resonance imaging (MRI) in brain (intracranial), spine and associated tissues in adult and pediatric patients (2 years of age and older) to detect and visualize areas with disruption of the blood brain barrier (BBB) and/or abnormal vascularity.

IMPORTANT SAFETY INFORMATION¹

WARNING: NEPHROGENIC SYSTEMIC FIBROSIS (NSF)

Gadolinium-based contrast agents (GBCAs) increase the risk for NSF among patients with impaired elimination of the drugs. Avoid use of GBCAs in these patients unless the diagnostic information is essential and not available with non-contrast MRI or other modalities. NSF may result in fatal or debilitating fibrosis affecting the skin, muscle and internal organs.

- The risk for NSF appears highest among patients with:
 - Chronic, severe kidney disease (GFR < 30 mL/min/1.73m²), or
 - Acute kidney injury.
- Screen patients for acute kidney injury and other conditions that may reduce renal function. For patients at risk for chronically reduced renal function (e.g. age > 60 years, hypertension, diabetes), estimate the glomerular filtration rate (GFR) through laboratory testing (5.1).
- For patients at highest risk for NSF, do not exceed the recommended DOTAREM dose and allow a sufficient period of time for elimination of the drug from the body prior to any re-administration (5.1).

Contraindicated in patients with a history of clinically important hypersensitivity reactions to DOTAREM.

The possibility of serious or life-threatening anaphylactoid/anaphylactic reactions with cardiovascular, respiratory or cutaneous manifestations, ranging from mild to severe, including death, should be considered. Monitor patients closely for need of emergency cardiorespiratory support.

In patients with chronically reduced renal function, acute kidney injury requiring dialysis has occurred with the use of GBCAs. The risk of acute kidney injury may increase with increasing dose of the contrast agent; administer the lowest dose necessary for adequate imaging. Screen all patients for renal impairment by obtaining a history and/or laboratory tests. Consider follow-up renal function assessments for patients with a history of renal dysfunction.

The most common adverse reactions associated with DOTAREM in clinical studies were nausea, headache, injection site pain, injection site coldness, and burning sensation.

For more information about DOTAREM, including full Boxed WARNING, please see the Full Prescribing Information.

Please see adjacent Brief Summary of Prescribing Information.

DOTAREM is a registered trademark of Guerbet and is available by prescription only.

GU07131063

References: 1. Dotarem [package insert]. Bloomington, IN: Guerbet LLC; 2013. 2. Data on file, Guerbet LLC.